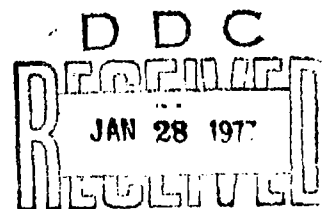


Mechanics and Materials Research Center  
TEXAS A&M UNIVERSITY  
College Station, Texas

ADA 034978

**VISCOELASTIC CHARACTERIZATION OF  
A NONLINEAR, GLASS/EPOXY  
COMPOSITE INCLUDING THE EFFECTS  
OF DAMAGE**

**S. W. BECKWITH**



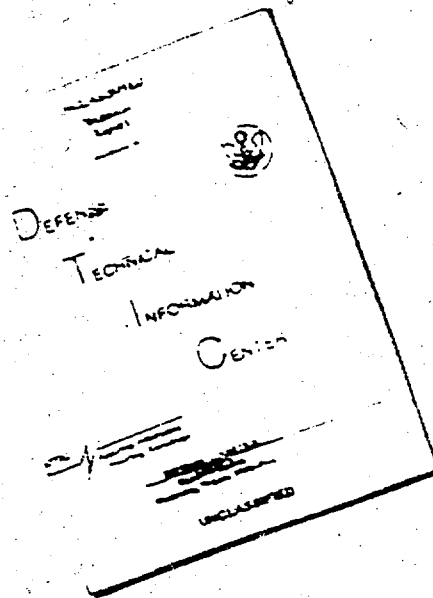
✓ Aerojet Solid Propulsion Company  
Sacramento, California  
Under Contract No. F04-611-72-C-0055 ✓  
Air Force Rocket Propulsion Laboratory  
Edwards Air Force Base, California

**MM 2895-74-8**

**October 1974**

Approved for public release; Distribution unlimited

# DISCLAIMER NOTICE



THIS DOCUMENT IS BEST  
QUALITY AVAILABLE. THE COPY  
FURNISHED TO DTIC CONTAINED  
A SIGNIFICANT NUMBER OF  
PAGES WHICH DO NOT  
REPRODUCE LEGIBLY.

REPRODUCED FROM  
BEST AVAILABLE COPY

(6) VISCOELASTIC CHARACTERIZATION OF A NONLINEAR, GLASS/EPOXY  
COMPOSITE INCLUDING THE EFFECTS OF DAMAGE.

A Dissertation

by

(10) SCOTT WILLIAMS/BECKWITH

Submitted to the Graduate College of  
Texas A&M University  
in partial fulfillment of the requirement for the degree of

DOCTOR OF PHILOSOPHY

Major Subject: Interdisciplinary Engineering

(11) F 405 706 - 0055

MM 2895-74-8

(11) October 1974  
(13) 423 p.

405 706  
key

Approved for public release; Distribution unlimited

FEDERAL GOVERNMENT PROPERTY	
Do not mark, destroy, or dispose of without authority	
A	

## ABSTRACT

Viscoelastic Characterization of a Nonlinear,  
Glass/Epoxy Composite Including the  
Effects of Damage. (December 1974)

Scott Williams Beckwith, B.S., Texas A&M University

M.S., California Institute of Technology

Chairman of Advisory Committee: Dr. R. A. Schapery

↓  
Isothermal creep and recovery tests were conducted on an epoxy resin and a glass fiber-reinforced composite made from the same bulk resin. The glass/epoxy which was studied included uni-directional and laminated (angle-ply) composites as well as samples removed from a Minuteman III solid rocket motor case. The creep and recovery tests were carried out at a series of stress levels well into the nonlinear region at temperatures of 20, 75 and 140°F for several fiber angles. Both the epoxy and glass/epoxy were found to be thermorheologically complex materials with a creep compliance which may be represented by a power law in time.

The linear viscoelastic principal creep compliances were determined for the glass/epoxy using fourth-order tensor transformations. Using the Halpin-Tsai relationships and the "rule of mixtures", the principal creep compliances were compared with those predicted by micromechanics. The experimental results were found to agree very well with the Halpin-Tsai model except at the highest temperatures and were within the upper and lower theoretical bounds



on compliance. Even at low stress levels the presence of micro-crack growth was found to produce appreciable softening at the highest temperatures.

The nonlinear properties were found to depend primarily on the stress normal to the fiber, suggesting a crack opening-mode as the essential mechanism of growth. Multiple cycles of creep and recovery showed a disproportionate amount of damage during the first cycle. Crack growth was found to reduce more rapidly and with less softening effect in the laminated (10) composites, probably as a result of the interfacial barrier between the layers. In general, the off-angle composites exhibit considerable softening due to micro-crack growth.

Bending tests conducted on glass/epoxy beam and plate specimens brought out a strong influence of the strain gradient. It was found that linear theory can be used for most of the useful engineering range of application. Nonlinear theory based on tensile tests of unidirection specimens predicts considerably more reduction in bending stiffness than observed experimentally.

Multiple cycling effects on the glass/epoxy composite were found to be more sensitive to the stress normal to the fibers than to the shear stress. The second-order Lebesgue norm ( $L_2$ ) was found to approximately characterize multiple cycling effects such as seen in a solid rocket motor case. The  $L_2$  norm which, at a given time, is proportional to the root mean square value of the stress is, therefore, proposed as a parameter for defining the damage produced by hydrotesting.

## ACKNOWLEDGMENTS

The author wishes to express his sincere gratitude for the support and assistance of the many individuals who made this work possible.

The author particularly wishes to acknowledge the guidance and valuable assistance given by his chairman, Dr. R. A. Schapery during this period. Additional thanks are due his committee members, Dr. R. Darby, Dr. J. S. Ham, Dr. J. E. Martinez and Dr. L. D. Webb for their valuable discussions and suggestions. The interest and assistance shown by Dr. H. R. Thornton was also appreciated. The author would like to extend a note of special appreciation for the technical guidance and moral support given by a close friend and associate, Dr. D. Saylak.

Additional acknowledgments are due to N. Conrad and J. B. Hattox for their aid in the development of the computer codes used in the analysis, to C. E. Fredericksen for his assistance with the electronic instrumentation and in the actual testing program, and special thanks to R. E. Milburn for his considerable help and untiring attitude during the data analysis and final drafting stages.

Acknowledgment is extended to Dr. J. S. Noel (currently at Texas A&M University), previously with Rockwell International, for conducting the thermal expansion tests.

Financial support for a portion of this work was provided by

the Air Force Materials Laboratory on a related project involving graphite/epoxy composites. The overall support for this work was provided by the Aerojet Solid Propulsion Company under contract to the Air Force Rocket Propulsion Laboratory. The author is indebted to the Project Manager, Mr. K. W. Bills, Jr., a close friend and associate, who fully supported the author's effort with the experimental materials and technical assistance throughout the length of the program.

Finally, and especially, appreciation is extended to the author's wife, Mary Lou, and family for their patience and encouragement.

## TABLE OF CONTENTS

	PAGE
ABSTRACT . . . . .	iii
ACKNOWLEDGMENTS . . . . .	v
TABLE OF CONTENTS . . . . .	vii
LIST OF TABLES . . . . .	x
LIST OF FIGURES . . . . .	xii
SECTION	
I INTRODUCTION . . . . .	1
II REVIEW OF CONSTITUTIVE THEORY FOR FIBROUS COMPOSITE MATERIALS . . . . .	6
Introduction . . . . .	6
Viscoelastic Behavior and Matrix Constitutive Theory . . . . .	9
Linear Viscoelastic Theory . . . . .	10
Nonlinear Viscoelastic Behavior . . . . .	29
Lamina Constitutive Theory . . . . .	39
Elastic Anisotropic Materials . . . . .	41
Viscoelastic Composite Material Behavior. Structure-Property Relationships . . . . .	52
71	
Laminate Constitutive Theory . . . . .	78
Elastic Orthotropic Materials . . . . .	80
Viscoelastic Orthotropic Materials . . . . .	82
Structure-Property Relationships . . . . .	84
III MECHANICAL CHARACTERIZATION TESTS . . . . .	86
Materials and Equipment . . . . .	87
Materials . . . . .	87
Specimen Preparation . . . . .	95
Equipment and Procedures . . . . .	100
Experimental Considerations . . . . .	114
Bending and Grip Effects . . . . .	114
Strain Gage Heating . . . . .	114
Humidity Effects . . . . .	115
Softening and Transition Temperatures . . . . .	115

## TABLE OF CONTENTS (Continued)

	PAGE
Preliminary Characterization Tests . . . . .	121
Fiber Properties . . . . .	121
Fiber Volumetric Content . . . . .	122
Tensile Coupon Stress-Strain Behavior . . . . .	125
Constant Crosshead Rate Tests . . . . .	137
Uniaxial Tension . . . . .	137
Four-Point Beam Bending . . . . .	137
Plate Twist Test . . . . .	139
Single and Multiple Cycle Creep and Recovery Tests . . . . .	140
Uniaxial Tension . . . . .	140
Four-Point Beam Bending . . . . .	147
Plate Twist Test . . . . .	148
IV DATA REDUCTION AND ANALYSIS OF RESULTS. . . . .	149
Uniaxial Creep and Recovery of Epoxy Matrix. . . . .	149
Determination of Material Constants . . . . .	149
Effect of Stress and Temperature. . . . .	153
Multiple Cycling Effects. . . . .	165
Matrix Creep Compliance . . . . .	169
Uniaxial Creep and Recovery of Unidirectional Glass/Epoxy Laminates and Laminated Composites . . . . .	170
Determination of Material Constants in Power Law Representation. . . . .	170
Linear Viscoelastic Creep Compliances . . . . .	176
Effect of Stress and Temperature. . . . .	178
Multiple Cycling Effects. . . . .	206
Lamina Angular Dependence and Principal Creep Compliances . . . . .	245
Comparison with Micromechanics Theory . . . . .	252
Constant Crosshead Rate Tests on Glass/Epoxy Laminates. . . . .	281
Effect of Temperature . . . . .	281
Effect of Multiple Cycling and Stress Level. . . . .	286
Four-Point Beam Bending Tests. . . . .	306
Creep and Recovery Tests. . . . .	307

## TABLE OF CONTENTS (Continued)

	PAGE
Constant Crosshead Rate Tests. . . . .	315
Plate Twist Tests . . . . .	332
Creep and Recovery Tests . . . . .	333
Constant Crosshead Rate Tests. . . . .	333
V APPLICATION TO MOTOR CASE DESIGN	349
Review of Present Technology. . . . .	349
Prediction of Multiple Cycling Effects. . .	352
VI CONCLUSIONS. . . . .	367
REFERENCES . . . . .	372
APPENDIX . . . . .	389
VITA . . . . .	397

## LIST OF TABLES

TABLE		PAGE
1	Conversion Between Tensor, Contracted and Mixed Contracted Notations . . . . .	43
2	Ingredients of Shell 58-68R Epoxy Resin [181]. .	89
3	Fiber Content of S-901 Glass/Shell 58-68R Epoxy Resin Materials. . . . .	123
4	Summary of Maximum Bending Moment, $M_x$ (in-lbs), for Four-Point Bending Tests (Constant Crosshead Rate). . . . .	139
5	Summary of Uniaxial Creep and Recovery Tests ( $T = 20^\circ\text{F}$ ) . . . . .	142
6	Summary of Uniaxial Creep and Recovery Tests ( $T = 75^\circ\text{F}$ ) . . . . .	143
7	Summary of Uniaxial Creep and Recovery Tests ( $T = 140^\circ\text{F}$ ). . . . .	145
8	Summary of Maximum Bending Moment, $M_x$ (in-lbs), for Four-Point Bending Tests (Creep and Recovery) . . . . .	147
9	Power Law Constants for Shell 58-68R Epoxy Resin. . . . .	154
10	Shift Factors, $a_T$ , for Shell 58-68R Epoxy Resin. . . . .	164
11	Shell 58-68R Epoxy Creep Compliances . . . . .	169
12	Linear Viscoelastic Creep Compliances for S-901 Glass/Shell 58-68R Epoxy . . . . .	177
13	Creep Compliances for S-901 Glass/Shell 58-68R Epoxy Composite at $140^\circ\text{F}$ . . . . .	228
14	Measured Properties $S_{12}$ , $v_{12}$ and $v_{21}$ for S-901 Glass/Shell 58-68R Epoxy . . . . .	251

## LIST OF TABLES

TABLE		PAGE
15	Experimental, Initial Principal Creep Compliances for S-901 Glass/Shell 58-68R Epoxy. . . . .	256
16	Stress History of Multiple Cycling, Constant Crosshead Rate Tests. . . . .	288
17	Beam Creep and Recovery Compliances Using Flexure Formula, Equation (153) . . . . .	314
18	Softening Parameters for S-901 Glass/Shell 58-68R Epoxy. . . . .	361



## LIST OF FIGURES

FIGURE		PAGE
1	Relation between creep and recovery of a linear viscoelastic material . . . . .	37
2	Surface layer of a typical glass-fiber/epoxy composite after removal of resin . . . . .	40
3	Glass fiber ends, or bundles after resin removal . . . . .	40
4	Anisotropic tensile specimen . . . . .	50
5	Section of solid rocket motor case (a) showing winding pattern and (b) hydrotest damage . . . . .	61
6	Evidence of fiber fracture in graphite/epoxy composite . . . . .	62
7	Matrix failure and interfacial adhesive failure in the same composite . . . . .	62
8	Crack arrest mechanism in an E-glass/epoxy composite subject to tensile stress [12] . . .	69
9	Enlarged view (220X) showing presence of significant fiber bending [12] . . . . .	69
10	Laminated plate notation . . . . .	79
11	Instrumented third stage Minuteman III solid rocket motor case undergoing prooftesting . .	92
12	Forward dome section of the third stage Minuteman III solid rocket motor case . . . .	94
13	Closeup view of the case region near a thrust termination port . . . . .	94
14	Typical tensile coupons used for creep and recovery and constant crosshead rate tests . .	97
15	Specimens used for four-point beam bending tests . . . . .	101

## LIST OF FIGURES (Continued)

FIGURE		PAGE
16	Orthotropic $\pm 45^\circ$ glass/epoxy plate specimen. .	101
17	(a) Multi-station, dead-weight creep tester with (b) closeup view of heat chambers and tensile coupon . . . . .	103
18	Lower grip and pin connections showing tensile coupon in (a) unloaded (recovery) and (b) loaded (creep) condition . . . . .	105
19	(a) Lever arm creep tester and (b) closeup of the sample and grip assembly . . . . .	106
20	Interior view of heat chamber. . . . .	109
21	Heat chamber mounted around sample in lever arm creep tester . . . . .	109
22	Four-point beam bending test setup for (a) creep and recovery test and (b) constant crosshead rate test. . . . .	110
23	Experimental setup for plate twist test for (a) constant crosshead rate and (b) creep and recovery tests . . . . .	113
24	Thermal expansion behavior of aluminum reference material . . . . .	118
25	Thermal expansion of Shell 58-68R epoxy resin. . . . .	119
26	Effect of thermal cycling on the thermal expansion of glass/epoxy composite . . . . .	120
27	Stress-strain behavior of Shell 58-68R epoxy .	126
28	Stress-strain behavior of unidirectional glass/epoxy ( $\theta = 0^\circ$ ) . . . . .	127
29	Stress-strain behavior of unidirectional glass/epoxy ( $\theta = 20^\circ$ ). . . . .	128

## LIST OF FIGURES (Continued)

FIGURE		PAGE
30	Stress-strain behavior of unidirectional glass/epoxy ( $\theta = 45^\circ$ ) . . . . .	129
31	Stress-strain behavior of unidirectional glass/epoxy ( $\theta = 90^\circ$ ) . . . . .	130
32	Stress-strain behavior of laminated glass/-epoxy ( $\theta = 0^\circ/90^\circ$ ) . . . . .	131
33	Stress-strain behavior of laminated glass/-epoxy ( $\theta = +10^\circ$ ) . . . . .	132
34	Stress-strain behavior of laminated glass/-epoxy ( $\theta = +30^\circ$ ) . . . . .	133
35	Stress-strain behavior of laminated glass/-epoxy ( $\theta = \pm 45^\circ$ ) . . . . .	134
36	Stress-strain behavior of laminated glass/-epoxy ( $\theta = \pm 60^\circ$ ) . . . . .	135
37	Stress-strain behavior of laminated glass/-epoxy ( $\theta = \pm 80^\circ$ ) . . . . .	136
38	Evaluation of $n$ using the recovery compliance for the Shell 53-68R epoxy . . . . .	152
39	Creep compliance for Shell 58-68R epoxy as a function of temperature . . . . .	155
40	Temperature dependence of initial compliance, $D_0$ , for Shell 58-68R epoxy . . . . .	156
41	Net creep compliance, $\Delta D$ , for Shell 58-68R epoxy at different temperatures . . . . .	158
42	Temperature dependence and evaluation of $n$ from recovery compliance of Shell 58-68R epoxy . . . . .	159
43	Master curve for net creep compliance, $\Delta D$ , for Shell 58-68R epoxy . . . . .	161

## LIST OF FIGURES (Continued)

FIGURE		PAGE
58	Creep compliance for different stress levels ( $\theta = \pm 30^\circ$ , $T = 75^\circ\text{F}$ ) . . . . .	184
59	Creep compliance for different stress levels ( $\theta = \pm 45^\circ$ , $T = 75^\circ\text{F}$ ) . . . . .	185
60	Creep compliance for different stress levels ( $\theta = \pm 60^\circ$ , $T = 75^\circ\text{F}$ ) . . . . .	186
61	Creep compliance for different stress levels ( $\theta = 20^\circ$ , $T = 140^\circ\text{F}$ ) . . . . .	187
62	Creep compliance for different stress levels ( $\theta = 45^\circ$ , $T = 140^\circ\text{F}$ ) . . . . .	188
63	Creep compliance for different stress levels ( $\theta = 90^\circ$ , $T = 140^\circ\text{F}$ ) . . . . .	189
64	Creep compliance for different stress levels ( $\theta = 0^\circ/90^\circ$ , $T = 140^\circ\text{F}$ ) . . . . .	190
65	Creep compliance for different stress levels ( $\theta = \pm 30^\circ$ , $T = 140^\circ\text{F}$ ) . . . . .	191
66	Creep compliance for different stress levels ( $\theta = \pm 45^\circ$ , $T = 140^\circ\text{F}$ ) . . . . .	192
67	Creep compliance for different stress levels ( $\theta = \pm 60^\circ$ , $T = 140^\circ\text{F}$ ) . . . . .	193
68	Creep compliances at low stress levels for various fiber angles ( $T = 75^\circ\text{F}$ ) . . . . .	197
69	Creep compliances at low stress levels for various fiber angles of laminated composites ( $T = 75^\circ\text{F}$ ) . . . . .	198
70	Creep compliance at low stress levels for various fiber angles ( $T = 140^\circ\text{F}$ ) . . . . .	199
71	Creep compliances at low stress levels for various fiber angles of laminated composites ( $T = 140^\circ\text{F}$ ) . . . . .	200

## LIST OF FIGURES (Continued)

FIGURE		PAGE
44	Time-temperature shift factor, $a_T$ , vs. inverse temperature for evaluation of activation energy, $\Delta F$ , for Shell 58-68R epoxy . . . . .	162
45	Temperature dependence of the shift factor, $a_T$ , for Shell 58-68R epoxy . . . . .	163
46	Effect of multiple loading cycles on creep compliance of epoxy resin ( $T = 75^\circ\text{F}$ ) . . . . .	166
47	Effect of multiple loading cycles on net creep compliance of epoxy resin ( $T = 75^\circ\text{F}$ ) . . . . .	167
48	Effect of multiple loading cycles on recovery compliance of epoxy resin ( $T = 75^\circ\text{F}$ ) . . . . .	168
49	Creep and recovery of $45^\circ$ glass/epoxy at $75^\circ\text{F}$ . . . . .	171
50	Creep and recovery of $\pm 45^\circ$ glass/epoxy at $75^\circ\text{F}$ . . . . .	172
51	Creep and recovery of $45^\circ$ glass/epoxy at $140^\circ\text{F}$ . . . . .	173
52	Creep and recovery of $\pm 45^\circ$ glass/epoxy at $140^\circ\text{F}$ . . . . .	174
53	Creep compliance for different stress levels ( $\theta = 0^\circ$ , $T = 75^\circ\text{F}$ ) . . . . .	179
54	Creep compliance for different stress levels ( $\theta = 20^\circ$ , $T = 75^\circ\text{F}$ ) . . . . .	180
55	Creep compliance for different stress levels ( $\theta = 45^\circ$ , $T = 75^\circ\text{F}$ ) . . . . .	181
56	Creep compliance for different stress levels ( $\theta = 90^\circ$ , $T = 75^\circ\text{F}$ ) . . . . .	182
57	Creep compliance for different stress levels ( $\theta = 0^\circ/90^\circ$ , $T = 75^\circ\text{F}$ ) . . . . .	183

## LIST OF FIGURES (Continued)

FIGURE		PAGE
72	Effect of temperature on creep compliance of glass/epoxy composite ( $\theta = 45^\circ$ ) . . . . .	201
73	Effect of temperature on creep compliance of glass/epoxy composite ( $\theta = \pm 45^\circ$ ) . . . . .	202
74	Temperature dependence of the initial creep compliances for the glass/epoxy composite. . .	203
75	Time-temperature shift factor, $a_T$ , for the glass/epoxy composite and epoxy resin (from Figure 44) . . . . .	205
76	Effect of multiple loading on the creep compliance of the glass/epoxy unidirectional laminae ( $\theta = 20^\circ$ , $T = 75^\circ\text{F}$ , $\sigma = 10,500$ psi) . .	207
77	Effect of multiple loading on the creep compliance of the glass/epoxy unidirectional laminae ( $\theta = 20^\circ$ , $T = 140^\circ\text{F}$ , $\sigma = 2000$ psi) . .	208
78	Effect of multiple loading on the creep compliance of the glass/epoxy unidirectional laminae ( $\theta = 20^\circ$ , $T = 140^\circ\text{F}$ , $\sigma = 4800$ psi) . .	209
79	Effect of multiple loading on the creep compliance of the glass/epoxy unidirectional laminae ( $\theta = 20^\circ$ , $T = 140^\circ\text{F}$ , $\sigma = 8500$ psi) . .	210
80	Effect of multiple loading on the creep compliance of the glass/epoxy unidirectional laminae ( $\theta = 20^\circ$ , $T = 140^\circ\text{F}$ , $\sigma = 10,500$ psi) .	211
81	Effect of multiple loading on the creep compliance of the glass/epoxy unidirectional laminae ( $\theta = 45^\circ$ , $T = 75^\circ\text{F}$ , $\sigma = 3015$ psi) . . .	212
82	Effect of multiple loading on the creep compliance of the glass/epoxy unidirectional laminae ( $\theta = 45^\circ$ , $T = 75^\circ\text{F}$ , $\sigma = 6350$ psi) . . .	213
83	Effect of multiple loading on the creep compliance of the glass/epoxy unidirectional laminae ( $\theta = 45^\circ$ , $T = 140^\circ\text{F}$ , $\sigma = 500$ psi) . . .	214

## LIST OF FIGURES (Continued)

FIGURE		PAGE
84	Effect of multiple loading on the creep compliance of the glass/epoxy unidirectional laminae ( $\theta = 45^\circ$ , $T = 140^\circ\text{F}$ , $\sigma = 5000$ psi) . .	215
85	Effect of multiple loading on the creep compliance of the glass/epoxy unidirectional laminae ( $\theta = 90^\circ$ , $T = 75^\circ\text{F}$ , $\sigma = 540$ psi) . . .	216
86	Effect of multiple loading on the creep compliance of the glass/epoxy unidirectional laminae ( $\theta = 90^\circ$ , $T = 75^\circ\text{F}$ , $\sigma = 2015$ psi) . . .	217
87	Effect of multiple loading on the creep compliance of the glass/epoxy unidirectional laminae ( $\theta = 90^\circ$ , $T = 75^\circ\text{F}$ , $\sigma = 4000$ psi) . . .	218
88	Effect of multiple loading on the creep compliance of the glass/epoxy unidirectional laminae ( $\theta = 90^\circ$ , $T = 140^\circ\text{F}$ , $\sigma = 480$ psi) . . .	219
89	Effect of multiple loading on the creep compliance of the glass/epoxy unidirectional laminae ( $\theta = 90^\circ$ , $T = 140^\circ\text{F}$ , $\sigma = 1480$ psi) . .	220
90	Effect of multiple loading on the creep compliance of the glass/epoxy unidirectional laminae ( $\theta = 90^\circ$ , $T = 140^\circ\text{F}$ , $\sigma = 2375$ psi) . .	221
91	Effect of multiple loading on creep compliance of the glass/epoxy laminated composite ( $\theta = 45^\circ$ , $T = 75^\circ\text{F}$ , $\sigma = 3010$ psi) . . . . .	222
92	Effect of multiple loading on creep compliance of the glass/epoxy laminated composite ( $\theta = \pm 45^\circ$ , $T = 75^\circ\text{F}$ , $\sigma = 7035$ psi) . . . . .	223
93	Effect of multiple loading on creep compliance of the glass/epoxy laminated composite ( $\theta = \pm 45^\circ$ , $T = 75^\circ\text{F}$ , $\sigma = 8495$ psi) . . . . .	224
94	Effect of multiple loading on creep compliance of the glass/epoxy laminated composite ( $\theta = \pm 45^\circ$ , $T = 140^\circ\text{F}$ , $\sigma = 500$ psi) . . . . .	225

## LIST OF FIGURES (Continued)

FIGURE		PAGE
95	Effect of multiple loading on creep compliance of the glass/epoxy laminated composite ( $\theta = \pm 45^\circ$ , $T = 140^\circ\text{F}$ , $\sigma = 7000$ psi). . . . .	226
96	Multiple loading effects on creep coefficient ( $T = 75^\circ\text{F}$ ) . . . . .	230
97	Initial nonlinear property, $g_0$ , compared to the normalized octahedral stress, $\tau_0$ ( $T = 75^\circ\text{F}$ ) . . . . .	231
98	Initial nonlinear property, $g_0$ , compared to the normalized octahedral stress, $\tau_0$ ( $T = 140^\circ\text{F}$ ) . . . . .	232
99	Multiple loading effects on creep coefficient showing dependence on the average shear stress, $\tau$ ( $T = 75^\circ\text{F}$ ) . . . . .	234
100	Initial nonlinear property, $g_0$ , as function of the stress normal to the fibers ( $T = 75^\circ\text{F}$ , Cycle 1). . . . .	235
101	Initial nonlinear property, $g_0$ , as function of the stress normal to the fibers ( $T = 75^\circ\text{F}$ , Cycle 2). . . . .	236
102	Initial nonlinear property, $g_0$ , as function of the stress normal to the fibers ( $T = 75^\circ\text{F}$ , Cycle 3). . . . .	237
103	Initial nonlinear property, $g_0$ , as function of the stress normal to the fibers ( $T = 140^\circ\text{F}$ , Cycle 1) . . . . .	238
104	Initial nonlinear property, $g_0$ , as function of the stress normal to the fibers ( $T = 140^\circ\text{F}$ , Cycle 2) . . . . .	239
105	Initial nonlinear property, $g_0$ , as function of the stress normal to the fibers ( $T = 140^\circ\text{F}$ , Cycle 3) . . . . .	240



## LIST OF FIGURES (Continued)

FIGURE		PAGE
106	Effect of multiple loading on the creep compliance of the case material ( $\theta = \pm 70^\circ$ , $T = 75^\circ\text{F}$ , $\sigma = 300$ psi) . . . . .	241
107	Effect of multiple loading on the creep compliance of the case material ( $\theta = \pm 70^\circ$ , $T = 75^\circ\text{F}$ , $\sigma = 1000$ psi) . . . . .	242
108	Net creep compliance for case material subjected to multiple loading ( $\theta = \pm 70^\circ$ , $T = 75^\circ\text{F}$ , $\sigma = 300$ psi) . . . . .	243
109	Net creep compliance for case material subjected to multiple loading ( $\theta = \pm 70^\circ$ , $T = 75^\circ\text{F}$ , $\sigma = 1000$ psi) . . . . .	244
110	Angular dependence of the linear viscoelastic creep compliance, $S_{11}$ ( $T = 20^\circ\text{F}$ ) . . .	247
111	Angular dependence of the linear viscoelastic creep compliance, $S_{11}$ ( $T = 75^\circ\text{F}$ ) . . .	248
112	Angular dependence of the linear viscoelastic creep compliance, $S_{11}$ ( $T = 140^\circ\text{F}$ ) . . .	249
113	Temperature dependence of principal shear compliance, $S_{66}$ . . . . .	253
114	Temperature dependence of net creep compliance, $\Delta S_{66}$ . . . . .	254
115	Temperature dependence of initial principal linear viscoelastic creep compliances . . . . .	257
116	Temperature dependence of initial transformed reduced stiffnesses (data from Figure 115) . .	259
117	Linear viscoelastic creep compliances of glass/epoxy composite ( $T = 20^\circ\text{F}$ ) . . . . .	260
118	Linear viscoelastic creep compliances of glass/epoxy composite ( $T = 75^\circ\text{F}$ ) . . . . .	261

## LIST OF FIGURES (Continued)

FIGURE		PAGE
119	Linear viscoelastic creep compliances of glass/epoxy composite ( $T = 140^{\circ}\text{F}$ ) . . . . .	262
120	Linear viscoelastic reduced stiffness of glass/epoxy composite ( $T = 20^{\circ}\text{F}$ ) . . . . .	264
121	Linear viscoelastic reduced stiffness of glass/epoxy composite ( $T = 75^{\circ}\text{F}$ ) . . . . .	265
122	Linear viscoelastic reduced stiffness of glass/epoxy composite ( $T = 140^{\circ}\text{F}$ ) . . . . .	266
123	Comparison of experimental initial compliance, $D_0$ , with "effective" compliances for Shell 58-68R epoxy resin . . . . .	269
124	Principal compliances, $S_{22}$ and $S_{66}$ , predicted with Halpin-Tsai equations using the $S_{66}$ "effective" resin compliance ( $T = 20^{\circ}\text{F}$ ) . . . .	270
125	Principal compliances, $S_{22}$ and $S_{66}$ , predicted with Halpin-Tsai equations using the $S_{66}$ "effective" resin compliance ( $T = 75^{\circ}\text{F}$ ) . . . .	271
126	Principal compliances, $S_{22}$ and $S_{66}$ , predicted with Halpin-Tsai equations using the $S_{66}$ "effective" resin compliance ( $T = 140^{\circ}\text{F}$ ) . . . .	272
127	Comparison of temperature dependence of initial compliance, $S_{22}$ , with theoretical bounds . . . . .	276
128	Comparison of temperature dependence of initial compliance, $S_{66}$ , with theoretical bounds . . . . .	277
129	Comparison of experimental compliances $S_{22}$ and $S_{66}$ with theoretical upper and lower bounds ( $T = 20^{\circ}\text{F}$ ) . . . . .	278
130	Comparison of experimental compliances $S_{22}$ and $S_{66}$ with theoretical upper and lower bounds ( $T = 75^{\circ}\text{F}$ ) . . . . .	279

## LIST OF FIGURES (Continued)

FIGURE		PAGE
131	Comparison of experimental compliances $S_{22}$ and $S_{66}$ with theoretical upper and lower bounds ( $T = 140^{\circ}\text{F}$ ) . . . . .	280
132	Effect of repeated tensile loading on stress-strain response ( $\theta = 45^{\circ}$ , $T = 75^{\circ}\text{F}$ ) . . . . .	282
133	Effect of repeated tensile loading on stress-strain response ( $\theta = \pm 45^{\circ}$ , $T = 75^{\circ}\text{F}$ ) . . . . .	283
134	Effect of repeated tensile loading on stress-strain response ( $\theta = 45^{\circ}$ , $T = 140^{\circ}\text{F}$ ) . . . . .	284
135	Effect of repeated tensile loading on stress-strain response ( $\theta = \pm 45^{\circ}$ , $T = 140^{\circ}\text{F}$ ) . . . . .	285
136	Effect of cyclic loading on $0^{\circ}/90^{\circ}$ tensile coupon; $\sigma_{\max} = 15,000$ psi (Cycle 1) . . . . .	289
137	Effect of cyclic loading on $0^{\circ}/90^{\circ}$ tensile coupon; $\sigma_{\max} = 42,000$ psi (Cycle 4) . . . . .	290
138	Effect of cyclic loading on $0^{\circ}/90^{\circ}$ tensile coupon; $\sigma_{\max} = 42,000$ psi (Cycle 5) . . . . .	291
139	Effect of cyclic loading on $45^{\circ}$ tensile coupon; $\sigma_{\max} = 8000$ psi (Cycle 1) . . . . .	293
140	Effect of cyclic loading on $45^{\circ}$ tensile coupon; $\sigma_{\max} = 8000$ psi (Cycle 3) . . . . .	294
141	Effect of cyclic loading on $45^{\circ}$ tensile coupon; $\sigma_{\max} = 10,000$ psi (Cycle 7) . . . . .	295
142	Effect of cyclic loading on $45^{\circ}$ tensile coupon; $\sigma_{\max} = 10,000$ psi (Cycle 8) . . . . .	296
143	Effect of cyclic loading on $\pm 45^{\circ}$ tensile coupon; $\sigma_{\max} = 11,500$ psi (Cycle 1) . . . . .	297
144	Effect of cyclic loading on $\pm 45^{\circ}$ tensile coupon; $\sigma_{\max} = 11,500$ psi (Cycle 2) . . . . .	298

## LIST OF FIGURES (Continued)

FIGURES		PAGE
145	Effect of cyclic loading on $\pm 45^\circ$ tensile coupon; $\sigma_{\max} = 11,500$ psi (Cycle 4). . . . .	299
146	Superimposed stress-strain curves (Figures 143 and 145) showing cycle-to-cycle damage effects on $\pm 45^\circ$ glass/epoxy tensile coupon ( $\sigma_{\max} = 11,500$ psi). . . . .	301
147	Effect of cyclic loading on $\pm 45^\circ$ tensile coupon; $\sigma_{\max} = 5000$ psi (Cycle 1). . . . .	302
148	Effect of cyclic loading on $\pm 45^\circ$ tensile coupon; $\sigma_{\max} = 12,000$ psi (Cycle 15). . . . .	303
149	Effect of cyclic loading on $\pm 45^\circ$ tensile coupon; $\sigma_{\max} = 12,000$ psi (Cycle 17). . . . .	304
150	Damage effects as a result of different stress histories. Open circle (○) represents multiple cycles at sequentially higher stresses; closed circle (●) data represents several cycles at $\sigma_{\max} = 11,500$ psi. . . . .	305
151	Effect of multiple cycling on the creep strain for the $\pm 45^\circ$ glass/epoxy beam for a 12.5 in-lb applied moment ( $T = 75^\circ\text{F}$ ). . . . .	308
152	Effect of multiple cycling on the creep strain for the $\pm 45^\circ$ glass/epoxy beam for a 55.5 in-lb applied moment ( $T = 75^\circ\text{F}$ ). . . . .	309
153	Effect of multiple cycling on the creep strain for the $\pm 20^\circ$ case material beam for a 10.5 in-lb applied moment ( $T = 75^\circ\text{F}$ ). . . . .	310
154	Effect of multiple cycling on the creep strain for the $\pm 70^\circ$ case material beam for a 1.5 in-lb applied moment ( $T = 75^\circ\text{F}$ ). . . . .	311
155	Effect of multiple cycling on the creep strain for the $\pm 70^\circ$ case material beam for a 5.5 in-lb applied moment ( $T = 75^\circ\text{F}$ ). . . . .	312

## LIST OF FIGURES (Continued)

FIGURE		PAGE
156	Typical loading strain history for constant crosshead rate beam test . . . . .	317
157	Effect of cyclic loading of $\pm 45^\circ$ glass/epoxy beam (Cycles 1 and 3). . . . .	318
158	Effect of cyclic loading of $\pm 45^\circ$ glass/epoxy beam (Cycles 4 and 6). . . . .	319
159	Effect of cyclic loading of $\pm 45^\circ$ glass/epoxy beam (Cycles 7 and 9). . . . .	320
160	Effect of cyclic loading of $\pm 45^\circ$ glass/epoxy beam (Cycles 10 and 11). . . . .	321
161	Effect of cyclic loading of $0^\circ/90^\circ$ glass/epoxy beam (Cycles 1 and 3). . . . .	322
162	Effect of cyclic loading of $0^\circ/90^\circ$ glass/epoxy beam (Cycles 4 and 5). . . . .	323
163	Effect of cyclic loading of $0^\circ/90^\circ$ glass/epoxy beam (Cycles 6 and 7). . . . .	324
164	Effect of cyclic loading of $\pm 20^\circ$ beam cut from motor case material (Cycles 1 and 2) . . . . .	325
165	Effect of cyclic loading of $\pm 20^\circ$ beam cut from motor case material (Cycles 3 and 4) . . . . .	326
166	Effect of cyclic loading of $\pm 20^\circ$ beam cut from motor case material (Cycles 5 and 6) . . . . .	327
167	Effect of cyclic loading of $\pm 70^\circ$ beam cut from motor case material (Cycles 1 and 2) . . . . .	328
168	Effect of cyclic loading of $\pm 70^\circ$ beam cut from motor case material (Cycles 3 and 4) . . . . .	329
169	Evaluation of load-deflection behavior of aluminum plate . . . . .	335

## LIST OF FIGURES (Continued)

FIGURE		PAGE
170	Large deflection contribution, $\Delta P$ , to total plate load versus deflection for aluminum plate. . . . .	336
171	Load-deflection curve for 6061-T6 Aluminum plate. . . . .	338
172	Load deflection behavior of $\pm 45^\circ$ glass/epoxy plate (Cycle 1). . . . .	339
173	Load-deflection behavior of $\pm 45^\circ$ glass/epoxy plate (Cycle 3). . . . .	340
174	Load-deflection behavior of $\pm 45^\circ$ glass/epoxy plate (Cycle 6). . . . .	341
175	Load versus average surface strain for $\pm 45^\circ$ glass/epoxy plate (Cycle 1). . . . .	343
176	Load versus average surface strain for $\pm 45^\circ$ glass/epoxy plate (Cycle 3). . . . .	344
177	Load versus average surface strain for $\pm 45^\circ$ glass/epoxy plate (Cycle 6). . . . .	345
178	Evaluation of load-deflection behavior of $\pm 45^\circ$ glass/epoxy plate . . . . .	346
179	Low load level creep and recovery test within linear range ( $\theta = \pm 45^\circ$ ). . . . .	347
180	High load level constant crosshead rate test after buckling ( $\theta = \pm 45^\circ$ ). . . . .	347
181	Softening function, $1 + f$ , for $\theta = 20^\circ$ at $75^\circ\text{F}$ . . . . .	356
182	Softening function, $1 + f$ , for $\theta = 45^\circ$ at $75^\circ\text{F}$ . . . . .	357
183	Softening function, $1 + f$ , for $\theta = 90^\circ$ at $75^\circ\text{F}$ . . . . .	358

## LIST OF FIGURES (Continued)

FIGURE		PAGE
184	Softening function, $1 + f$ , for $\phi = 20^\circ$ at $140^\circ\text{F}$ . . . . .	359
185	Softening function, $1 + f$ , for $\phi = 45^\circ$ at $140^\circ\text{F}$ . . . . .	360
186	Normal stress dependence of the softening parameter, $A$ , at $75^\circ\text{F}$ . . . . .	362
187	Normal stress dependence of the softening parameter, $B$ , at $75^\circ\text{F}$ . . . . .	363
188	Normal stress dependence of the softening parameter, $A$ , at $140^\circ\text{F}$ . . . . .	364
189	Normal stress dependence of the softening parameter, $B$ , at $140^\circ\text{F}$ . . . . .	365

## SECTION I

### INTRODUCTION

During the past fifteen years there has been an increased emphasis on the development and structural application of composite materials. In general, there are two primary divisions of composite materials, viz., particulate and fibrous composites. These classes and several others are discussed in detail by Holliday [1]; however, this study is limited to fibrous composites. Typical fibrous composites in current use within the aerospace and commercial fields consist of composites made from continuous, parallel fibers embedded in a matrix material. The use of fiber-reinforced plastic composites such as glass/epoxy and graphite/epoxy for structural components has evolved as a result of increased interest in their mechanical properties relative to conventional materials. Of particular interest are their high strength-to-weight and high modulus-to-weight characteristics. This type of composite is discussed in detail by Ashton, Halpin and Petit [2], Lubin [3], Tsai, Halpin and Pagano [4] and [5]. This interest is also mirrored in the large number of published works on this class of materials as evidenced in the abstracts of recent literature surveys conducted specifically on the mechanics of fiber-reinforced plastics by

---

The format of this dissertation follows the style of the Journal of Composite Materials.



Beckwith et al. [6-8].

Although the constituent materials are usually assumed to exhibit linear elastic behavior up to failure, the overall fiber-reinforced plastic composite exhibits a significant amount of time and temperature dependent mechanical behavior in many service environments. The efficient and safe design and utilization of these composites demand a good understanding of their viscoelastic behavior. The surveys by Beckwith et al. [6-8] point out that while a significant amount of research has been conducted on the viscoelastic behavior of polymers and particulate composite polymers, there have been only a limited number of investigations of the viscoelastic behavior of plastic composites.

It has further been established by Lou and Schapery [9], Ashton [10], Halpin [11] and Schapery, Beckwith and Conrad [12], that the behavior of many of these composites is not linearly viscoelastic except at small strains, often well below the design limits normally imposed for structural applications. More recent studies of the nonlinear viscoelastic behavior of unidirectional glass/-epoxy composites [9] seem to indicate that the nonlinearity can be attributed to internal crack growth within the matrix (or at the fiber/matrix interface) and viscous flow in the plastic matrix.

Composites have typically found their way into several areas involving pressure vessels through the process of filament winding techniques [13-16]. The early emphasis on fiber-reinforced

composites can be attributed to their application in solid rocket motor cases in the late 1950's and early 1960's. This interest is currently at a very high level as evidenced by the use of some of the "advanced" composites such as graphite/epoxy [15]. Part of the motor case design problem rests in the complete mechanical characterization of the material and subsequent application after the vessel has been subjected to one or more cycles of "hydrotesting" to pressure levels about 10-25% above the expected operating conditions [17]. This technique of "non-destructive testing" (NDT) has, in fact, been shown to cause considerable internal damage to the composite and in glass/epoxy composites creates a condition for further damage due to moisture [14, 15].

The importance of the nonlinearity due to crack growth is considered significant, particularly during the first few cycles when a considerable amount of non-recoverable deformation occurs. There is also an associated softening of the composite from cycle-to-cycle, which should be accounted for in determining subsequent deformations during the application of the service conditions.

Constitutive theory for fibrous composite materials is reviewed in Section II. In addition to reviewing the basis for linear elastic constitutive theory, the definition of linear viscoelastic behavior is presented and the effects of temperature on the overall composite response are discussed. Schapery [18] has recently reviewed many of the major areas of viscoelastic behavior

normally observed in fibrous composite materials. Some of the more important areas are reviewed here, with particular emphasis on permanent damage as a result of crack propagation [12, 19, 20]. Finally, the prediction of effective properties using some of the current micromechanics theories [2, 4, 5] are discussed.

The experimental program, which was designed to provide the mechanical characterization data necessary for the evaluation of the glass/epoxy composite material currently used in the third stage Minuteman III solid rocket motor case [17], is described in Section III. The program consists of mechanical characterization tests on unidirectional and laminated glass/epoxy composites as well as the matrix material. A small number of tests were also conducted on samples of the laminated glass/epoxy composite taken from the actual motor case.

Reported in Section IV are the experimental results from a series of uniaxial creep and recovery tests and several beam tests designed to emphasize the effects of temperature, stress level and load history. The linear viscoelastic constitutive properties are established for the various materials and compared with several of the micromechanics theories used to predict the effective properties. The observed effects of material nonlinearities as a result of crack propagation are discussed.

The effects of the observed nonlinear material behavior of the glass/epoxy composite on the design and analysis of typical

solid rocket motor cases are reviewed in Section V. The current approach to motor case design and the effects of hydrotesting and temperature on the case properties are discussed. A method of accounting for the effects of multiple loading using second-order Lebesgue norms is proposed.

## SECTION II

REVIEW OF CONSTITUTIVE THEORY FOR  
FIBROUS COMPOSITE MATERIALS

## Introduction

The analysis of any structure or body in terms of a resultant stress (strain) field requires the satisfaction of a set of equilibrium and strain-displacement equations [21-23]. This set of equations is independent of the particular material makeup but the general solution depends on the relationship between the stress and strain tensors. This relationship is known as the constitutive equation and in the theory of linear anisotropic elasticity is referred to as generalized Hooke's law [22] and simply as Hooke's law in the case of isotropic materials. The application of Hooke's law has been extensively studied during the past century, particularly for homogeneous, isotropic materials.

Indeed, several excellent treatments of the subject are given in Love [21], Sokolnikoff [22] and Fung [23] to mention only a few of the more classic references. These references, developed primarily along the lines of classical elasticity theory, treat Hooke's law in generalized terms initially and then tend to concentrate on the more specialized case of isotropic materials.

The analysis of anisotropic materials is obviously more complicated due to the nature of the constitutive theory and therefore

has not received the same degree of attention until recent years. The works of Lekhnitskii [24, 25] and Ambartsumyan [26] concentrate on the development of anisotropic theory. With the current interest in the use of fiber-reinforced composite materials at an all-time high, their works have served as primary references for current analytical developments in areas where fibrous composites are being used as structural materials.

It has, in fact, only been within the last few years that these works have been translated and presented to the Western world. Some of the more notable presentations of their works in the engineering terminology were done by Ashton et al. [2], Ashton and Whitney [27], Dong et al. [28] and [5]. The use of fibrous composites by the aerospace industry for structural applications has resulted in several analytical developments and a complete reassessment of the overall design philosophy.

Fibrous composites have been developed along two different paths classified by the matrix material holding the load carrying fibers; namely, metal matrix and plastic matrix. The metal matrix composites are of interest primarily for their higher temperature capability, although they often possess potentially higher strength and stiffness due to the matrix properties. Plastic matrix composites have a lower density and can be readily fabricated into more complex shapes than metal matrix composites, thus making them more attractive for filament-wound pressure vessels and similar

structures. We shall be more concerned in this dissertation with the plastic (polymeric) matrix composites which exhibit a significant amount of time-dependent mechanical behavior in many service environments. This behavior, termed viscoelasticity, has only recently been investigated with regard to fibrous composites [9, 11, 12, 18, 29] although considerable attention has been given to particulate composites [20, 30, 31] (e.g. solid propellants). Glass fiber/epoxy and graphite fiber/epoxy composites are typical of this class of materials.

The application of linear, anisotropic viscoelastic theory to fibrous composites in recent years is evident in the works of Schapery [18, 32], Halpin [11, 33] and Hashin [34]. Unfortunately, as a result of the high volume fraction of fibers in the composite and the gross difference in both physical and mechanical properties of the constituents, linear theory is not always adequate to predict the response to various loading situations. In many cases linear theory at least provides the starting point. Nonlinear viscoelastic behavior is reported by Schapery [35] and Ashton [10] in the United States and by Ogibalov and Tiuneeva [36, 37], Rabotnov et al. [38] and Martirosian [39-42] in the Soviet Union. The nonlinear behavior may be "reversible" or "nonreversible", the latter normally considered to be due to "microcracking". "Reversible nonlinearities" are usually attributed to secondary bond failure within the polymer and essentially consist of polymer molecules sliding

past one another. On the other hand, primary bond failure in which the molecules are actually torn apart leads to microstructural damage. During fabrication there are a number of voids and flaws which develop as a result of the polymer's curing process and the difference in the physical properties of the various constituents. As a result, microstructural damage in fibrous composites is thought to be due primarily to the growth of these small flaws or "microcracks" [18].

Analysis of fibrous composite structures requires a careful consideration of the constitutive theory of the material. The decision to use linear or nonlinear anisotropic viscoelastic theory depends on the particular application and material. The development of viscoelastic theory with regard to fibrous composites will be reviewed in this section. Particular attention will be given to the contribution of the polymeric matrix to the overall response and the influence of microstructural damage on the composite constitutive relationship. Thermal effects will also be discussed since they strongly affect the behavior of the polymeric phase.

#### Viscoelastic Behavior and Matrix Constitutive Theory

Typical polymeric matrix materials fall into several classes of epoxies, phenolics, polyesters, etc. depending on the particular strength characteristics desired and many other design considerations. All of the materials exhibit some degree of viscoelasticity



and are generally considered to be of a homogeneous, isotropic nature. Therefore, in addition to reviewing matrix constitutive theory for this class of materials, it is also fitting that several ground rules be defined in terms of what is meant by the term "linear viscoelasticity".

The behavior of viscoelastic materials falls into two major divisions; linear and nonlinear. Farris and Schapery [20] recently conducted an extensive review of the entire field of linear and nonlinear viscoelastic constitutive theory and the reader is referred to this excellent review article. The authors noted that although an extensive amount of work, both theoretical and experimental, had been conducted during the last decade toward the development of a nonlinear viscoelastic constitutive theory, the definition of linearity was often incomplete or misunderstood. As a starting point we shall review linear viscoelastic theory and proceed from there.

#### Linear Viscoelastic Theory

An understanding of linear viscoelastic theory is important for two reasons. First of all, linear theory is at least an approximation to real behavior and one should be familiar with its range of applicability. Second, the exact definition of material linearity should be firmly established before one can assess the significance of nonlinear behavior. All too often it has been

found that only part of the definition of linearity has been applied [43, 44] while in actuality, the material is indeed non-linear. A definition of linearity compatible with that used in current literature [18, 20] will be given in order to provide a precise statement of linear viscoelastic behavior. We shall neglect the effects of large strains since the strains in fibrous composites are usually below 3-5 percent.

Statement of linearity. Following [18], the mechanical behavior of a linear viscoelastic material can be described in the form of a general input-response relationship. By applying the definition of linearity along these lines we treat the material as a "black-box" without specifying a priori its physical makeup and the physical significance of the input and response quantities. The representation of a response function,  $R$ , due to an input function,  $I$ , is given by

$$R = R\{I\} \quad (1)$$

in which the brackets  $\{ \}$  indicate that the current value of  $R$  is dependent upon the entire history of  $I$ , and not just its current value.

The response  $R$  is said to be linear, and the material consequently, linearly viscoelastic, if and only if it satisfies the property of homogeneity and obeys the superposition principle [18]. The property of homogeneity, or proportionality is given by

$$R\{cI\} = cR\{I\} \quad ; \quad c = \text{constant} \quad (2)$$

while the superposition principle is given by

$$R\{I_a + I_b\} = R\{I_a\} + R\{I_b\} \quad (3)$$

where  $I_a$  and  $I_b$  are arbitrary input histories.

Although the use of Equation (2) alone is not sufficient to prove linearity, many standard characterization methods used today use only this criterion to establish linearity. However, if the material obeys Equation (3), it can be shown to automatically satisfy homogeneity for all rational values of  $c$  (including  $c = 0$ ). Thus, the primary condition for a material to be linear is that it satisfies superposition.

Knowledge that a material is linear is sufficient to establish explicit single-integral expressions connecting responses to inputs [45]. The response  $R$  can be written as an integral containing the actual input  $I$  and the response of one preselected input history. For use in the characterization of viscoelastic materials it is customary and convenient to use the Heaviside unit step function,  $H$ , as the preselected input history. The step function is given as

$$H(t - t') = \begin{cases} 0, & t < t' \\ 1, & t > t' \end{cases} \quad (4)$$

where  $t$  is the current time and  $t'$  the time at which the input  $i$  is applied. The response to  $H$  is usually denoted by  $R_H$ , and, for many applications where aging considerations are not important, the

representation of  $R_H$  becomes

$$R_H = R_H(t - t') \quad (5)$$

As a consequence of the definition of the step function,  $R_H$  vanished when  $t < t'$  in as much as aging effects are excluded.

If the input is time varying, the response is found by considering the input to be the limit of a sum of step-inputs. An integral relationship between input and response immediately follows in the form given by Volterra [45] and Pipkin [46] as

$$R = \int_{-\infty}^t R_H(t - t') \frac{dI}{dt'} dt' \quad (6)$$

Equation (6) is called a hereditary law and is sometimes referred to as the convolution integral, the Duhamel integral or the Boltzmann superposition integral.

The superposition integral may be generalized to represent multiple responses due to several inputs when the response of the material or body is linear with respect to all inputs. This generalized form of the response is given by

$$R_\alpha = \int_{-\infty}^t R_{H\alpha\beta}(t - t') \frac{dI_\beta}{dt'} dt' \quad (7)$$

in which  $R_\alpha$  is the cumulative response due to all inputs  $I_\beta$  and where  $R_{H\alpha\beta}$  is the unit response of  $R_\alpha$  when only  $I_\beta = H(t)$  is applied. The summation convention over the range of indices  $\alpha$  and  $\beta$  will be implied whenever the index is repeated in a term.

Isothermal constitutive equations. The general linear relations between the stresses,  $\sigma_{ij}$ , ( $i, j = 1, 2, 3$ ) and infinitesimal strains,  $\epsilon_{kl}$ , may be found by replacing the responses and inputs in Equation (7) with these variables, respectively, hence

$$\sigma_{ij} = \int_{-\infty}^t C_{ijk\ell}(t - t') \frac{\partial \epsilon_{k\ell}}{\partial t'} dt' \quad (8)$$

where  $C_{ijk\ell}$  is the "effective relaxation modulus tensor". The spatial dependence of  $\sigma_{ij}$ ,  $\epsilon_{kl}$  and  $C_{ijk\ell}$  are implied although not shown for simplicity in the notation scheme, and the stress,  $\sigma_{ij}$ , and strain,  $\epsilon_{kl}$ , may be any time-dependent functions. The inverse relations, in terms of the "creep compliance tensor",  $S_{ijk\ell}$ , are given by

$$\epsilon_{ij} = \int_{-\infty}^t S_{ijk\ell}(t - t') \frac{\partial \sigma_{k\ell}}{\partial t'} dt'. \quad (9)$$

The compliances  $S_{ijk\ell}$  and moduli  $C_{ijk\ell}$  are fourth-order tensors which possess symmetry with respect to index changes of  $i$  with  $j$  and  $k$  with  $\ell$  due to the symmetry of the stress and strain tensors [23],

$$C_{ijk\ell}(t) = C_{jik\ell}(t) = C_{ij\ell k}(t) = C_{ji\ell k}(t) \quad (10a)$$

$$S_{ijk\ell}(t) = S_{jik\ell}(t) = S_{ij\ell k}(t) = S_{ji\ell k}(t). \quad (10b)$$

Additional symmetry of the tensor with respect to an interchange of

the first two (ij) and second two (kl) indices, i.e.,

$$C_{ijkl}(t) = C_{klij}(t) \quad (11a)$$

$$S_{ijkl}(t) = S_{klij}(t) \quad (11b)$$

has been shown by Biot [47] based on the thermodynamics of stable, irreversible systems. These symmetries considerably reduce the number of material properties required to completely characterize linear material behavior.

In order to bring out the significance of the material properties in Equation (9), consider a generalized creep test where the time-dependent input stress is given by

$$\sigma_{ij} = \sigma'_{ij} H(t) \quad (12)$$

where all the  $\sigma'_{ij}$  are constant. Substitution of Equation (12) into the constitutive relation, Equation (9), leads to the function  $\frac{dH}{dt}$ , which is the Dirac delta function  $\delta(t')$  given by

$$\delta(t') = \begin{cases} 0, & t' \neq 0 \\ \infty, & t' = 0 \end{cases} \quad (13)$$

Consequently, Equation (9) becomes

$$\epsilon_{ij} = \int_0^t S_{ijkl}(t - t') \sigma'_{kl} \delta(t') dt'. \quad (14)$$

Using the sifting property associated with the Dirac delta function,

Equation (14) reduces to

$$\epsilon_{ij} = S_{ijkl}(t)\sigma'_{ij} \quad (15)$$

If the test is a uniaxial creep test then  $\sigma'_{ij} = \sigma'_{11}$  and we find that

$$\epsilon_{11} = S_{1111}(t)\sigma'_{11} \quad (16)$$

or, with single-index notation for stress and strain [22],

$$\epsilon_1 = S_{11}(t)\sigma'_1 \quad (17)$$

where  $\epsilon_1$  is used to denote the strain in the  $x_1$  direction, and  $\sigma'_1$  is the constant value of stress in this direction;  $S_{11}(t)$  is called the "uniaxial creep compliance". When the material is isotropic it is often common to rewrite Equation (17) after a change in notation to

$$\epsilon = D(t)\sigma \quad (18)$$

where the corresponding terms still have the same significance as before.

Nonisothermal constitutive equations. It has generally been found that viscoelastic materials exhibit significant temperature dependence. The influence of temperature on viscoelastic behavior can be divided into reversible and irreversible effects. Irreversible effects result in permanent changes such as primary bond

rupture and weight loss, brought about by thermal degradation. These effects will not be considered within this discussion.

Reversible effects, on the other hand, consist of thermal expansion and temperature dependence of those mechanical properties which appear in the constitutive equations, i.e., Equations (8) and (9). Thermal expansion effects will not be treated here; a detailed analysis of these effects is presented by Schapery [48] for anisotropic materials in the context of irreversible thermodynamics. We shall concentrate on the temperature dependence of the mechanical properties in our discussion of reversible thermal effects. In general, these effects further divide material behavior into two categories: thermorheologically simple behavior and thermorheologically complex behavior.

The simplest realistic representation of material response for viscoelastic materials under transient temperatures is that for a "thermorheologically simple material" (TSM). Morland and Lee [49] originally defined a TSM for an isotropic material and Schapery [50] extended the concept to anisotropic materials using irreversible thermodynamic principles. By definition [50] for a TSM, the constitutive equation is given by

$$\sigma_{ij} = \int_0^{\xi} C_{ijkl}(\xi - \xi') \frac{\partial \epsilon_{kl}}{\partial \xi'} d\xi' \quad (19a)$$

or, equivalently,



$$\sigma_{ij} = \int_0^t C_{ijkl} (\xi - \xi') \frac{\partial \epsilon_{kl}}{\partial t'} dt' \quad (19b)$$

where  $\xi$  is the so-called "reduced time" defined by

$$\xi = \xi(t) \equiv \int_0^t \frac{dt'}{a_T} ; \quad \xi' = \xi'(t') \equiv \int_0^{t'} \frac{dt'}{a_T} . \quad (20)$$

The scalar function  $a_T$  reflects the influence of temperature on internal viscosity and is quite sensitive to temperature changes.

The so-called "temperature shift-factor" is given by

$$a_T = a_T[T(t')] \quad (21)$$

and is used to evaluate the reduced times  $\xi$  and  $\xi'$ . For isothermal tests, Equation (20) becomes

$$\xi = \frac{t}{a_T} ; \quad \xi' = \frac{t'}{a_T} \quad (22)$$

since  $a_T$  is constant in this case. By rewriting Equation (22), (where  $\log \equiv \log_{10}$ ),

$$\log \xi = \log t - \log a_T \quad (23)$$

we find that plots of isothermal moduli, or compliances, can be shifted horizontally along the time scale with the magnitude of the shift equal to  $\log a_T$ . It is interesting to note that Schwarzl and Staverman [51] shifted isothermal data in this manner to obtain

a single, "master", curve as a function of  $\xi$  and subsequently defined a TSM as one which behaved in this manner. A reference temperature is usually selected with  $a_T$  defined as  $a_T \equiv 1$ .

The shift-factor  $a_T$  is usually obtained by graphically shifting the data horizontally along the time scale as noted by Equation (23). However, several analytical representations have been postulated over the years for polymers. When  $T < T_g$ , an Arrhenius type of temperature dependence is usually observed [11, 52]. This shift factor has exponential dependence with respect to the inverse of absolute temperature ( $1/T$ ),

$$\log a_T = \frac{\Delta H}{2.303R} \left( \frac{1}{T} - \frac{1}{T_R} \right) \quad (24)$$

where  $\Delta H$  is the activation energy (per mole),  $R$  is the universal gas constant, and  $T_R$  is an arbitrary reference temperature. By plotting  $\log a_T$  against the reciprocal of absolute temperature,  $1/T$ , a straight line results and the activation energy,  $\Delta H$ , may be found.

When  $T > T_g$  the so-called WLF equation normally applies [52],

$$\log a_T = \frac{-C_1(T - T_R)}{C_2 + T - T_R} \quad (25)$$

where  $C_1$  and  $C_2$  are constants. The form of the equation is similar regardless of the choice of  $T_R$ , only the values of  $C_1$  and  $C_2$  change. When  $T_R$  is chosen to be approximately  $50^\circ\text{C}$  above the  $T_g$ , the values of  $C_1$  and  $C_2$  have been found to be universal constants

for many polymer systems [52, 53] with the following values,

$$C_1 = 8.86 \text{ } (^{\circ}\text{K}^{-1}) \quad (26)$$

$$C_2 = 101.6 \text{ } (^{\circ}\text{K})$$

Schapery [32] has used a power law form of  $a_T$  when  $T > T_g$ ,

$$a_T = \left[ \frac{(T_R - T_a)}{(T - T_a)} \right]^{\mu} \quad (27)$$

where  $T_a$  and  $\mu$  are material constants. Again, the value of  $T_R$  is arbitrary and it has been found that  $\mu$  assumes a typical range of 12-15.  $T_a$  takes on values several degrees below the  $T_g$ . This power law has been found to be a good approximation of experimental data over a wide range of temperature for filled polymers [54] and enables the reduced time, viz., Equation (20), to be evaluated analytically for constant rates of change of temperature whereas the WLF equation does not.

The inverse representation of Equations (19a) and (19b), in terms of the creep compliance tensor,  $S_{ijkl}$ , is given by

$$\epsilon_{ij} = \int_0^{\xi} S_{ijkl}(\xi - \xi') \frac{\partial \sigma_{kl}}{\partial \xi'} d\xi' \quad (28a)$$

or, equivalently,

$$\epsilon_{ij} = \int_0^t S_{ijkl}(\xi - \xi') \frac{\partial \sigma_{kl}}{\partial t'} dt'. \quad (28b)$$

In both cases, Equations (19) and (28), we have neglected the effects of thermal expansion, however, these terms generally represent only a simple addition to the strain tensor as shown in [32]. Furthermore, by specializing these relations to isotropic materials and changing notation to correspond with that used in Equation (18) we find

$$\sigma = \int_0^{\xi} E(\xi - \xi') \frac{d\xi}{dt'} dt' \quad (29)$$

and

$$\epsilon = \int_0^{\xi} D(\xi - \xi') \frac{d\sigma}{dt'} dt' \quad (30)$$

for the uniaxial stress-strain behavior of a TSM. These relationships correspond to the constitutive theory proposed originally by Morland and Lee [49].

There is a significant amount of published data to verify isothermal curve shifting of relaxation moduli and creep compliances from several sources [52, 55]. Moehlenpah et al. [56] treated isothermal relaxation moduli for an epoxy resin to form a master curve in terms of  $\xi$ . The superposition of individual isothermal responses to form a master curve is not sufficient to establish the behavior of a TSM although most characterization methods tend to totally ignore this fact. Transient temperature tests are necessary to completely define the TSM behavior. Only recently tests of this type have been conducted by Leeming [57] and

Farris [58] on solid propellants, Johnson et al. [59] and Watkins [60] on epoxy resins, and by Kabelka and Vejchar [61] and Schapery et al. [12] on fibrous composites.. With few exceptions [12, 60] the behavior of the materials characterized using transient temperature tests have been TSM.

The data of Moehlenpah et al. [56], Schapery et al. [12], Watkins [60], and Sims and Halpin [62] definitely show that horizontal shifting along the time scale is not entirely sufficient to form a smooth, well-defined master curve. However, by using vertical and horizontal translations, it is possible to superpose the data over a large time-temperature range [18].

Viscoelastic materials whose temperature dependence cannot be characterized by Equations (29) and (30) for isotropic materials and Equations (19) and (28) for general, multiaxial behavior of anisotropic materials are defined as "thermorheologically complex materials" (TCM). Some materials are composed of several constituents or phases, each behaving as a TSM with different  $a_T$  shift factors. This particular type of TCM has been designated by Schapery [18] as TCM-1. The behavior of materials in this class has been studied only under isothermal conditions which, as we noted earlier, is not sufficient to completely verify behavior under transient temperature conditions [33, 63].

Schapery [18] has also defined a second class, TCM-2, composed of materials which by definition satisfy the uniaxial stress-strain

behavior under isothermal or transient temperatures as given by

$$\epsilon = D_0 \sigma + \int_0^t \Delta D(\xi - \xi') \frac{d}{dt'} \left( \frac{\sigma}{a_G} \right) dt' \quad (31)$$

where  $\xi$  and  $\xi'$  are given by Equation (20),  $\sigma$  is any arbitrary stress input, and  $D_0 = D_0(T)$  is the initial value of the creep compliance. For the case of an isothermal creep test, the creep compliance becomes

$$D = D_0(T) + \frac{\Delta D(\xi)}{a_G(T)} \quad (32)$$

where  $\xi = \frac{t}{a_T}$ . Most data reduction techniques follow a normalization condition by assuming  $a_G = a_T \equiv 1$  at some arbitrary reference temperature,  $T_R$ , which results in

$$\Delta D(t) = D(t, T_R) - D_0(T_R) \quad (33)$$

where  $\Delta D(t)$  is the transient component of the compliance at temperature  $T_R$ .

In order to determine  $a_T$  and  $a_G$  from experimental data at different temperatures Schapery [18] rewrote Equation (32) in the form

$$\log [D - D_0] = \log \Delta D - \log a_G. \quad (34)$$

A plot of  $\log [D - D_0]$  against  $\log t$  for isothermal tests at various temperatures,  $T$ , will be identical to that at  $T_R$  except for a rigid horizontal translation of  $\log a_T$  and a similar vertical translation

of  $\log a_G$ . The final result is, again, a master curve similar to that obtained for a TSM.

A special case of Equation (31) occurs when the temperature dependence of  $D_0$  is given by

$$D_0 = \frac{D_0(T_R)}{a_G(T)} \quad (35)$$

which results in

$$D = \frac{D(\xi)}{a_G(T)} \quad (36a)$$

where

$$D(\xi) = D_0(T_R) + \Delta D(\xi) . \quad (36b)$$

As a result the constitutive relation given in Equation (31) becomes

$$\epsilon = \int_0^t D(\xi - \xi') \frac{d}{dt} \left( \frac{\sigma}{a_G} \right) dt' \quad (37)$$

which is the same as Equation (30) except for  $a_G$ .

Superposition procedures or normalization techniques, in addition to that of Schapery's based on Equation (34), have been suggested for accounting for the behavior of TCM [64-69]. McCrum and Pogany [70] have reviewed several of these procedures and compared the master curve predictions for an epoxy resin over a temperature range which included the glass transition temperature,  $T_g$ . Four of these different techniques are given in the following discussion.

## 1. Tobolsky-Ferry procedure [65, 65]:

$$D_o(T) \equiv \frac{D_o(T_R)}{a_G(T)} \quad (38)$$

$$a_G(T) \equiv \frac{T}{T_R} \frac{\rho}{\rho_R}$$

where  $\rho$  and  $\rho_R$  are the densities at temperatures  $T$  and  $T_R$ , respectively.

## 2. Ferry-Fitzgerald procedure [68]:

$$D_o(T) \equiv D_o(T_R) \quad (39)$$

$$a_G(T) \equiv \frac{T}{T_R} \frac{\rho}{\rho_R}$$

## 3. Kê procedure [66]:

$$D_o(T) \equiv \frac{D_o(T_R)}{a_G(T)} \quad (40)$$

$$a_G(T) \equiv \frac{D_o(T_R)}{D_o(T)}$$

## 4. McCrum-Morris procedure [67]:

$$D_o(T) \equiv D(0, T) \quad (41)$$

$$a_G(T) \equiv \frac{D_\infty(T_R) - D_o(T_R)}{D_\infty(T) - D_o(T)}$$

The Tobolsky-Ferry and Ferry-Fitzgerald procedures are based on the kinetic theory of rubber elasticity; the Kê procedure uses



the initial compliance to define the temperature dependence of  $a_G$ , and the McCrum-Morris procedure contains the first three as special cases by allowing for arbitrary variations of the initial and long-term compliances with temperature. The most successful of these procedures is the McCrum-Morris normalization although the specific reduction technique given by McCrum and Pogany [70] requires knowledge of the initial and long-term compliances which are not always available because of experimental limitations. Another form of  $a_G$  proposed by Schapery and Martin [69] is based on kinetic theory and is given as

$$a_G(T) = \frac{\gamma \ln\left(\frac{T}{T_R}\right)}{e^{\frac{\gamma}{T} - \frac{\gamma}{T_R}} - 1} \quad (42)$$

where  $\gamma$  is a factor related to pressure, volume and excess molar energy and  $\ln \equiv \log_e$ .

Graphical shift-methods [18] appear to be the easiest procedure for providing the best "average" material properties in the absence of the limiting values of compliance. The general technique involves the use of Equation (32) by making preliminary estimates of  $D_0$  and then forming master curves of  $\Delta D(\xi)$ . By using a smoothing technique, the best master curve may be found by adjusting the values of the initial estimate of  $D_0$ .

Analytical representation of time-dependent properties. No mention has been made up to this point about the representation of

the relaxation and creep functions in Equations (8) and (9).

According to thermodynamic theory [47], they have the following time-dependence,

$$C_{ijkl}(t) = C_{ijkl}^{\infty} + \sum_s C_{ijkl}^{(s)} e^{-t/\rho_s} \quad (43a)$$

$$S_{ijkl}(t) = S_{ijkl}^0 + S_{ijkl}^F t + \sum_s S_{ijkl}^{(s)} (1 - e^{-t/\tau_s}) \quad (43b)$$

where the range of the summation index,  $s$ , depends on the particular material,  $\rho_s$  are relaxation times and  $\tau_s$  are retardation times. The constants  $C_{ijkl}^{\infty}$  are elastic moduli which produce long-term stress response to strains whereas the constants  $S_{ijkl}^0$  are elastic compliances which produce the short-term strain response to stresses. The exponential coefficients  $C_{ijkl}^{(s)}$  and  $S_{ijkl}^{(s)}$  and the corresponding constants  $\rho_s$  and  $\tau_s$  define the time and rate-dependence of the material. The coefficients  $S_{ijkl}^F$  lead to steady-flow under constant stress such as might be found in uncrosslinked polymer systems.

Thermodynamics gives us the general form, Equations (43a) and (43b), of the material properties. Although there may be a large number of time constants as a result of the polymer's molecular configuration, creep and relaxation functions are often approximated by exponential series [71] consisting of relatively few terms (typically ten to twenty).

The modified power law [72]

$$E(t) = E_{\infty} + \frac{E_0 - E_{\infty}}{\left(1 + \frac{t}{\tau_0}\right)^n} \quad (44)$$

where  $E_{\infty}$ ,  $E_0$ ,  $\tau_0$  and  $n$  are independent of time, often provides an excellent approximation to polymer behavior above their  $T_g$ . Also, when  $t/\tau_0 \gg 1$  then Equation (44) reduces to

$$E(t) = E_{\infty} + (E_0 - E_{\infty})\left(\frac{t}{\tau_0}\right)^{-n} \quad (45)$$

and further to

$$E(t) = E_0\left(\frac{t}{\tau_0}\right)^{-n} \quad (46)$$

when  $E_{\infty} \ll E_0$ . A similar form for the compliance is [72]

$$D(t) = D_0 + \frac{(D_{\infty} - D_0)}{\left(1 + \frac{t}{\tau_0}\right)^n} \left(\frac{t}{\tau_0}\right)^n \quad (47)$$

where  $D_0$ ,  $D_{\infty}$ ,  $\tau_0$ , and  $n$  are material properties. If  $t/\tau_0 \ll 1$  then Equation (47) reduced to

$$D(t) = D_0 + (D_{\infty} - D_0)\left(\frac{t}{\tau_0}\right)^n \quad (48)$$

and further to

$$D(t) = D_{\infty}\left(\frac{t}{\tau_0}\right)^n \quad (49)$$

when  $D_{\infty} \gg D_0$ .

The forms of Equations (48) and (49) have often been found in

the literature as

$$D(t) = D_0 + D_1 t^n \quad (50)$$

and

$$D(t) = D_1 t^n \quad (51)$$

respectively. These particular forms have been found to represent the behavior of many rigid plastics with and without reinforcement [73-76].

#### Nonlinear Viscoelastic Behavior

We have already defined the conditions necessary for linearity, viz. Equations (8) and (9), and have further commented on the usefulness of linear viscoelasticity. However, the behavior of most materials is generally nonlinear prior to complete fracture and, for some materials, this nonlinearity exists even at small stress levels well within the design range of structural applications. There are many theoretical works on constitutive theory, both linear and nonlinear, such as those of Green, Rivlin and Spencer [77, 78], Coleman and Noll [79, 80], Truesdell [81, 82], Wang [83, 84], Volterra [45], Pipkin [85, 86], Hermann [87], Lianis and co-workers [88, 89], Schapery [90, 91], Huang and Lee [92], Dong [93, 94], Williams [72], Tobolsky [65, 95], Alfrey [96], Ferry [52] and others [97-107]. The development of nonlinear constitutive

theory has also resulted in several applications to various materials such as reported in the works of Findley, Lai and Onaran [108-113], Gottenberg et al. [114], Lockett [115, 116], Valanis and Landel [117], Lee and Huang [92], Schapery [35, 91], Freudenthal [118], Ward [119-121] and others [122-127]. It would be a formidable task to comment on all of these works; therefore, in the sections to follow, we shall comment only on observed deviations from linear behavior and discuss some of the more general approaches taken to describe nonlinear viscoelastic behavior.

Equations (2) and (3), homogeneity and superposition, respectively, completely define the mathematical rules of linear material response. Linear viscoelastic behavior is achieved through the use of these relationships to derive Equations (8) and (9). Nonlinearity is defined only as the failure to satisfy one or both of these rules. It is therefore possible for a material to satisfy the homogeneity rule and fail the superposition rule [128, 129].

Multiple-integral theories. Because of its generality, the various approaches to multiple-integral theory have received widespread attention in recent years. These mathematical theories are probably general enough to account for almost all types of observed nonlinearities, but they are very impractical with strong nonlinearities. This type of representation was developed by Green, Rivlin and Spencer [77, 130] and has been applied by several investigators over the years [110, 119, 124, 131].

For the case of uniaxial loading, the multiple-integral representation takes the following form,

$$\begin{aligned} \epsilon = & \int_0^t K_1(t-\tau_1) \frac{d\sigma(\tau_1)}{d\tau_1} d\tau_1 + \\ & \int_0^t \int_0^t K_2(t-\tau_1, t-\tau_2) \frac{d\sigma(\tau_1)}{d\tau_1} \frac{d\sigma(\tau_2)}{d\tau_2} d\tau_1 d\tau_2 + \\ & \int_0^t \int_0^t \int_0^t K_3(t-\tau_1, t-\tau_2, t-\tau_3) \frac{d\sigma(\tau_1)}{d\tau_1} \frac{d\sigma(\tau_2)}{d\tau_2} \frac{d\sigma(\tau_3)}{d\tau_3} d\tau_1 d\tau_2 d\tau_3 + \\ & \int_0^t \int_0^t \int_0^t \int_0^t \dots \end{aligned} \quad (52)$$

where  $K_1, K_2, K_3, \dots$  are the kernel functions containing time ( $t$ ) and material constants, and  $\tau_1, \tau_2, \tau_3, \dots$  are the dummy time variables of integration. The corresponding creep relation (constant stress) takes the form

$$\epsilon = K_1(t)\sigma + K_2(t,t)\sigma^2 + K_3(t,t,t)\sigma^3 + \dots \quad (53)$$

For a linear viscoelastic representation the higher order kernels  $K_2$  and  $K_3$  do not appear; however in published applications of this theory, the series is usually truncated at three integrals for the representation of nonlinear behavior.

In order to define the material behavior one may either solve the relations by numerical techniques or assume some form of the kernel functions  $K_1$ ,  $K_2$  and  $K_3$ . Findley and Onaran [110] used a product form suggested by Nakada [107] where the kernels take the form

$$K_1 = \alpha_1(t-\tau_1) \quad (54)$$

$$K_2 = \alpha_2(t-\tau_1)^{1/2} (t-\tau_2)^{1/2}$$

$$K_3 = \alpha_3(t-\tau_1)^{1/3} (t-\tau_2)^{1/3} (t-\tau_3)^{1/3}$$

where  $\alpha_1$ ,  $\alpha_2$  and  $\alpha_3$  are material constants. Nolte and Findley [132] have also used creep kernel functions of the form

$$K_1 = \alpha_1 + \beta_1(t-\tau_1)^n \quad (55)$$

$$K_2 = \alpha_2 + \beta_2(t-\tau_1)^n(t-\tau_2)^n$$

$$K_3 = \alpha_3 + \beta_3(t-\tau_1)^n(t-\tau_2)^n(t-\tau_3)^n$$

where  $\alpha_1$ ,  $\alpha_2$ ,  $\alpha_3$ ,  $\beta_1$ ,  $\beta_2$ ,  $\beta_3$  and  $n$  are again material constants.

A more general form of Equation (55) was recently proposed by Smart and Williams [133] where the kernel functions may be written

$$K_1 = \alpha_1(t-\tau_1)^l \quad (56)$$

$$K_2 = \alpha_2(t-\tau_1)^{p+m}(t-\tau_2)^{-p}$$

$$K_3 = \alpha_3(t-\tau_1)^{q+n}(t-\tau_2)^r(t-\tau_3)^s$$

with  $q + r + s = 0$  and where  $\alpha_1, \alpha_2, \alpha_3$  and  $l, m, p, q, r$  and  $s$  are the material constants.

Without going further into multiple-integral representation of nonlinear viscoelastic materials, one must be impressed at this point with the complex nature of such an approach. In fact, the representation of nonlinear behavior often requires more than three integrals, particularly if a strong nonlinearity exists. The solution of boundary value problems and the inversion of even the simplest formulation becomes very involved and complex. In addition, the determination of the material functions requires an experimental program consisting of many multiple step loading sequences. Generally speaking, the multiple-integral approach has not found its way into serious engineering consideration with regard to material characterization and subsequent structural applications of composites. As a result we shall not consider this approach any further.

Single-integral theories. Several methods exist which fall into a class called single-integral theories of nonlinear viscoelasticity. The modified superposition principle (MSP) was first suggested by Leaderman [134] who observed that the creep behavior of certain fibers and plastics could be separated into time and stress-dependent parts so that the creep response to a stress,  $\sigma$ , could be written as



$$\epsilon = D_0 \sigma + \int_0^t \Delta D(t-\tau) \frac{dg_0}{d\tau} d\tau \quad (57)$$

where  $D_0$  is the initial value of the compliance,  $\Delta D$  is the transient component of the compliance and  $g$  is a nonlinear function of the stress,  $\sigma$ . This theory has met with varying degrees of success, the accuracy depending on the particular material as well as on the type of loading. The MSP cannot represent a material which possesses permanent memory effects which exist as a result of permanent internal changes such as microcracking.

Schapery [90, 91, 135] used thermodynamic theory to develop a nonlinear constitutive theory which has been successfully applied to several materials [9, 35]. When stress is treated as the independent state variable, then the theory can be written as

$$\epsilon = g_0 D_0 \sigma + g_1 \int_0^t \Delta D(\psi - \psi') \frac{dg_2 \sigma}{d\tau} d\tau \quad (58)$$

where  $D_0$  and  $\Delta D$  are the initial and transient components of the linear viscoelastic creep compliance,  $\psi$  is the so-called reduced-time defined by

$$\psi = \psi(t) \equiv \int_0^t \frac{dt'}{a_\sigma[\sigma(t')]} \quad (59a)$$

and

$$\psi' = \psi'(\tau) \equiv \int_0^\tau \frac{dt'}{a_\sigma[\sigma(t')]} \quad (59b)$$

and the material properties  $g_0$ ,  $g_1$ ,  $g_2$  and  $a_\sigma$  are functions of stress. When the applied stress is sufficiently small,  $g_0 = g_1 = g_2 = a_\sigma = 1$ , and Equation (60) reduces to the familiar Boltzmann superposition integral for linear viscoelastic behavior,

$$\epsilon = D_0 \sigma + \int_0^t \Delta D(t-\tau) \frac{d\sigma}{d\tau} d\tau. \quad (60)$$

The MSP, i.e., Equation (57), is obtained from Equation (58) by setting  $g_0 = g_1 = a_\sigma = 1$  and allowing all of the nonlinearity to be contained in  $g_2$ . The stress-dependent properties have specific thermodynamic significance; changes in  $g_0$ ,  $g_1$  and  $g_2$  reflect third and higher order dependence of the Gibbs free energy on the applied stress, and  $a_\sigma$  arises from similar high-order effects in both entropy production and free energy.

A constitutive equation with strain-dependent properties has also been developed [90] and can be put in the form

$$\sigma = h_e E_e \epsilon + h_1 \int_0^t \Delta E(\rho - \rho') \frac{dh_2 \epsilon}{d\tau} d\tau \quad (61)$$

with the reduced-time,  $\rho$ , defined as

$$\rho = \rho(t) \equiv \int_0^t \frac{dt'}{a_e[\epsilon(t')]} \quad (62a)$$

and

$$\rho' = \rho'(\tau) \equiv \int_0^\tau \frac{dt'}{a_e[\epsilon(t')]} \quad (62b)$$

The strain-dependent properties are  $h_e$ ,  $n_1$ ,  $h_2$  and  $a_e$ ; variations of the first three are due to third and higher order strain effects in the Helmholtz free energy, while changes in  $a_e$  arise from similar strong strain influences in both entropy production and free energy.

Schapery's theory involves only a limited amount of experimental testing in addition to that normally required by linear theory. The determination of the nonlinear properties does not represent much in the way of additional work, especially considering the improvement over MSP when significant nonlinearity exists.

Consider the case of a creep and recovery test as shown in Figure 1, where the stress input is given by

$$\sigma = \sigma_0 [H(t) - H(t - t')]. \quad (63)$$

Equation (58) yields the creep strain

$$c = g_0 D_0 \sigma_0 + g_1 g_2 \Delta D \left( \frac{t}{a_\sigma} \right) \sigma_0, \quad 0 < t < t' \quad (64)$$

and the recovery strain

$$c_r = g_2 [\Delta D(\psi) - \Delta D(\psi - \psi')] \sigma_0, \quad t > t' \quad (65)$$

where in Equation (65)

$$\psi' = \frac{t'}{a_\sigma}; \quad \psi = \frac{t'}{a_\sigma} + t - t'. \quad (66)$$

We have already noted, e.g. Equation (50), that many metals and plastics obey a power law in time where the transient component

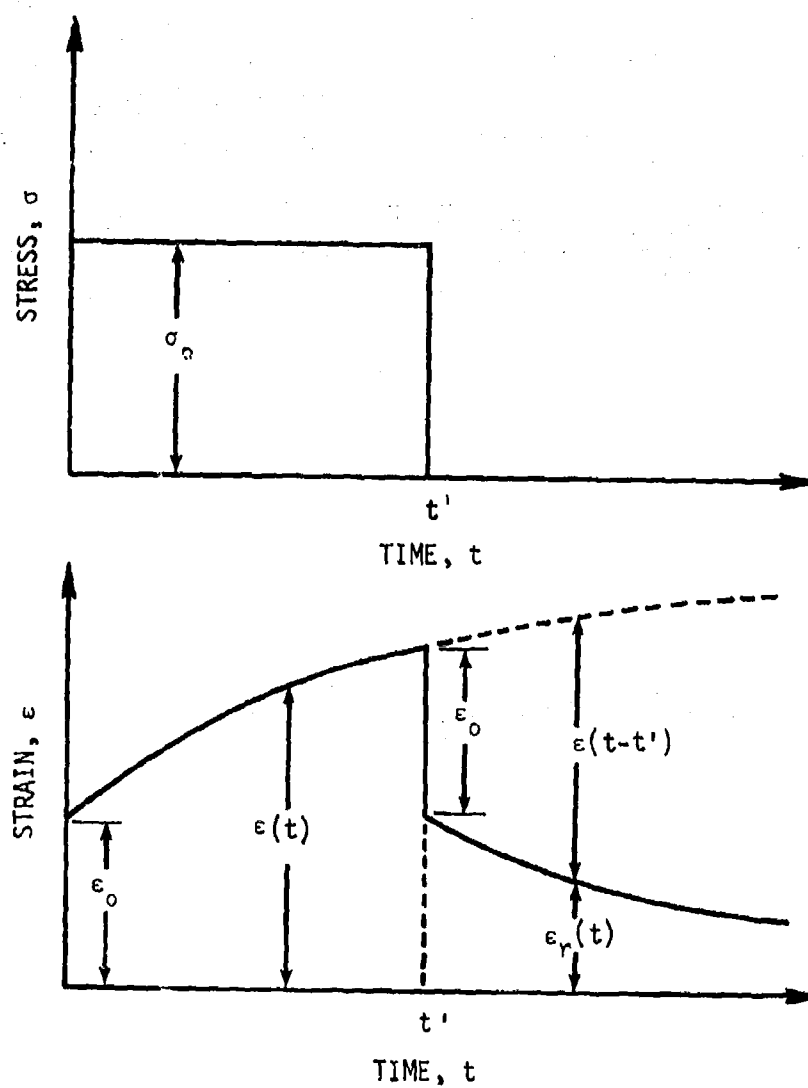


Figure 1. Relation between creep and recovery of a linear viscoelastic material.

may be represented as

$$\Delta D(\psi) = D_1 \psi^n \quad (67)$$

where  $D_1$  and  $n$  are independent of stress level and time. Rewriting Equation (64) using Equation (67) we find

$$\epsilon = g_0 D_0 \sigma_0 + \frac{g_1 g_2}{a_\sigma^n} D_1 t^n \sigma_0 \quad (68)$$

and also by a similar substitution into Equation (65),

$$\epsilon_r = \frac{\Delta \epsilon_1}{g_1} [(1 + a_\sigma \lambda)^n - (a_\sigma \lambda)^n] \quad (69)$$

where

$$\lambda = \frac{t - t'}{t'} \quad (70)$$

and

$$\Delta \epsilon_1 \equiv \epsilon(t') - \epsilon_0 = g_1 g_2 D_1 \psi'^n \sigma_0 \quad (71)$$

is the transient component of strain existing immediately before the stress is removed.

Findley and co-workers [76] have found that several of the material properties obey a hyperbolic sine function as suggested by Eyring's rate theory,

$$g_0 = \frac{\sinh \sigma/\sigma_e}{\sigma/\sigma_e} \quad (72a)$$

and

$$\frac{g_1 g_2}{a_\sigma^n} = \frac{\sinh \sigma/\sigma_m}{\sigma/\sigma_m} \quad (72b)$$

where the constants  $\sigma_e$  and  $\sigma_m$  have values which depend on the particular material. The function  $g_0$  is generally close to  $g_0 = 1$  and consequently,  $\sigma_e \gg \sigma_m$  for many materials. Schapery [35] has shown that  $a_\sigma$  contributes most of the stress dependence in Equation (72b) with  $g_1 = g_2 = 1$  for a glass fiber-reinforced phenolic composite.

### Lamina Constitutive Theory

In order to study the behavior of laminated fiber-reinforced composites, it is first necessary to establish the constitutive theory of the lamina (or laminae) using linear, elastic, anisotropic theory [24, 25]. We shall first review the basis for elastic theory before proceeding on to viscoelastic behavior and subsequent discussions on structure-property relationships. In describing the behavior of fibrous composites, it is often helpful to keep in mind the general nature of the material at hand. Figure 2 shows the surface of a typical glass fiber/epoxy lamina which has had the epoxy matrix removed by a resin-burnoff process. Evidence of some degree of fiber misalignment is clearly visible. The fiber ends are shown in Figure 3, and it can be seen that there are actually groups or bundles of fibers. This is common in glass/epoxy



Figure 2. Surface layer of a typical glass-fiber/-epoxy composite after removal of resin.



Figure 3. Glass fiber ends, or bundles after resin removal.

composites because of the fabrication technique, but generally does not exist with boron/epoxy and graphite/epoxy composites.

### Elastic Anisotropic Materials

Governing equations of anisotropic elasticity. Since the principles of anisotropic elasticity represent the foundation for the mathematical description of the elastic response of composite materials, the governing equations for this theory will be presented here.

Using the notation of Timoshenko and Goodier [136] we can denote the stresses acting on a small cubic element of the material in the following manner; the three normal stresses are  $\sigma_x$ ,  $\sigma_y$  and  $\sigma_z$  and the shearing stresses are  $\tau_{xy}$ ,  $\tau_{xz}$  and  $\tau_{yz}$  where we have assumed symmetry with respect to  $\tau_{ij} = \tau_{ji}$ . The basic equations of static equilibrium for an anisotropic body are the same as those given for an isotropic body,

$$\begin{aligned}\frac{\partial \sigma_x}{\partial x} + \frac{\partial \tau_{xy}}{\partial y} + \frac{\partial \tau_{xz}}{\partial z} + X &= 0 \\ \frac{\partial \tau_{xy}}{\partial x} + \frac{\partial \sigma_y}{\partial y} + \frac{\partial \tau_{yz}}{\partial z} + Y &= 0 \\ \frac{\partial \tau_{xz}}{\partial x} + \frac{\partial \tau_{yz}}{\partial y} + \frac{\partial \sigma_z}{\partial z} + Z &= 0\end{aligned}\tag{73}$$

where  $X$ ,  $Y$  and  $Z$  designate body forces referred to a unit volume in the directions  $x$ ,  $y$  and  $z$  respectively.



The infinitesimal linear strain-displacement relations are defined in the same way as in isotropic elasticity, namely,

$$\epsilon_x = \frac{\partial u}{\partial x} ; \quad \epsilon_y = \frac{\partial v}{\partial y} ; \quad \epsilon_z = \frac{\partial w}{\partial z} \quad (74)$$

$$\gamma_{xy} = \frac{\partial u}{\partial y} + \frac{\partial v}{\partial x} ; \quad \gamma_{yz} = \frac{\partial w}{\partial y} + \frac{\partial v}{\partial z} ; \quad \gamma_{xz} = \frac{\partial w}{\partial x} + \frac{\partial u}{\partial z} .$$

In the conventional engineering definition of strain, the components are the same as the general tensor notation, e.g. Sokolnikoff [22], except for the shear strain components which are multiplied by a factor of 2. Equations (73) and (74) are tensors of order two and, along with the boundary conditions and constitutive equations, specify the state of stress and strain at any point within the body. The transformation relations are found in the reference by Ashton et al. [2] and will not be repeated here for the sake of space.

Generalized Hooke's law. Equations (73) and (74) are insufficient to solve problems of equilibrium, motion or stability of an elastic body without defining the relations between the components of stress,  $\sigma_{ij}$ , and the strain,  $\epsilon_{ij}$ . As in Equations (8) and (9), we can formulate the relations for an elastic body to obtain

$$\sigma_{ij} = C_{ijkl} \epsilon_{kl} \quad (75a)$$

and

$$\epsilon_{ij} = S_{ijkl} \sigma_{kl} \quad (75b)$$

where the  $C_{ijkl}$  are the elastic moduli and the  $S_{ijkl}$  are the

elastic compliances. Each set of material constants defines a fourth-order tensor and possesses the symmetry discussed earlier, namely, Equations (10) and (11). As a result, for a general anisotropic material there are 21 independent elastic constants.

A contracted notation has frequently appeared in the literature. In dealing with fourth-order tensors, this notation reduces the number of indices from four to two but expands the range from three to six. In contracted notation, engineering strain is used instead of tensorial strain. Table 1 shows the correlation between normal and contracted notation where  $e_{ij}$  represents tensorial strain given by

$$e_{ij} = 1/2(u_{i,j} + u_{j,i}) \quad (76)$$

and the comma denotes differentiation. A mixed notation used by Ashton et al. [2] is also shown.

Table 1. Conversion Between Tensor, Contracted and Mixed Contracted Notations

Tensor		Contracted		Mixed [2]	
$\sigma_{11}$	$e_{11}$	$\sigma_1$	$\epsilon_1$	$\sigma_1$	$\epsilon_1$
$\sigma_{22}$	$e_{22}$	$\sigma_2$	$\epsilon_2$	$\sigma_2$	$\epsilon_2$
$\sigma_{33}$	$e_{33}$	$\sigma_3$	$\epsilon_3$	$\sigma_3$	$\epsilon_3$
$\sigma_{23}$	$2e_{23}$	$\sigma_4$	$\epsilon_4$	$\tau_{23}$	$\gamma_{23}$
$\sigma_{31}$	$2e_{31}$	$\sigma_5$	$\epsilon_5$	$\tau_{31}$	$\gamma_{31}$
$\sigma_{12}$	$2e_{12}$	$\sigma_6$	$\epsilon_6$	$\tau_{12}$	$\gamma_{12}$

After changing to the mixed contracted notation, the constitutive relation is given

$$\begin{bmatrix} \epsilon_1 \\ \epsilon_2 \\ \epsilon_3 \\ \gamma_{23} \\ \gamma_{31} \\ \gamma_{12} \end{bmatrix} = \begin{bmatrix} S_{11} & S_{12} & S_{13} & S_{14} & S_{15} & S_{16} \\ & S_{22} & S_{23} & S_{24} & S_{25} & S_{26} \\ & & S_{33} & S_{34} & S_{35} & S_{36} \\ & & & S_{44} & S_{45} & S_{46} \\ \text{Symmetric} & & & & S_{55} & S_{56} \\ & & & & & S_{66} \end{bmatrix} \begin{bmatrix} \sigma_1 \\ \sigma_2 \\ \sigma_3 \\ \tau_{23} \\ \tau_{31} \\ \tau_{12} \end{bmatrix} \quad (77)$$

where use has been made of the symmetry conditions. This represents the most general case of an anisotropic material.

Various kinds of geometric symmetry are often present, which, in turn, lead to elastic symmetry. Elastic symmetry is expressed by the property that under certain coordinate rotations the elastic moduli or compliances remained unchanged. Some of the constants  $S_{ij}$  become equal to zero and dependencies appear between other constants.

A monoclinic material has a single plane of symmetry, which by selecting a suitable reference system yields

$$\begin{bmatrix} \epsilon_1 \\ \epsilon_2 \\ \epsilon_3 \\ \gamma_{23} \\ \gamma_{31} \\ \gamma_{12} \end{bmatrix} = \begin{bmatrix} S_{11} & S_{12} & S_{13} & 0 & 0 & S_{16} \\ & S_{22} & S_{23} & 0 & 0 & S_{26} \\ & & S_{33} & 0 & 0 & S_{36} \\ & & & S_{44} & S_{45} & 0 \\ \text{Symmetric} & & & & S_{55} & 0 \\ & & & & & S_{66} \end{bmatrix} \begin{bmatrix} \sigma_1 \\ \sigma_2 \\ \sigma_3 \\ \tau_{23} \\ \tau_{31} \\ \tau_{12} \end{bmatrix} \quad (78)$$

with 13 independent elastic constants.

If an anisotropic material possesses two orthogonal planes of symmetry, the material is called orthotropic and has the following constitutive relation

$$\begin{bmatrix} \epsilon_1 \\ \epsilon_2 \\ \epsilon_3 \\ \gamma_{23} \\ \gamma_{31} \\ \gamma_{12} \end{bmatrix} = \begin{bmatrix} S_{11} & S_{12} & S_{13} & 0 & 0 & 0 \\ & S_{22} & S_{23} & 0 & 0 & 0 \\ & & S_{33} & 0 & 0 & 0 \\ & & & S_{44} & 0 & 0 \\ & \text{Symmetric} & & & S_{55} & 0 \\ & & & & & S_{66} \end{bmatrix} \begin{bmatrix} \sigma_1 \\ \sigma_2 \\ \sigma_3 \\ \tau_{23} \\ \tau_{31} \\ \tau_{12} \end{bmatrix} \quad (79)$$

with 9 independent elastic constants. This form occurs in many structural materials such as wood, plywood, fiber-reinforced rubber and plastics, etc.

When a material has a plane in which the coefficient matrix is isotropic, it is called a transversely isotropic material. If we assume that the  $y - z$  (or  $2 - 3$ ) plane is isotropic, then there is no preferred orientation in this plane and the constitutive relation becomes

$$\begin{bmatrix} \epsilon_1 \\ \epsilon_2 \\ \epsilon_3 \\ \gamma_{23} \\ \gamma_{31} \\ \gamma_{12} \end{bmatrix} = \begin{bmatrix} S_{11} & S_{12} & S_{12} & 0 & 0 & 0 \\ & S_{22} & S_{23} & 0 & 0 & 0 \\ & & S_{22} & 0 & 0 & 0 \\ & & & 2(S_{22}-S_{23}) & 0 & 0 \\ & \text{Symmetric} & & & S_{66} & 0 \\ & & & & & S_{66} \end{bmatrix} \begin{bmatrix} \sigma_1 \\ \sigma_2 \\ \sigma_3 \\ \tau_{23} \\ \tau_{31} \\ \tau_{12} \end{bmatrix} \quad (80)$$

The number of independent elastic constants for this material is 5 if we assume that  $S_{12} = S_{21}$  or 6 if complete symmetry is not assumed, e.g., Schapery [18]. The inverse constitutive relation for the transversely isotropic material is given by [5]

$$\begin{bmatrix} \sigma_1 \\ \sigma_2 \\ \sigma_3 \\ \tau_{23} \\ \tau_{31} \\ \tau_{12} \end{bmatrix} = \begin{bmatrix} C_{11} & C_{12} & C_{12} & 0 & 0 & 0 \\ & C_{22} & C_{23} & 0 & 0 & 0 \\ & & C_{22} & 0 & 0 & 0 \\ & & & \frac{(C_{22}-C_{23})}{2} & 0 & 0 \\ & \text{Symmetric} & & & C_{66} & 0 \\ & & & & & C_{66} \end{bmatrix} \begin{bmatrix} \epsilon_1 \\ \epsilon_2 \\ \epsilon_3 \\ \gamma_{23} \\ \gamma_{31} \\ \gamma_{12} \end{bmatrix} \quad (81)$$

In the case of complete material symmetry, the material is isotropic and we obtain

$$\begin{bmatrix} \epsilon_1 \\ \epsilon_2 \\ \epsilon_3 \\ \gamma_{23} \\ \gamma_{31} \\ \gamma_{12} \end{bmatrix} = \begin{bmatrix} S_{11} & S_{12} & S_{12} & 0 & 0 & 0 \\ & S_{11} & S_{12} & 0 & 0 & 0 \\ & & S_{11} & 0 & 0 & 0 \\ & & & 2(S_{11}-S_{12}) & 0 & 0 \\ & \text{Symmetric} & & & 2(S_{11}-S_{12}) & 0 \\ & & & & & 2(S_{11}-S_{12}) \end{bmatrix} \begin{bmatrix} \sigma_1 \\ \sigma_2 \\ \sigma_3 \\ \tau_{23} \\ \tau_{31} \\ \tau_{12} \end{bmatrix} \quad (82)$$

with 2 independent elastic constants.

Engineering constants usually refer to Young's moduli, Poisson's ratio and shear moduli which can be measured from simple tests. The following relations between the components of  $S_{ij}$  and

$C_{ij}$  ( $i, j = 1, 2, 6$ ) and the engineering constants can be established immediately from the nature of uniaxial and simple shear tests for the case of a transversely isotropic material:

$$\begin{aligned}
 S_{11} &= 1/E_{11} \\
 S_{22} &= S_{33} = 1/E_{22} \\
 S_{12} &= S_{13} = -\nu_{12}/E_{11} = -\nu_{21}/E_{22} \\
 S_{23} &= -\nu_{23}/E_{22} \\
 S_{44} &= 2(1 + \nu_{23})/E_{22} \\
 S_{55} &= S_{66} = 1/G_{12}
 \end{aligned} \tag{83a}$$

and

$$\begin{aligned}
 C_{11} &= (1 - \nu_{23}^2)VE_{11} \\
 C_{22} &= C_{33} = (1 - \nu_{12}\nu_{21})VE_{22} \\
 C_{12} &= C_{13} = \nu_{21}(1 + \nu_{23})VE_{11} \\
 &= \nu_{12}(1 + \nu_{23})VE_{22} \\
 C_{23} &= (\nu_{23} + \nu_{12}\nu_{21})VE_{22} \\
 C_{44} &= (C_{22} - C_{33})/2 \\
 &= (1 - \nu_{23} - 2\nu_{12}\nu_{21})VE_{22}/2 \\
 C_{55} &= C_{66} = G_{12}
 \end{aligned} \tag{83b}$$

where

$$V = [(1 + \nu_{23})(1 - \nu_{23} - 2\nu_{12}\nu_{21})]^{-1} \tag{83c}$$

Two-dimensional composites. Fibrous composites are generally used in a manner such that the stress state is essentially two-dimensional. As a result, the assumptions of plane strain or plane stress are often invoked. We shall review the constitutive relations given in Equations (80) and (81) for the transversely isotropic material in terms of plane stress assumptions. This state exists more often than most since the composite generally is a thin laminated structure used in plates or shells.

The plane stress problem can be formulated by assuming

$$\sigma_3 = \tau_{23} = \tau_{31} = 0 \quad (84)$$

and we note that

$$\gamma_{23} = \gamma_{31} = 0 \quad (85)$$

as a result of Equation (84). Equation (80) now becomes

$$\begin{bmatrix} \epsilon_1 \\ \epsilon_2 \\ \gamma_{12} \end{bmatrix} = \begin{bmatrix} S_{11} & S_{12} & 0 \\ S_{12} & S_{22} & 0 \\ 0 & 0 & S_{66} \end{bmatrix} \begin{bmatrix} \sigma_1 \\ \sigma_2 \\ \tau_{12} \end{bmatrix} \quad (86a)$$

and

$$\begin{bmatrix} \sigma_1 \\ \sigma_2 \\ \tau_{12} \end{bmatrix} = \begin{bmatrix} Q_{11} & Q_{12} & 0 \\ Q_{12} & Q_{22} & 0 \\ 0 & 0 & Q_{66} \end{bmatrix} \begin{bmatrix} \epsilon_1 \\ \epsilon_2 \\ \gamma_{12} \end{bmatrix} \quad (86b)$$

Thus, for plane stress, the  $S_{ij}$  remains the same as a three-dimensional material, whereas the  $C_{ij}$  must be replaced by a "reduced stiffness" denoted as the  $Q_{ij}$ . The  $Q_{ij}$  ( $i, j = 1, 2, 6$ ) are given by

$$Q_{ij} = C_{ij} - \frac{C_{i3}C_{j3}}{C_{33}} \quad (87a)$$

where

$$\begin{aligned} Q_{11} &= E_{11}/(1 - \nu_{12}\nu_{21}) \\ Q_{22} &= E_{22}/(1 - \nu_{12}\nu_{21}) \\ Q_{12} &= \nu_{21}E_{11}/(1 - \nu_{12}\nu_{21}) = \nu_{12}E_{22}/(1 - \nu_{12}\nu_{21}) \\ Q_{56} &= G_{12} \end{aligned} \quad (87b)$$

This is the constitutive relationship for a specialy orthotropic material in a plane stress state. It is called specially orthotropic when the lamina principal axes (1, 2) coincide with the reference axes. When the material axes are referred to any other direction (x, y) as in Figure 4, the constitutive relations must be transformed accordingly, e.g. Ashton et al. [2],

$$\begin{bmatrix} \epsilon_x \\ \epsilon_y \\ \gamma_{xy} \end{bmatrix} = \begin{bmatrix} S_{11}^l & S_{12}^l & S_{16}^l \\ S_{12}^l & S_{22}^l & S_{26}^l \\ S_{16}^l & S_{26}^l & S_{66}^l \end{bmatrix} \begin{bmatrix} \sigma_x \\ \sigma_y \\ \tau_{xy} \end{bmatrix} \quad (88a)$$

and



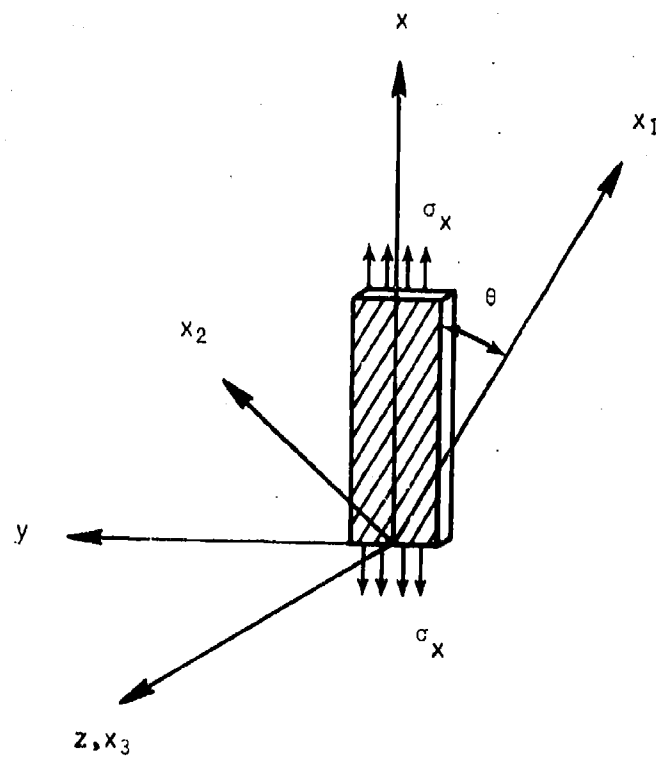


Figure 4. Anisotropic tensile specimen.

$$\begin{bmatrix} \sigma_x \\ \sigma_y \\ \tau_{xy} \end{bmatrix} = \begin{bmatrix} Q'_{11} & Q'_{12} & Q'_{16} \\ Q'_{12} & Q'_{22} & Q'_{26} \\ Q'_{16} & Q'_{26} & Q'_{66} \end{bmatrix} \begin{bmatrix} \epsilon_x \\ \epsilon_y \\ \gamma_{xy} \end{bmatrix} \quad (88b)$$

where the  $S_{ij}$  and  $Q_{ij}$  matrices are now fully populated and the  $S'_{ij}$  and  $Q'_{ij}$  are the transformed compliances and stiffnesses, respectively.  $S'_{ij}$  and  $Q'_{ij}$  are related to the orthotropic lamina properties  $S_{ij}$  and  $Q_{ij}$  and the angle of orientation of the lamina,  $\theta$ . The transformation equations are found in the reference by Ashton et al. [2] and are repeated here for convenience,

$$\begin{aligned} S'_{11} &= S_{11}\cos^4\theta + (2S_{12}+S_{66})\sin^2\theta\cos^2\theta + S_{22}\sin^4\theta \\ S'_{22} &= S_{11}\sin^4\theta + (2S_{12}+S_{66})\sin^2\theta\cos^2\theta + S_{22}\cos^4\theta \\ S'_{12} &= S_{12}(\sin^4\theta+\cos^4\theta) + (S_{11}+S_{22}-S_{66})\sin^2\theta\cos^2\theta \\ S'_{66} &= 2(2S_{11}+2S_{22}-4S_{12}-S_{66})\sin^2\theta\cos^2\theta + S_{66}(\sin^4\theta+\cos^4\theta) \\ S'_{16} &= 2(2S_{11}-2S_{12}-S_{66})\sin\theta\cos^3\theta - 2(2S_{22}-2S_{12}-S_{66})\sin^3\theta\cos\theta \\ S'_{26} &= 2(2S_{11}-2S_{12}-S_{66})\sin^3\theta\cos\theta - 2(2S_{22}-2S_{12}-S_{66})\sin\theta\cos^3\theta \end{aligned} \quad (89a)$$

and

$$\begin{aligned} Q'_{11} &= Q_{11}\cos^4\theta + 2(Q_{12}+2Q_{66})\sin^2\theta\cos^2\theta + Q_{22}\sin^4\theta \\ Q'_{22} &= Q_{11}\sin^4\theta + 2(Q_{12}+2Q_{66})\sin^2\theta\cos^2\theta + Q_{22}\cos^4\theta \\ Q'_{12} &= (Q_{11}+Q_{22}-4Q_{66})\sin^2\theta\cos^2\theta + Q_{12}(\sin^4\theta+\cos^4\theta) \\ Q'_{66} &= (Q_{11}+Q_{22}-2Q_{12}-2Q_{66})\sin^2\theta\cos^2\theta + Q_{66}(\sin^4\theta+\cos^4\theta) \\ Q'_{16} &= (Q_{11}-Q_{12}-2Q_{66})\sin\theta\cos^3\theta + (Q_{12}-Q_{22}+2Q_{66})\sin^3\theta\cos\theta \\ Q'_{26} &= (Q_{11}-Q_{12}-2Q_{66})\sin^3\theta\cos\theta + (Q_{12}-Q_{22}+2Q_{66})\sin\theta\cos^3\theta \end{aligned} \quad (89b)$$

### Viscoelastic Composite Material Behavior

The fibers and matrix materials used to form fiber-reinforced composites are usually assumed by most investigators to exhibit linear elastic behavior until they fail. In many cases, the matrix material is actually a viscoelastic material which will exhibit a significant amount of time dependence within certain ranges of stress and temperature. However, it has only been within the past decade that serious attention has been given to the viscoelastic behavior of fibrous composites.

The works of Hashin [34, 137], Schapery [9, 18, 32] and Halpin [11, 33] have done much to bring out the significance of anisotropic viscoelasticity. In several recent literature surveys on fiber-reinforced plastic composites by Beckwith et al. [6-8], it is evident that these effects cannot be neglected in many design situations. Experimental studies on the mechanical behavior of fibrous composites have been reported by Hanson [138], Bott and Barker [139], Delmonte [140], Zvonar and Tamchyna [141], Martirosian [39-42] and Ogibalov and Tiuneeva [36, 37]. Some of the work done in the Soviet Union, namely that of Antans and Skudra [142, 143], Bulavs and Skudra [144] and Smotrin and Chebanov [145], have attempted to model the viscoelastic behavior of glass/epoxy composites using simple spring and dashpot models consisting of only a few elements typical of a Maxwell or Voigt model [147]. Perhaps the best documented work on reinforced polymers done in the Soviet

Union is contained in Rabinovich [146] and Tarnopolskiy and Skudra [147]. Both references contain a vast amount of experimental and theoretical research on glass and cotton fiber-reinforced composites. Time and temperature dependence are treated by using spring and dashpot models. In most cases it is difficult to assess the accuracy of these models since their data do not cover a very long time scale and is almost always plotted against real time rather than log time. Bryzgalin [148, 149] used the modified superposition principle to predict the creep behavior of glass/-epoxy plates, however, his work is not typical of the main approach used by Soviet researchers, namely, mechanical modeling.

Kaye and Saunders [150] investigated the creep behavior of a glass/epoxy laminate in the linear viscoelastic range and over a small temperature range. They were not able to ascertain the symmetry of the creep compliance, i.e.,  $S_{12} = S_{21}$ , as a result of experimental limitations. Cessna [151], who studied a glass/-polypropylene composite and Findley and Worley [152, 153], who studied a glass fabric/resin composite both used the activation energy theory of Eyring [154] and the hyperbolic sine law to describe the creep behavior, e.g. Equation (74).

Schapery [18, 32] has recently reviewed the use of viscoelastic analysis of fiber-reinforced composite materials and comments on the techniques required to characterize the material in terms of linear and nonlinear viscoelastic behavior. Sims [29] and McQuillan [155]

have also recently applied viscoelastic theory to composite materials using several approximate methods developed earlier by Schapery [18, 32].

Linear constitutive theory. Throughout this discussion we shall limit ourselves to the viscoelastic behavior of an orthotropic material in a state of plane stress, viz. Equations (86) and (88). However, it should be kept in mind that the general, three-dimensional state of stress (strain) can be described in a similar manner for a linear viscoelastic anisotropic material by Equations (8) and (9),

$$\sigma_{ij} = \int_{-\infty}^t C_{ijkl}(t - \tau) \frac{\partial \epsilon_{kl}}{\partial \tau} d\tau \quad (8)$$

and

$$\epsilon_{ij} = \int_{-\infty}^t S_{ijkl}(t - \tau) \frac{\partial \sigma_{kl}}{\partial \tau} d\tau. \quad (9)$$

In an analogous fashion we can rewrite Equation (86a) as

$$\begin{aligned} \epsilon_1 &= \int_0^t S_{11}(t - \tau) \frac{\partial \sigma_1}{\partial \tau} d\tau + \int_0^t S_{12}(t - \tau) \frac{\partial \sigma_2}{\partial \tau} d\tau \\ \epsilon_2 &= \int_0^t S_{12}(t - \tau) \frac{\partial \sigma_1}{\partial \tau} d\tau + \int_0^t S_{22}(t - \tau) \frac{\partial \sigma_2}{\partial \tau} d\tau \\ \gamma_{12} &= \int_0^t S_{66}(t - \tau) \frac{\partial \tau_{12}}{\partial \tau} d\tau \end{aligned} \quad (90)$$

If the stress inputs are of the type  $\sigma_{ij} = \sigma'_{ij}H(t)$ , i.e., creep test, then we obtain

$$\begin{aligned}\epsilon_1 &= S_{11}(t)\sigma_1 + S_{12}(t)\sigma_2 \\ \epsilon_2 &= S_{12}(t)\sigma_1 + S_{22}(t)\sigma_2 \\ \gamma_{12} &= S_{66}(t)\tau_{12}\end{aligned}\tag{91}$$

where all of the stresses are time-wise constant. If the lamina coordinate system is referred to an arbitrary set of coordinates  $(x, y)$  which are not aligned with the principal material directions  $(1, 2)$  then Equation (88a) becomes

$$\begin{aligned}\epsilon_x &= \int_0^t S'_{11}(t-\tau) \frac{\partial \sigma_x}{\partial \tau} d\tau + \int_0^t S'_{12}(t-\tau) \frac{\partial \sigma_y}{\partial \tau} d\tau + \int_0^t S'_{16}(t-\tau) \frac{\partial \tau_{xy}}{\partial \tau} d\tau \\ \epsilon_y &= \int_0^t S'_{12}(t-\tau) \frac{\partial \sigma_x}{\partial \tau} d\tau + \int_0^t S'_{22}(t-\tau) \frac{\partial \sigma_y}{\partial \tau} d\tau + \int_0^t S'_{26}(t-\tau) \frac{\partial \tau_{xy}}{\partial \tau} d\tau \\ \gamma_{xy} &= \int_0^t S'_{16}(t-\tau) \frac{\partial \sigma_x}{\partial \tau} d\tau + \int_0^t S'_{26}(t-\tau) \frac{\partial \sigma_y}{\partial \tau} d\tau + \int_0^t S'_{66}(t-\tau) \frac{\partial \tau_{xy}}{\partial \tau} d\tau\end{aligned}\tag{92}$$

where the  $S'_{ij}$  are related to the  $S_{ij}$  compliances in the same manner as given by Equation (89a) except that they are time-dependent. As in Equation (91), when the stress inputs are of the type  $\sigma_{ij} = \sigma'_{ij}H(t)$ , then we have

$$\begin{aligned}
 \epsilon_x &= S_{11}'\sigma_x + S_{12}'\sigma_y + S_{16}'\tau_{xy} \\
 \epsilon_y &= S_{12}'\sigma_x + S_{22}'\sigma_y + S_{26}'\tau_{xy} \\
 \gamma_{xy} &= S_{16}'\sigma_x + S_{26}'\sigma_y + S_{66}'\tau_{xy}
 \end{aligned}
 \tag{93}$$

The solution of the field equations, e.g., Equations (73) and (74), along with any boundary conditions and either Equation (90) or (92) for isothermal conditions can be accomplished with the use of Laplace transforms in order to reduce the problem to an equivalent elasticity problem. This analogy is called the "correspondence principle" and is limited to problems in which:

1. The boundaries do not move except by infinitesimal displacements,
2. the stress boundary conditions do not change to displacement boundary conditions with time, or vice-versa, and
3. the differential equations relating stress and strain have time independent coefficients. If the stress-strain relations are characterized by integral relations, then the integral relations must be of the convolution type.

This principle was shown by Lee [156] for isotropic media, and by Biot [157] for anisotropic materials. Unfortunately conventional Laplace transform inversion is often not feasible because the elastic solution is known only numerically, or is so analytically

complex that standard methods are not adequate [18]. Schapery [158] proposed two methods of transform inversion, the collocation method and the direct method.

Another procedure which has been used very extensively is the "quasi-elastic" method of analysis proposed by Schapery [159]. The method is easy to use in that transform inversion is avoided. In the most general form, the method is equivalent to approximating the constitutive Equations (8) and (9) by

$$\sigma_{ij}(t) = C_{ijk\ell}(t)\epsilon_{k\ell}(t) \quad (94)$$

and

$$\epsilon_{ij}(t) = S_{ijk\ell}(t)\sigma_{k\ell}(t) \quad (95)$$

where we have assumed

$$S_{ijk\ell}(t) = [C_{ijk\ell}(t)]^{-1}. \quad (96)$$

This procedure has been applied successfully by Schapery [32] and Sims [29] to fibrous composites.

In terms of general stress and strain inputs, Equations (90) and (92) may be rewritten as

$$\begin{aligned} \epsilon_1(t) &= S_{11}(t)\sigma_1(t) + S_{12}(t)\sigma_2(t) \\ \epsilon_2(t) &= S_{12}(t)\sigma_1(t) + S_{22}(t)\sigma_2(t) \\ \gamma_{12}(t) &= S_{66}(t)\tau_{12}(t) \end{aligned} \quad (97)$$



and

$$\begin{aligned}\epsilon_x(t) &\approx S'_{11}(t)\sigma_x(t) + S'_{12}(t)\sigma_y(t) + S'_{16}(t)\tau_{xy}(t) \\ \epsilon_y(t) &\approx S'_{12}(t)\sigma_x(t) + S'_{22}(t)\sigma_y(t) + S'_{26}(t)\tau_{xy}(t) \\ \gamma_{xy}(t) &\approx S'_{16}(t)\sigma_x(t) + S'_{26}(t)\sigma_y(t) + S'_{66}(t)\tau_{xy}(t)\end{aligned}\quad (98)$$

Three-dimensional, nonisothermal constitutive equations for an anisotropic TSM have already been given as

$$\sigma_{ij} = \int_0^t C_{ijkl}(\xi - \xi') \frac{\partial \epsilon_{kl}}{\partial \tau} d\tau \quad (19b)$$

and

$$\epsilon_{ij} = \int_0^t S_{ijkl}(\xi - \xi') \frac{\partial \sigma_{kl}}{\partial \tau} d\tau \quad (28b)$$

where  $\xi$  and  $\xi'$  are defined by Equation (20). The correspondence principle exists for a TSM if the temperature is spacewise constant; however, it may be transient as long as the first condition is satisfied. When the temperature is both transient and spacewise nonuniform, then the correspondence principle does not exist. When the material is a TCM of the form of Equation (37), then the correspondence principle is similar to that for a TSM where all the stresses are divided by  $a_G$ . The same conditions required by a TSM must be met by the TCM [18].

If one (or more) phases of the composite is of the type TCM-2, then a correspondence principle does not exist under transient

temperatures. The overall composite behavior will generally be more complex than TCM-2 under these conditions. Schapery [18] discusses several other aspects of nonisothermal behavior of composite materials in terms of predicting effective properties.

Nonlinear constitutive theory. We shall follow the previous definition of material nonlinearity, i.e., failure to satisfy homogeneity and/or superposition. In some fibrous composites one important source of nonlinearity appears to be the growth of cracks as part of the phenomena we shall call microstructural damage. These cracks are generally a result of the fabrication process and the mismatch in physical and mechanical properties of the matrix and fiber. The latter problem leads to significant thermal, or residual, stress in the matrix material surrounding the fibers [160] and is further aggravated by the high volume fraction of fibers which creates triaxial stresses between the fibers. This damage and consequent nonlinearity may be quite significant at relatively small strains (stresses) compared to ultimate values. In particulate composites, e.g., solid propellant, an advanced stage of crack growth causes a large amount of measurable dilatation [161, 162]. Studies on several glass/epoxy and graphite/-epoxy composites by Beckwith [163] at room temperature on both laminae and laminates show no detectable (greater than 0.1% volume change) dilatation prior to ultimate failure.

Lou and Schapery [9] and Schapery [35] have reported reversible

nonlinearities in glass/epoxy composites due primarily to highly stress-dependent viscosity behavior. Their experiments were conducted after mechanically conditioning the specimens until crack growth effects reached a steady state, i.e., damage reached a constant. No attempt has been made to date to explicitly predict time-dependent microstructural damage using experimental data from fibrous composite materials.

Figure 5a shows the forward dome of a typical solid rocket motor case made from a glass/epoxy composite. A closeup view (Figure 5b) shows the winding pattern and the light areas represent regions of visible damage after the pressure vessel has been loaded just short of failure. The light areas represent severe damage as evidenced by very fine cracks in the epoxy resin, limited fiber fracture, and delamination. The fiber fracture, which is presumed to occur only in areas where the local stress is close to the ultimate fiber strength, is shown in Figure 6 for a graphite/epoxy composite [12]. Matrix failure and interfacial adhesive failure is clearly visible in another region of the same composite as shown in Figure 7. Microstructural damage of this type is not always as severe as shown here; however, the same mechanisms are thought to exist at very low stress (strain) levels within most structural composites in use today.

Perhaps at this point we should recognize that there are additional classifications of viscoelastic materials and divide

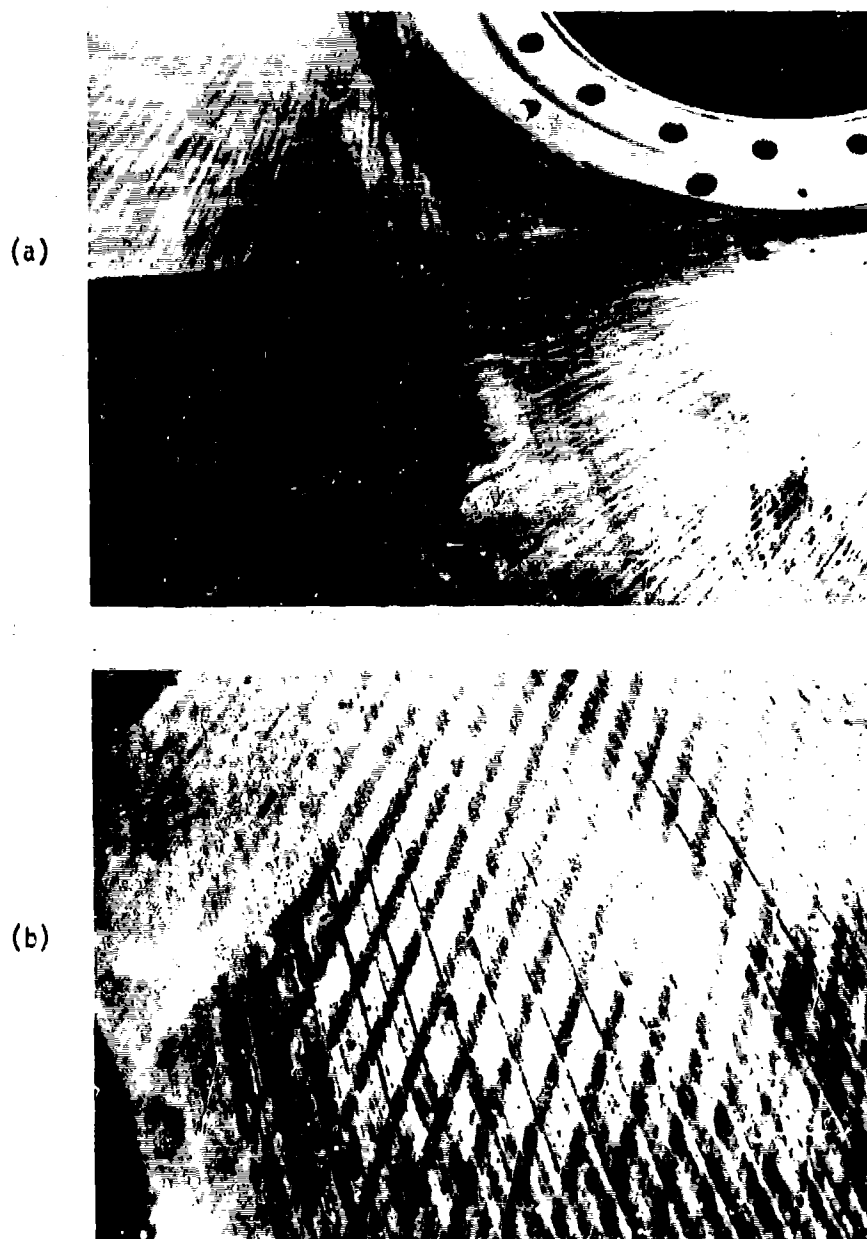


Figure 5. Section of solid rocket motor case (a) showing winding pattern and (b) hydrotest damage.

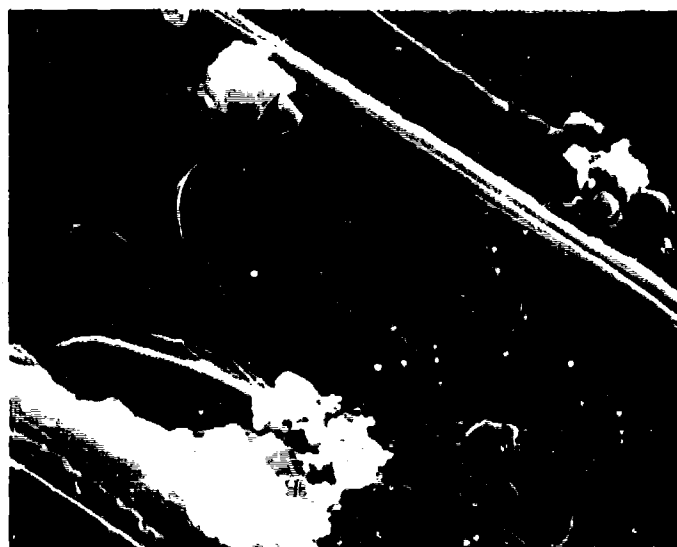


Figure 6. Evidence of fiber fracture in graphite/-epoxy composite.



Figure 7. Matrix failure and interfacial adhesive failure in the same composite.

them into categories of fading memory and nonfading or permanent memory.

1. Fading memory viscoelastic theories are valid for viscoelastic materials whose time effects are reversible, such as those caused by internal viscosity effects.
2. Permanent memory viscoelastic theories are required for viscoelastic materials possessing additional time effects or memory phenomena not caused by internal viscosity and are more permanent in nature, e.g., microstructural damage.

A single-integral, fading memory representation was used by Lou and Schapery [9] to characterize a glass/epoxy composite in the absence of significant crack growth and similarly by Schapery [35] on a glass/phenolic fabric composite. Equation (60), along with Equations (61), (69) and (74b), were used to describe the material behavior. It was found that the nonlinear, uniaxial creep compliances obeyed a power law in time with the exponent being independent of fiber orientation and stress level. The nonlinear material properties, e.g.,  $g_0$ ,  $g_1$ ,  $g_2$  and  $a_g$ , depended mainly on the average octahedral shear stress in the matrix. They were able to determine the principal creep compliances, e.g.,  $S_{11}(t)$ ,  $S_{22}(t)$  and  $S_{12}(t)$ , directly from experiments and calculated  $S_{66}(t)$  using fourth-order tensor transformations and additional creep

compliance data. In [164], some preliminary work was done to relate the viscoelastic behavior at various temperatures using the Arrhenius form of  $a_T$  given by Equation (24). Additional work done on a graphite/epoxy in [12] gave similar results, indicating good agreement when  $T < T_g$ . The main conclusion appears to be that the single-integral, fading memory representation used in [9] describes the material behavior only in the absence of time-dependent microstructural damage. A constitutive theory which contains permanent memory effects is needed to describe the behavior of fibrous composites which generally exhibit time-dependent crack growth. There are currently two approaches to modeling this type of behavior; the theories put forth by Farris [44, 58, 128, 129, 161, 162, 165, 166] and those by Schapery [12, 19, 20].

Fitzgerald and Farris [44] proposed the theory originally for filled elastomers such as solid propellant. Farris successfully applied the theory under isothermal [44, 165] and, subsequently, nonisothermal [58] conditions. Farris based his theory on a linear cumulative damage model (viz. Miner's law) for the failing microstructure using the form

$$D'(t) = \sum_{k=1}^n (t_k/t_{fk}) \quad (99)$$

where  $D'(t)$  is the accumulating damage,  $t_k$  is the time the sample spent at strain level  $\epsilon_k$  and  $t_{fk}$  is the time-to-failure for the

constant history of strain level  $\epsilon_k$ . An important parameter in this theory which results from Equation (99) is the so-called  $p^{\text{th}}$  order Lebesgue norm of strain,

$$||\epsilon||_p \equiv \left[ \int_0^t |\epsilon(t')|^p dt' \right]^{1/p} \quad (100)$$

where  $|\epsilon|$  is the absolute value of strain. By judicious selection of the Lebesgue norm functions, one is able to satisfy the proportionality (homogeneity) condition, but not superposition. This behavior is similar to that seen in fiber-reinforced composites except that stress, rather than strain, is the predominant factor. Motivated by these results and his own earlier work, Schapery et al. [12, 20] used fracture mechanics, which resulted in Lebesgue norms of stress, to model the microstructural damage in composite materials.

The basic mathematical concepts which describe the crack growth behavior in viscoelastic media are presented in [19]. Using these concepts, Schapery [20] developed the constitutive equations for particulate composites, viz. solid propellant, with microstructural damage. The theory was developed to predict microstructural damage effects during the initial stages of crack growth, prior to extensive dilatation within the propellant. It was assumed that the cracks propagated in an "opening mode" and that an initial distribution of cracks existed within the matrix, or



possibly between the matrix and filler particles. It was further assumed that during most of the time required for local fracture, the creep compliance is given by the power law,

$$D_m = D_1 (t/a_T)^n \quad (101)$$

where  $D_1$  and  $n$  are material constants. Fracture mechanics predicted Lebesgue norms of stress,  $||\sigma||_p$ , rather than strain, appear in the general constitutive theory.

If linearity for a fixed crack length is assumed, then the total strain is the sum of the strain due to the externally applied stress acting on the undamaged composite material plus the strain due to microcracking. The resultant constitutive relation is given by

$$\epsilon = \int_0^{\xi} D_m(\xi - \xi') \frac{d}{d\xi'} \left\{ \sigma \left[ 1 + \int_{g'}^{\infty} G(g) dg \right] \right\} d\xi' \quad (102)$$

where  $\xi$  and  $\xi'$  take on the normal definitions for reduced-time, viz. Equation (20),  $G(g)$  is a distribution function which reflects the distribution of the crack lengths and stress concentrations in the matrix, and

$$g' \equiv g(\xi') = \left\{ \int_0^{\xi'} M^{1/n} \sigma^n d\xi \right\}^{-1/q} \quad (103)$$

where

$$g(\xi') = \frac{1}{||\sigma||_{Mq}}. \quad (104)$$

The exponent  $q$  is given

$$q \equiv 2(1 + 1/n) \quad (105)$$

and  $||\sigma||_{Mq}$  is a "weighted" Lebesgue norm where  $M = M(\xi)$  accounts for aging and rehealing effects. In the absence of these effects  $M$  is unity.

Equation (102) may be rewritten as

$$\epsilon = \int_0^{\xi} D_m(\xi - \xi') \frac{d\sigma_{ef}}{d\xi'} d\xi' \quad (106)$$

where  $\sigma_{ef}$  is the "effective stress" seen by the material and is given by

$$\sigma_{ef} = \sigma \left[ 1 + \int_{g'}^{\infty} G(g) dg \right] \quad (107a)$$

or,

$$\sigma_{ef} = \sigma \left[ 1 + f ||\sigma|| \right]. \quad (107b)$$

The effective stress exhibits both time and temperature dependence in the usual manner but also is stress-dependent through the Lebesgue norm function represented by  $f ||\sigma||$ . It may also be convenient to work with the inverse relationship given by

$$\sigma_{ef} = \int_0^{\epsilon} E_m (\epsilon - \epsilon') \frac{d\epsilon}{d\epsilon'} d\epsilon' \quad (108)$$

The constitutive theory represented by Equations (106) and (108) was developed under the assumption that the particles are rigid relative to the matrix. Therefore, the crack growth is governed by the stress intensity factor and fracture energy associated with the matrix material. The theory represents the condition of cracks which are initially isolated from each other and do not interact.

It has been found that the cracks actually interact in some materials depending on the constituent material properties. Studies using a scanning electron microscope on graphite/epoxy and glass/epoxy composites show that a crack arrest mechanism is present under certain loading conditions [12]. Figures 8 and 9 show the crack arrest mechanism and the degree of fiber bending present in an E-glass/epoxy laminae which has been subject to a stress normal to the fibers.

Motivated by this possibility, Schapery et al. [12] studied the effects of fiber bending on the overall strain energy release rate as a function of the loading condition and composite properties. The energy associated with matrix stretching was ultimately neglected and the effects of fiber bending and shear stress were used to model the crack growth. Equation (101) was again used to model the matrix creep compliance and the distribution function representing

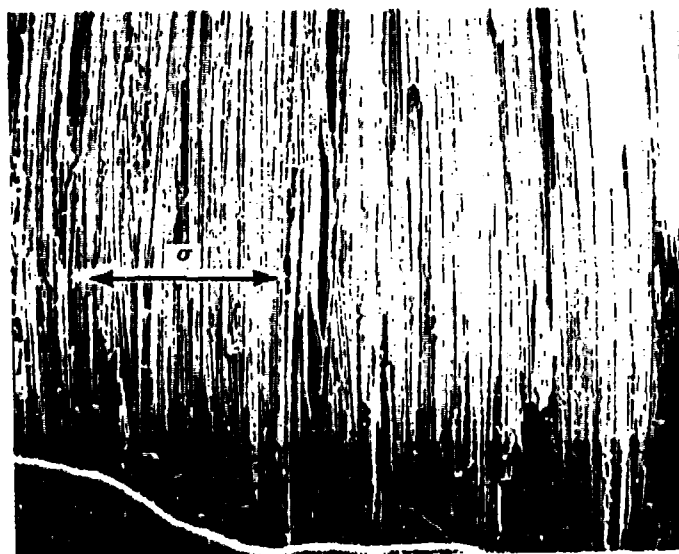


Figure 8. Crack arrest mechanism in an E-glass/epoxy composite subject to tensile stress [12].



Figure 9. Enlarged view (220X) showing presence of significant fiber bending [12].

crack lengths and stress concentrations was assumed, as an example, to be

$$F_1 = K_1 r^{-p} \quad (108)$$

where  $K_1$  and  $p$  are positive constants with  $p > 1$ . The model allows for the possibility of crack arrest, a phenomenon which is clearly evident in the behavior of multiple cycle creep and recovery tests on fibrous composites [12, 167] in which most of the damage is done during the first loading cycle.

The principle compliance parallel to the fibers,  $S_{11}$ , and the Poisson's ratio for loading in the fiber direction will not be affected by cracks parallel to the fibers. Therefore, as long as appreciable fiber failure does not occur, the principal stress-strain equations are identical to those for linear viscoelasticity except for additional terms of  $\Delta\gamma_{12}$  and  $\Delta\epsilon_2$ . Hence, the principal relations are

$$\begin{aligned} \epsilon_1 &= \int_0^t S_{11}(t-\tau) \frac{\partial \sigma_1}{\partial \tau} d\tau + \int_0^t S_{12}(t-\tau) \frac{\partial \sigma_2}{\partial \tau} d\tau \\ \epsilon_2 &= \int_0^t S_{12}(t-\tau) \frac{\partial \sigma_1}{\partial \tau} d\tau + \int_0^t S_{22}(t-\tau) \frac{\partial \sigma_2}{\partial \tau} d\tau + \Delta\epsilon_2 \\ \gamma_{12} &= \int_0^t S_{66}(t-\tau) \frac{\partial \tau_{12}}{\partial \tau} d\tau + \Delta\gamma_{12} \end{aligned} \quad (109)$$

As an example [12], we can rewrite the shear strain as

$$\gamma_{12} = \int_0^t S_{66}^*(t-\tau) \frac{\partial \tau_{12}}{\partial \tau} d\tau \quad (110)$$

where  $S_{66}^*$  is the principal nonlinear compliance, and is given by

$$S_{66}^* = S_{66} + \frac{D_m K_1}{(p-1)(2-p)} \left\{ \frac{4A \sin^4 \theta + B \sin^2 2\theta}{4r} \right\}^{\frac{2-p}{n}} \sigma_0^{\frac{4-2p}{n}} \left( \frac{t}{a_T} \right)^{2-p} \quad (111)$$

for the case of a uniaxial creep test where  $\sigma = \sigma_0 H(t)$ . In Equation (111),  $r$  is the fracture energy of the matrix, and  $A$  and  $B$  are constants which depend on the constituent properties and fracture properties. Their explicit definition is given by Equation (39) of [12].

Neither theory, Equations (102-108) or Equations (109-111), has been compared with a specific fibrous composite material although they appear to be general enough to predict the types of nonlinearity presently observed.

#### Structure-Property Relationships

Micromechanics deals with the mechanical interaction between the constituent materials of a composite. The study of micromechanics of composite materials has received considerable attention since the early 1960's in an attempt to relate constituent properties to the overall, macromechanical response of a single

ply, or lamina. We have already shown, viz., Equation (86), that the constitutive relation for an orthotropic material in a state of plane stress depends on the determination of four compliances, namely,  $S_{11}$ ,  $S_{12}$ ,  $S_{22}$ , and  $S_{66}$ . It has also been noted in Equation (83) that these material properties can be related to functions of the engineering constants  $E_{11}$ ,  $E_{22}$ ,  $G_{12}$  and either  $\nu_{12}$  or  $\nu_{21}$ . The latter two are related through the symmetry condition that requires

$$\nu_{12}E_{22} = \nu_{21}E_{11} \quad (112)$$

so that there are again only four independent material constants to be determined. As we noted earlier, the viscoelastic nature of the polymeric matrix also makes these properties time and temperature dependent, with  $G_{12}$  (or  $S_{66}$ ) generally exhibiting the predominant viscoelastic effects.

Schapery [18] discusses the measurement of the principal compliances experimentally using off-angle unidirectional composites and fourth-order tensor transformations. The direct measurement of  $S_{11}$ ,  $S_{22}$ ,  $S_{12}$  and  $S_{66}$  falls into the classification of macro-mechanics where the ply or lamina is treated as a single material with anisotropic properties, neglecting the overall constitution of the lamina. Several experimental techniques have been proposed for the measurement of these properties directly or indirectly [2, 9, 18, 33, 168].

In the subsections which follow we shall discuss some of the aspects of current micromechanics theory, paying particular attention to the relationship between the constituent properties and the overall response observed experimentally.

Basic assumptions. There are several basic assumptions which are common to almost all of the theories presently in use today with regard to elastic behavior, namely:

1. The ply is macroscopically homogeneous, linearly elastic and orthotropic.
2. The fibers are linearly elastic and homogeneous.
3. The matrix is linearly elastic and homogeneous.
4. Both the fiber and matrix are free of voids.
5. There is complete bonding at the interface of the constituents and there is no transitional region between them.
6. The fibers are (a) regularly spaced and (b) aligned.
7. In-situ mechanical properties are the same as the properties of the constituents when not in the composite.

In general, it is realized that the lamina often exhibits behavior which is nonlinearly viscoelastic, particularly at high stress levels and temperatures. There are, of course, a great number of possible deviations from these assumptions and the net result is an abundance of theories based on relaxing one or more



of the basic assumptions.

Prediction of effective properties. We shall not attempt to critique the various micromechanics theories since time and space do not permit even a minimal treatment. The interested reader is referred to several excellent critiques of the area given by Chamis and Sendeckyj [169], Ashton et al. [2], Pagano and Tsai [170] and others [171, 172]. The various theories which have been proposed to date can be classified as follows: netting analysis, mechanics of materials, self-consistent models, variational methods, exact (elasticity) methods, statistical methods, discrete element methods and semi-empirical approaches. An exhaustive bibliography of many of these theories can be found in [6-8, 169] and will, therefore, not be repeated here.

The prediction of the longitudinal composite properties, viz.,  $E_{11}$  and  $\nu_{12}$ , has generally proceeded along the classical lines of parallel element models [137, 173-176]. The longitudinal composite modulus,  $E_{11}$ , is given by [137, 174]

$$E_{11} = v_f E_f + v_m E_m + v_m v_f G_m \frac{\left[ \frac{G_f}{K_f} - \frac{G_m}{K_m} \right]^2}{\left[ \frac{v_m G_m}{K_f} + \frac{v_f G_m}{K_m} + 1 \right]} \quad (113)$$

where  $E$  is the modulus of elasticity,  $G$  is the shear modulus,  $K$  is the plane strain bulk modulus,  $v$  is the volume fraction, and the subscripts  $f$  and  $m$  signify the fiber and matrix respectively.

Hill [174] demonstrated that  $E_{11}$  is actually bounded from below by the "rule of mixtures" and that the last term can be neglected such that

$$E_{11} = v_f E_f + v_m E_m \quad (114)$$

Tsai [172] allowed for the possibility for fiber misalignment by applying a correction factor to Equation (114)

$$E_{11} = k(v_f E_f + v_m E_m) \quad (115)$$

however, the value of  $k$  is often very close to unity for present composites considering the fabrication techniques used.

The major Poisson's ratio,  $v_{12}$ , was also derived in a form similar to Equation (113), namely, [137, 174]

$$v_{12} = v_f v_f + v_m v_m + \frac{v_m v_f (v_f - v_m) \left[ \frac{1}{K_m} - \frac{1}{K_f} \right]}{\left[ \frac{v_m}{K_f} + \frac{v_f}{K_m} + \frac{1}{G_m} \right]} \quad (116)$$

where  $v$  is Poisson's ratio and the other symbols are the same as previously defined. Again, neglecting the last term we have

$$v_{12} = v_f v_f + v_m v_m \quad (117)$$

Most experimental evidence indicates that the "rule of mixtures" representation, viz., Equations (114) and (117), are quite accurate for the calculation of  $E_{11}$  and  $v_{12}$  respectively. Extension to

include viscoelastic behavior can be readily accomplished using the quasi-elastic approach,

$$E_{11}(t) \approx v_f E_f(t) + v_m E_m(t) \quad (118a)$$

and

$$v_{12}(t) \approx v_f v_f(t) + v_m v_m(t) \quad (118b)$$

where, for most advanced composites, the properties of the fiber are taken to be independent of time, except possibly at very high temperatures.

The representation of the composite transverse modulus,  $E_{22}$ , and shear modulus,  $G_{12}$ , is not quite so elementary; also, these properties are much more sensitive to voids and fiber geometric arrangement. Many investigators have looked at square arrays, rectangular arrays, hexagonal arrays and random fiber geometries in various attempts to model the actual behavior. Halpin [171] and Ashton et al. [2] developed some approximate forms based on Herman's work [177] who originally used a method developed by Kerner [178]. These equations are based on the application of semi-empirical adjustment factors to the theoretical representations of the orthotropic engineering parameters. These adjustment factors depend on the fiber geometry and spacing and can possibly account for void and microstructural damage effects. The "Halpin-Tsai equations" are given by

$$E_{22} = E_m \left[ \frac{E_f(1+\zeta_E v_f) + \zeta_E E_m(1-v_f)}{E_f(1-v_f) + E_m(\zeta_E + v_f)} \right] \quad (119a)$$

$$G_{12} = G_m \left[ \frac{G_f(1+\zeta_G v_f) + \zeta_G G_m(1-v_f)}{G_f(1-v_f) + G_m(\zeta_G + v_f)} \right] \quad (119b)$$

where  $\zeta_E$  and  $\zeta_G$  are the adjustment factors. Reliable estimates for the  $\zeta$ -factor can be obtained by Equations (119a) and (119b) with various numerical micromechanics solutions. Typical values for elastic composites are  $\zeta_E = 2$  and  $\zeta_G = 1$  [2]. Deviations from these values account for differences in the assumed microstructural arrangement of the fibers and microstructural damage. As in Equation (118) a quasi-elastic viscoelastic solution may be obtained as

$$E_{22}(t) = E_m(t) \left[ \frac{E_f(t)(1+\zeta_E v_f) + \zeta_E E_m(t)(1-v_f)}{E_f(t)(1-v_f) + E_m(t)(\zeta_E + v_f)} \right] \quad (120a)$$

$$G_{12}(t) = G_m(t) \left[ \frac{G_f(t)(1+\zeta_G v_f) + \zeta_G G_m(t)(1-v_f)}{G_f(t)(1-v_f) + G_m(t)(\zeta_G + v_f)} \right] \quad (120b)$$

where we can normally assume that  $E_f$  and  $G_f$  are independent of time.

The principal elastic compliances  $S_{11}$ ,  $S_{22}$ ,  $S_{12}$ , and  $S_{66}$  can be found by applying Equation (83) to the engineering properties. Corresponding viscoelastic compliances are derived by using Equation (83) and the quasi-elastic method to obtain  $S_{11}(t)$ ,  $S_{22}(t)$ ,  $S_{12}(t)$  and  $S_{66}(t)$ . We can also include temperature dependence by using the

reduced-time,  $\epsilon$ , provided we do not violate the correspondence principle discussed earlier. Halpin [33] has used the Halpin-Tsai equations to predict  $S_{22}$  and  $S_{66}$  for a viscoelastic rubber reinforced with unidirectional, nylon fibers over a temperature range using isothermal data. Sims [29] has also employed these relations analytically to calculate the relaxation moduli for unidirectional graphite and boron fiber-reinforced epoxy composites.

#### Laminate Constitutive Theory

The behavior of laminated composite materials is directly related to the response of the various laminae after taking into account the geometry and individual properties of the layers. Laminated composite theory is given in Ashton et al. [2], Ashton and Whitney [27], Ambartsumyan [26], and Lekhnitskii [25] for elastic materials and may be extended to linear viscoelastic behavior by using the correspondence principle or the quasi-elastic approach.

A typical laminate consisting of  $n$  layers, or lamina, is shown in Figure 10. The strain-displacement relationships are generally derived for small deformations of the laminate and are written in terms of the midplane strains  $\epsilon_x^0$ ,  $\epsilon_y^0$ ,  $\epsilon_{xy}^0$  and the plate curvatures  $k_x$ ,  $k_y$  and  $k_{xy}$  as follows,

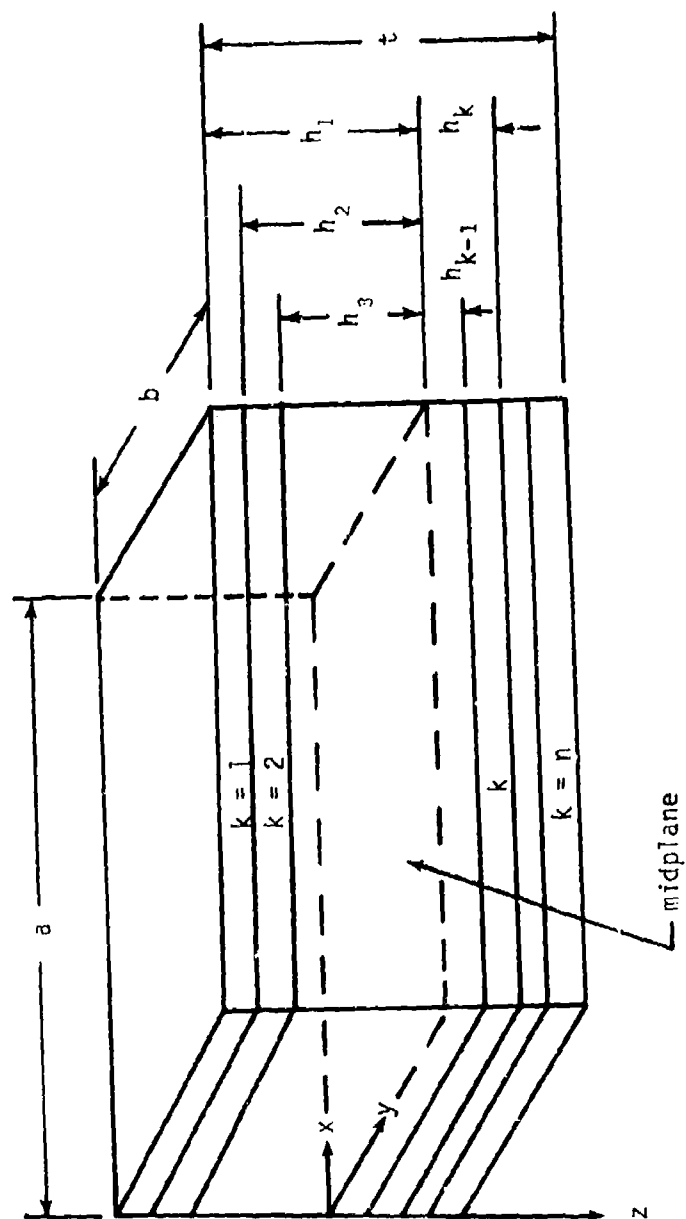


Figure 10. Laminated plate notation.

$$\begin{aligned}
\epsilon_x^0 &= \frac{\partial u}{\partial x} & k_x &= -\frac{\partial^2 w}{\partial x^2} \\
\epsilon_y^0 &= \frac{\partial v}{\partial y} & k_y &= -\frac{\partial^2 w}{\partial y^2} \\
\gamma_{xy}^0 &= \frac{\partial u}{\partial y} + \frac{\partial v}{\partial x} & k_{xy} &= -2\frac{\partial^2 w}{\partial x \partial y}
\end{aligned} \tag{121}$$

where  $u_0$  and  $v_0$  are the midplane displacements and  $w$  is the transverse displacement. The strains in any given layer are related to the midplane strains and curvatures in Equation (121) by the relationships

$$\begin{aligned}
\epsilon_x &= \epsilon_x^0 + zk_x \\
\epsilon_y &= \epsilon_y^0 + zk_y \\
\gamma_{xy} &= \gamma_{xy}^0 + zk_{xy}
\end{aligned} \tag{122}$$

where  $z$  is the coordinate distance measured perpendicular to the laminate reference surface as shown in Figure 10.

#### Elastic Orthotropic Materials

Under the assumption that plane sections remain plane the constitutive equations for an elastic, orthotropic laminate consisting of  $n$  laminae having the constitutive relationship which obeys Equations (88b) and (89b) are given as (see, for example, Ashton et al. [2]),

$$\begin{bmatrix} N_x \\ N_y \\ N_{xy} \\ M_x \\ M_y \\ M_{xy} \end{bmatrix} = \begin{bmatrix} A_{11} & A_{12} & A_{16} & B_{11} & B_{12} & B_{16} \\ A_{12} & A_{22} & A_{26} & B_{12} & B_{22} & B_{26} \\ A_{16} & A_{26} & A_{66} & B_{16} & B_{26} & B_{66} \\ B_{11} & B_{12} & B_{16} & D_{11} & D_{12} & D_{16} \\ B_{12} & B_{22} & B_{26} & D_{12} & D_{22} & D_{26} \\ B_{16} & B_{26} & B_{66} & D_{16} & D_{26} & D_{66} \end{bmatrix} \begin{bmatrix} \epsilon_x^o \\ \epsilon_y^o \\ \gamma_{xy}^o \\ k_x \\ k_y \\ k_{xy} \end{bmatrix} \quad (123)$$

where  $N_x$ ,  $N_y$  and  $N_{xy}$  are the in-plane forces (stress resultants) and  $M_x$ ,  $M_y$  and  $M_{xy}$  are the moments (moment resultants) given by

$$N_x = \int_{-h/2}^{h/2} \sigma_x dz$$

$$M_x = \int_{-h/2}^{h/2} \sigma_x z dz$$

$$N_y = \int_{-h/2}^{h/2} \sigma_y dz \quad (124a)$$

$$M_y = \int_{-h/2}^{h/2} \sigma_y z dz \quad (124b)$$

$$N_{xy} = \int_{-h/2}^{h/2} \tau_{xy} dz$$

$$M_{xy} = \int_{-h/2}^{h/2} \tau_{xy} z dz$$

The quantities  $A_{ij}$ ,  $B_{ij}$  and  $D_{ij}$  are the laminate extensional stiffnesses, coupling stiffnesses and bending stiffnesses, respectively. These laminate stiffnesses can be defined in terms of the lamina stiffnesses given in Equation (89b) as



$$\begin{aligned}
 A_{ij} &= \sum_{k=1}^n (Q'_{ij})_k (h_k - h_{k-1}) \\
 B_{ij} &= \frac{1}{2} \sum_{k=1}^n (Q'_{ij})_k (h_k^2 - h_{k-1}^2) \\
 D_{ij} &= \frac{1}{3} \sum_{k=1}^n (Q'_{ij})_k (h_k^3 - h_{k-1}^3)
 \end{aligned} \tag{125}$$

where  $h_k$  is the coordinate distance to a lamina from the reference surface as shown in Figure 10. The  $Q'_{ij}$ 's are the transformed stiffnesses which depend on the orthotropic lamina stiffness and the angle of orientation of the lamina as shown in Equation (89b).

The most important feature of Equation (123) is the coupling phenomena which exists between stretching and bending through the  $B_{ij}$  matrix. If the  $(Q'_{ij})_k$  is an even function of  $z$  (symmetric layup of the laminate), then  $B_{ij} = 0$  and coupling is eliminated. Many laminates are constructed in this manner and, therefore, the governing constitutive equations are considerably simplified.

#### Viscoelastic Orthotropic Materials

The constitutive equations for a linear viscoelastic laminate can be formulated by replacing the products of the time-dependent quantities in Equation (123) by superposition integrals of the form

$$\begin{aligned}
 A'_{ij} &= \int_0^t A_{ij}(t - \tau) \frac{\partial}{\partial \tau} d\tau \\
 B'_{ij} &= \int_0^t B_{ij}(t - \tau) \frac{\partial}{\partial \tau} d\tau \\
 D'_{ij} &= \int_0^t D_{ij}(t - \tau) \frac{\partial}{\partial \tau} d\tau
 \end{aligned} \tag{126}$$

and, similarly,

$$\begin{aligned}
 A_{ij}(t) &= \sum_{k=1}^n [Q'_{ij}(t)]_k (h_k - h_{k-1}) \\
 B_{ij}(t) &= \frac{1}{2} \sum_{k=1}^n [Q'_{ij}(t)]_k (h_k^2 - h_{k-1}^2) \\
 D_{ij}(t) &= \frac{1}{3} \sum_{k=1}^n [Q'_{ij}(t)]_k (h_k^3 - h_{k-1}^3)
 \end{aligned} \tag{127}$$

where the  $Q'_{ij}$ 's are the time-dependent transformed stiffnesses defined by Equation (89b).

In the application of Equations (123), (126) and (127) for the solution of many viscoelastic problems, the procedure often becomes time consuming. Under certain conditions when the time-dependent material functions or input quantities are slowly varying functions of time, the convolution integral may be omitted. The quasi-elastic approach used earlier to derive the lamina constitutive equations

may also be used here. The procedure involves direct substitution of the time-dependent properties of the  $A'_{ij}$ ,  $B'_{ij}$  and  $D'_{ij}$  matrices.

### Structure-Property Relationships

In order to apply the micromechanics theory derived earlier to the behavior of the laminate, it is necessary to establish the relation between the  $S_{ij}$  and  $Q_{ij}$ . These relations are given in [2] as

$$\begin{aligned} Q_{11} &= \frac{S_{22}}{S_{11}S_{22} - S_{12}^2} \\ Q_{12} &= \frac{-S_{12}}{S_{11}S_{22} - S_{12}^2} \\ Q_{22} &= \frac{S_{11}}{S_{11}S_{22} - S_{12}^2} \\ Q_{66} &= \frac{1}{S_{66}} \end{aligned} \quad (128)$$

where  $S_{11}$ ,  $S_{22}$ ,  $S_{12}$  and  $S_{66}$  may either be measured directly or predicted by the various micromechanics theories already discussed. The Halpin-Tsai relations, Equations (114), (117) and (119), are often used because of their relative simplicity. We may also relate the  $Q_{ij}$  to the common engineering constants and apply the Halpin-Tsai relations directly, [2]

$$Q_{11} = \frac{E_{11}}{1 - \nu_{12}\nu_{21}}$$

$$Q_{22} = \frac{E_{22}}{1 - \nu_{12}\nu_{21}} \quad (87b)$$

$$Q_{12} = \frac{\nu_{21}E_{11}}{1 - \nu_{12}\nu_{21}} = \frac{\nu_{12}E_{22}}{1 - \nu_{12}\nu_{21}}$$

$$Q_{66} = G_{12}$$

In either case, the application of the quasi-elastic approach to the solution of viscoelastic problems proceeds by inputting time-dependent properties in Equations (128) and (87b) by using, for example, time-dependent Halpin-Tsai relations, Equations (118) and (120).

### SECTION III

#### MECHANICAL CHARACTERIZATION TESTS

The experimental program was designed to provide the necessary isothermal data required to evaluate the effective (overall) laminate stiffness of a typical glass/epoxy composite material. The glass/epoxy fibrous composite studied is currently being used in the construction of the third stage Minuteman III solid rocket motor case. State-of-the-art filament winding techniques are used to fabricate the actual case. The basic barrel (cylindrical section) consists of 14 layers of hoop-oriented S-901 glass<sup>1</sup> wraps and 8 layers of glass wraps oriented  $14.63^\circ$  to the longitudinal motor axis. The S-901 glass filament rovings are used in a tape prepreg system consisting of a Shell 58-68R epoxy resin.

Glass cloth is interwoven between hoop layers at the barrel ends to provide stub skirts for attachment purposes. In the forward and aft dome regions the fiber or wrap angle is variable because of the shape of the end closures. The geometry is further complicated with the provision for six thrust termination ports in the forward dome. These areas are reinforced locally with a glass tape/epoxy during the winding process.

As a result, the effects of both variable thickness and wrap angle must be taken into account in the forward dome area in order

---

<sup>1</sup>Formerly designated as S-HTS or S-994-HTS glass. Owens-Corning Fiberglas Corporation trademark.

to determine the effective stiffness as a function of the fiber angle. In the discussion of effective stiffness in Section II it was noted that the controlling factors are primarily constituent properties, volumetric content and stacking sequence. The fiber content may be somewhat variable in the dome regions due to the fabrication technique which causes both fiber slippage ("gaps") and shingling ("overlapping"). Current motor case analysis conducted by the Aerojet Solid Propulsion Company (ASPC)<sup>2</sup> assumes a nominal 65.7% fiber content (volume) as representative of the actual motor case [17].

The mechanical characterization tests described in this section were conducted in a manner that would permit the evaluation of the effective stiffness in the glass/epoxy composite as a function of fiber angle, stacking sequence and load history. The effects of multiple loading cycles, typical of the prooftesting of glass/epoxy rocket motor cases, and temperature were considered in the latter area.

### Materials and Equipment

#### Materials

The prediction of effective properties through the use of the Halpin-Tsai Equation (119) and other associated micromechanics theories rely very heavily upon accurate measurements of the

<sup>2</sup>Aerojet Solid Propulsion Company, Sacramento, California.

constituent properties. In the glass/epoxy system, the glass fiber properties are generally assumed to be linearly elastic up to failure. Epoxy matrix properties, on the other hand, exhibit considerable time and temperature dependence.

The materials tested were representative of both the constituent materials as well as the actual rocket motor case. Four materials were used in the experimental program:

1. Shell 58-68R epoxy resin.
2. S-901 glass/Shell 58-68R epoxy resin unidirectional composite laminae.
3. S-901 glass/Shell 58-68R epoxy resin composite laminates.
4. S-901 glass/Shell 58-68R epoxy resin laminate sections removed from a third stage Minuteman III solid rocket motor case.

The first three materials were fabricated by Structural Composites Industries (SCI)<sup>3</sup> for the experimental program and furnished under a subcontract with the ASPC. All of these materials were made according to the current ASPC specifications pertaining to the materials preparation and method of construction as actually used in the third stage Minuteman III motor case.

Epoxy resin. The Shell 58-68R epoxy resin system was originally developed by SCI in the early Polaris solid rocket motor

---

<sup>3</sup>Structural Composites Industries, Azusa, California.

cases and has been used by NASA in several filament-wound tank applications for cryogenic fuels [179,180]. The epoxy system used in our tests employs the standard formulation given in Table 2.

Table 2. Ingredients of Shell 58-68R Epoxy Resin [181]

Material	Formulation: Parts by Weight
Epon 828	50
Epon 1031	50
Nadic Methyl Anhydride (NMA)	90 $\pm$ 5
Benzyltrimethylamine (BDMA)	0.55 $\pm$ 0.05

The epoxy mixture was prepared by mixing the Epon 828 and Epon 1031 components in an oven at 150°F and then blending them together once the Epon 1031 was completely melted. While the components were still warm, the NMA (curing agent) and BDMA (accelerator) were added separately and mixed thoroughly after each addition. The resulting mixture was placed in a vacuum bell jar in order to remove any entrapped air bubbles.

After the initial mixing and degassing, the epoxy mixture was poured into flat casting molds with 8" x 8" x 1/8" dimensions. Sufficient quantity of the epoxy was prepared to cast three sheets from the same batch. The molds were then placed in an oven in a vertical position and cured for 2 hours at 200°F and then 2 hours at 350°F. Upon removal from the molds, the plates were visually established to be void free and found to have a uniform thickness of



0.125  $\pm$  0.003 inches. The density of the cured plates, measured by water displacement method, was found by SCI to be 1.24 grams/cc [181]. This is consistent with other studies using the same resin system with slight variations of cure times and temperatures [179, 180].

Glass/epoxy composites. Both the unidirectional laminae and the composite laminates were prepared by using the Shell 58-68R epoxy resin and Owens-Corning S-901 Glass roving (20-end)<sup>4</sup>. The 20-end roving is used in the actual motor case because experience has shown it to have a higher strength than the 12-end roving which is also available [179].

All prepreg broadgoods materials required for panel fabrication were prepared by a drum-winding process. This process involved winding the S-901 Glass roving onto a Mylar-film-lined, 24-inch diameter cylinder at a controlled winding speed and load, and then applying a quantity of the Shell 58-58R epoxy resin uniformly over the entire surface. The amount of glass roving and epoxy required for the prepregs was precalculated to yield a desired ply thickness and glass volume percent close to 65% in the molded panels. To facilitate processing, a 50% resin solution was made in methyl-ethyl-ketone (MEK). Residual solvents in the prepregs were removed by heating in an oven at 150°F prior to the final layup.

---

<sup>4</sup>An "end" is defined as the smallest commercially available bundle of glass filaments; each "end" generally consists of 204 monofilaments in a single, continuous, untwisted strand.

The prepreg broadgoods were cut into 13-inch strips with the fibers running at the required angle of the molded panel. Single ply patterns approximately 13" x 13" were cut and fifteen (15) plies were laid up in a single stack. All panels, unidirectional and laminated, had fifteen plies such that the outer layers were oriented in the same direction in order to reduce warpage during the curing process. The plies were also stacked symmetrically such that the bending-stretching (coupling) stiffness,  $B_{ij}$ , is zero. The prepreg plies were laid up on polished aluminum plates, covered with a Teflon-impregnated release fabric, followed by another 13" x 13" x 0.065" aluminum cover plate over the outer layers, and then subsequently covered with 2 plies of glass bleeder cloth. The entire assembly was bagged with a Nylon film and placed in an autoclave for cure. Curing was executed for 2 hours at 200°F and then 2 hours at 350°F in a 75 psig autoclave pressure in addition to the vacuum-bag pressure.

The cured panels were inspected for visible defects. The panel thickness was measured at 25 locations and then trimmed to a net delivery size of 12" x 12" x 1/8". Unidirectional glass/epoxy panels were fabricated at fiber angles of 0, 20, 45 and 90° while the laminated glass/epoxy panels were made in symmetric layups of 0/90, ±10, ±30, ±45, ±60 and ±80°.

Filament-wound case materials. The third stage Minuteman III solid rocket motor case is shown in Figure 11. The motor shown is

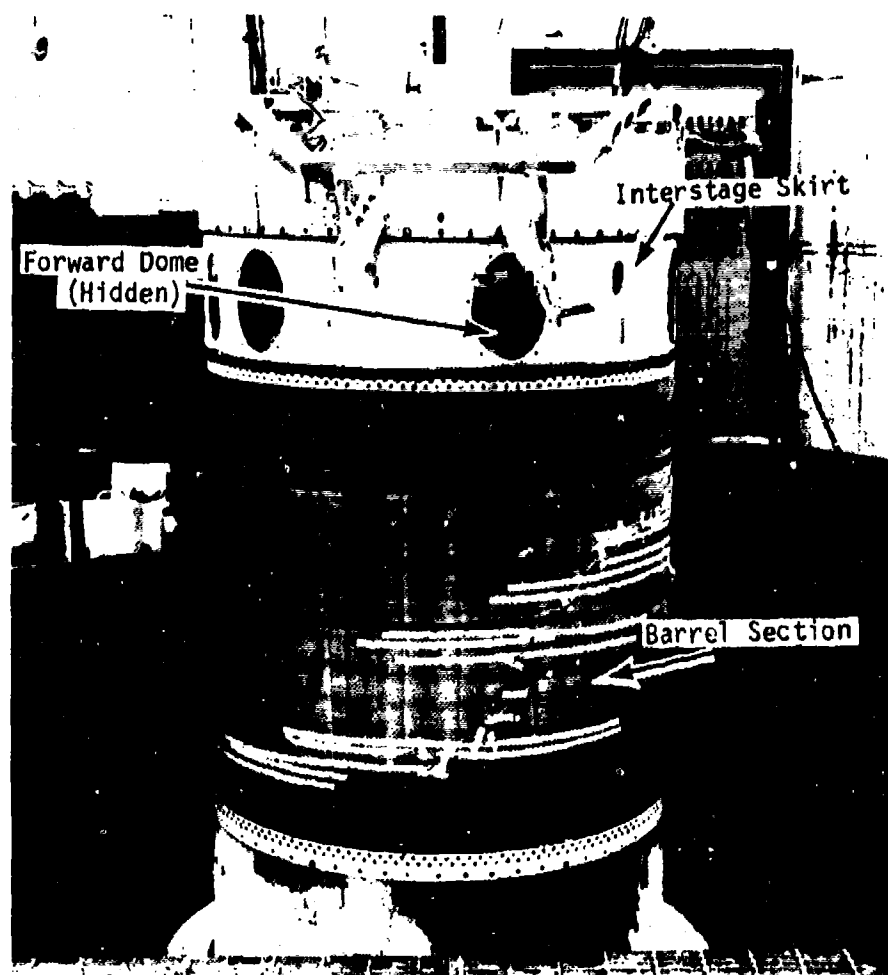


Figure 11. Instrumented third stage Minuteman III solid rocket motor case undergoing proof testing.

instrumented and being prooftested by ASPC prior to casting the solid propellant. The barrel section along with the strain gage instrumentation can be clearly seen. Figure 12 shows the section of the forward dome which has been removed from the barrel section. The thrust termination ports and igniter adapter are shown in more detail. In Figure 11 they are hidden by the interstage assembly in the forward end of the motor case. A closeup of the area between two of the thrust termination ports is shown in Figure 13.

In order to make a comparison between the effective stiffness of the composite plates and the actual motor case, the ASPC furnished both the forward dome (Figure 12) and the aft end of a third stage motor case which had undergone prooftesting ("hydrotesting"). Although the effects of the hydrotesting damage may be significant with regard to the first loading cycle, the results of subsequent loading cycles (second through  $n^{\text{th}}$  cycle) could be compared directly with the glass/epoxy plates fabricated by SCI. For these series of tests the forward dome was chosen since the aft end has an outer layer of cork insulation which could not easily be removed without damaging the case material.

Samples were obtained from an area between two of the thrust termination ports similar to that shown in Figure 13. In this region the motor case does not possess mid-plane symmetry since there are eight (8) alternating layers and hence  $B_{ij} \neq 0$ . The fiber angles of samples taken from the meridional and

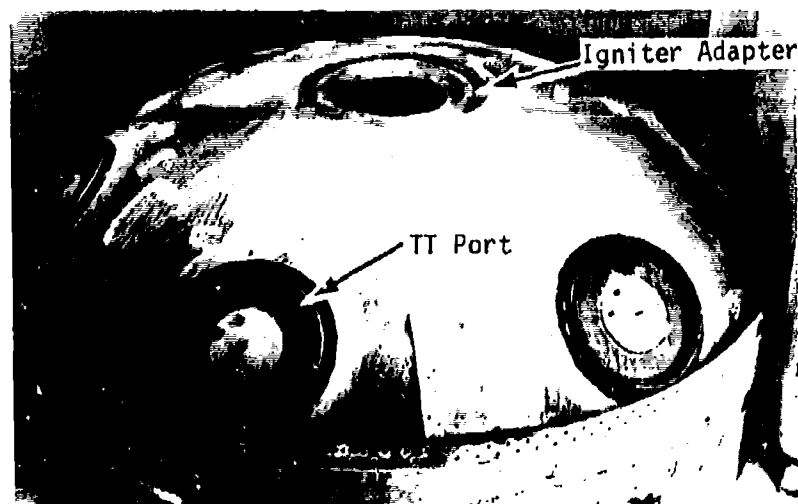


Figure 12. Forward dome section of the third stage Minuteman III solid rocket motor case.

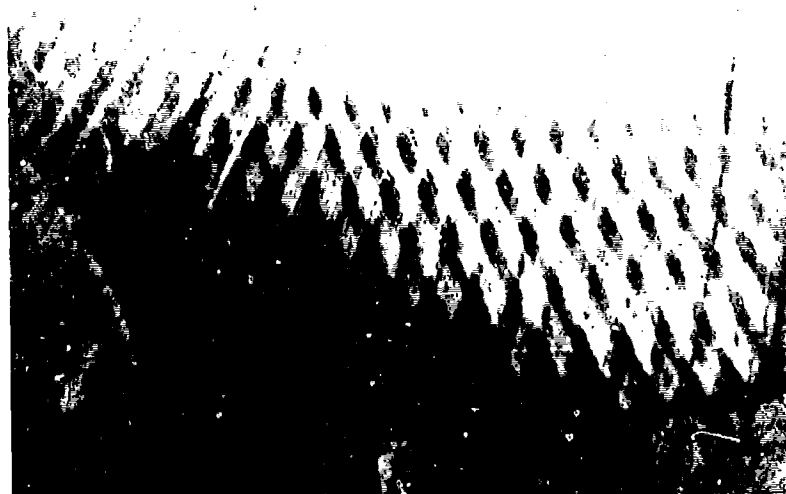


Figure 13. Closeup view of the case region near a thrust termination port.

circumferential directions were approximately  $\pm 20$  and  $\pm 70^\circ$  respectively.

Aluminum. A 6061-T6 aluminum plate was also used as a reference material for comparison with the glass/epoxy plate tests which are discussed in a subsequent section.

#### Specimen Preparation

Uniaxial tensile coupons. The majority of the tests conducted during the course of the experimental program utilized uniaxial tensile coupons cut from the plates fabricated by SCI. Sample preparation technique for both the Shell 58-68R epoxy resin and S-901 glass/Shell 58-68R epoxy resin materials was the same.

The surfaces of the plates which were to be used were first taped completely with masking tape. A sample layout corresponding to the desired fiber angle and coupon dimensions was drawn directly on one taped surface. All sample dimensions were drawn slightly oversize to allow for final trimming. Using a tungsten carbide band saw blade and a slow band speed, the samples were rough cut from each plate used in the tests. After carefully removing the masking tape, several samples were mounted in a vertical mill and machined to the final dimensions using a fly cutting attachment. Visual inspection of the sample edges showed little damage from the cutting operation provided the cutting tool was resharpened after each surface was completed.

Several sets of samples were prepared from the SCI plates at different fiber angles,  $\theta$ , with the emphasis placed on the off-angle specimens ( $0^\circ < \theta < 90^\circ$ ). These latter specimens exhibit significant creep and nonlinearity. All of the samples were cut to the nominal dimensions of  $6" \times 1/2" \times 1/8"$ .

Specimens for the failure tests, constant crosshead rate tests and the creep and recovery tests required end tabs to be bonded to coupons in order to transfer the applied load to the specimen. Aluminum end tabs were sandblasted and bonded to the coupon ends using Micro-Measurements' M-Bond AE-15<sup>5</sup> adhesive cured under slight pressure for 2 hours at 170°F. The end tabs for the constant crosshead rate tests were basically 5° wedges measuring  $1.5" \times 1" \times 1/8"$  and the tabs for the failure and creep and recovery tests measured  $1" \times 5/8" \times 1/8"$  with the edge tapered to about 20-30° (Figure 14). Different types of tabs were used because of the difference in grips.

Tensile coupons used for the creep and recovery tests were loaded by means of pin-connected grips while the constant crosshead rate coupons were held by a set of wedge-action grips. In order to reduce the possibility of load-induced bending due to any pin misalignment, an alignment fixture was used to clamp and align the ends while a 1/8- or 3/16-inch hole was drilled through the tabs. These holes were actually drilled slightly oversize to accommodate

---

<sup>5</sup>Micro-Measurements, Romulus, Michigan.

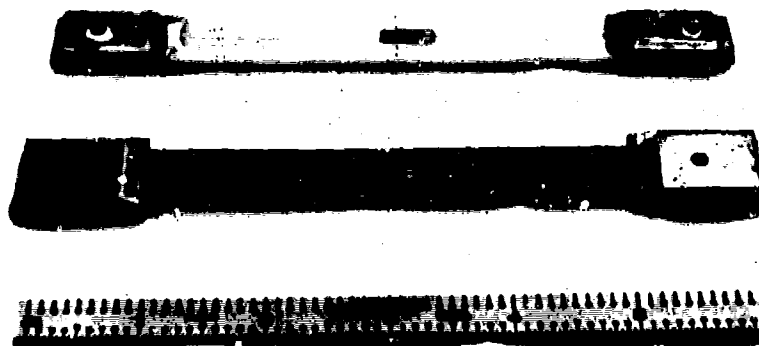
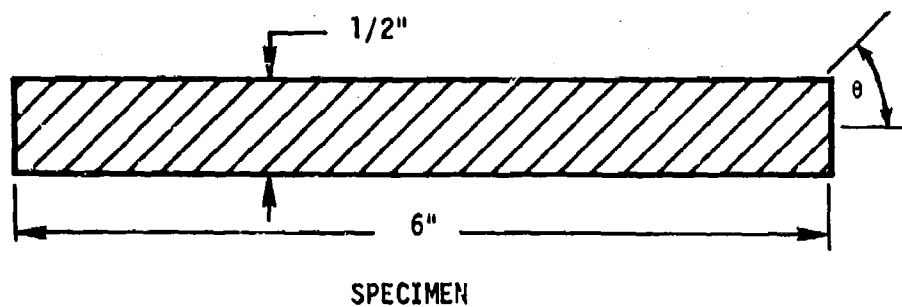


Figure 14. Typical tensile coupons used for creep and recovery and constant crosshead rate tests.



the pin easily. The larger pin size was used for the higher loads to prevent pin failure.

All of the samples were strain-gaged using standard techniques. The same adhesive system and cure conditions used to bond the end tabs was employed during the strain-gaging. Axial strain was measured by two Micro-Measurements' strain gages, type EA-06-125BZ-350. They were bonded along the longitudinal direction of the sample (Figure 14), one on each side, and connected to the signal conditioning system individually so that the strain on each gage was known at all times in order to assess the effects of bending, if present. Some of the epoxy specimens, as well as the  $\theta = 0^\circ$  and  $\theta = 90^\circ$  glass/epoxy specimens, were strain-gaged with the type EA-06-100VA-350 gages. These gages had an additional transverse gage for measuring Poisson's ratio,  $\nu$ , in the epoxy resin, and  $\nu_{12}$  and  $\nu_{21}$  in the glass/epoxy for the two respective fiber angles.

Beam bending specimens. Several specimens of the glass/epoxy laminates were also prepared for four-point beam bending tests. These specimens were all cut and prepared in a manner similar to the tensile coupons with several exceptions. The sample configuration was slightly larger, namely, 7" x 1" x 1/8" and no end tabs were necessary. For comparison purposes only the 0/90 and  $\pm 45^\circ$  fiber angle layups were prepared. Only the bottom (tension), central section of the beam was strain-gaged for these tests using type EA-06-125BZ-350 gages.

Filament-wound case material specimens. Preparation of the specimens from the forward dome required considerably more care because of the case flexibility, curvature and lack of support during the cutting operation. The case thickness varies from a minimum of 0.08 inches (eight plies) near the barrel section and thrust termination (TT) ports to approximately 0.375 inches near the igniter adapter and other areas of local reinforcement (Figure 13). An area between two of the thrust termination ports was selected because of the uniform thickness (0.08 inches) and relatively small curvature. The interior of the forward dome had a 1/2-inch layer of rubber insulation bonded over the complete dome area which had to be removed from the case material.

Two areas measuring 10" x 10" were marked to be cut out. One section was to be used for samples with a fiber angle of  $\pm 20^\circ$  (meridional direction) while the other was oriented at  $\pm 70^\circ$  (circumferential direction). Each section was cut out by using a saber saw with a special tungsten carbide blade. Before further sectioning into useable sample sizes could be accomplished, the rubber insulation had to be removed. Removal was done with a high speed, electric hand grinder in such a manner that only a thin layer of the insulation was left to protect the fiber surface. The sections were then marked and further cut such that at least four beam specimens, of nominal dimensions 7" x 1" x 0.08", and two tensile specimens, measuring approximately 6" x 3/4" x 0.08", were obtained from each section. Final trimming and smoothing of the edges was

done with a high speed router.

All of the samples were strain-gaged by following the techniques established previously for the tensile coupons and beams, respectively, with one exception. The surface of the filament-wound case material was very irregular compared to the SCI plate materials, and therefore, the surface was first coated with an epoxy filler material and sanded smooth prior to gaging. Several of the completed samples are shown in Figure 15.

Plate twist specimens. Two samples were used for these tests, a  $\pm 45^\circ$  glass/epoxy and 6061-T6 aluminum plate. Both plates were 12" x 12" x 1/8". The glass/epoxy plate was one of the original SCI plates described earlier and therefore possessed midplane symmetry, i.e.,  $B_{ij} = 0$ . The plates were strain-gaged on both surfaces at the intersection of their diagonals using a Micro-Measurements' EA-06-125RD-350 rectangular rosette gage configuration. The gages were mounted with the AE-15 adhesive with the two principal gages oriented in the direction of the diagonals (Figure 16). A room temperature cure for 24 hours followed by postcuring at 140°F for 4 hours was used for these samples in order to reduce plate warping.

#### Equipment and Procedures

All of the tests involved the use of strain-gaged specimens. Whenever a test was conducted, a dummy sample and identical gage was mounted in the same environment in order to compensate for both thermal expansion and humidity changes. Strain gage measurements

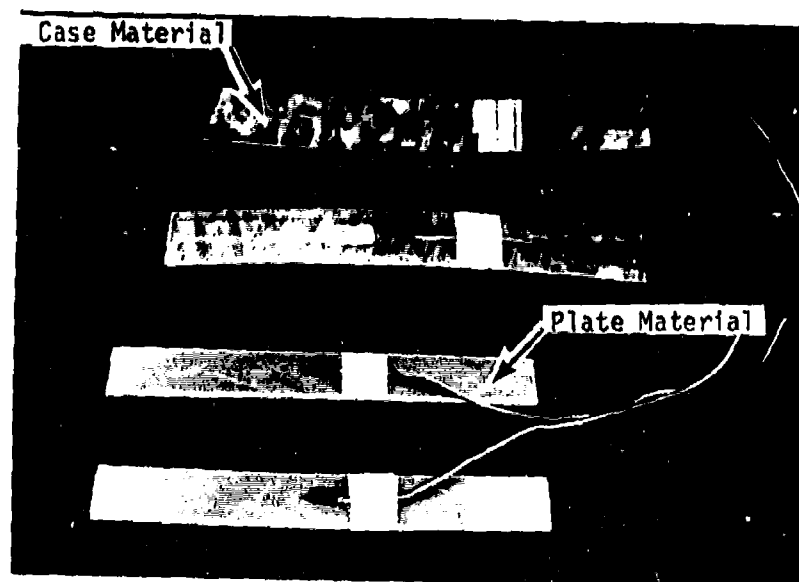


Figure 15. Specimens used for four-point beam bending tests.

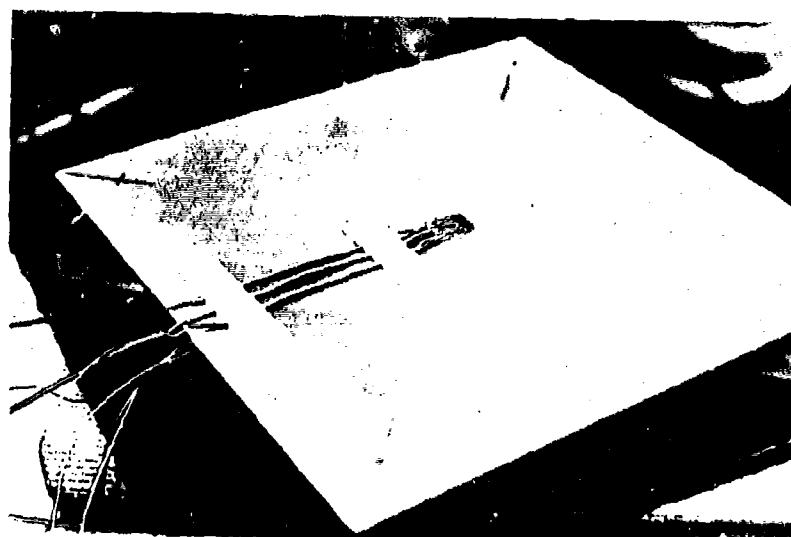


Figure 16. Orthotropic  $\pm 45^\circ$  glass/epoxy plate specimen.

were recorded using a B & F Instruments' Strain Gage Acquisition System<sup>6</sup> and a modified Hewlett-Packard 561 Digital Printer<sup>7</sup>. The printer was modified to include an input from a timing clock. The system operated at a rate of two channels per second, accommodating up to ten channels of strain gage signal conditioning, and providing reliable data within a few seconds of the actual loading.

Creep and recovery testers. The variation of fiber angle and stress level studied during the program required the use of several creep testers in order to provide the maximum amount of data in a reasonable time period. Three sets of creep testers were designed and fabricated for the test program:

1. Multi-station, dead-weight test unit (500 pounds maximum).
2. Single unit, lever arm system for medium loads (2000 pounds maximum).
3. Single unit, lever arm system for heavy loads (6000 pounds maximum).

The multi-station, dead-weight creep tester consists of five test stations, each capable of sample loads up to about 500 pounds. This unit, shown in Figure 17, was used for the majority of the testing where the low load (stress) levels were of interest. For the tensile coupon configuration shown in Figure 14 this

---

<sup>6</sup>B & F Instruments, Inc., Cornwells Heights, Pennsylvania.  
<sup>7</sup>Hewlett-Packard, Palo Alto, California.

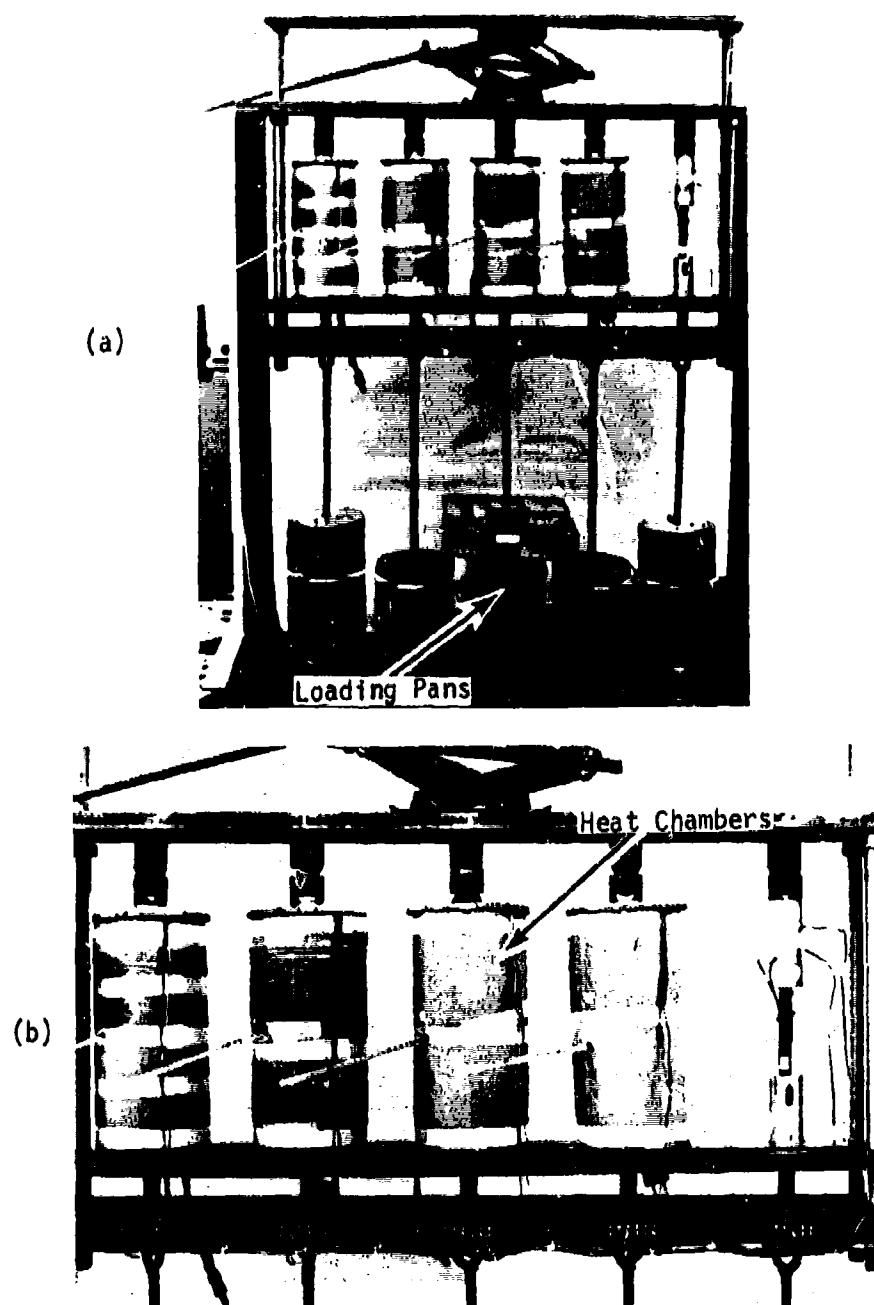


Figure 17. (a) Multi-station, dead-weight creep tester with (b) closeup view of heat chambers and tensile coupon.

corresponded to a stress level of almost 8000 psi.

The dead weights were connected to the lower grips which in turn were lowered (creep-load application) and raised (recovery-load removal) by means of a scissors jack which controlled the motion of the base plate directly under the grips. Figure 18 shows a typical tensile coupon mounted in the tester without the heating chamber. The specimen was pin-connected, both at the top and bottom, and a universal joint located at the top was used to minimize bending. The lower grips contained an oversized slot so that the sample was completely free of any loads during the recovery period. Details of the lower grip and pin-connection are also shown in Figure 18.

Several tests required load (stress) levels higher than 500 pounds which in turn lead to the design of the lever arm creep testers. Five single unit, lever arm systems were built such that two load ranges could be obtained by simply changing the lever advantage. The basic unit, shown in Figure 19, consisted of a lever arm, counter-weight and essentially the same grips as used in the dead-weight creep tester. The unit shown in Figure 19 is set up for the intermediate load range of 2000 pounds and has a 9:1 lever advantage. By making a suitable change in lever arms and connections, these same units have a 30:1 lever advantage and can be used with wedge-action grips to achieve 6000 pounds. The exact lever arm advantage, necessary for accurate determination of the

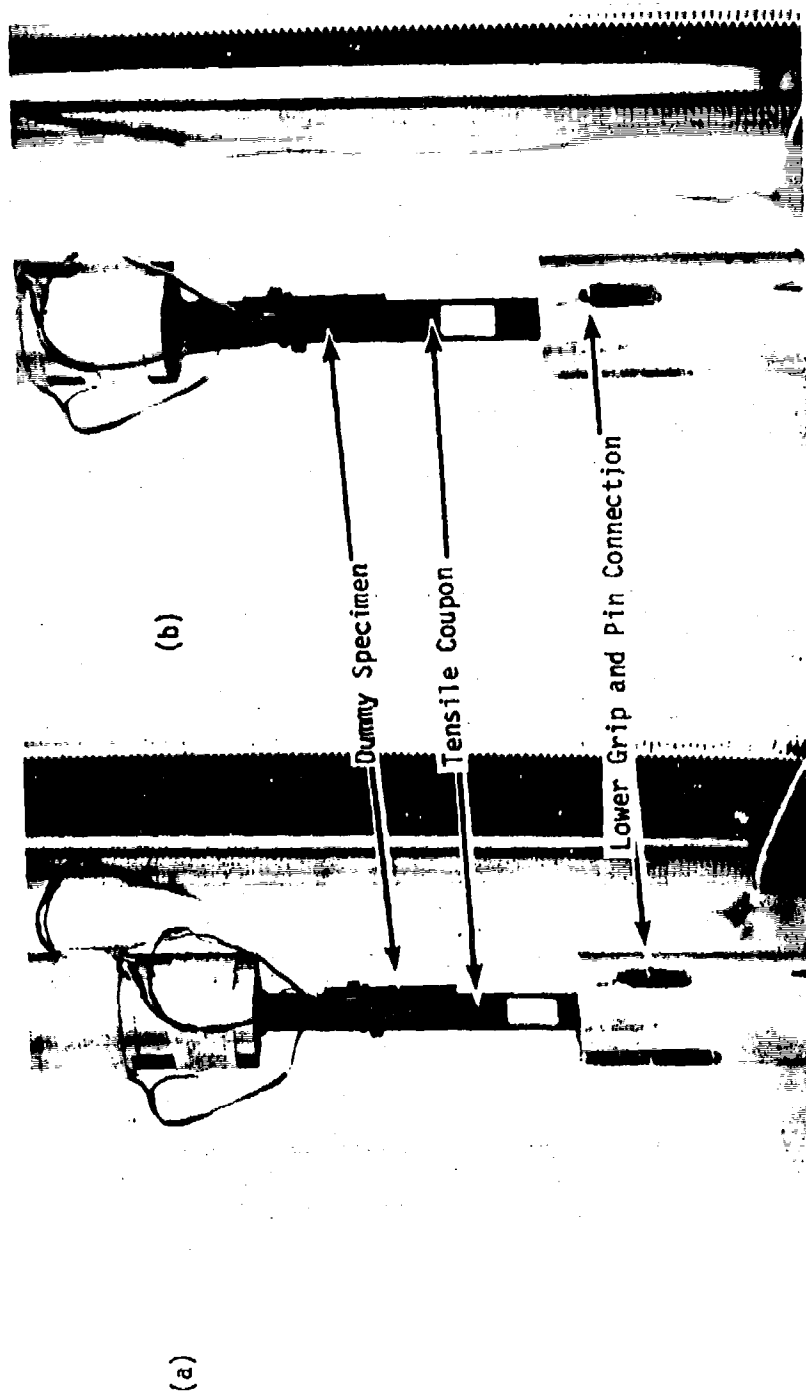


Figure 18. Lower grip and pin connections showing tensile coupon in (a) unloaded (recovery) and (b) loaded (creep) condition.



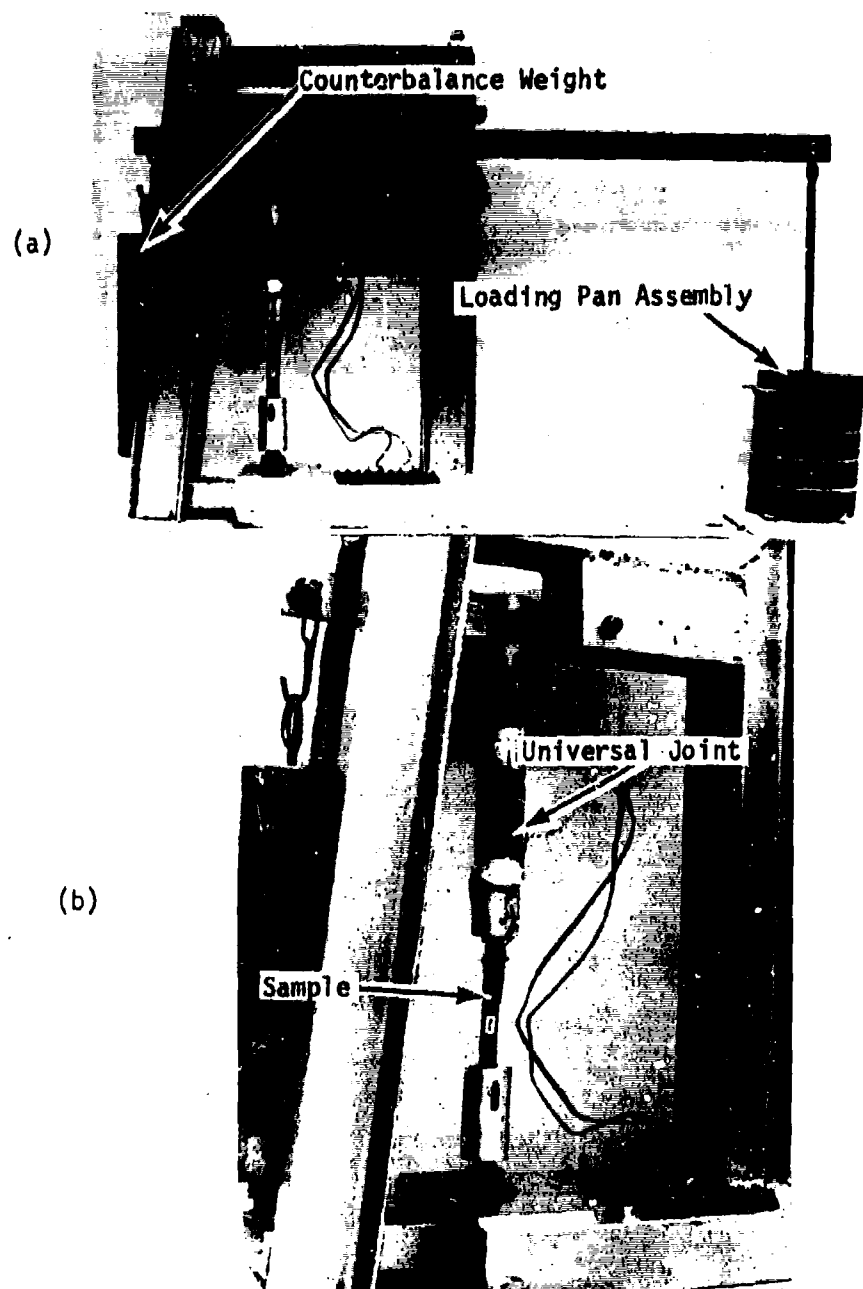


Figure 19. (a) Lever arm creep tester and (b) closeup of the sample and grip assembly.

stress, was obtained through an extensive series of calibration tests using dead weights on the loading pan assembly and strain-gaged aluminum and steel specimens mounted on the grips.

Even with the care taken to assure perfectly aligned loading pin holes, it was not always possible to prevent some degree of hole misalignment. In order to further reduce the bending effect, a small load was applied to the sample prior to the actual test (usually enough to induce about  $50\mu\epsilon$ ). The strains on both sides of the sample were recorded and then the lower grip pin alignment was changed until both strain readings were approximately equal. This was accomplished by adjusting two small Allen screws which engaged the pin vertically in the upper end of the slot until the strains were equivalent. The entire procedure yielded strains which were usually within 5-10% of each other.

Temperature conditioning. The creep and recovery tests as well as some of the constant crosshead rate tests were performed at several temperatures. Most of the tests at temperatures between  $-20^{\circ}\text{F}$  to  $140^{\circ}\text{F}$  were conducted in the large walk-in environmental rooms located in Texas A & M University's McNew Laboratory. These rooms had controls for the humidity as well as temperature, therefore providing a stable environment for long term tests. Almost all of the creep and recovery tests on the glass/epoxy composites were conducted in these rooms.

High temperature creep and recovery tests on the Shell 58-68R

epoxy resin were run by enclosing each specimen within individual heaters such as the ones shown in Figures 20 and 21. The cylindrical heating elements were constructed with electrical heating tape wrapped around a pre-formed wire cylinder serving as the inner wall. The exterior was insulated with two layers of asbestos tape and two layers of cardboard. During testing the ends of the chambers were covered with asbestos plates to minimize heat losses. Temperature control was accomplished with the use of a small thermistor sensor located near the specimen center and an RFL Industries Model 70 Proportional Controller<sup>2</sup>. Temperature measurement was achieved by inserting a glass thermometer through a small hole in the side of the heat chamber. These heating chambers were capable of temperatures up to and exceeding 260°F [12] with control to ±2°F or better. Previous calibration tests showed that the axial temperature gradient at the center of the chambers was small.

Beam tests. Four-point bending tests were conducted in a manner which essentially followed that given in the ASTM D790-71 procedure for determining the flexural properties of plastics [182]. These tests were conducted for both creep and recovery and constant crosshead rate bending using the same basic loading fixture shown in Figure 22. The support was a section of 5-inch heavy aluminum channel with the edges sanded smooth and rounded. The loading points were the tips of a small section of 3-inch steel channel

---

<sup>2</sup>RFL Industries, Inc., Boonton, New Jersey.



Figure 20. Interior view of heat chamber.

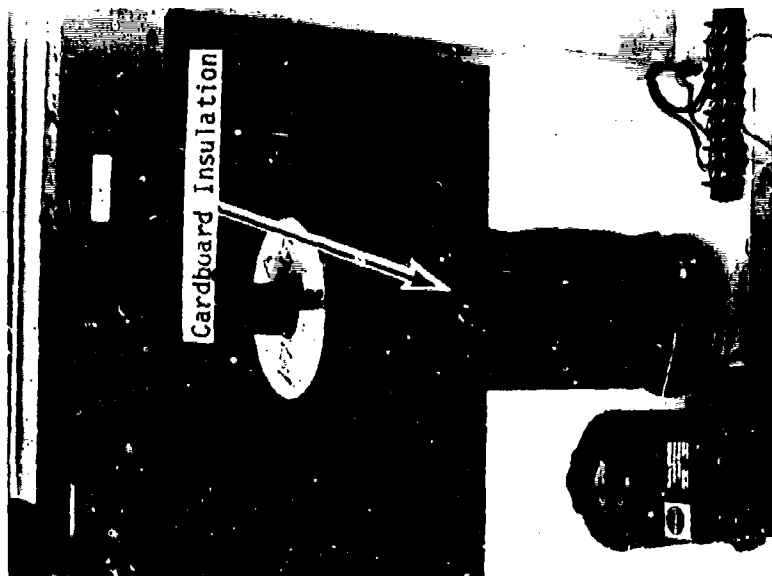


Figure 21. Heat chamber mounted around sample in lever arm creep tester.

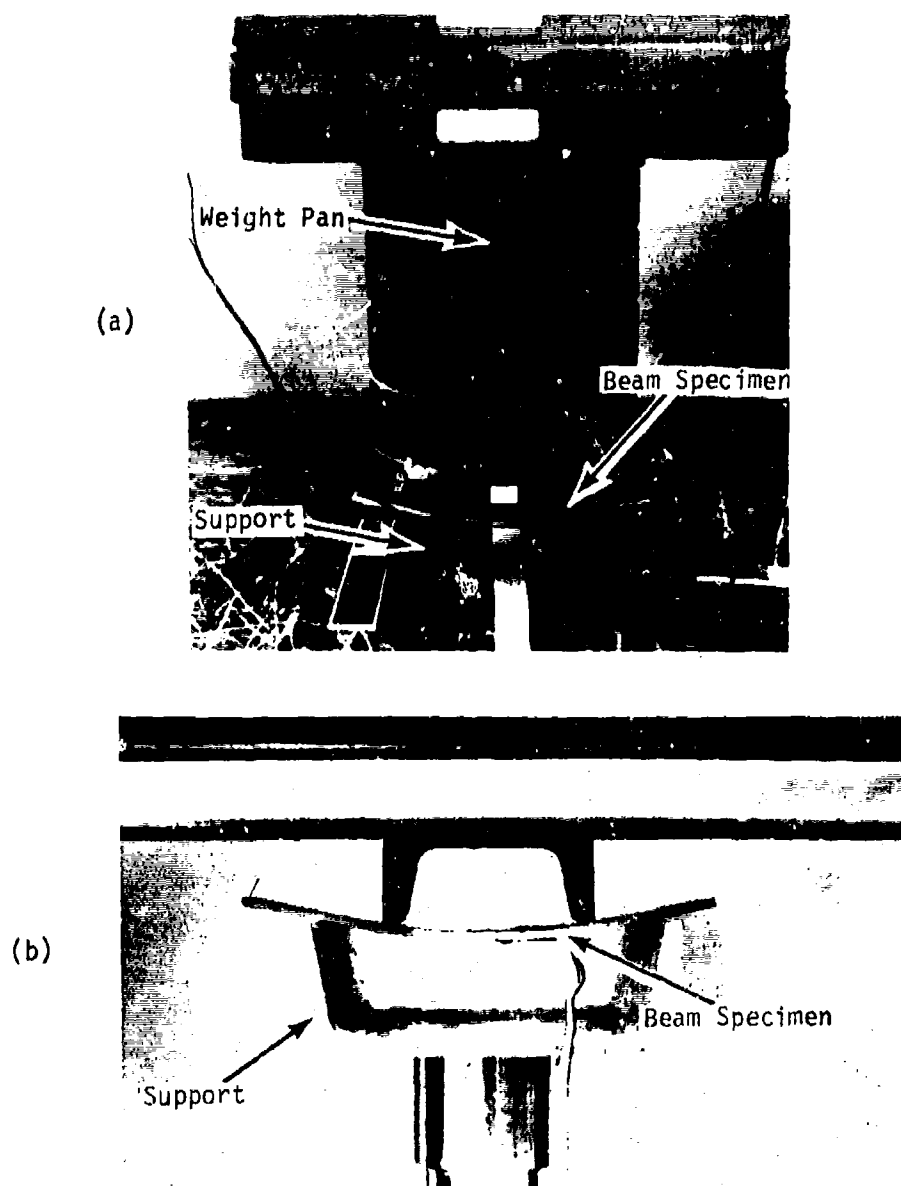


Figure 22. Four-point beam bending test setup for (a) creep and recovery test and (b) constant crosshead rate test.

which had also been sanded. All of the loading and support points were covered with a 1-inch wide strip of Teflon tape to minimize the friction.

The loading channel was fastened to the bottom of one of the load pans in the multi-station, dead weight creep tester described earlier and then lowered onto the upper surface of the sample. In the constant crosshead rate tests the channel was bolted to the lower moveable crosshead of an Instron<sup>9</sup> Testing Machine. A cross-head rate of 0.2 inches per minute was used for these tests.

Plate twist tests. Some of the previous background and interest in the plate twist tests has already been discussed in Section II. Experimentally, the test is relatively simple to perform, provided that the theoretical limitations concerning large deflections and localized loading conditions are considered. In the plate twist test, a pure twisting moment is imposed on a square plate by loading all four corners with equal forces. The forces are perpendicular to the plate with those forces at the first and third (diagonal) corners being upward and the other two forces downward. The corner loads cause the square plate to assume a hyperbolic paraboloid or saddle-shaped surface [183, 184].

The vertical upward forces were applied through the base support. The support consisted of a heavy steel plate about 1/2-inch thick with two large steel blocks welded to it at the ends

---

<sup>9</sup>Instron Corporation, Canton, Massachusetts.

of one diagonal (see Figure 23 for detail). A hole was countersunk into each block, making sure that the distance between hole centers was 14 inches. A 3/4-inch diameter steel ball bearing was then welded into the countersunk hole to provide a rounded loading support which would reduce the effect of a concentrated load. The vertical downward forces were applied in a similar manner. The ball bearings and blocks were welded 14 inches apart to the ends of a section of 3-inch steel channel. A 1/2-inch diameter steel rod was welded to the inside of the channel, midway between the ball bearings. This rod was used to bolt the channel to the upper crosshead of the Instron (constant crosshead rate tests) and served as a guide for a load bucket (creep tests). All of the ball bearing surfaces were covered with Teflon tape to minimize the frictional effects.

The displacement of the corners under the downward forces was monitored by two linear variable differential transformers (LVDT). Placement of the spring-loaded LVDT's was very critical, as was the alignment of the channel loading fixture. They were mounted 14 inches apart, directly under the applied downward forces. Cross-head deflections from the Instron tests were also used and found to be in excellent agreement with the LVDT deflections.

The constant crosshead rate tests on the Instron testing machine were performed by mounting the base support plate on a compression load cell and the loading channel to the upper crosshead. Dead-weight creep tests were run in a similar manner by carefully

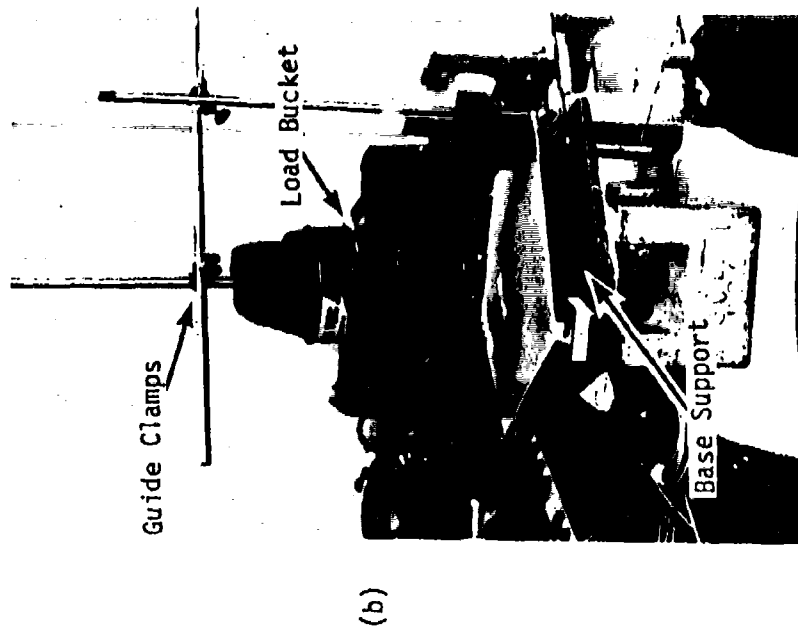
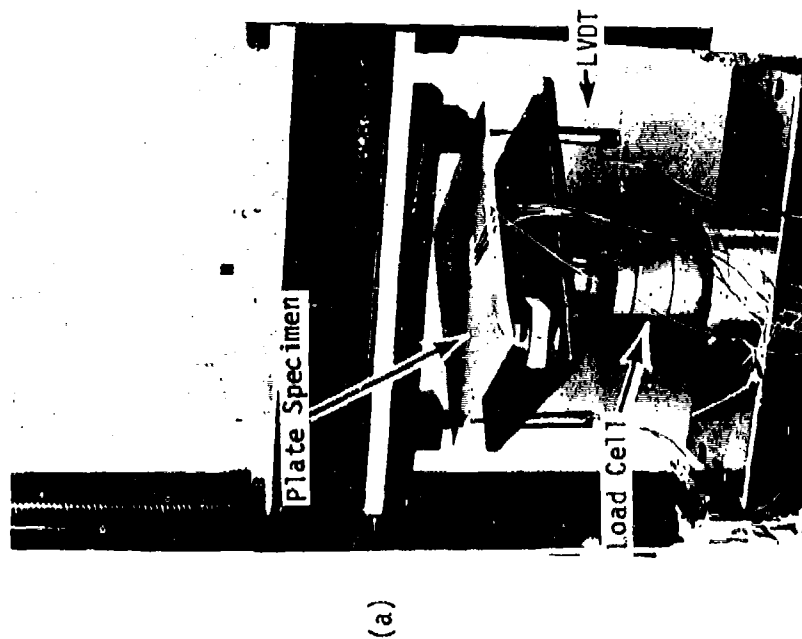


Figure 23. Experimental setup for plate twist test for (a) constant crosshead rate and (b) creep and recovery tests.



weighing the entire loading channel assembly (channel, load bucket, weights, etc.) before the test. The load was lowered onto the plate diagonal as rapidly as possible, using several guide clamps to assure the alignment of the applied load.

### Experimental Considerations

#### Bending and Grip Effects

The use of off-angle tensile specimens ( $0^\circ < \theta < 90^\circ$ ) under uniaxial loads creates bending moment and shear stress distributions along the length of the specimen due to the existence of rigid clamps which are prevented from rotating. The clamping condition was investigated in [167,185] and it was shown in [167] that the difference between the actual compliance and the compliance defined by the centerline strain and the axial stress (axial force divided by the cross-sectional area) was less than 1% for an E-glass/epoxy composite. It was pointed out that the effect is a strong function of the geometry of the tensile coupon as well as its anisotropy. For the materials and specimens employed in this program this condition was found to be negligible.

#### Strain Gage Heating

The use of bonded foil resistance strain gages has been found to lead to significant gage-specimen interaction if the material is near the softening or transition temperatures. High resistance

gages of 350 ohms were used to minimize the local heating. An earlier study [60] conducted on the Shell 58-68R epoxy resin showed that local heating for these same gages was on the order of 3-5°F for a 2.5 volt bridge excitation voltage. The gages used had a lower power output than some other available gages such as the more common 120 ohm foil gages.

#### Humidity Effects

Humidity has been shown to affect polymeric materials in much the same way as temperature [11]. An increase in relative humidity, or water content, is equivalent to an increase in temperature. Several experiments were conducted on an E-glass/epoxy composite [186] which showed that humidity control should be considered during any characterization test program. In view of this fact, the samples were always allowed to reach an equilibrium in the test environment for a period of at least 24 hours. The humidity in the environmental chambers was held constant during the experiments. However, it was not possible to maintain a given relative humidity level at all of the temperatures tested because of equipment limitations.

#### Softening and Transition Temperatures

The softening temperature of a material has generally been defined as the approximate value at which a rapid increase in creep

rate begins as the specimen is slowly heated. Above the softening temperature the composite becomes extremely soft and loses its practical structural value. One way to obtain an estimate of this temperature has been to conduct a low stress level creep test on an off-angle specimen while slowly increasing the temperature [9, 12]. The point or region at which the creep rate rapidly increases is then defined as the "softening temperature".

Another temperature, the glass transition temperature,  $T_g$ , represents the point at which the physical mechanism of deformation within the polymer changes due to a significant change in free volume [52]. As an epoxy resin or composite system is heated through the transition temperature, the expansion coefficient has been found to increase by a factor of two or three. The  $T_g$  represents a more physical change in the polymeric system and is always below the softening temperature. It was necessary to determine the region where the transition took place in order to define the maximum temperature for the characterization tests.

The thermal expansion behavior of the test materials (Shell 58-68K epoxy resin, S-901 glass/epoxy resin and aluminum) was determined with a DuPont Thermal-Mechanical Analyzer (TMA)<sup>10</sup>. The TMA consists of a fused quartz holding tube and an LVDT probe to measure the expansion characteristics of small samples under variable heating and cooling rates. A sample of each material measuring

---

<sup>10</sup>E.I. DuPont de Nemours and Co., Inc., Wilmington, Delaware.

approximately  $1/4" \times 1/4" \times 1/8"$  was cut from a representative section of the plates. The specimen was a unidirectional laminae with the expansion measured in the direction of the plate thickness. The aluminum sample was used primarily as a reference standard. Each sample was thermally cycled (heating followed by cooling) several times at a rate of  $10^{\circ}\text{C}/\text{minute}$ . The results of these tests are shown in Figures 24 through 26.

All of the materials exhibited a thermal hysteresis loop which was believed to have resulted from the high heating rate used. Even with the small sample dimensions employed, the temperature of the specimen was not expected to be completely uniform at that rate. However, the tests showed several distinct trends which were considered important. The hysteresis loop in the epoxy resin and glass/epoxy composite can be attributed to some degree to the shrinkage and weight loss associated with the initial moisture content of the materials. Freeman and Campbell [187] reported the same effects on epoxy resin and graphite/epoxy composites using a quartz tube dilatometer and slow heating (cooling) rates. After several cycles above the boiling point of water,  $212^{\circ}\text{F}$ , the material appeared to reach a stable state. It is not known at this time if the process is reversible or if any permanent damage has been done.

In the glass/epoxy composite (Figure 26), the effect was more pronounced. The relaxation of thermal stresses (originally developed during curing) and drying out could possibly explain the

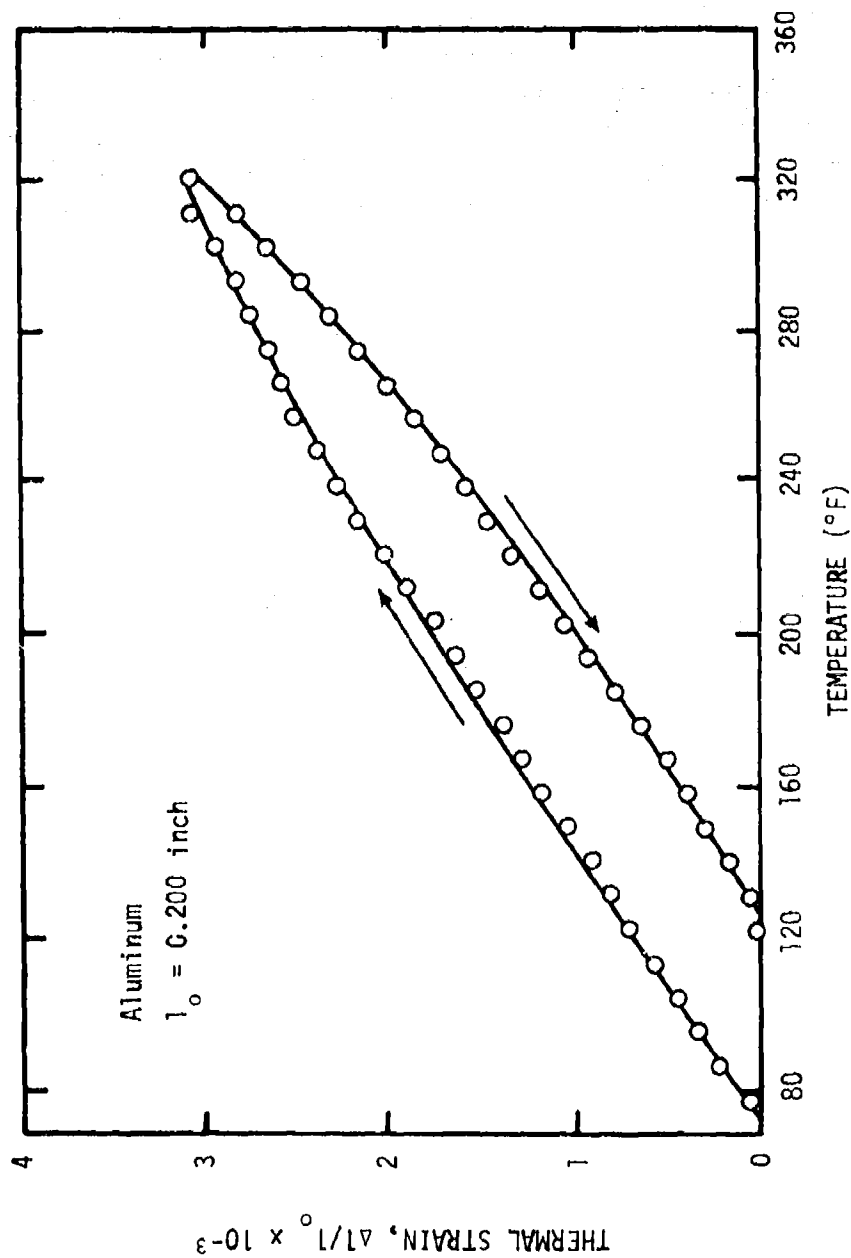


Figure 24. Thermal expansion behavior of aluminum reference material.

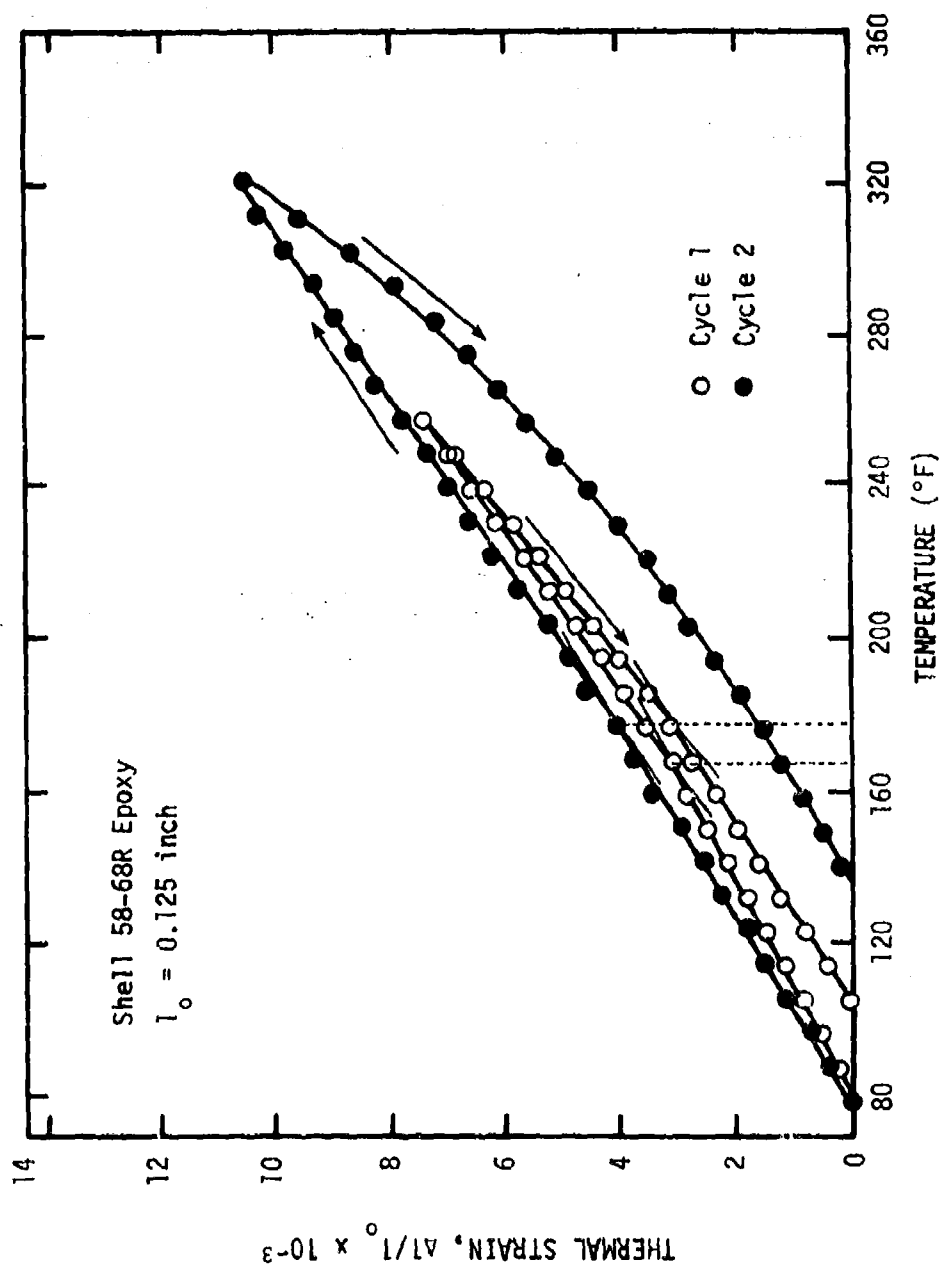


Figure 25. Thermal expansion of Shell 58-68R epoxy resin.

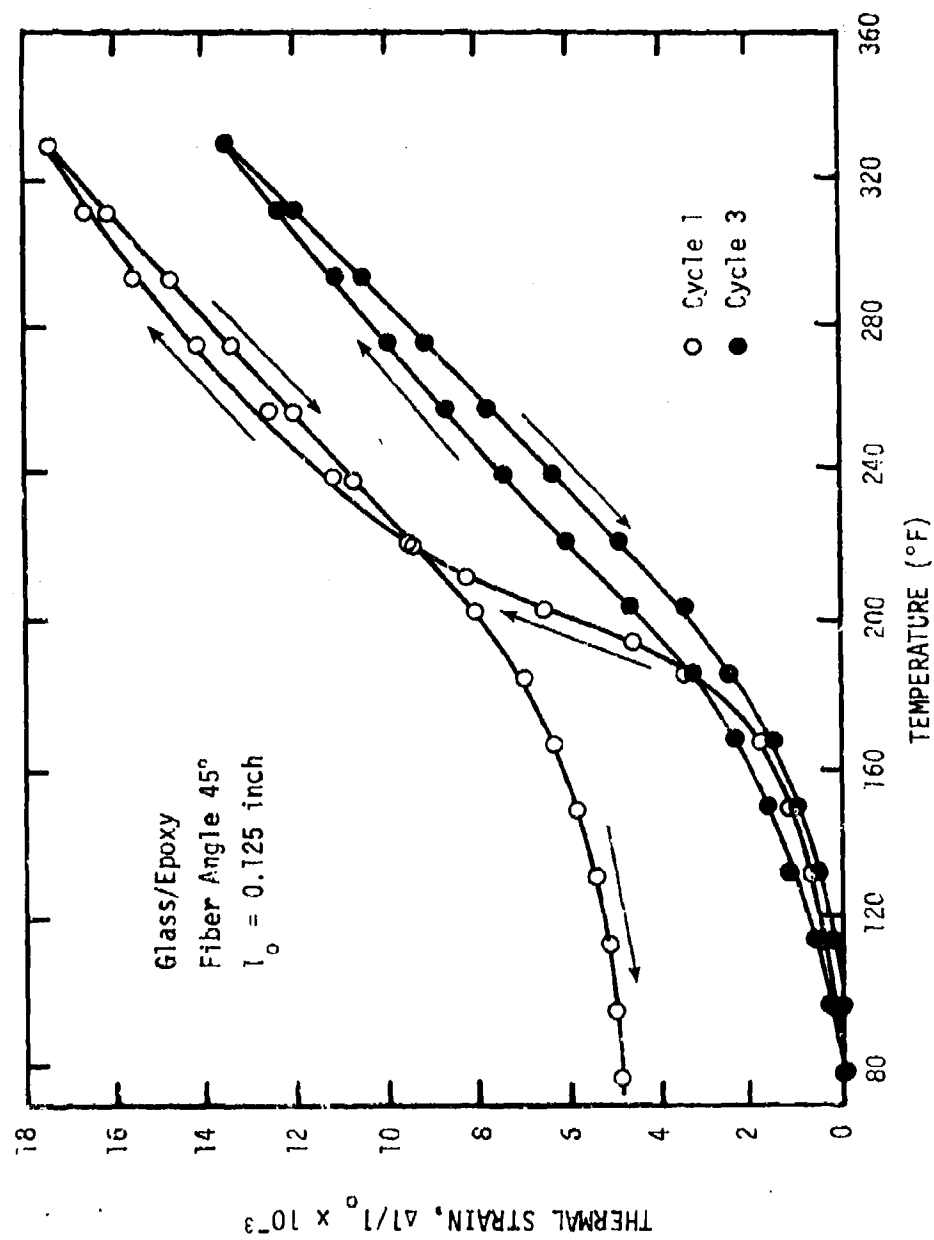


Figure 26. Effect of thermal cycling on the thermal expansion of glass/epoxy composite.

relatively large changes in the first and second thermal cycles. The third cycle appeared to be very stable. The  $T_g$  for these materials appears to be around 180°F or so, while the softening temperature was at a higher temperature. As a result, all of the characterization tests were conducted below 160°F after drying the samples for at least 24 hours. These effects are discussed in Section V with regard to composite design and analysis.

#### Preliminary Characterization Tests

Several preliminary tests were conducted to determine some of the basic properties of the S-901 glass and glass/epoxy composite system. These properties were used as a guide in establishing various test parameters.

#### Fiber Properties

The determination of the fiber properties by SCI was considered necessary to insure that the S-901 glass used in the laminates was within the normal specifications. Consequently, SCI conducted several strength tests on the 20-end, S-901 glass roving taken from each of the three spools used in the fabrication. These strand tensile tests indicated that the tensile strength was nominally 525,000 psi, well above the minimum specification of 500,000 psi [181].

The specific gravity, tensile modulus and Poisson's ratio of the glass fibers were not determined by SCI since this data has been



reported previously [179, 188]

$$\gamma_f = 2.465$$

$$E_f = 12.4 \times 10^6 \text{ psi} \quad (129)$$

$$v_f = 0.22$$

The value used for the specific gravity represents an average of the reported values. These properties are used in subsequent analysis of the overall composite behavior as discussed in Section IV.

#### Fiber Volumetric Content

The fiber content (by volume),  $v_f$ , of a composite material, strongly influences the overall mechanical and physical behavior of the composite as shown by the Halpin-Tsai Equation (119). As a result of its importance in the analysis of the data, glass volumetric tests were run at SCI and TAMU. SCI conducted gravimetric tests on the edge trimmings taken from each panel and determined the resin content, voids and glass volume. Void determinations were generally found to be less than 0.1% and were discontinued after the first four panels [181]. The SCI data is shown in Table 3 along with the values determined by TAMU. Glass fiber content values determined by SCI are considered questionable with regard to being representative of the panel since the samples were edge trimmings.

Table 3. Fiber Content of S-901 Glass/Shell  
58-68R Epoxy Resin Materials

Material or Fiber Angle	Fiber Content (Volume Fraction)	
	$V_f$ SCI [181]	$V_f$ TAMU
0°	.625	.622
20°	.616	.603
45°	.642	.609
90°	.625	.623
0/90°	.667	.615
±10°	.609	.624
±30°	.624	.625
±45°	.665	.613
±60°	.624	.609
±80°	.609	.618
Forward Dome	----	.635

Fiber content values more representative of the actual test samples were determined from samples cut from the interior of the panels (i.e., away from the edges). These tests were conducted on samples which had been tested and were not needed for further testing. Specimens were generally cut from the center sections of the tensile coupons after removing the strain gage. Each sample was carefully weighed and then heated in a muffle furnace at 600°F for 4 hours and then 1200°F for 24 hours [179]. After this sequence the resin was completely burned off. The sample was removed to a dessicator where it cooled to ambient temperature. The sample was weighed again and the fiber content determined from the values of specific gravity and measured weights. These values are shown in Table 3 and were considered to be more representative of the actual glass/epoxy composite use in the program.

The fiber content of samples taken from the forward dome of the Minuteman III case was determined after removing the rubber insulation material and the adjacent glass/epoxy lamina. Using the same procedure as before, the fiber content shown in Table 3 was found to be very close to the SCI panels. This makes the comparison of plate and case properties more valid since the volumetric contents of the constituents are almost exactly the same. A value of 0.616, representing the average of the TAMU fiber volume content on the panel specimens, was used for analytical purposes.

### Tensile Coupon Stress-Strain Behavior

In order to establish the creep stress levels and approximate strains for the test program, constant strain rate tests were conducted on the various materials which were used during the program. These tests were run using an Instron tensile tester at a crosshead rate of 0.02 inches per minute at temperatures of 75°F and 140°F. These temperatures essentially represent the range investigated during the program.

The rectangular tensile coupons described in an earlier subsection were used for the tests. Wedge-action grips were used rather than the pin-connected creep grips since the samples were taken to complete failure. It should be noted that this particular specimen design provides excellent mechanical characterization data for a uniaxial stress field; however, because the specimen does not have a reduced test section, the specimen will usually fail prematurely near the grips or end tabs. Consequently, these specimens were not used to generate failure stress-strain information and the constant rate tests employed here served only as a guide for establishing test limit conditions.

The stress-strain behavior of the Shell 58-68R epoxy resin and S-901 glass/epoxy resin is shown in Figures 27 through 37. The influence of temperature is evident, and the possible presence of nonlinear, viscoelastic material behavior is particularly noticeable for the off-angle glass/epoxy orientations. Strain data past

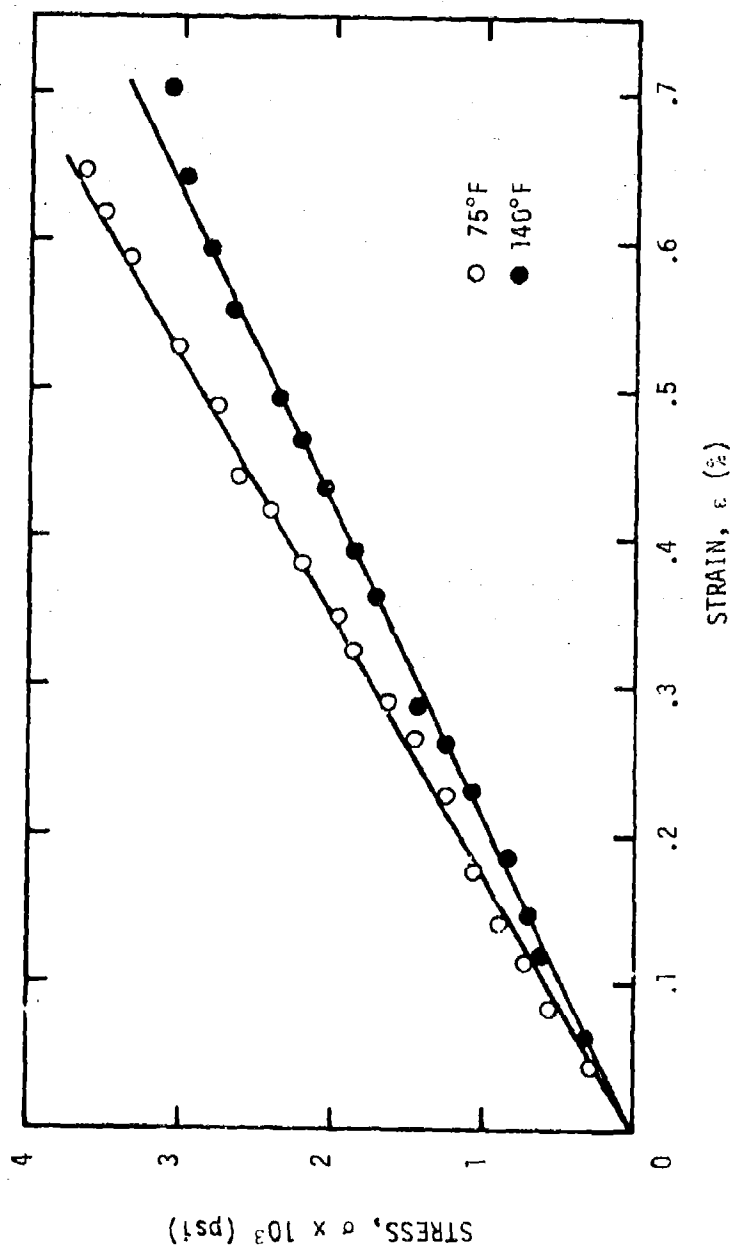


Figure 27. Stress-strain behavior of Shell 58-68R epoxy.

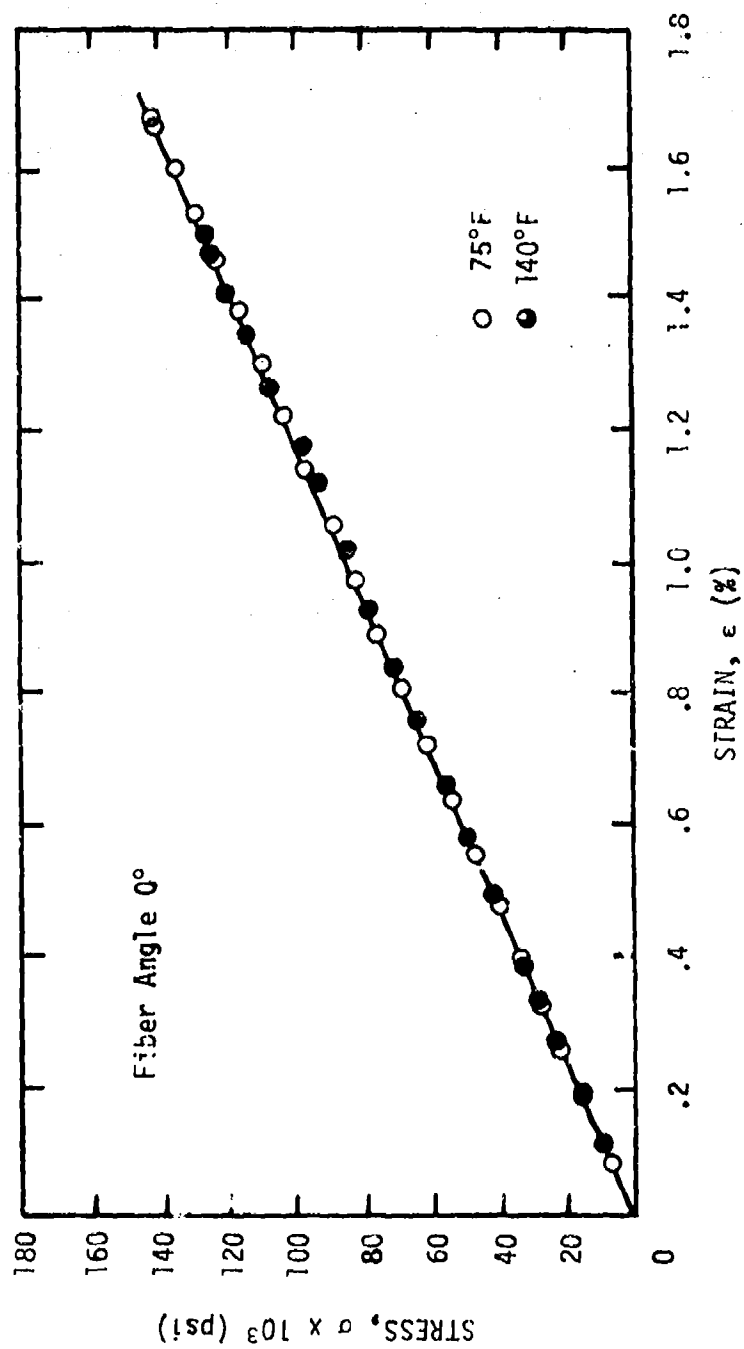


Figure 28. Stress-strain behavior of unidirectional glass/epoxy ( $\theta = 0^\circ$ ).

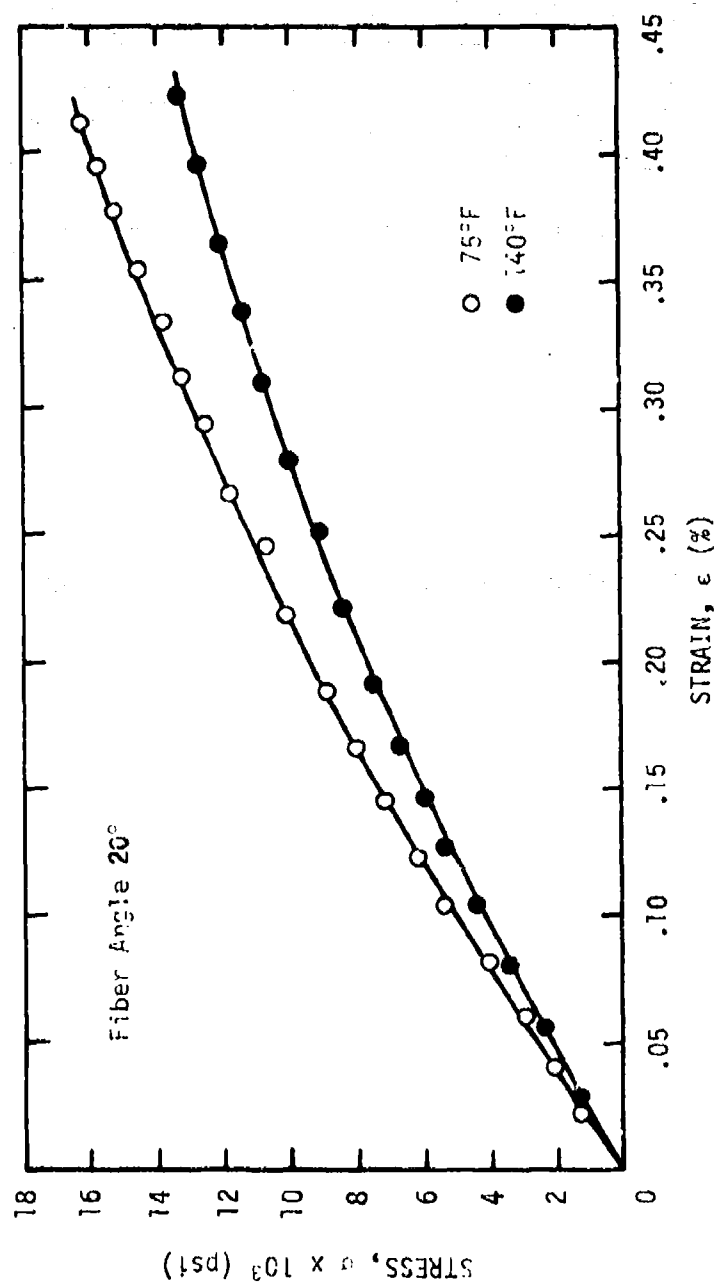


Figure 29. Stress-strain behavior of unidirectional glass/epoxy ( $\theta = 20^\circ$ ).

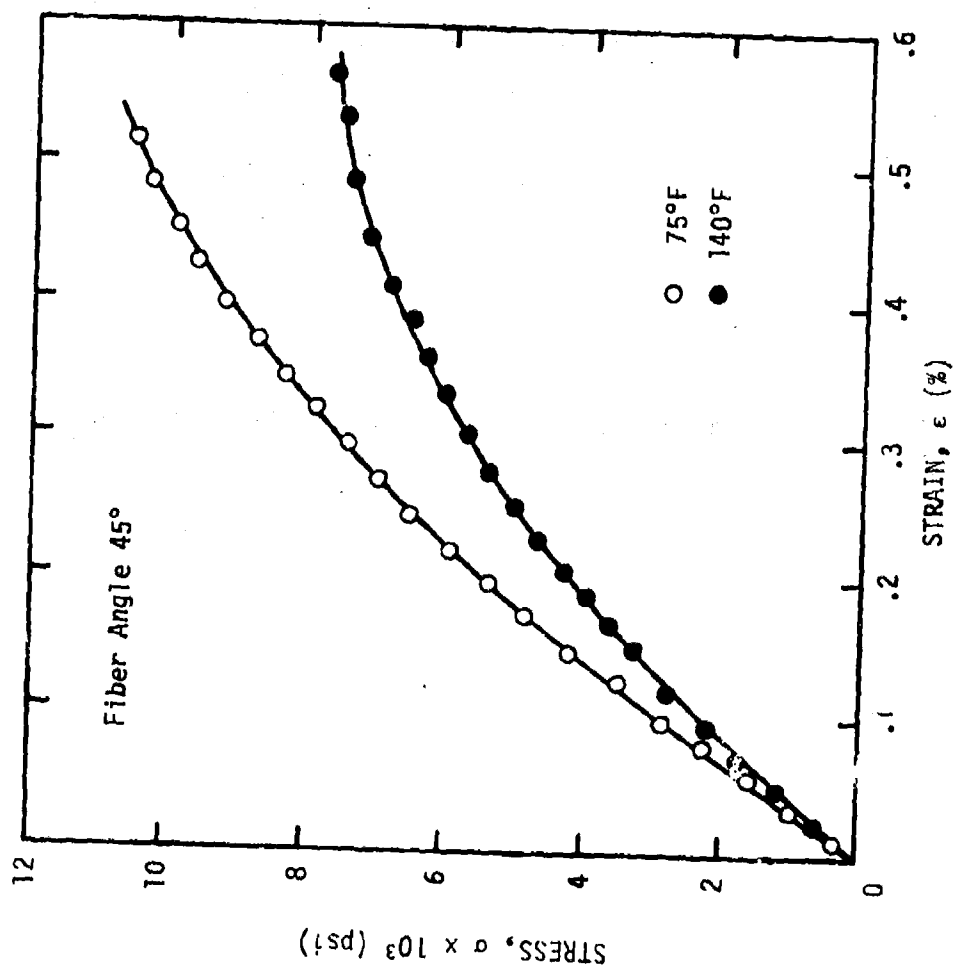


Figure 30. Stress-strain behavior of unidirectional glass/epoxy ( $\theta = 45^\circ$ ).



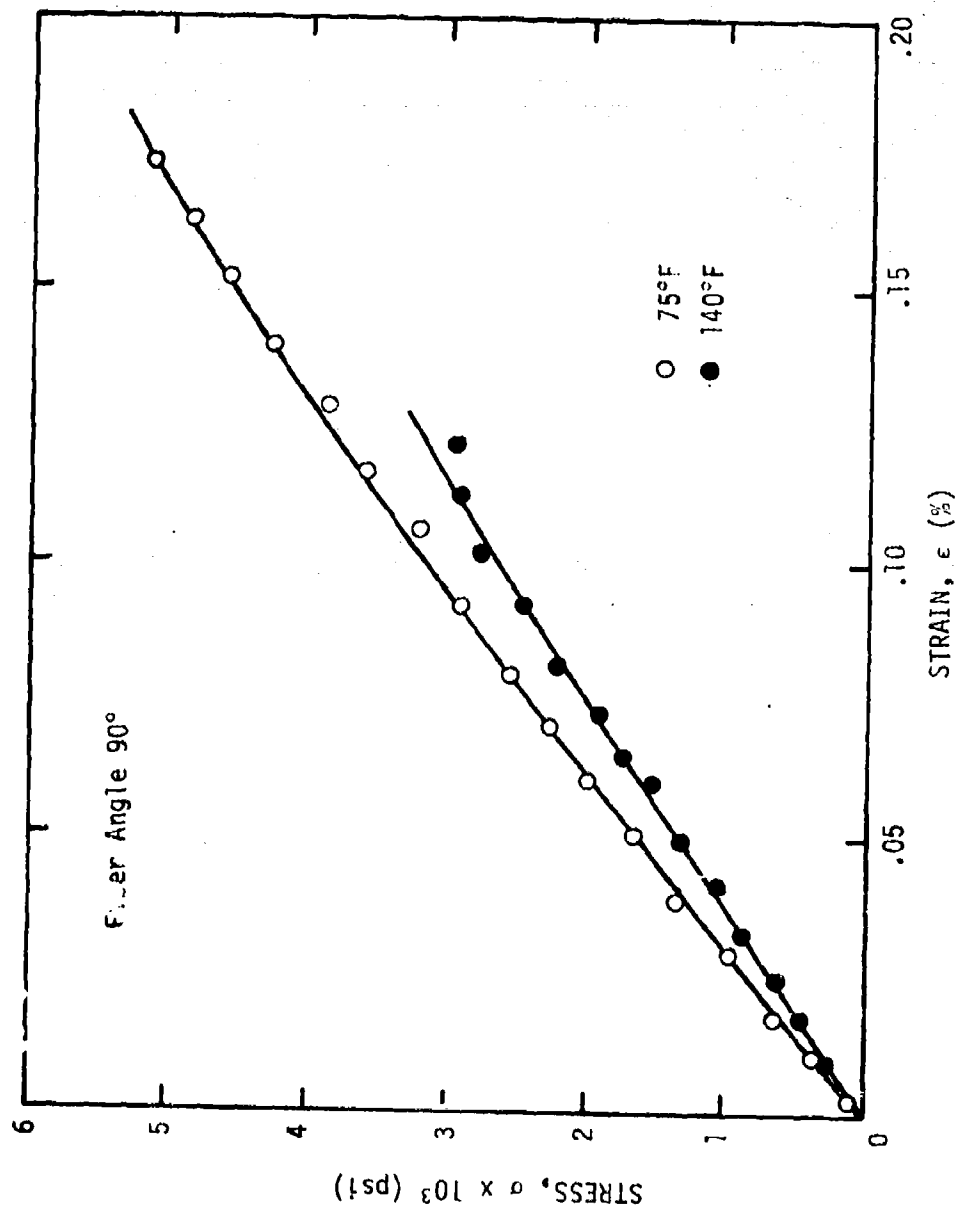


Figure 31. Stress-strain behavior of unidirectional glass epoxy ( $\theta = 90^\circ$ ).

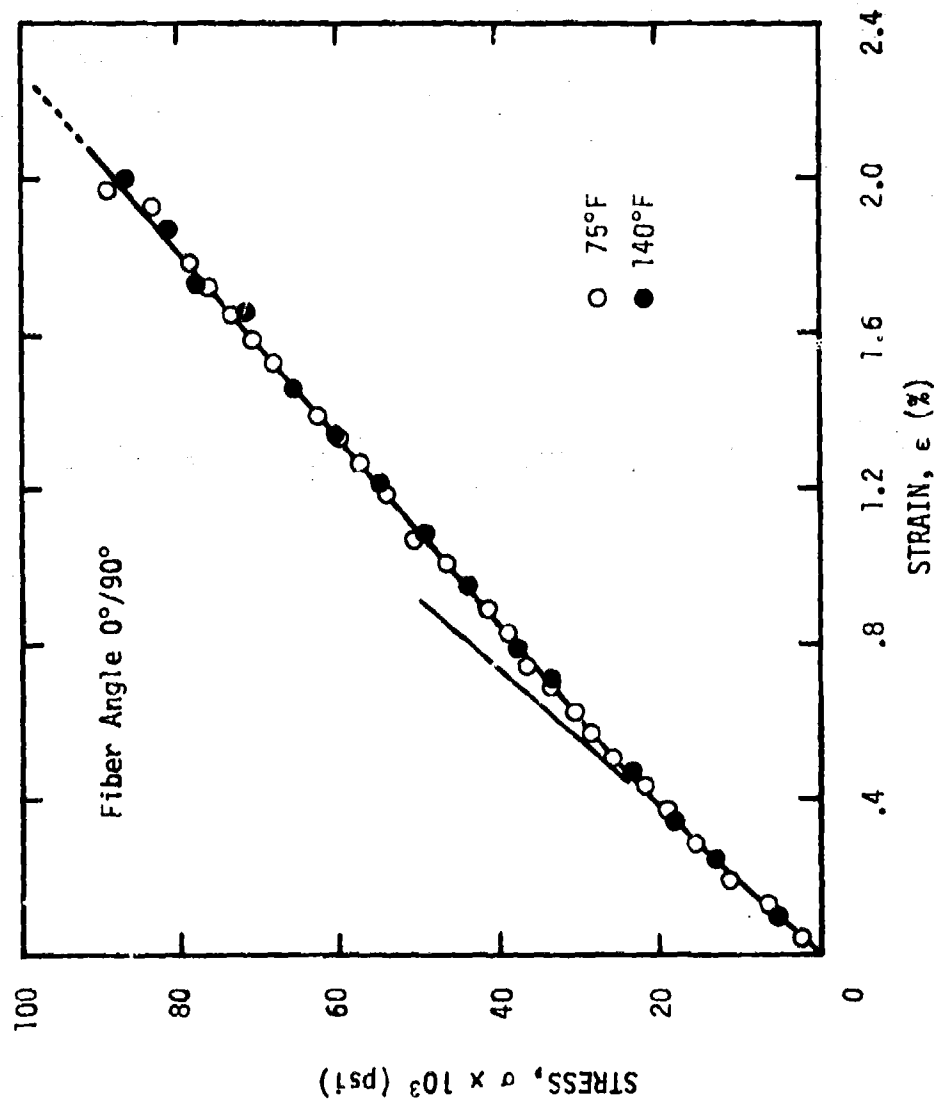


Figure 32. Stress-strain behavior of laminated glass/epoxy  
( $\theta = 0^\circ/90^\circ$ ).

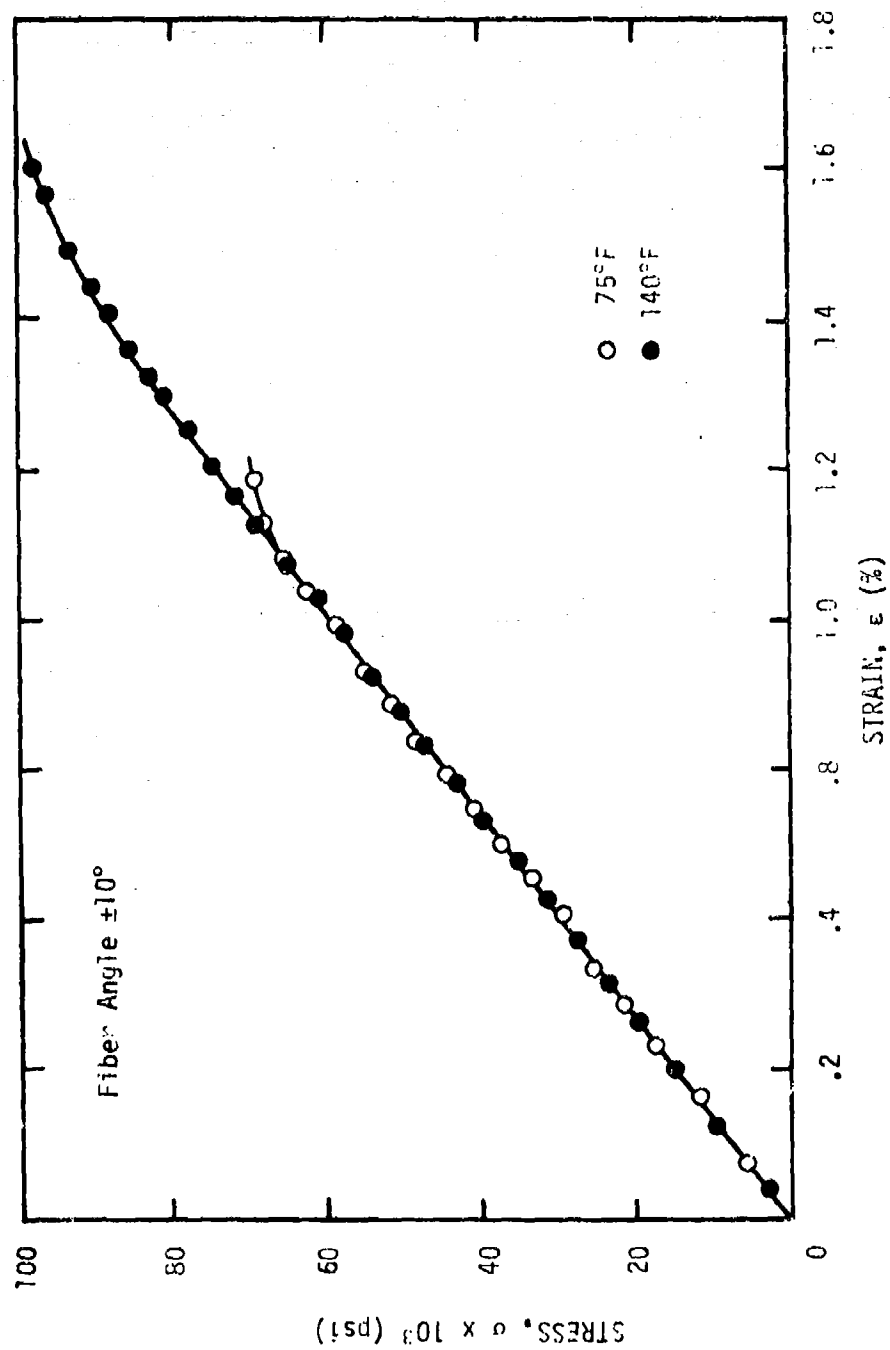


Figure 33. Stress-strain behavior of laminated glass/epoxy ( $\theta = \pm 10^\circ$ ).

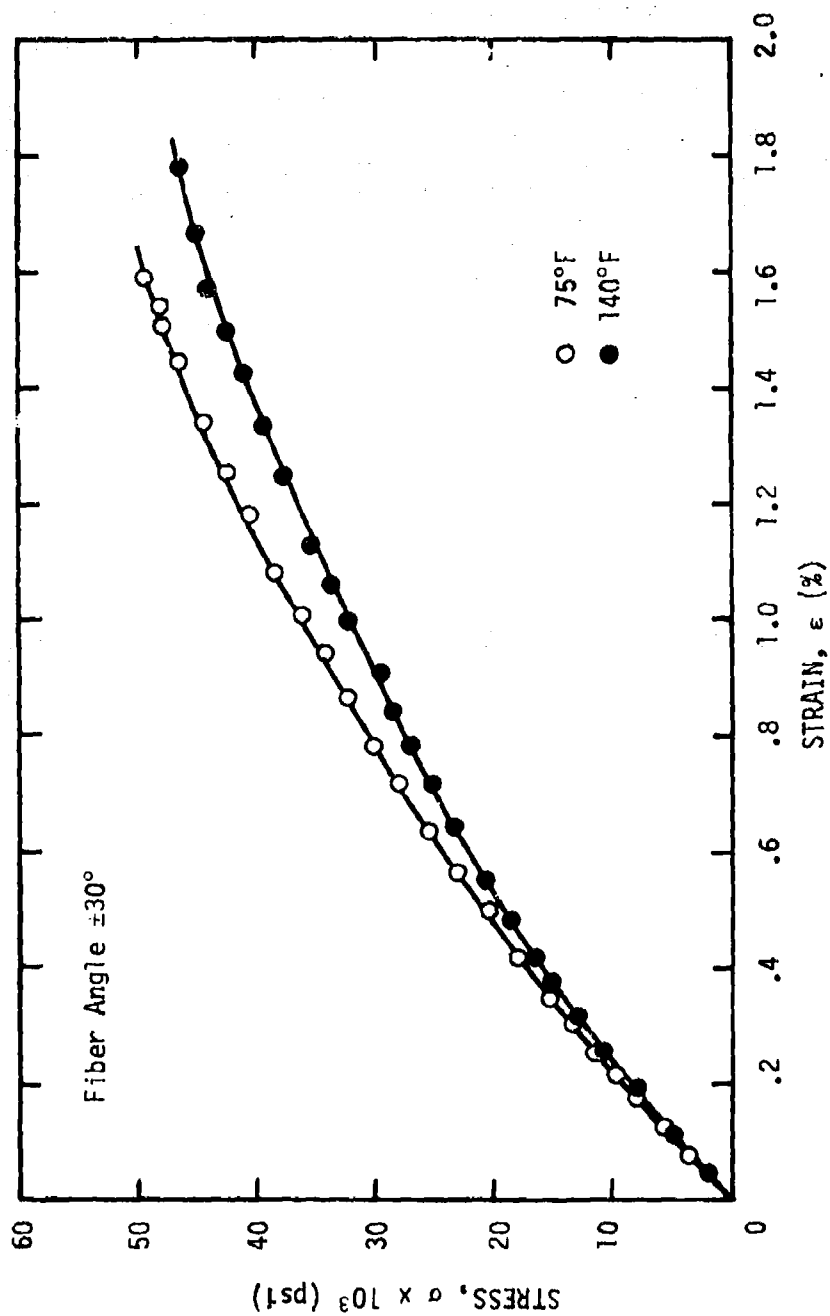


Figure 34. Stress-strain behavior of laminated glass/epoxy ( $\theta = \pm 30^\circ$ ).

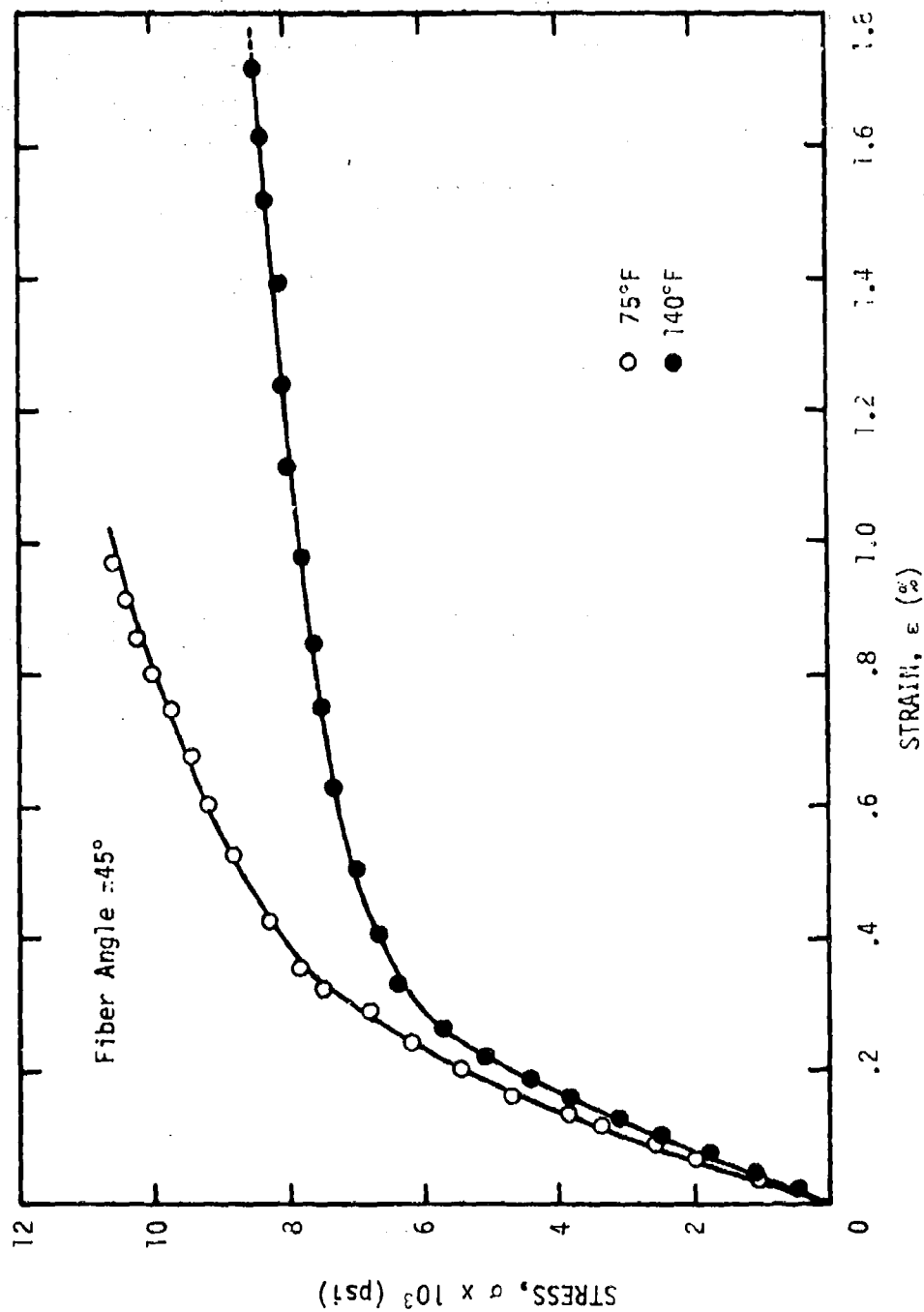


Figure 35. Stress-strain behavior of laminated glass/epoxy ( $\theta \approx 45^\circ$ ).

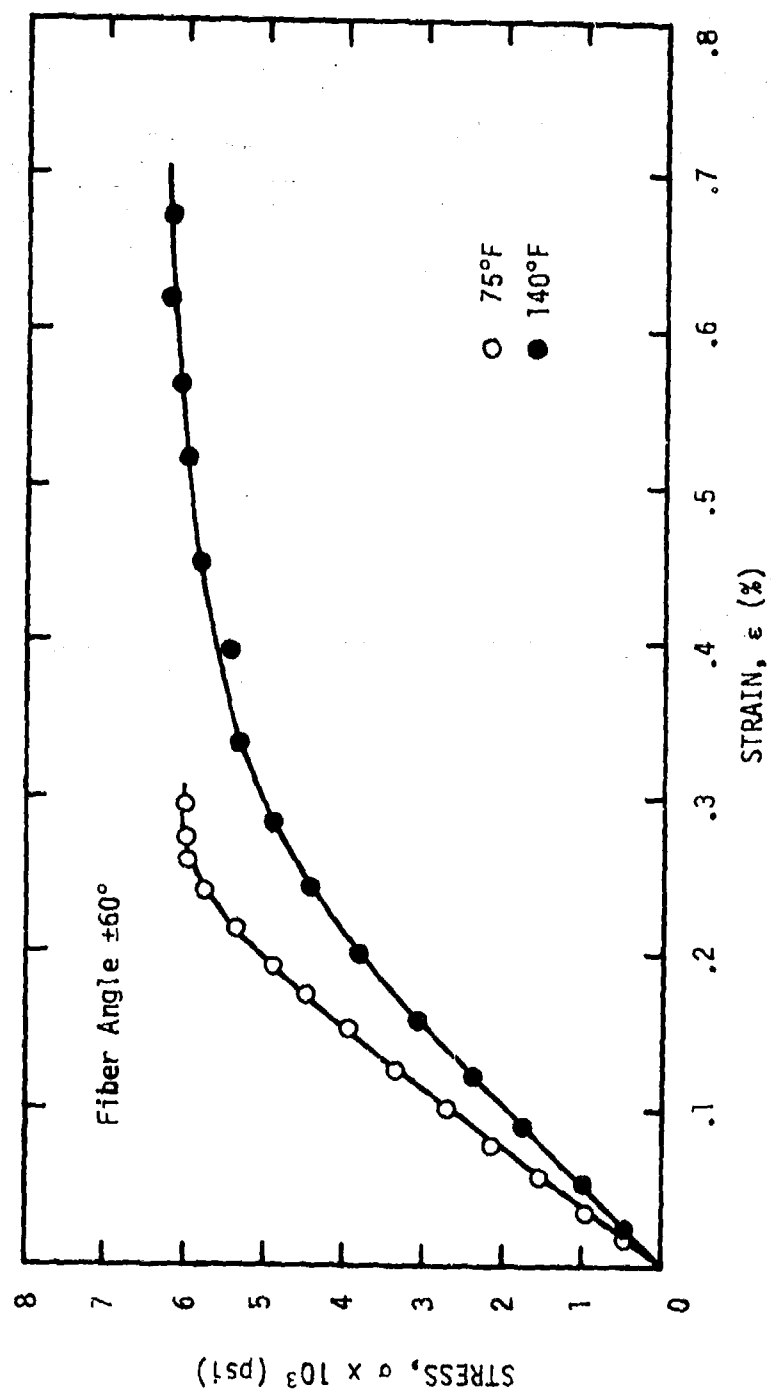


Figure 36. Stress-strain behavior of laminated glass/epoxy ( $\theta = \pm 60^\circ$ ).

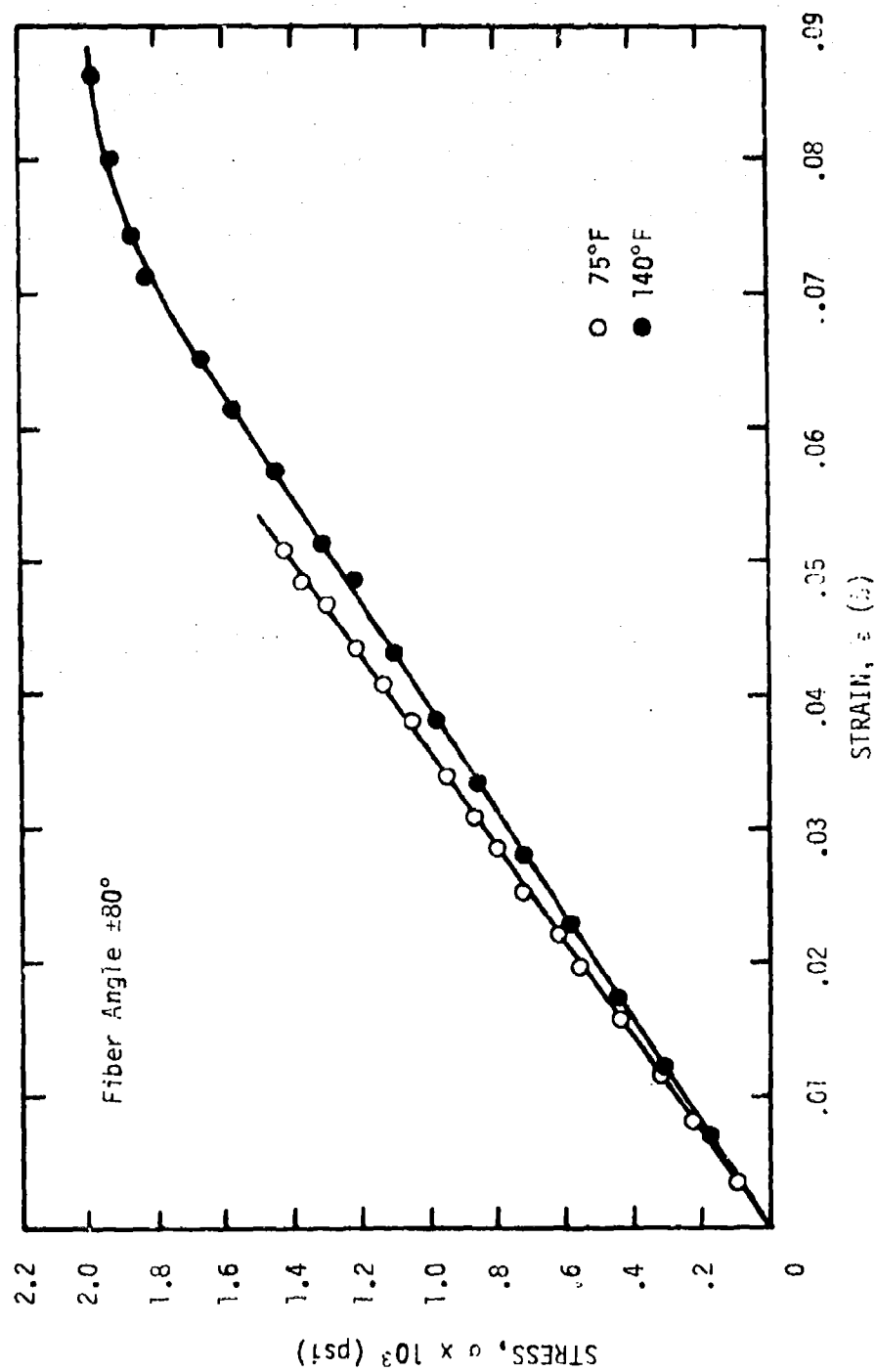


Figure 37. Stress-strain behavior of laminated glass/epoxy ( $\theta = \pm 80^\circ$ ).

2% was not available for the  $0^\circ/90^\circ$  and  $\pm 45^\circ$  fiber angles because of equipment limitations, but the extrapolated behavior is shown as a dotted line in the respective figures.

### Constant Crosshead Rate Tests

#### Uniaxial Tension

Using the tensile coupons with the  $5^\circ$  wedge-shaped end tabs, a series of constant crosshead rate tests were conducted on several  $45^\circ$  and  $\pm 45^\circ$  glass/epoxy samples. These tests were carried out at temperatures of  $75^\circ\text{F}$  and  $140^\circ\text{F}$  using the Instron and the environmental rooms. Each sample was tested at a crosshead rate of 0.02 inches per minute to a stress level of 6000 psi and then unloaded to zero stress at a crosshead rate of 0.2 inches per minute. Three cycles were run on each sample after waiting approximately 5 minutes between cycles. All of the tests were conducted with the Instron wedge-action grips. A second set of  $5^\circ$  wedges, placed in the grips with a piece of Teflon tape facing the sample end tabs, permitted the sample to hang free of obstructions upon unloading. This technique gave more consistent results and allowed the specimen to recover unhindered (zero stress).

#### Four-Point Beam Bending

All of the beam bending tests were performed at  $75^\circ\text{F}$  using the Instron tensile tester and a crosshead rate of 0.2 inches



per minute. Glass/epoxy specimens with fiber angles of  $\pm 45^\circ$  and  $0^\circ/90^\circ$  and filament-wound specimens with nominal fiber angles of  $\pm 20^\circ$  and  $\pm 70^\circ$  were used in the tests. Since only one side of the specimen was strain-gaged, the side with the gage was mounted face downward in order to record the tension strain. In the case of the filament-wound specimen this corresponded to the surface without the rubber insulation material. The temperature compensating specimens were mounted on the end of the support fixture in the same position so as to compensate for creep effects due to the sample weight. This procedure was necessary primarily for the thinner filament-wound case materials which were more flexible.

The beam samples were loaded to a preselected maximum stress (load) and then unloaded completely, always at the same crosshead rate. Strain and load information were recorded continuously during this period and at specified time intervals following the complete unloading. A recovery period of approximately three times the complete cycle time was allowed before starting the next load cycle. Each maximum stress (load) cycle was repeated in the same manner until two or three cycles were completed. The beam was then subjected to another preselected, higher, maximum stress (load) cycle following the previous procedure.

The maximum stress (load) levels for each of the beams tested are given in Table 4 in terms of the bending moment,  $M_x$  (in-lbs), which existed at the center section of the beam.

Table 4. Summary of Maximum Bending Moment,  $M_x$  (in-lbs), for Four-Point Bending Tests (Constant Crosshead Rate)

Fiber Angle	$\pm 45^\circ$	$0^\circ/90^\circ$	$\pm 20^\circ$ (case)	$\pm 70^\circ$ (case)
$M_x$	10	10	5	3
	25	50	10	6
	40	90	25	
	70	150		

#### Plate Twist Test

Constant crosshead rate tests conducted at 75°F and 0.1 inches per minute were carried out on a 6061-T6 aluminum and a  $\pm 45^\circ$  glass/epoxy plate. During the tests the outputs from the Instron load cell, the surface strain gages and the corner LVDT's were monitored continuously. The aluminum plate was used primarily as an isotropic reference material and was loaded only within its linear elastic range.

Each test consisted of loading and unloading the plate to a preselected maximum load level at the same crosshead rate. After unloading, the plate was allowed to recover for a period of approximately three times the complete cycle time before starting the next cycle. In the case of the aluminum, the plate was cycled twice to a load level of about 50 pounds. This corresponded to a twisting moment,  $M_{xy}$ , of almost 25 in-lbs. The  $\pm 45^\circ$

glass/epoxy plate was cycled in a similar manner. Each cycle was repeated three times before increasing the maximum load level. Three load levels were studied, corresponding to twisting moments,  $M_{xy}$ , of 25, 42 and 53 in-lbs in succession.

### Single and Multiple Cycle Creep and Recovery Tests

#### Uniaxial Tension

In order to characterize the epoxy resin and glass/epoxy composites, both single and multiple cycle creep and recovery tests were conducted. The creep test consisted of rapidly applying a constant uniaxial load to the tensile coupon and measuring the resultant strain for one hour. This test was immediately followed by a recovery test where the constant load was suddenly removed and the strain was measured for two hours. Each specimen underwent several creep-recovery cycles in order to assess the effects of internal microcracking.

Earlier studies conducted on an E-glass/epoxy composite [9] indicated that a significant amount of internal microcracking occurs during the first few loading cycles with consistent creep behavior occurring only after as many as ten loading cycles. The effects of multiple cycling were investigated for approximately three creep-recovery cycles in order to model typical hydrotesting damage in filament-wound motor cases.

After completion of one cycle (creep and recovery), the total strain was recorded, the strain electrically rezeroed and the next cycle was initiated. The strain was therefore referred to the specimen length which existed at the end of each cycle and little time was permitted for bond reformation between flaw surfaces. This last point was considered important since the earlier work on the E-glass/epoxy indicated that long recovery periods created a necessity for repeating the mechanical conditioning due to re-healing.

Tests on the Shell 58-68R epoxy resin matrix material were conducted over a temperature range from 20°F to 160°F for two cycles of creep and recovery. Several stress levels ranging between 200 psi and 2000 psi were investigated during this phase of the program. Most of the creep and recovery tests carried out on the S-901 glass/Shell 58-68R epoxy resin were performed at 75°F and 140°F with the exception of a few tests conducted on 45° and ±45° glass/epoxy specimens at 20°F to establish the validity of time-temperature superposition (Tables 5 through 7). Three cycles of creep and recovery were completed for each sample. As many as five different stress levels were studied for each fiber angle studied, depending on the degree of nonlinearity observed in the constant crosshead rate stress-strain behavior. Most of the work centered around the 20°, 45°, ±30° and ±45° glass/epoxy composite layups.

Table 5. Summary of Uniaxial Creep and Recovery Tests (T = 20°F)

Fiber Angle ( $\theta$ )	Stress (psi)	Number of Cycles
Epoxy	600	2
	1200	2
0	7000	2
45	520	3
	3010	3
90	500	3
±45	520	3
	3270	3

Table 6. Summary of Uniaxial Creep and Recovery Tests ( $T = 75^{\circ}\text{F}$ )

Fiber Angle ( $\theta$ )	Stress (psi)	Number of Cycles
Epoxy	200	2
	400	2
	600	2
	1200	2
	2000	3
0	7000	3
	42,000	3
20	2000	2
	4800	3
	8700	3
	10,500	3
	12,500	3
45	500	3
	3000	3
	5000	2
	6400	3
	8500	1
90	550	3
	2000	3
	4000	3

Table 6. (Continued)

Fiber Angle (°)	Stress (psi)	Number of Cycles
0/90	4500	3
	29,000	3
	69,300	3
±30	2500	3
	15,000	3
	30,000	3
	40,000	3
±45	500	3
	3000	2
	5000	3
	7000	3
	8500	3
±60	300	3
	2000	3
	5100	3
±80	300	3

Table 7. Summary of Uniaxial Creep and Recovery Tests ( $T = 140^{\circ}\text{F}$ )

Fiber Angle ( $\theta$ )	Stress (psi)	Number of Cycles
Epoxy ( $145^{\circ}\text{F}$ )	200	2
	400	2
	600	2
	1200	2
	2200	2
0	42,600	3
20	2000	3
	4800	3
	8500	2
	10,500	2
45	500	3
	3000	2
	5000	3
	6500	1
90	500	2
	1500	2
	2400	2



Table 7. (Continued)

Fiber Angle ( $\theta$ )	Stress (psi)	Number of Cycles
0/90	4500	3
	26,000	2
	69,000	1
$\pm 30$	2500	2
	15,000	3
	30,000	2
	40,000	1
$\pm 45$	500	3
	3000	2
	5200	2
	7000	3
$\pm 60$	300	3
	2000	3
	5000	1

Creep and recovery tests were also conducted on specimens of the filament-wound case material at 75°F. A fiber angle of  $\pm 70^\circ$  was used for this series of tests because of the lower specimen curvature in the circumferential direction. Stress levels of 300 psi and 1000 psi were used for this series of tests. Three creep and recovery cycles were run on each specimen at the selected stress level.

#### Four-Point Beam Bending

Using basically the same procedures applied in the constant crosshead rate tests, three cycles of creep and recovery were run on samples of the same fiber orientation at 75°F. The maximum creep stress (load) levels for each of the beams tested are given in Table 8 in terms of the bending moment,  $M_x$  (in-lbs), which existed at the center section of the beam.

Table 8. Summary of Maximum Bending Moment,  $M_x$  (in-lbs), for Four-Point Bending Tests (Creep and Recovery)

Fiber Angle	$\pm 45^\circ$	$0^\circ/90^\circ$	$\pm 20^\circ$ (case)	$\pm 70^\circ$ (case)
$M_x$	1.25	1.25	3.0	1.5
	55.5	85.0	10.5	5.5

### Plate Twist Test

Creep and recovery tests on the  $\pm 45^\circ$  glass/epoxy plate were conducted at load levels corresponding to a maximum twisting moment,  $M_{xy}$ , of 3.0 and 16.7 in-lbs successively. Each cycle was repeated three times before increasing the maximum load level. The strain output from the surface gages and the corner deflections from the LVDT's were monitored on a logarithmic time scale during the creep and recovery phases. The loads were set in place on the surface of the plate manually, using the guide fixtures in Figure to assure alignment. Recorded data was taken only after the loads were completely aligned; usually on the order of 20-30 seconds after initial application.

## SECTION IV

## DATA REDUCTION AND ANALYSIS OF RESULTS

## Uniaxial Creep and Recovery of Epoxy Matrix

## Determination of Material Constants

In Section II several analytical forms used to represent the compliance of viscoelastic materials were discussed. The power law form given by Equation (50) has been found to represent the behavior of many rigid plastics with and without reinforcement [73-76]. The compliance given by Equation (50), repeated here for convenience, is

$$D(t) = D_0 + D_1 t^n \quad (50)$$

where  $D_0$ ,  $D_1$  and  $n$  are positive constants which are independent of time. The values of the material constants may reflect temperature dependence if the material is a TCM, as was noted earlier.

In the case of fiber-reinforced plastic composites where the fiber is considerably stiffer than the plastic matrix, the net compliance is relatively small and the initial compliance,  $D_0$ , is not easily discernable from experimental data. This also is true of the epoxy matrix without reinforcement when the epoxy is relatively stiff, i.e.,  $E_0 \approx 0.5(10^6)$  psi. As a result, the constants defining the power law cannot be found accurately from short-term data.

Lou and Schapery [9] developed an analytical procedure for evaluating the constants by employing the power law form of the compliance with experimental data from both creep and recovery tests. The procedure uses the superposition principle in order to represent the recovery compliance defined by (see Figure 1)

$$D_r(t) = \frac{\epsilon_r(t)}{\sigma_0} \quad (130)$$

which results in

$$D_r(t) = D_1 t'^n [(1+\lambda)^n - \lambda^n] \quad (131)$$

where

$$\lambda \equiv \frac{t - t'}{t'} \quad (70)$$

Equation (131) is of the same form as Equation (69) when  $g_1 = g_2 = a_\sigma = 1$  for the linear viscoelastic region and  $t'$  is the time at which the recovery initiates. When Equation (131) is plotted on log-log scales, the result is a standardized curve whose shape is dependent only on the value of  $n$  through the function in the brackets. The exponent  $n$  may be determined by plotting

$$D_{ref} = (1+\lambda)^n - \lambda^n \quad (132)$$

for several values of  $n$  (typically  $0 < n < 0.5$ ) and then overlaying these curves on the experimental recovery data curves to select an

n value as shown in Figure 38. The theoretical curve that fits all of the data most accurately was found to be  $n = 0.19$ . This value appeared to be independent of both stress and temperature.

There are two methods which may be used to evaluate  $D_0$  and  $D_1$  once the value of  $n$  is known. The first uses recovery data plotted on log-log scales and Equation (131). The vertical shift, along the compliance, is equal to  $\log (D_1 t'^n)$ . With the values of  $n$  and  $t'$  already known, the shift value may be used to determine  $D_1$ .  $D_0$  may be found by choosing any point on the creep curve and using Equation (50). The second method for evaluating  $D_0$  and  $D_1$  involves the use of Equation (50) and any two points from the creep data, which are then used to yield two simultaneous equations with  $D_0$  and  $D_1$  as the unknowns.

There are several points which must be made with regard to these procedures, all of which are designed to provide accurate results in the analysis of the creep and recovery data. First of all, it should be noted that, at least for cases where the amount of net creep strain is relatively small, one should always work with data points taken from a smooth curve drawn through the experimental data rather than the individual data points. This is particularly true when the recording equipment can only record strain in units of 1, 2 or 5 microstrain, which at low stress levels is inadequate to show the changes continuously over the time scale. As a result, the data often appears in quantum, or discrete, jumps.

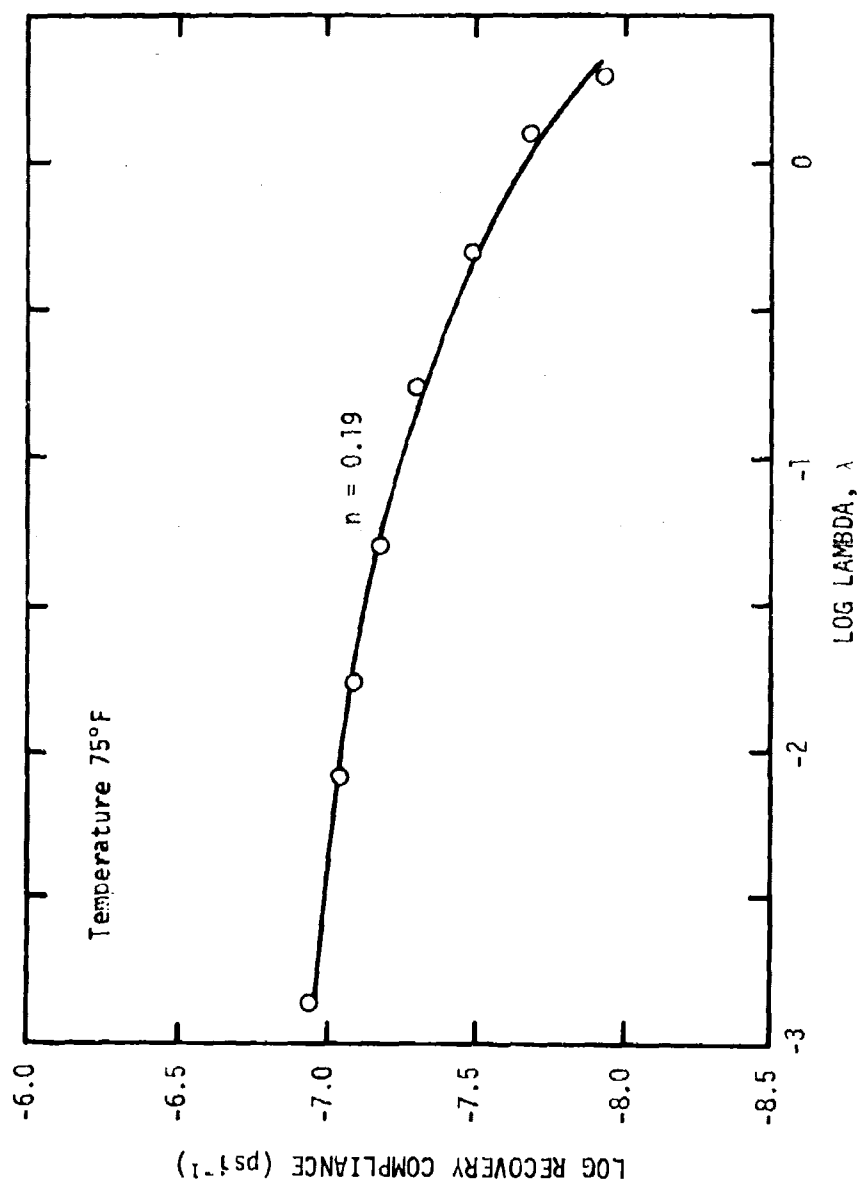


Figure 38. Evaluation of  $n$  using the recovery compliance for the Shell 58-68R epoxy.

Determination by the second method, solution of two simultaneous equations, was found to be easier since the epoxy behaved in a linear viscoelastic manner. In order to accurately determine  $D_0$  and  $D_1$ , creep data were taken at 21 time points, approximately evenly spaced on a log time scale. A computer program was developed to solve pairs of simultaneous equations taken at several time points. This procedure was easier and less time consuming than the method which involved recovery data.

The values of  $D_0$ ,  $D_1$  and  $n$  may be checked by rewriting Equation (50) in the form

$$D(t) - D_0 = D_1 t^n \quad (133)$$

which, if plotted on log-log scales should result in a straight line with a slope of  $n$  and a value of  $D_1$  at  $t = 1$ .

#### Effect of Stress and Temperature

Creep and recovery tests were conducted over a temperature range from 20°F to 160°F at stress levels up to approximately 3000 psi. In all cases the epoxy satisfied both the homogeneity and superposition requirements for linearity up to the maximum stress level studied. The ultimate stress for the epoxy has generally been reported to be in the 9,000-11,000 psi range [179, 180] although the present tensile coupon design did not allow us to reach these levels prior to failure near the grips. Therefore,



it is possible that nonlinearity is present at the higher stress levels. The exponent in the power law,  $n$ , was found to be equal to 0.19 under all test conditions investigated.

The creep compliances for several temperatures are shown in Figure 39 for the epoxy resin using data taken at various stress levels. The  $D_0$  values determined from the solution of simultaneous equations, i.e., Equation (50), are given in Table 9. Also given are the values of  $D_1$  obtained in the same manner and the values of  $D_1$  obtained from the recovery data, i.e., Equation (131).

Table 9. Power Law Constants for Shell 58-68R Epoxy Resin

Temperature (°F)	$D_0 \times 10^{-6}$ (psi <sup>-1</sup> )	$D_1 \times 10^{-6}$ (from creep data)	$D_1 \times 10^{-6}$ (from recovery data)
20	1.726	.019	.025
75	1.883	.069	.069
110	1.934	.124	.142
130	2.022	.161	.171
145	2.012	.198	.201
160	2.070	.232	.247

The temperature dependence of  $D_0$  can be seen in Figure 40 to increase linearly with temperature. As a result the epoxy must be treated as a TCM-2 where  $D_0 = D_0(T)$ . This is particularly important when conditions of transient temperature exist in a structure.

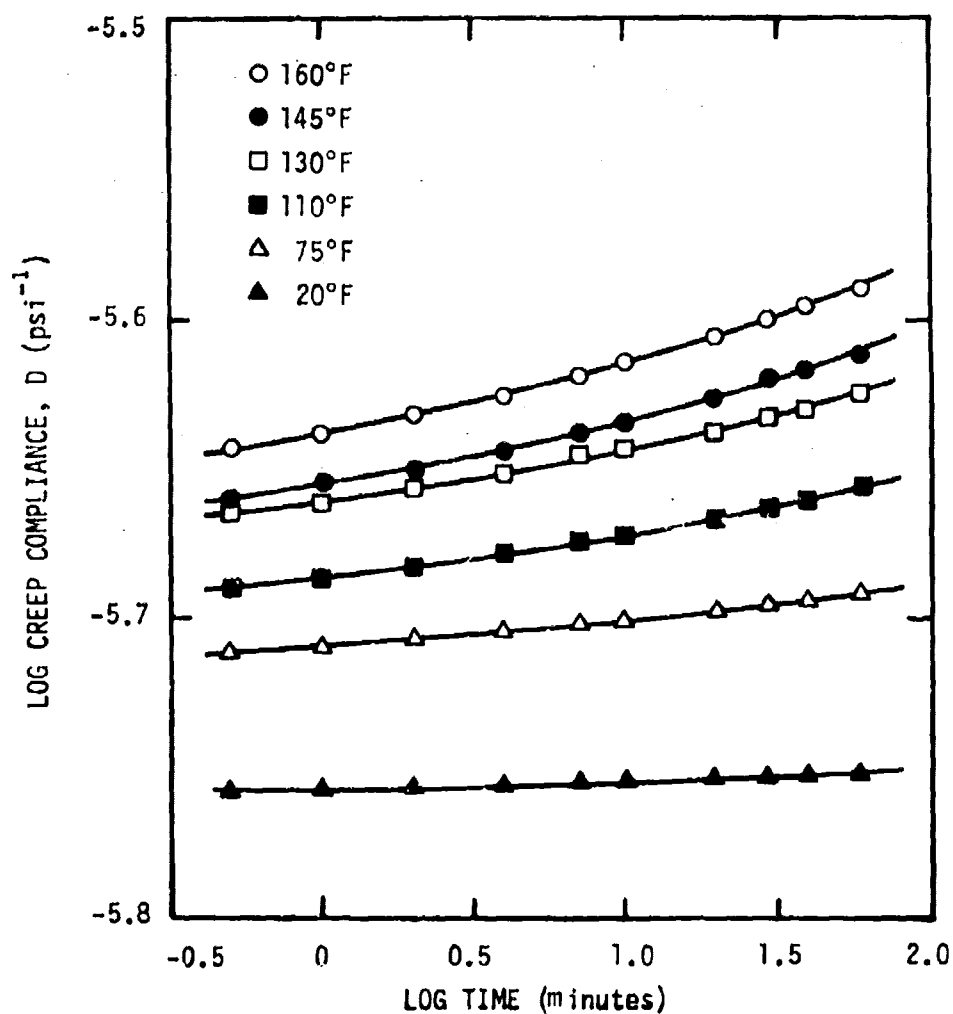


Figure 39. Creep compliance for Shell 58-68R epoxy as a function of temperature.

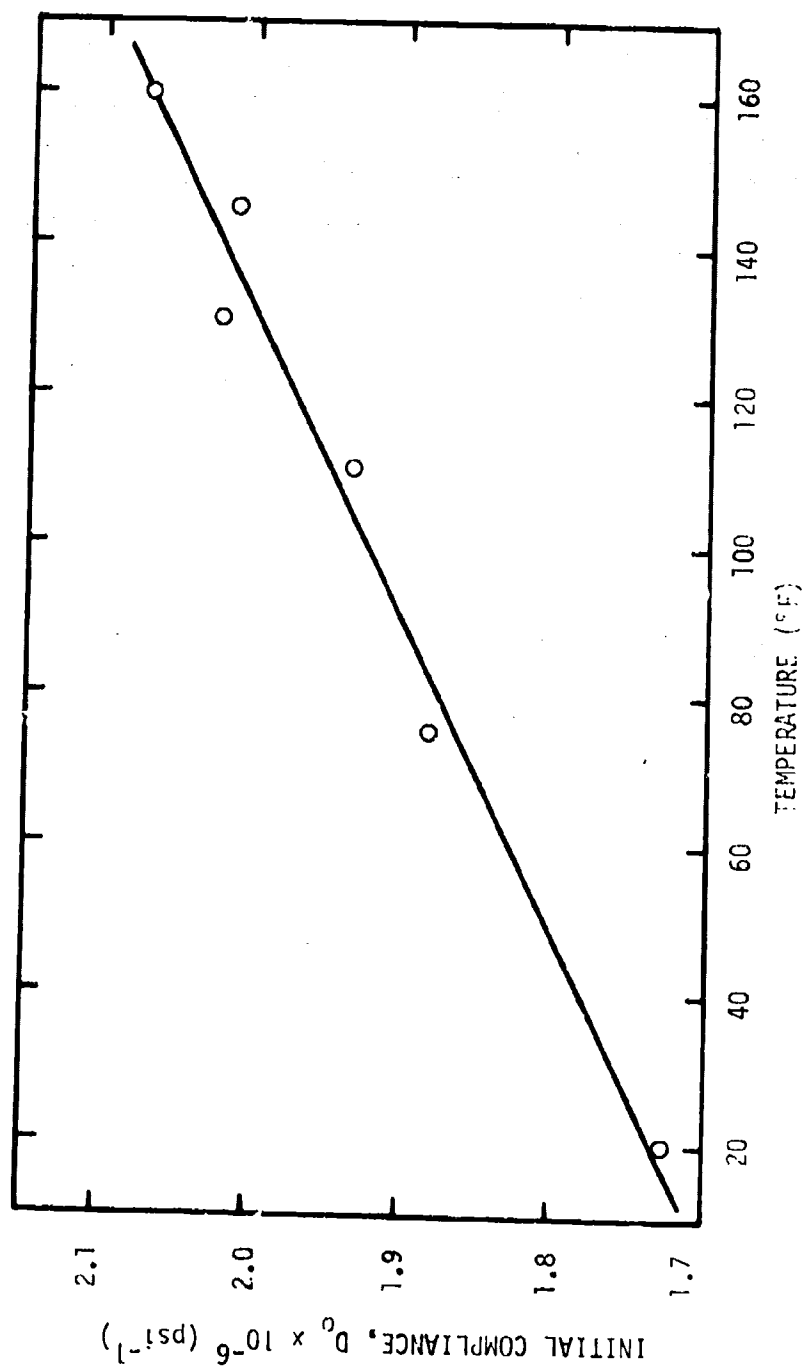


Figure 40. Temperature dependence of initial compliance,  $D_0$ , for Shell 58-68R epoxy.

In all future analysis, the value of  $D_0$  for a specific temperature was obtained from the curve drawn in Figure 40 and not the individual data points. It should also be noted that Watkins [60] shows a somewhat different relationship for  $D_0(T)$  in some earlier work. The difference appears to be the result of only a limited amount of preliminary data at the time the earlier work was done. The preliminary work was done on several samples which were not adequately temperature compensated; however, the general trend is the same in both cases.

After subtracting the initial compliance,  $D_0$ , the net creep compliance,  $\Delta D$ , given by Equation (133) was determined and is shown in Figure 41. The data appears to validate the  $n$  value of 0.19 found from recovery data. The recovery compliances given by Equation (130) are also shown in Figure 42 for the epoxy as a function of the nondimensional time,  $\lambda$ .

The values of the shift factors,  $a_G$  and  $a_T$ , were also found from the isothermal creep data. Actually it is not possible to separately determine  $a_G$  and  $a_T$  for the power law material using isothermal creep data alone. However, Watkins [60] found that the value of  $a_G = 1$  fit the data taken from transient temperature tests on the same epoxy over a large portion ( $70^\circ\text{F} \leq T \leq 160^\circ\text{F}$ ) of the temperature range investigated in this study. As a result, the evaluation of the time-temperature shift factor,  $a_T$ , can be easily determined by employing a graphical shift along the time axis of

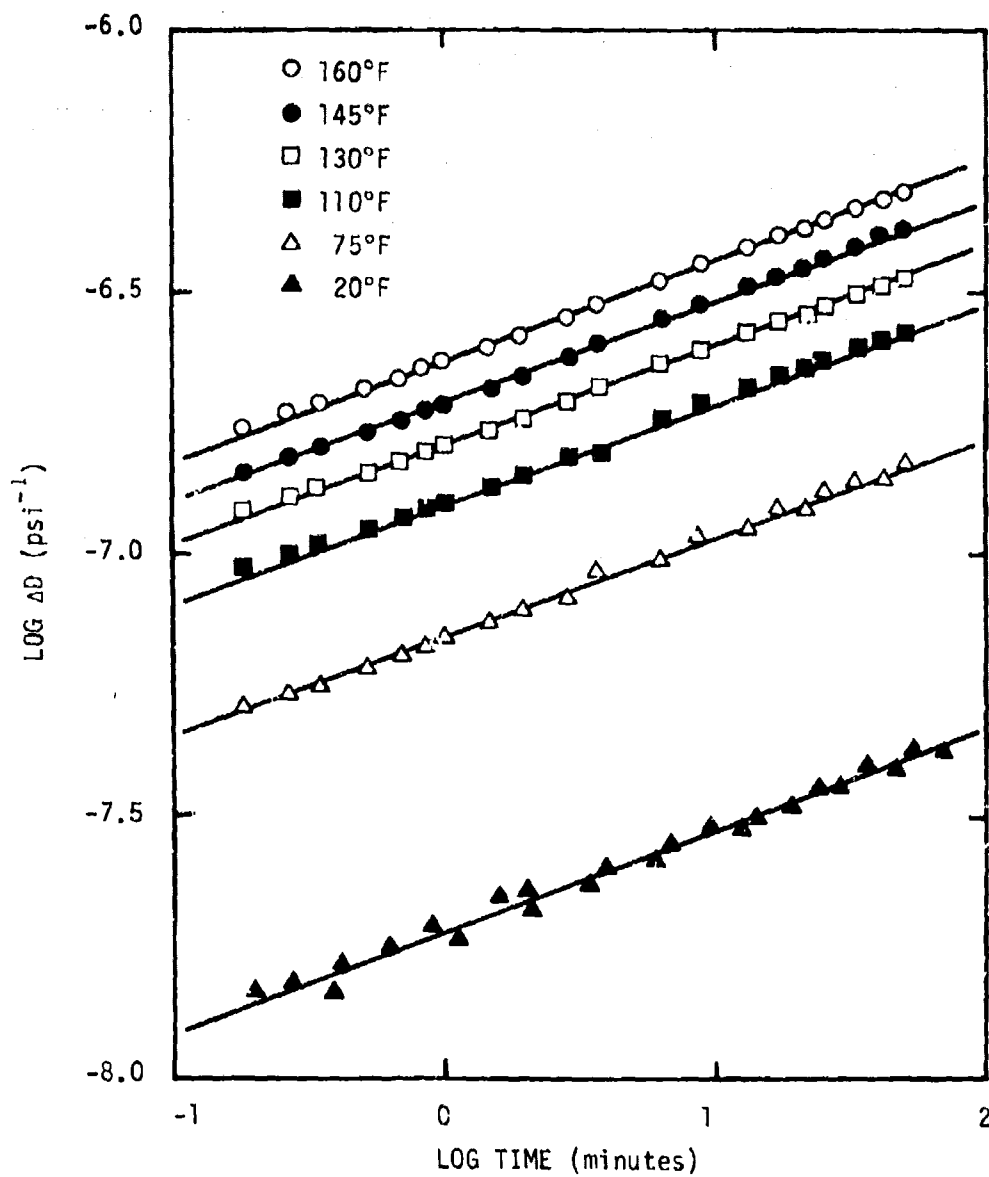


Figure 41. Net creep compliance,  $\Delta D$ , for Shell 58-68R epoxy at different temperatures.

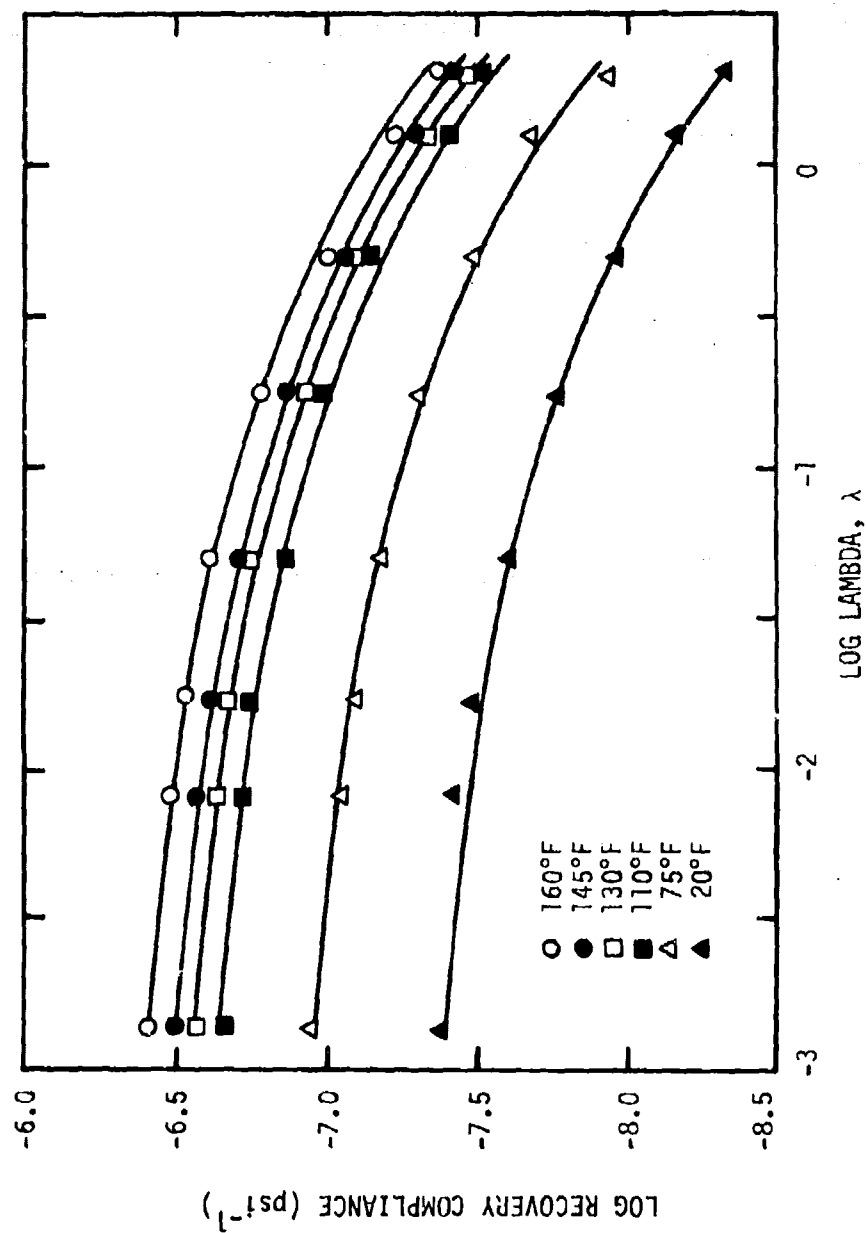


Figure 42. Temperature dependence and evaluation of  $n$  from recovery compliance of Shell 58-68R epoxy.

the net creep compliance,  $\Delta D$  (Figure 41), as well as evaluating the ratios of  $D_1$  at different temperatures.

The graphical shifting of the isothermal net creep compliances to obtain a smooth master curve is shown by Figure 43 where only a few of the data points have been shown for illustration purposes. The second procedure involves the use of the  $D_1$  values shown in Table 9 for the various temperatures. Since the values of  $D_1$  for both creep and recovery are close, only one set, the recovery  $D_1$  values, was used for reduction purposes. The value of  $D_1$ , as used in Equation (130) in this instance, reflects temperature dependence. In order to place the temperature dependence where it should be, in the reduced time, it should be realized that the values given in Table 9 are really

$$D_1 = \frac{D_1'}{a_T^n} \quad (134)$$

where  $D_1'$  is a constant. Thus, by choosing  $D_1'$  at 75°F as a reference value ( $a_T \equiv 1$ ), the ratios of  $D_1$  at other temperatures to  $D_1$  at 75°F will yield the value of  $a_T^n(T)$  where  $a_T^n(75)$  has been given the value of unity.

The shift factors found by these procedures are shown in Table 10 and Figures 44 and 45. Good agreement between the two methods is indicated. The shift factor is plotted against the inverse temperature (Figure 44) in order to determine the activation energy using Equation (24). The activation energy was found

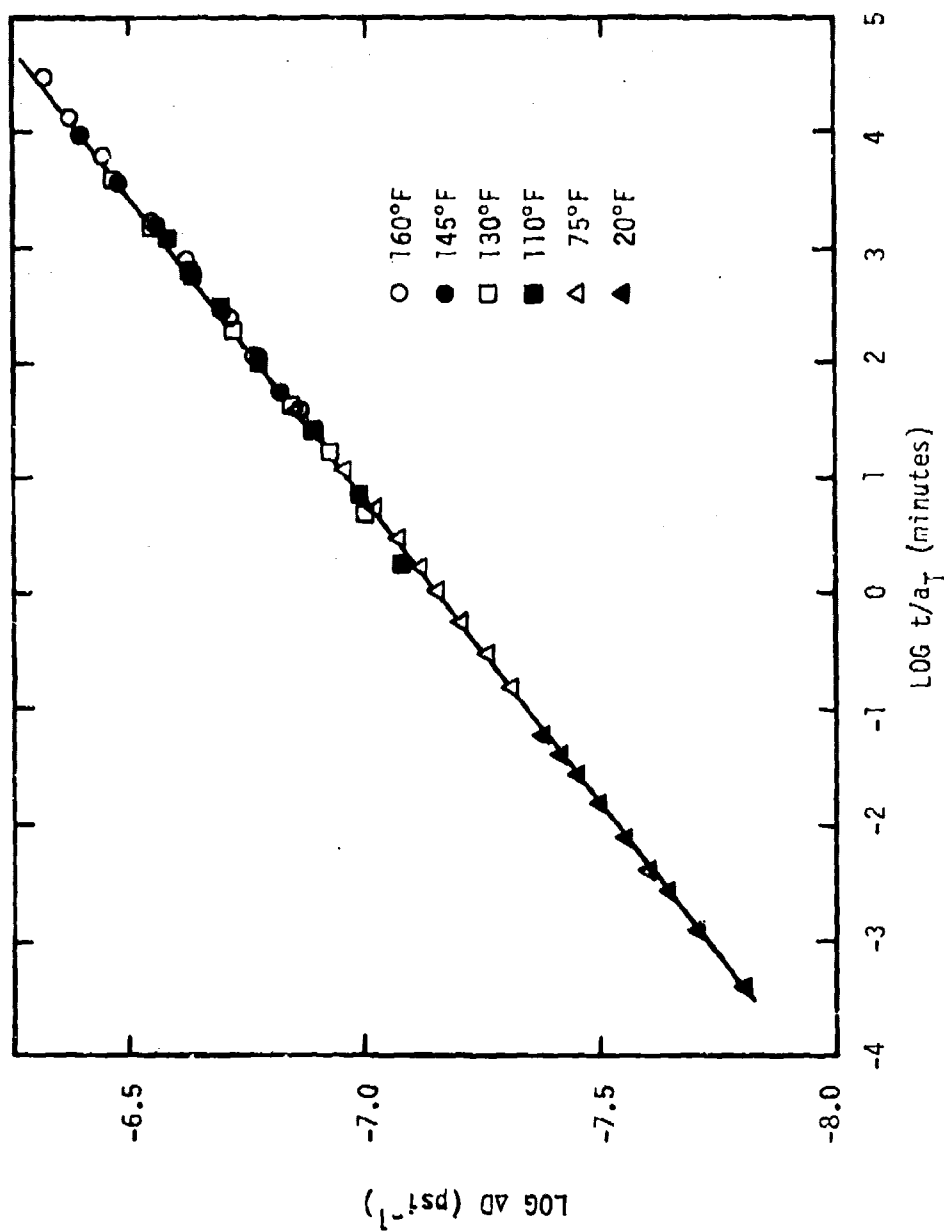


Figure 43. Master curve for net creep compliance,  $\Delta D$ , for Shell 58-68R epoxy.



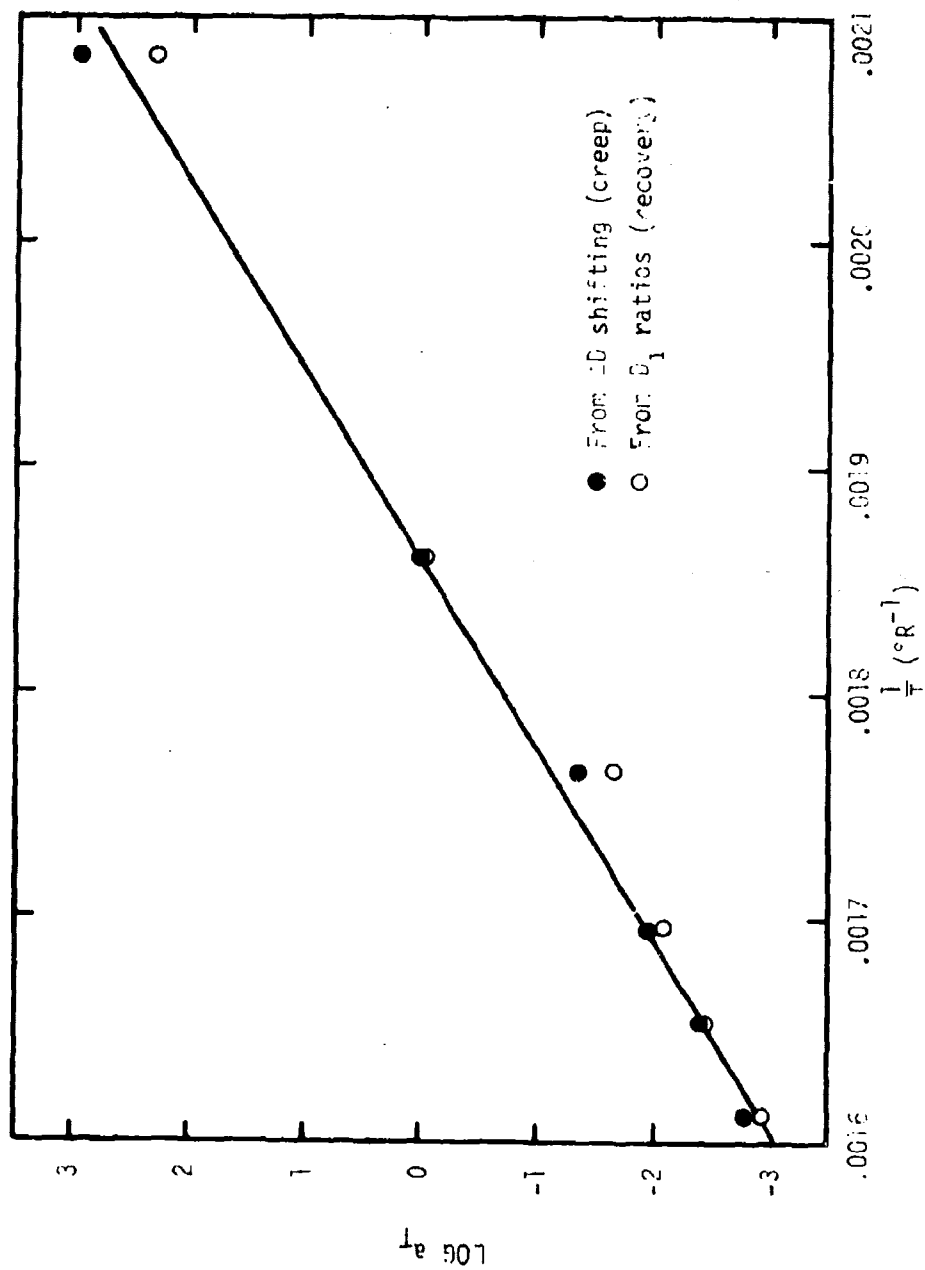


Figure 44. Time-temperature shift factor,  $a_T$ , vs. inverse temperature for evaluation of activation energy,  $\Delta F$ , for Shell 58-68R epoxy.

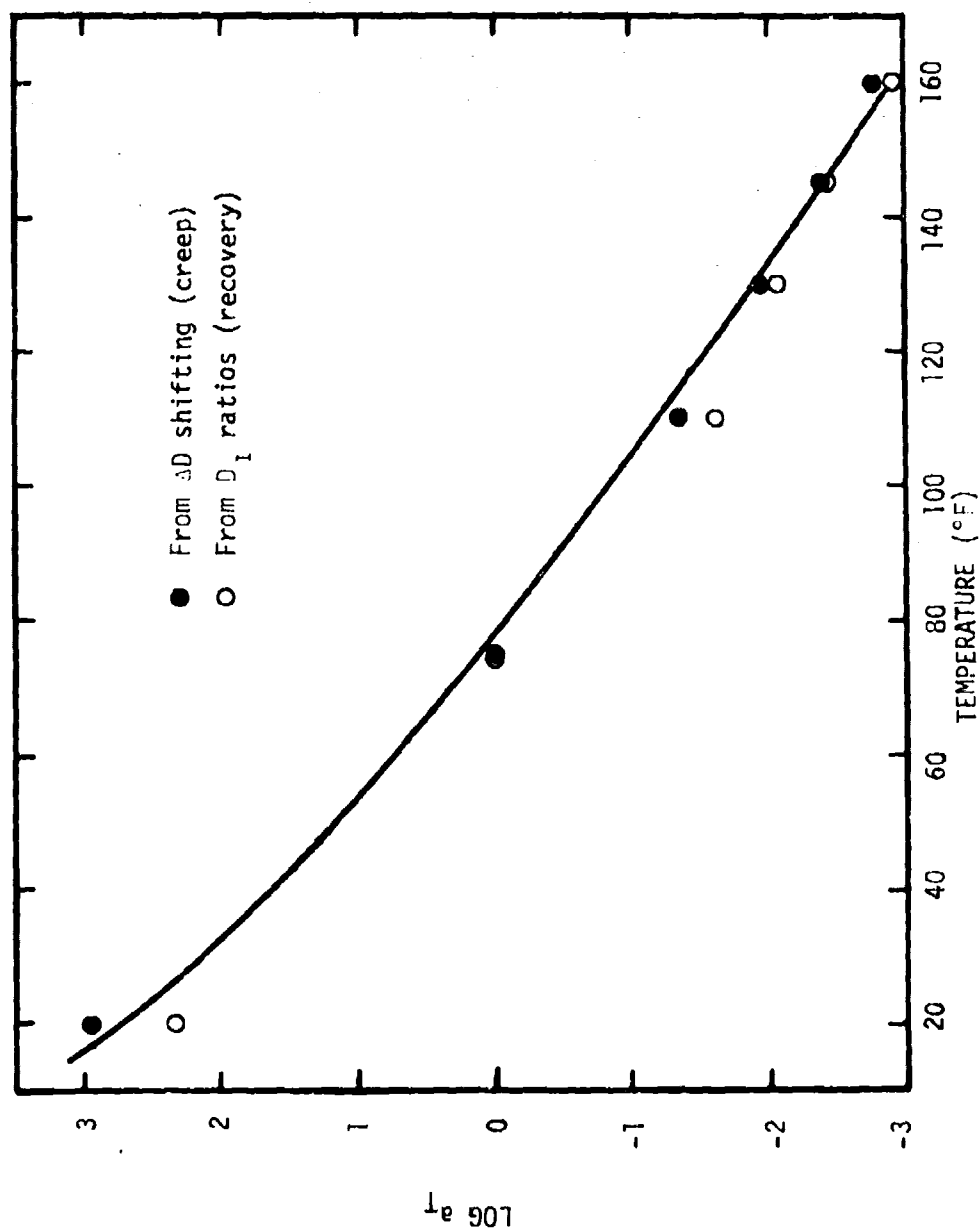


Figure 45. Temperature dependence of the shift factor,  $a_T$ , for Shell 58-68R epoxy.

to be 30 K cal/g-mole which is typical of that generally reported for epoxy resin materials [11].

Table 10. Shift Factors,  $a_T$ , for Shell 58-68R Epoxy Resin

Temperature (°F)	$\log a_T$	$\log a_T$
	(from $\Delta D$ shift)	(from $D_1$ ratios)
20	2.95	2.32
75	0	0
110	-1.34	-1.65
130	-1.94	-2.07
145	-2.41	-2.44
160	-2.77	-2.92

The Poisson's ratio,  $\nu$ , of the epoxy was measured at 20, 75 and 140°F at several stress levels below 600 psi. No appreciable time dependence was noted although some of the tests lasted as long as 60 minutes. A value of  $\nu = 0.393$ , which represents the average of tests at all three temperatures, will be used for all future analysis. There was no strong temperature dependence of Poisson's ratio and the value quoted represents a  $\pm 5\%$  variation of the experimental values.

### Multiple Cycling Effects

All of the creep and recovery tests on the epoxy resin were conducted for at least two cycles in order to assess any effects from multiple cycling. The data from two cycles are shown in Figures 46, 47 and 48 for the creep compliance, net creep compliance and recovery compliance, respectively. Two different stress levels are shown for comparison; however, as noted before, there does not appear to be any strong nonlinearity due to stress present at the levels investigated. The main difference in the two creep compliance curves shown in Figure 46 for the different stress levels represents less than 0.6% which is probably sample variation. When the strain during the creep portion of the test is referenced to the sample length existing just prior to the start of the cycle, the epoxy appears to have become stiffer after the first cycle. However, by always referencing the creep strain to the initial sample length, the material softens slightly. This becomes more evident in looking at the net creep compliance,  $\Delta D$ , in Figure 47 where it is evident that the value of  $D_1$  has decreased. In general, the value of  $D_1$  was found to decrease by about 15% from the first to the second cycle, regardless of the temperature range. This behavior is not clearly understood at this time.

The previously quoted values for  $D_0$  and  $D_1$  are all based on the second cycle data, which should be more representative of the actual material in the glass/epoxy composite as a result of the

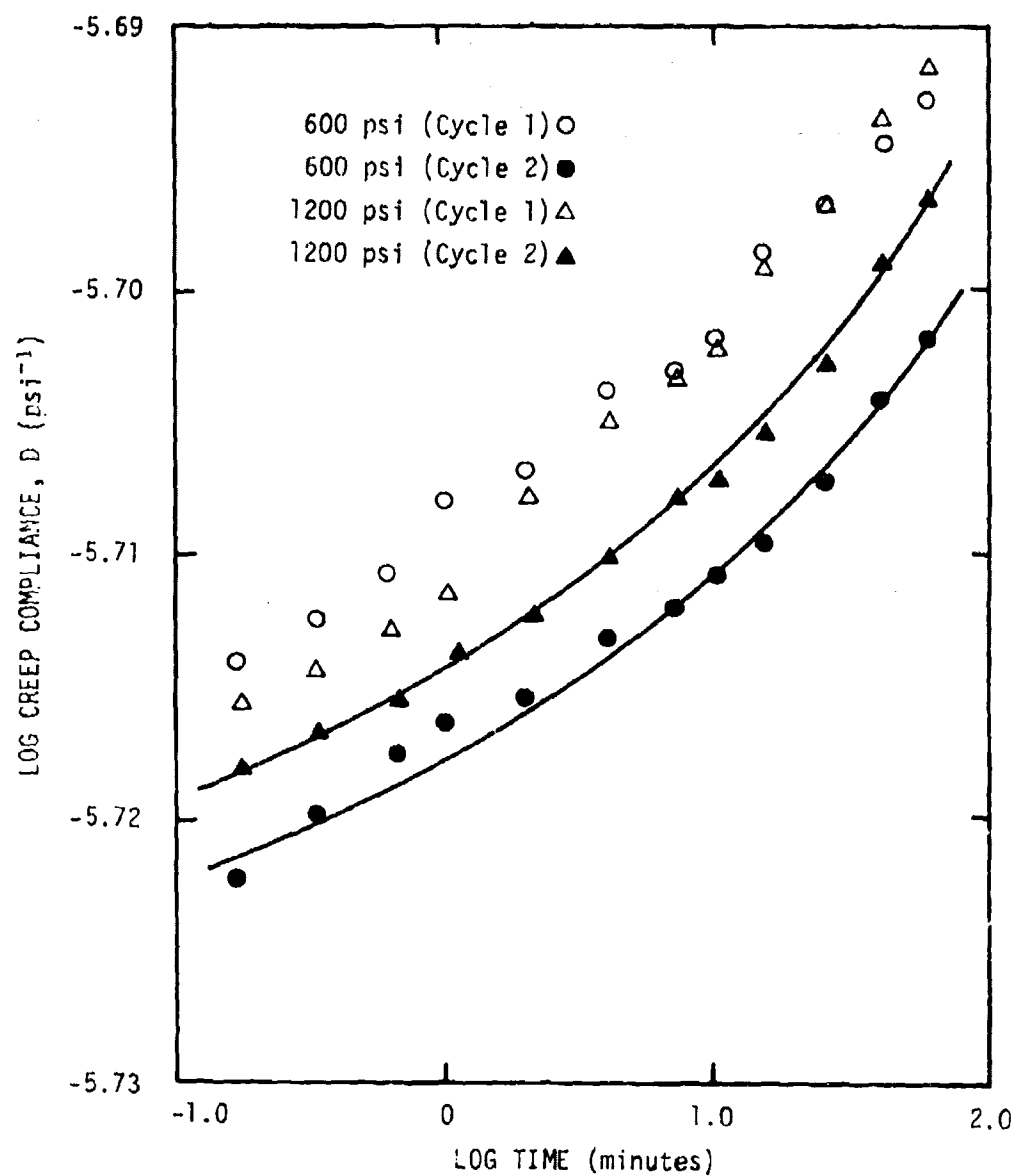


Figure 46. Effect of multiple loading cycles on creep compliance of epoxy resin ( $T = 75^{\circ}\text{F}$ ).

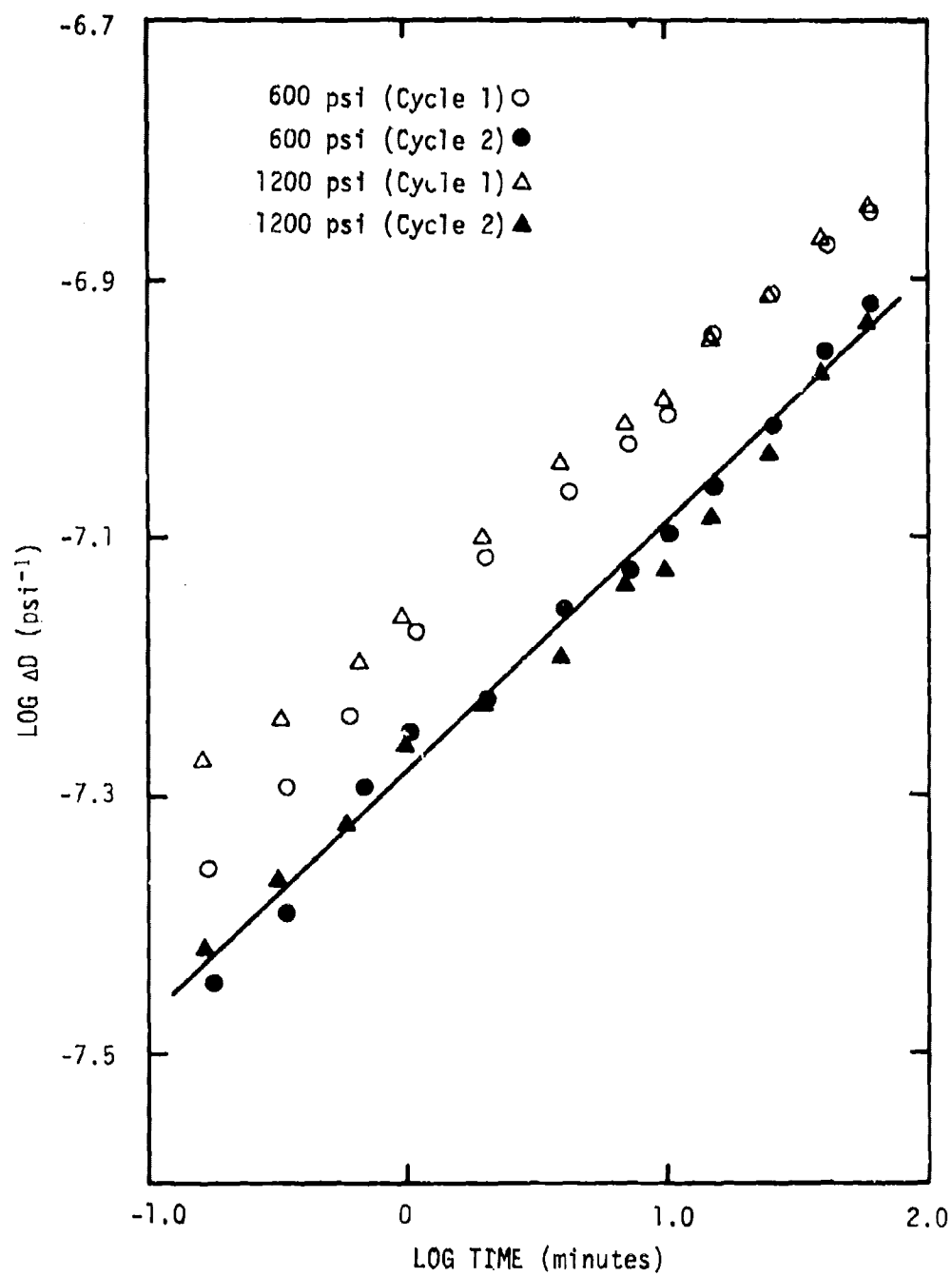


Figure 47. Effect of multiple loading cycles on net creep compliance of epoxy resin ( $T = 75^{\circ}\text{F}$ ).

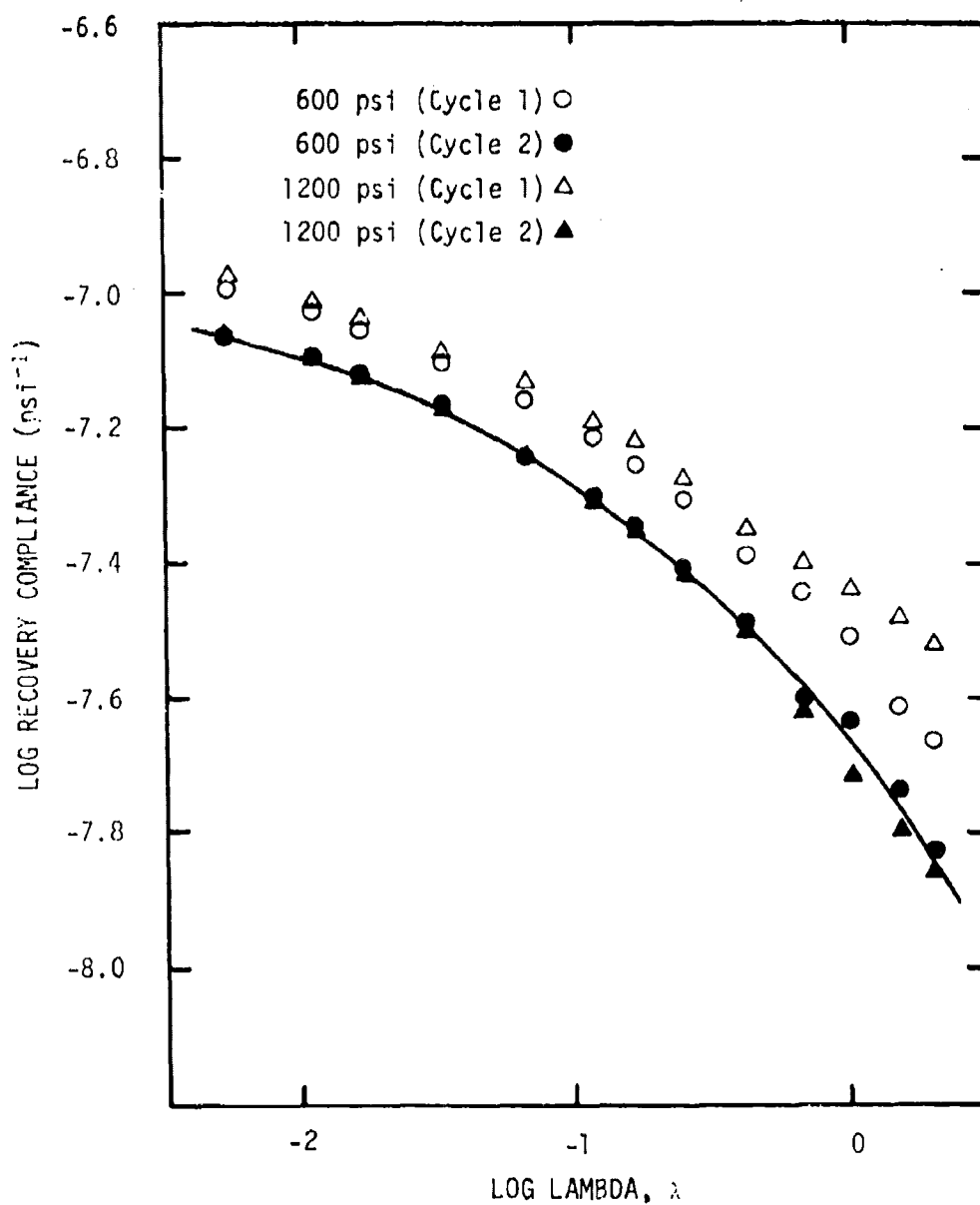


Figure 48. Effect of multiple loading cycles on recovery compliance of epoxy resin ( $T = 75^{\circ}\text{F}$ ).

fabrication process which induces stresses during cure.

#### Matrix Creep Compliance

The creep compliance for the Shell 58-68R epoxy can be determined for analytical purposes by using the  $D_0$  values taken directly from the solid line in Figure 40 and the values of  $D_1$  determined using  $D_1(75) = 0.069(10^{-6})$  and the specific  $a_T$  values defined by the solid line in Figure 44 (or Figure 45). The total creep compliance is then defined by Equation (50) with  $n = 0.19$ .

Later on we shall need to know the creep compliances for 20, 75 and 140°F in order to evaluate the various micromechanics theories. Following the approach outlined above, we find the values of the epoxy creep compliances as shown in Table 11.

Table 11. Shell 58-68R Epoxy Creep Compliances

Temperature (°F)	Creep Compliance $D(t) \times 10^{-6} \text{ (psi}^{-1}\text{)}$
20	$1.732 + .021t^{.19}$
75	$1.865 + .069t^{.19}$
140	$2.021 + .184t^{.19}$



## Uniaxial Creep and Recovery of Unidirectional Glass/Epoxy Laminae and Laminated Composites

### Determination of Material Constants in Power Law Representation

The power law representation, Equation (50), has been found to describe the behavior of several glass/epoxy and graphite composites [9, 12] and will be used here to model the S-901 glass/-Shell 58-68R epoxy composite system. Moreover, the use of viscoelastic micromechanics theory implies that the composite obeys the same power law, i.e.,  $t^{0.19}$ , at least in the absence of any significant crack growth and fiber deformation. When the fiber angle,  $\theta$ , is not close to zero degrees the glass/epoxy exhibits an appreciable amount of time dependence, particularly at the higher temperatures and stress levels. Figures 49 through 52 represent the typical strain response for  $\theta = 45^\circ$  and  $\theta = \pm 45^\circ$  at two of the temperatures investigated. Since the transient part of the creep strain obeys a power law in time, the strain does not actually level off in time, as it appears to do in these figures.

In the case of the off-angle specimens,  $0^\circ < \theta < 90^\circ$ , the creep compliance measured was  $S'_{11}$ . For  $\theta = 0^\circ$  and  $\theta = 90^\circ$ ,  $S_{11}$  and  $S_{22}$  were measured directly for the respective angles. The use of a transversely mounted strain gage on the latter fiber angles also gave us the values of the compliances  $S_{12}$  and  $S_{21}$ , respectively. The power law creep compliance can be rewritten as

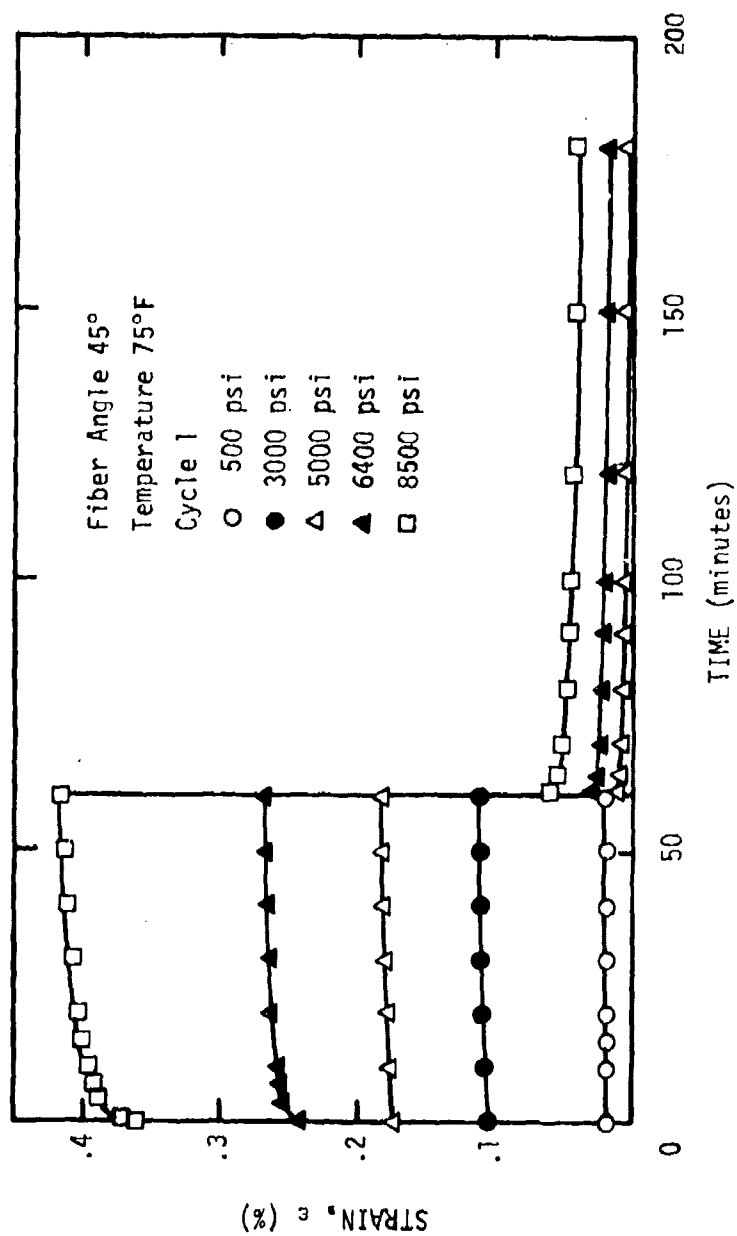
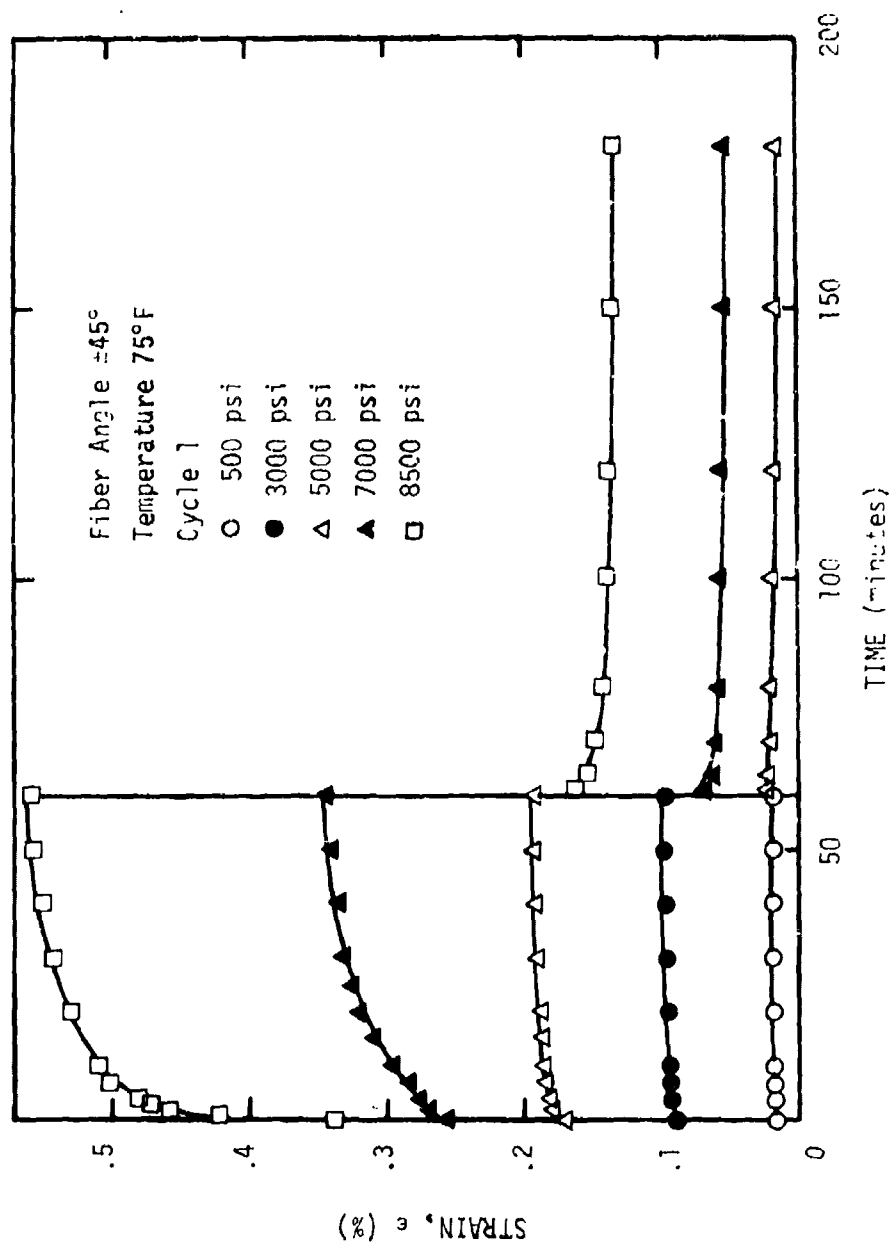


Figure 49. Creep and recovery of 45° glass/epoxy at 75°F.

Figure 50. Creep and recovery of  $\pm 45^\circ$  glass/epoxy at  $75^\circ\text{F}$ .

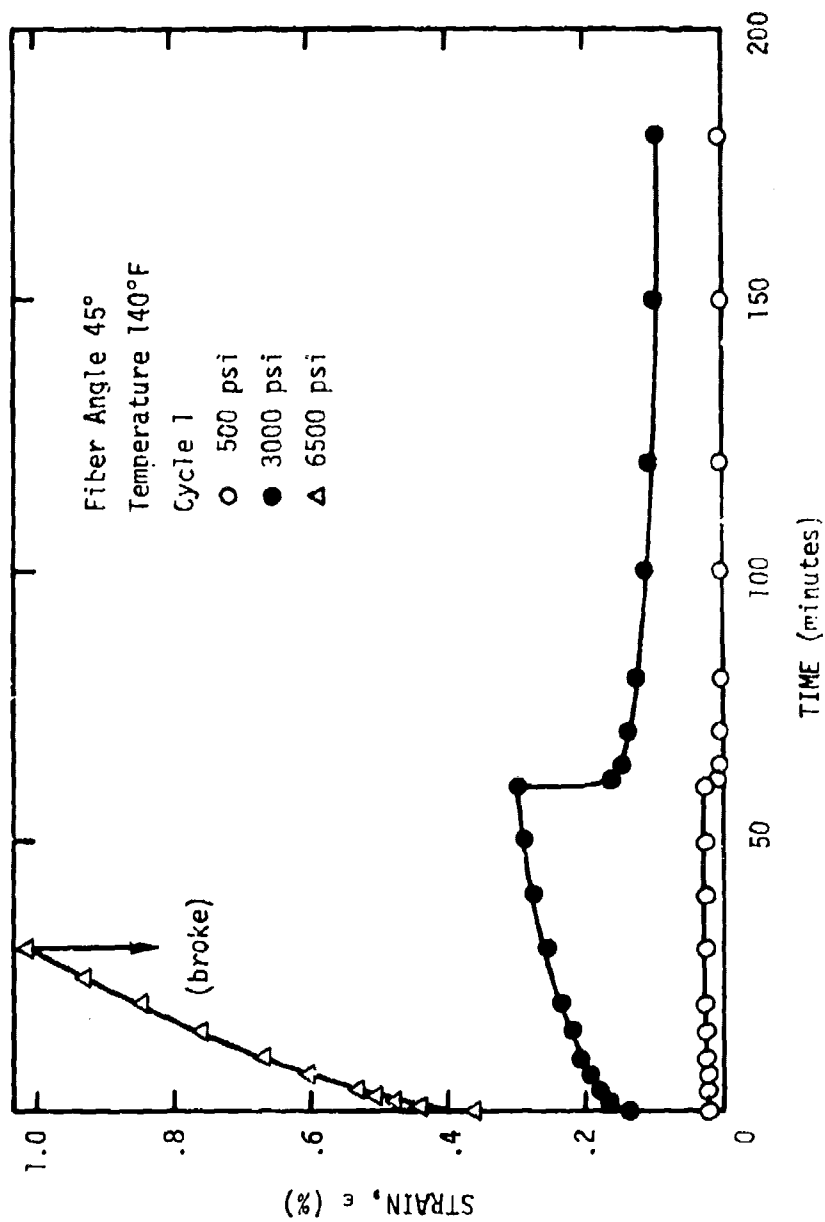


Figure 51. Creep and recovery of 45° glass/epoxy at 140°F.

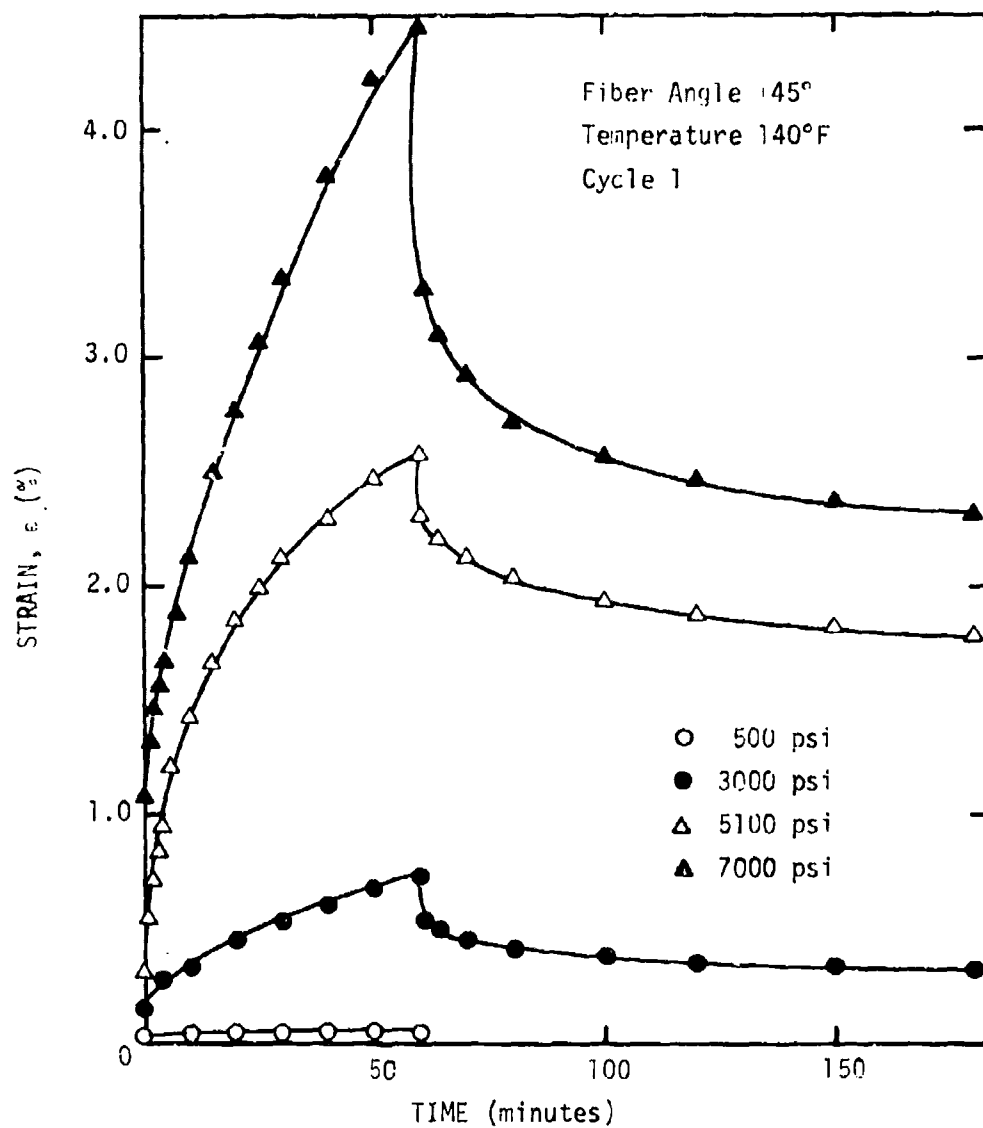


Figure 52. Creep and recovery of  $\pm 45^\circ$  glass/epoxy at  $140^\circ\text{F}$ .

$$S(t) = S_0 + S_1 t^n \quad (135)$$

where the notation more closely represents that commonly used in the composite area, and where

$$S_0 \equiv S'_{11}(0) \quad (136a)$$

and

$$\Delta S = S_1 t^n \quad (136b)$$

The  $S_1$  coefficient is normally called the "creep coefficient". By solving pairs of simultaneous equations using the creep data, in the same manner used for the epoxy creep tests, it is possible to determine both  $S_0$  and  $S_1$  with the assumption that  $n = 0.19$ . The computer program was modified in order to account for values of  $n$  greater than 0.19 when crack growth appeared to be significant. All of the strain-time data was first plotted on semi-log paper and a smooth curve was drawn through each data set. The new data points, taken from the smooth curve, were used in all subsequent analysis. The computer program solved the simultaneous equations for each data set and various values of  $n$  from 0.19 to 0.59. In order to determine the best fit for  $S_0$ ,  $S_1$  and  $n$  the program output was set up to give the correlation coefficient between the experimental  $\Delta S$  defined by

$$\Delta S_{\text{exp}} = S(t)_{\text{exp}} - S_0 \quad (137)$$

and the theoretical  $\Delta S$  given by Equation (136b). The ratio of  $\Delta S_{\text{exp}}/\Delta S$  was also printed out to assist in the evaluation of the fit.

#### Linear Viscoelastic Creep Compliances

In Section III it was noted that the residual, or permanent, strain was rezeroed just prior to the start of the next loading cycle, and, therefore, the resulting creep compliance was referred to the sample length existing at the start of the cycle. For the purpose of the analysis to follow, the creep compliance will always be referred to the total strain referenced to the initial, first cycle length. This procedure is more desirable for engineering applications and comparisons with nonlinear theory.

At sufficiently low stress levels the behavior of the glass/-epoxy composite can be considered linearly viscoelastic. The stress range of linearity depends on the temperature as well as the fiber angle. The linear viscoelastic creep compliances were determined at stress levels between 500 and 2500 psi, depending on the fiber angle. In all cases the value of  $n$  was found to be 0.19 with good agreement in the correlation coefficient in the third or fourth decimal point, e.g., 0.9995. The linear viscoelastic creep compliances found experimentally are tabulated in Table 12.

Examination of the experimental data taken from various tensile coupons showed that there is some variation between samples

Table 12. Linear Viscoelastic Creep Compliances  
for S-901 Glass/Shell 58-68R Epoxy

Temperature (°F)	Fiber Angle (°)	Creep Compliance, $S'_{11}$ ( $\times 10^{-6}$ psi $^{-1}$ )
20	0	.1210 + .0003t $^{.19}$
	45	.3021 + .0046t $^{.19}$
	90	.3115 + .0025t $^{.19}$
	$\pm 45$	.2876 + .0023t $^{.19}$
75	0	.1213 + .0004t $^{.19}$
	20	.1990 + .0038t $^{.19}$
	45	.3260 + .0124t $^{.19}$
	90	.3315 + .0081t $^{.19}$
	0/90	.1793 + .0015t $^{.19}$
	$\pm 30$	.2037 + .0037t $^{.19}$
	$\pm 45$	.3061 + .0082t $^{.19}$
	$\pm 60$	.3534 + .0103t $^{.19}$
140	$\pm 80$	.3416 + .0152t $^{.19}$
	0	.1265 + .0003t $^{.19}$
	20	.1957 + .0439t $^{.19}$
	45	.3524 + .0503t $^{.19}$
	90	.3490 + .1468t $^{.19}$
	0/90	.1829 + .0096t $^{.19}$
	$\pm 30$	.2042 + .0345t $^{.19}$
	$\pm 45$	.1881 + .3032t $^{.19}$
	$\pm 60$	.3181 + .1786t $^{.19}$



within the same plate as well as plate-to-plate variability. This variability is reflected somewhat by the differences in the fiber contents shown in Table 3 and can account for the approximately 3-7% variation in initial compliances. Strain gage misalignment, small deviations from the desired fiber angle and loading misalignment all are thought to contribute to the differences in initial compliance, as well as effecting the transient compliance if the errors are high enough.

The creep behavior of the  $0^\circ$  fiber angle, although very small (less than 0.5%), can probably be attributed to the straightening out of any misaligned fibers. The effect is larger than would normally be predicted by the rule of mixtures, viz., Equation (114). Antans and Skudra [142] also noted this behavior in a glass/epoxy composite although their matrix material was considerably softer than the present epoxy. In fact, the net creep compliance was on the order of several percent of the initial compliance even at slightly elevated temperatures.

#### Effect of Stress and Temperature

The general effect of stress and temperature causes an increased degree of reversible (temperature) and irreversible (stress) changes. Figures 53 through 67 show the effects of stress level for the various fiber angles during the first cycle of loading. Data is shown for the  $75^\circ\text{F}$  and  $140^\circ\text{F}$  only, since the lower

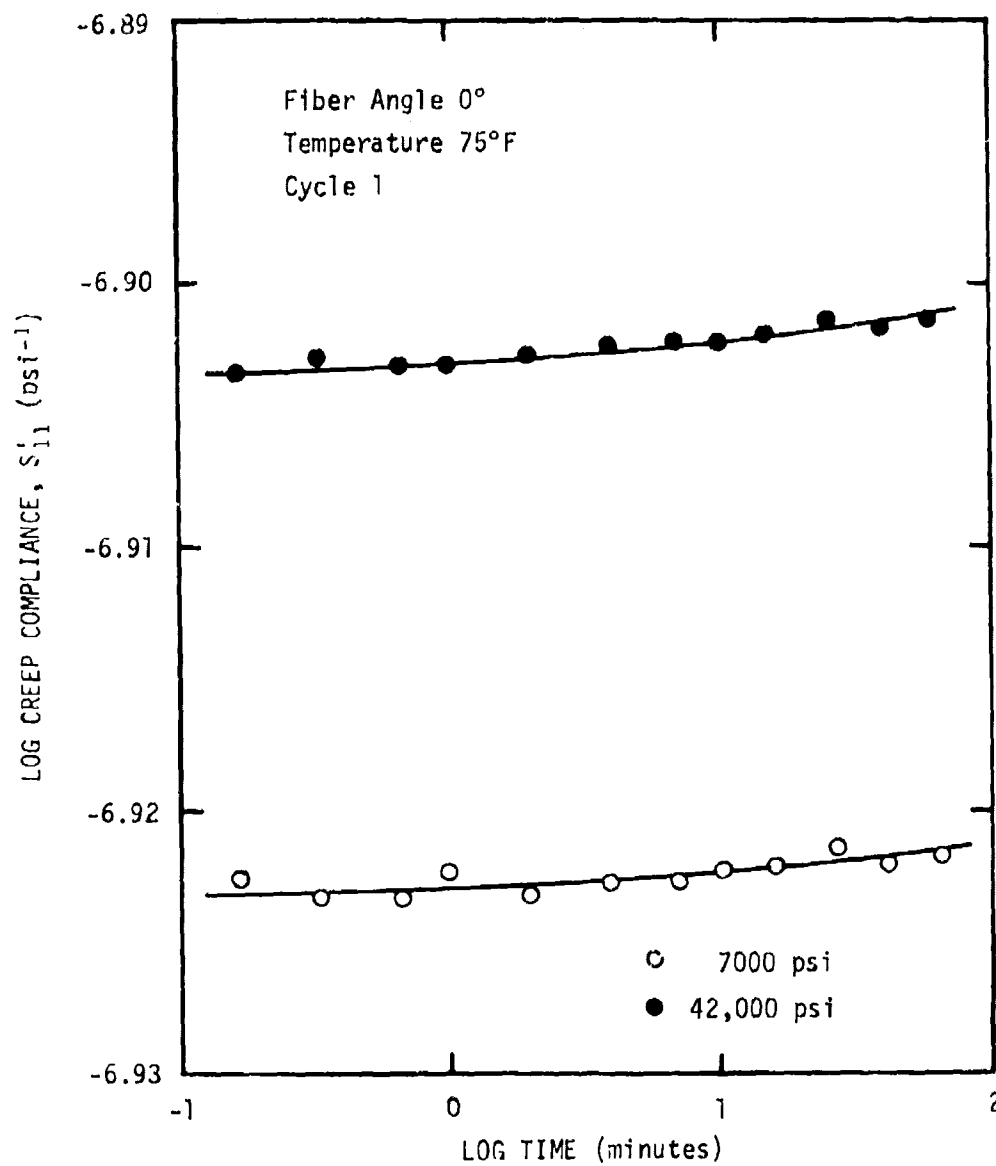


Figure 53. Creep compliance for different stress levels ( $\theta = 0^\circ$ ,  $T = 75^\circ\text{F}$ ).

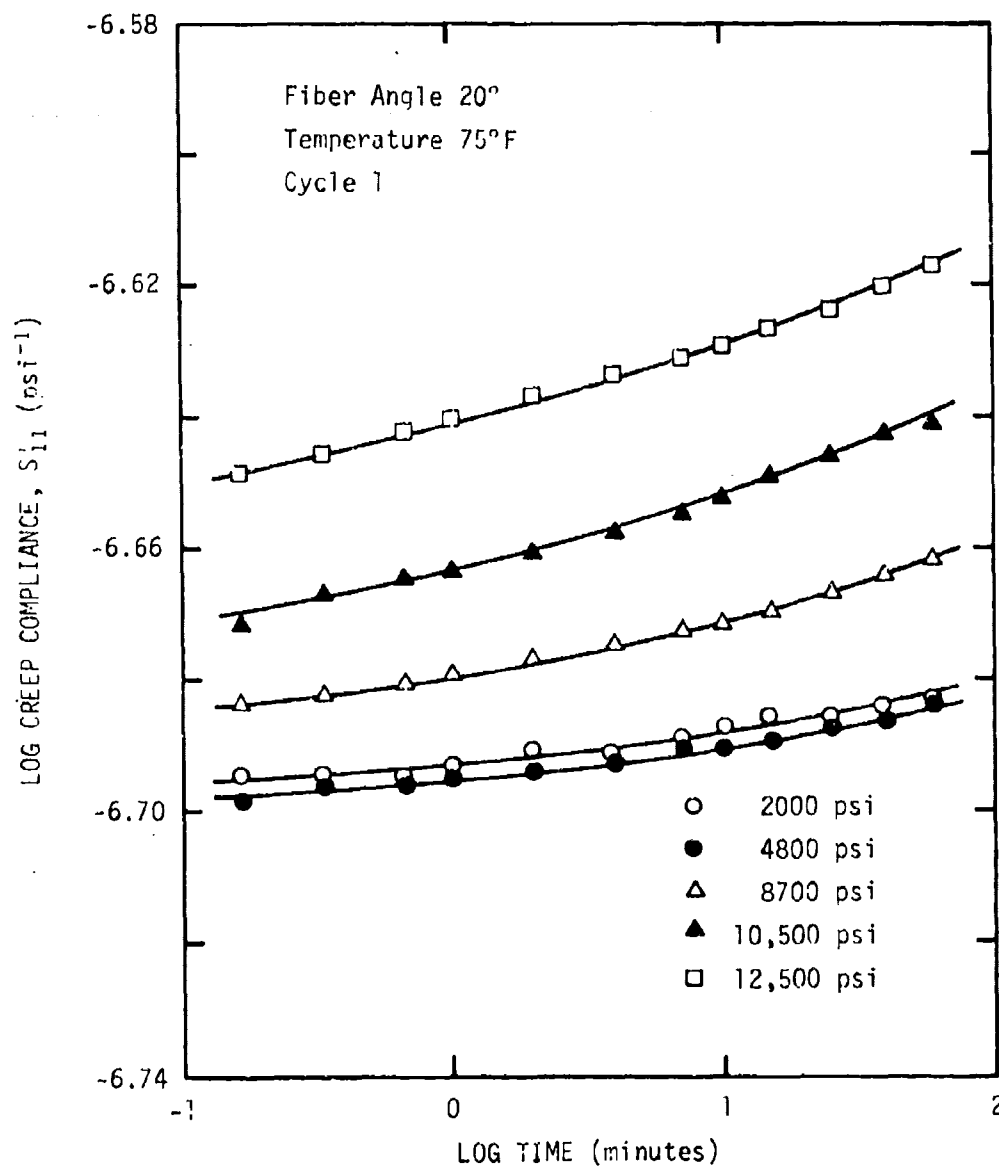


Figure 54. Creep compliance for different stress levels ( $\theta = 20^\circ$ ,  $T = 75^\circ\text{F}$ ).

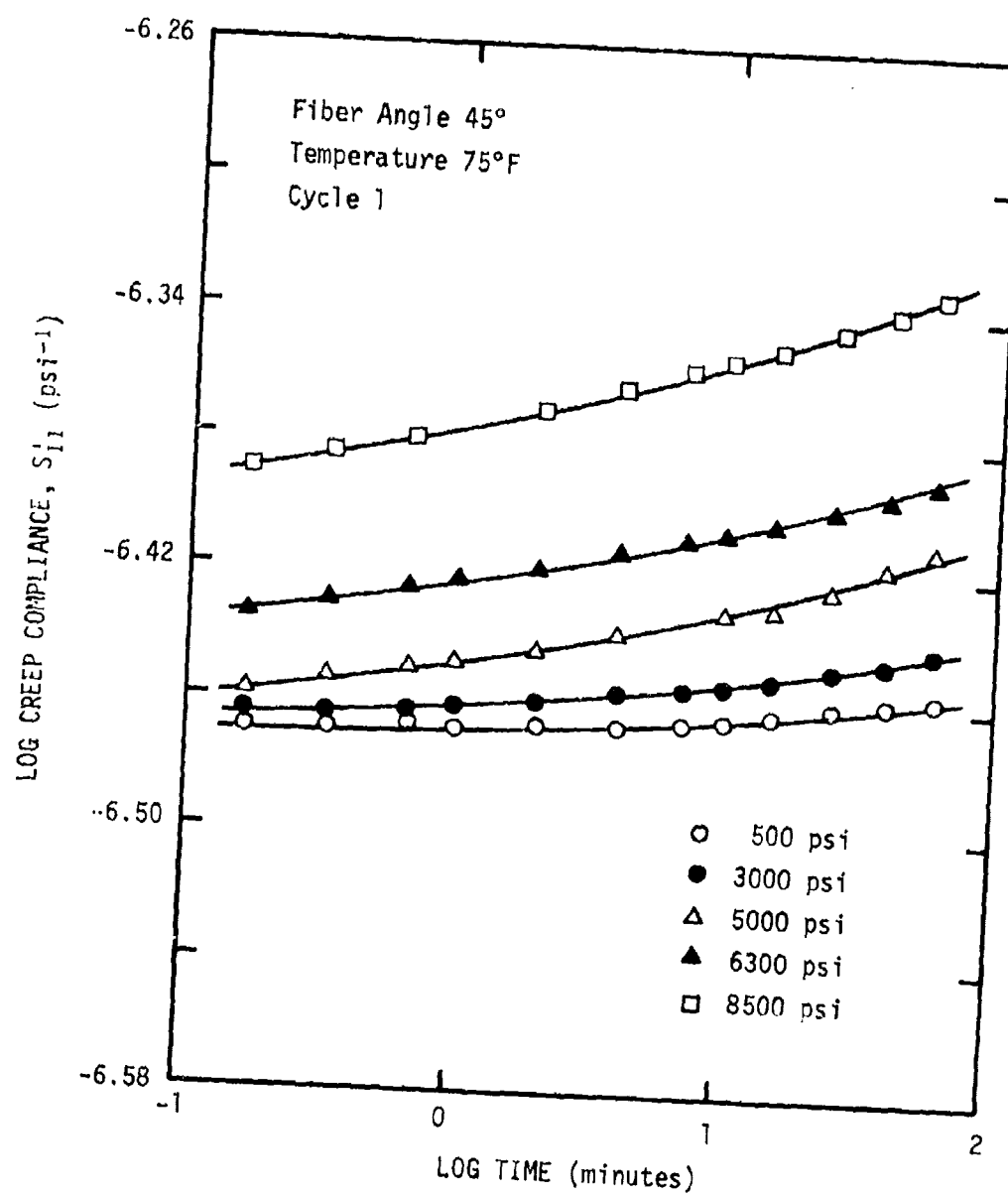


Figure 55. Creep compliance for different stress levels ( $\theta = 45^\circ$ ,  $T = 75^\circ\text{F}$ ).

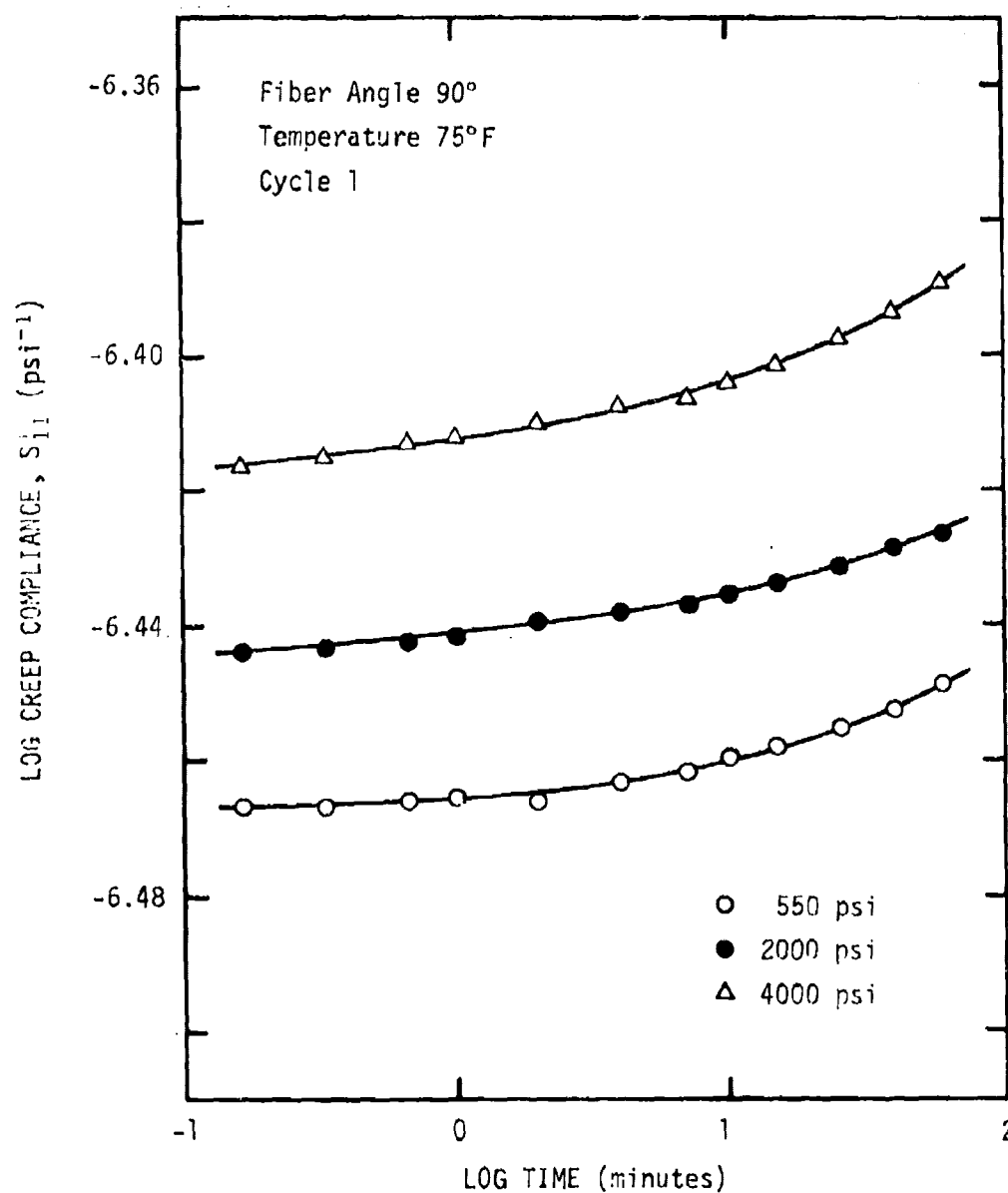


Figure 56. Creep compliance for different stress levels ( $\theta = 90^\circ$ ,  $T = 75^\circ\text{F}$ ).

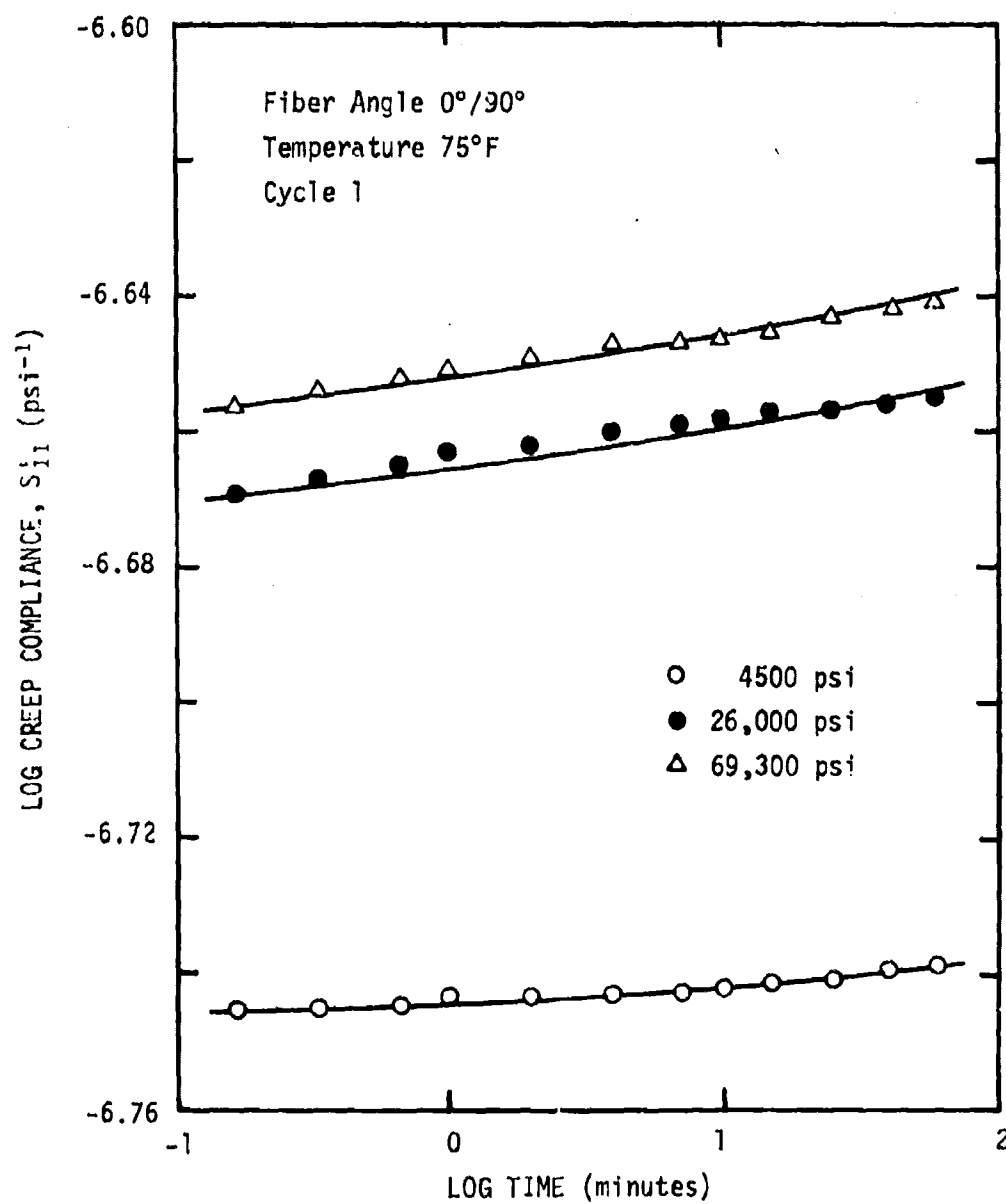


Figure 57. Creep compliance for different stress levels ( $\theta = 0^\circ/90^\circ$ ,  $T = 75^\circ\text{F}$ ).

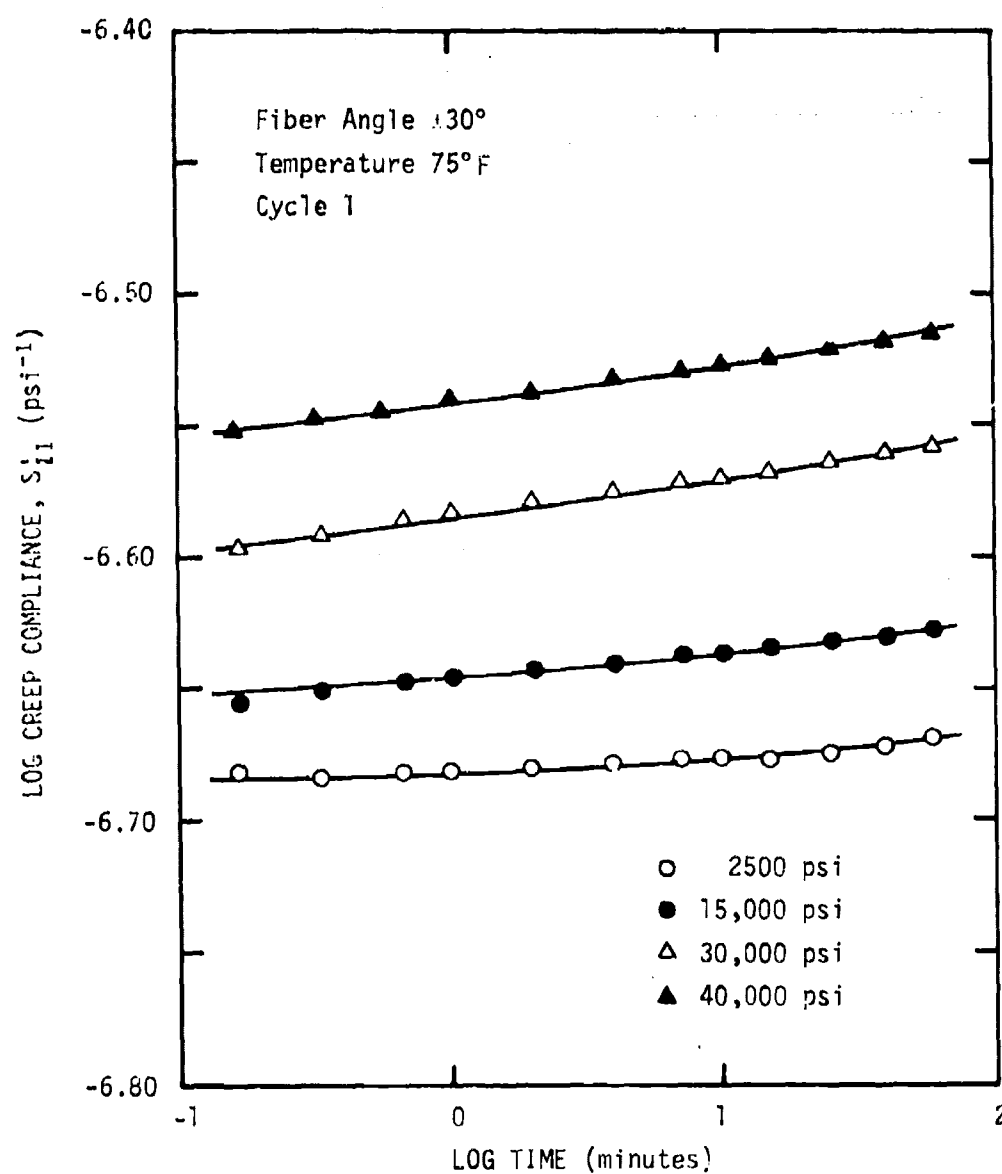


Figure 58. Creep compliance for different stress levels ( $\theta = \pm 30^\circ$ ,  $T = 75^\circ\text{F}$ ).

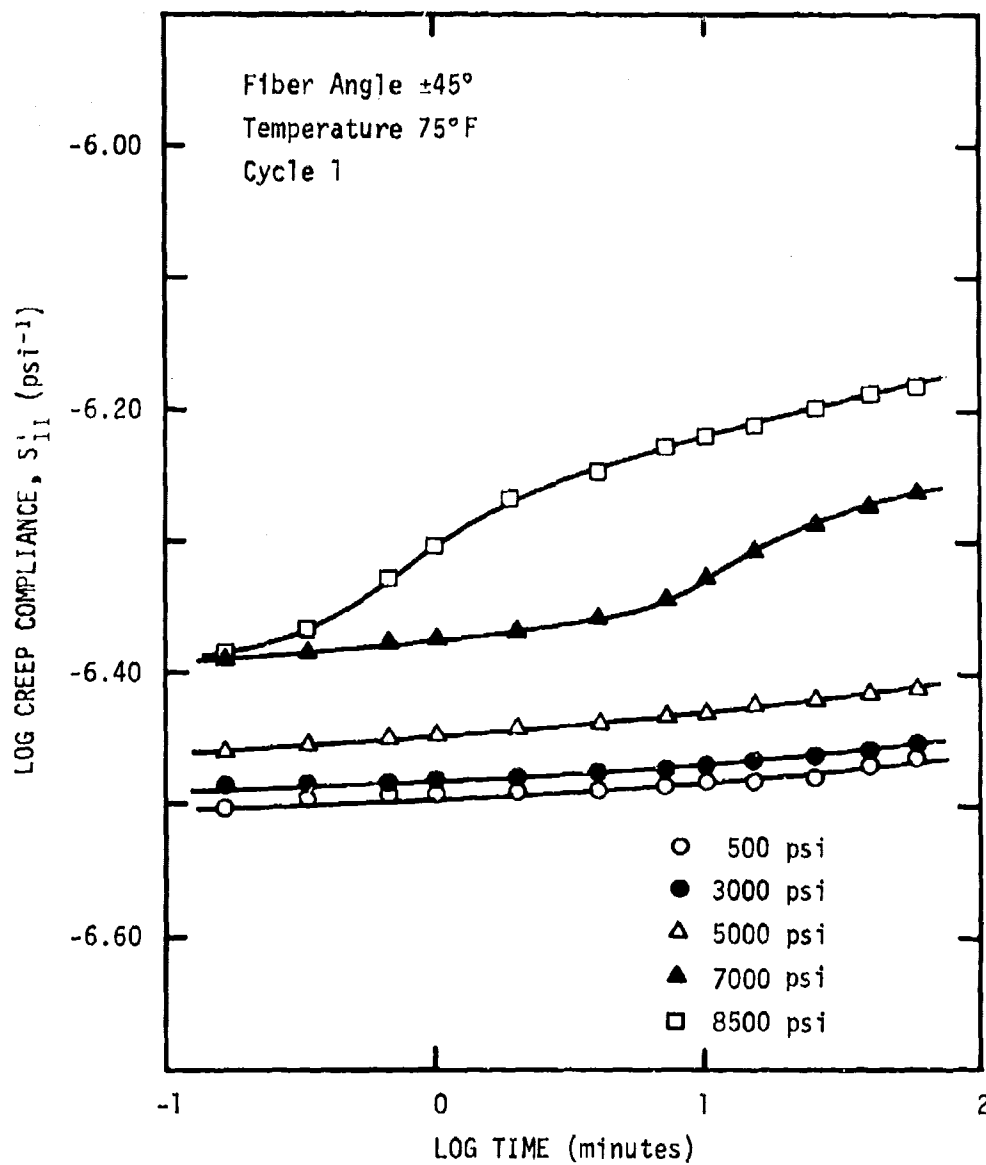


Figure 59. Creep compliance for different stress levels ( $\theta = \pm 45^\circ$ ,  $T = 75^\circ\text{F}$ ).



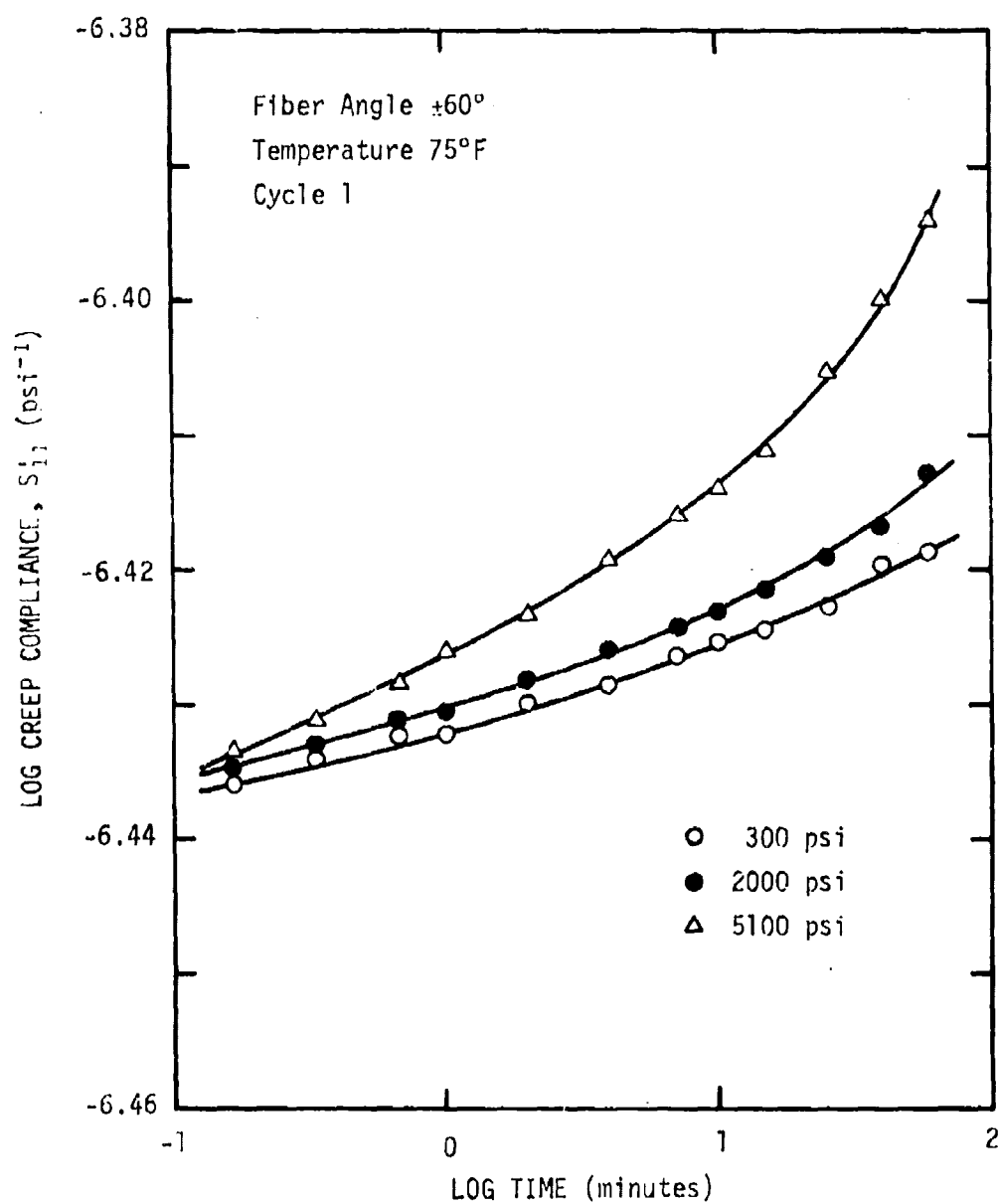


Figure 60. Creep compliance for different stress levels ( $\theta = \pm 60^\circ$ ,  $T = 75^\circ\text{F}$ ).

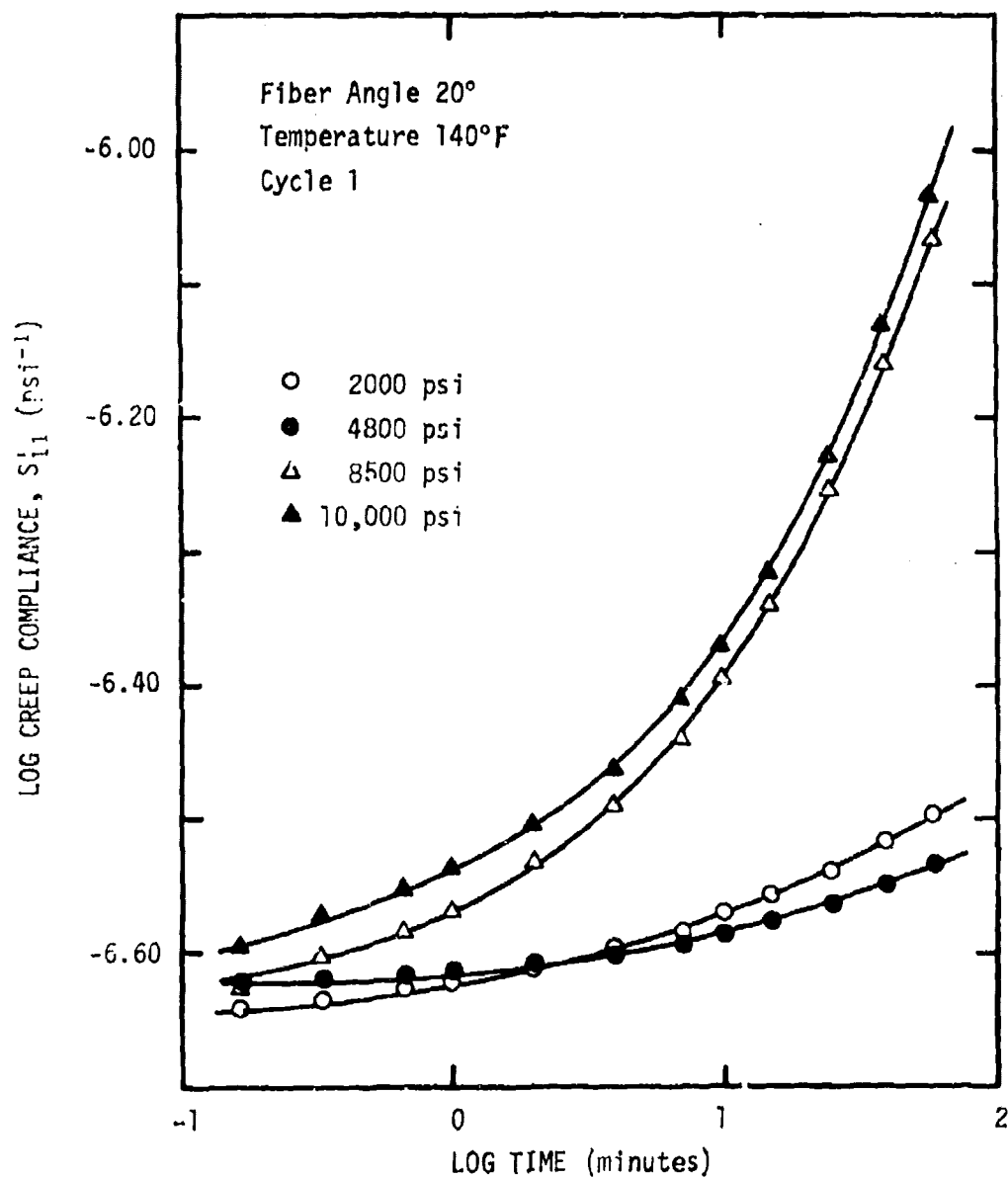


Figure 61. Creep compliance for different stress levels ( $\theta = 20^\circ$ ,  $T = 140^\circ\text{F}$ ).

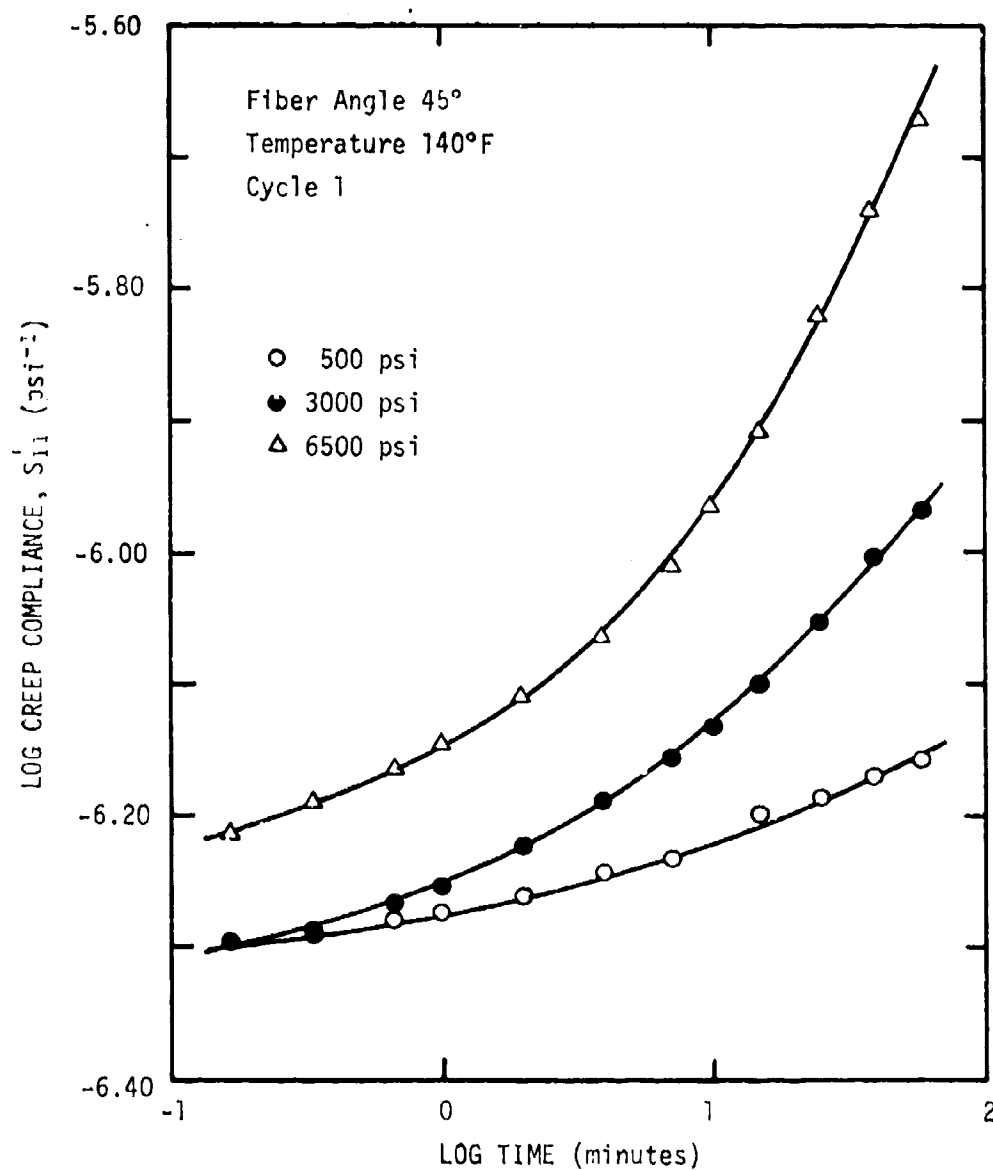


Figure 62. Creep compliance for different stress levels ( $\theta = 45^\circ$ ,  $T = 140^\circ\text{F}$ ).

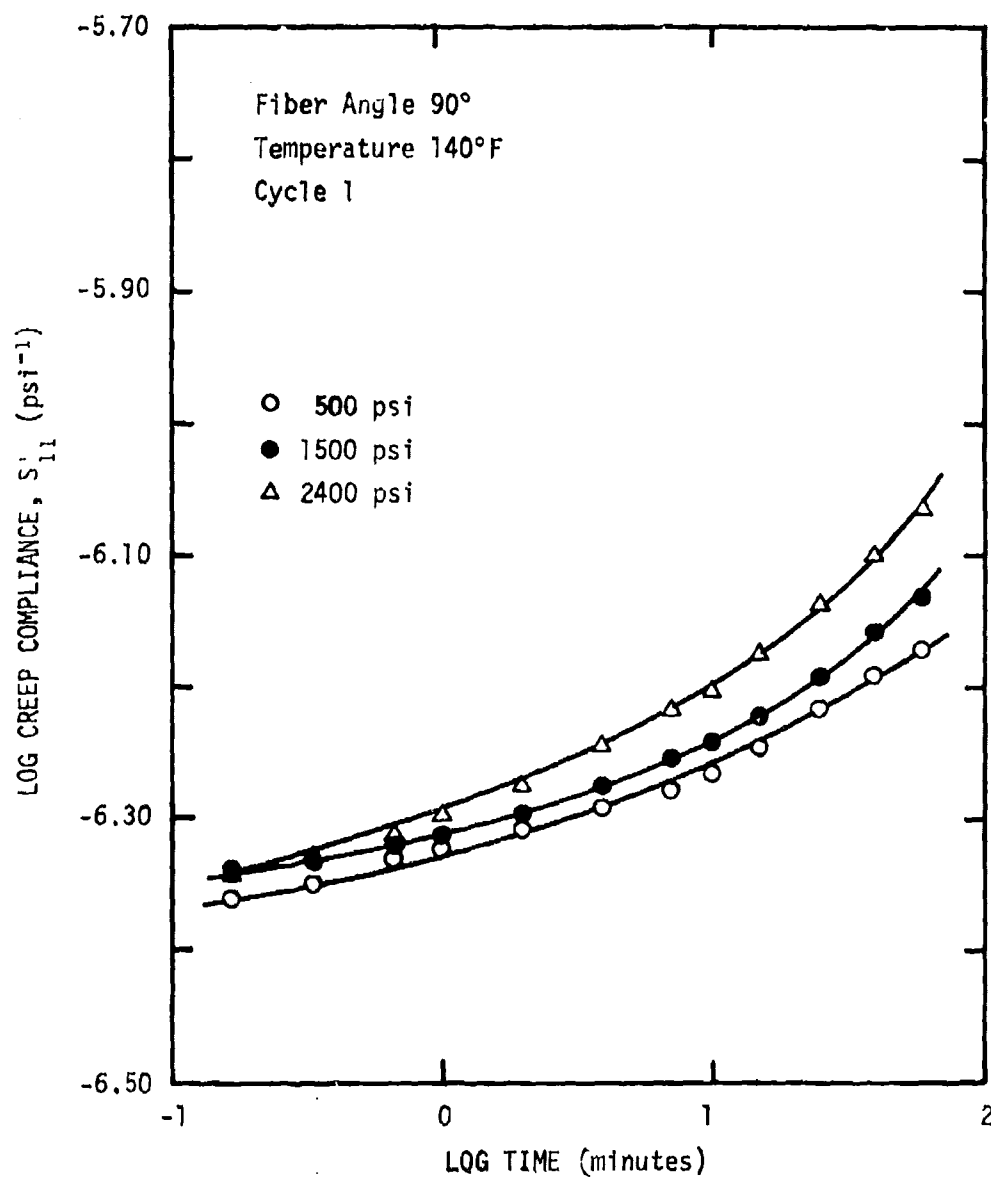


Figure 63. Creep compliance for different stress levels ( $\theta = 90^\circ$ ,  $T = 140^\circ\text{F}$ ).

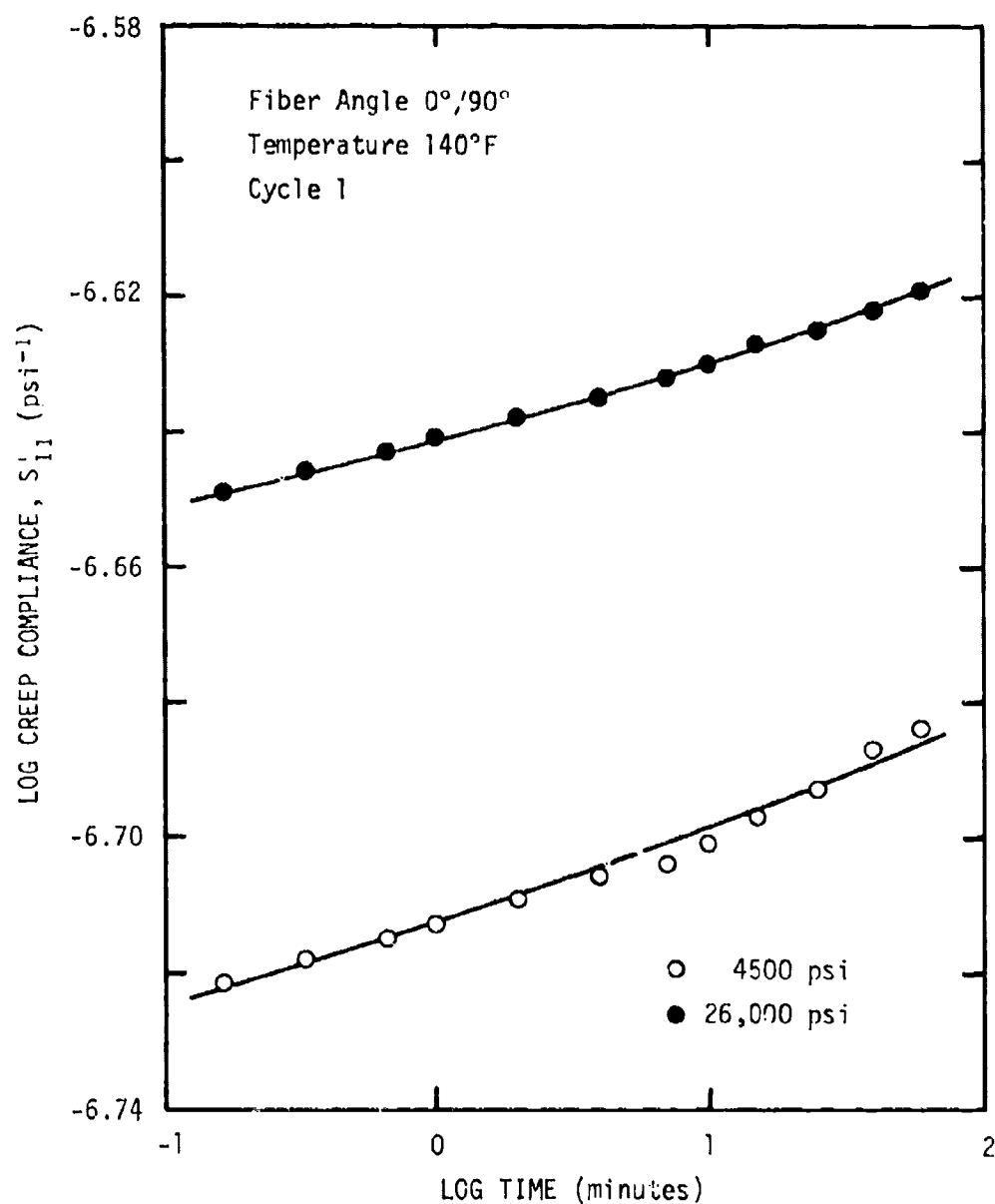


Figure 64. Creep compliance for different stress levels ( $\theta = 0^\circ/90^\circ$ ,  $T = 140^\circ\text{F}$ ).

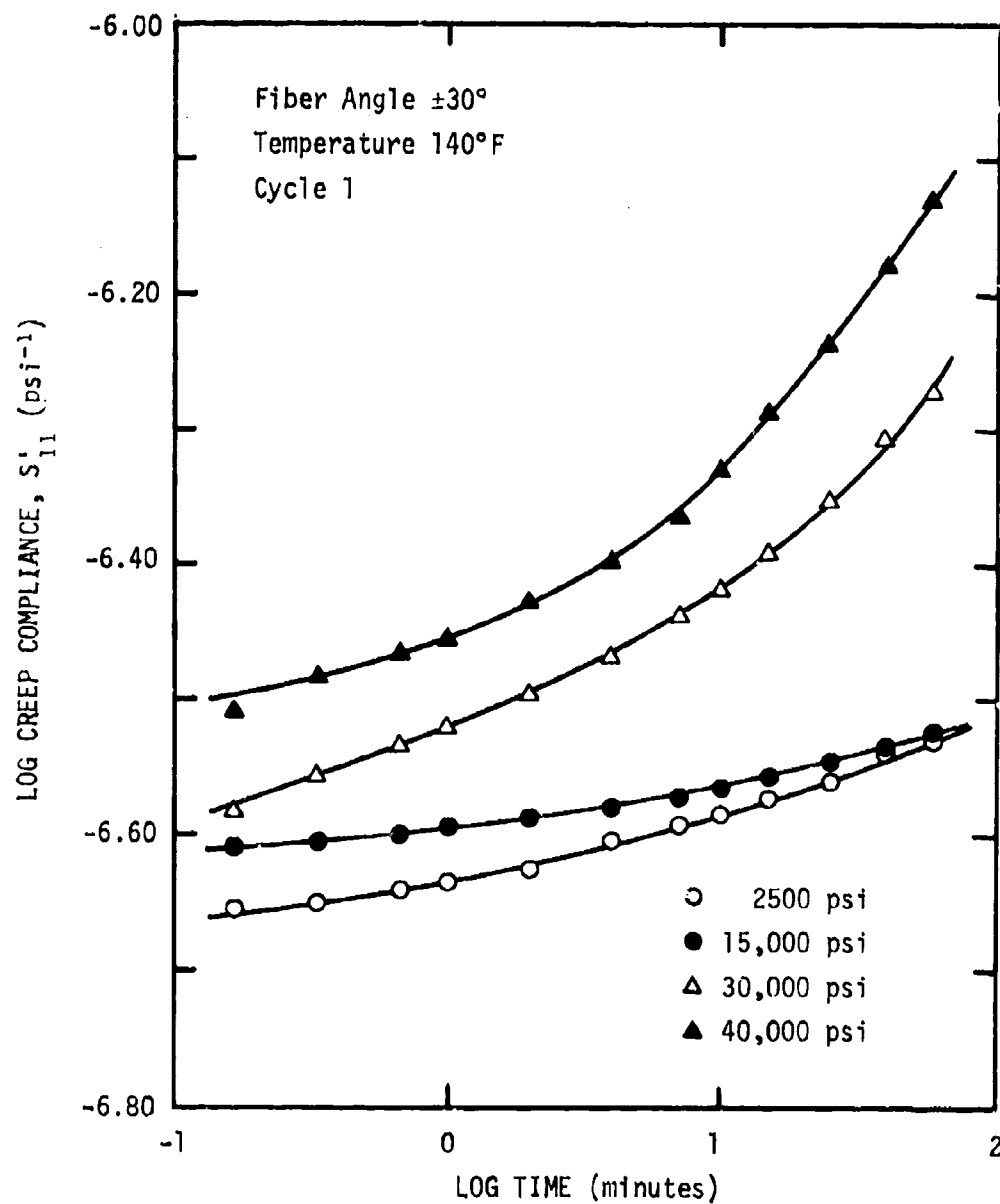


Figure 65. Creep compliance for different stress levels ( $\theta = \pm 30^\circ$ ,  $T = 140^\circ\text{F}$ ).

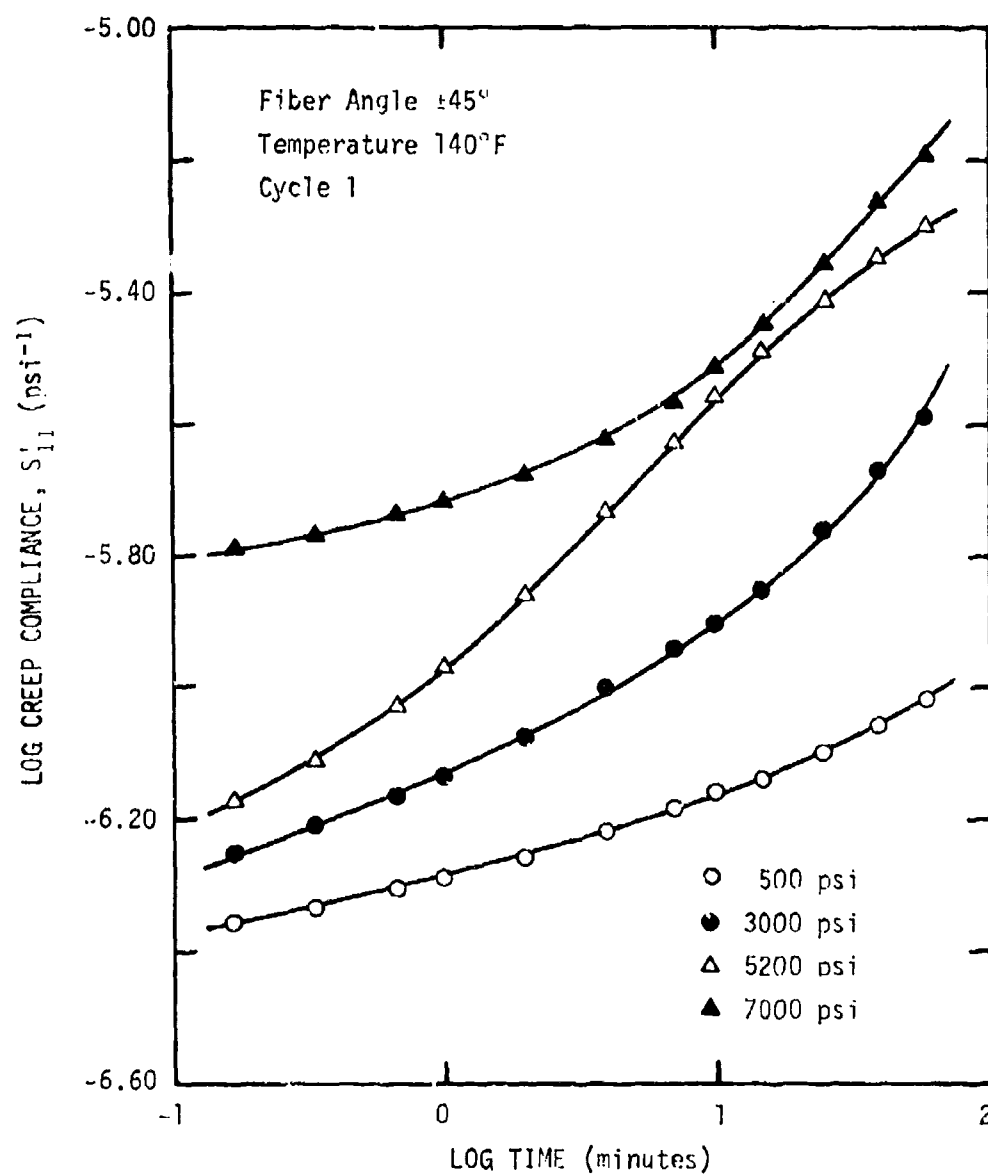


Figure 66. Creep compliance for different stress levels ( $\theta = \pm 45^\circ$ ,  $T = 140^\circ\text{F}$ ).

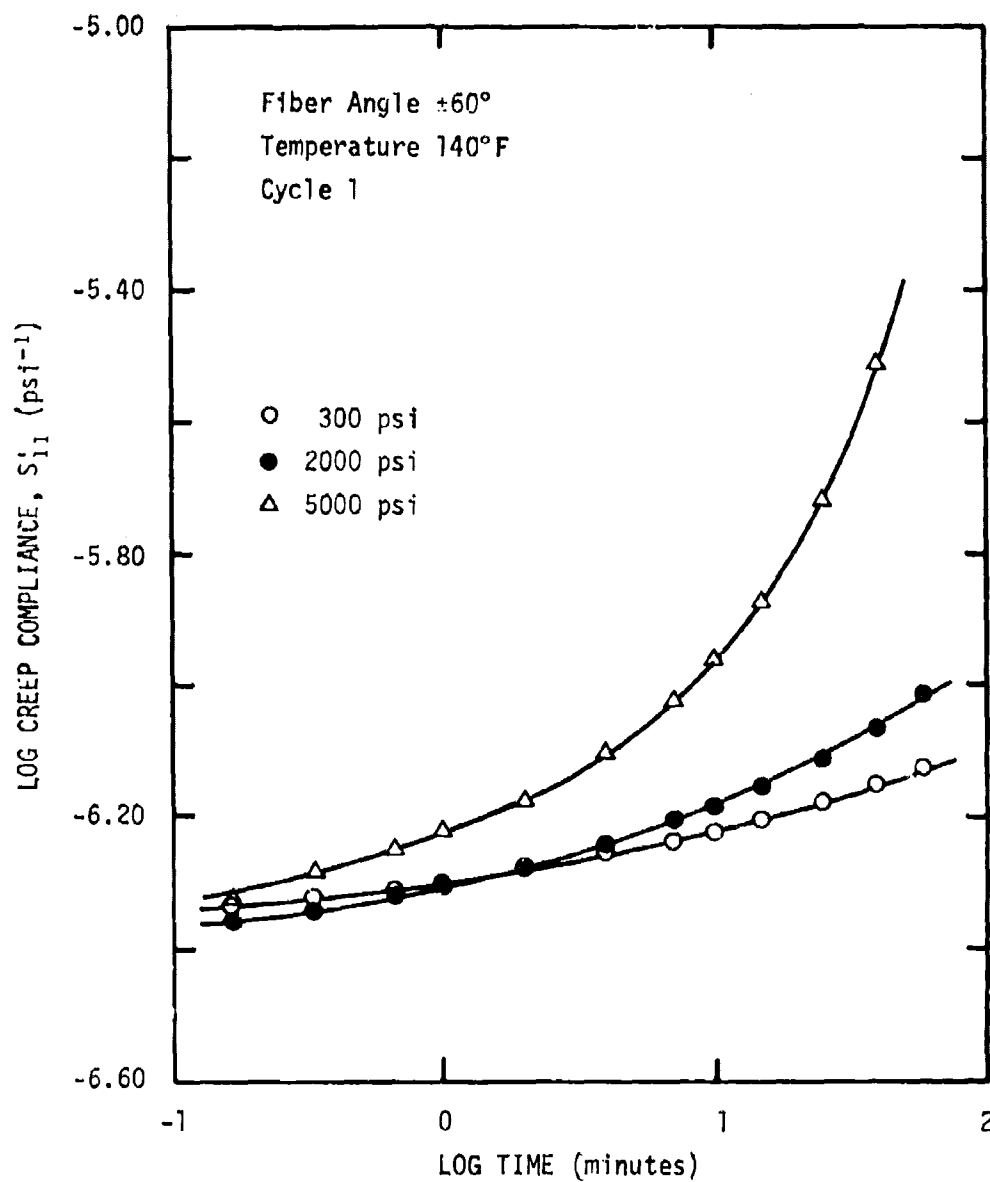


Figure 67. Creep compliance for different stress levels ( $\theta = \pm 60^\circ$ ,  $T = 140^\circ\text{F}$ ).



temperature (20°F) does not exhibit as strong a time dependence. All of the 20°F and 75°F data obey the power law with  $n = 0.19$ . However, both the initial creep compliance and the creep coefficient increase with stress level. This behavior is evident for both the unidirectional laminae and the laminated composites at all stress levels. Equation (106) qualitatively reflects this behavior although allowing  $n$  to remain unchanged.

If it is hypothesized that an initial distribution of small, microcracks already exist within the composite as a result of fabrication, then the initial softening effect can be thought of in terms of crack growth and arrest. Actually, with power law creep compliance behavior the crack growth occurs continuously. However, the application of stress probably causes the existing crack distribution to grow while at the same time creating an additional number of new crack surfaces. The initial compliance, therefore, reflects crack growth (existing cracks) and crack initiation (new crack surfaces). It is natural to expect that the creep coefficient would increase with stress level since there is continuous propagation of the cracks within the material. The possibility of crack arrest would be reflected by reduction in creep rate from cycle-to-cycle, particularly in the off-angle composites where the crack growth would tend to be limited by the fiber spacing.

Figure 57 reflects the damage done within the 90° layers of the 0°/90° composite. At an applied tensile stress level of

4500 psi the strains within the  $90^\circ$  layers are considerably below that which would cause failure in a  $90^\circ$  unidirectional sample (see Figure 31). In Figure 32 this is the region below the "knee" in the stress-strain curve. At the higher stress levels, the  $90^\circ$  layers have failed and the  $0^\circ$  layers are carrying the load. This is typical of the behavior in the barrel region of the motor case where the layers are predominantly  $0^\circ/90^\circ$ .

Crack arrest is not visibly evident during the first loading cycles for any of the unidirectional composites shown in Figures 53 through 56. However, the behavior of the  $\pm 45^\circ$  laminated composite (Figure 59) at the two highest stress levels shows a definite decrease in the relative rate of creep after a period of time. It is hypothesized that some of the cracks arrest under conditions where they (i) move toward the fiber where the crack tip is arrested and/or (ii) the crack moves away from the fiber/matrix interface toward an adjacent fiber, with arrest occurring when it reaches this fiber. The laminated composite provides additional crack arrest boundaries in terms of the individual layers oriented at an angle of  $2\theta$  with respect to the adjacent layer. This layering may tend to cause the cracks to develop and propagate between layers, causing considerable delamination at the higher stress levels. This delamination is clearly visible as an edge effect at stresses near failure when the top layers begin to curl upwards at the outer edge of the tensile coupons.

The creep compliances which were measured at the lowest stress levels are summarized in Figures 68 through 71 for the unidirectional and laminated composites. These compliances were denoted as the linear viscoelastic creep compliances previously listed in Table 12; however, at 140°F even the lowest stress level tests conducted on the 45, 90, ±45 and ±60° samples indicated some degree of irreversible damage. Tests at lower stress levels were not possible as a result of the lack of strain gage sensitivity coupled with the effect of small temperature changes during the test. With the small changes in creep strain at lower stress levels, even minor changes in temperature ( $\pm 1^\circ\text{F}$ ) create cyclic readings of a few microstrain. A stress level of 300 psi was considered to be the minimum.

The effect of temperature can be seen more readily in Figures 72 and 73 which show the creep compliance measured at a stress level of 3000 psi for both the 45° unidirectional and ±45° laminated glass/epoxy composite. Both figures show the strong influence of temperature on the material's internal viscosity which affects the creep coefficient through the reduced time, or  $a_T$  shift function. The vertical offset indicates at first glance that the initial compliance may be temperature dependent. The initial compliances,  $S'_{11}(0)$ , for the 45, 90 and ±45° fiber angles are shown in Figure 74. Since the behavior of the initial matrix compliance is that of a TCM, it is not unexpected that the glass/epoxy composite

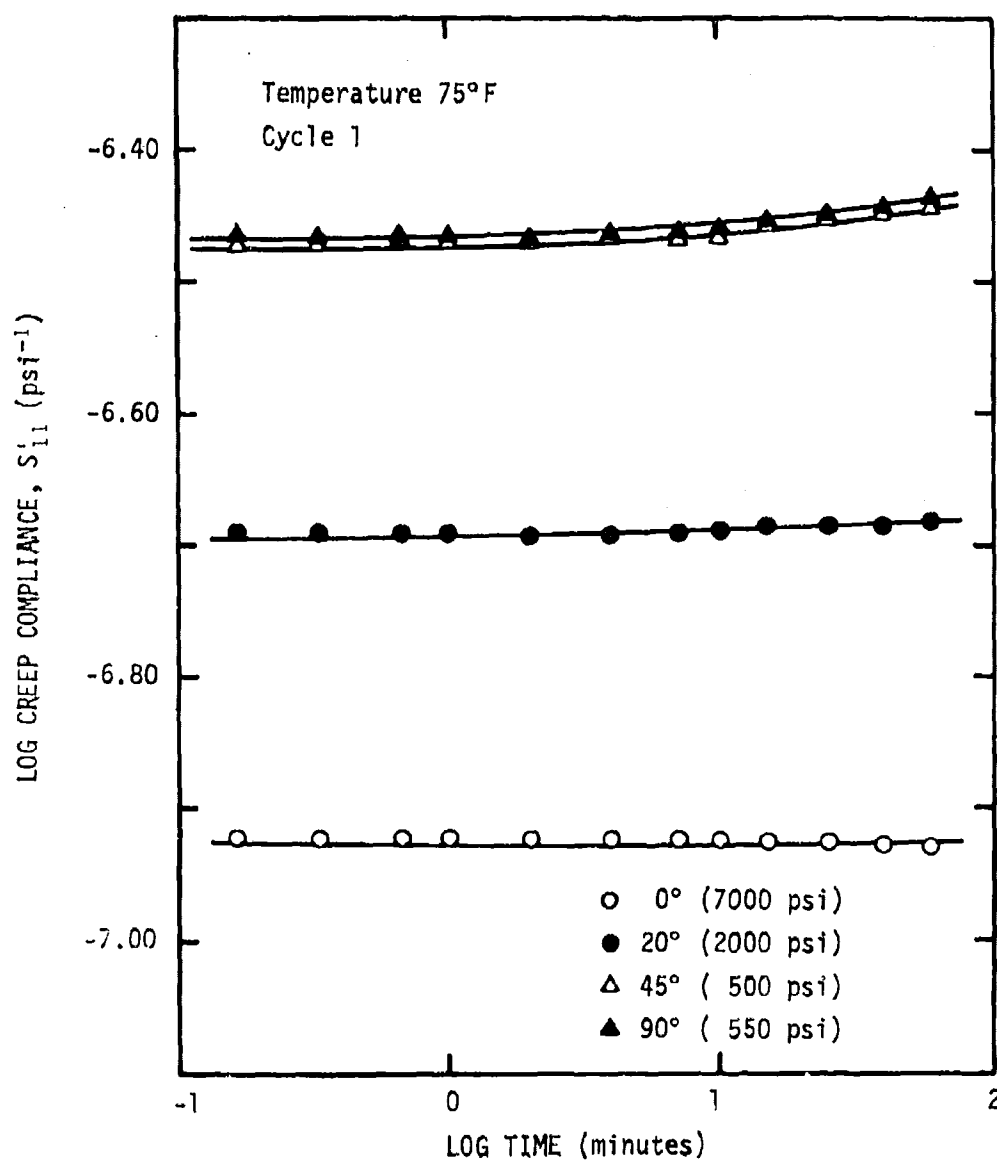


Figure 68. Creep compliances at low stress levels for various fiber angles ( $T = 75^\circ\text{F}$ ).

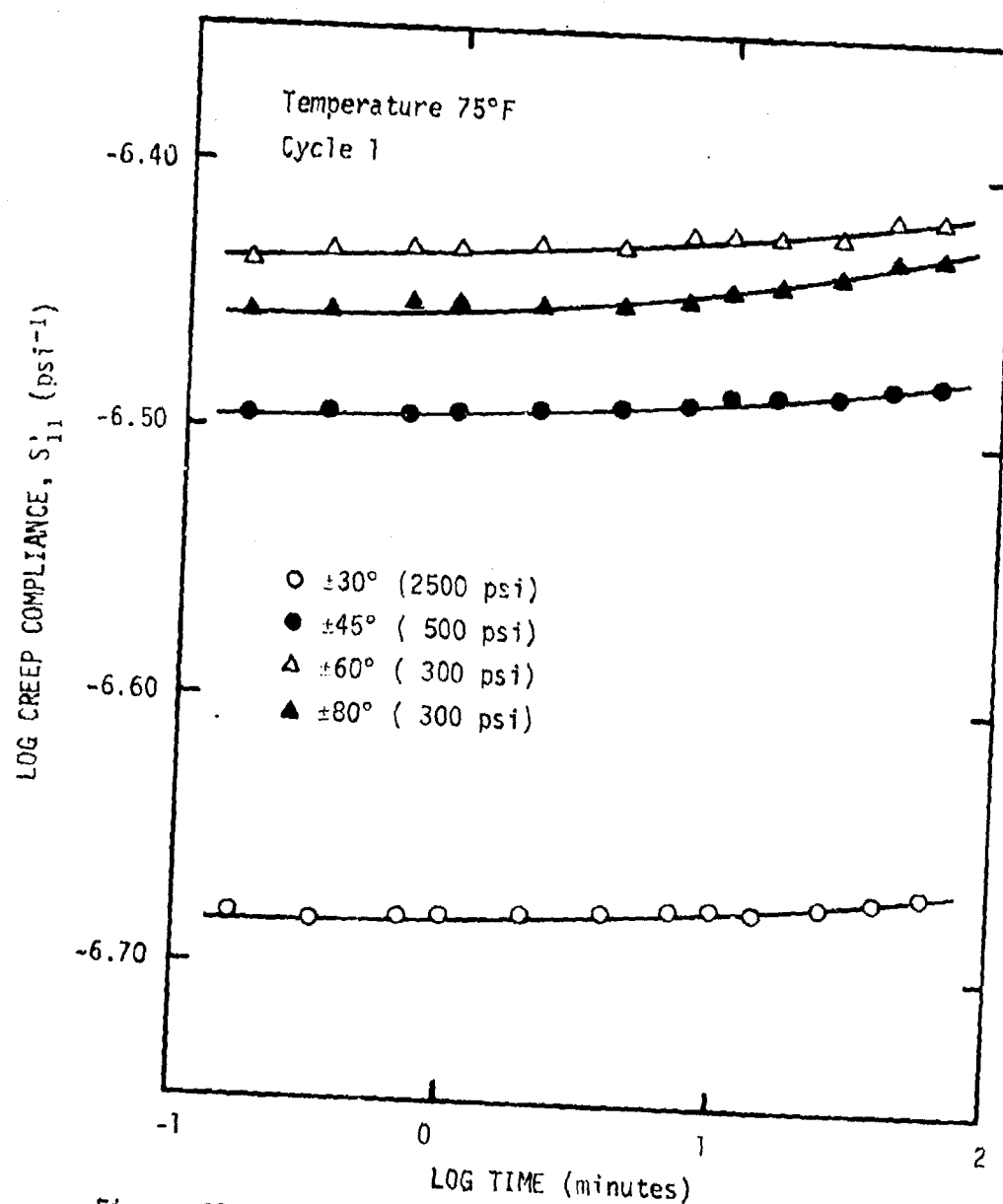


Figure 69. Creep compliances at low stress levels for various fiber angles of laminated composites ( $T = 75^\circ\text{F}$ ).

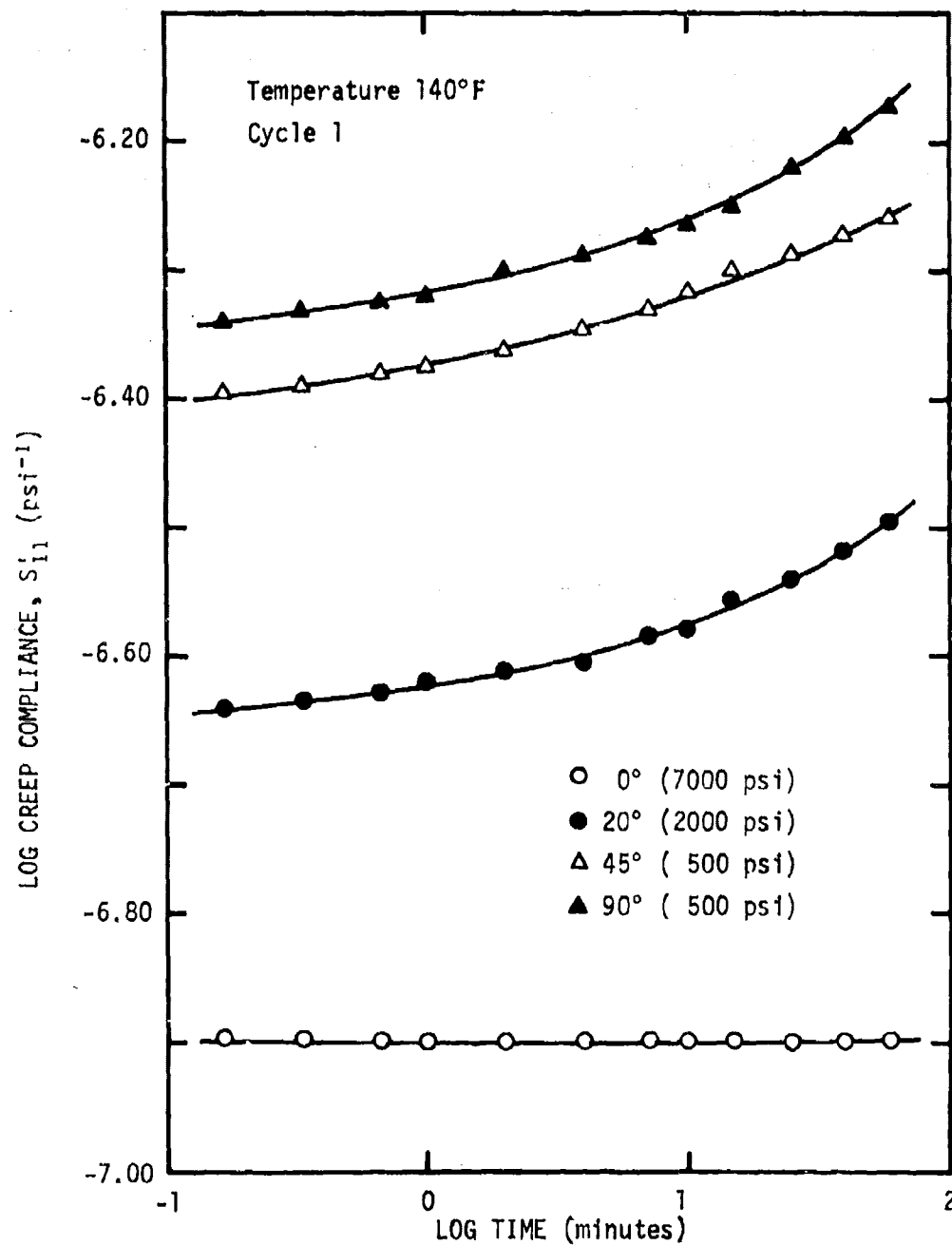


Figure 70. Creep compliance at low stress levels for various fiber angles ( $T = 140^\circ\text{F}$ ).

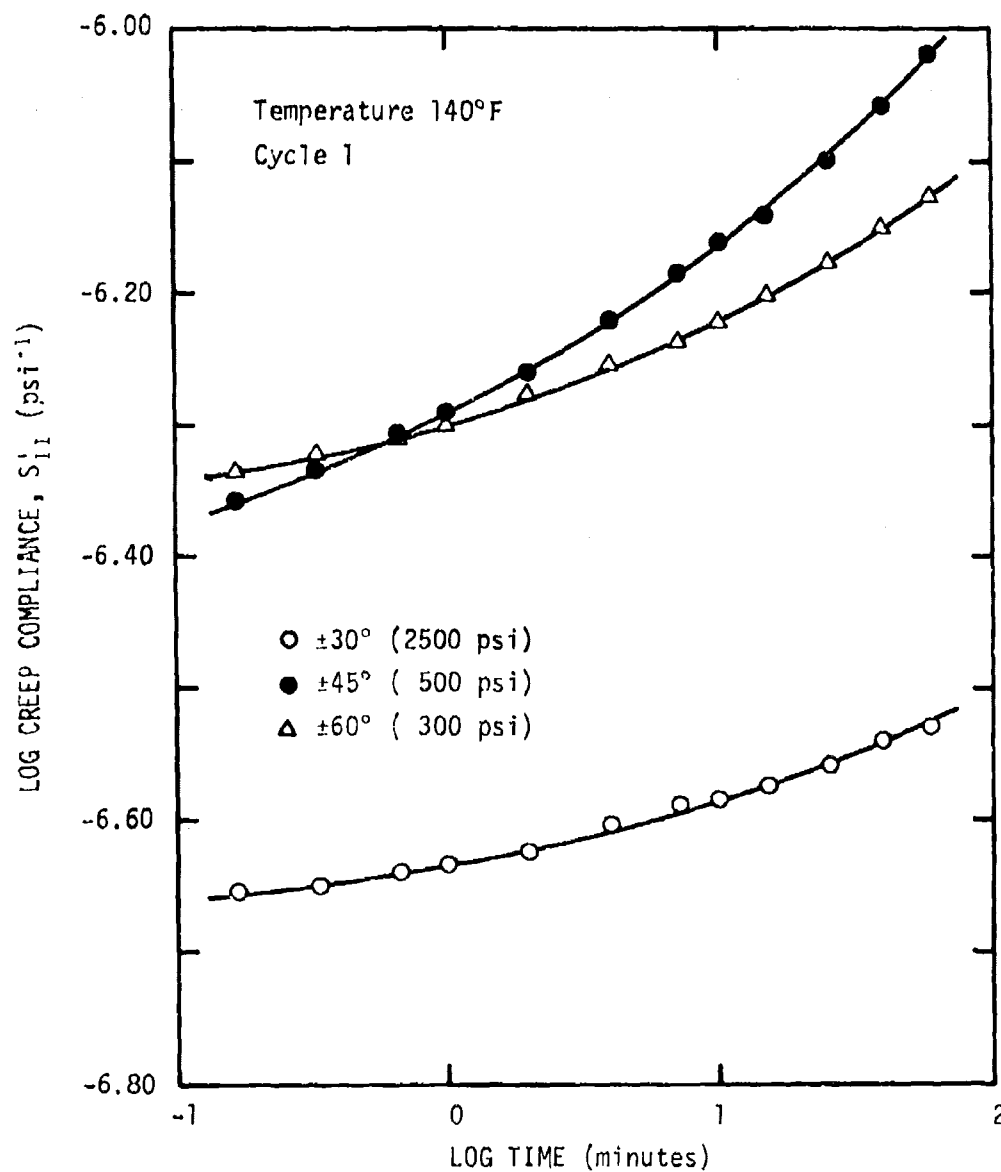


Figure 71. Creep compliances at low stress levels for various fiber angles of laminated composites ( $T = 140^\circ\text{F}$ ).

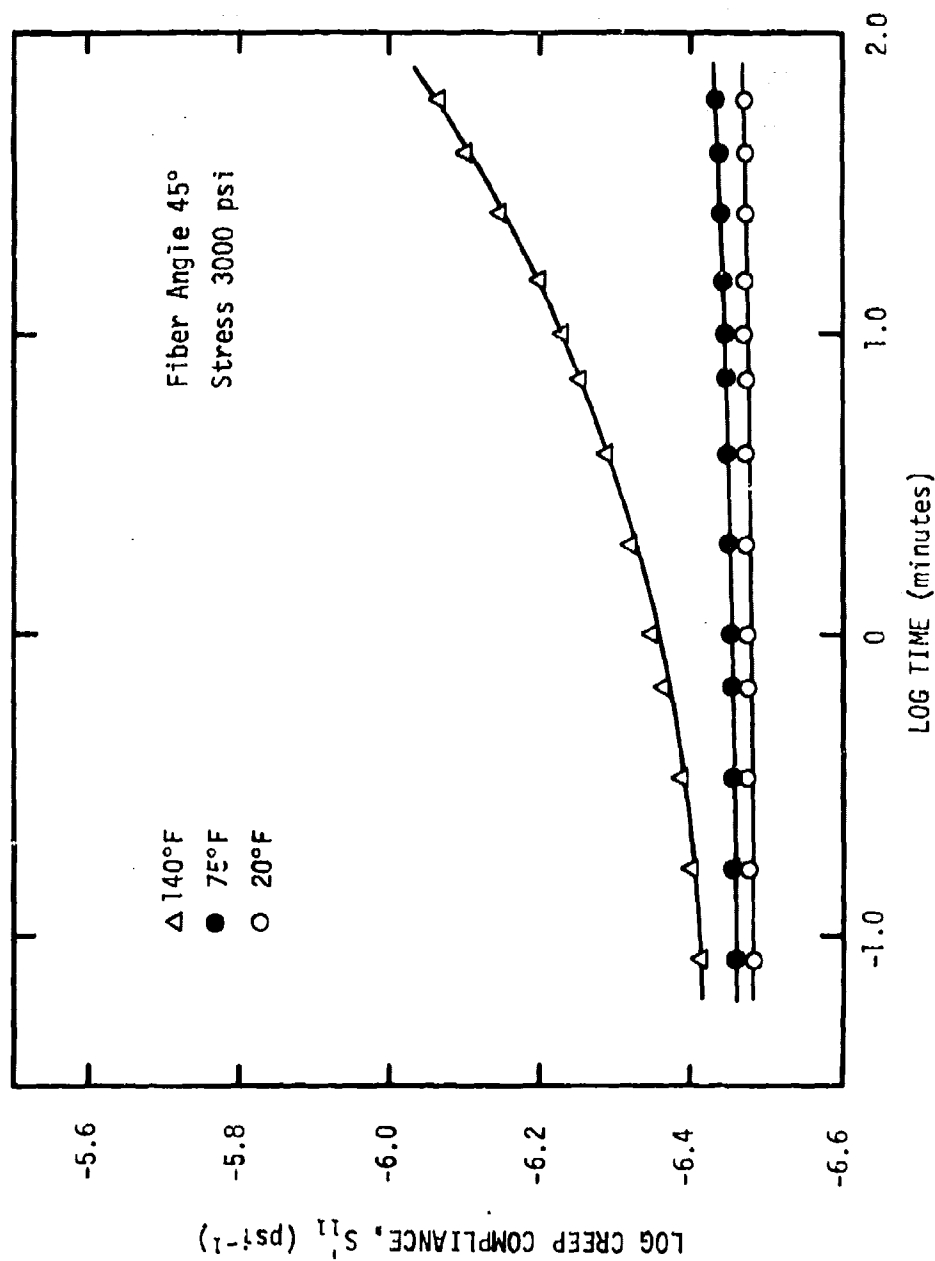


Figure 72. Effect of temperature on creep compliance of glass/epoxy composite ( $\theta = 45^\circ$ ).



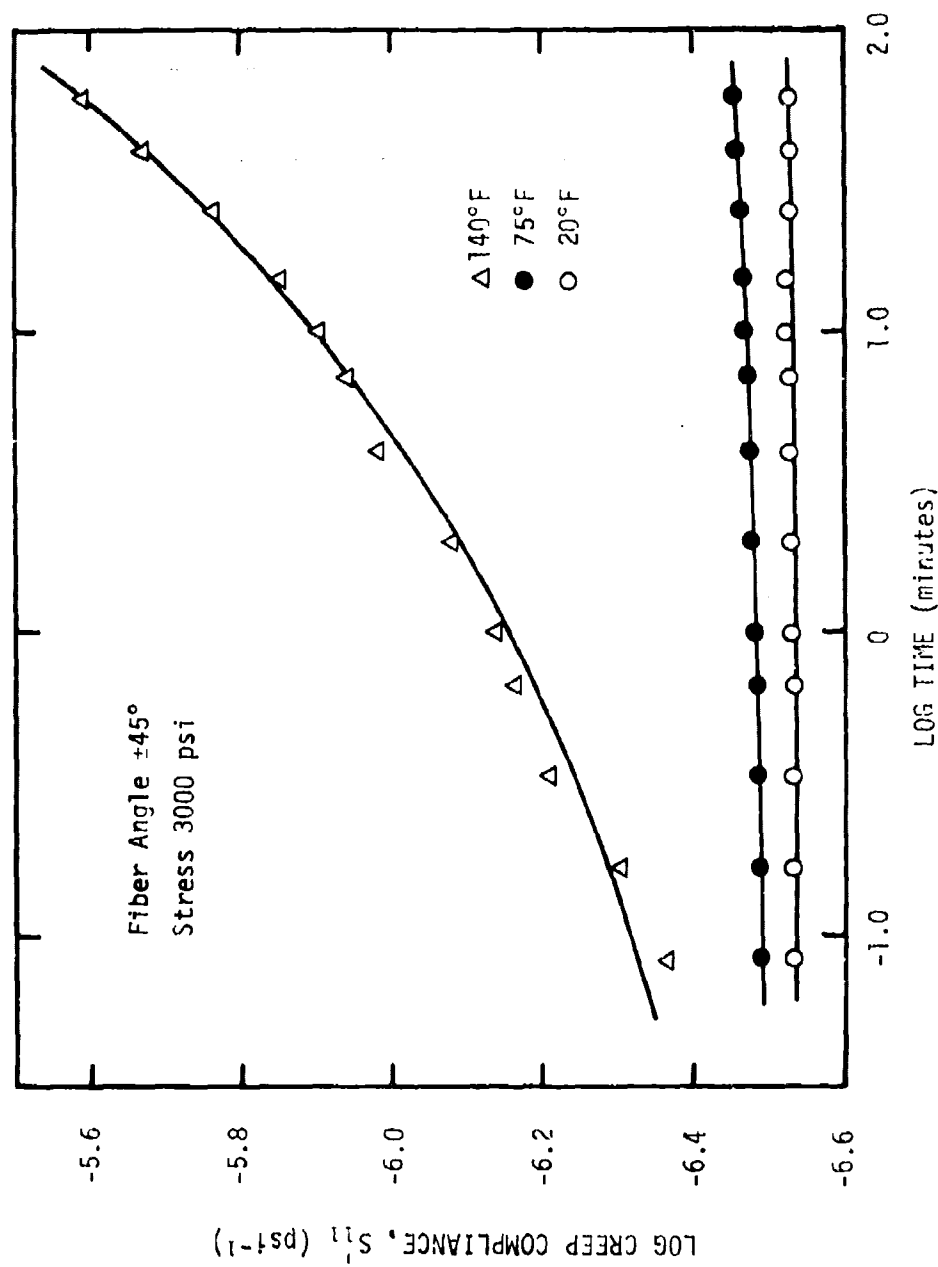


Figure 73. Effect of temperature on creep compliance of glass/epoxy composite ( $\theta = \pm 45^\circ$ ).

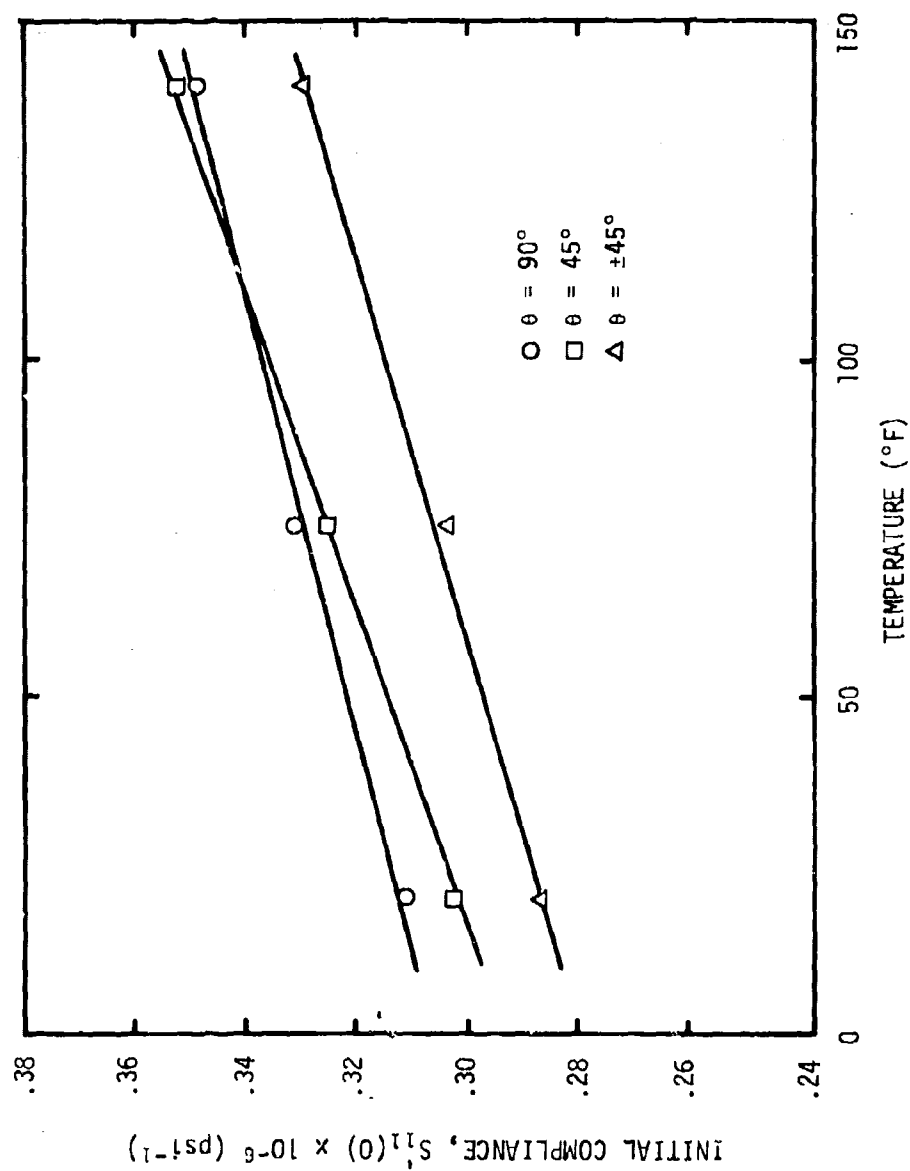


Figure 74. Temperature dependence of the initial creep compliances for the glass/epoxy composite.

exhibits a similar behavior. The glass/epoxy composite, therefore, is a TCM-2 by definition that the initial compliance is temperature dependent. Similar behavior was noted for a graphite/epoxy [12] and an E-glass/epoxy [9]. Unfortunately, many investigators do not recognize this temperature dependence when trying to separate out the elastic and transient components. This results in a series of discontinuities in the experimental data when one attempts to form a master curve using isothermal data from several temperatures [62].

The time-temperature shift factor,  $a_T$ , was determined for the glass/epoxy by using the method of the creep coefficient ratios for the  $45^\circ$  unidirectional and  $\pm 45^\circ$  laminated composite. These particular fiber angles were selected primarily because it was felt that the crack growth had essentially ceased by the third cycle at low stress levels. Lesser fiber angles were expected to give more scatter since the creep coefficient was smaller. The  $a_T$  factor is compared in Figure 75 with the epoxy resin shift factor. An activation energy of 37 Kcal/g-mole was found for the glass/epoxy. This corresponds to the values of 38 Kcal/g-mole and 35 Kcal/g-mole found for an E-glass/epoxy [9] and a graphite/epoxy [12] earlier. The value is physically consistent in terms of the fiber stiffnesses in the three systems. It should be noted that the values of  $a_T$  determined for all of the laminated composites and the  $90^\circ$  unidirectional composite at  $140^\circ\text{F}$  were considerably below the  $\log a_T$ -temperature curve for the epoxy.

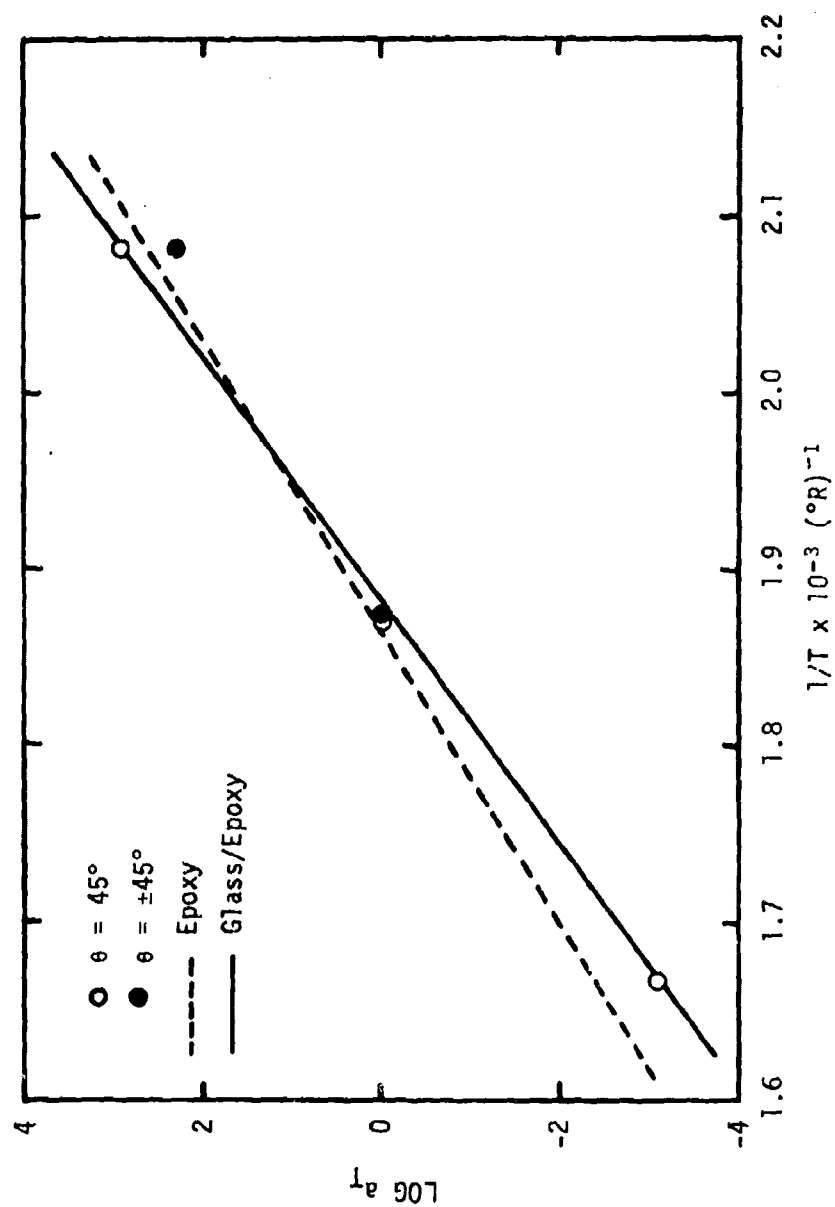


Figure 75. Time-temperature shift factor,  $a_T$ , for the glass/epoxy composite and epoxy resin (from Figure 44).

Studies conducted on the 170° motor case materials were carried out only at 75°F; however, the same behavior is expected in terms of material response at the higher temperatures. The linear creep compliance could not be determined for this material since the motor case had previously been pressurized to a high level. From Figures 5 and 13 one can see that the case material has undergone some degree of permanent damage already. However, the results of some multiple cycling tests carried out at low and high stress levels will be discussed in the next subsection.

#### Multiple Cycling Effects

All of the glass/epoxy composite samples were tested for several creep and recovery cycles. In order to simulate the actual conditions in the motor case, at least two, and as many as three cycles were run on the tensile coupons at all stress levels and temperatures. Since the total number of tests was well into the hundreds, it would not be possible to present the results from all of them. The principal results from the tests conducted at 75°F and 140°F on the 20, 45, 90 and  $\pm 45^\circ$  glass/epoxy composites are shown in Figures 76 through 95. These results are also limited to only a few representative stress levels.

Several general comments appear to be in order upon inspection of the results. In all of the tests the initial compliance continuously increases with each cycle, with a disproportionate change

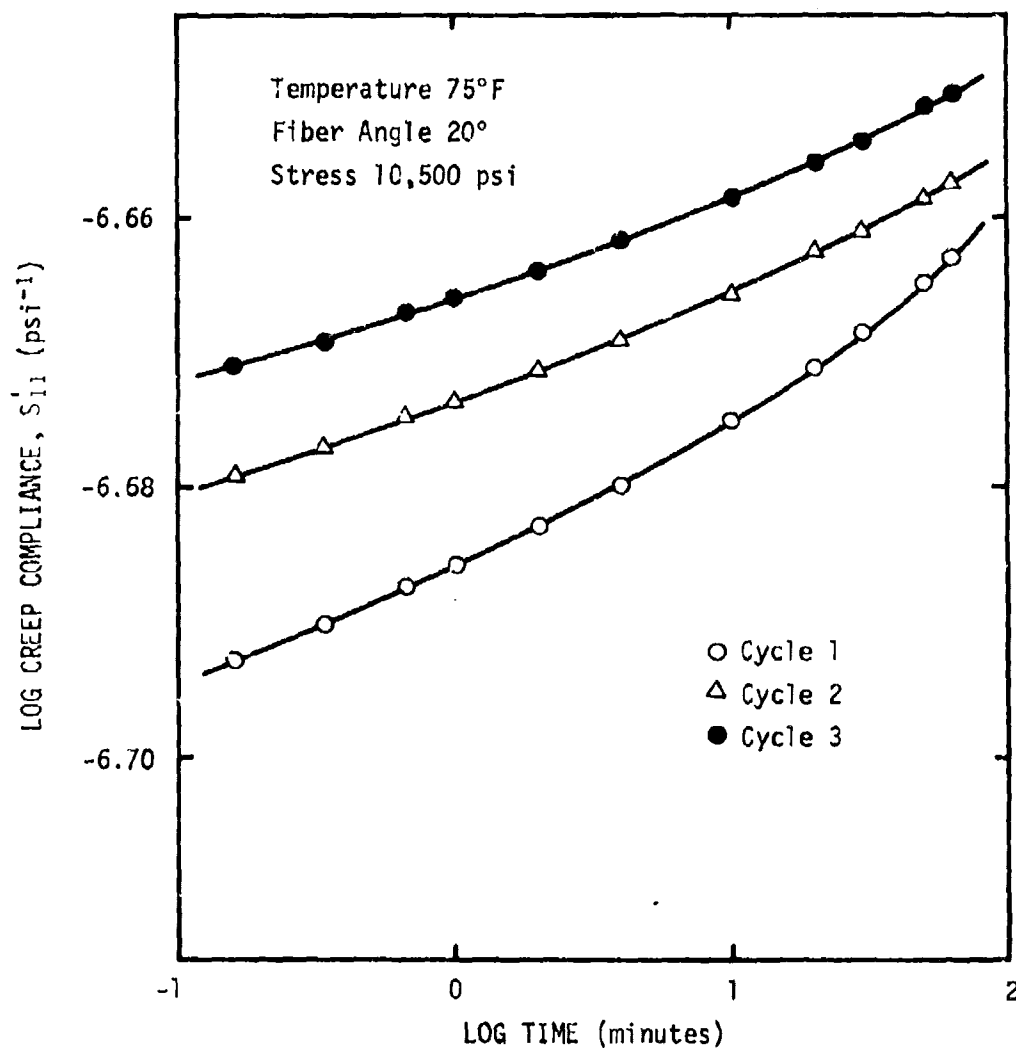


Figure 76. Effect of multiple loading on the creep compliance of the glass/epoxy unidirectional laminae ( $\theta = 20^\circ$ ,  $T = 75^\circ\text{F}$ ,  $\sigma = 10,500$  psi).

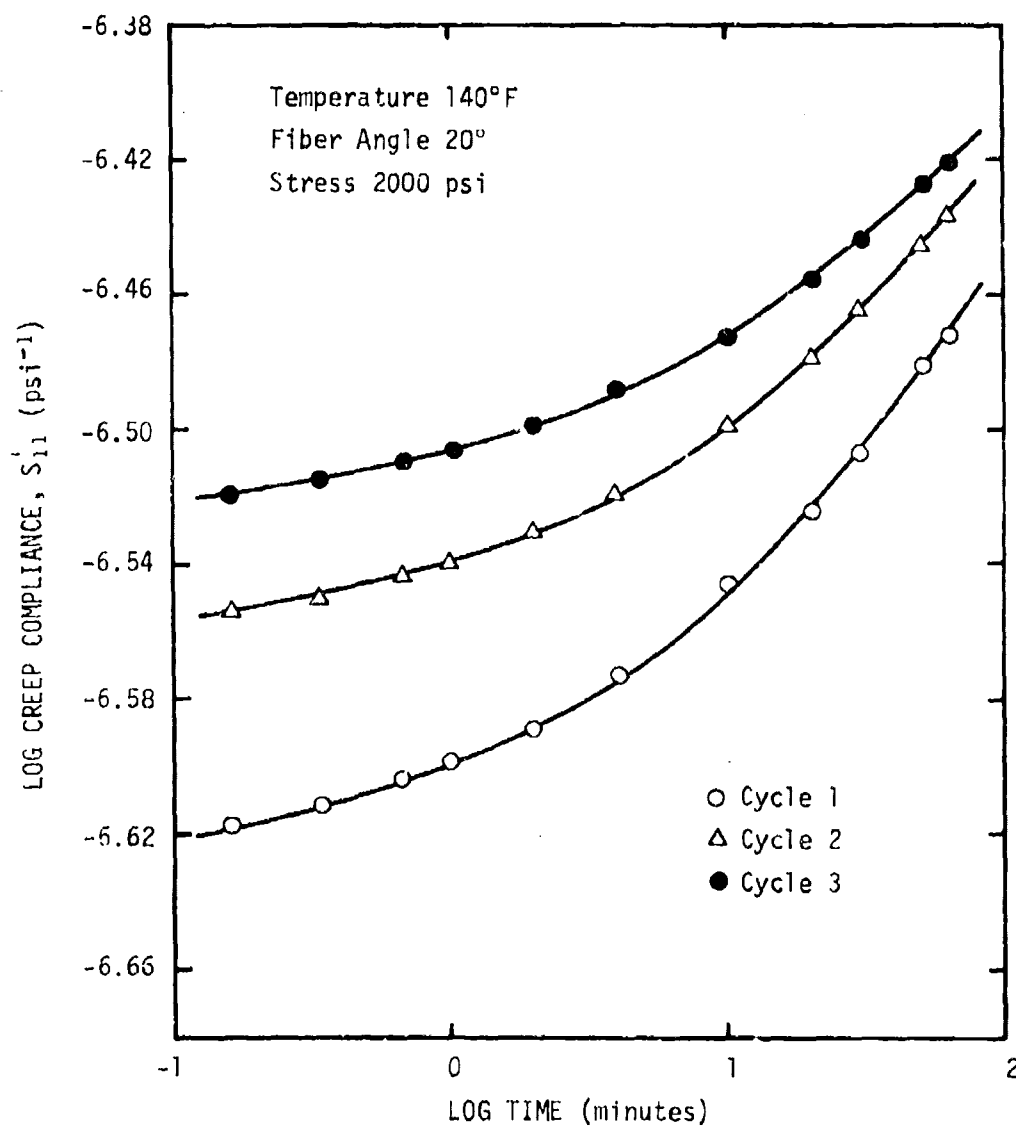


Figure 77. Effect of multiple loading on the creep compliance of the glass/epoxy unidirectional laminae ( $\theta = 20^\circ$ ,  $T = 140^\circ\text{F}$ ,  $\sigma = 2000$  psi).

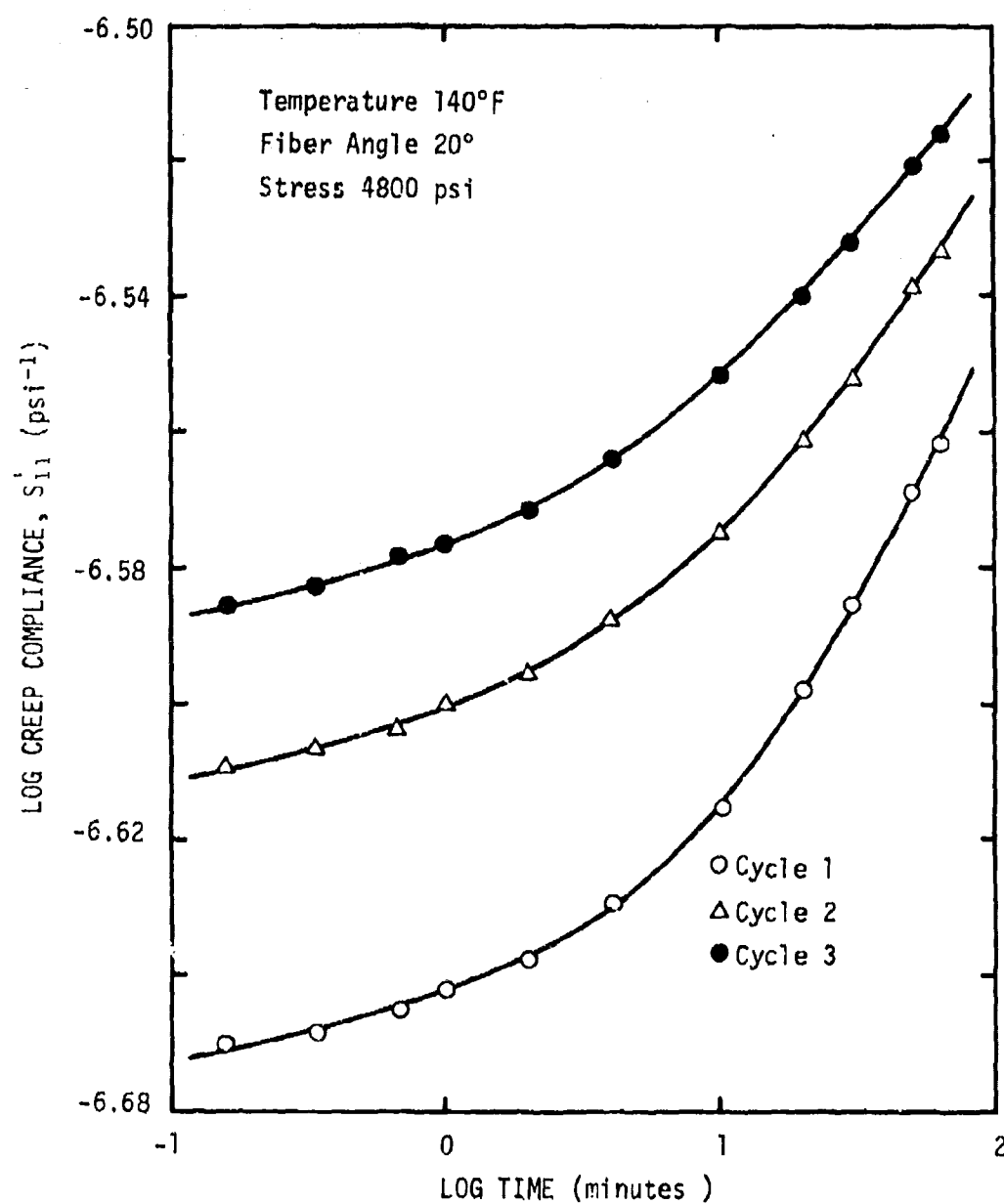


Figure 78. Effect of multiple loading on the creep compliance of the glass/epoxy unidirectional laminae ( $\theta = 20^\circ$ ,  $T = 140^\circ\text{F}$ ,  $\sigma = 4800$  psi).



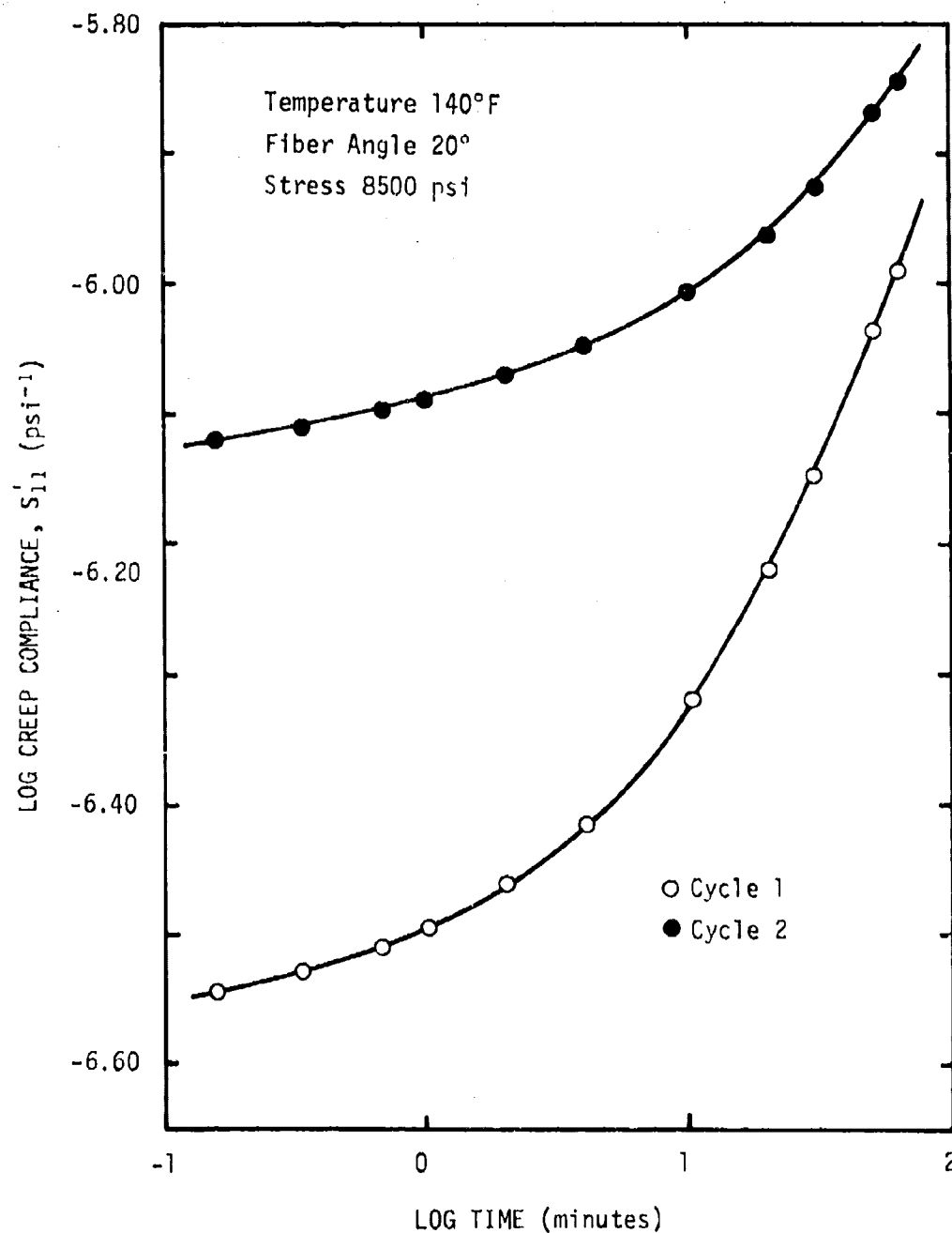


Figure 79. Effect of multiple loading on the creep compliance of the glass/epoxy unidirectional laminae ( $\theta = 20^\circ$ ,  $T = 140^\circ\text{F}$ ,  $\sigma = 8500$  psi).

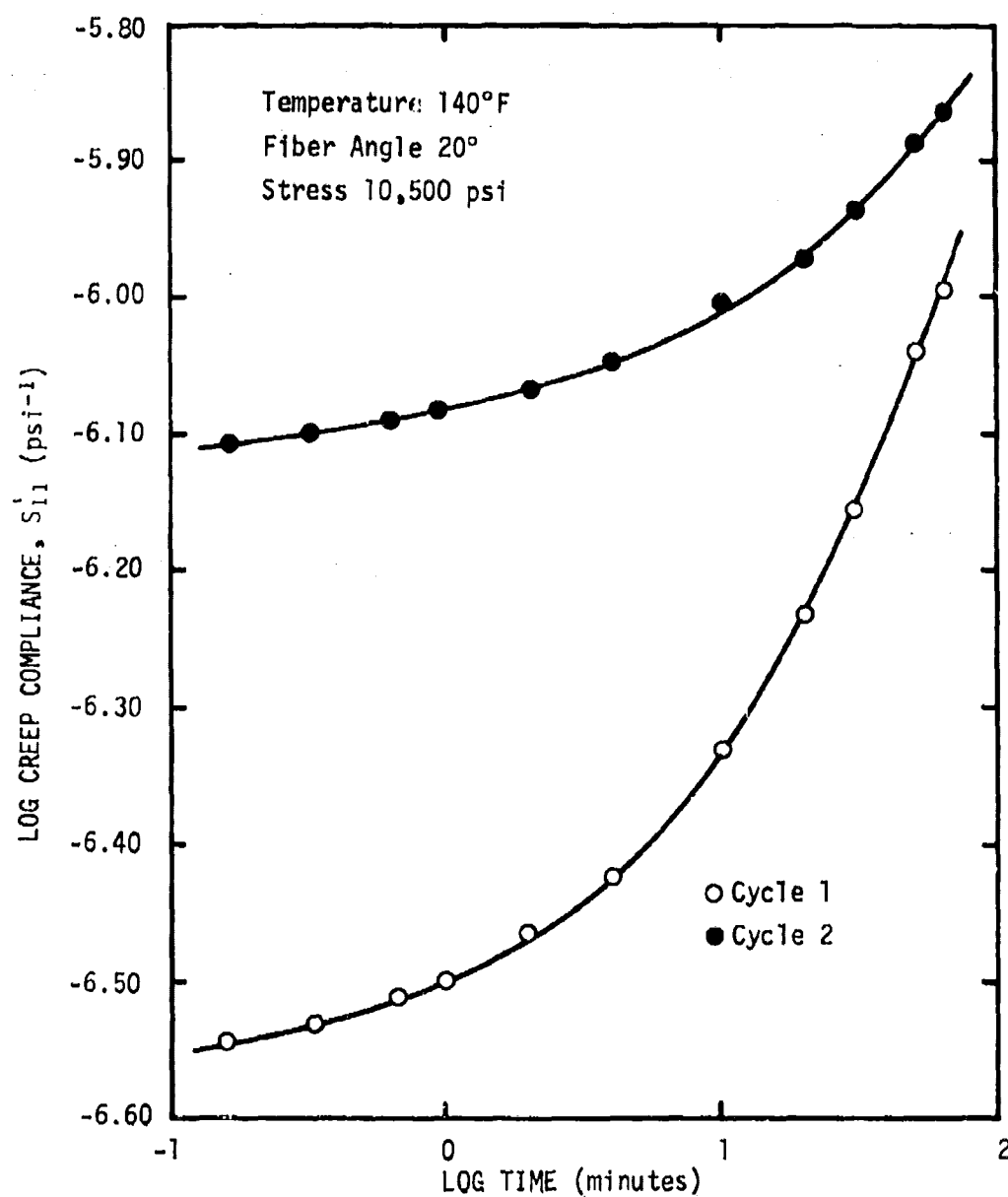


Figure 80. Effect of multiple loading on the creep compliance of the glass/epoxy unidirectional laminae ( $\theta = 20^\circ$ ,  $T = 140^\circ\text{F}$ ,  $\sigma = 10,500$  psi).

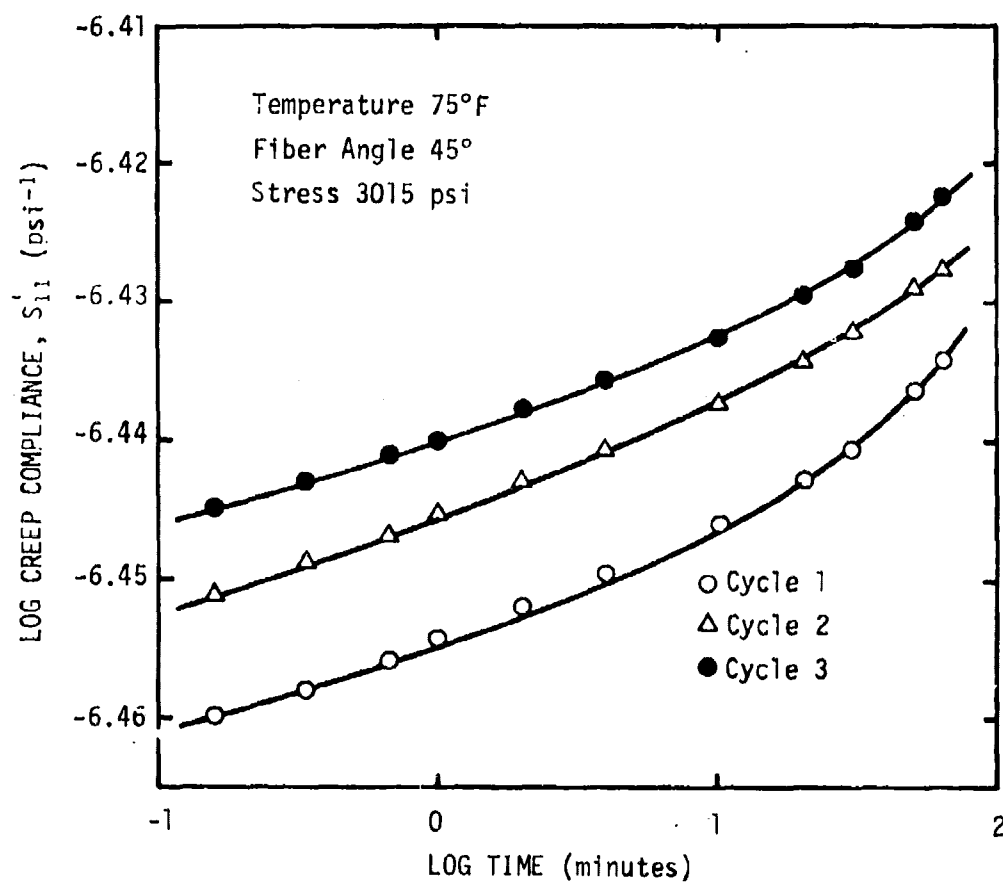


Figure 81. Effect of multiple loading on the creep compliance of the glass/epoxy unidirectional laminae ( $\theta = 45^\circ$ ,  $T = 75^\circ\text{F}$ ,  $\sigma = 3015 \text{ psi}$ ).

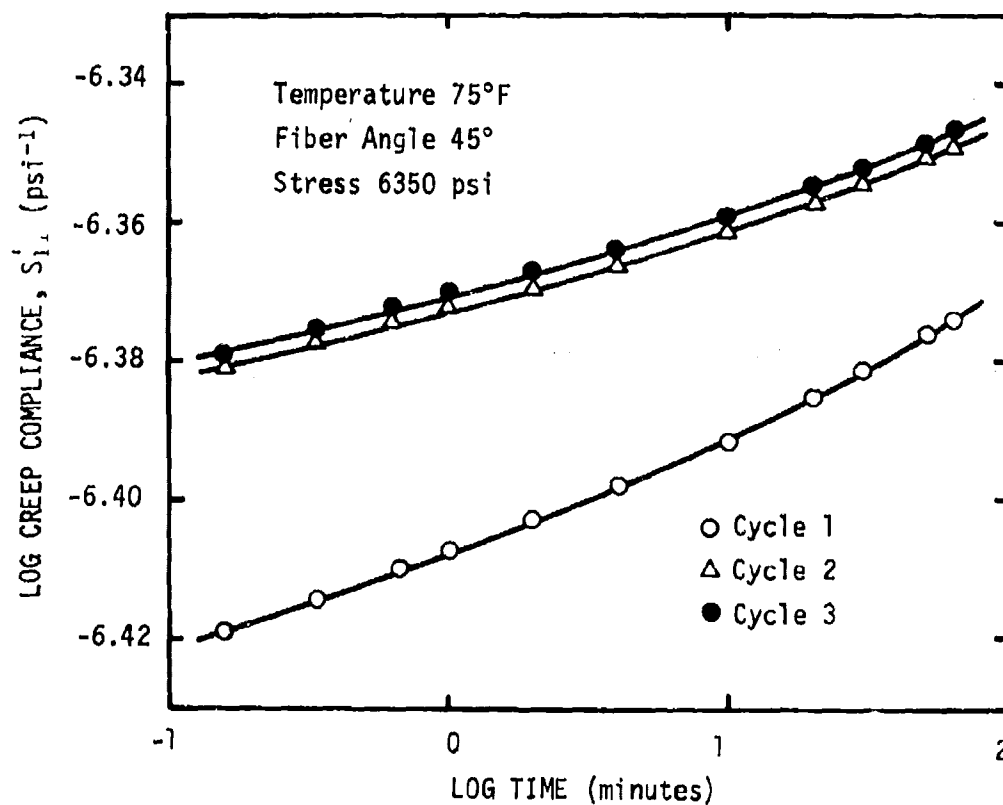


Figure 82. Effect of multiple loading on the creep compliance of the glass/epoxy unidirectional laminae ( $\theta = 45^\circ$ ,  $T = 75^\circ\text{F}$ ,  $\sigma = 6350$  psi).

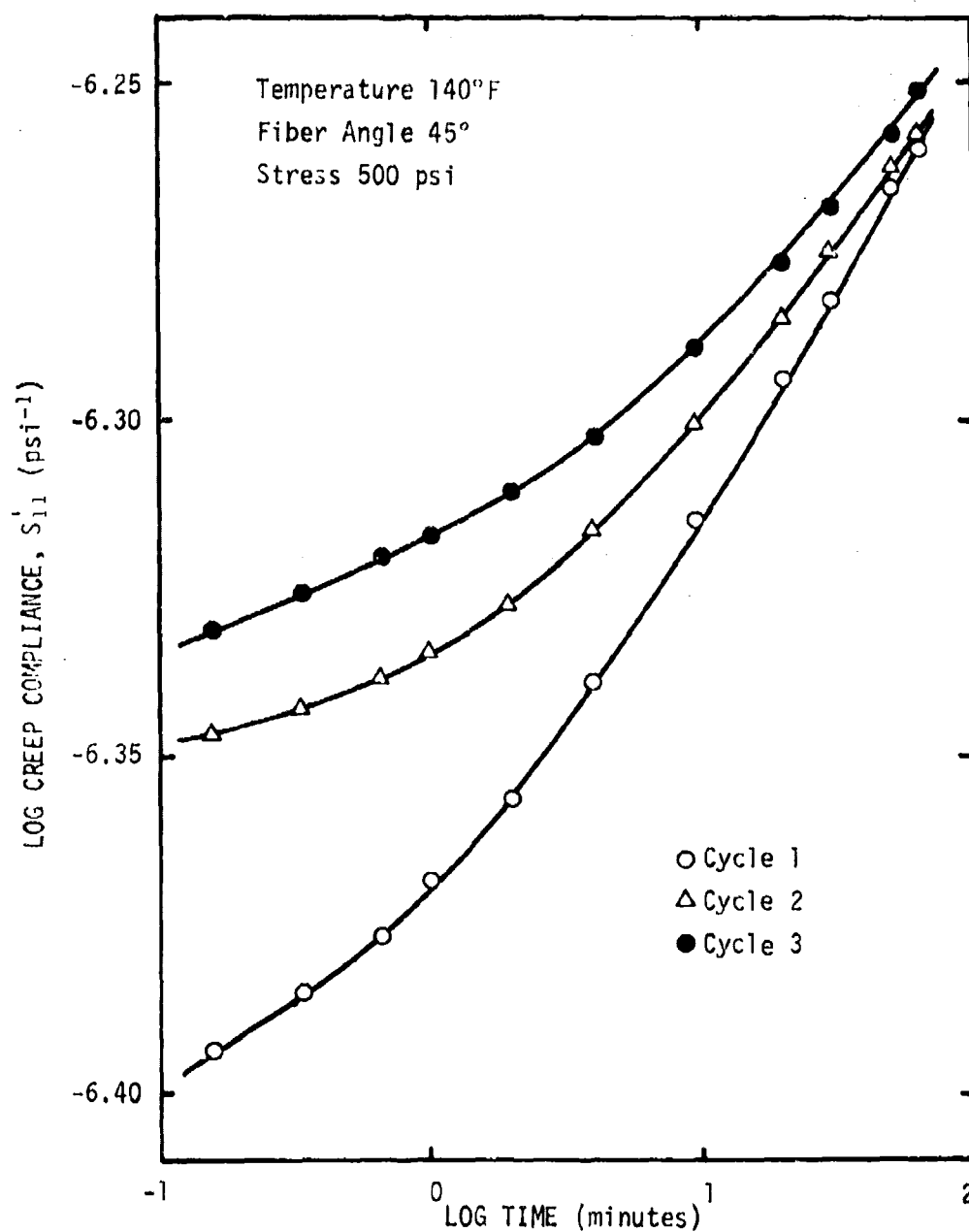


Figure 83. Effect of multiple loading on the creep compliance of the glass/epoxy unidirectional laminae ( $\theta = 45^\circ$ ,  $T = 140^\circ\text{F}$ ,  $\sigma = 500$  psi).

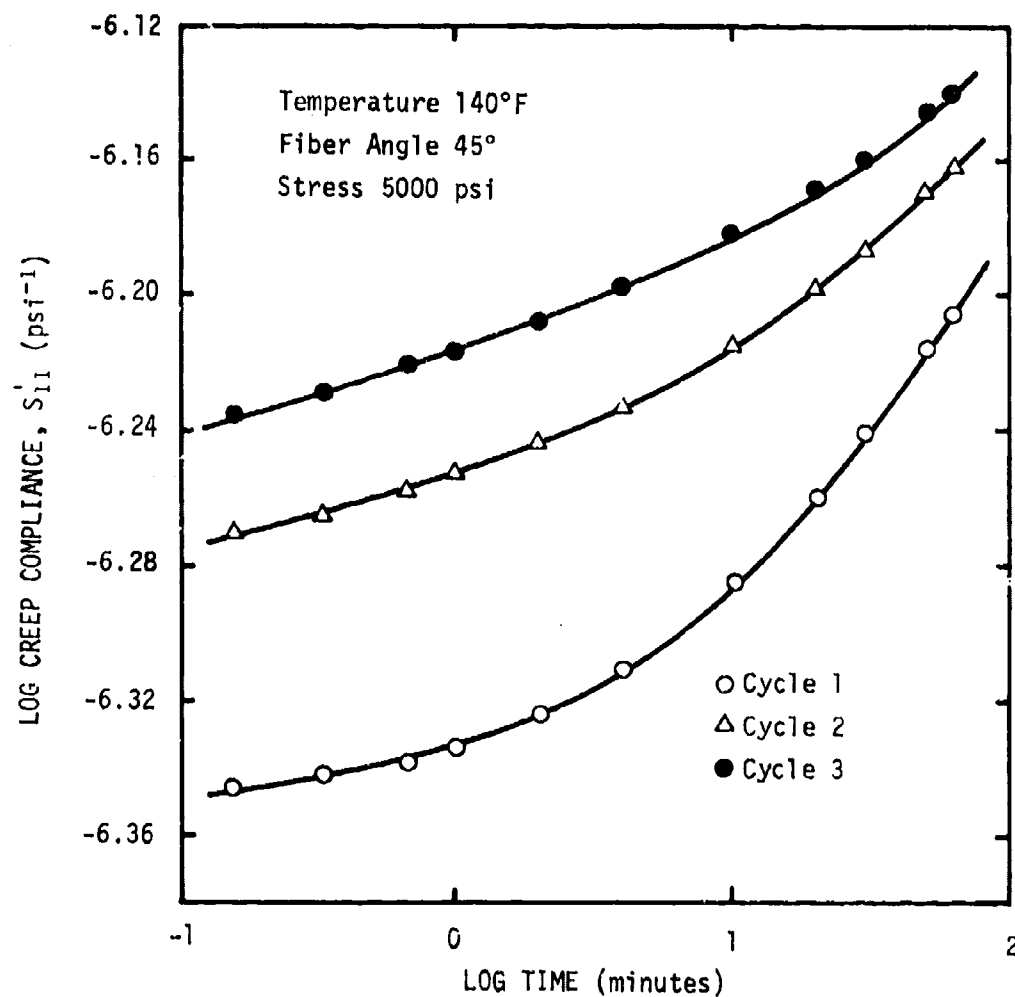


Figure 84. Effect of multiple loading on the creep compliance of the glass/epoxy unidirectional laminae ( $\theta = 45^\circ$ ,  $T = 140^\circ\text{F}$ ,  $\sigma = 5000 \text{ psi}$ ).

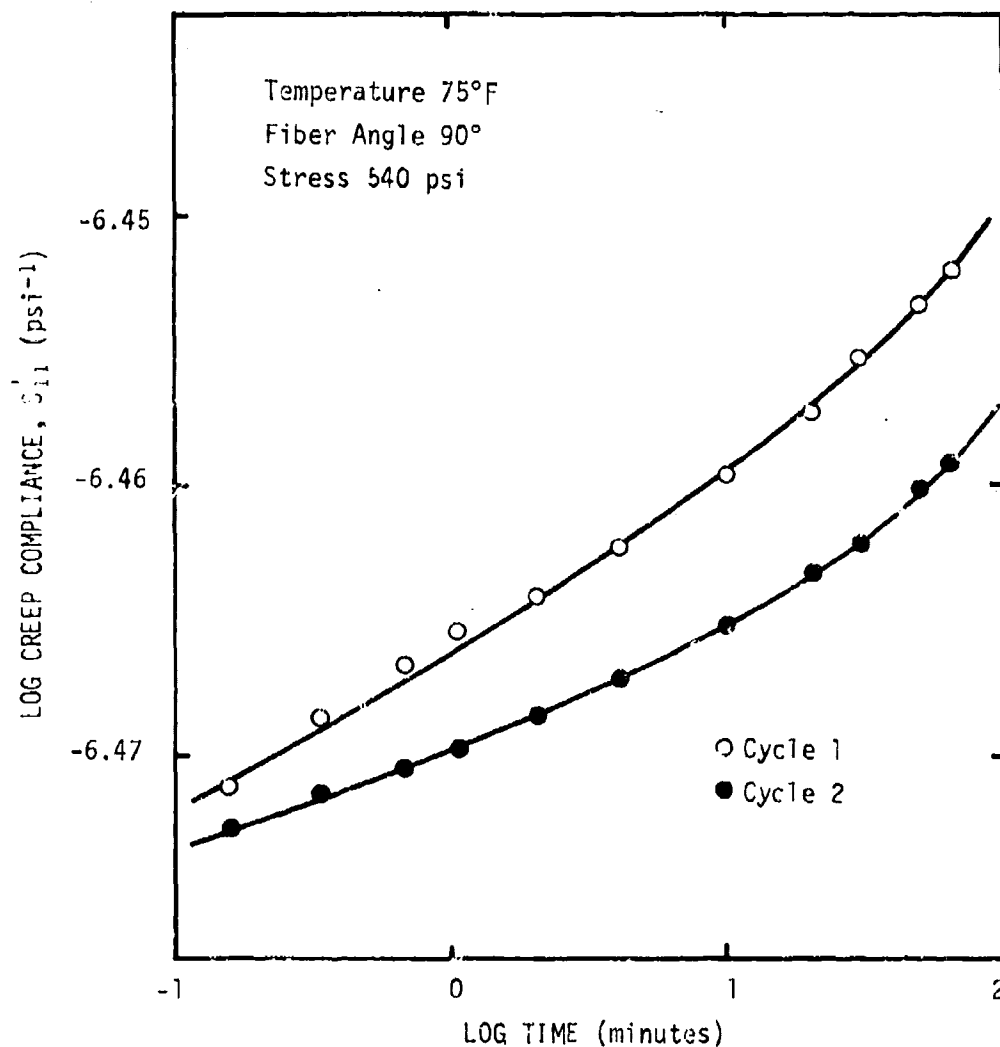


Figure 85. Effect of multiple loading on the creep compliance of the glass/epoxy unidirectional laminae ( $\theta = 90^\circ$ ,  $T = 75^\circ\text{F}$ ,  $\sigma = 540$  psi).

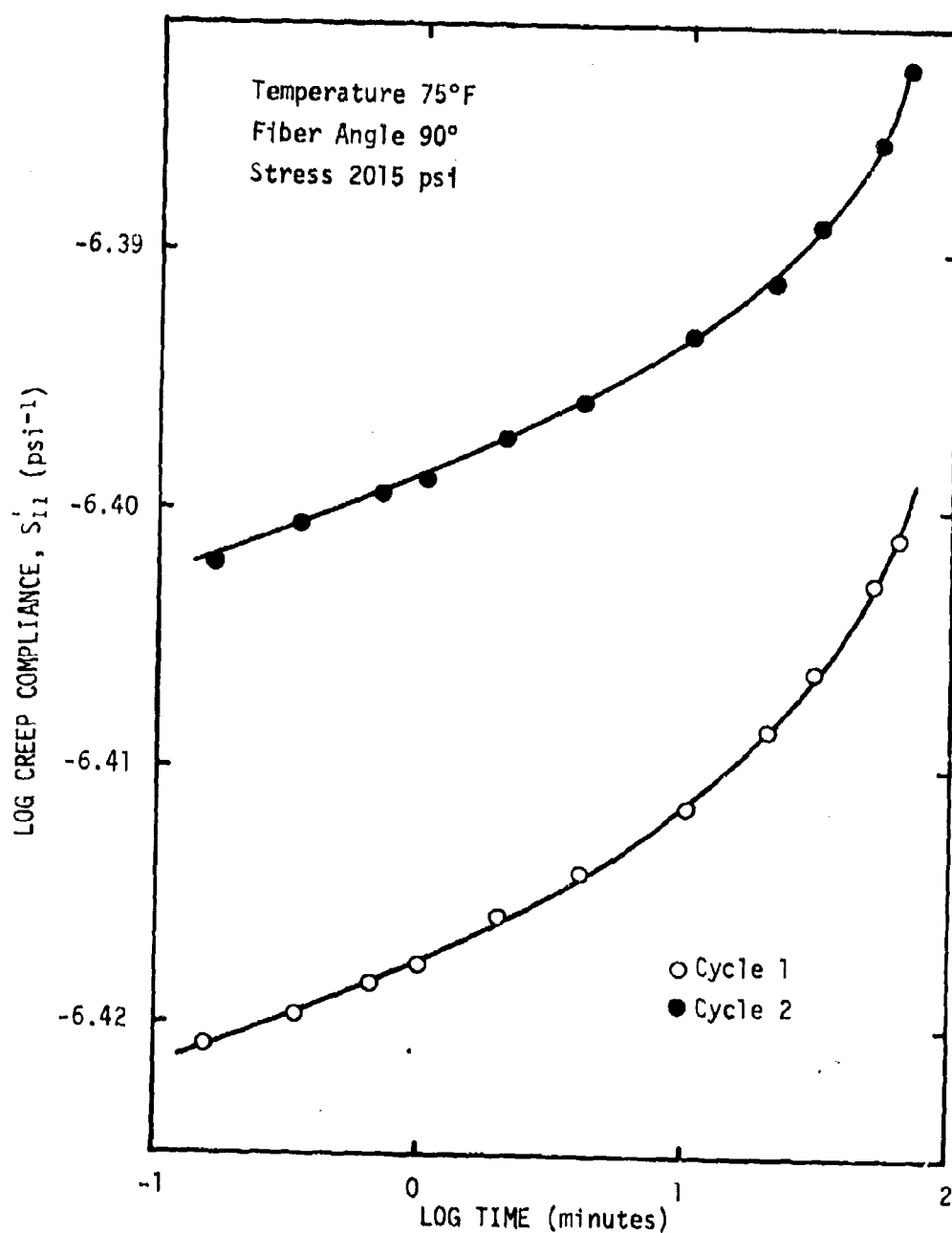


Figure 86. Effect of multiple loading on creep compliance of the glass/epoxy unidirectional laminae ( $\theta = 90^\circ$ ,  $T = 75^\circ\text{F}$ ,  $\sigma = 2015$  psi).



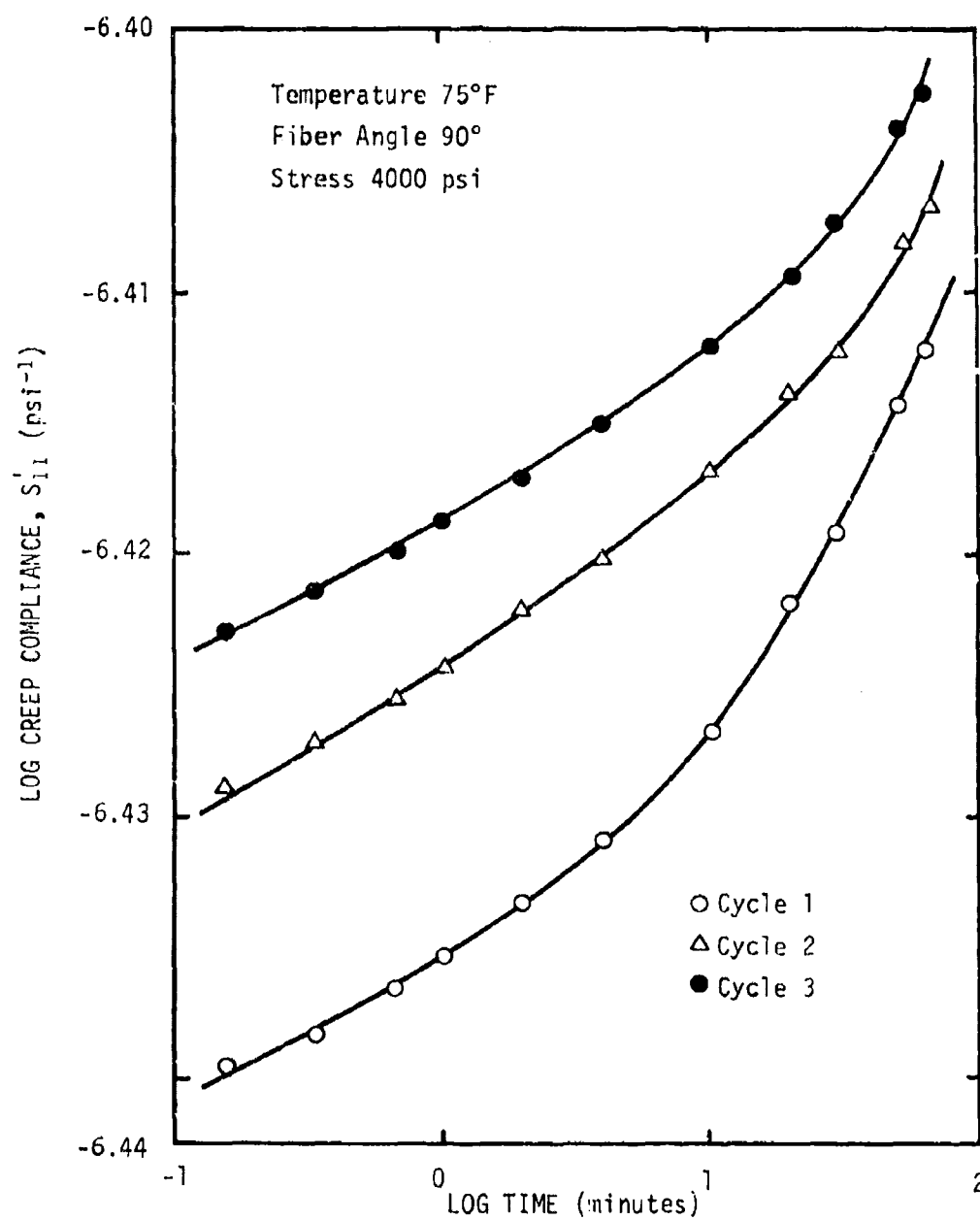


Figure 87. Effect of multiple loading on creep compliance of the glass/epoxy unidirectional laminae ( $\theta = 90^\circ$ ,  $T = 75^\circ\text{F}$ ,  $\sigma = 4000\text{ psi}$ ).

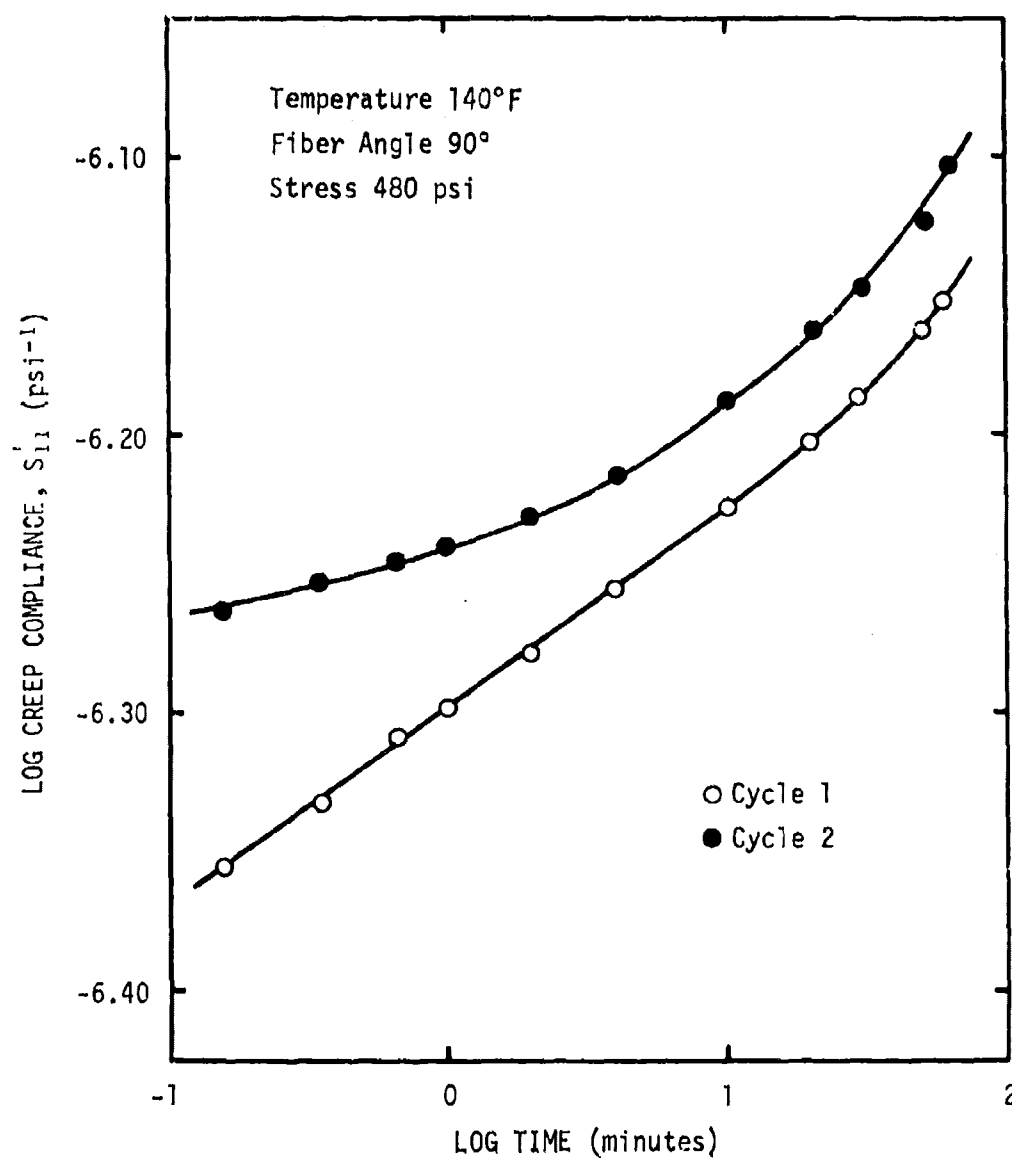


Figure 88. Effect of multiple loading on creep compliance of the glass/epoxy unidirectional laminae ( $\theta = 90^\circ$ ,  $T = 140^\circ\text{F}$ ,  $\sigma = 480$  psi).

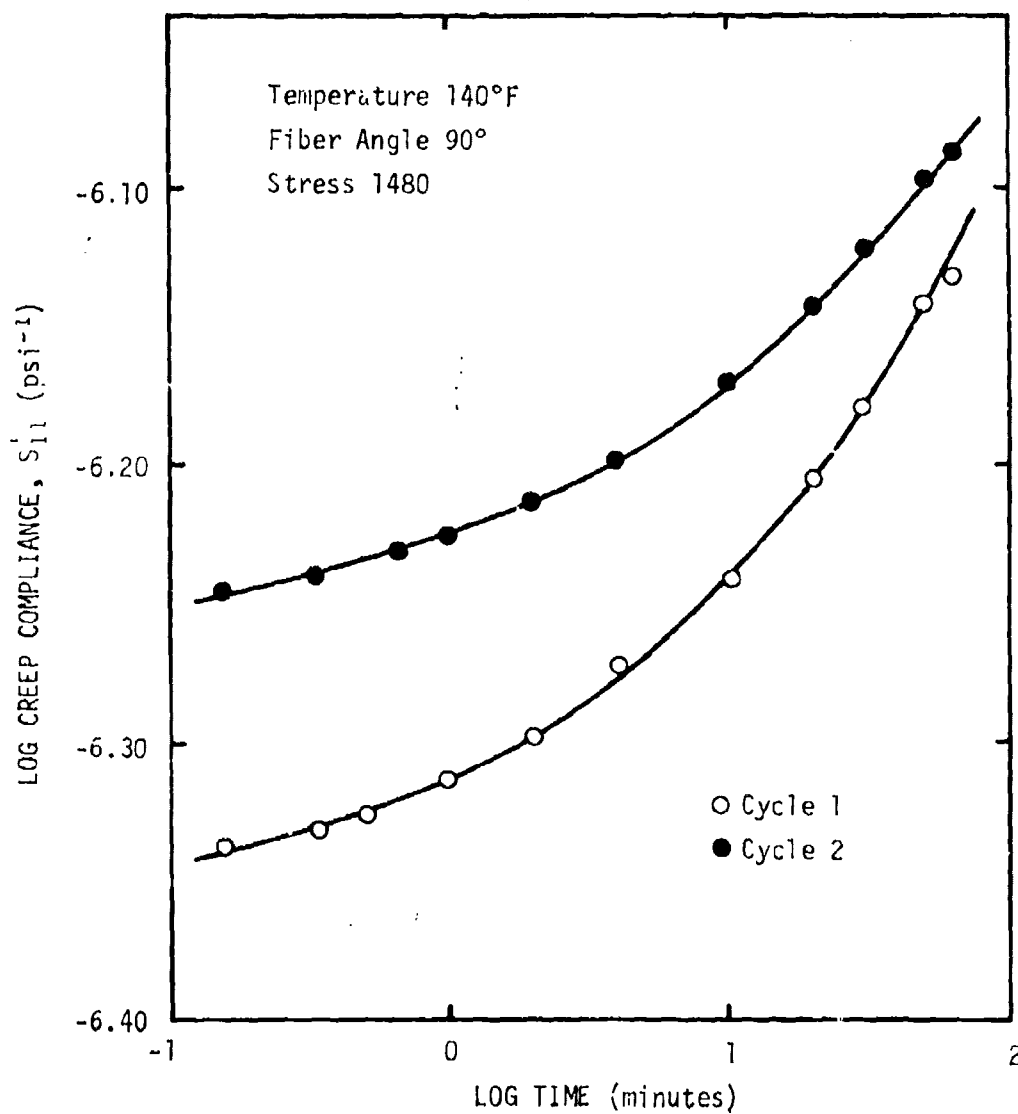


Figure 89. Effect of multiple loading on creep compliance of the glass/epoxy unidirectional laminae ( $\theta = 90^\circ$ ,  $T = 140^\circ\text{F}$ ,  $\sigma = 1480$  psi).

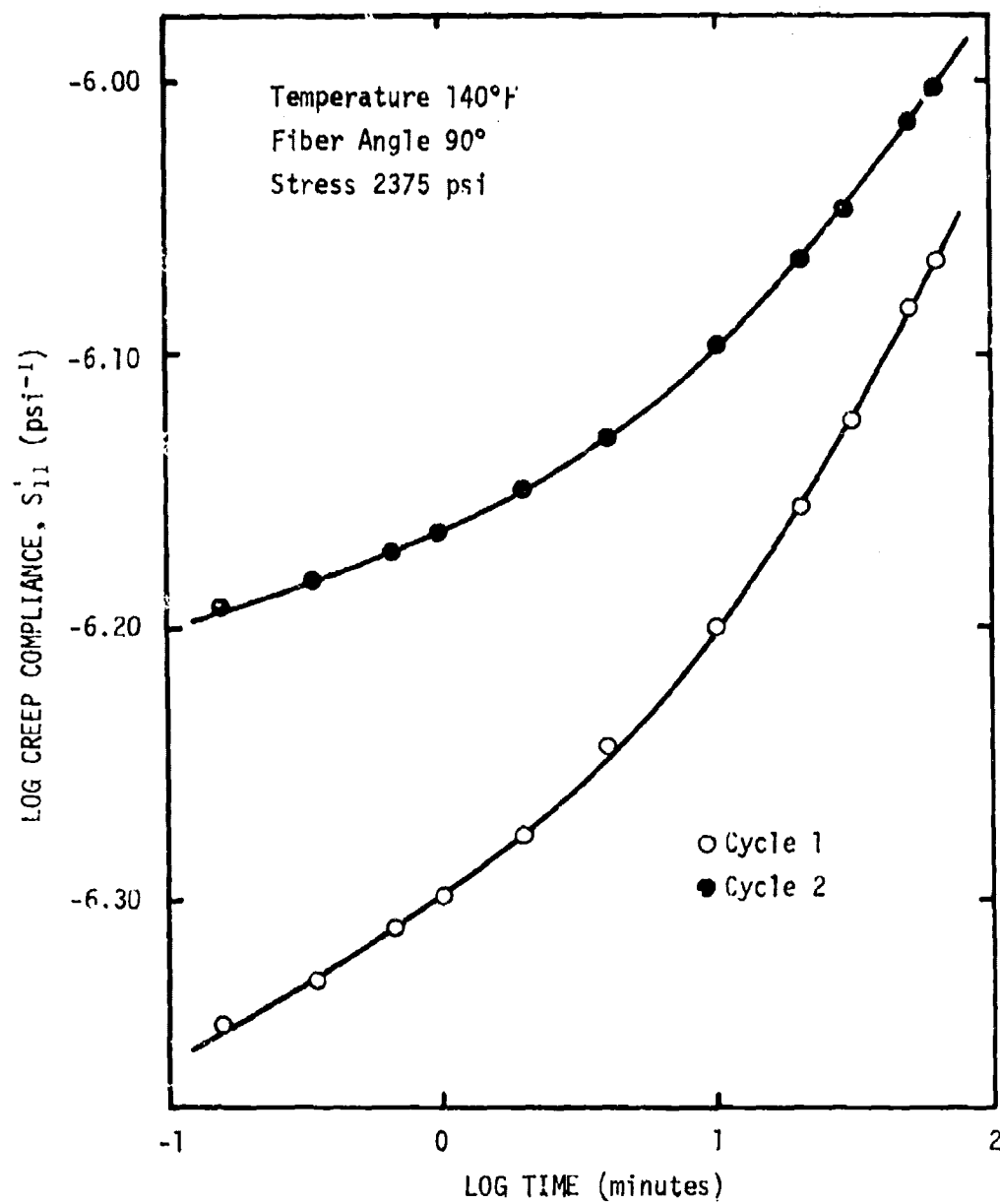


Figure 90. Effect of multiple loading on creep compliance of the glass/epoxy unidirectional laminae ( $\theta = 90^\circ$ ,  $T = 140^\circ\text{F}$ ,  $\sigma = 2375$  psi).

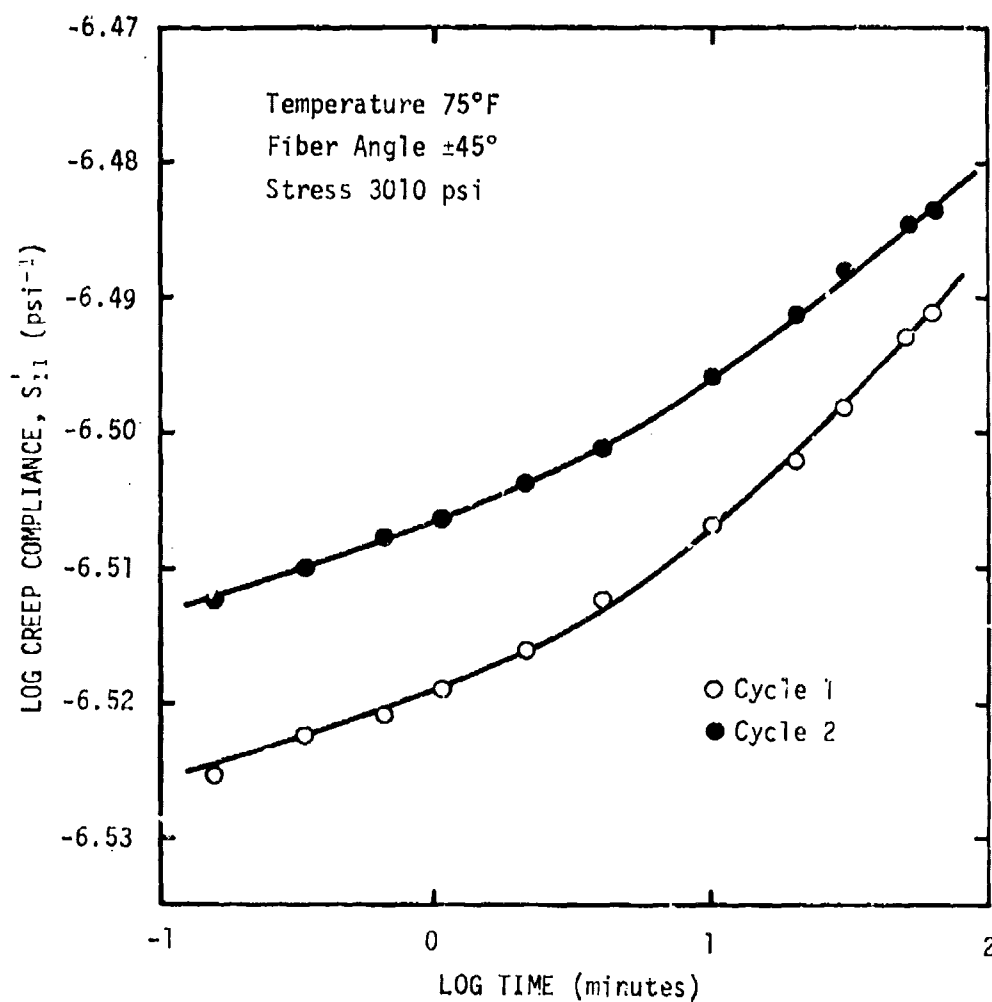


Figure 91. Effect of multiple loading on creep compliance of the glass/epoxy laminated composite ( $\theta = \pm 45^\circ$ ,  $T = 75^\circ\text{F}$ ,  $\sigma = 3010$  psi).

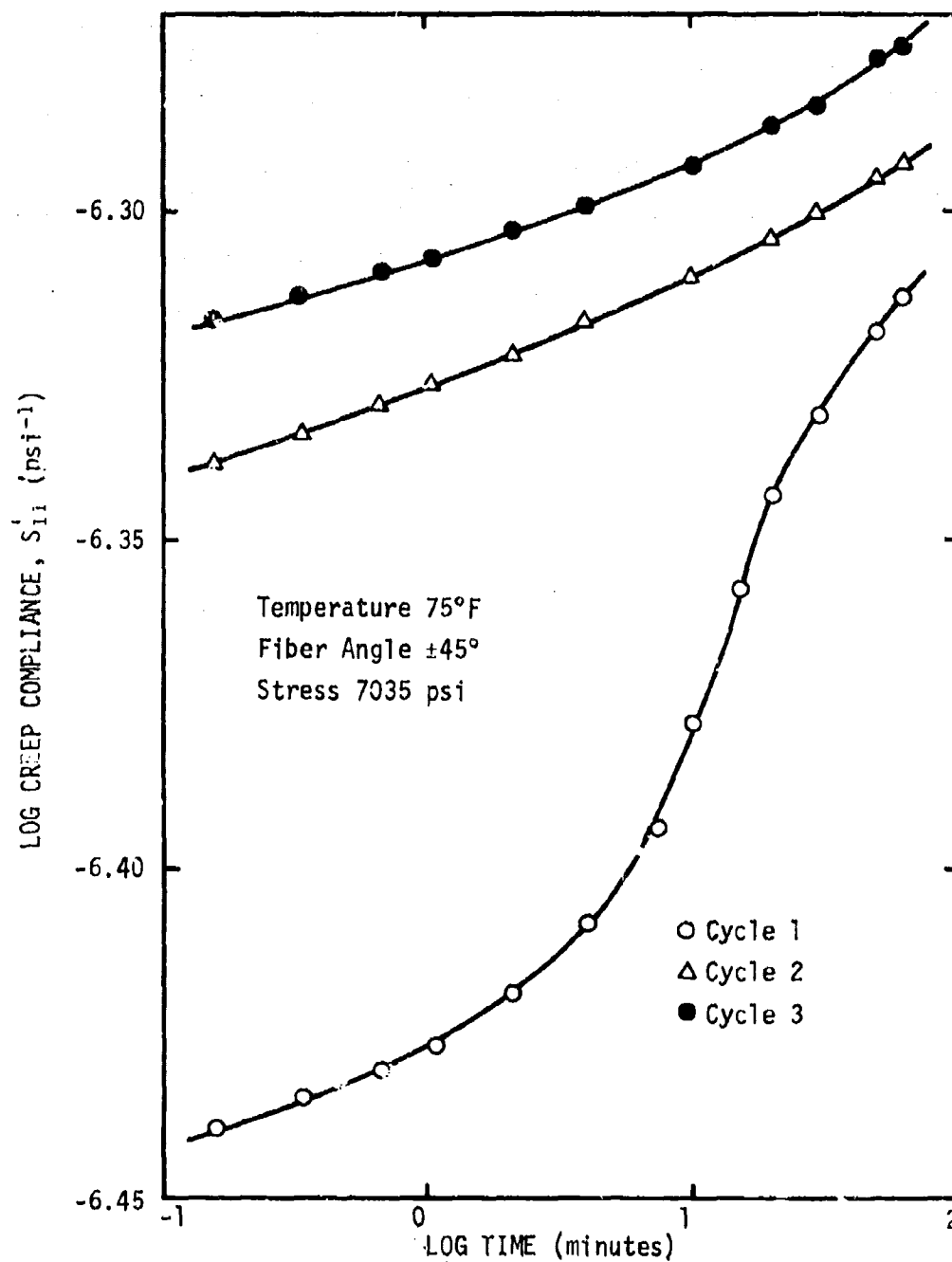


Figure 92. Effect of multiple loading on creep compliance of the glass/epoxy laminated composite ( $\theta = \pm 45^\circ$ ,  $T = 75^\circ\text{F}$ ,  $\sigma = 7035$  psi).

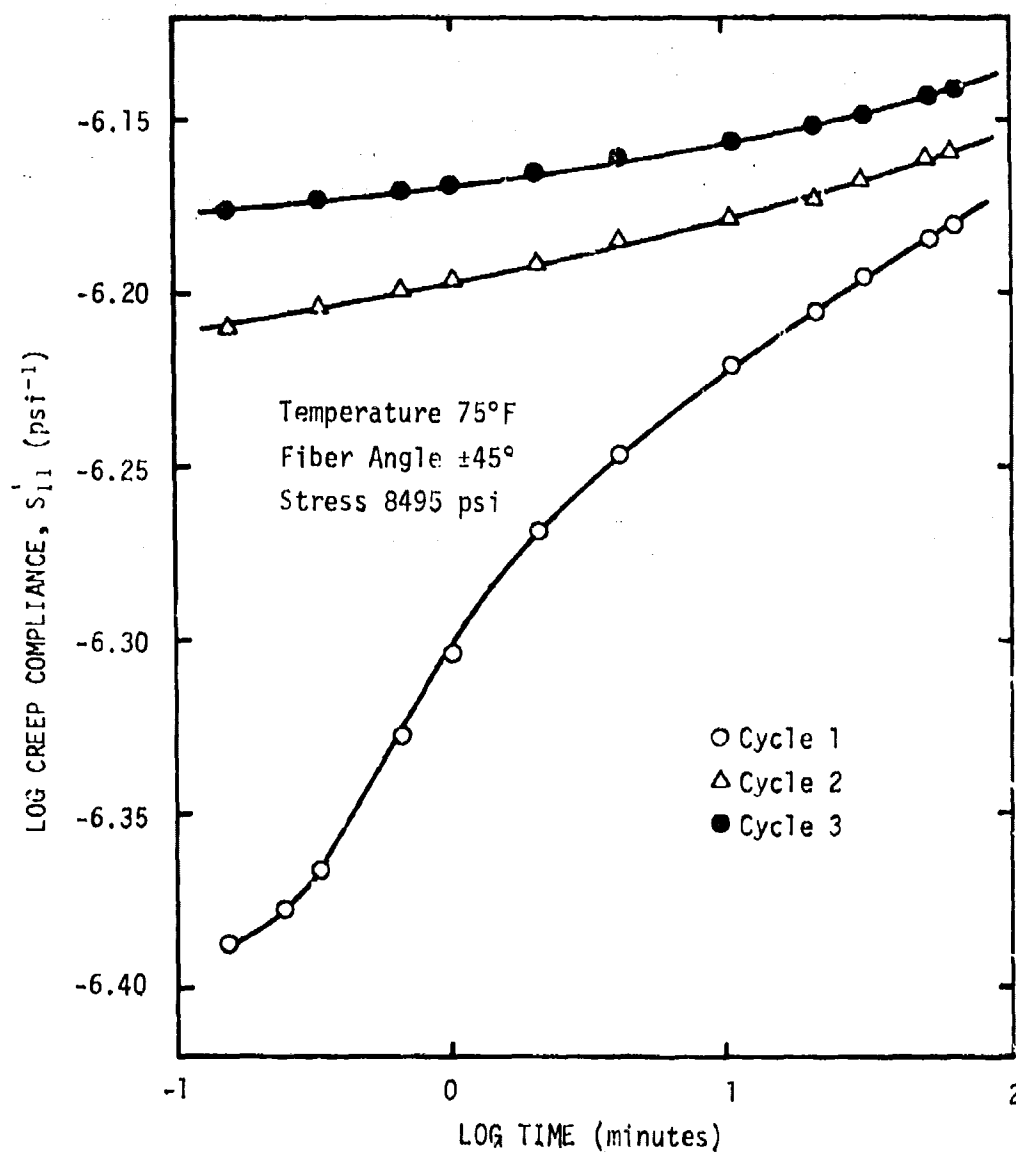


Figure 93. Effect of multiple loading on creep compliance of the glass/epoxy laminated composite ( $\theta = \pm 45^\circ$ ,  $T = 75^\circ\text{F}$ ,  $\sigma = 8495$  psi).

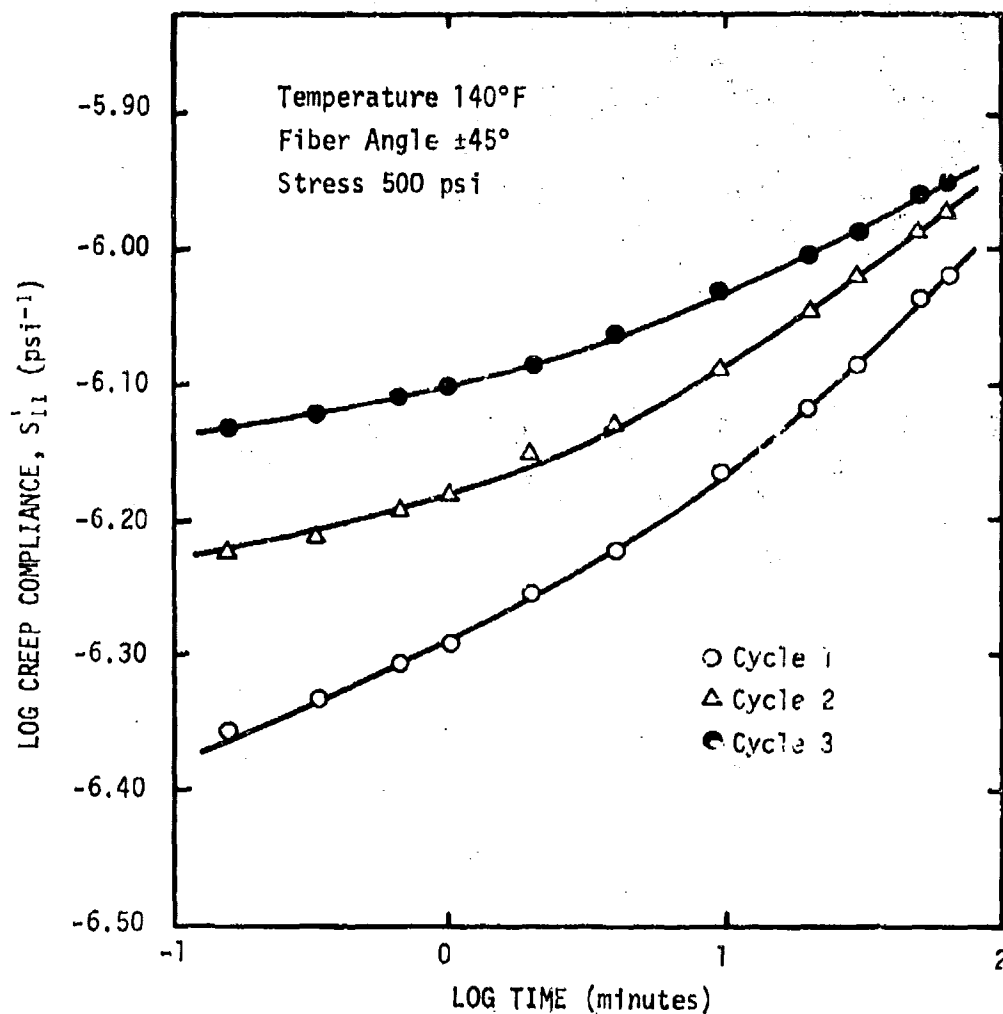


Figure 94. Effect of multiple loading on creep compliance of the glass/epoxy laminated composite ( $\theta = \pm 45^\circ$ ,  $T = 140^\circ\text{F}$ ,  $\sigma = 500$  psi).



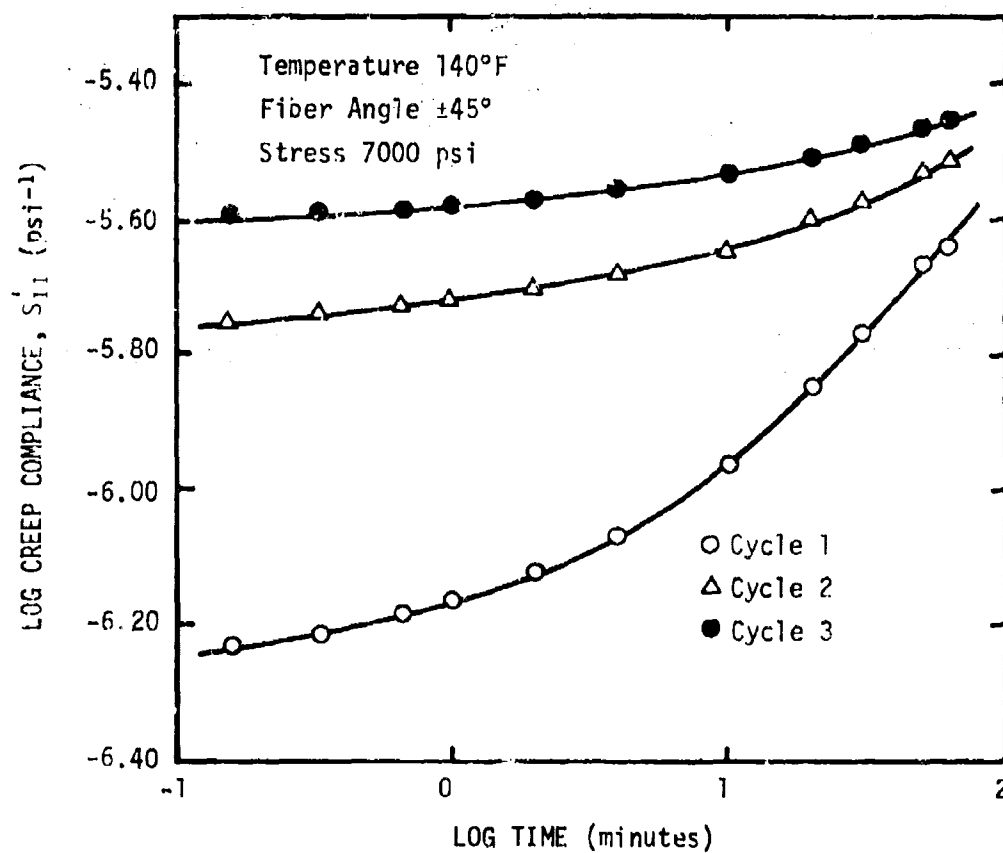


Figure 95. Effect of multiple loading on creep compliance of the glass/epoxy laminated composite ( $\theta = \pm 45^\circ$ ,  $T = 140^\circ\text{F}$ ,  $\sigma = 7000$  psi).

occurring between the first and second cycle. The initial compliance, when plotted as a function of the loading cycle, appears to asymptotically level off after a number of cycles. At the high stress levels three cycles does not represent an equilibrium. Even at moderately low levels it appears that three cycles are not enough to generate data from which one can truly measure the effects of stress level in the absence of crack growth.

Also evident is the change in the net creep compliance with each cycle. During the first cycle a considerable amount of crack propagation and possible fiber realignment occurs. The latter is believed to occur more predominantly at the elevated temperatures where the matrix viscosity is considerably reduced and fiber rearrangement is feasible. All of the 75°F tests obeyed a power law with  $n = 0.19$  regardless of fiber angle or stress level for all loading cycles. However, the value of the creep coefficient generally decreased very rapidly from the first cycle. The creep coefficient for the second cycle was usually about 50-80% of the value during the first cycle, depending on the stress level. At 140°F the glass/epoxy obeyed a power law in time where the exponent  $n$  varied from cycle to cycle. The value of  $n$  for tests at the highest stress level sometimes reached as high as  $n = 0.59$ . As an example of this behavior, the creep compliances determined by analytically fitting the data to a power law of the form in Equation (135) are shown in Table 13 for several fiber angles and

Table 13. Creep Compliances for S-901 Glass/-  
Shell 58-68R Epoxy Composite at 140°F

Fiber Angle ( $\theta$ )	Stress (psi)	Cycle	Creep Compliance, $S_{11}$ ( $\times 10^{-6}$ psi $^{-1}$ )
20	4800	1	.2185 + .0097t <sup>.41</sup>
		2	.2406 + .0105t <sup>.39</sup>
		3	.2531 + .0123t <sup>.35</sup>
20	8501	1	.2633 + .0582t <sup>.59</sup>
		2	.7196 + .0944t <sup>.47</sup>
20	10,501	1	.2642 + .0555t <sup>.59</sup>
		2	.7422 + .0873t <sup>.45</sup>
45	3000	1	.4102 + .1077t <sup>.41</sup>
		2	.6947 + .0879t <sup>.35</sup>
45	5000	1	.4419 + .0221t <sup>.53</sup>
		2	.4997 + .0602t <sup>.27</sup>
		3	.5349 + .0722t <sup>.23</sup>
45	6501	1	.5264 + .1441t <sup>.57</sup>
90	1480	1	.4357 + .0498t <sup>.45</sup>
		2	.5318 + .0649t <sup>.35</sup>

stress levels.

It can be seen that  $n$  decreases rapidly with each succeeding cycle, with the creep coefficient generally increasing. The overall result is a decrease in the net creep compliance with each subsequent cycle. Given enough loading cycles the crack growth should stabilize such that one could measure the effects of stress

and temperature alone as did Lou and Schapery [9]. It was noted in their work that as many as ten cycles were necessary to get repeatable results, i.e., the same strain output under the same load for every creep test thereafter.

Lou and Schapery [9] were able to express their data in terms of Equation (68) and a normalized octahedral shear stress given by

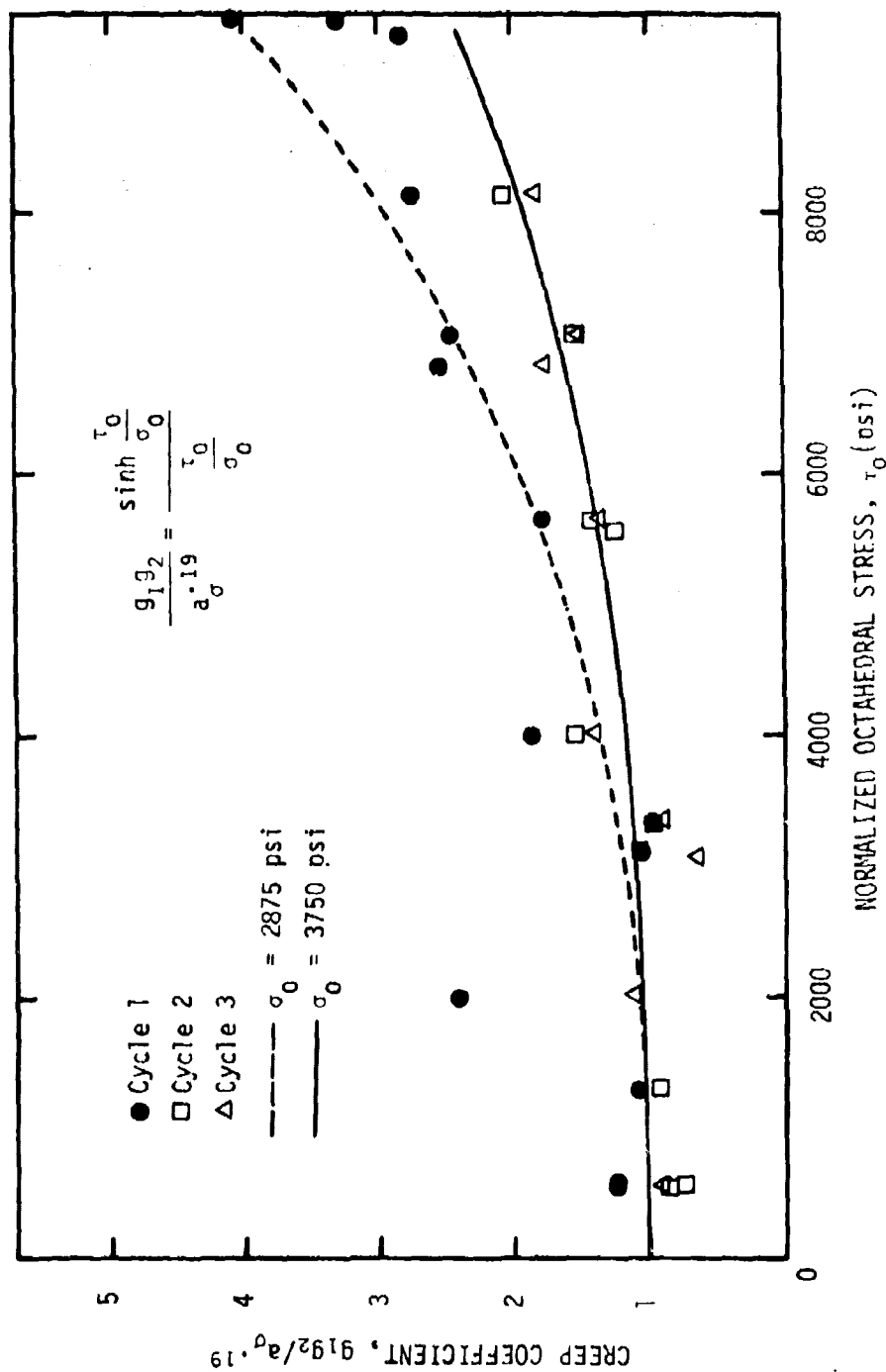
$$\tau_o = \sigma \sin\theta[\gamma - (\gamma-1)\sin^2\theta]^{1/2} \quad (138)$$

where  $\sigma$  is the applied stress,  $\theta$  the fiber angle, and  $\gamma$  is defined in terms of the effective matrix Poisson's ratio,  $\nu_e$ ,

$$\gamma = \frac{3}{1 - \nu_e + \nu_e^2} \quad (139)$$

The nonlinear initial compliance,  $S'_{11}(0)$ , in [9] was written in terms of the linear viscoelastic creep compliance and a scalar factor,  $g_o$ , as defined in Equation (68). In a similar manner the creep coefficient was also defined using the linear viscoelastic creep coefficient and the scalar factor  $(g_1 g_2 / a_\sigma^n)$ . The latter factor was found to roughly follow a hyperbolic sine function as in Equation (72b) with  $\sigma = \tau_o$  and  $\sigma_m = \sigma_o$  (Figure 96).

An attempt was made to model the early loading cycles using this approach; however, Figures 97 and 98 show that  $g_o$  is a strong function of fiber angle and  $\tau_o$  does not collapse the curves into a single, invariant function for either test temperature. The creep

Figure 96. Multiple loading effects on creep coefficient ( $T = 75^{\circ}\text{F}$ ).

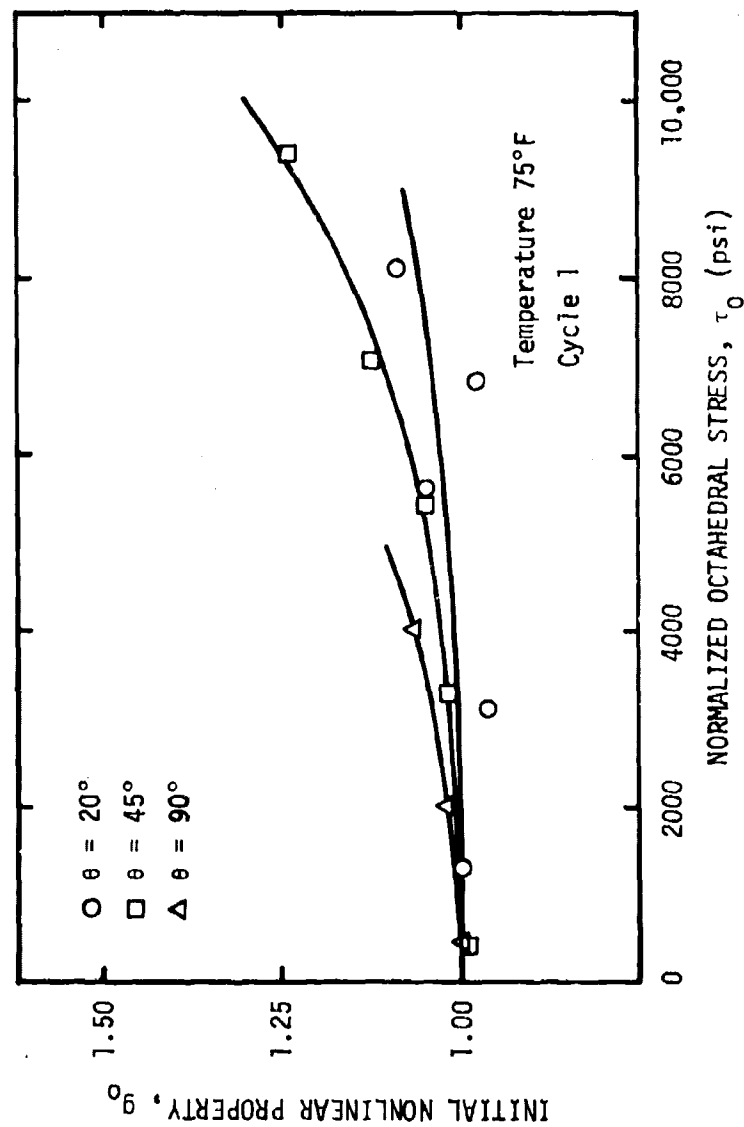


Figure 97. Initial nonlinear property,  $g_0$ , compared to the normalized octahedral stress,  $\tau_0$  ( $T = 75^\circ\text{F}$ ).

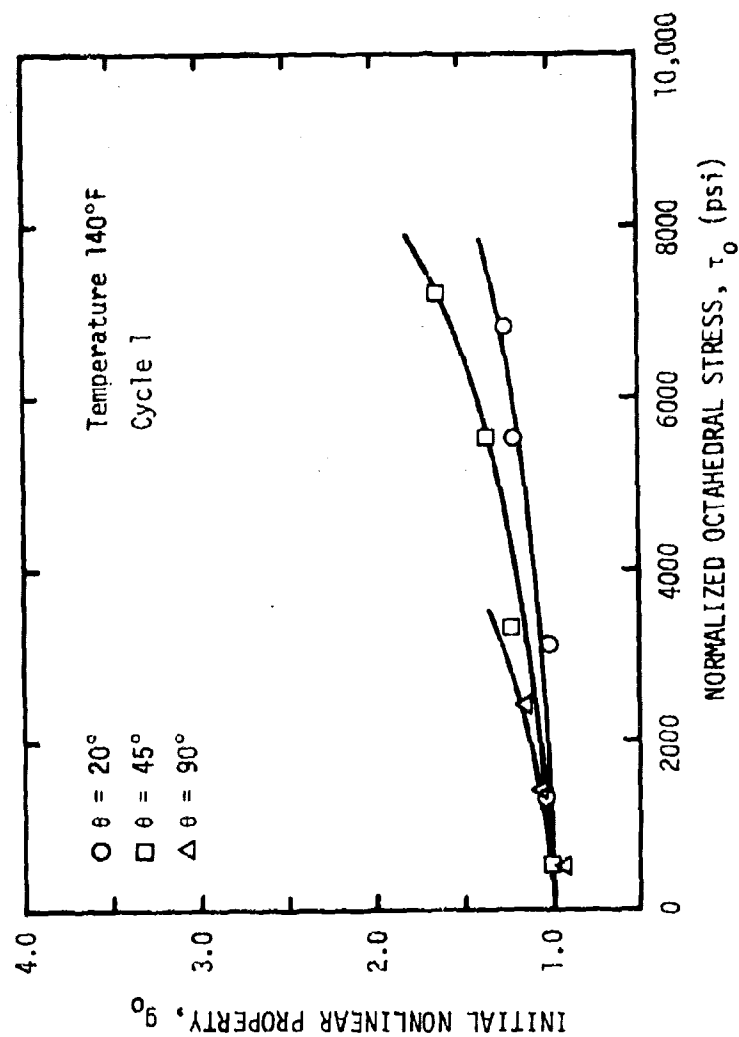


Figure 98. Initial nonlinear property,  $g_0$ , compared to the normalized octahedral stress,  $\tau_o$  ( $T = 140^\circ\text{F}$ ).

coefficient appears to fit the hyperbolic sine function fairly well. Unfortunately, several points, especially for  $\theta = 90^\circ$ , are not very close to the analytical function. The creep coefficient appears to depend primarily on the shear stress,  $\tau$ , existing parallel to the fibers (see Figure 99). As might be expected, this arises from the matrix contribution. However, this does not explain the  $\theta = 90^\circ$  behavior where the shear stress is zero. The initial creep compliance appears to be controlled primarily by the stress normal to the fibers through the nonlinear parameter,  $g_0$ , as shown in Figures 100 through 105. The behavior of the two high stress level points for the  $20^\circ$  fiber angle shown in Figures 104 and 105 is not understood at this time. We shall point out later how these curves may be used as correction factors in the actual motor case analysis.

The effect of multiple cycling on the creep compliance of the case material for the  $\pm 70^\circ$  fiber angle is shown in Figures 106 and 107 for two stress levels. Remember that these materials have already been stressed to a high level during the actual motor hydro-testing. As a result, the creep compliances for both stress levels are considerably higher than would be predicted by linear viscoelastic analysis. However, the trends from cycle to cycle as well as stress level follow the same pattern established for the tensile coupons cut from the plates. The net creep compliances are shown in Figures 108 and 109 and are found to obey the power law



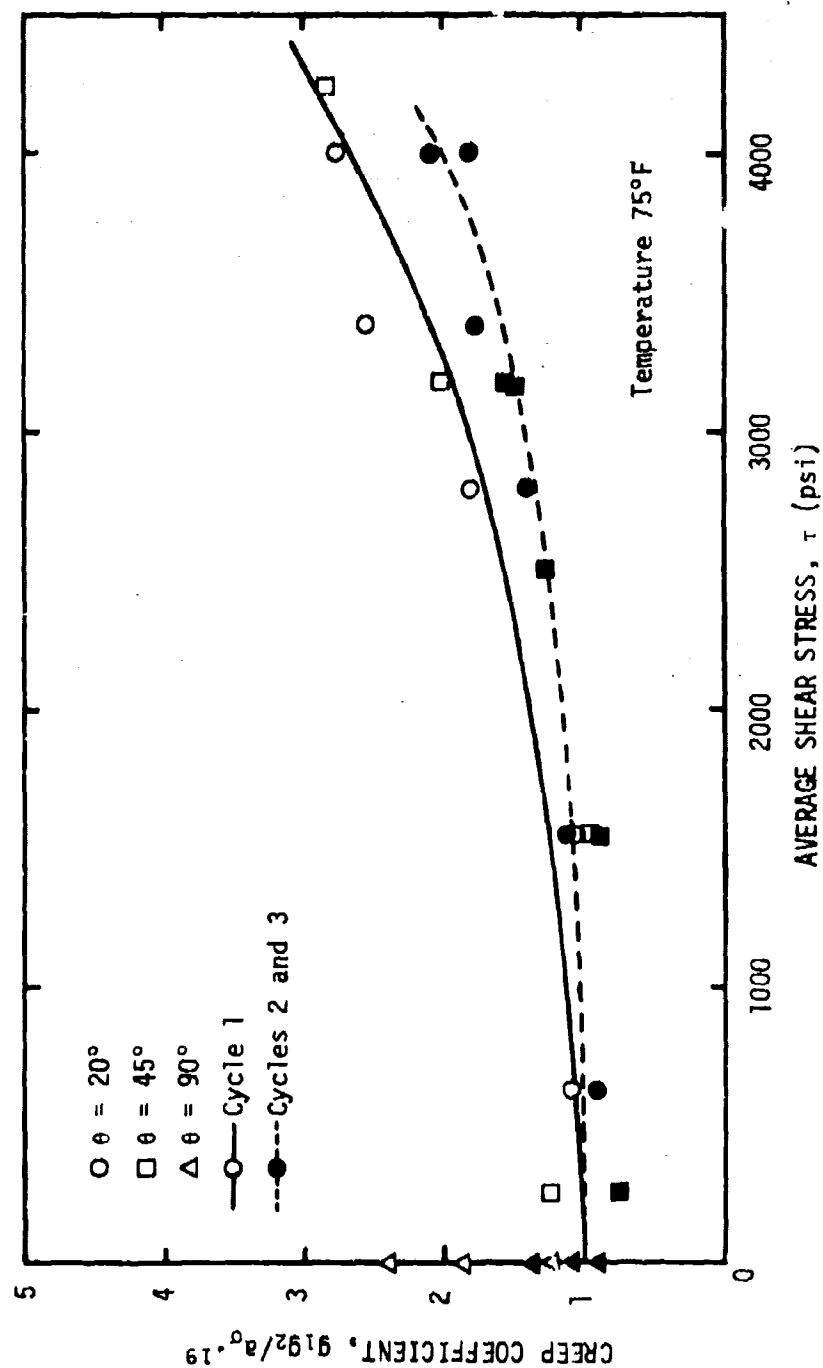


Figure 99. Multiple loading effects on creep coefficient showing dependence on the average shear stress,  $\tau$  ( $T = 75^\circ\text{F}$ ).

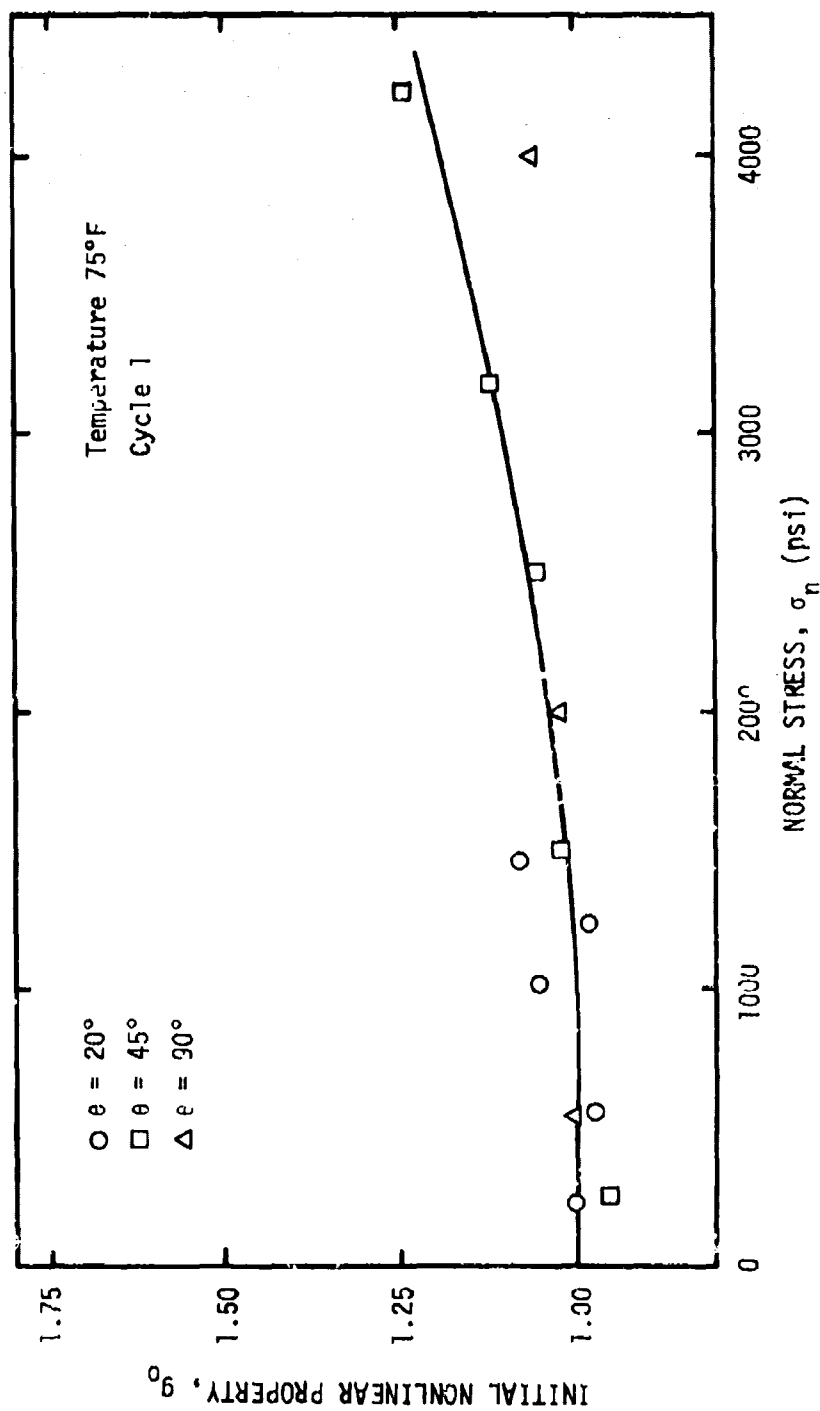


Figure 100. Initial nonlinear property,  $g_0$ , as a function of the stress normal to the fibers ( $\tau = 75^\circ\text{F}$ , Cycle 1).

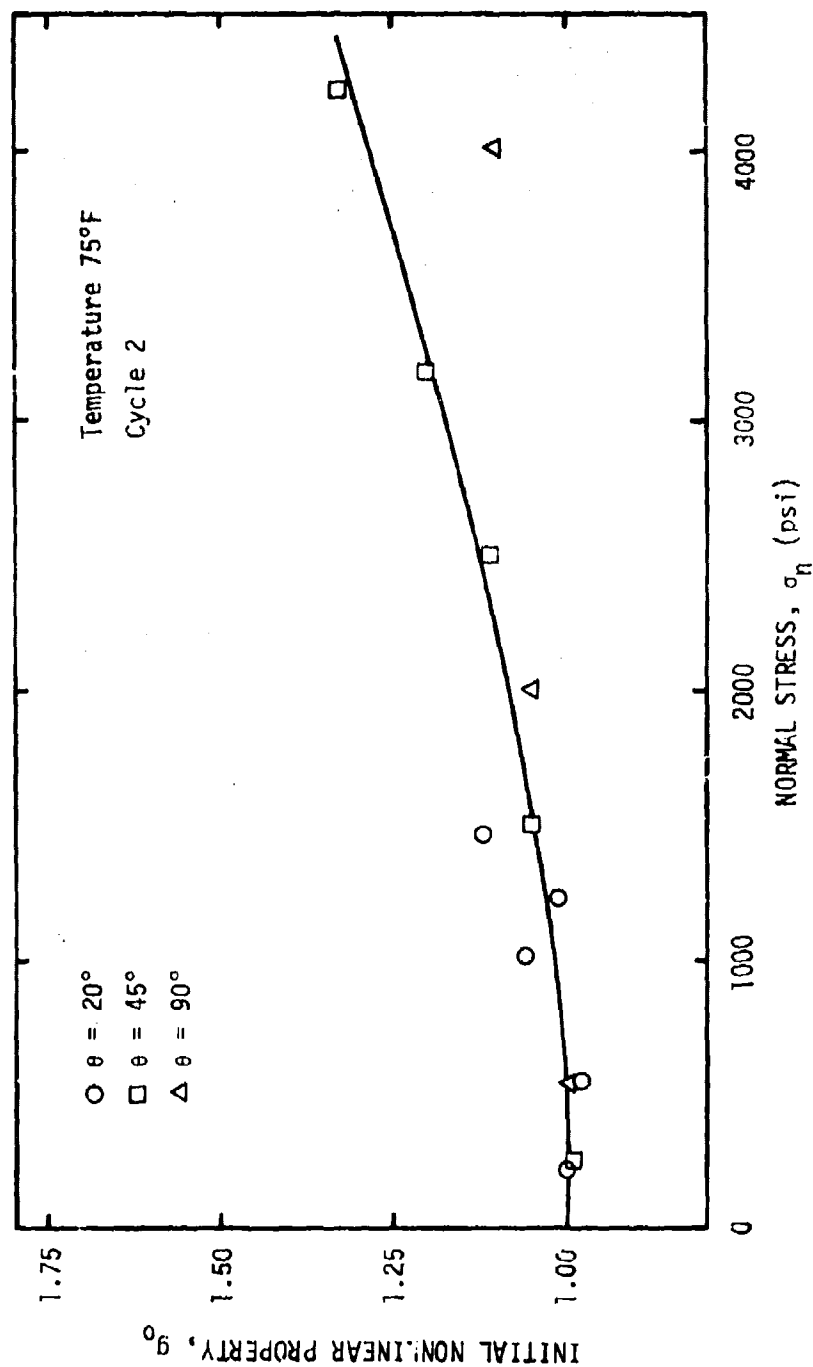


Figure 101. Initial nonlinear property,  $g_0$ , as a function of the stress normal to the fibers ( $T = 75^\circ\text{F}$ , Cycle 2).

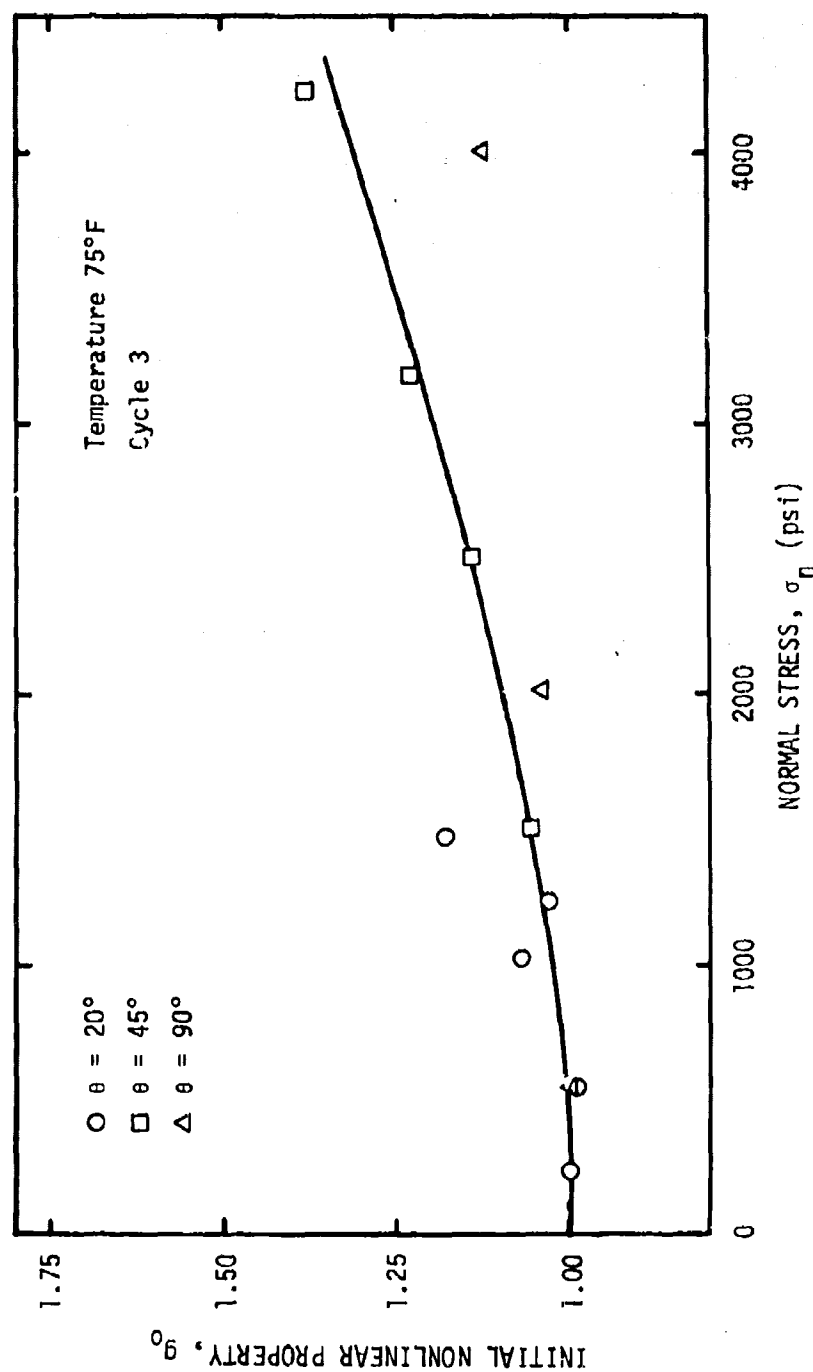


Figure 102. Initial nonlinear property,  $g_0$ , as a function of the stress normal to the fibers ( $T = 75^\circ\text{F}$ , Cycle 3).

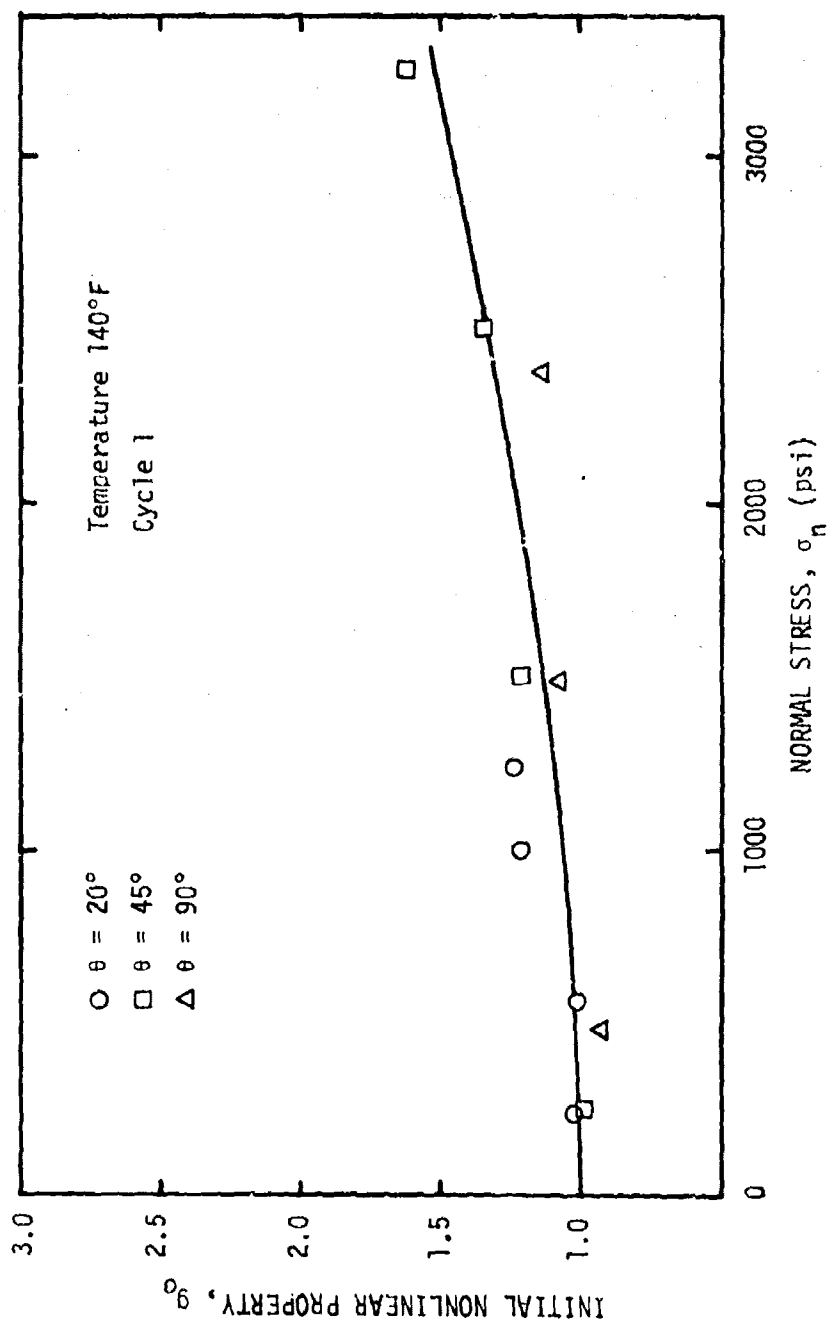


Figure 103. Initial nonlinear property,  $g_0$ , as a function of the stress normal to the fibers ( $T = 140^\circ\text{F}$ , Cycle 1).

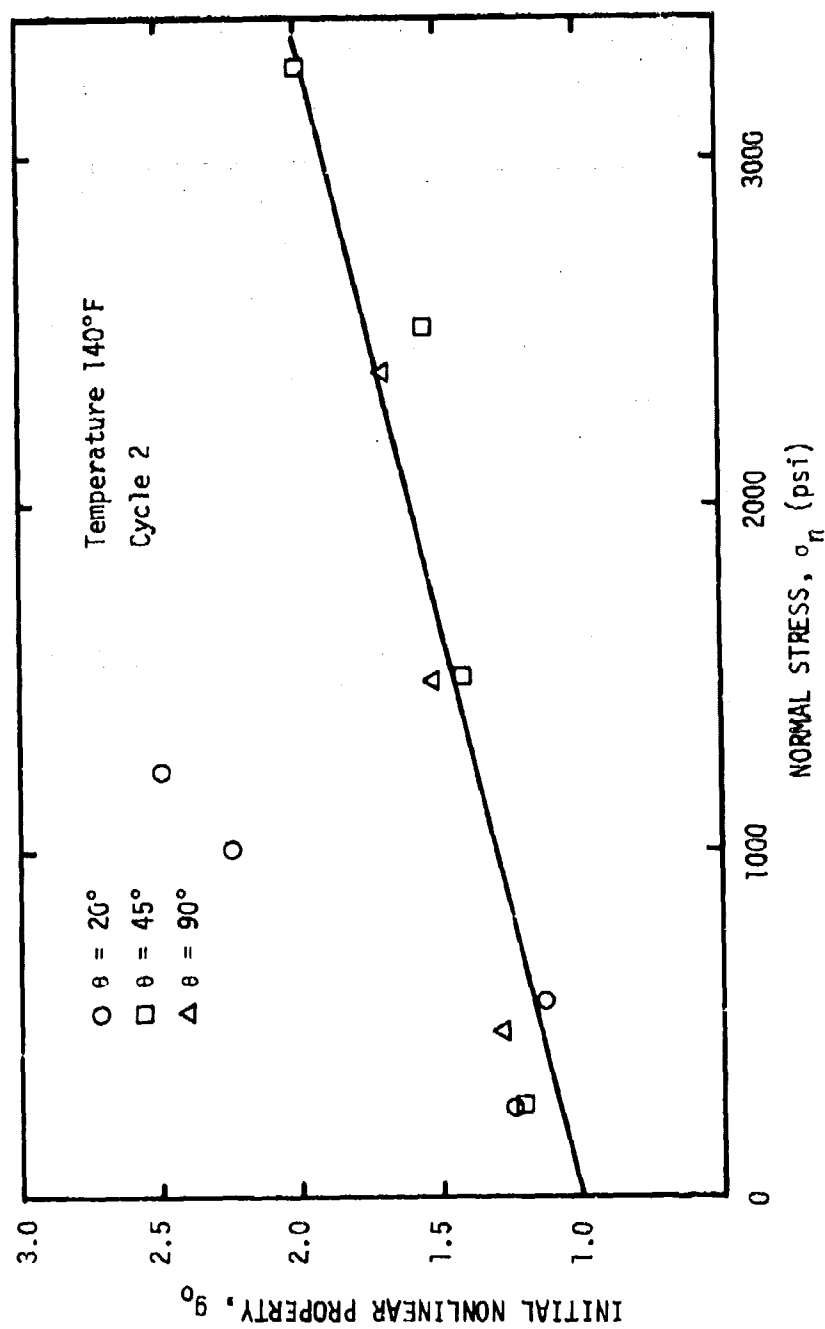


Figure 104. Initial nonlinear property,  $g_0$ , as a function of the stress normal to the fibers ( $T = 140^\circ\text{F}$ , Cycle 2).

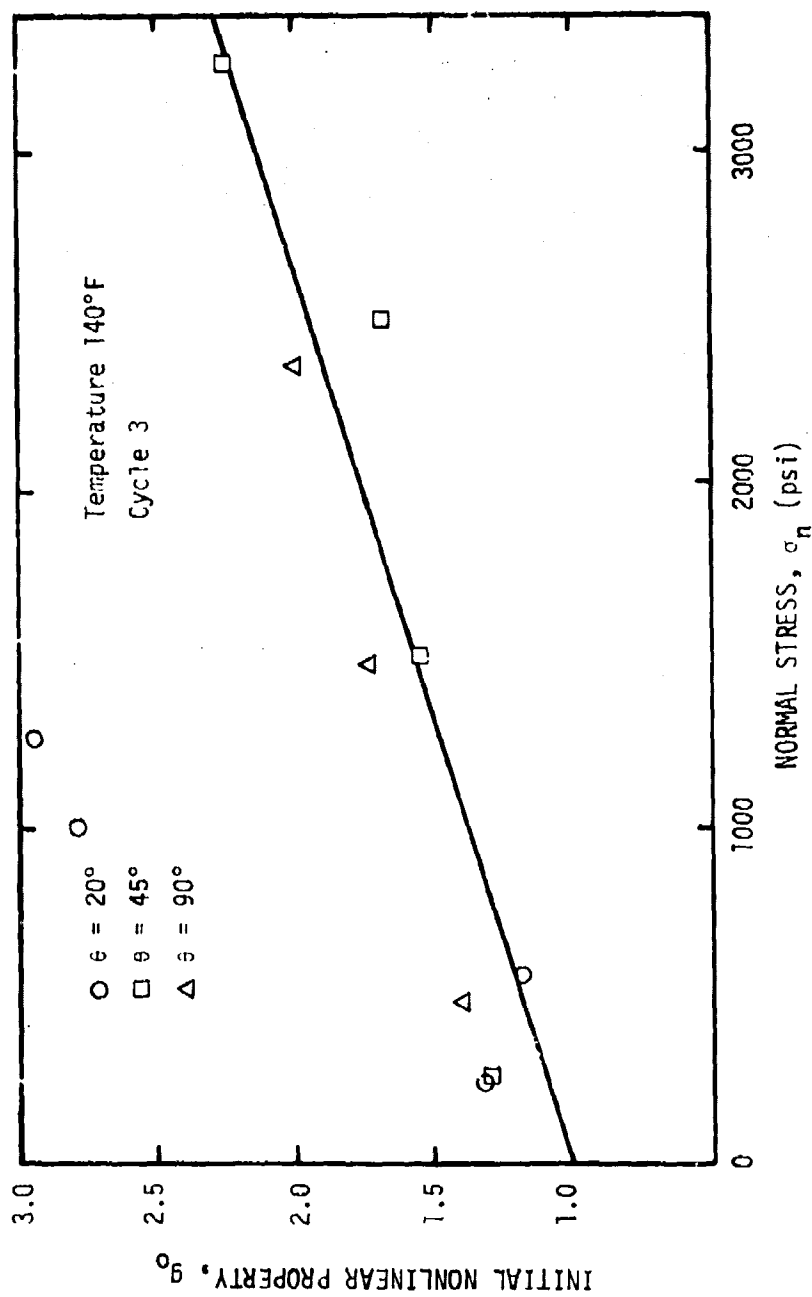


Figure 105. Initial nonlinear property,  $g_0$ , as a function of the stress normal to the fibers ( $T = 140^\circ\text{F}$ , Cycle 3).

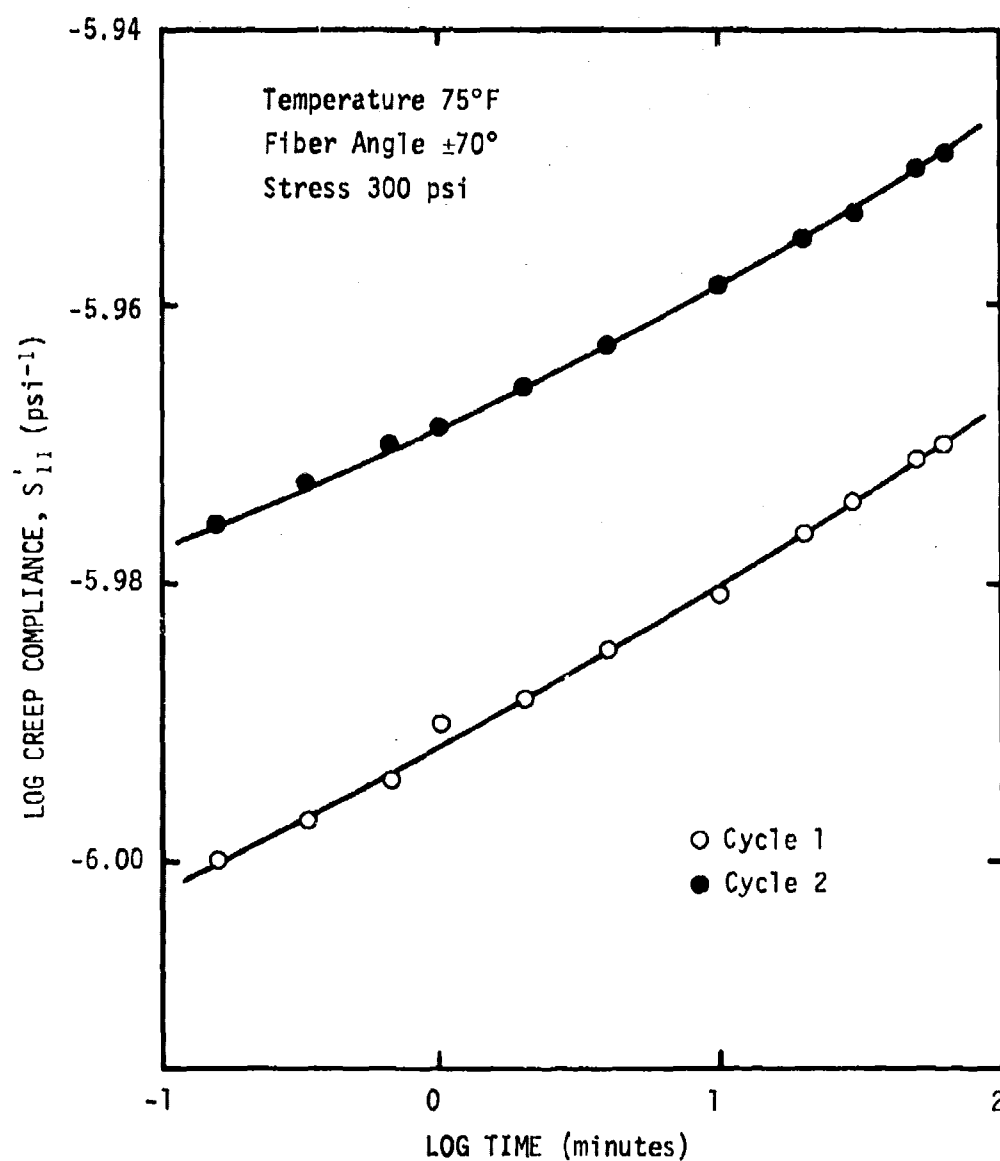


Figure 106. Effect of multiple loading on the creep compliance of the case material ( $\epsilon = \pm 70^\circ$ ,  $T = 75^\circ\text{F}$ ,  $\sigma = 300 \text{ psi}$ ).



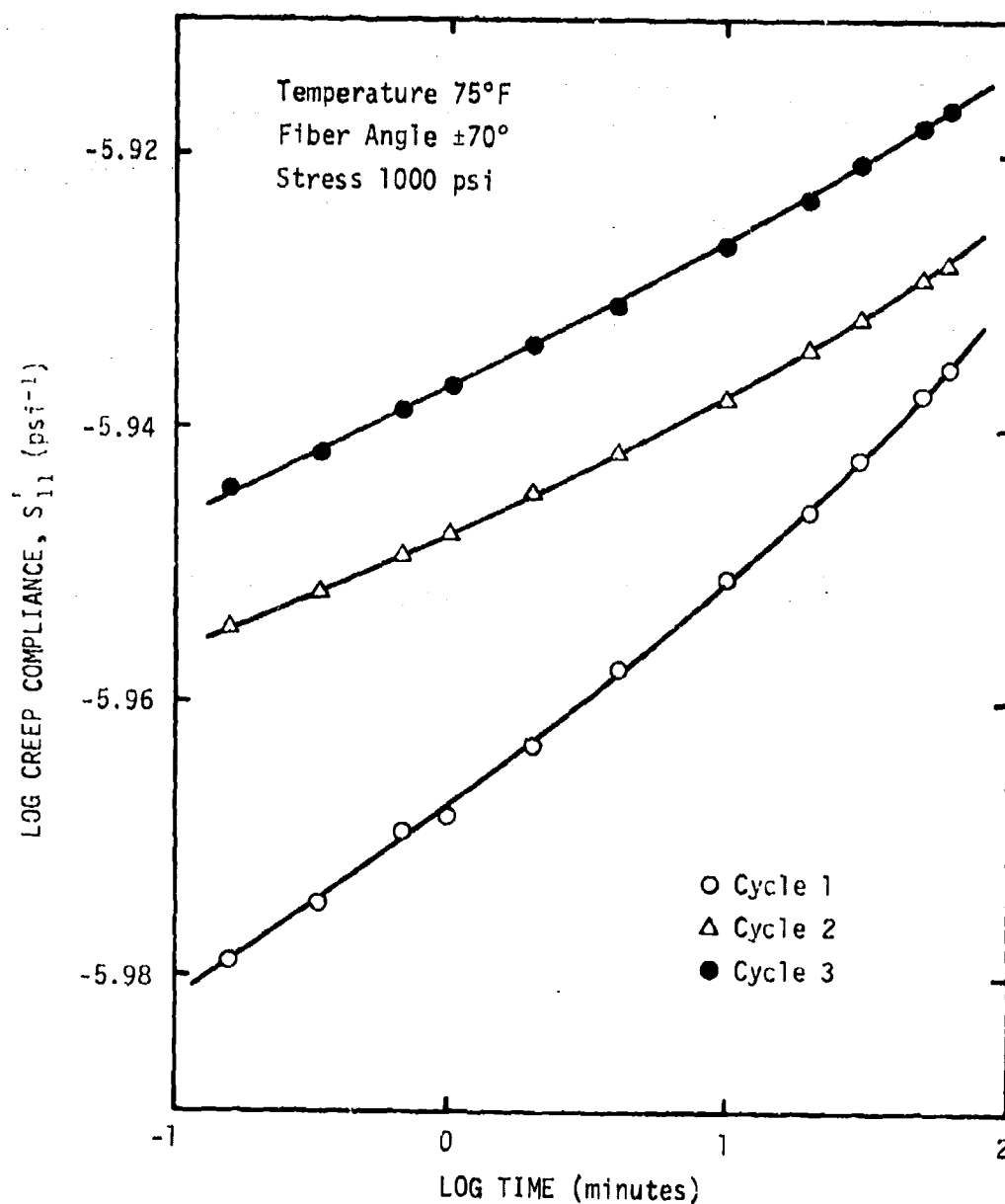


Figure 107. Effect of multiple loading on the creep compliance of the case material ( $\theta = \pm 70^\circ$ ,  $T = 75^\circ\text{F}$ ,  $\sigma = 1000$  psi).

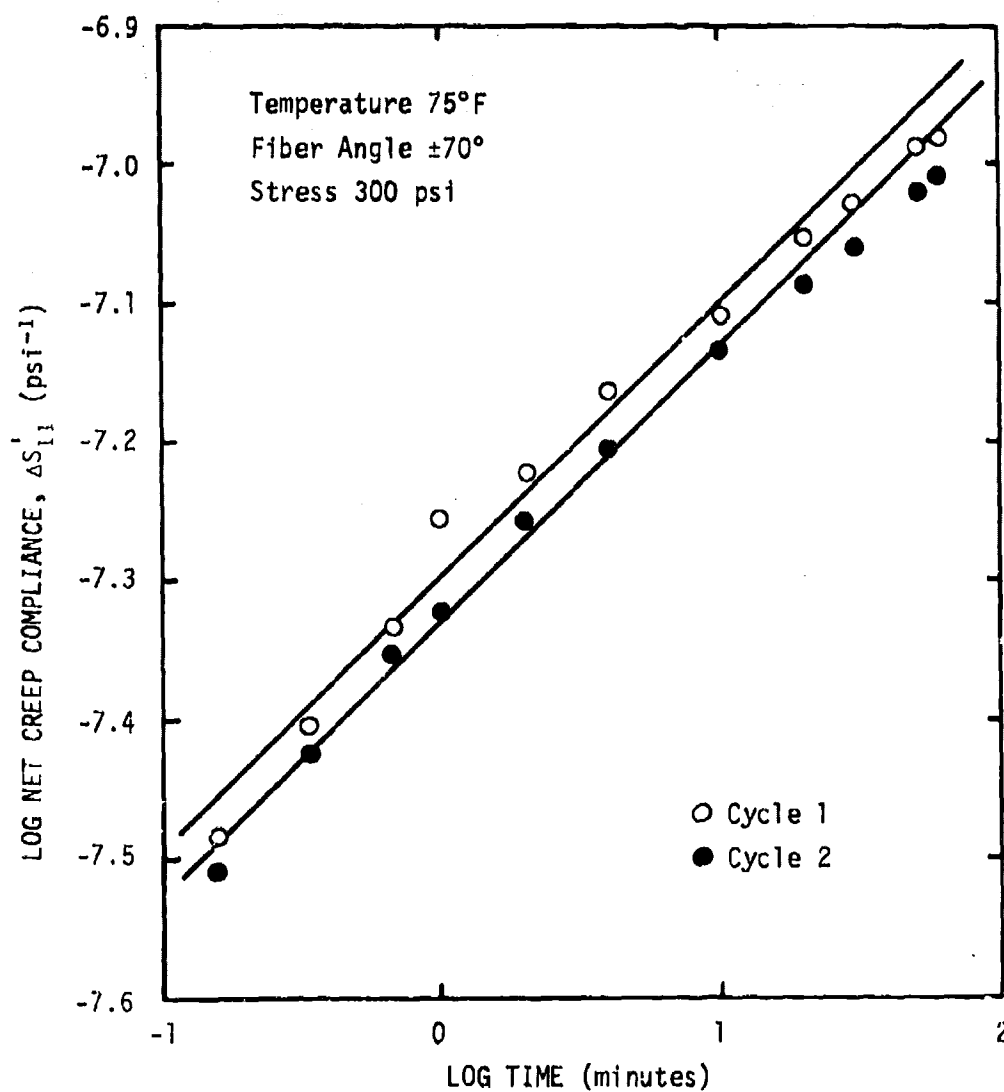


Figure 108. Net creep compliance for case material subjected to multiple loading ( $\theta = \pm 70^\circ$ ,  $T = 75^\circ\text{F}$ ,  $\sigma = 300$  psi).

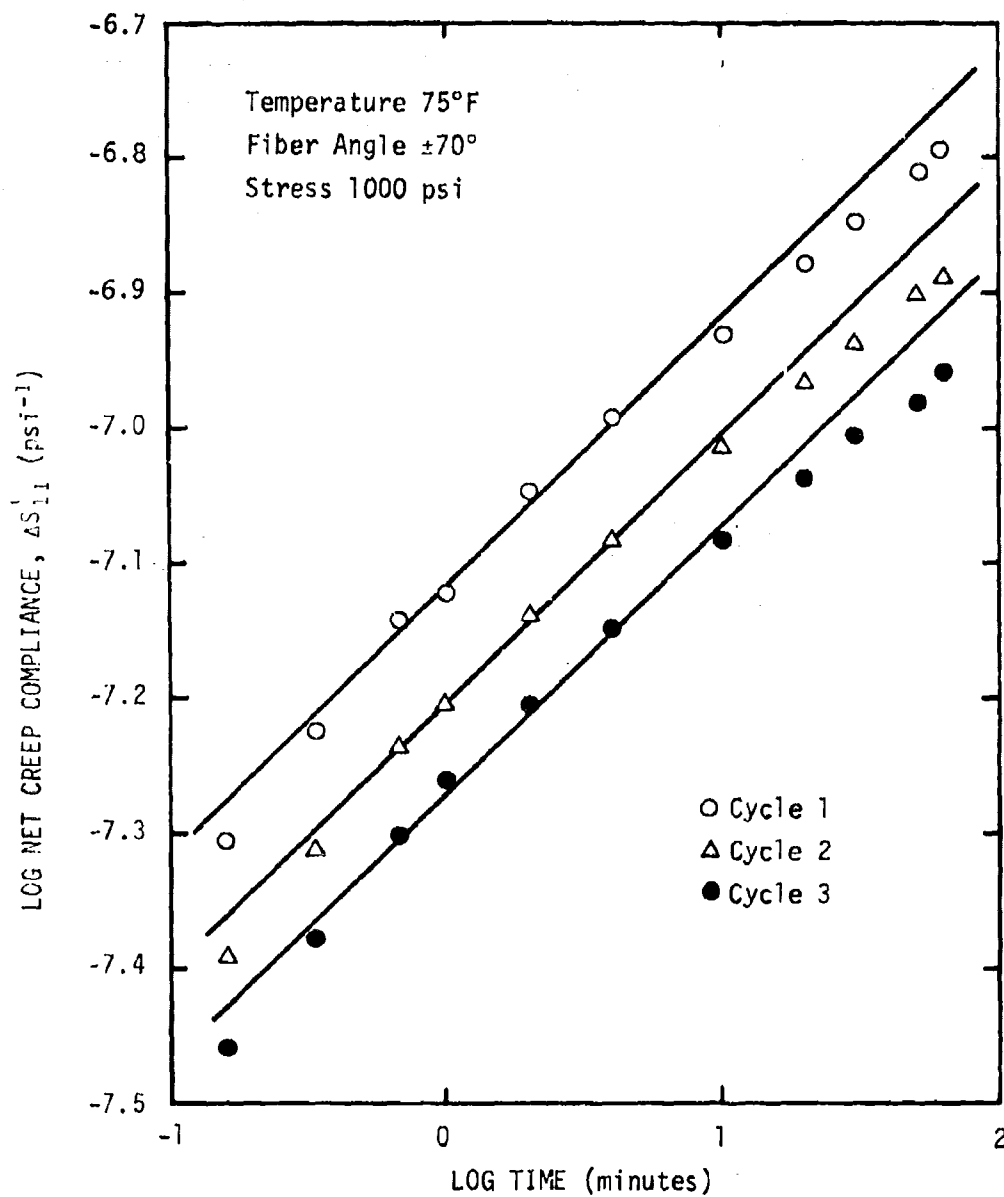


Figure 109. Net creep compliance for case material subjected to multiple loading ( $\theta = \pm 70^\circ$ ,  $T = 75^\circ\text{F}$ ,  $\sigma = 1000$  psi).

with  $n = 0.19$ . The data from the plate material, therefore, yields comparable results to that seen in the filament wound motor case materials.

#### Lamina Angular Dependence and Principal Creep Compliances

The angular dependence of the compliances are given by Equation (89a). The uniaxial compliance,  $S'_{11}(\theta)$ , may be expressed in terms of the two principal compliances  $S_{11}$  and  $S_{22}$  and the uniaxial compliance  $S'_{11}(\theta_1)$  where  $\theta_1 \neq \theta$ . By eliminating the term containing  $S_{66}$  and solving for  $S'_{11}(\theta)$  we find that

$$S'_{11}(\theta) = \frac{\ell^2 m^2}{\ell_1^2 m_1^2} S'_{11}(\theta_1) + \left[ \ell^4 - \frac{\ell^2 m^2 \ell_1^2}{m_1^2} \right] S_{11} + \left[ m^4 - \frac{\ell^2 m^2 m_1^2}{\ell_1^2} \right] S_{22} \quad (140)$$

where

$$\ell = \cos \theta \quad m = -\sin \theta \quad (141)$$

$$\ell_1 = \cos \theta_1 \quad m_1 = -\sin \theta_1$$

and

$$S_{11} = S_{0^\circ} \quad (142a)$$

$$S_{22} = S_{90^\circ} \quad (142b)$$

Therefore, in order to predict the angular dependence of the creep compliance from experimental data, one only needs experimental compliances for  $S_{0^\circ}$ ,  $S_{90^\circ}$  and one more angle, say  $S'_{11}(\theta)$ . For the present analysis the measured compliance  $S_{45^\circ}$  was used to predict the other compliances. For this special case Equation (140) with  $\theta_1 = 45^\circ$  becomes

$$S'_{11}(\theta) = 4\ell^2m^2S_{45^\circ} + (\ell^4 - \ell^2m^2)S_{0^\circ} + (m^4 - \ell^2m^2)S_{90^\circ} \quad (143)$$

The initial compliance and the one-hour creep compliance have been calculated from Equation (143) for different fiber angles for the three test temperatures and are shown in Figures 110 through 112. The values for  $S_{0^\circ}$ ,  $S_{90^\circ}$  and  $S_{45^\circ}$  were taken from the linear viscoelastic creep compliances shown in Table 12. The experimentally determined compliances for the last cycle of the low stress level tests are shown on the figures for both the unidirectional and angle-ply glass/epoxy composites. The predictions agree reasonably well with the experimental points at 20°F and 75°F. The one-hour curves for the 20°F and 140°F predictions were also derived by applying the  $a_T$  factor from the epoxy data to the 75°F creep coefficient in the  $S_{45^\circ}$  and  $S_{90^\circ}$  compliances. The 20°F prediction was essentially the same; however, the 140°F indicates what appears to be considerable crack growth nonlinearity. It should also be realized that a value of  $n = 0.19$  was used for the predictions and it was noted earlier that  $n > 0.19$  for most of the 140°F data as a

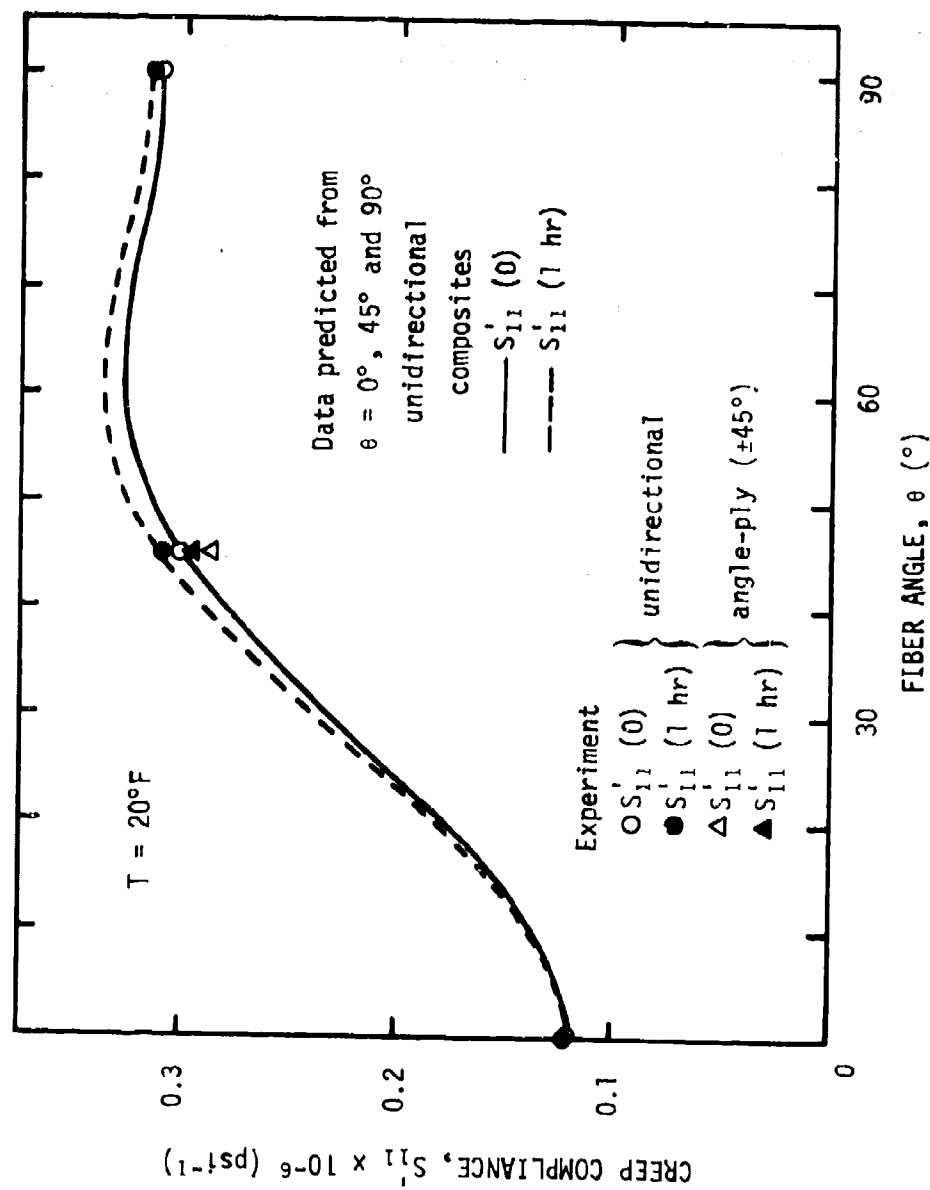


Figure 110. Angular dependence of the linear viscoelastic creep compliance,  $S'_{11}$  ( $T = 20^{\circ}\text{F}$ ).

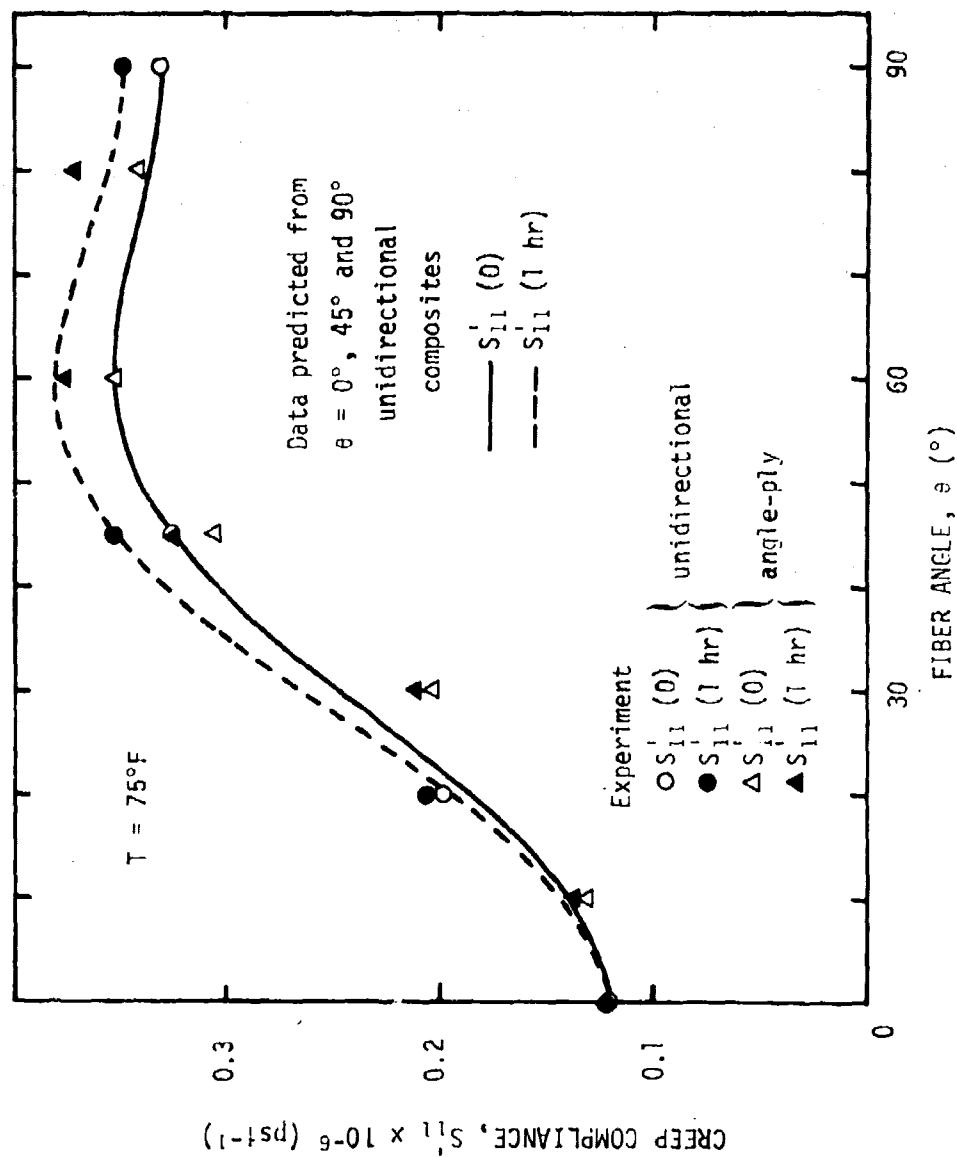


Figure 111. Angular dependence of the linear viscoelastic creep compliance,  $S'_{11}$  ( $T = 75^\circ\text{F}$ ).

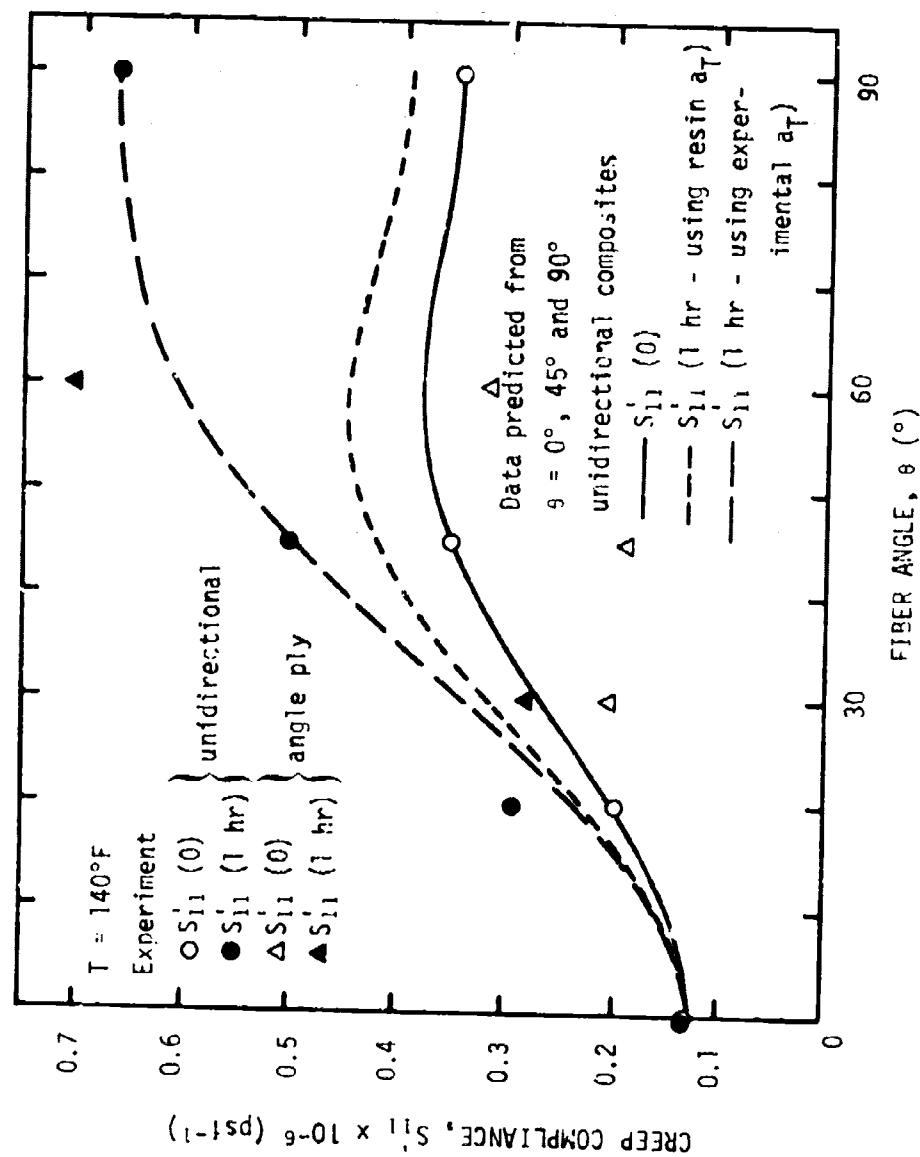


Figure 112. Angular dependence of the linear viscoelastic creep compliance,  $S'_{11}$  ( $T = 140^\circ\text{F}$ ).



result of the apparent crack growth. In the absence of the crack growth, it appears that the power law representation adequately predicts the creep compliances.

The principal creep compliances, necessary for the complete definition of the fibrous composite under conditions of plane stress, are given by Equation (86a) for a transversely isotropic material. They are  $S_{11}$ ,  $S_{22}$ ,  $S_{12}$  and  $S_{66}$ . The values of  $S_{11}$  and  $S_{22}$ , which are the compliances for  $\theta = 0^\circ$  and  $\theta = 90^\circ$ , respectively, have already been given in Table 12 for the linear viscoelastic region. The principal creep compliance  $S_{12}$  is given by Equation (83a)

$$S_{12} = \frac{-\nu_{12}}{E_{11}} = \frac{-\nu_{21}}{E_{22}} \quad (83a)$$

which may be rewritten as

$$S_{12} = -\nu_{12}S_{11} = -\nu_{21}S_{22} \quad (144)$$

Both relationships assume that the compliance matrix is symmetric, i.e.,  $S_{12} = S_{21}$ . Experimentally,  $S_{12}$  may be found from the transverse strain,  $\epsilon_y$ , measured during a creep test on a specimen with  $\theta = 0^\circ$  under an axial stress,  $\sigma_x$ ,

$$S_{12} = -\left(-\frac{\epsilon_y}{\epsilon_x}\right)\left(\frac{\sigma_x}{\sigma_x}\right) = \frac{\epsilon_y}{\sigma_x} \quad (145)$$

The experimental values were found to be independent of time and

are given in Table 14 along with the values of  $\nu_{12}$  and  $\nu_{21}$  measured during the creep of a  $0^\circ$  and  $90^\circ$  sample, respectively.

Table 14. Measured Properties  $S_{12}$ ,  $\nu_{12}$  and  $\nu_{21}$  for S-901 Glass/Shell 58-60R Epoxy

Temperature (°F)	$S_{12}$ ( $\times 10^{-6}$ )(psi $^{-1}$ )	$\nu_{12}$	$\nu_{21}$
20	-.0329	.272	.151
75	-.0330	.273	.096
140	-.0359	.283	.051

The values of  $S_{12}$  and  $\nu_{12}$  are reasonable; however, the values of  $\nu_{21}$ , when used with the  $S_{22}$  compliance in Equation (144) give values of  $S_{21}$  which differ significantly from  $S_{12}$ . It is felt that most of the error is due to the small transverse strain associated with  $\nu_{21}$  measurements and possibly microstructural damage at the  $140^\circ\text{F}$  temperature. The average value of  $S_{21}$  over the temperature range is within 15% of the  $S_{12}$  values. All subsequent analysis assumed that  $S_{12} = S_{21}$  and the values of  $S_{12}$  given in Table 14 were used.

The last principal compliance,  $S_{66}$ , can be calculated from the transformation relation, Equation (89a), from the known values of  $S_{11}$ ,  $S_{22}$ ,  $S_{12}$  and the compliance from one other angle,  $S'_{11}(\theta)$ . Using the  $45^\circ$  creep compliance,  $S_{45^\circ}$ , yields the following relationship,

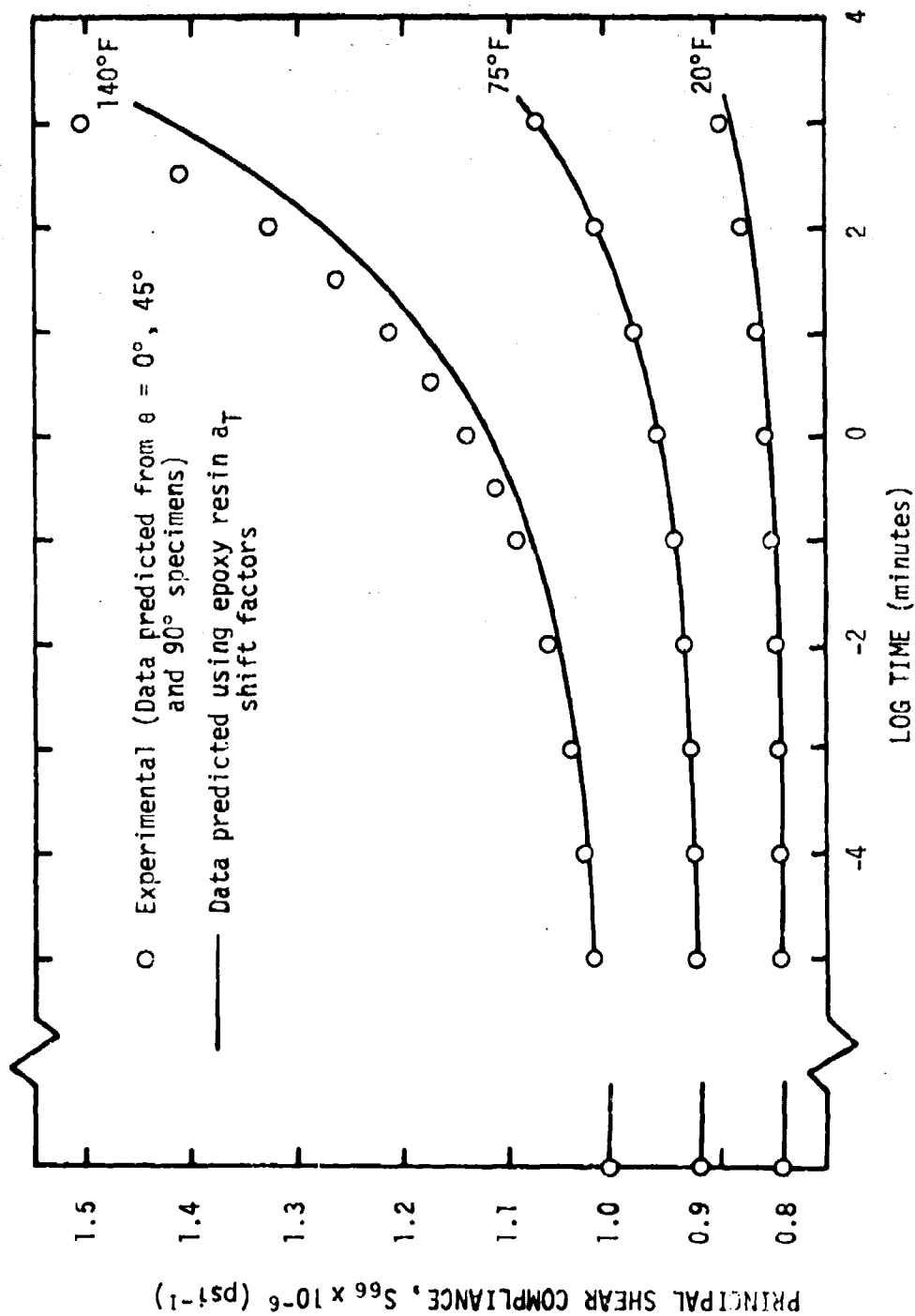
$$S_{66} = 4S_{45^\circ} - 2S_{12} - S_{11} - S_{22} \quad (146)$$

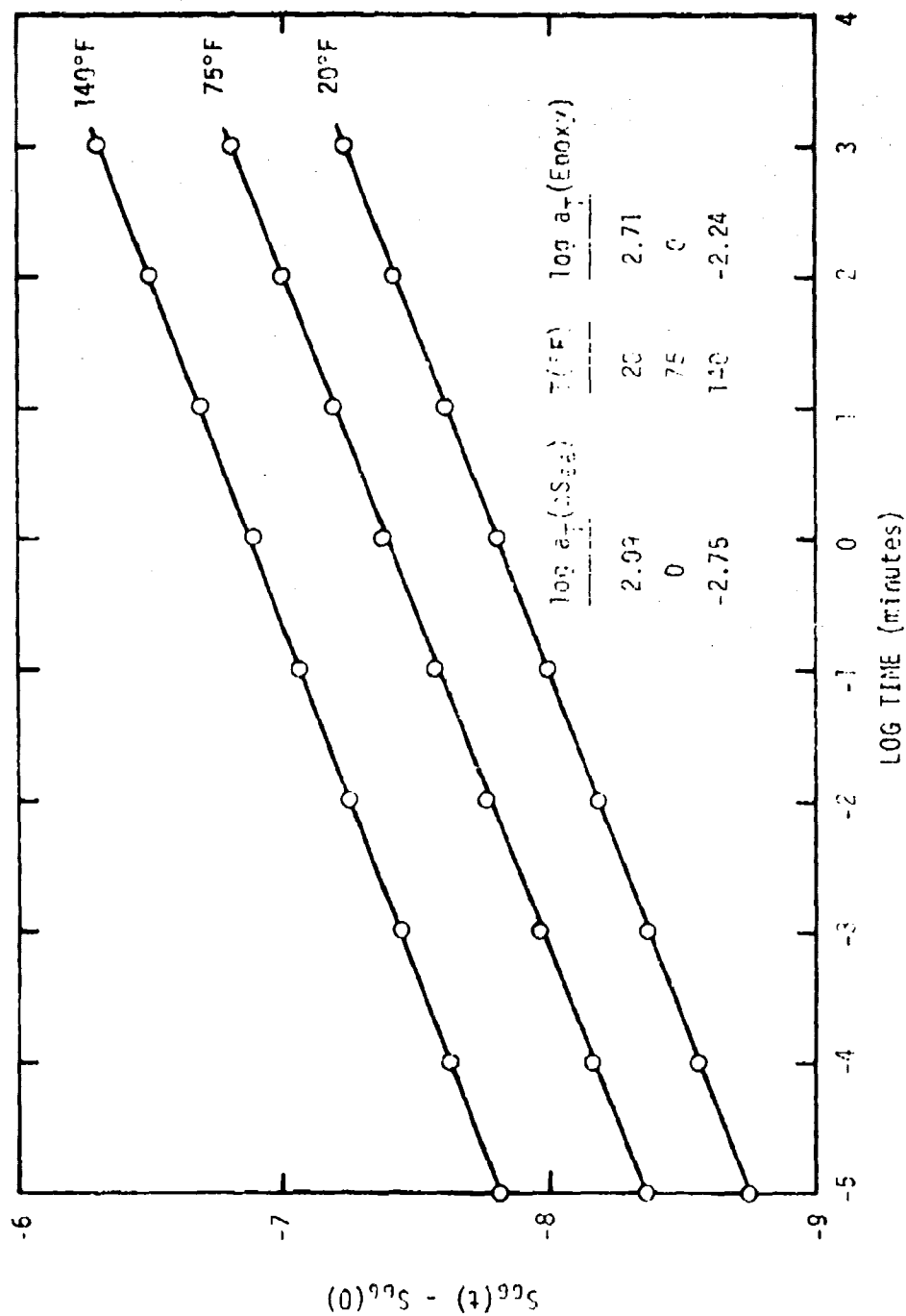
The experimental creep compliance,  $S_{66}$ , was calculated using the linear viscoelastic creep compliance for  $S_{45^\circ}$ ,  $S_{0^\circ}(S_{11})$ ,  $S_{90^\circ}(S_{22})$  and  $S_{12}$  (Table 14). The time dependence of  $S_{66}$  is shown in Figure 113. The solid curve represents the predicted behavior if one were to use the epoxy  $a_T$  shift factors on the 75°F creep coefficient to obtain the creep coefficients at 20°F and 140°F. The initial compliance remains unchanged. The net compliance,  $S_{66}(t) - S_{66}(0)$ , shown in Figure 114 can be seen to obey the power law in time with  $n = 0.19$  as expected. The  $a_T$  shift factors determined by a horizontal shifting of  $\Delta S_{66}$  along the time scale are given in the figure.

All of the four principal compliances have been determined experimentally, with  $S_{66}$  predicted from experimental data and not measured directly. Our attention will now be turned toward the prediction of the principal compliances using the various micromechanics theories.

#### Comparison with Micromechanics Theory

The "rule of mixtures" representation, viz., Equations (114) and (117), was used to predict the major Poisson's ratio,  $\nu_{12}$ , and longitudinal modulus,  $E_{11}$ . For the glass/epoxy composite studied here the last terms in Equations (113) and (116) may be dropped

Figure 113. Temperature dependence of principal shear compliance,  $S_{66}$ .

Figure 114. Temperature dependence of net creep compliance,  $S_{ss}$ .

with only negligible error in order to arrive at the "rule of mixtures" relationships. This error is on the order of 0.1 and 2.4% for the respective equations. The fiber properties,  $E_f$  and  $\nu_f$ , given by Equation (129) were considered independent of time and temperature. A fiber volume fraction,  $\nu_f$ , of 0.616 was used for the analysis (see Table 3 for experimental values of various plates). The matrix volume fraction was 0.384. The viscoelastic behavior of  $E_{11}$  and  $\nu_{12}$  was readily found by employing the quasi-elastic approach given by Equations (118a) and (118b). The matrix modulus was determined using the quasi-elastic approach

$$E_m(t) = \frac{1}{D_m(t)} \quad (147)$$

where the values of  $D_m(t)$  are given in Table 11.

The principal creep compliances,  $S_{11}$  and  $S_{12}$ , are expressed in terms of  $E_{11}$  and  $\nu_{12}$  through Equation (83a) and were predicted with the use of a computer for several decades of time. Calculation of the other two principal creep compliances,  $S_{22}$  and  $S_{66}$ , is more involved. Several micromechanics theories were considered; however, the Halpin-Tsai Equations given by Equations (119) and (120) for the elastic and quasi-elastic cases, respectively, are relatively popular. The Halpin-Tsai relations are a semi-empirical approach which has been used by several investigators [29, 33, 62]. The adjustment factors,  $\zeta_E$  and  $\zeta_G$ , are selected to give the best fit with experimental data. The factors are known to be functions of fiber

geometry and spacing; their time-dependence, if any, has not been investigated by others.

The initial principal creep compliances which were measured are summarized in Table 15 for future reference.

Table 15. Experimental, Initial Principal Creep Compliances for S-901 Glass/Shell 58-68R Epoxy

Temperature (°F)	$S_{11} \times 10^{-6}$ (psi <sup>-1</sup> )	$S_{12} \times 10^{-6}$ (psi <sup>-1</sup> )	$S_{22} \times 10^{-6}$ (psi <sup>-1</sup> )	$S_{66} \times 10^{-6}$ (psi <sup>-1</sup> )
20	.121	-.0329	.3115	.8417
75	.121	-.0330	.3315	.9175
140	.127	-.0359	.3490	1.0054

In order to determine the optimum values for  $\zeta_E$  and  $\zeta_G$ , Equations (147) and (120) were solved for several values of the adjustment factors using initial properties. Equation (83a) was used to convert  $E_{22}$  and  $G_{12}$  to the compliances  $S_{22}$  and  $S_{66}$ . The analytical values of  $S_{22}$  and  $S_{66}$  were plotted as a function of the adjustment factor. It was found that  $\zeta_E \approx \zeta_G = 3.14$  gave the best fit over the entire temperature range, never exceeding an error of  $\pm 4\%$ .

The temperature dependence of the initial, principal creep compliances is shown in Figure 115 along with the corresponding analytical predictions. It is evident that the "rule of mixtures" and the Halpin-Tsai relations give excellent results. The dotted line, shown for  $S_{22}$  and  $S_{66}$ , represents the predicted Halpin-Tsai

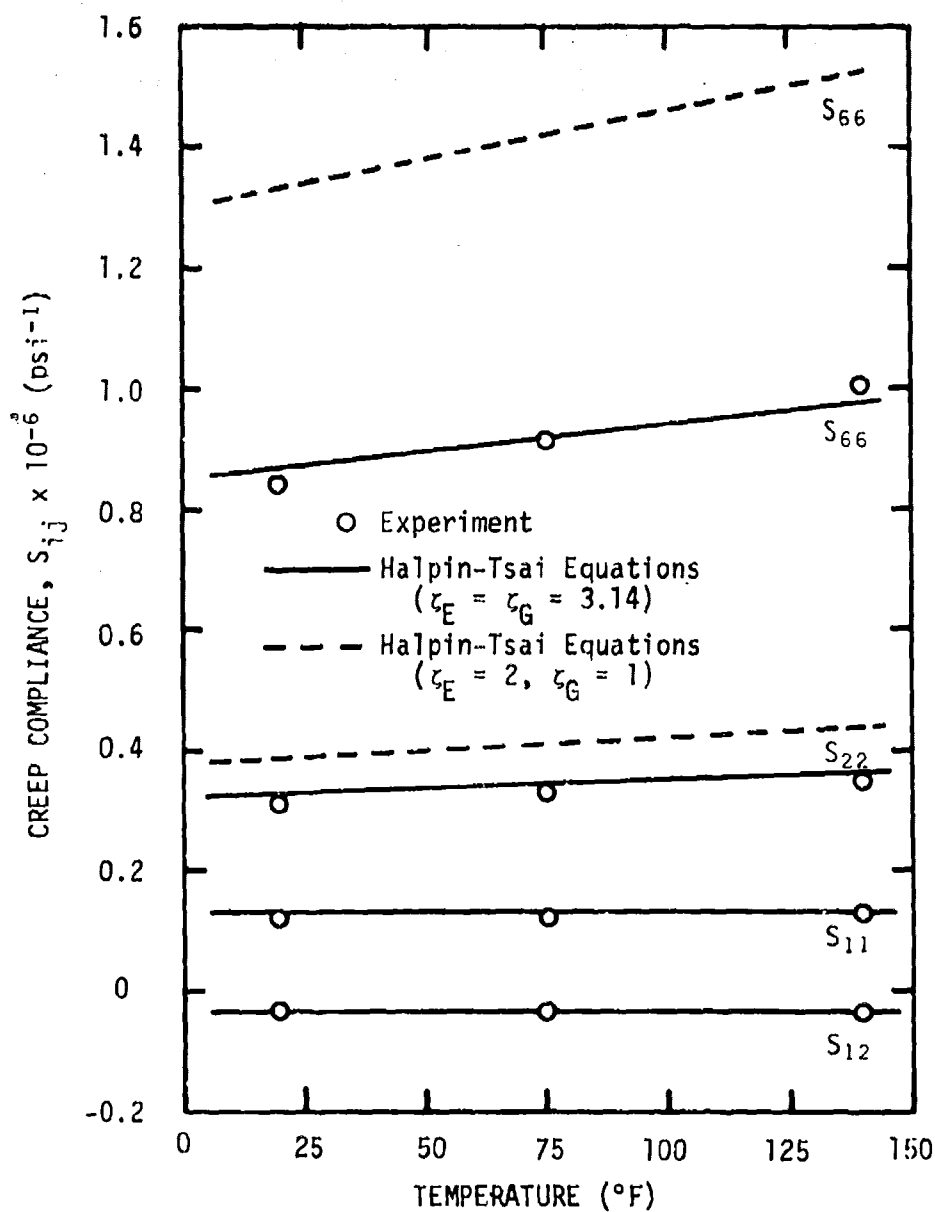


Figure 115. Temperature dependence of initial principal linear viscoelastic creep compliances.



compliances when  $\zeta_E = 2$  and  $\zeta_G = 1$  are used. The specific values are based on numerical solutions [2] but it is evident that they do not give good predictions for the glass/epoxy composite. We shall comment later concerning the use of these specific values. The reduced stiffnesses,  $Q_{ij}$ , are related to the  $S_{ij}$  by Equation (128) and are shown in Figure 116. Again, the agreement with the predicted values (solid line) is good.

The time dependence of the principal compliances was found by using a quasi-elastic analysis and the linear viscoelastic creep compliance for the epoxy matrix (see Table 11). Data over several decades of time was obtained by using the linear viscoelastic power law coefficients and extrapolation to times beyond the actual experimental time. The "rule of mixtures", Equations (114) and (117), and Halpin-Tsai Equations (120) were solved for several decades of time. Equation (83a) was used to convert the engineering properties,  $E_{11}$ , etc., to the principal creep compliances,  $S_{ij}$ . Figures 117, 118 and 119 show the time and temperature dependence of the predicted (solid and dotted lines) and experimental (open circles) compliances. All of the curves are based on the last cycle of creep. Except for 140°F where a significant amount of crack growth occurs, the agreement is good over several decades of time. At 140°F the strong time dependence exhibited by the  $S_{22}$  compliance is evident. The applied stress is normal to the fibers and, therefore, does not provide any known mechanism for crack

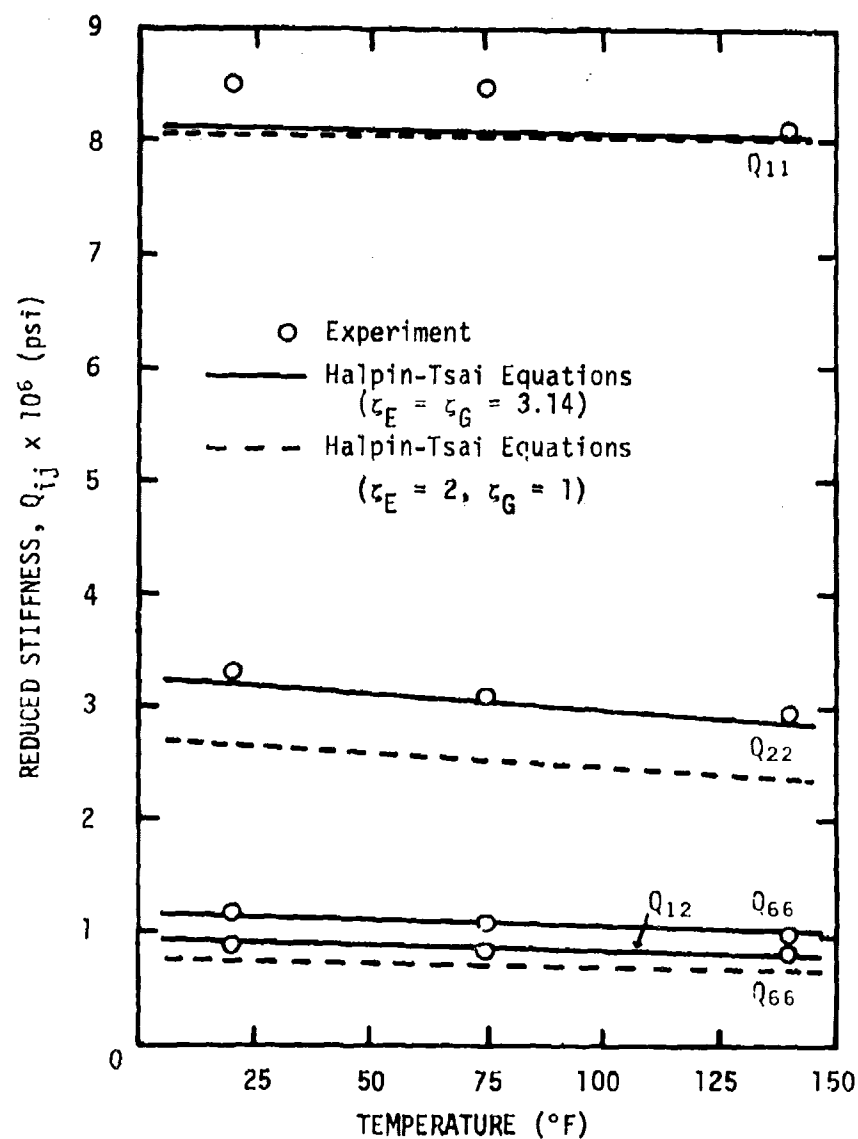


Figure 116. Temperature dependence of initial transformed reduced stiffnesses (data from Figure 115).

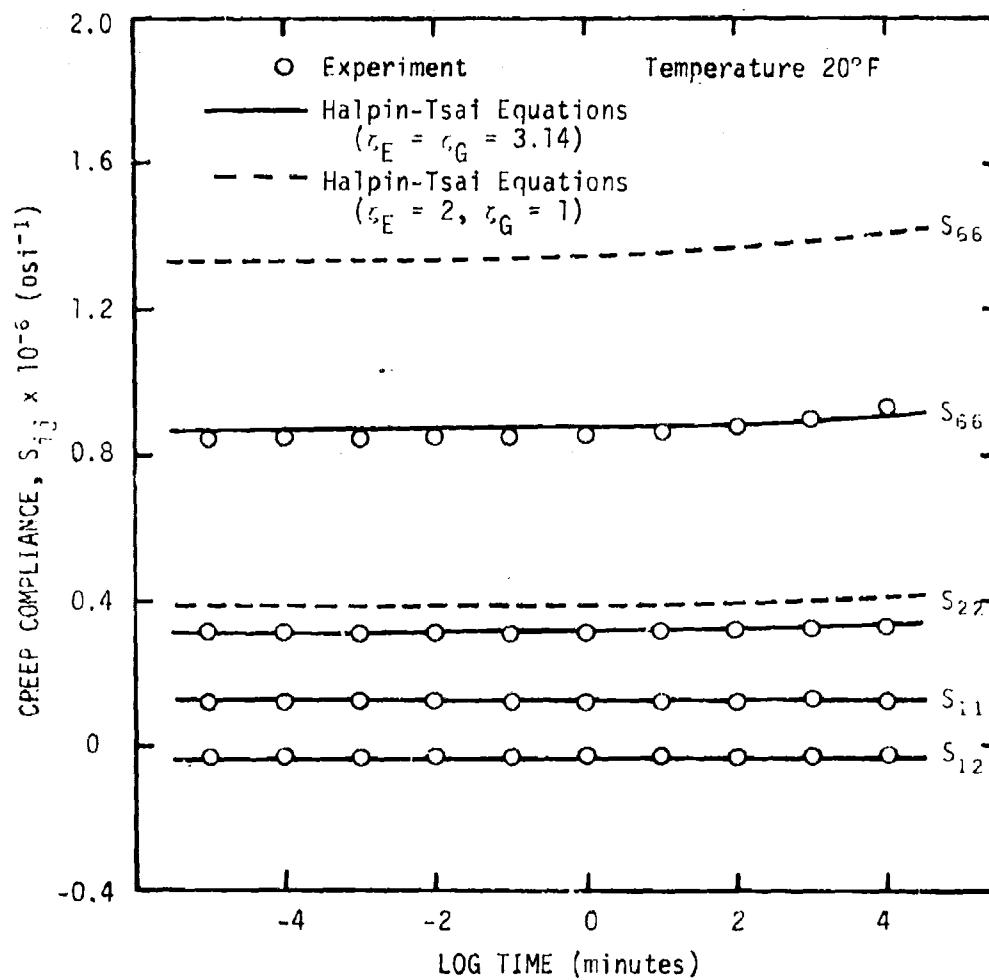


Figure 117. Linear viscoelastic creep compliances of glass/epoxy composite ( $T = 20^\circ\text{F}$ ).

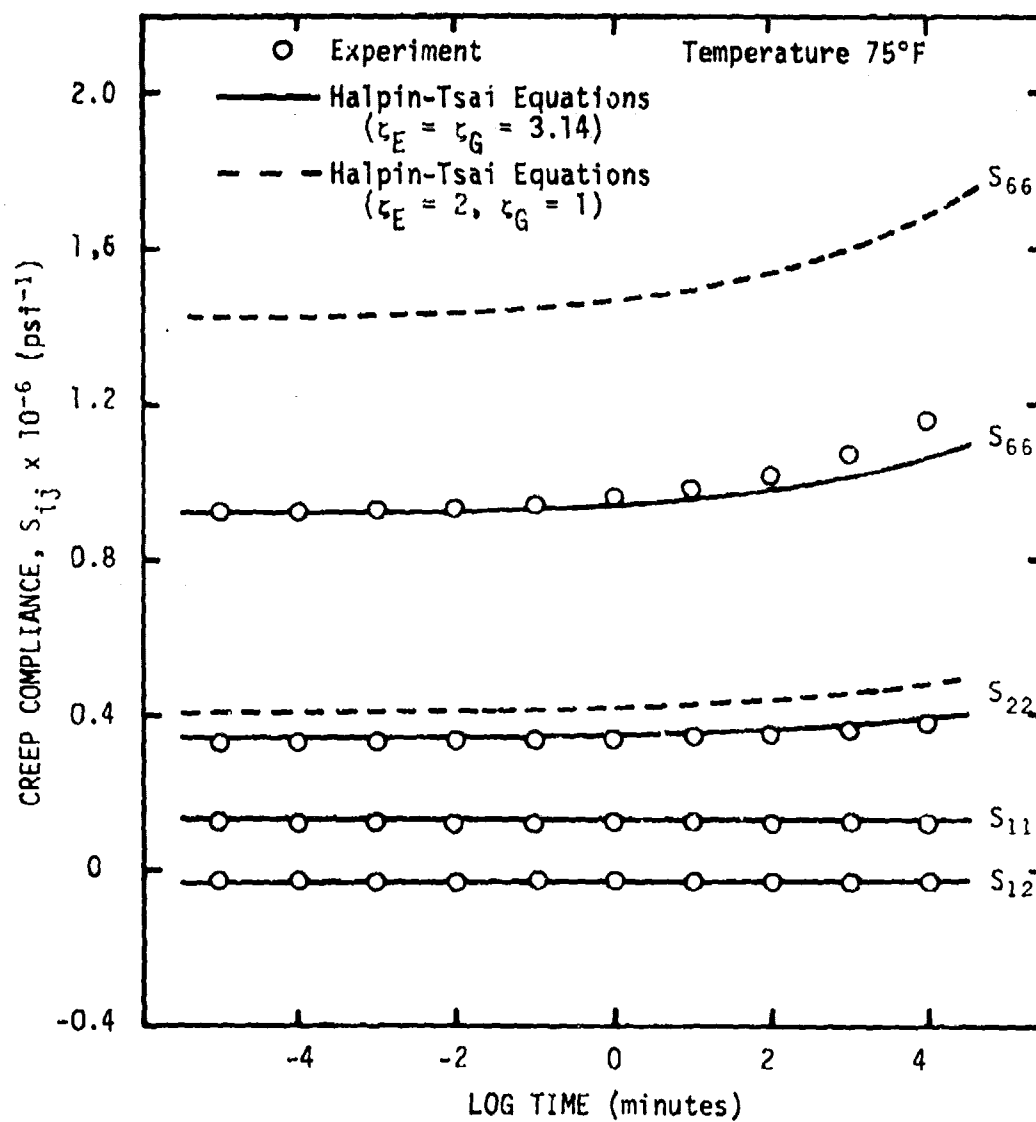


Figure 118. Linear viscoelastic creep compliances of glass/epoxy composite ( $T = 75^\circ\text{F}$ ).

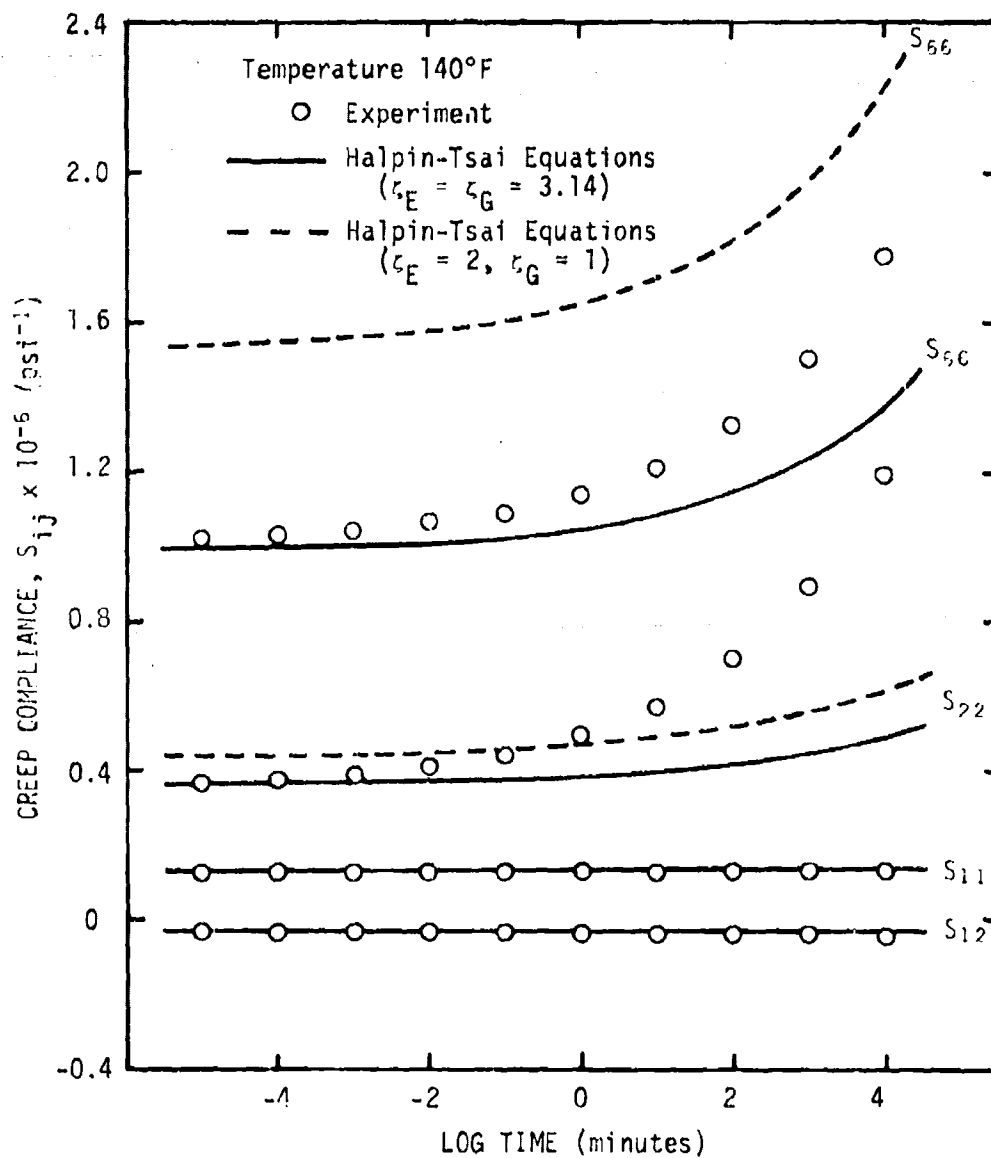


Figure 119. Linear viscoelastic creep compliances of glass/epoxy composite ( $T = 140^\circ\text{F}$ ).

arrest in the absence of any shear stress component. The opening mode crack growth is hypothesized to predominate very strongly. Further evidence of crack growth as a result of the normal stress can be seen in the behavior of the creep compliance for the  $\theta = 90^\circ$  specimen. Although the initial compliance appears to be reasonable, the experimentally determined creep coefficient appears to be high. As an example, from Figure 75 we can determine the value of  $\log a_T$  at  $140^\circ\text{F}$  to be about  $-3.25$ . Using this value of  $a_T$  and the creep coefficient at  $75^\circ\text{F}$ , the  $140^\circ\text{F}$  creep coefficient is predicted to be  $0.0336 (10^{-6})$ . The experimental value shown in Table 12, for the last creep cycle at a stress level of 475 psi is more than 4 times greater than predicted. At  $140^\circ\text{F}$  crack growth is significant and the stress level used to define the linear viscoelastic creep compliance, namely 475 psi, already is creating a strong nonlinearity.

The corresponding reduced stiffnesses,  $Q_{ij}$ , found by using Equation (128) are shown in Figures 120, 121 and 122. Again, the agreement is good except at  $140^\circ\text{F}$ .

It was noted earlier that the values of  $\zeta_E = 2$  and  $\zeta_G = 1$  are often used in the Halpin-Tsai relations. These values appear to work reasonably well when the ratio of fiber to matrix properties is high, e.g., graphite/epoxy and boron/epoxy. A comparison of the relative stiffness for these two materials gives a range of 50 to 120 typically. Glass/epoxy composites generally lie in the range from 20-25 at the lower end of the spectrum. Several investigators

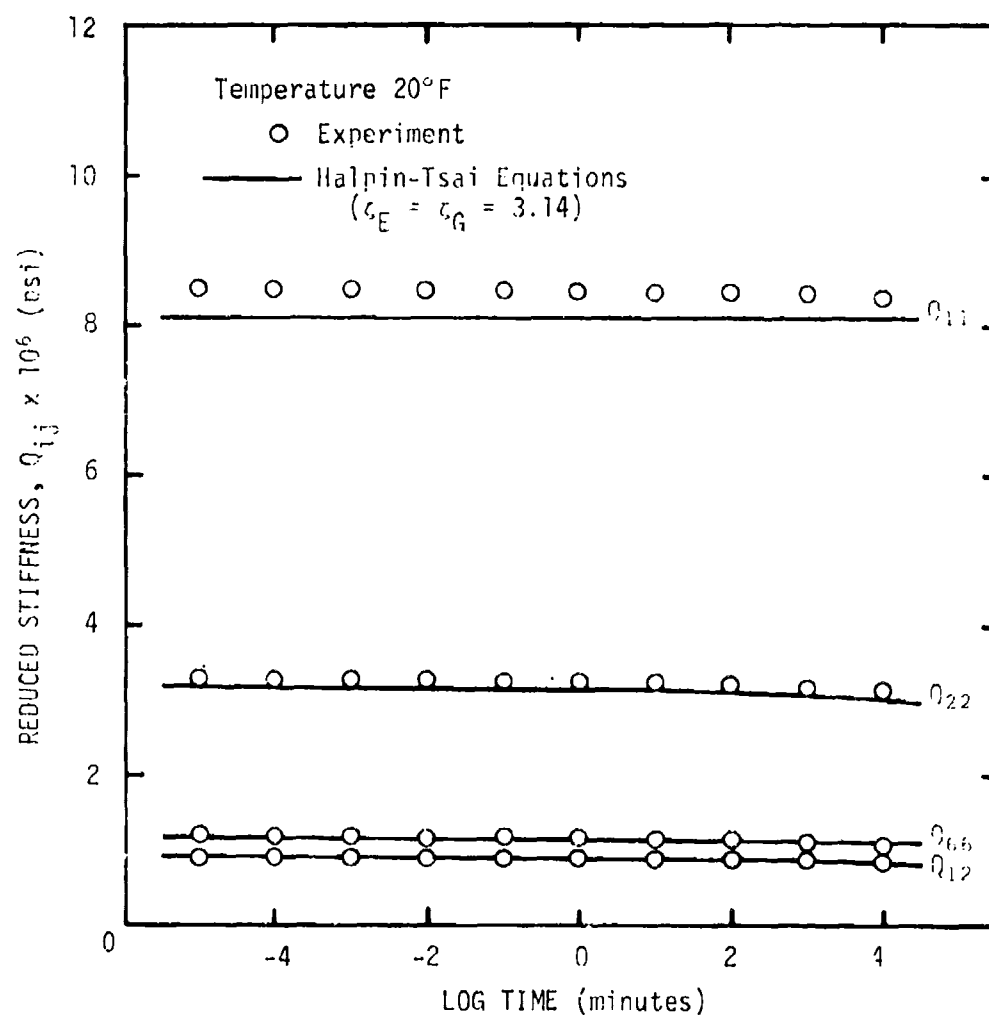


Figure 120. Linear viscoelastic reduced stiffness of glass/epoxy composite ( $T = 20^\circ\text{F}$ ).

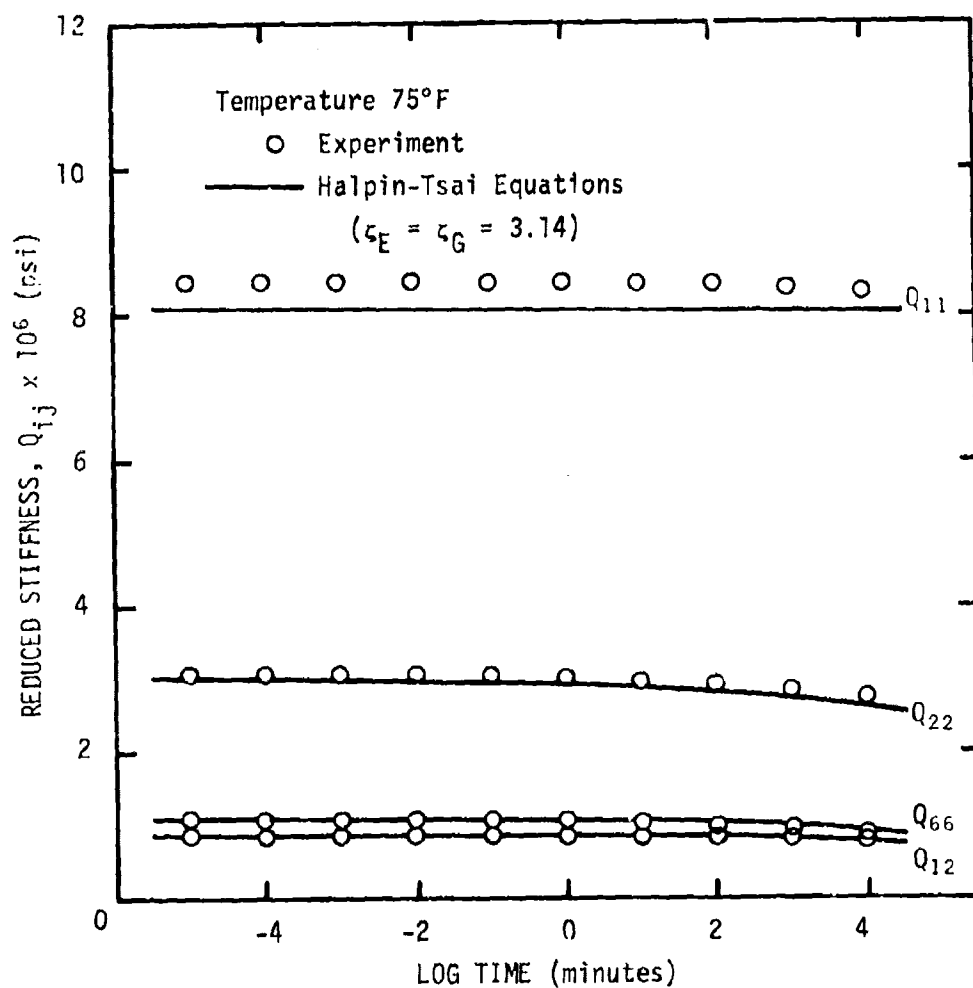


Figure 121. Linear viscoelastic reduced stiffness of glass/epoxy composite ( $T = 75^\circ\text{F}$ ).



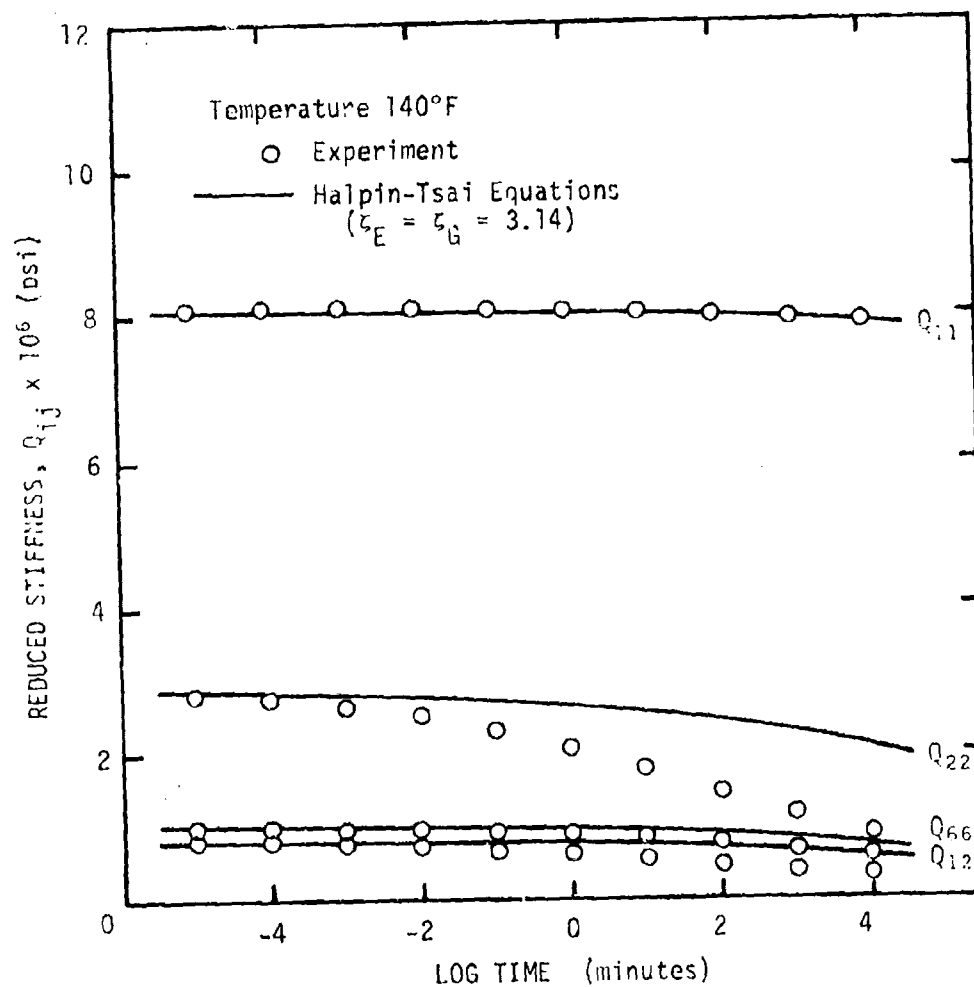


Figure 122. Linear viscoelastic reduced stiffness of glass/epoxy composite ( $T = 140^\circ\text{F}$ ).

[33, 62] further justify the use of these specific values in order to determine an "effective" resin compliance. This procedure involves the solution of the Halpin-Tsai Equations (119) or (120) in terms of the "effective" resin properties  $E_m$  and  $G_m$ . The argument for this approach is based on a consideration that:

1. The bulk epoxy resin properties are generally not available.
2. The mechanical properties of the bulk resin and the resin in the composite may be different because of curing conditions and chemical composition.
3. The effect of stress concentrations around the fibers may affect the resin properties.

Sims and Halpin [62] used this approach on an E-glass/epoxy and a graphite/epoxy composite with fiber volume fractions on the order of 0.56. A comparison of the "effective" resin properties with measured bulk resin properties showed that the "effective" properties were within  $\pm 10\%$ . A careful examination of Figures 117, 118 and 119 shows that the time-dependence of the experimental data, especially for  $S_{66}$ , agrees more closely with the Halpin-Tsai relations when one uses  $\zeta_E = 2$  and  $\zeta_G = 1$ .

The primary difference, with the exception of  $S_{22}$  at  $140^\circ\text{F}$ , appears to be in the value of the initial compliances. In order to check this behavior, the Halpin-Tsai Equation (120) was solved for

the "effective" resin compliance using  $\zeta_E = 2$  and  $\zeta_G = 1$ . Only the initial compliance,  $D_0$  of the epoxy resin was determined. The solution of Equation (120) yields two real roots, one positive and the other negative. Only the positive value of  $D_0$  was considered on the basis of physical reasons. Figure 123 compares the experimental initial compliances with the "effective" compliances predicted from the  $S_{22}$  and  $S_{66}$  principal compliances. Note that there is a considerable difference in the  $S_{22}$  and  $S_{66}$  predictions; however, the  $S_{22}$  compliance is not nearly as sensitive to changes in the matrix  $D_0$  as  $S_{66}$ . The "effective" resin properties indicate approximately a twofold increase in stiffness from the bulk material. This appears to be unreasonably high and it is felt that the fibers are creating most of the stiffening effect. However, a closer examination of the theoretical bounds on the principal compliances will be discussed later in order to justify this hypothesis.

The time-dependence of  $S_{22}$  and  $S_{66}$  using the "effective"  $S_{66}$  resin compliances and the Halpin-Tsai relations with  $\zeta_E = 2$  and  $\zeta_G = 1$  are shown in Figures 124, 125 and 126. Remember that only the value of  $D_0$  was changed, retaining the original  $D_1$  values found experimentally. The time-dependence of  $S_{66}$  agrees remarkably well over several decades of time. The predicted  $S_{22}$  response is in close agreement except where considerable crack growth is present at the 140°F temperature.

The theoretical upper and lower bounds for  $S_{66}$  and  $S_{22}$  have

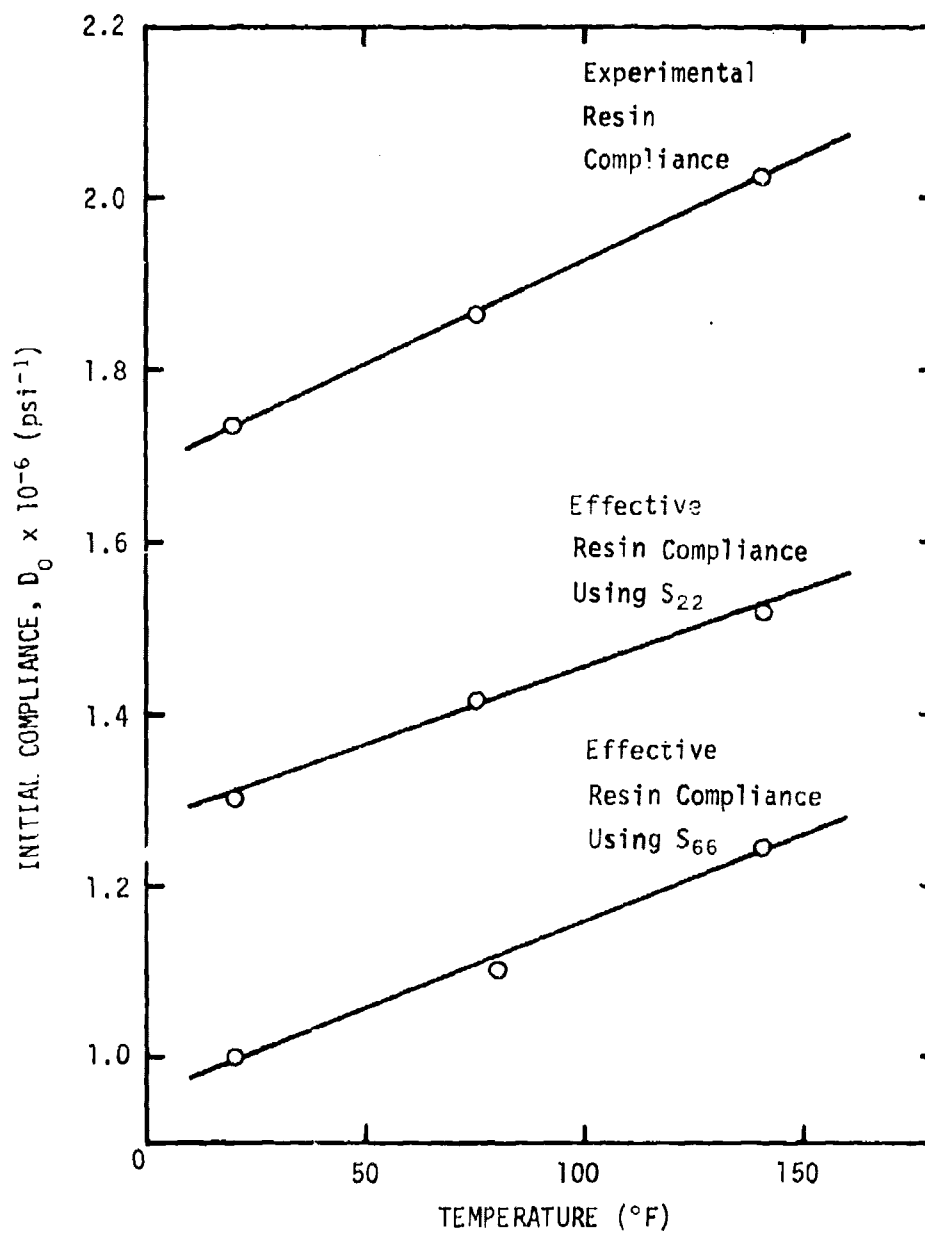


Figure 123. Comparison of experimental initial compliance,  $D_0$ , with "effective" compliances for Shell 58-68R epoxy resin.

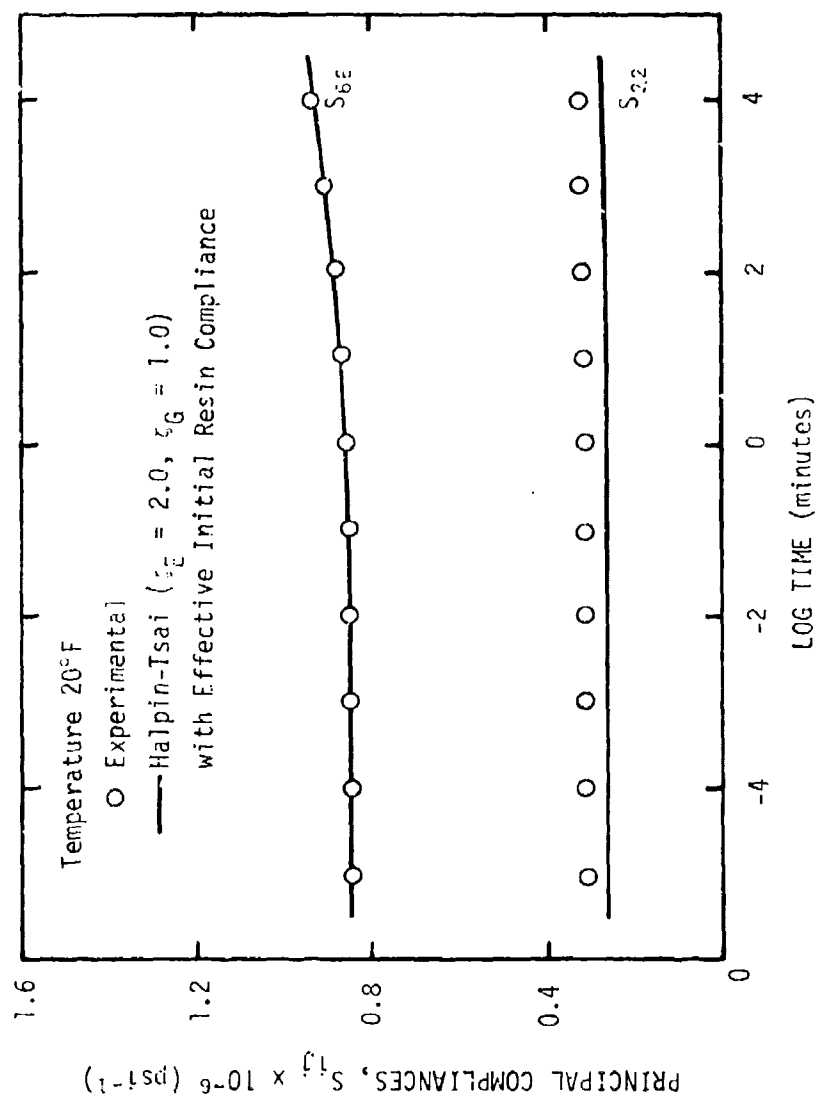


Figure 124. Principal compliances,  $S_{22}$  and  $S_{66}$ , predicted with Halpin-Tsai equations using the  $S_{66}$  "effective" resin compliance ( $T = 20^\circ\text{F}$ ).

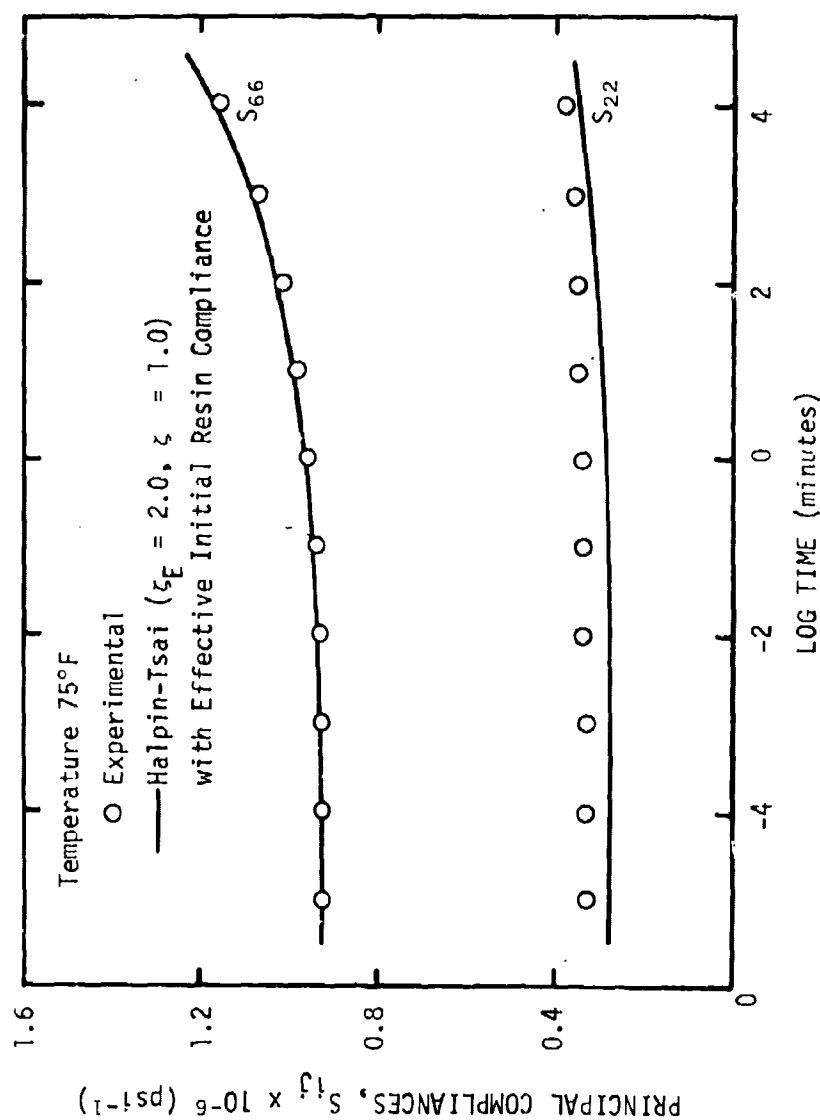


Figure 125. Principal compliances,  $S_{22}$  and  $S_{66}$ , predicted with Halpin-Tsai equations using the  $S_{66}$  "effective" resin compliance ( $T = 75^\circ\text{F}$ ).

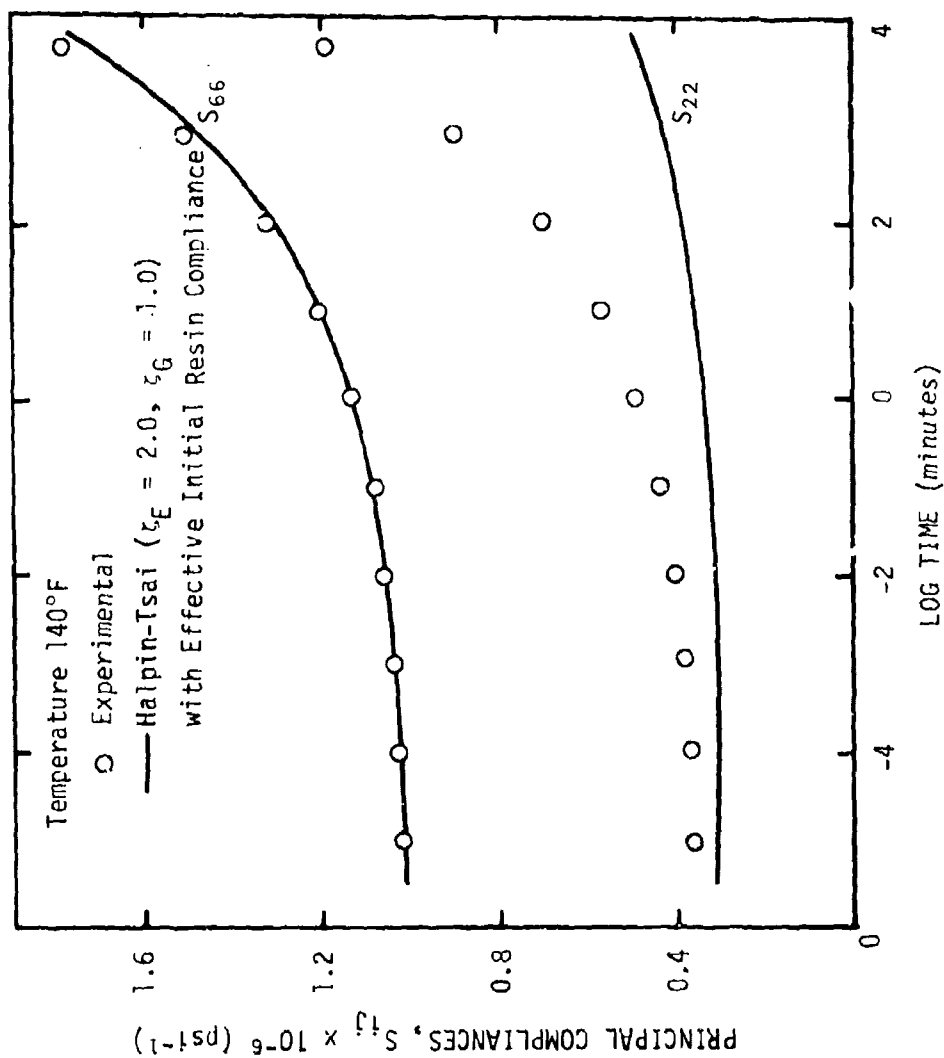


Figure 126. Principal compliances,  $S_{22}$  and  $S_{66}$ , predicted with Halpin-Tsai equations using the  $S_{66}$  "effective" resin compliance ( $T = 140^\circ\text{F}$ ).

been established by Hashin and Rosen [189]. The "composite cylinder assemblage" (CCA) model corresponds to the upper bounds on compliance. The CCA model is obtained by progressively filling out a cylindrical specimen with composite circular cylinders. Each cylinder consists of a circular fiber and concentric matrix shell having the same fiber volume fraction as the overall composite and is filled out in such a manner that the assemblage is statistically homogeneous and transversely isotropic. The upper and lower bounds for the shear modulus in the plane parallel to the fibers,  $G_{12}$ , are given by (after some rearrangement)

$$G_{12}(+) = G_f \left[ \frac{G_f(1-v_m) + G_m(1+v_m)}{G_f(1+v_m) + G_m(1-v_m)} \right] \quad (148a)$$

$$G_{12}(-) = G_m \left[ \frac{G_f(1+v_f) + G_m(1-v_f)}{G_f(1-v_f) + G_m(1+v_f)} \right] \quad (148b)$$

where the subscripts  $f$  and  $m$  refer to the fiber and matrix, respectively, and  $G$  and  $v$  are the shear modulus and volume fraction, respectively.

Determination of the bounds on the transverse modulus,  $E_{22}$  (or  $S_{22}$ ), is more involved since it requires the evaluation of the effective plane strain transverse bulk modulus,  $k_t^*$  as well as bounds on the transverse shear modulus,  $G_t^*$ . The effective plane strain transverse bulk modulus is given by



$$k_t^* = k_m + \frac{v_f}{\left[ \frac{1}{k_f - k_m} + \frac{v_m}{k_m + G_m} \right]} \quad (149)$$

where  $k$ , the bulk modulus of the fiber (f) and matrix (m) is defined by

$$k = \frac{E}{3(1-2\nu)} \quad (150)$$

In Equation (150),  $E$  is the tensile modulus and  $\nu$  is the Poisson's ratio of the individual constituents.

The upper and lower bounds on the transverse shear modulus are given by

$$G_t^*(+) = G_f + \frac{v_m}{\left[ \frac{1}{G_m - G_f} + \frac{(k_f + 2G_f)v_f}{2G_f(k_f + G_f)} \right]} \quad (151a)$$

and

$$G_t^*(-) = G_m + \frac{v_f}{\left[ \frac{1}{G_f - G_m} + \frac{(k_m + 2G_m)v_m}{2G_m(k_m + G_m)} \right]} \quad (151b)$$

The upper and lower bounds on the transverse modulus,  $E_{22}$ , may now be expressed in terms of  $k_t^*$ ,  $G_t^*$  and the major Poisson's ratio,  $\nu_{12}$ , and longitudinal modulus,  $E_{11}$ , given by Equations (117) and (114), respectively. These bounds become

$$E_{11}(+) = \frac{4k_t^* G_t^*(+)}{k_t^* + G_t^*(+) [1 + 4k_t^* \nu_{12}^2/E_{11}]} \quad (152a)$$

and

$$E_{22}(-) = \frac{4k_t^* G_t^*(-)}{k_t^* + G_t^*(-) [1 + 4k_t^* \nu_{12}^2/E_{11}]} \quad (152b)$$

Using Equation (83a) to convert  $E_{22}$  and  $G_{12}$  to  $S_{22}$  and  $S_{66}$ , respectively, the temperature dependence of the initial compliances, now using the experimental  $D_0$  and not the "effective" initial compliance, is compared with the experimental data as shown in Figures 127 and 128. The previous predictions for the Halpin-Tsai relations are also shown for reference. It should be noted that the upper bounds (+) on the compliances are the values determined from the lower bounds (-) on the moduli due to the inversion. The opposite is true for the lower (-) compliance bounds. The upper bound on  $S_{66}(+)$  also corresponds to using  $\zeta_G = 1$  in the Halpin-Tsai relationships.

Time-dependence may be represented by using the associated relationships and the quasi-elastic analysis approach. Figures 129 through 131 show that the response of  $S_{22}$  and  $S_{66}$  is well within the upper and lower bounds with the exception of  $S_{22}$  at 140°F. Rather than force the Halpin-Tsai relations to fit the experimental data by requiring the matrix compliance to change significantly, it seems more reasonable to adjust the factor  $\zeta_E$  and  $\zeta_G$  according

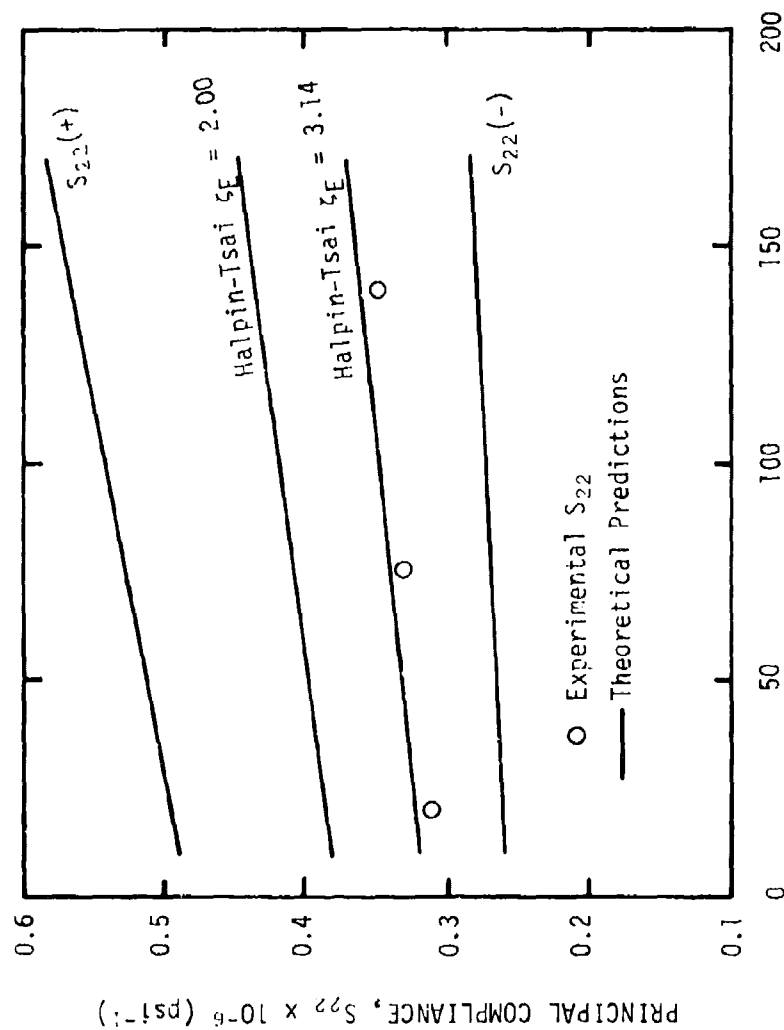


Figure 127. Comparison of temperature dependence of initial compliance,  $S_{22}$ , with theoretical bounds.

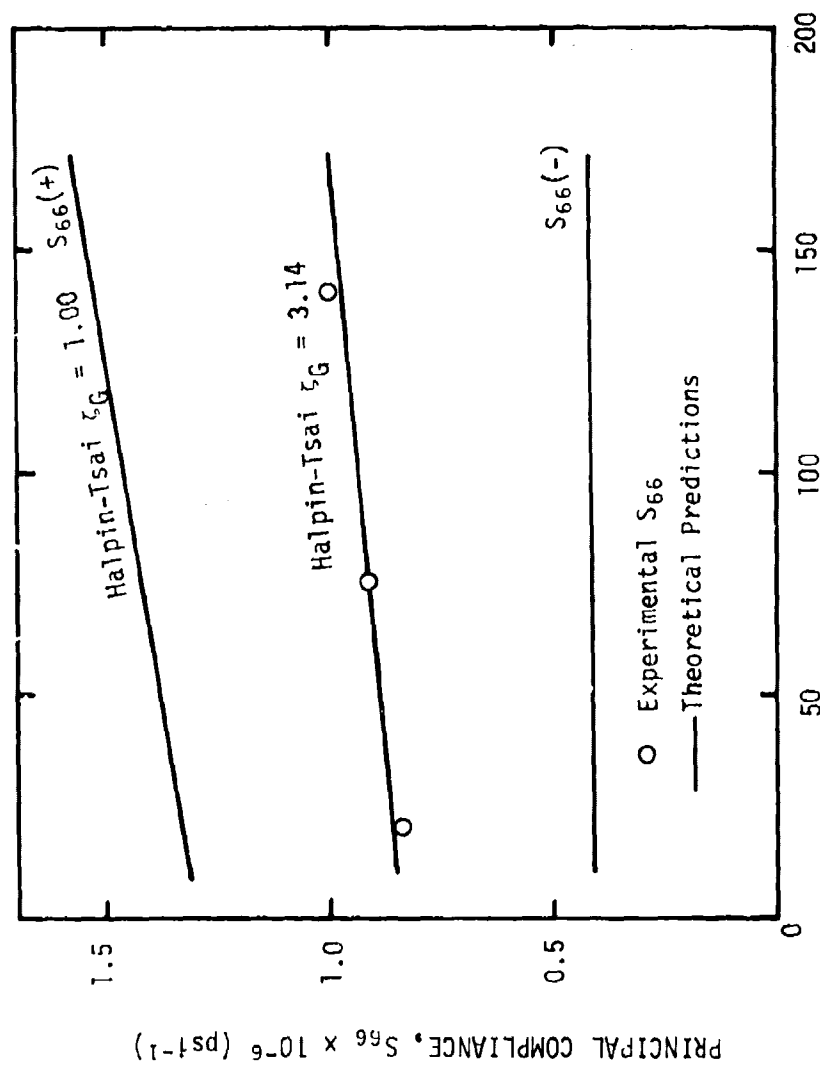


Figure 128. Comparison of temperature dependence of initial compliance,  $S_{66}$ , with theoretical bounds.

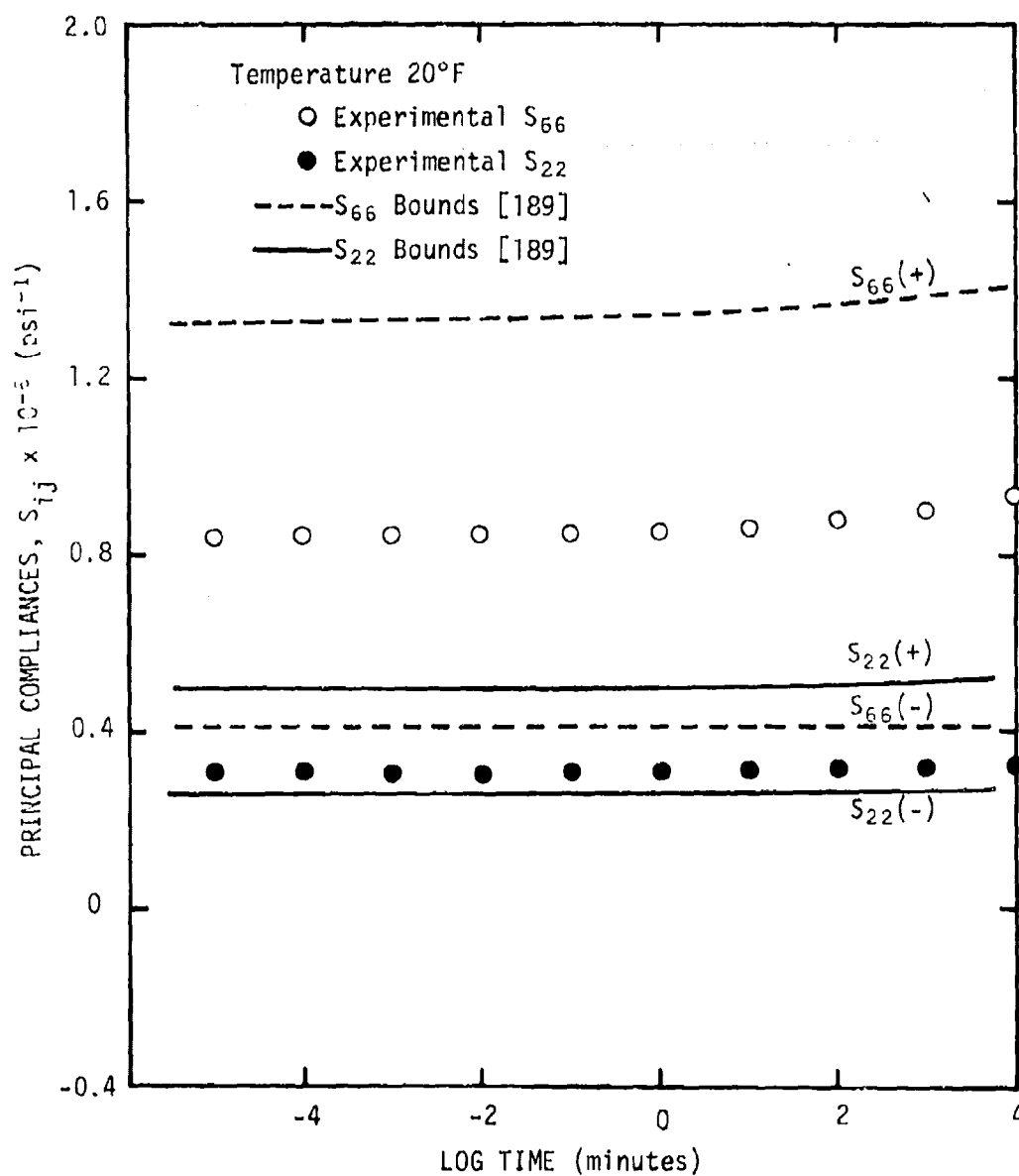


Figure 129. Comparison of experimental compliances  $S_{22}$  and  $S_{66}$  with theoretical upper and lower bounds ( $T = 20^\circ\text{F}$ ).

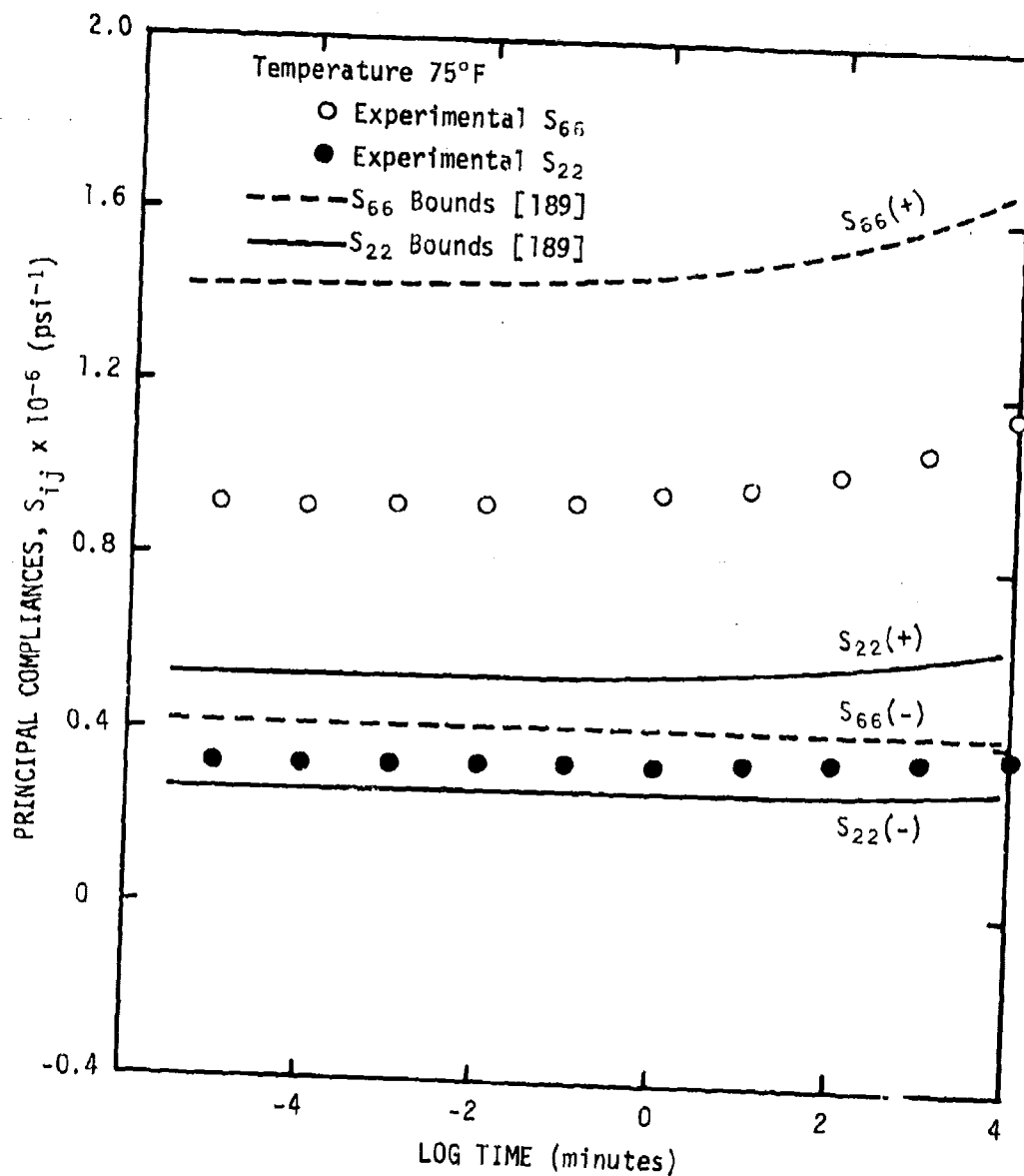


Figure 130. Comparison of experimental compliances  $S_{22}$  and  $S_{66}$  with theoretical upper and lower bounds ( $T = 75^\circ\text{F}$ ).

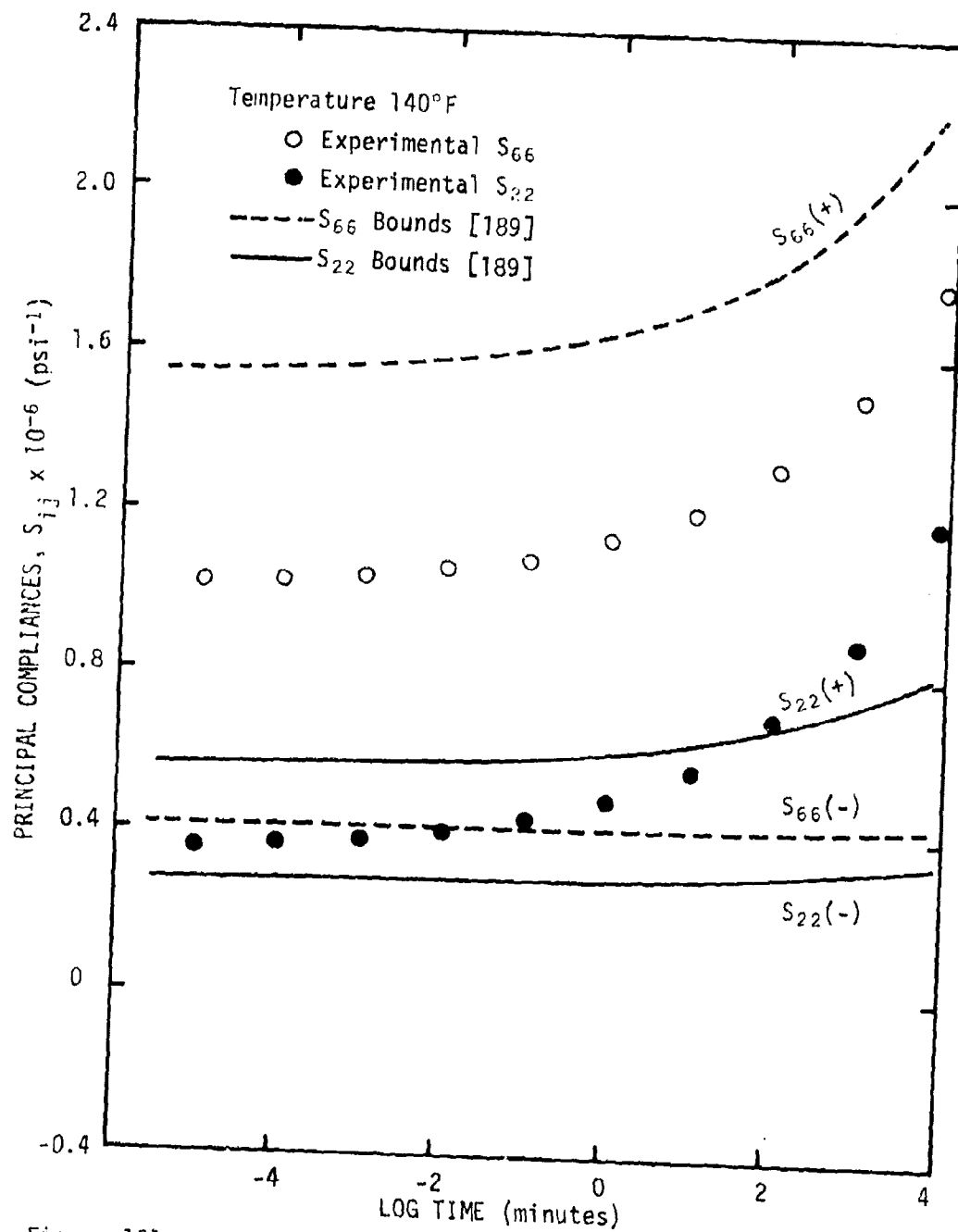


Figure 131. Comparison of experimental compliances  $S_{22}$  and  $S_{66}$  with theoretical upper and lower bounds ( $T = 140^\circ\text{F}$ ).

to the best fit over the desired time scale of engineering interest. The experimental data falls between the bounds, suggesting that upper bounds for  $S_{66}(\zeta_G = 1)$  does not represent the actual model for the glass/epoxy composite within the theoretical constraints originally imposed.

### Constant Crosshead Rate Tests on Glass/Epoxy Laminates

#### Effect of Temperature

The effects of temperature on the multiple cycling of a 45 and  $\pm 45^\circ$  glass/epoxy composite tensile coupon is shown in Figures 132 through 135. For these figures only, the stress-strain curve has been drawn for each specimen with the strain always referenced to the sample length at the start of each cycle, i.e., the strain at the beginning of each cycle is rezeroed ( $\epsilon = 0$ ). The net result, as we noted earlier, causes the material to appear to become stiffer with each succeeding cycle. This effect is misleading and is cited here only to show the trend in cycle-to-cycle behavior. In Figures 132 and 133 the glass/epoxy appears to become nonlinear as a result of irreversible damage at a stress level near 4000 psi (75°F). However, at 140°F it appears that this damage occurs at extremely low stress levels for the 45° unidirectional composite (Figure 134), approaching zero stress. The  $\pm 45^\circ$  laminated composite, possibly because of the layering effect on crack arrest, becomes nonlinear near 2000 psi (Figure 135).



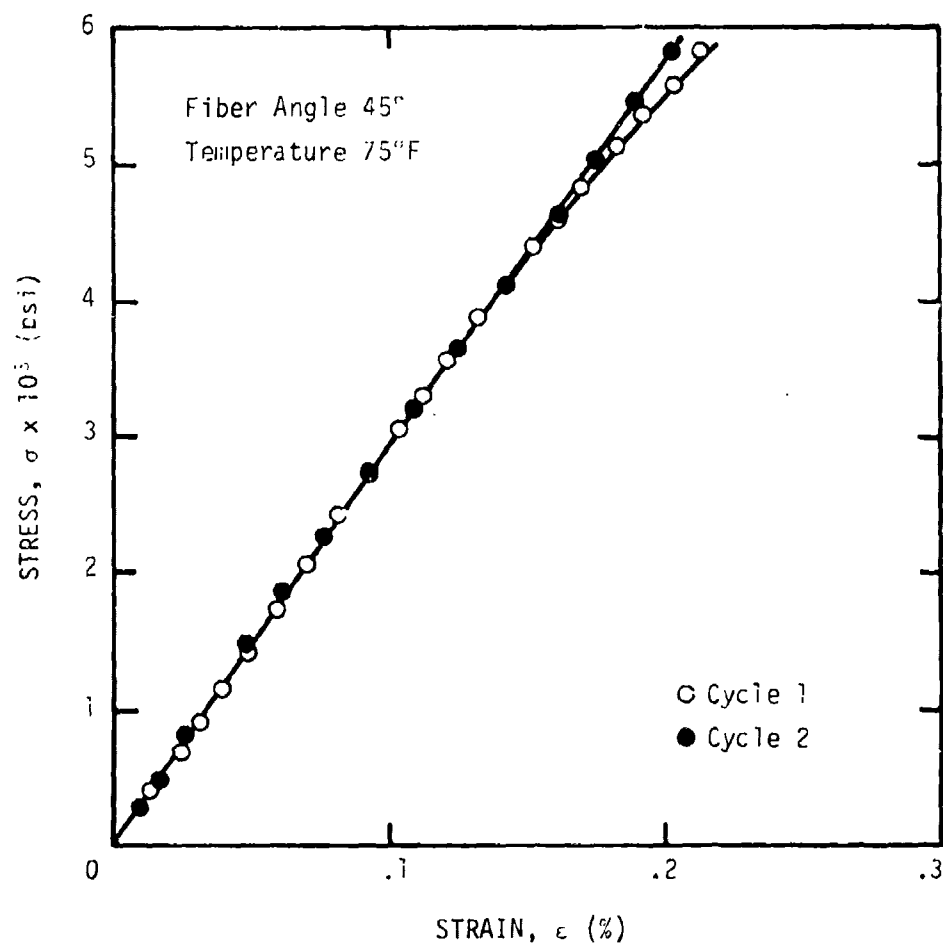


Figure 132. Effect of repeated tensile loading on stress-strain response ( $\theta = 45^\circ$ ,  $T = 75^\circ\text{F}$ ).

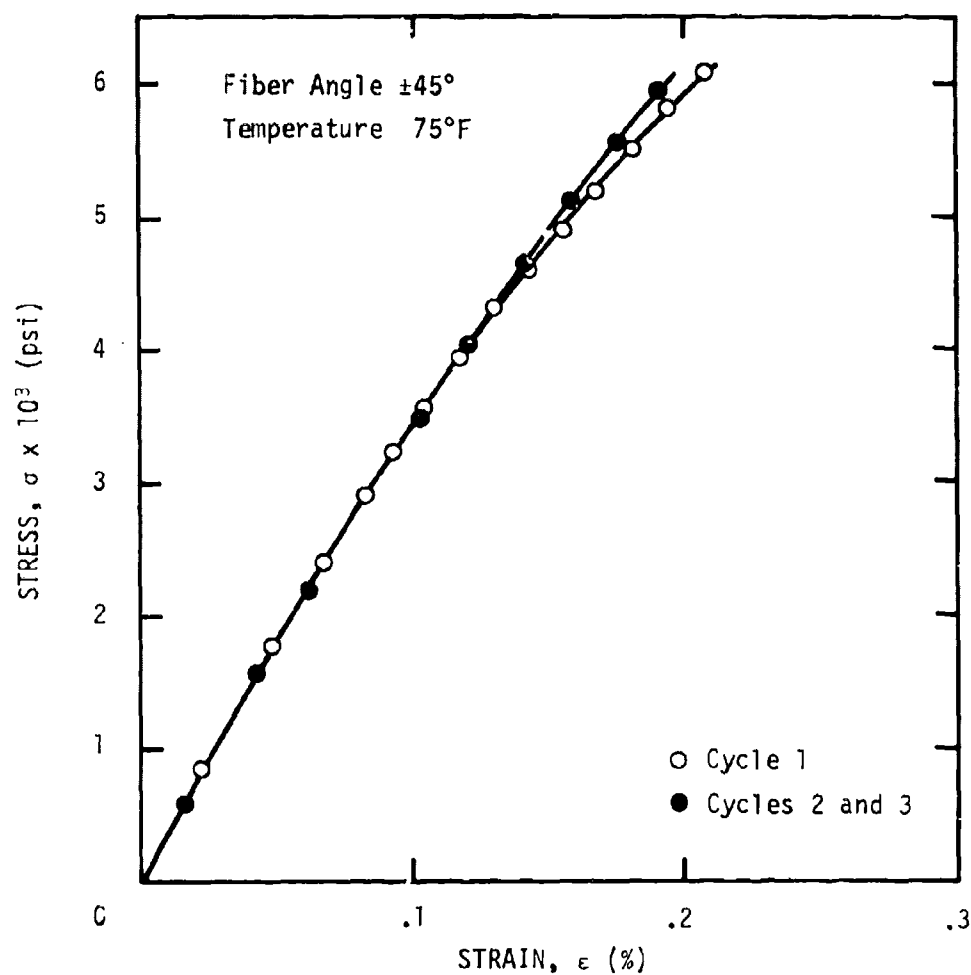


Figure 133. Effect of repeated tensile loading on stress-strain response ( $\theta = \pm 45^\circ$ ,  $T = 75^\circ\text{F}$ ).

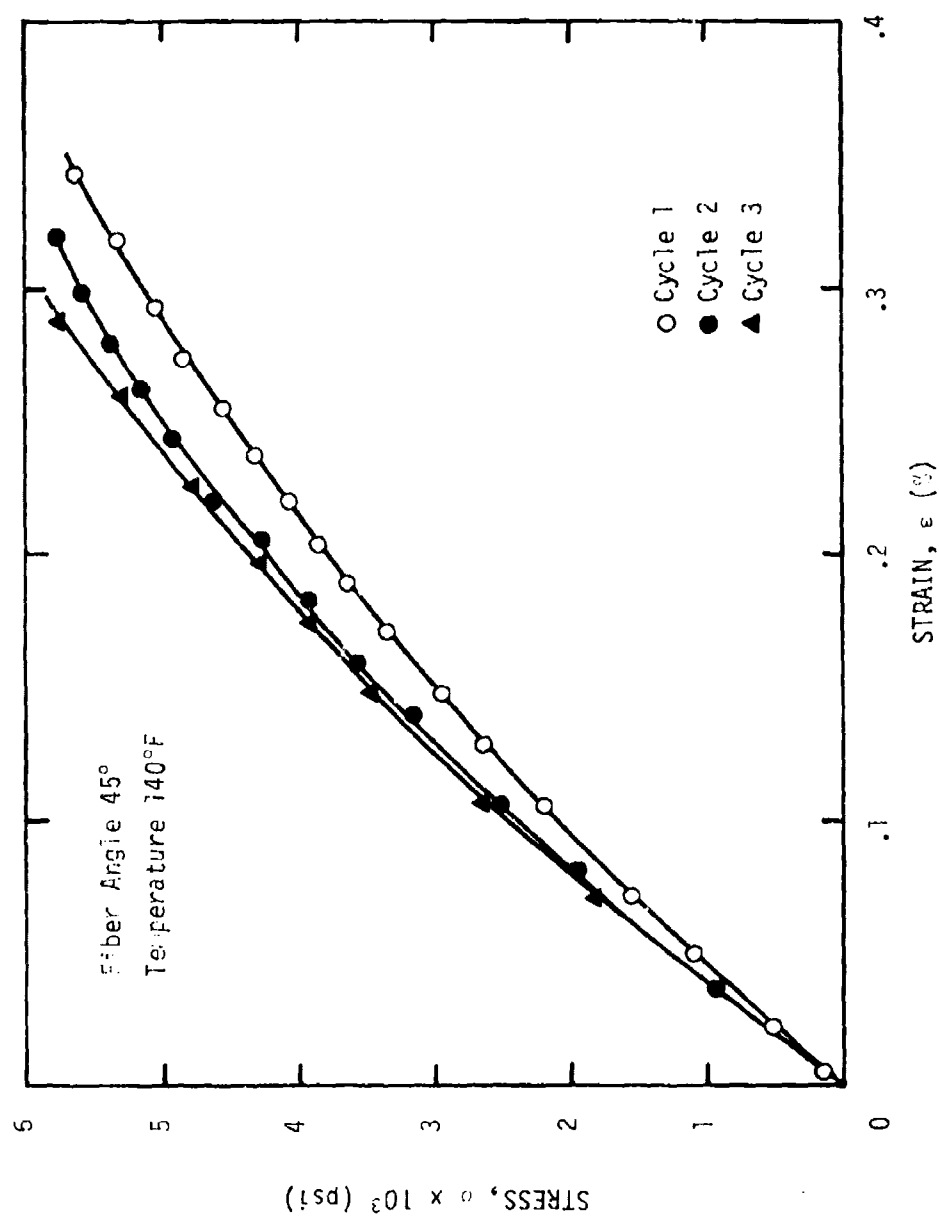


Figure 134. Effect of repeated tensile loading on stress-strain response ( $\theta = 45^\circ$ ,  $T = 140^\circ\text{F}$ )

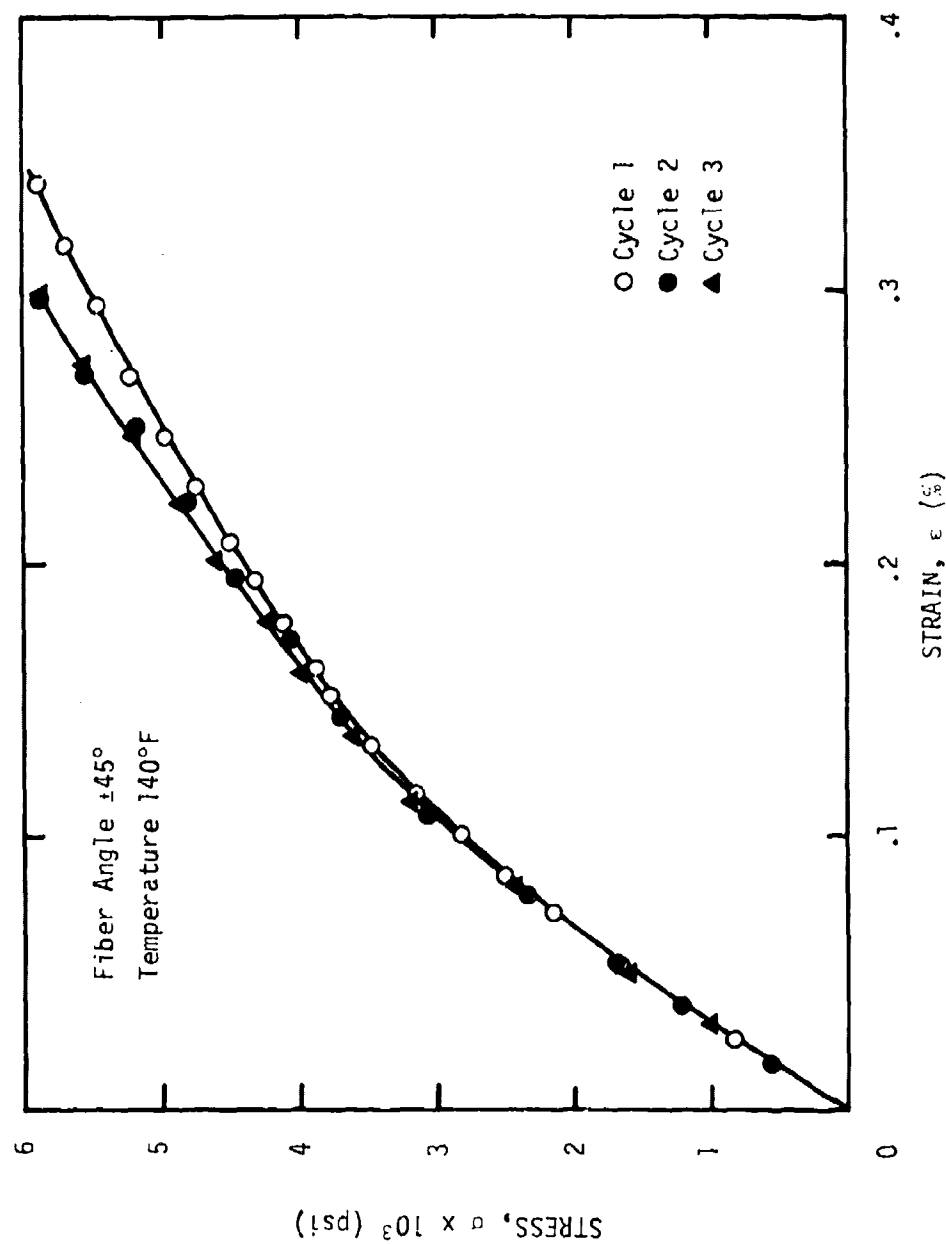


Figure 135. Effect of repeated tensile loading on stress-strain response ( $\theta = \pm 45^\circ$ ,  $T = 140^\circ\text{F}$ ).

At 75°F it appears that the degree of crack growth and arrest are on the same order of magnitude for the second and subsequent cycles for both the 45 and  $\pm 45^\circ$  composites. This is supported by the relative change from the first to second cycles as seen in Figures 132 and 133, along with the similarity in stress levels at which the two cycles begin to differ, viz. 4000 psi. Earlier it was reported in Table 12 that the initial creep compliance for the  $\pm 45^\circ$  laminated composite was slightly lower (6.5%) than the 45° unidirectional composite. The differences in fiber volume fraction, although in the correct direction of the experimental results, are only on the order of 1% (TAMU data) to 3.5% (SCI data). A comparison of the two tensile stress-strain curves also shows the same trend in the stiffness.

The layering effect seems to cause the material to become stiffer at both 75 and 140°F. At 140°F crack arrest occurs more rapidly in the  $\pm 45^\circ$  laminated composite which displays the same behavior in the second and third cycle. The 45° unidirectional composite, on the other hand, still shows significant change between the second and third cycle. The effect of temperature appears to strongly affect the crack growth behavior in the unidirectional 45° composite more than the  $\pm 45^\circ$  laminated composite.

#### Effect of Multiple Cycling and Stress Level

After the initial set of experiments were completed, it was

decided to conduct another series of tests on 45, 0/90 and  $\pm 45^\circ$  glass/epoxy tensile coupons in order to further study the effects of multiple cycling and stress level, including the unloading phase. All of these tests were conducted at 75°F using a ramp loading and unloading rate of 0.02 inches per minute followed by a recovery period (no load) equal to two times the total time under load. The stress histories used for this series of tests are shown in Table 16.

The first series of tests were carried out on the 0°/90° laminated composite. The results of these tests are shown in Figures 136, 137 and 138. Only the first cycle is shown for the stress level of 15,000 psi since there was no visible evidence of irreversible damage present. All three cycles exhibited nearly elastic behavior within the time scale of the experiment. Considering the maximum strain level induced in the 90° layers, one would not expect any significant damage, at least not visible damage in this type of test. The total experimental time for one complete cycle (neglecting recovery) was less than three minutes; therefore, the viscoelastic effects for the 0°/90° fiber angle are negligible.

The next two cycles at the 42,000 psi level reflect the breakdown of the 90° layers at a strain level close to 0.3%. Once the layers are broken the succeeding cycles (Figure 13C) show a permanent strain and little if any hysteresis. This condition is probably representative of the behavior in the barrel region of the

Table 16. Stress History of Multiple Cycling,  
Constant Crosshead Rate Tests

Fiber Angle ( $\theta$ )	Sample Number	Cycle Number	Maximum Stress (psi)
0°/90°	090.11	1,2,3	15,000
		4,5	42,000
45°	45.13	1,2,3	8000
		4,5	5000
		6	8000
		7,8	10,000
		9(broke)	12,000
±45°	AP45.18	1,2,3,4	11,500
		5(broke)	10,500
±45°	AP45.11	1,2	5000
		3,4,5	6500
		6,7,8	8100
		9,10,11	9700
		12,13,14	10,500
		15,16,17	12,000
		18	12,900
		19(broke)	13,100

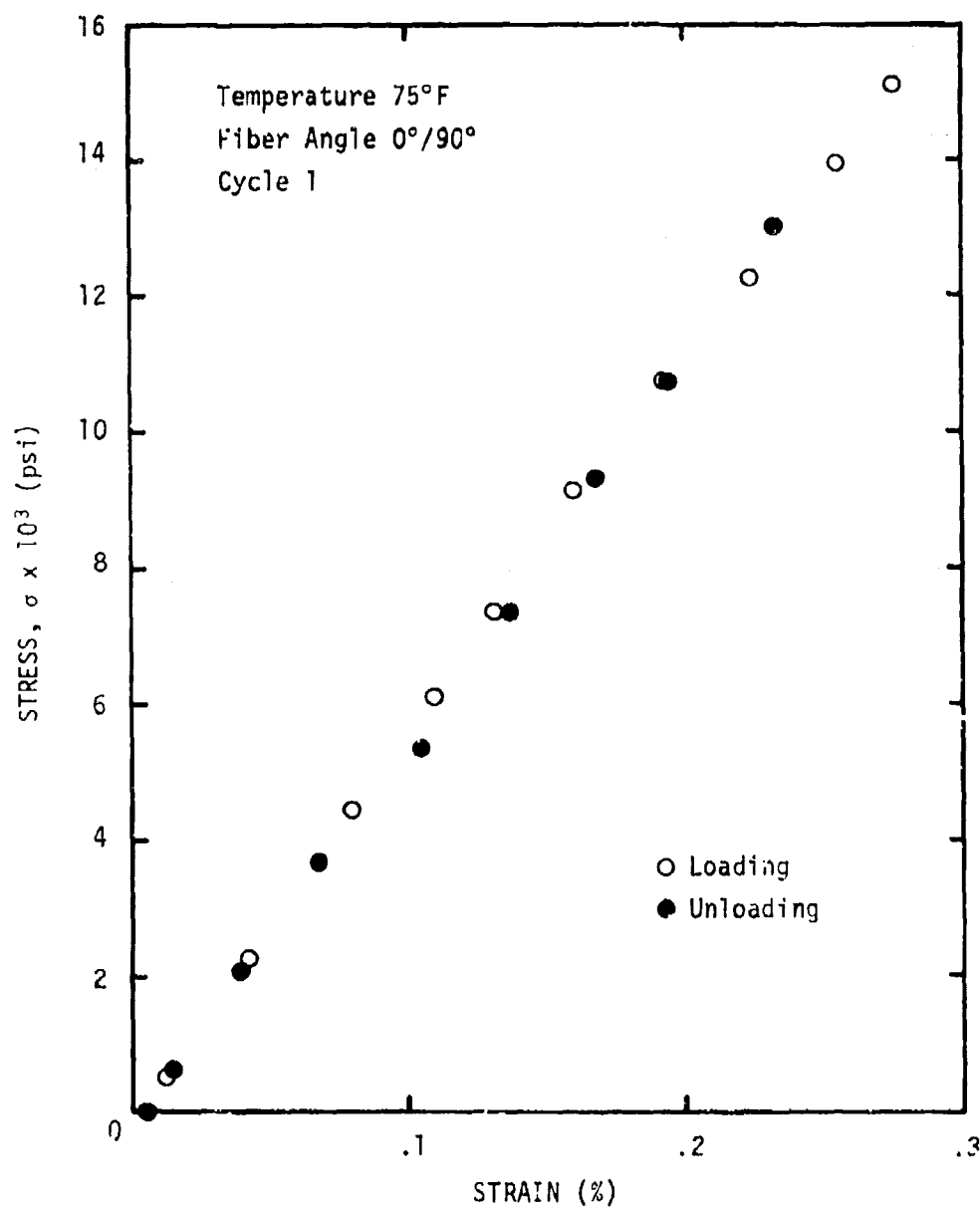


Figure 136. Effect of cyclic loading on 0°/90° tensile coupon;  $\sigma_{\max} = 15,000$  psi (Cycle 1).



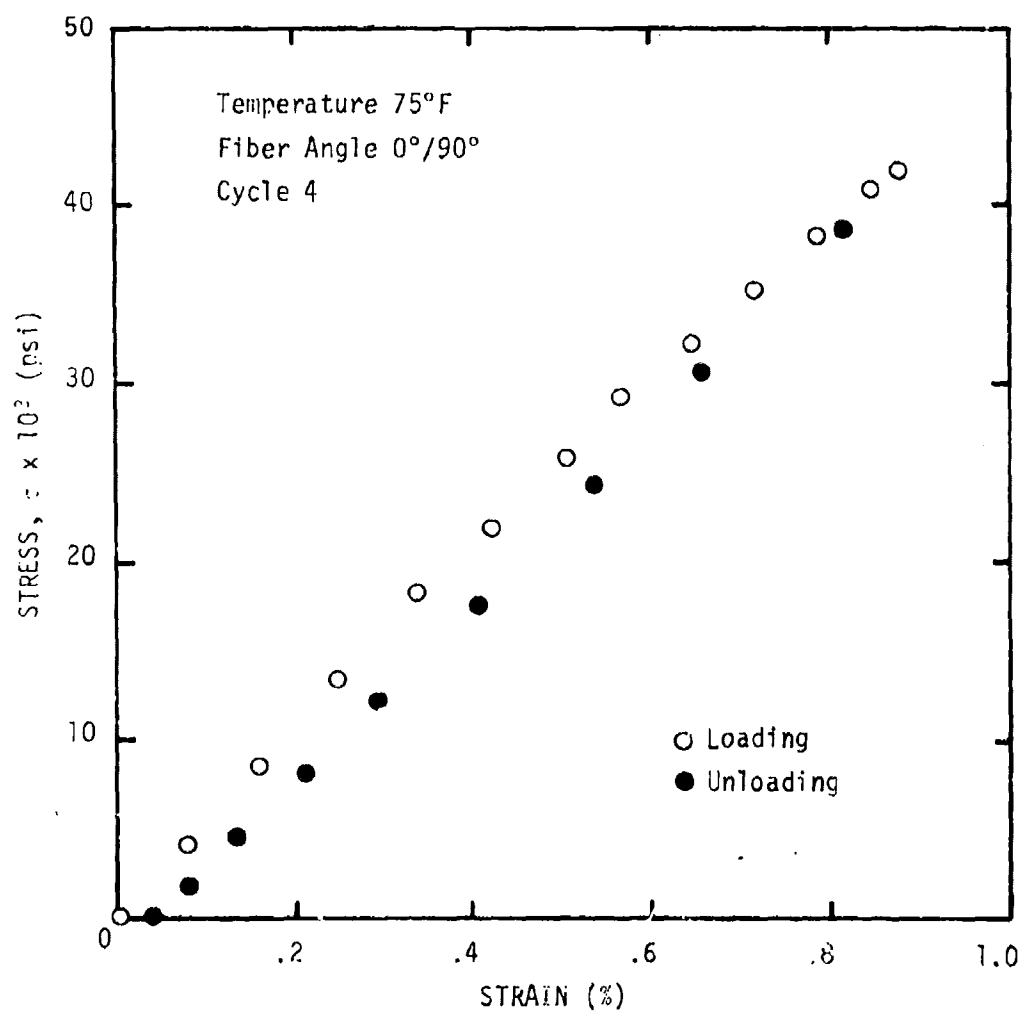


Figure 137. Effect of cyclic loading on 0°/90° tensile coupon;  $\sigma_{\max} = 42,000$  psi (Cycle 4).

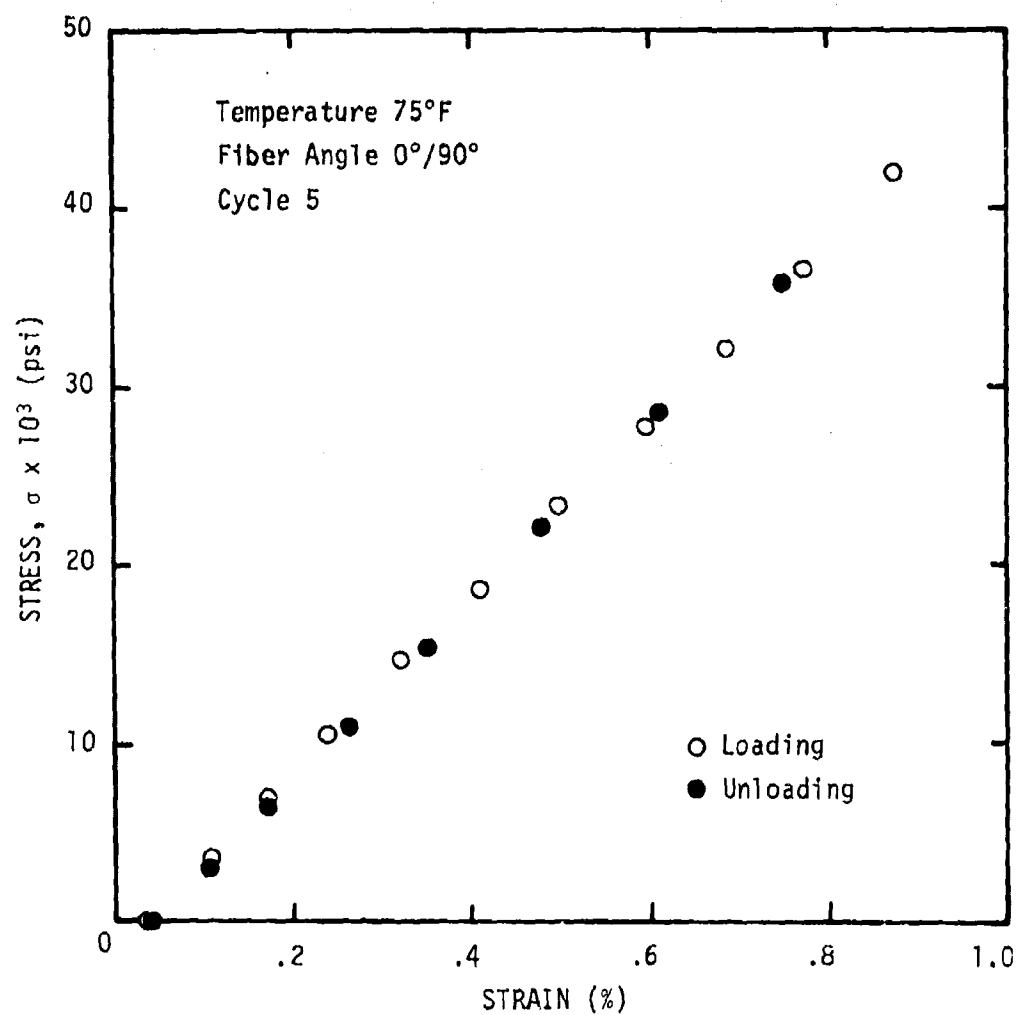


Figure 138. Effect of cyclic loading on 0°/90° tensile coupon;  $\sigma_{\max} = 42,000$  psi (Cycle 5).

motor case during the first cycle (hydrotest) and subsequent cycles (motor handling and firing).

In the initial test series on  $45^\circ$  unidirectional glass/epoxy laminates the maximum stress was about 6000 psi. This series was conducted to study the effects of successively higher stress levels up to complete fracture. The first three cycles shown in Figures 139 and 140 indicate the amount of irreversible damage as a result of crack growth. The accumulation of permanent strain and the decrease in the hysteresis loop is clearly shown. Figures 141 and 142 show the two cycles conducted at a stress level of 10,000 psi. The relative change in the hysteresis loop appears to be on the same order of magnitude as the cycles conducted at the lower stress levels.

The last test series was run on two  $\pm 45^\circ$  laminated composites using two different stress histories. Sample AP45.18 was tested completely at a high stress level without cycling at lower levels. A maximum stress of 11,500 psi was selected for this sample. The stress history for sample AP45.11 consisted of several cycles at 5000 psi followed by several additional cycles at increasingly higher stress levels until fracture occurred. Figures 143, 144 and 145 show the rather dramatic changes which occur through the first four cycles of loading. It is evident that a disproportionate amount of damage is done in the first cycle. This fact agrees with the results shown earlier for the creep and recovery tests.

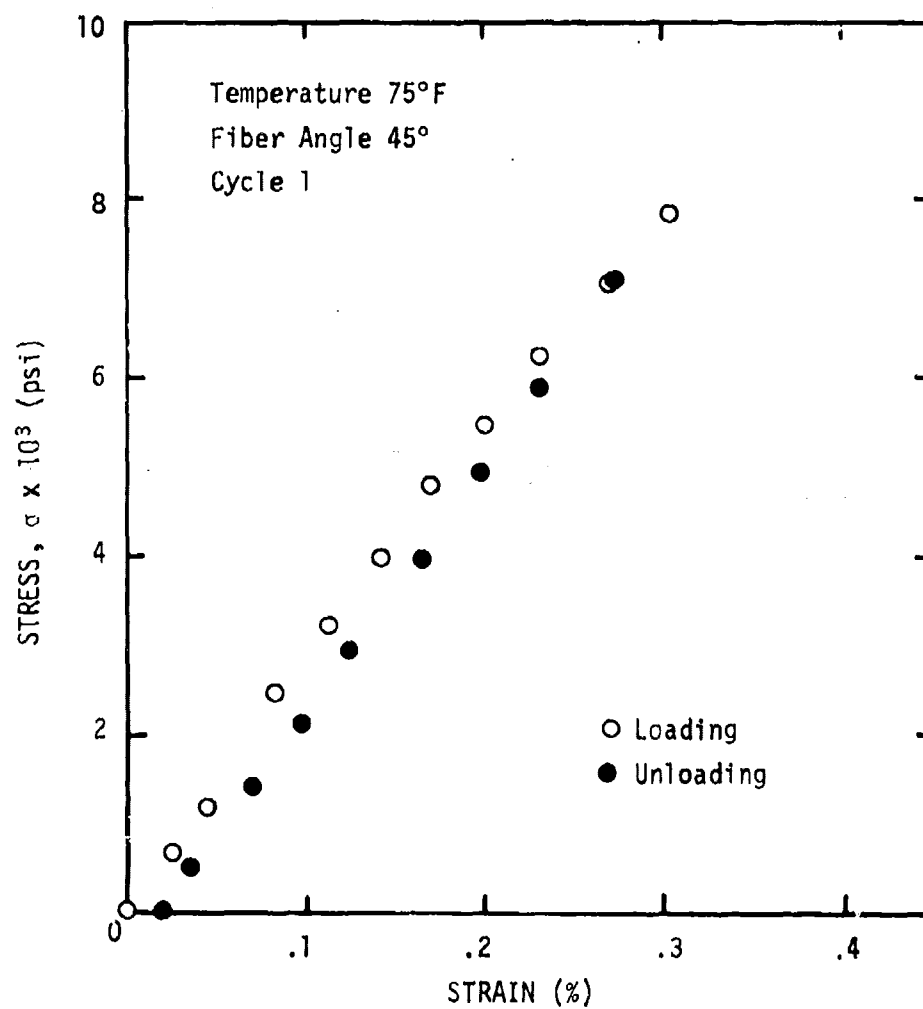


Figure 139. Effect of cyclic loading on 45° tensile coupon;  $\sigma_{\max} = 8000$  psi (Cycle 1).

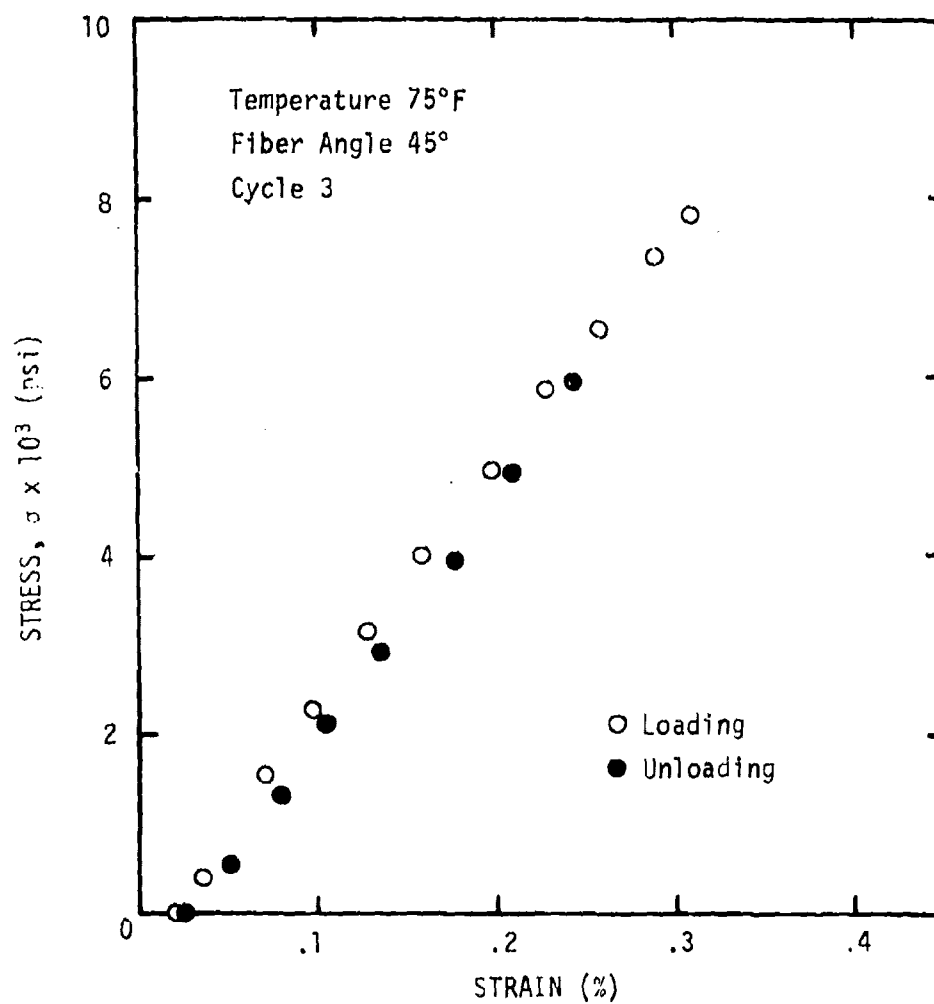


Figure 140. Effect of cyclic loading on 45° tensile coupon;  $\sigma_{\max} = 8000$  psi (Cycle 3).

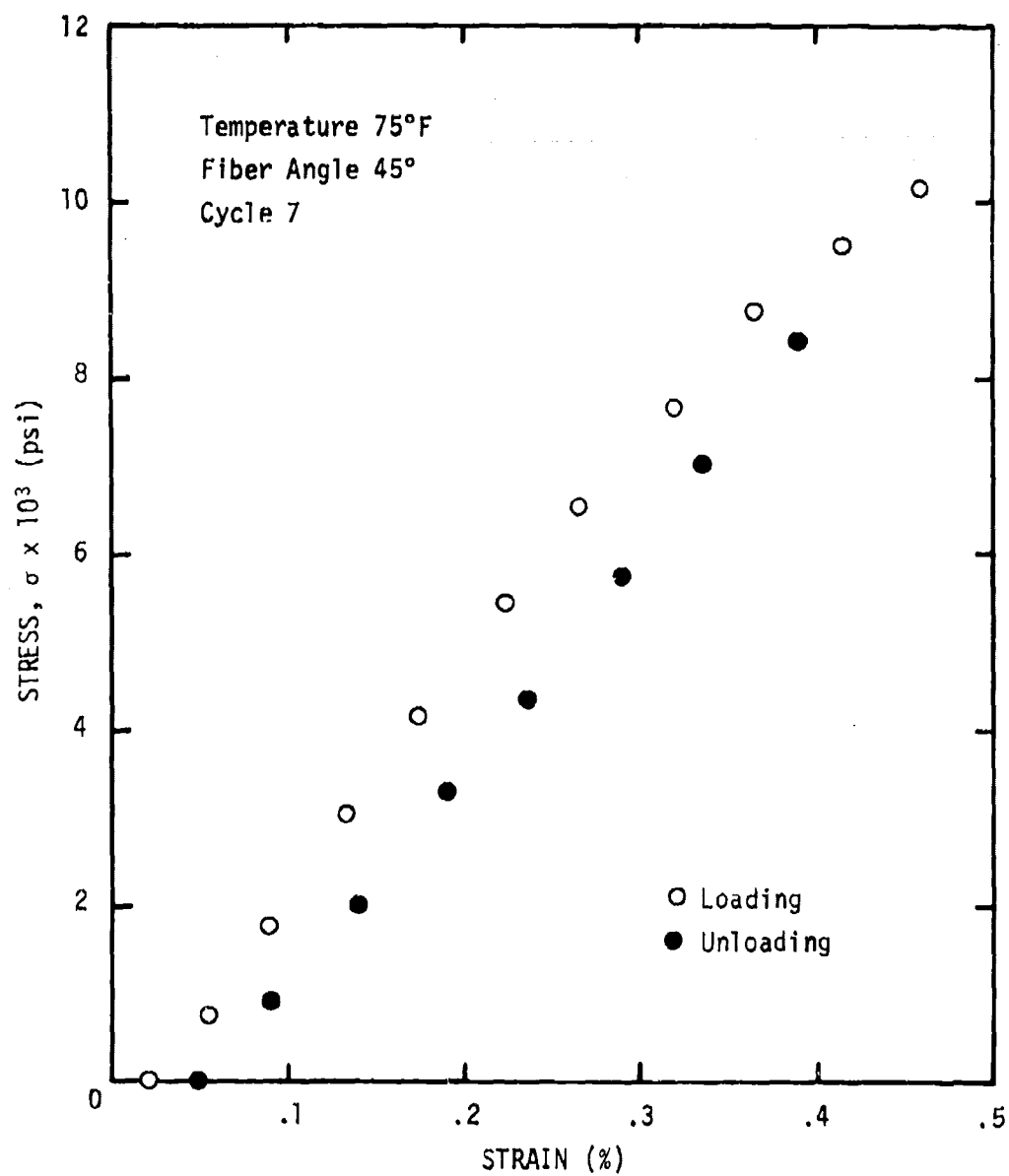


Figure 141. Effect of cyclic loading on 45° tensile coupon;  $\sigma_{\max} = 10,000$  psi (Cycle 7).

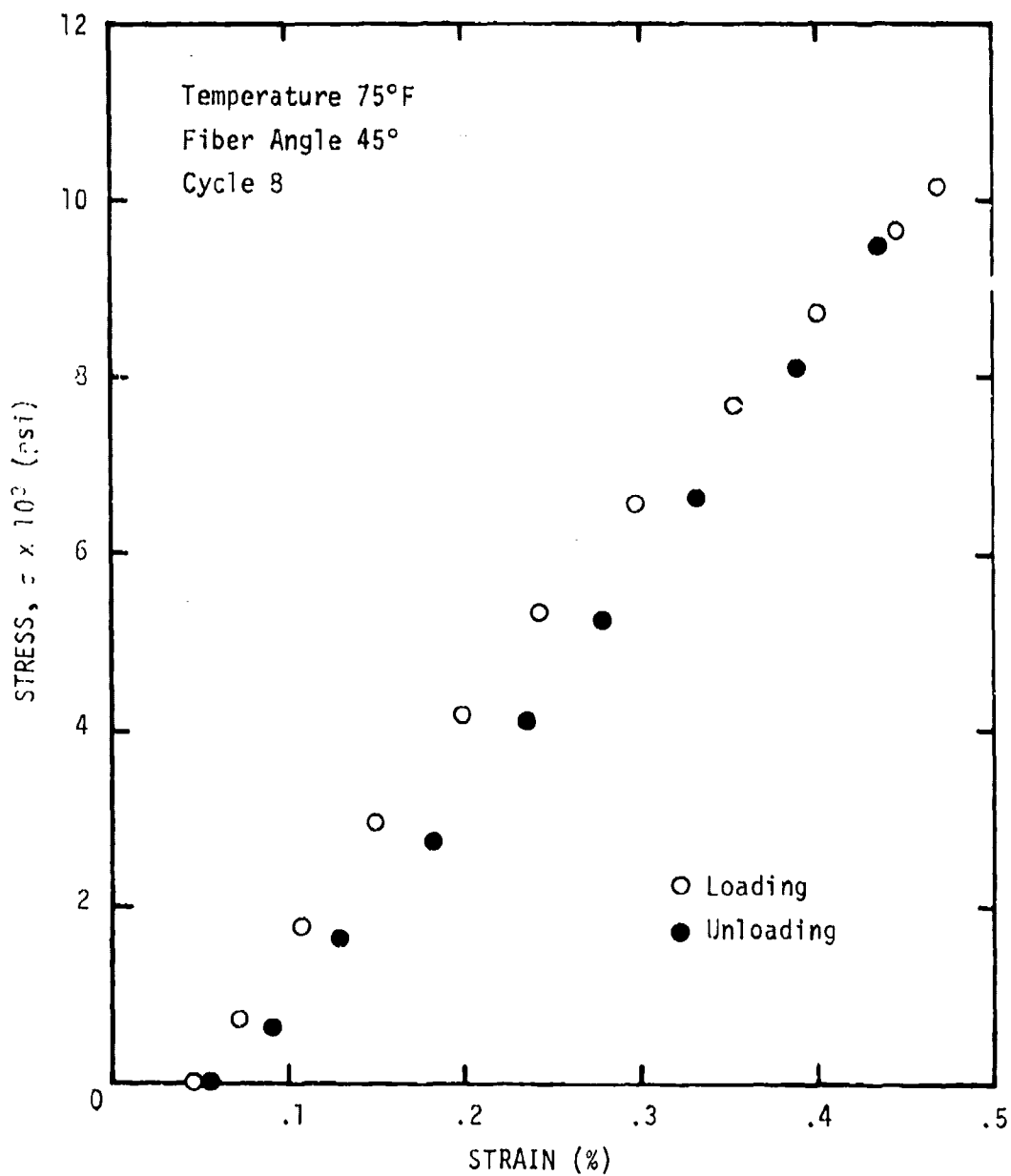


Figure 142. Effect of cyclic loading on 45° tensile coupon;  $\sigma_{\max} = 10,000$  psi (Cycle 8).

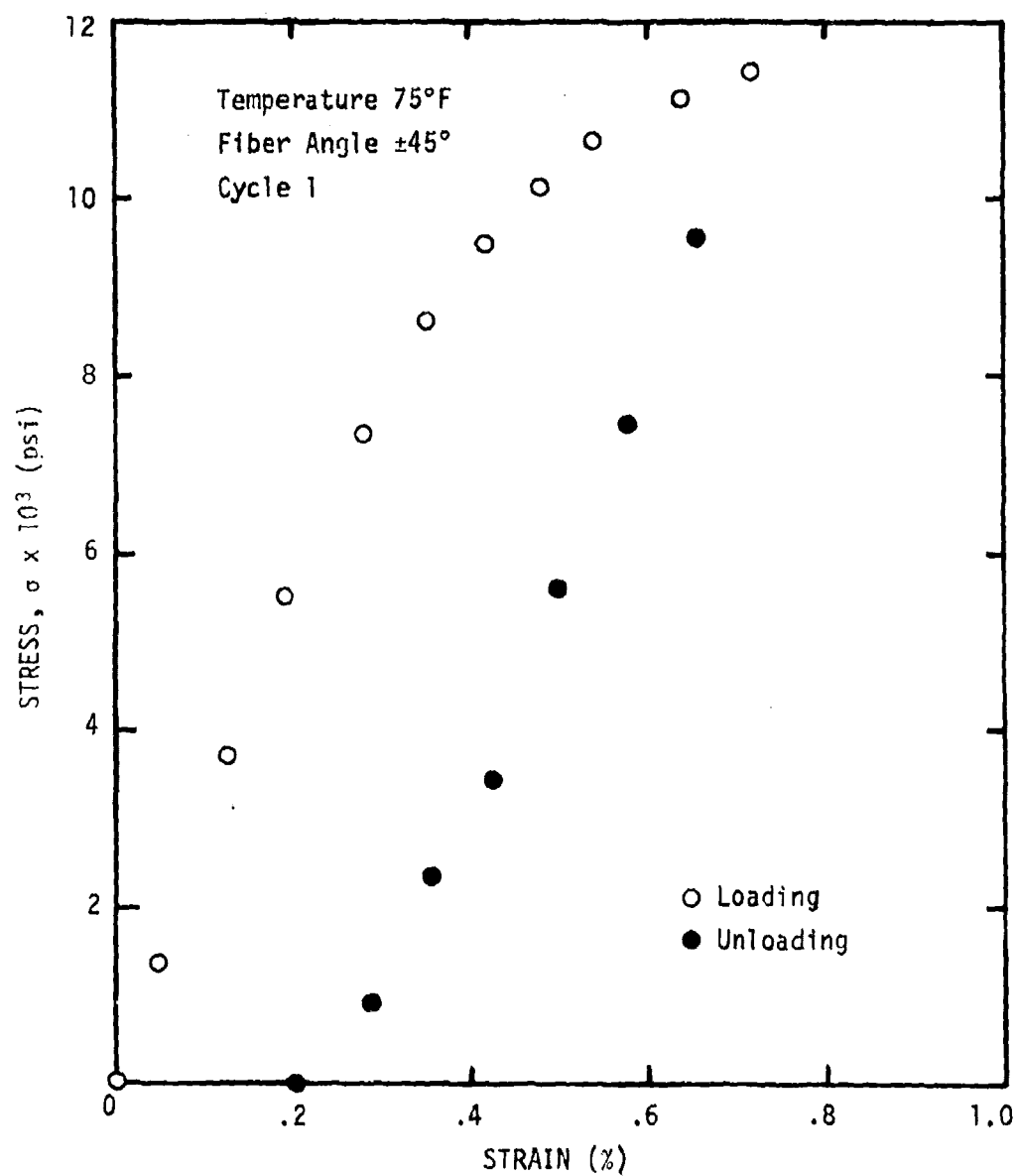


Figure 143. Effect of cyclic loading on  $\pm 45^\circ$  tensile coupon;  $\sigma_{\max} = 11,500$  psi (Cycle 1).



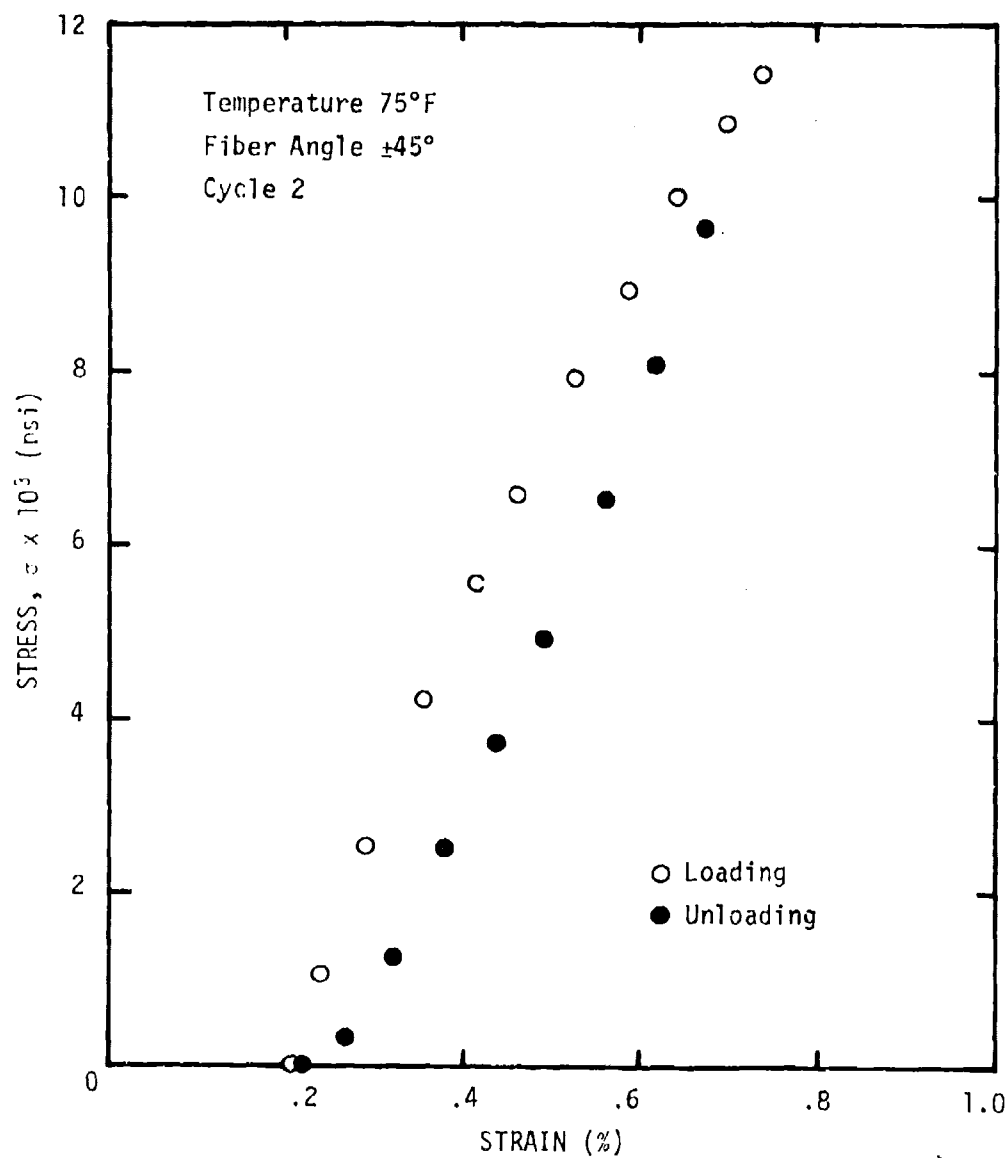


Figure 144. Effect of cyclic loading on  $\pm 45^\circ$  tensile coupon;  $\sigma_{\max} = 11,500$  psi (Cycle 2).

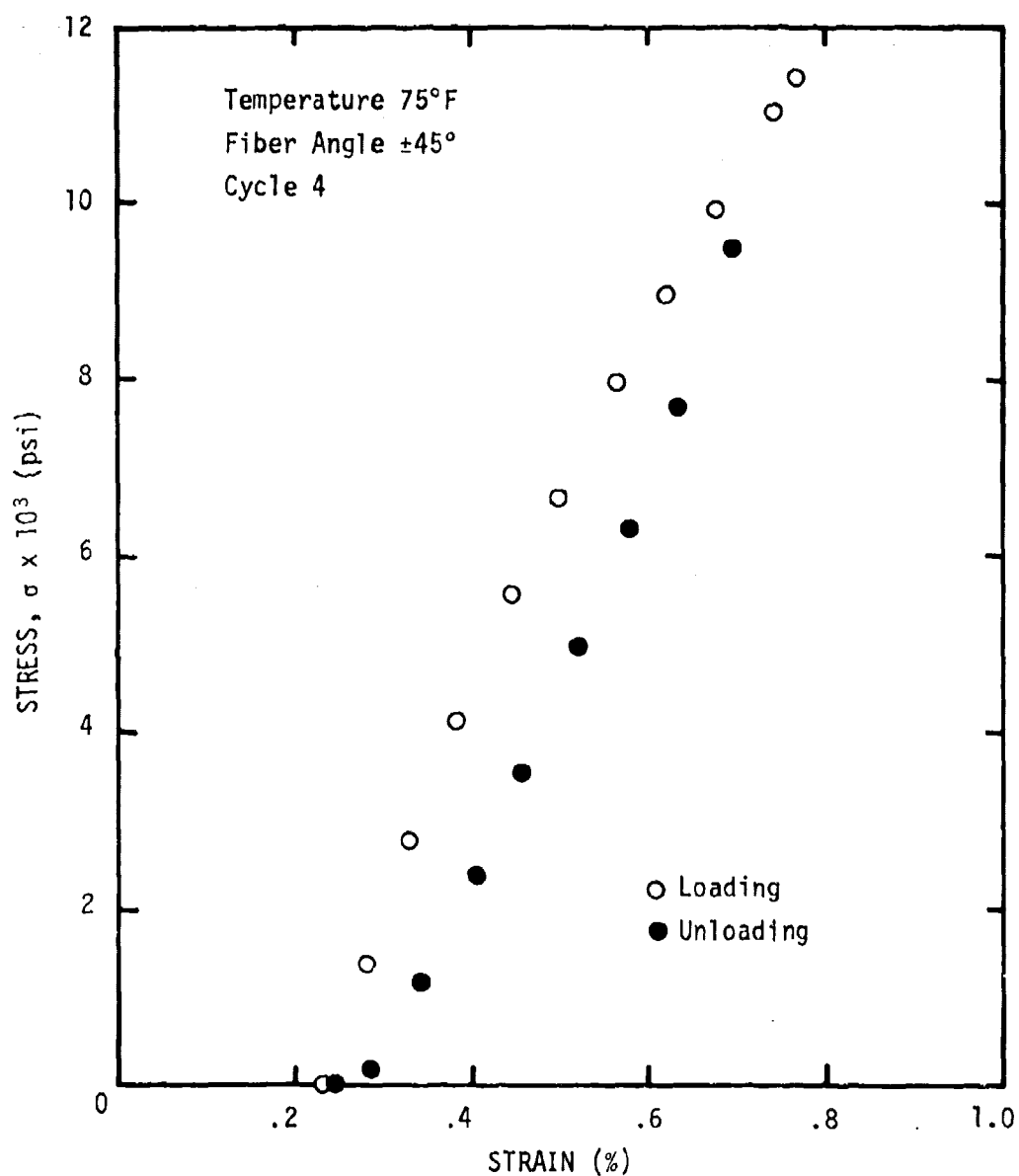


Figure 145. Effect of cyclic loading on  $\pm 45^\circ$  tensile coupon;  $\sigma_{\max} = 11,500$  psi (Cycle 4).

Close comparison of the second and fourth cycle indicates that the shape of the hysteresis loop is almost identical, differing only by a slight shift along the strain axis. This corresponds primarily to slight changes in the initial compliance with the net creep compliance remaining essentially constant. Crack growth, therefore, appears to be arrested very rapidly in the  $\pm 45^\circ$  glass/epoxy even at extremely high stress levels. Figure 146 was drawn to graphically show the effect of the cycle-to-cycle damage by superimposing the first and fourth cycle stress-strain curves.

The last series of tests, on sample AP45.11, was conducted to show the effects of multiple cycles at low stress levels followed by cycles at sequentially higher stress levels until ultimate fracture. Figure 147 shows that cyclic response up to 5000 psi stress levels are relatively insensitive to cycle-to-cycle damage. Figures 148 and 149 represent the first and third cycle at a maximum stress of 12,000 psi. However, the sample has already been subjected to fourteen previous cycles at stress levels below 12,000 psi as noted in Table 16. Let us now compare the behavior of the two samples, AP45.11 and AP45.18. Remember that one sample has seen only four high stress levels near 11,500 psi while the other sample has seen a total of seventeen cycles, all at or above 5000 psi. The last cycles for the two samples, conducted at or near a maximum stress of 11,500 psi, are shown superimposed in Figure 150. Except for slight differences in maximum stress level and sample

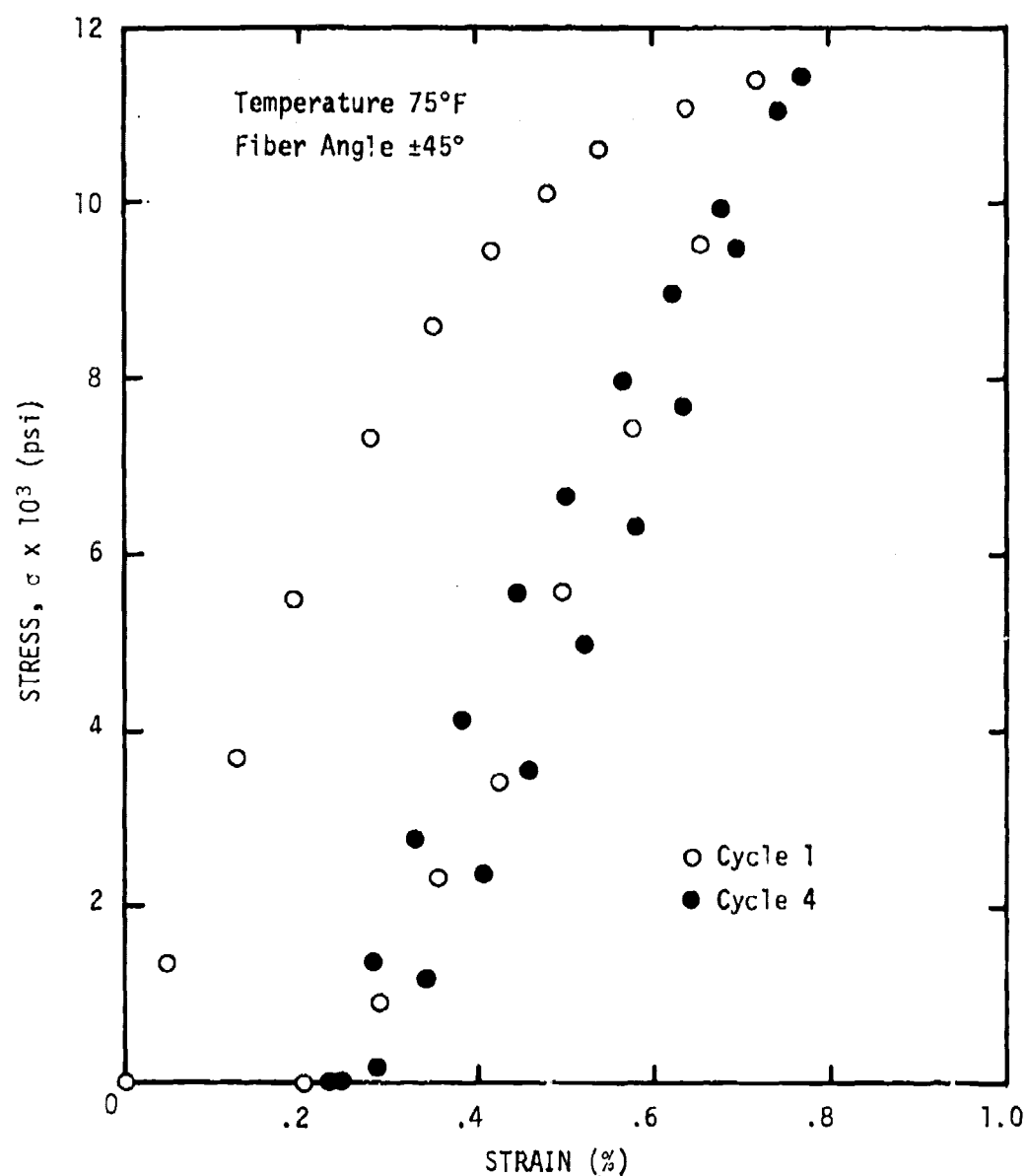


Figure 146. Superimposed stress-strain curves (Figures 143 and 145) showing cycle-to-cycle damage effects on  $\pm 45^\circ$  glass/epoxy tensile coupon ( $\sigma_{\max} = 11,500$  psi).

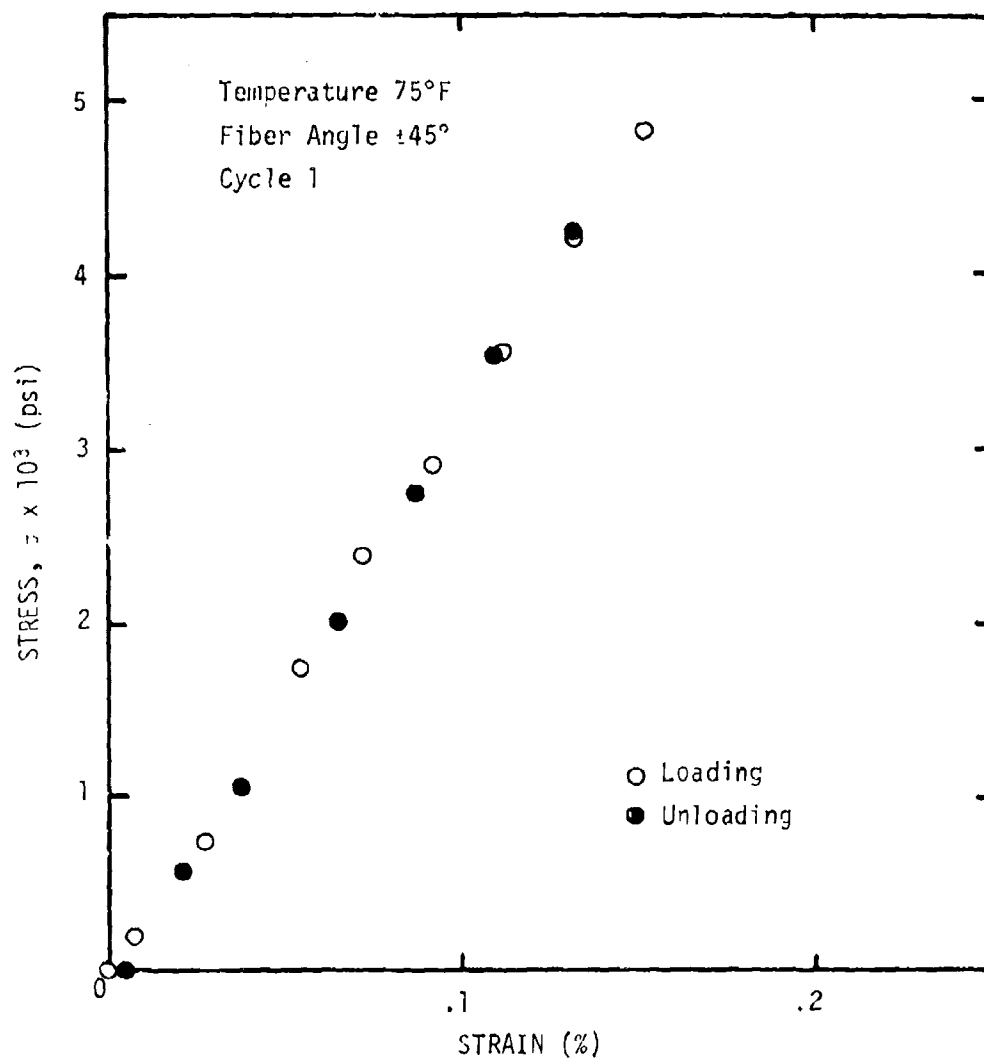


Figure 147. Effect of cyclic loading on  $\pm 45^\circ$  tensile coupon;  $\sigma_{\max} = 5000$  psi (Cycle 1).

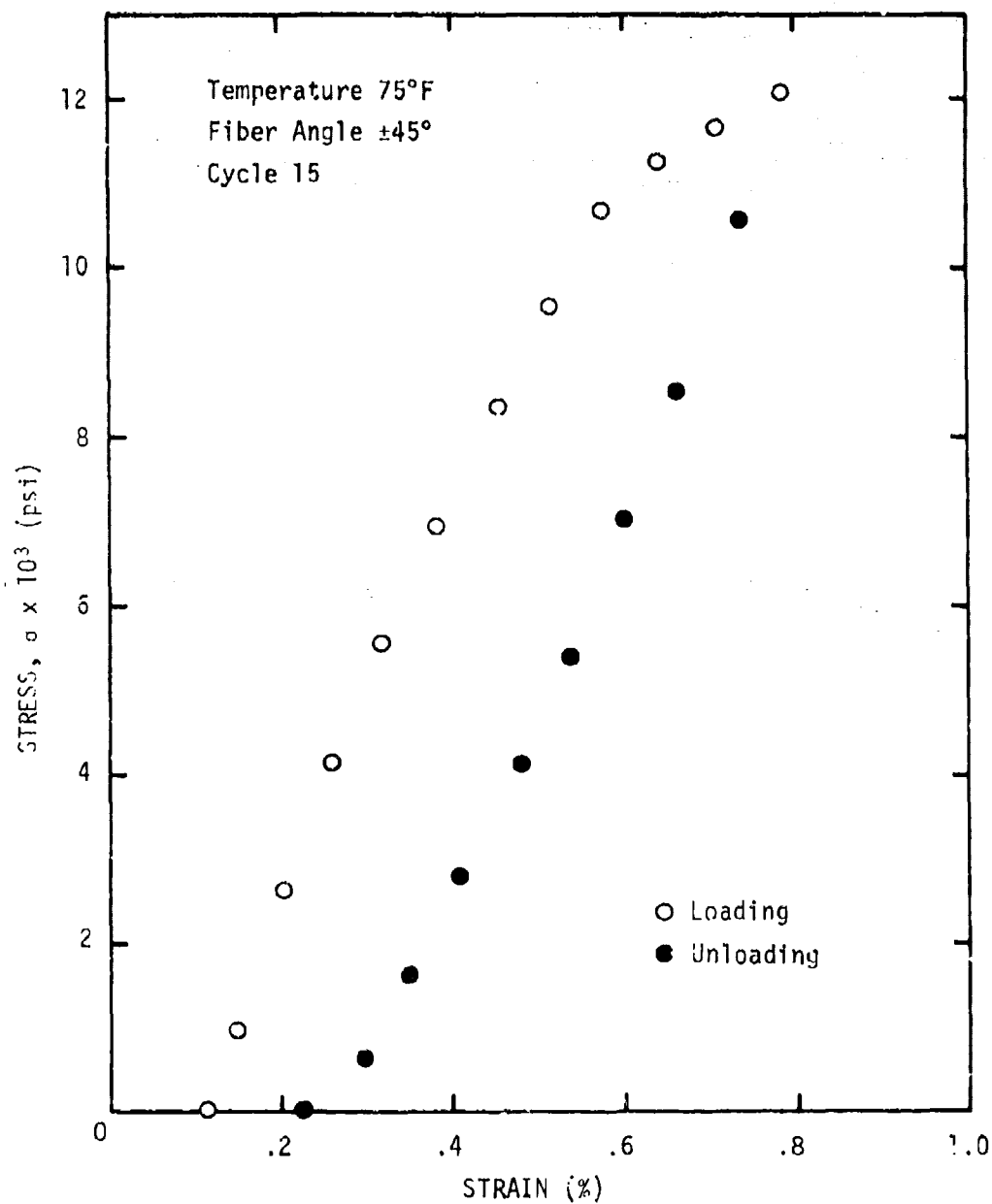


Figure 148. Effect of cyclic loading on  $\pm 45^\circ$  tensile coupon;  $\sigma_{\max} = 12,000$  psi (Cycle 15).

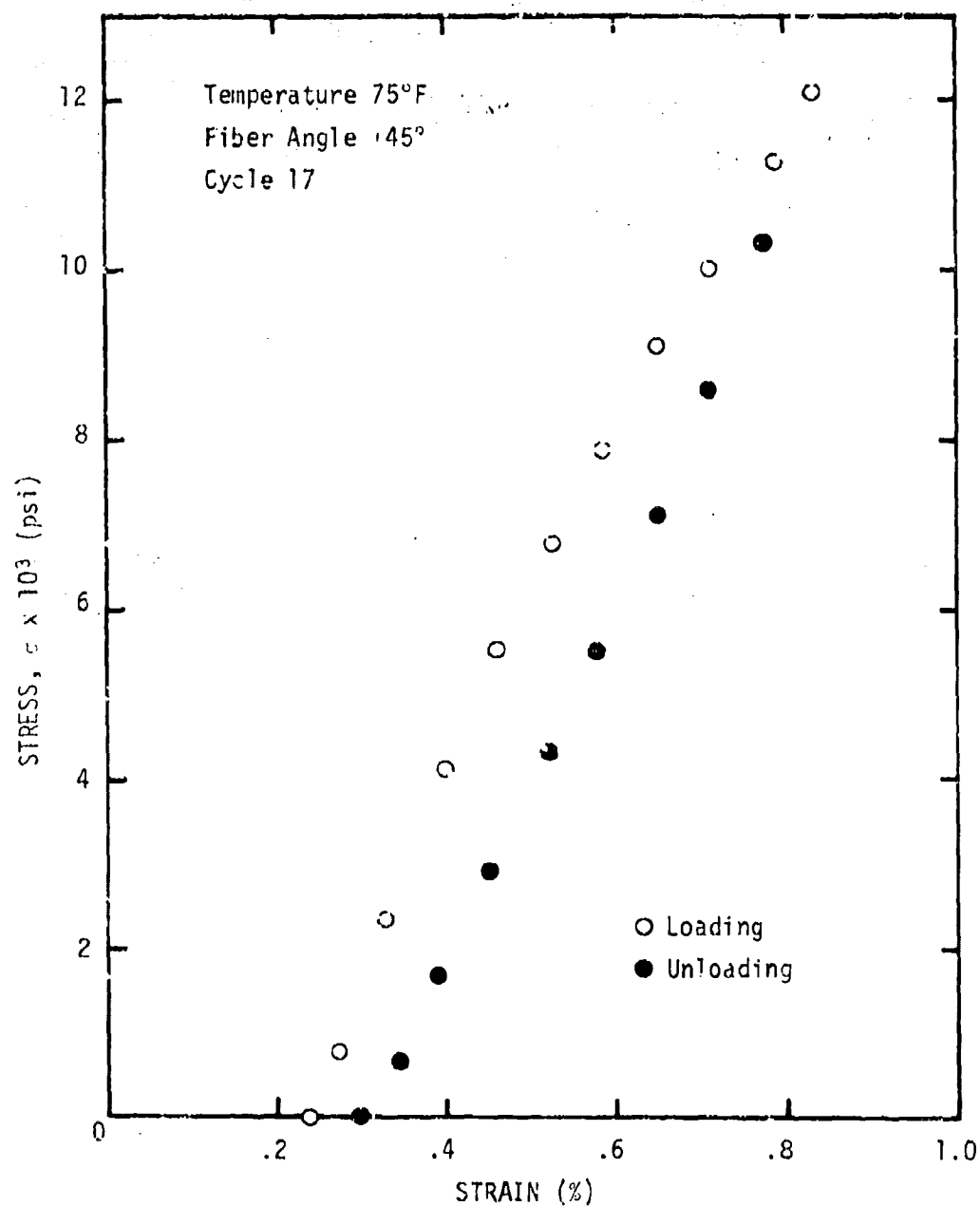


Figure 149. Effect of cyclic loading on  $\pm 45^\circ$  tensile coupon;  $\sigma_{\max} = 12,000$  psi (Cycle 17).

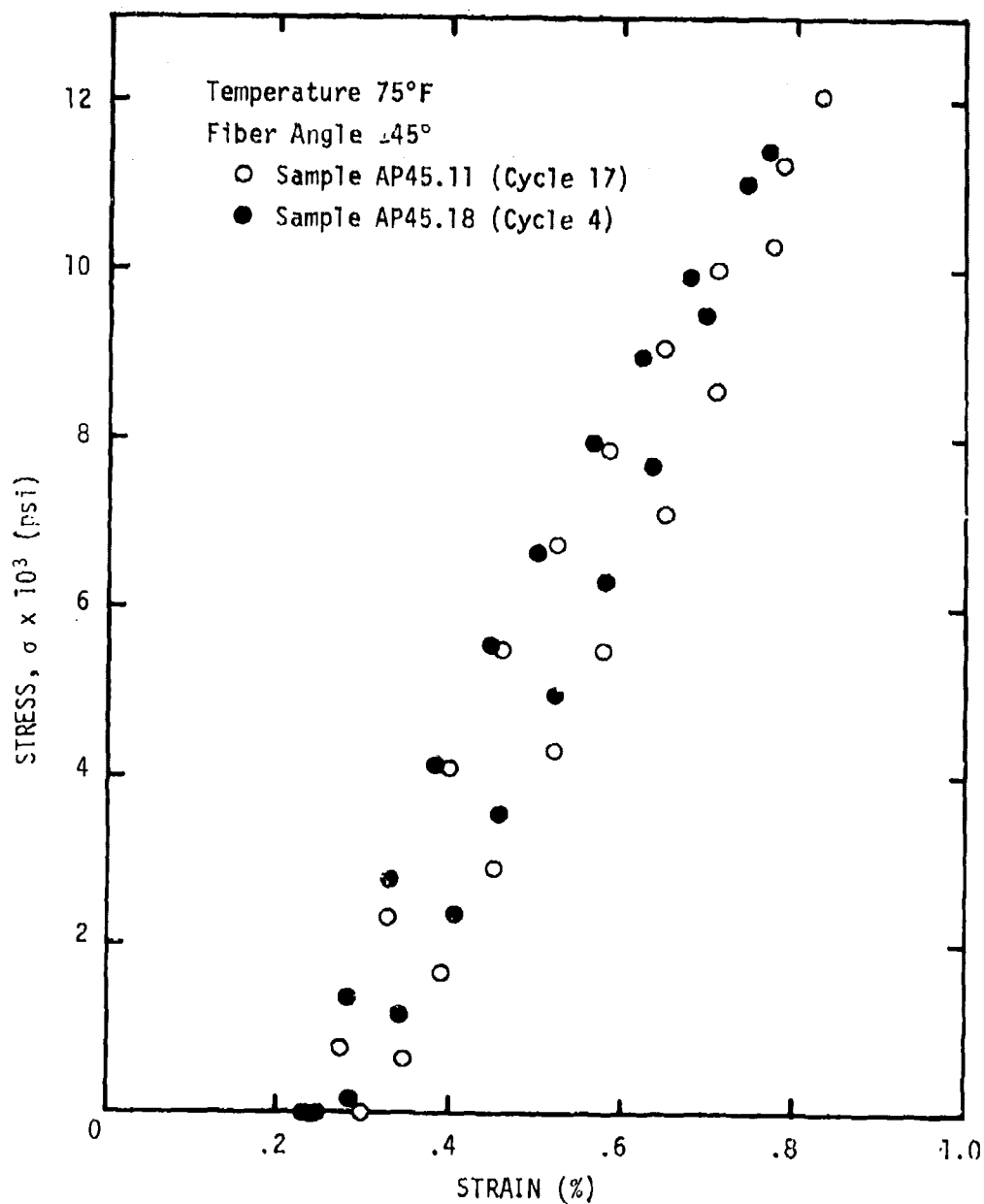


Figure 150. Damage effects as a result of different stress histories. Open circle (○) represents multiple cycles at sequentially higher stresses; closed circle (●) data represents several cycles at  $\sigma_{\max} = 11,500$  psi.



variability the stress-strain behavior appears to be a function of the maximum stress level achieved during the sample's history. This behavior is typical of that reported by Farris et al. [20, 128] for propellant materials although he proposed the dependence on strain using Lebesgue norms. Schapery [12, 20] has proposed the use of Lebesgue norms of stress rather than strain to model this behavior. The functional behavior of the Lebesgue norm is such that it appears ideally suited for the representation of the response seen in Figure 150; namely, that it is more influenced by the maximum stress level than the entire past history.

#### Four-Point Beam Bending Tests

The previously described uniaxial tensile tests were conducted in order to investigate the time and temperature dependence of the glass/epoxy composites. The studies have shown that the glass/epoxy materials are nonlinearly viscoelastic, in part, probably due to the time-dependent development and growth of microscopic cracks. The degree of nonlinearity depends on many factors which already have been cited, namely, stress level, temperature, fiber angle, etc. However, the uniaxial tensile test differs significantly from a bending test in that a strain gradient exists across the thickness which is not present in the former one (neglecting a slight amount of bending due to grip effects). This series of tests was conducted in order to determine the effect of the strain

gradient on material nonlinearity.

### Creep and Recovery Tests

The results from some of the creep and recovery tests are shown in Figures 151 through 155. The data is plotted as usual for the previous tests of this type except that strain,  $\epsilon$ , rather than compliance is used. Strictly speaking, we cannot assume that all of the layers of the beam are within the linear viscoelastic range, particularly in the presence of a significant strain gradient. Neglecting this situation for the moment, we shall study some of the behavior shown by the beam tests. Remember also that the strain used here represents the output from the strain gage on the tension side of the beam.

In general, the beam cycle-to-cycle variation behaves in the same manner as the tensile coupons, showing a disproportionate change between the first and second loading cycles. It has been found that the strain can be represented by the power law in time with  $n = 0.19$  for all of the tests, regardless of fiber angle or stress level, with excellent correlation at each cycle.

With the behavior pattern now established, let us assume that the stress,  $\sigma$ , at the outer fibers of the beam is still within the linear range. Consequently, we can use the flexure formula

$$\sigma = \frac{Mc}{I} \quad (153)$$

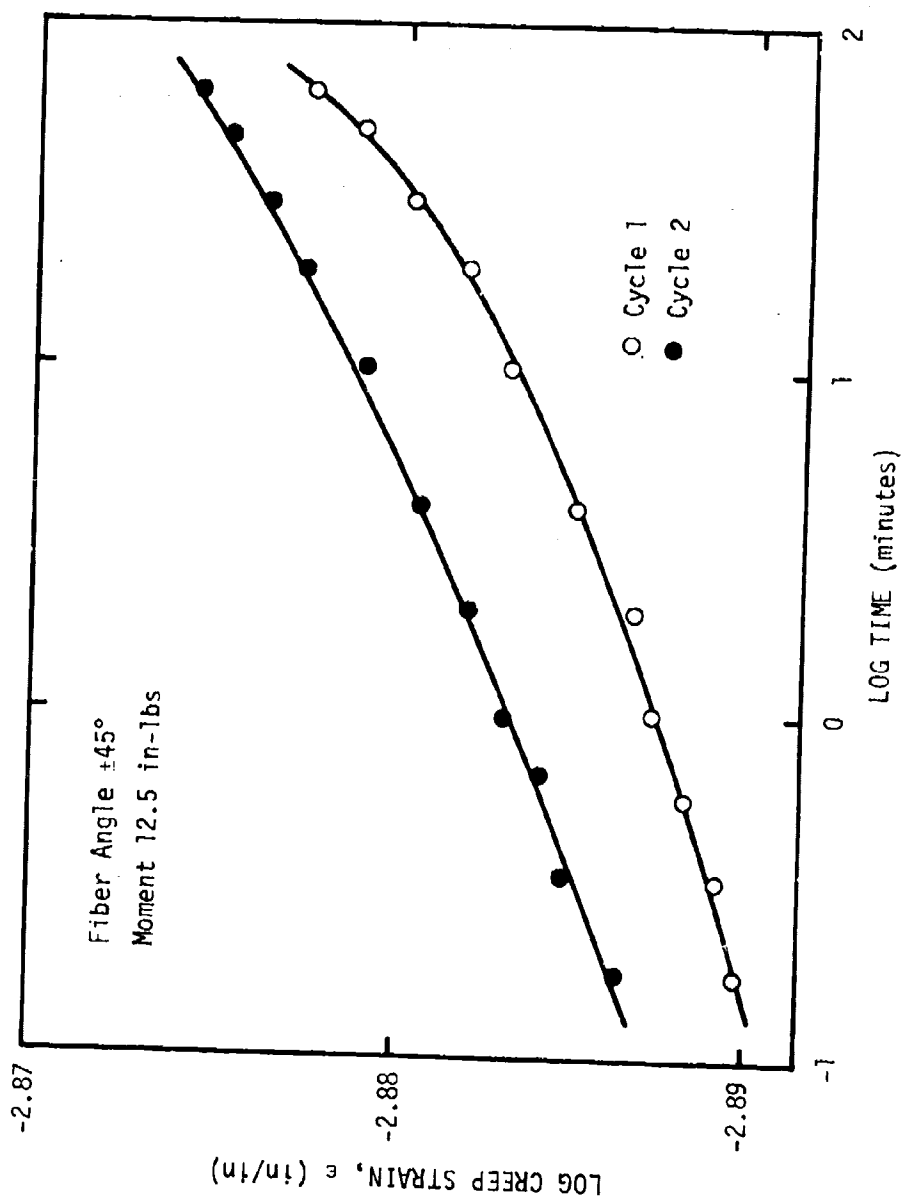


Figure 151. Effect of multiple cycling on the creep strain for the  $\pm 45^\circ$  glass/epoxy beam for a 12.5 in-lb applied moment ( $T = 75^\circ\text{F}$ ).

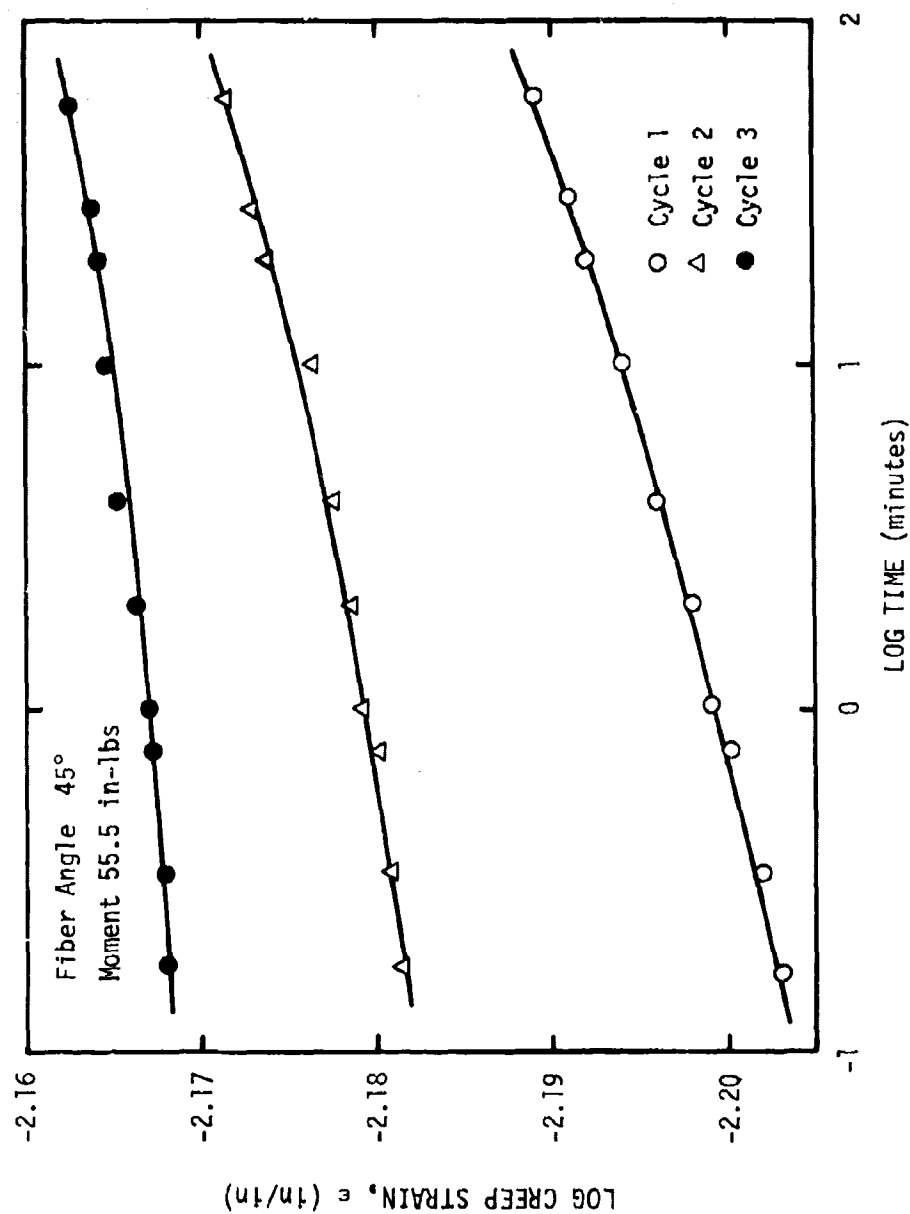


Figure 152. Effect of multiple cycling on the creep strain for the 45° glass/epoxy beam for a 55.5 in-lb applied moment ( $T = 75^\circ\text{F}$ ).

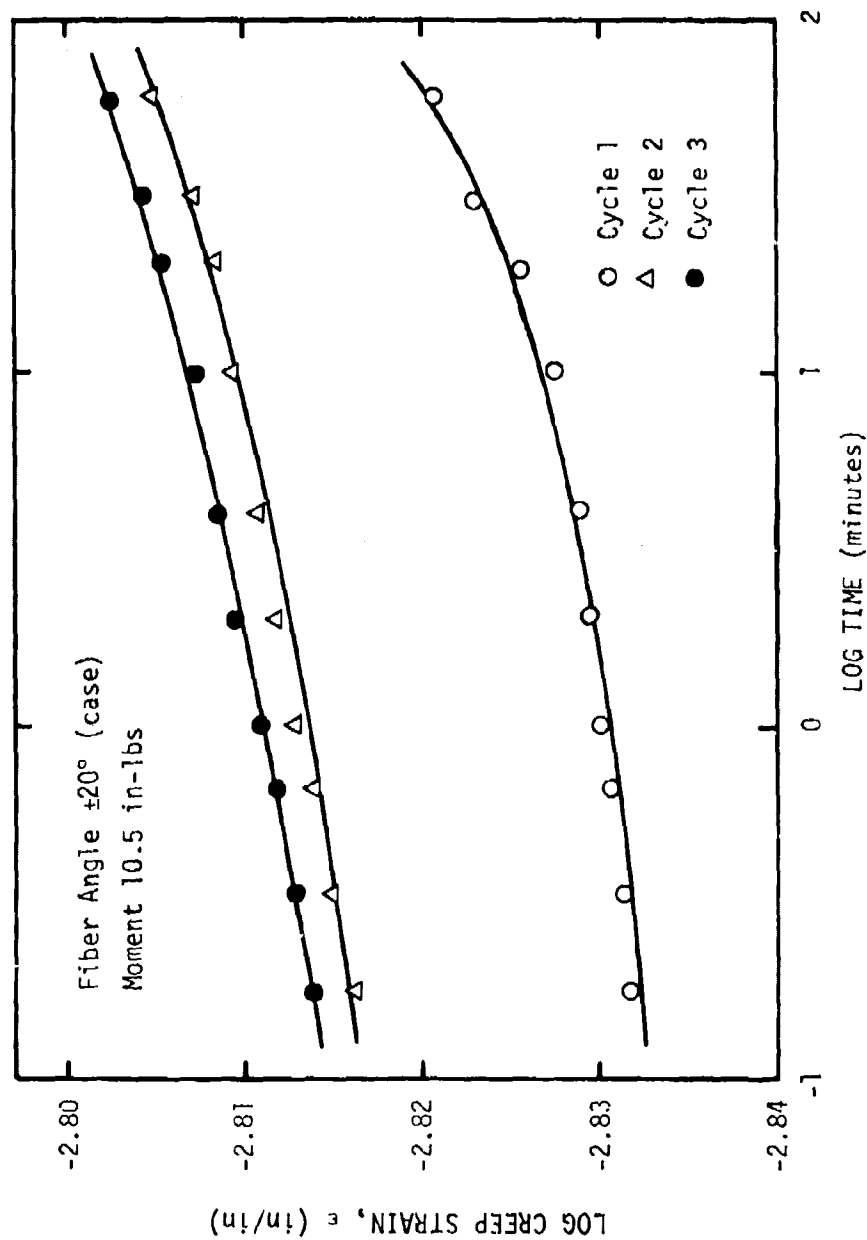


Figure 153. Effect of multiple cycling on the creep strain for the  $\pm 20^\circ$  case material beam for a 10.5 in-lb applied moment ( $T = 75^\circ\text{F}$ ).

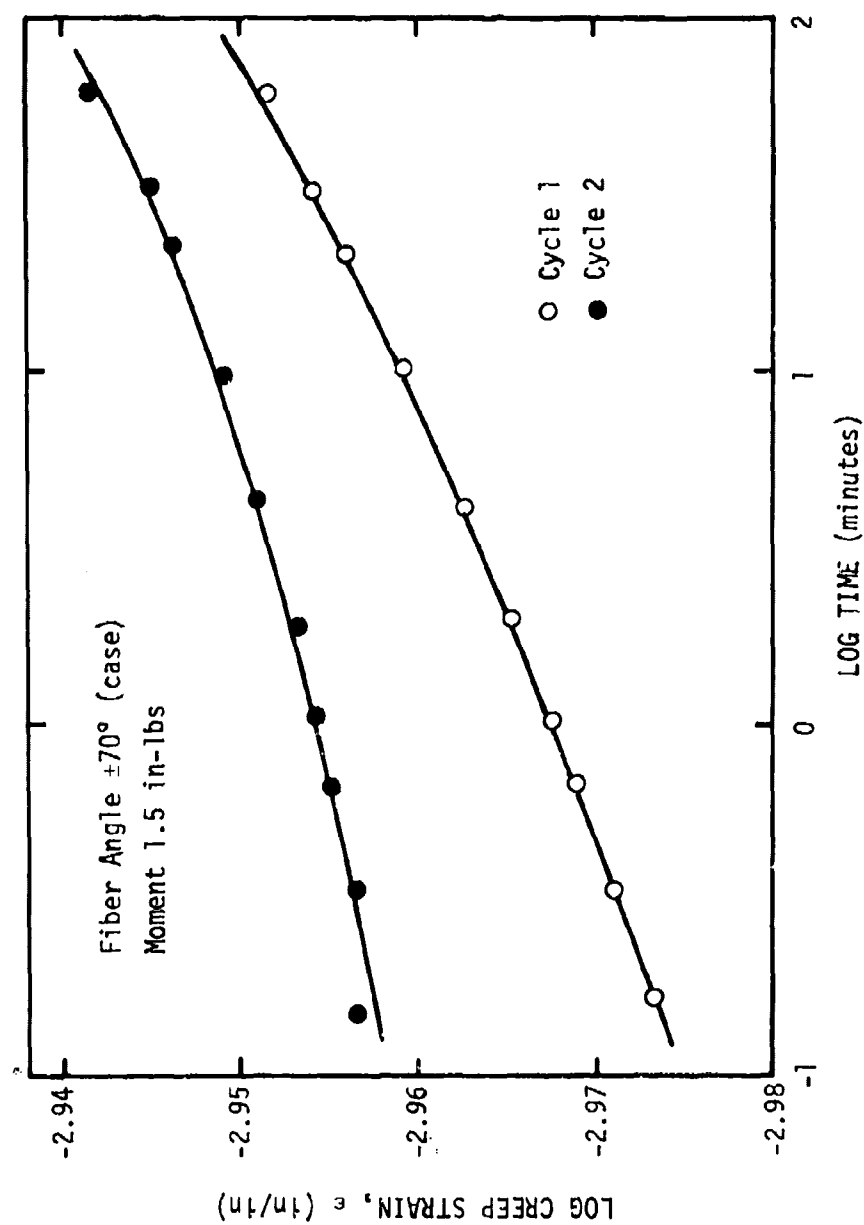


Figure 154. Effect of multiple cycling on the creep strain for the  $\pm 70^\circ$  case material beam for a 1.5 in-lb applied moment ( $T = 75^\circ F$ ).

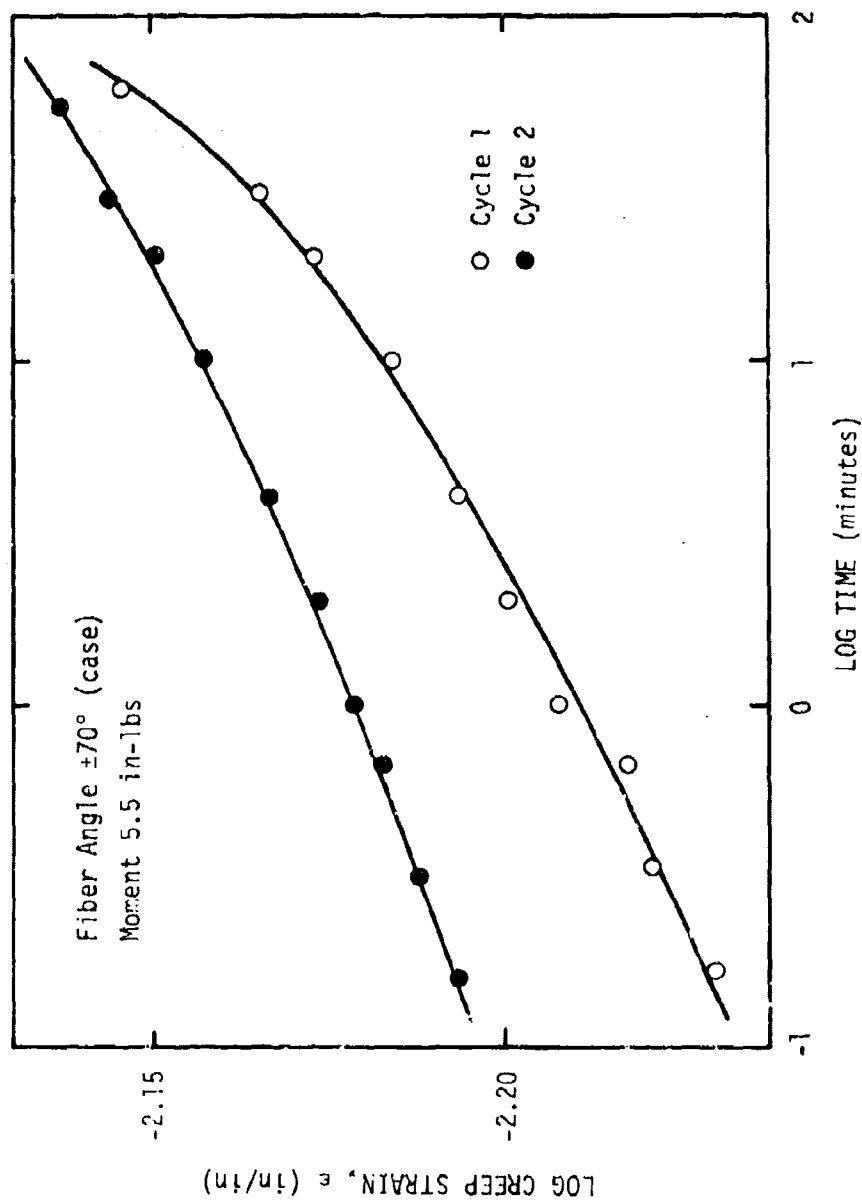


Figure 155. Effect of multiple cycling on the creep strain for the  $\pm 70^\circ$  case material beam for a 5.5 in-lb applied moment ( $T = 75^\circ\text{F}$ ).

where  $M$  is the applied moment (constant for the creep test),  $I$  is the moment of inertia of the cross-section about the neutral axis and  $C$  is the distance from the neutral axis to the outer fibers. We are, of course, assuming linear elastic (viscoelastic) behavior although at the higher stress levels this will not be true. The creep compliance may be determined in the same manner as we have in the previous tests for the constant applied stress. Table 17 shows the effective creep compliance found by using the stress defined by Equation (153).

The initial creep compliance for the  $\pm 45^\circ$  glass/epoxy tested at the bending moment of 12.5 in-lbs is within 2% of the value shown in Table 12 for the uniaxial creep and recovery tests. The creep coefficient which does not change significantly with subsequent cycles also agrees with the uniaxial data. At the higher stress levels (moments) the  $\pm 45^\circ$  glass/epoxy exhibits the softening effect seen in the tensile coupons.

Consider the  $\pm 20^\circ$  glass/epoxy case material next. Earlier we predicted the angular dependence of the linear viscoelastic creep compliances in Figure 111. From the predicted curve based on third cycle data we find the initial compliance to be  $0.187 \times 10^{-6}(\text{psi}^{-1})$ , which agrees reasonably well with the beam values. The agreement is within 4.5% after correcting for the difference in the fiber volume fraction using the experimental data in Table 3. The third cycle beam data was corrected by simply multiplying by the ratio of



Table 17. Beam Creep and Recovery Compliances  
Using Flexure Formula, Equation (153)

Fiber Angle ( $\theta$ )	Moment (in-lbs)	Cycle	Compliance ( $\times 10^{-6}$ )(psi $^{-1}$ )
$\pm 45$	12.5	1	.3000 + .0083t $^{.19}$
		2	.3027 + .0085t $^{.19}$
$\pm 45$	55.5	1	.3980 + .0097t $^{.19}$
		2	.4205 + .0067t $^{.19}$
		3	.4371 + .0032t $^{.19}$
$\pm 20$ (case)	10.5	1	.1657 + .0024t $^{.19}$
		2	.1724 + .0025t $^{.19}$
		3	.1735 + .0028t $^{.19}$
$\pm 70$ (case)	1.5	1	.7694 + .0291t $^{.19}$
		2	.7753 + .0295t $^{.19}$
		3	.8085 + .0212t $^{.19}$
$\pm 70$ (case)	5.5	1	1.5060 + .1899t $^{.19}$
		2	1.6394 + .1758t $^{.19}$

the fiber volume fractions, i.e., 0.635/0.616, to obtain an estimated initial creep compliance.

The  $\pm 70^\circ$  case material does not show good agreement with the initial linear creep compliance of  $0.348 \times 10^{-6}$  ( $\text{psi}^{-1}$ ) which would be predicted from Figure 111, being in error by about 100%. However, the strain which exists at the outer fibers of the beam is on the same order of magnitude as the earlier tensile creep and recovery tests which had also indicated significant softening. It is not unreasonable to expect severe softening after one considers the prior history of the case as a result of hydrotesting.

There is a considerable number of surface cracks present in the case materials as a result of the earlier hydrotesting (see Figure 5b). The material is, therefore, much softer in the dome region of the motor case where the fiber angles are greater ( $\pm 20^\circ$  to  $\pm 70^\circ$ ) than in the barrel section ( $0^\circ/90^\circ$ ).

Another interesting feature is the relative growth in the initial creep compliance for the  $\pm 70^\circ$  glass/epoxy with each cycle while the creep coefficient remains virtually unchanged from cycle to cycle. The normal stress is considerably higher than the shear stress for the  $\pm 70^\circ$  fiber angle and would tend to explain this behavior in terms of sudden (rather than slow) crack growth.

#### Constant Crosshead Rate Tests

The constant crosshead rate tests were conducted to study the

effects of multiple cycling under controlled displacement conditions. The test has been observed to be essentially a constant strain rate test for the sample stiffnesses encountered. A plot of the outer fiber strain (tension side) as a function of time indicates that the strain rate is constant (Figure 156). The effects of multiple cycles and applied moment are shown in Figures 157 through 168 for fiber angles of  $\pm 45^\circ$ ,  $0/90^\circ$ ,  $\pm 20^\circ$  (case) and  $\pm 70^\circ$  (case).

In all situations the strain shown is the output from the tension side of the beam. Additional tests conducted using strain gages on both sides of the beam (tension and compression) indicated the compression strain to be less than the tension strain for the  $0^\circ/90^\circ$  specimen. The neutral axis, therefore, shifts slightly toward the compression side as a result of the softening which occurs under tension in the  $90^\circ$  layers. This effect, however, appears to be very small and is not considered further in the analysis of the beam data.

Therefore, by assuming that the strain is a linear function of the distance from the centroidal axis (plane sections remain plane) and that the effect of tension and compression stresses is the same, we can predict the linear and nonlinear behavior by using the data from constant crosshead rate tensile stress-strain curves. The moment-strain response for the  $\pm 45^\circ$  glass/epoxy beam was predicted by using the constant rate-to-failure stress-strain curve

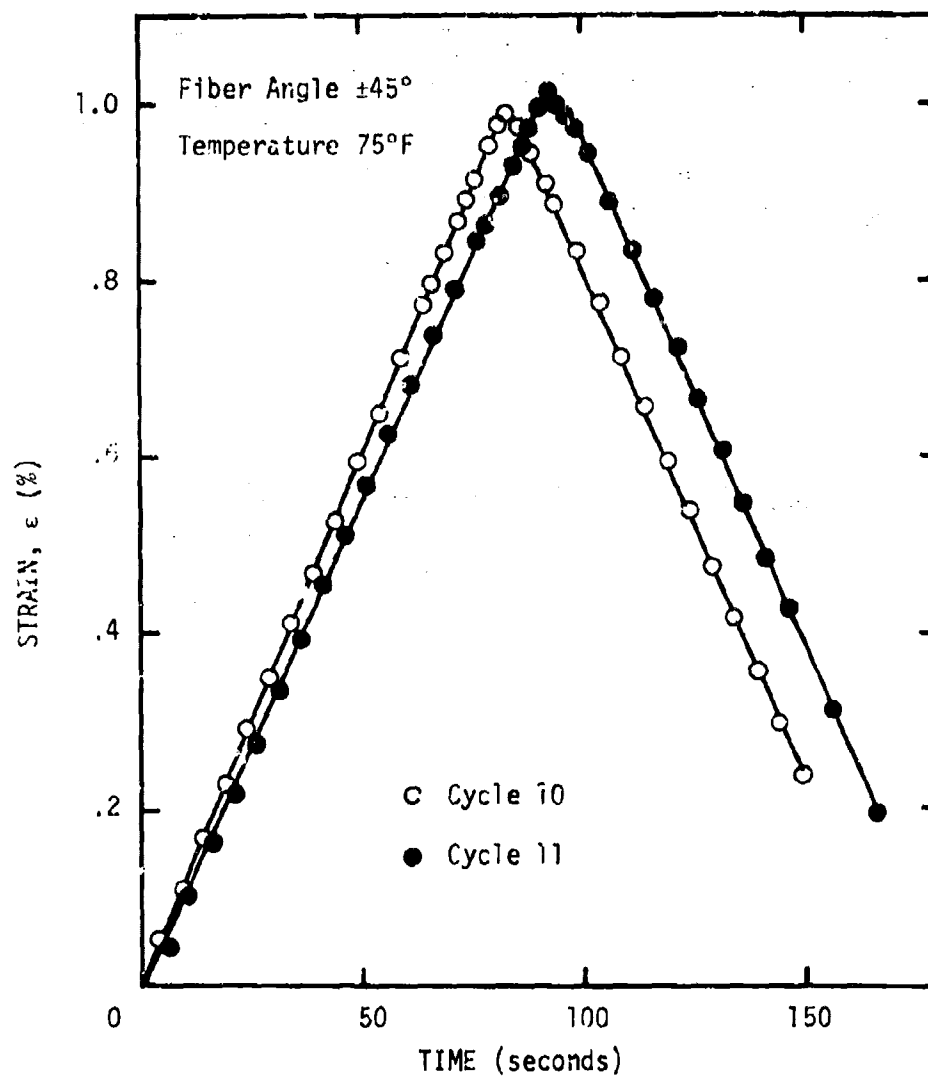


Figure 156. Typical loading strain history for constant crosshead rate beam test.

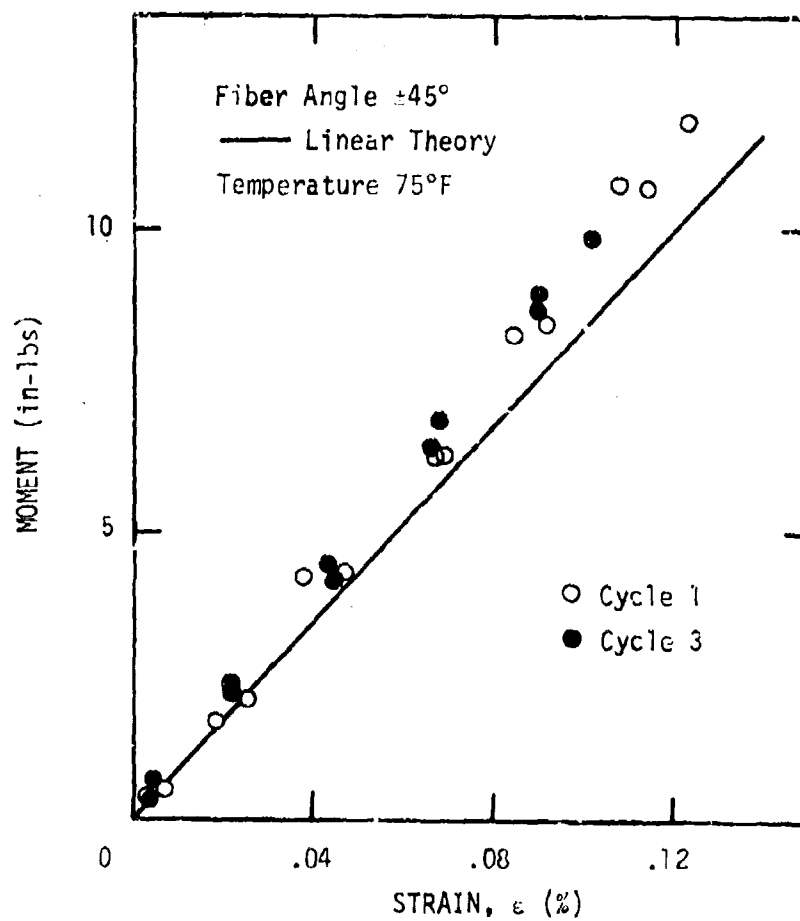


Figure 157. Effect of cyclic loading of  $\pm 45^\circ$  glass/epoxy beam (Cycles 1 and 3).

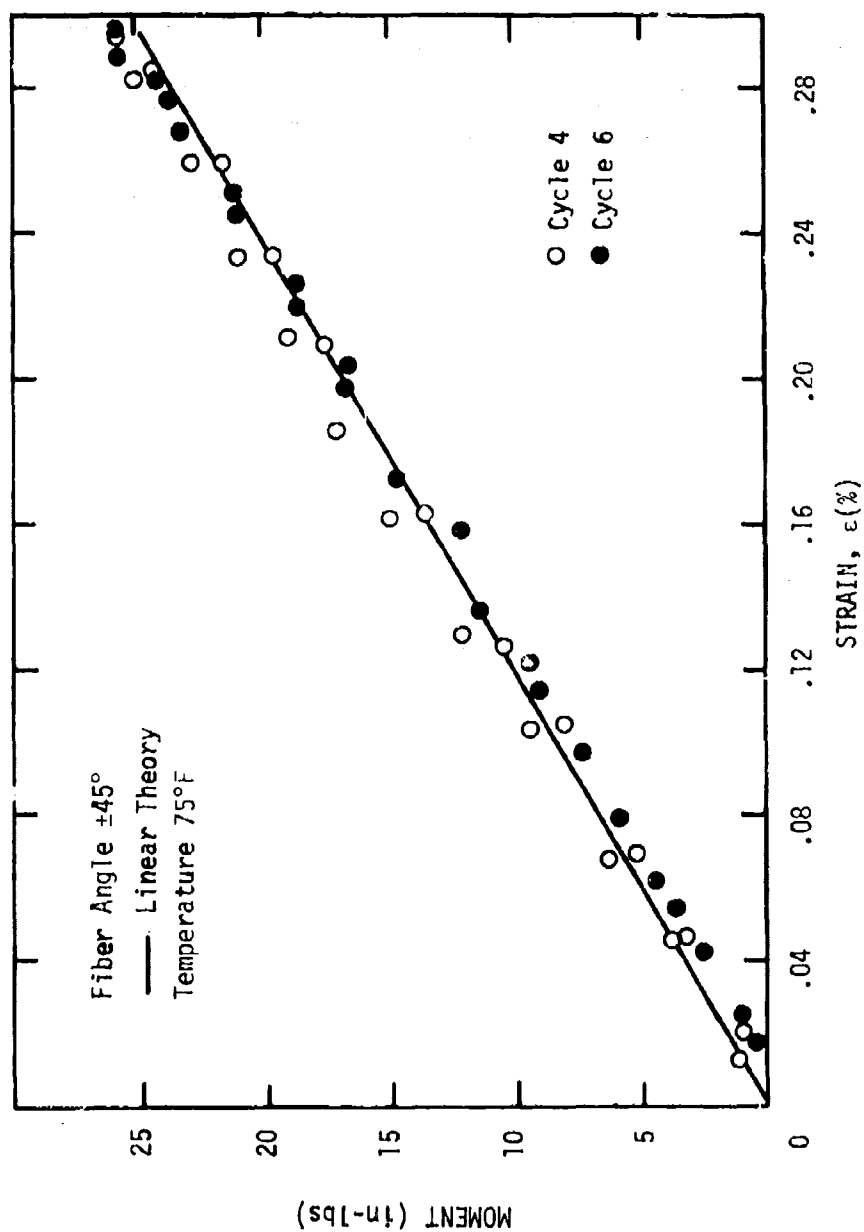


Figure 158. Effect of cyclic loading of  $\pm 45^\circ$  glass/epoxy beam (Cycles 4 and 6).

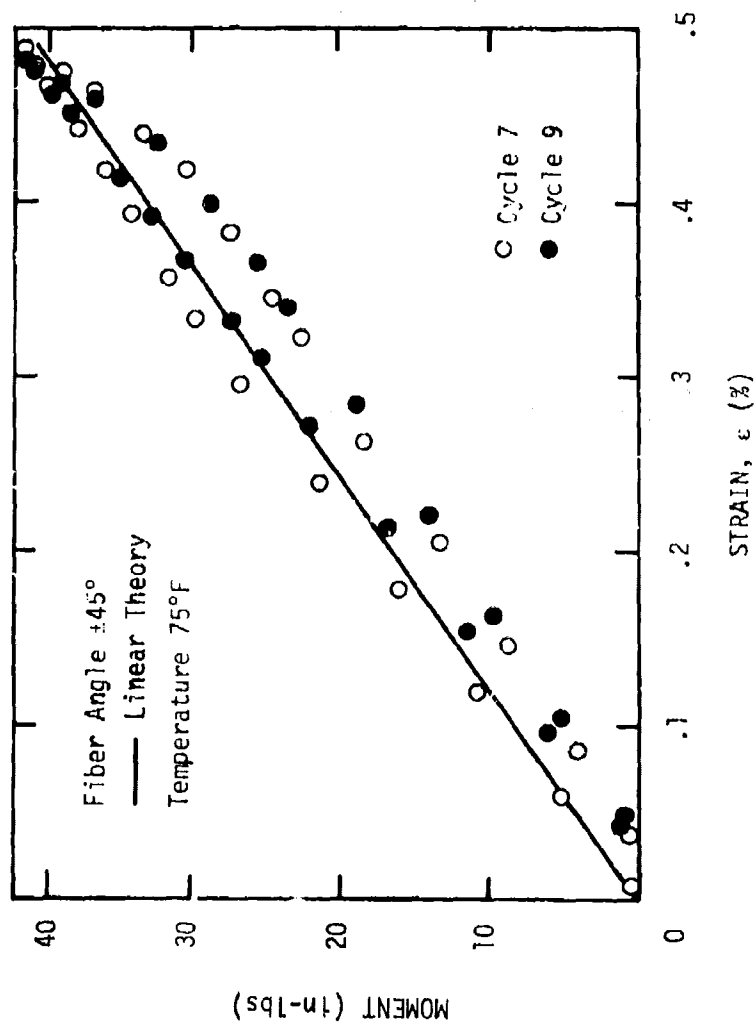


Figure 159. Effect of cyclic loading of  $\pm 45^\circ$  glass/epoxy beam (Cycles 7 and 9).

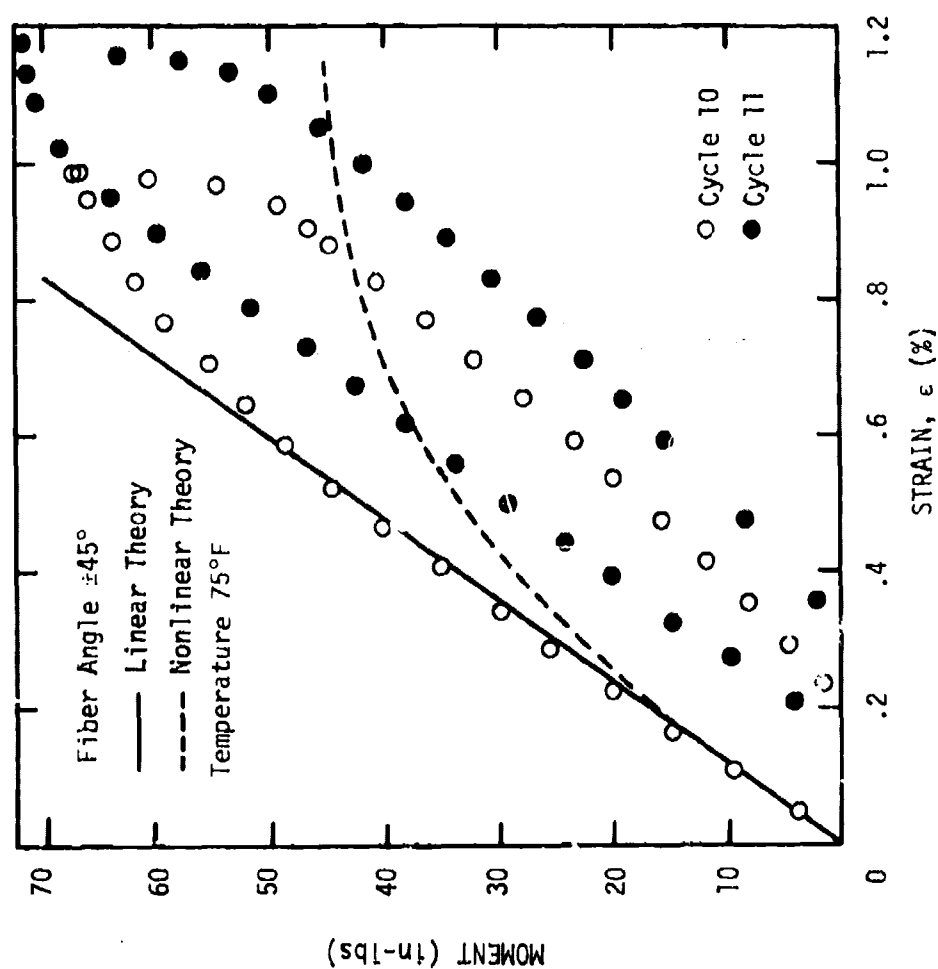


Figure 160. Effect of cyclic loading of  $\pm 45^\circ$  glass/epoxy beam (Cycles 10 and 11).



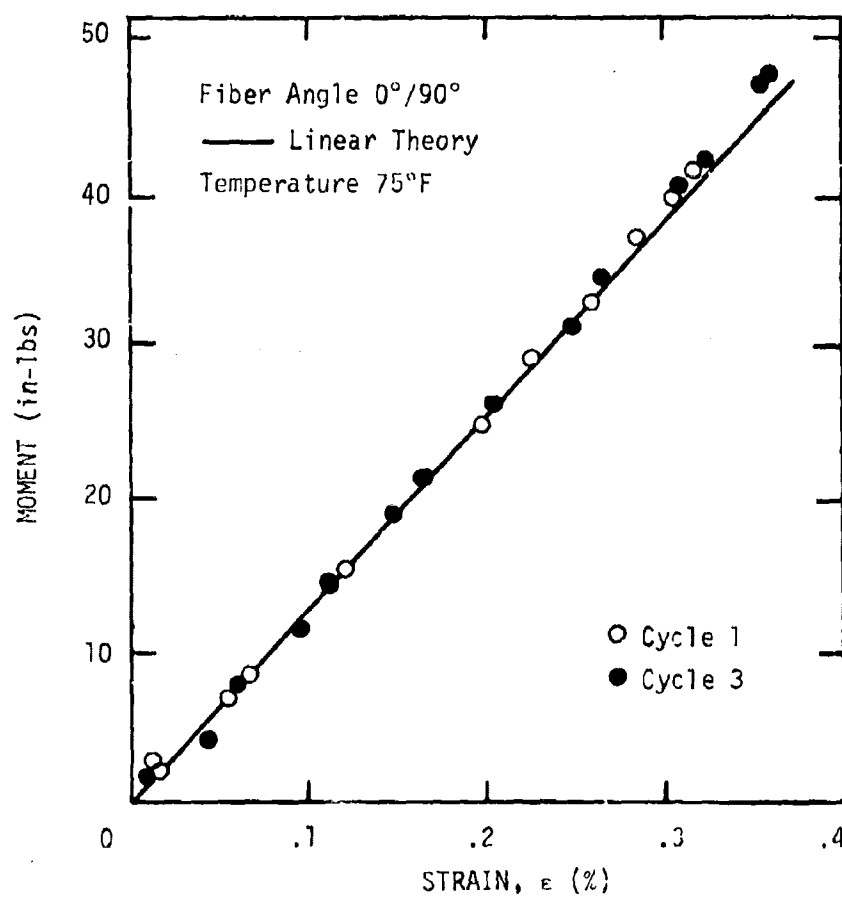


Figure 161. Effect of cyclic loading of 0°/90° glass/epoxy beam (Cycles 1 and 3).

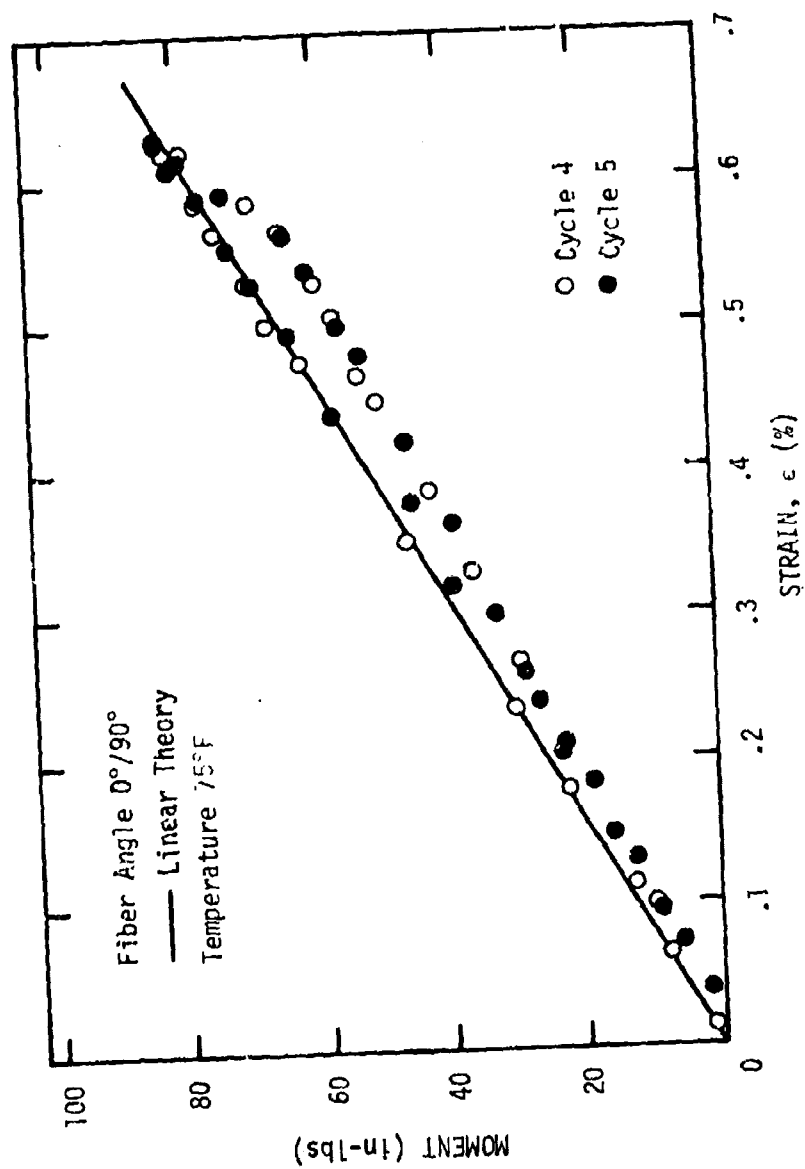


Figure 162. Effect of cyclic loading of 0°/90° glass/epoxy beam (Cycles 4 and 5).

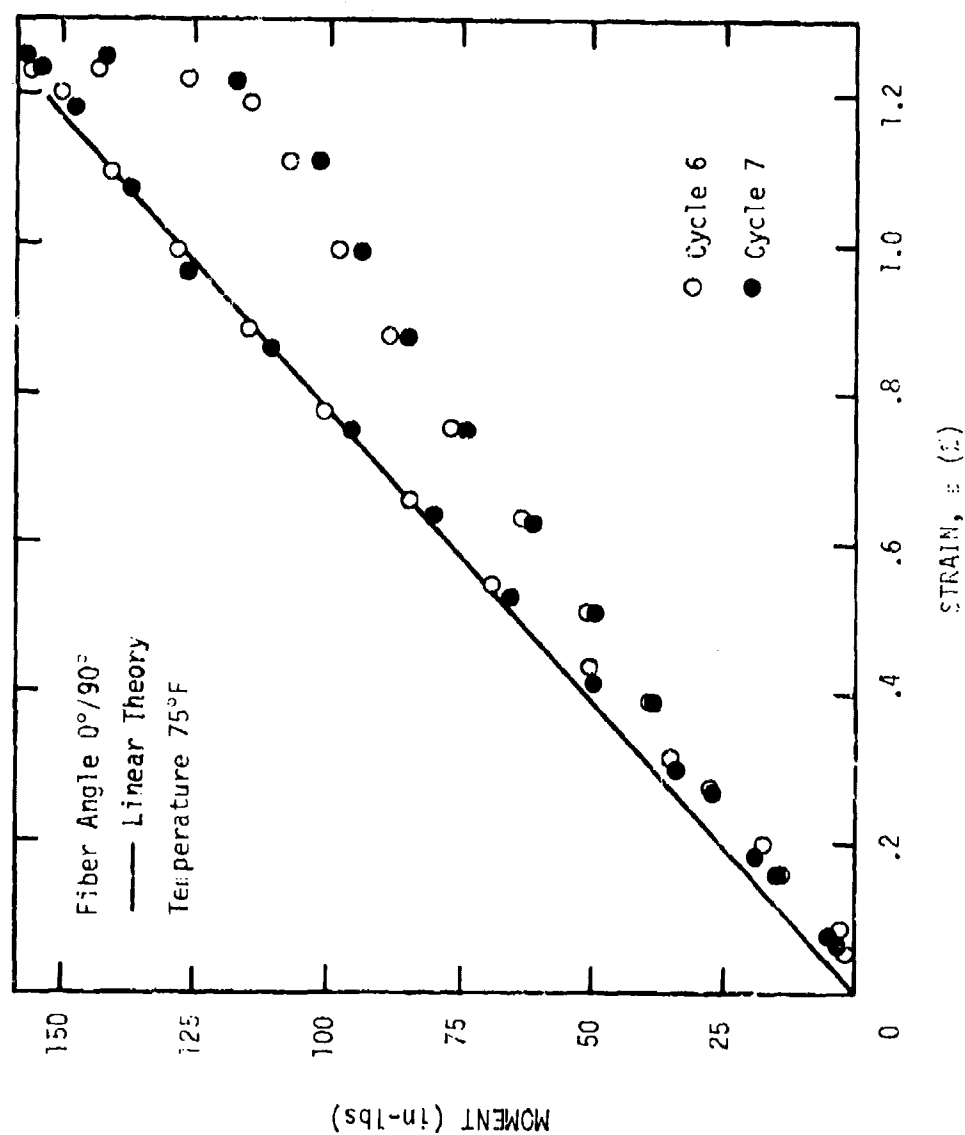


Figure 163. Effect of cyclic loading of 0°/90° glass/epoxy beam (Cycles 6 and 7).

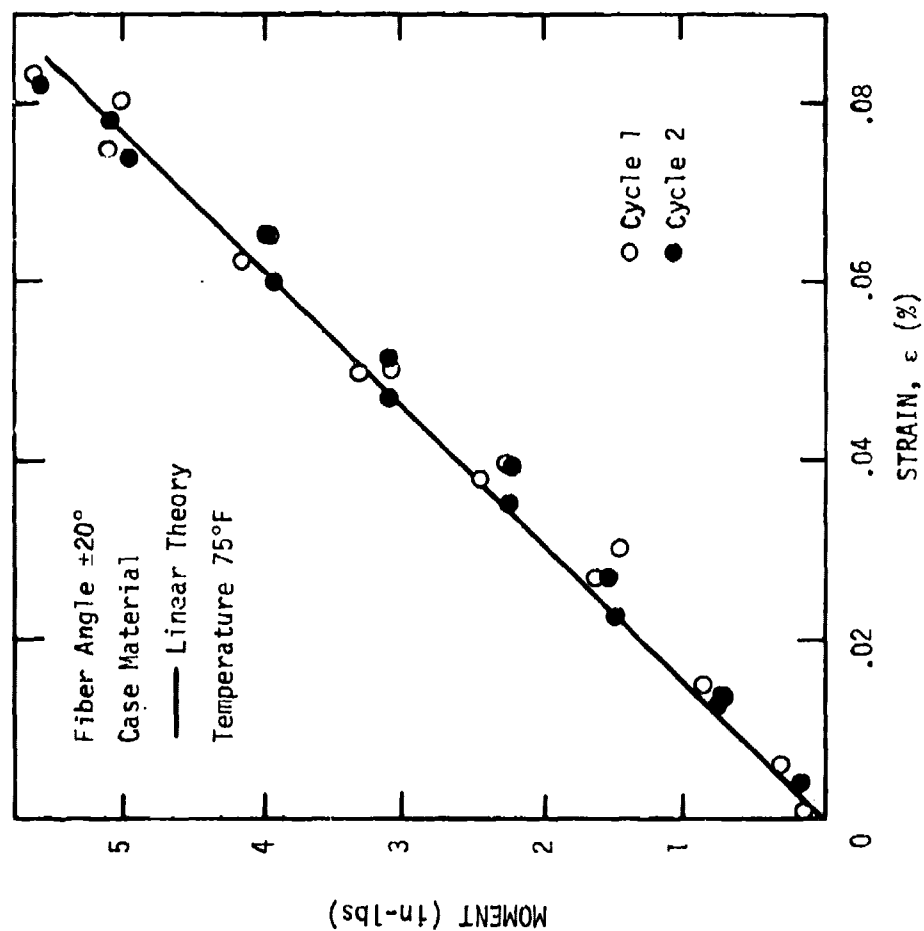


Figure 164. Effect of cyclic loading of  $\pm 20^\circ$  beam cut from motor case material (Cycles 1 and 2).

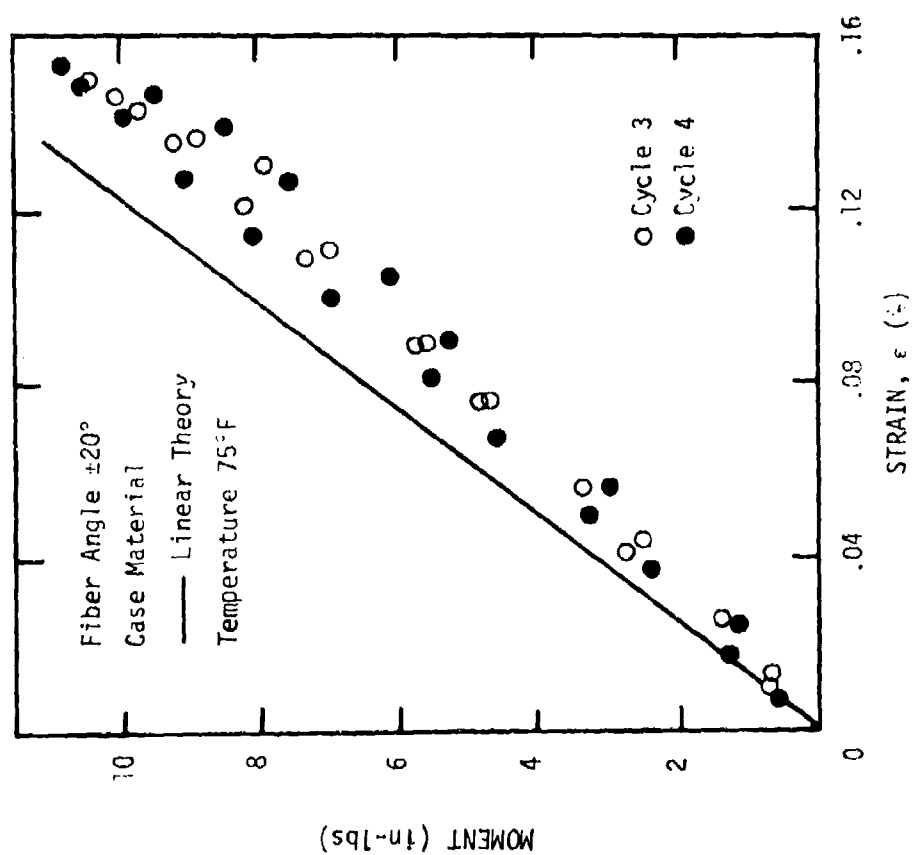


Figure 165. Effect of cyclic loading of  $\pm 20^\circ$  beam cut from motor case material (Cycles 3 and 4).

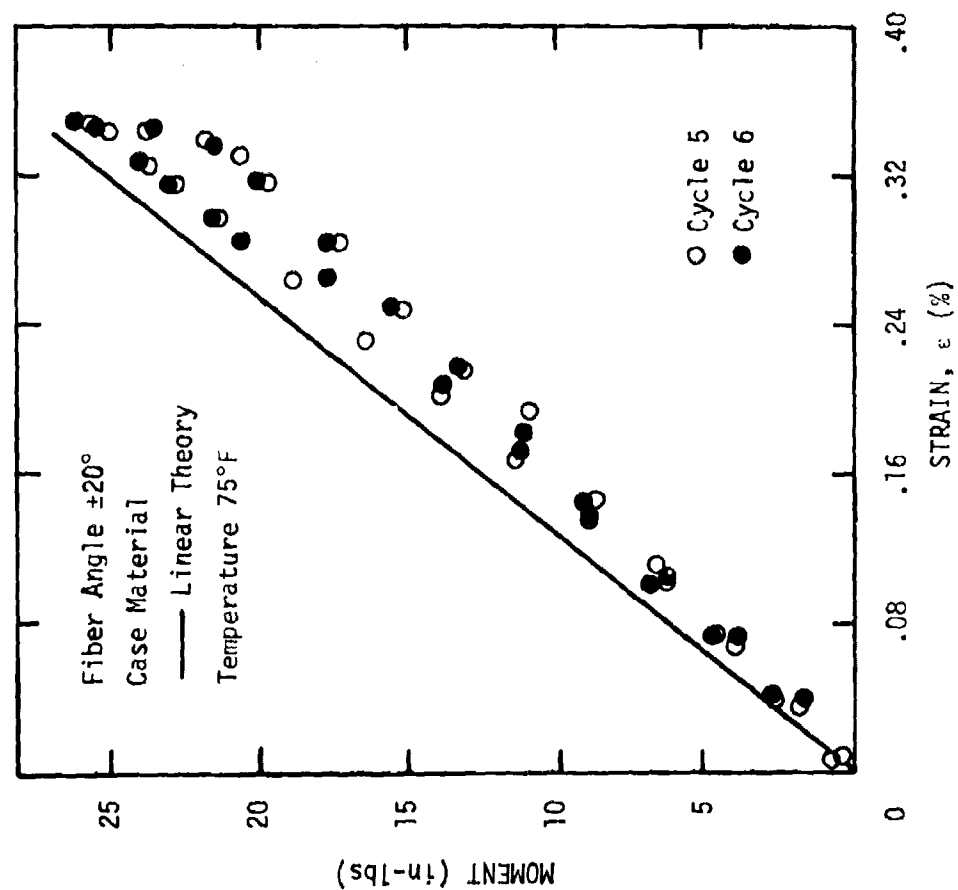


Figure 166. Effect of cyclic loading of  $\pm 20^\circ$  beam cut from motor case material (Cycles 5 and 6).

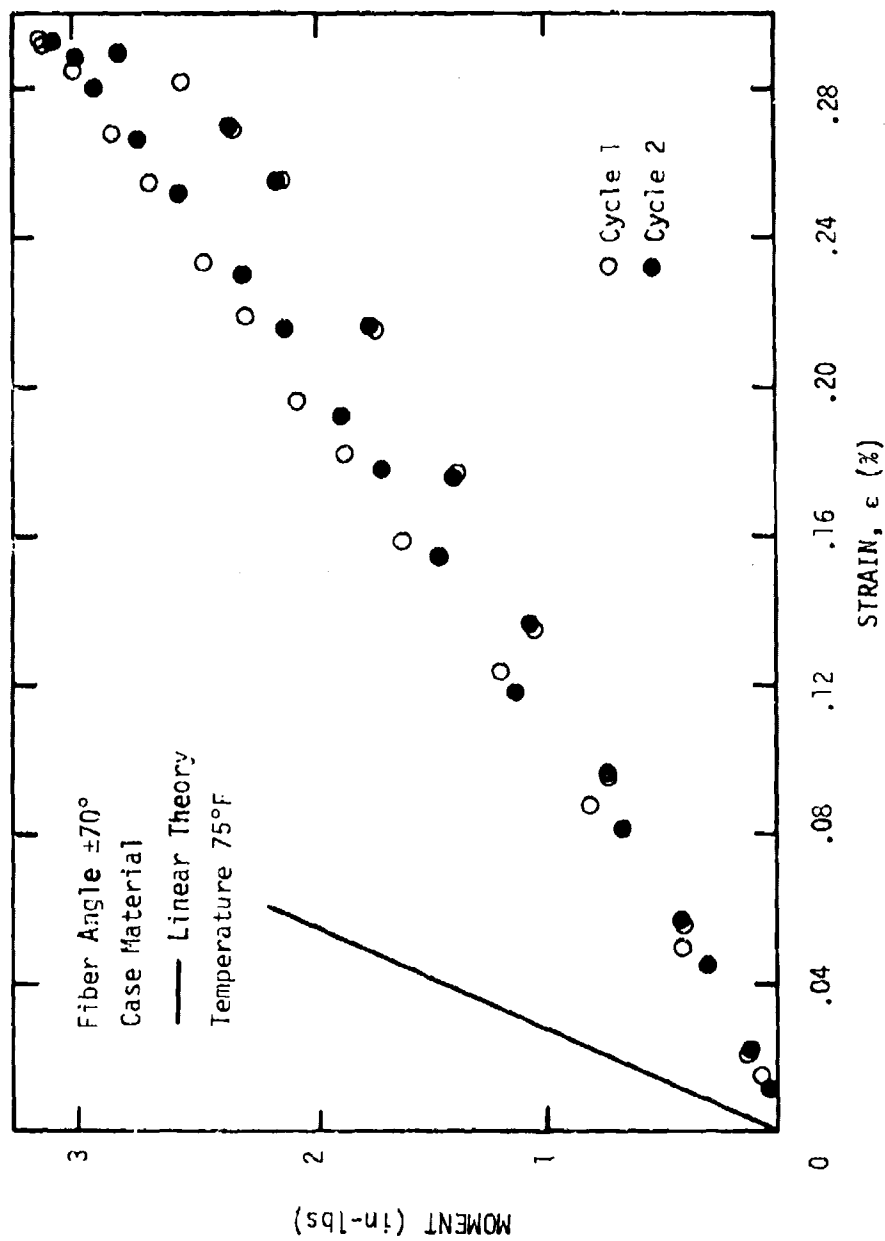


Figure 167. Effect of cyclic loading of  $\pm 70^\circ$  beam cut from motor case material (Cycles 1 and 2).

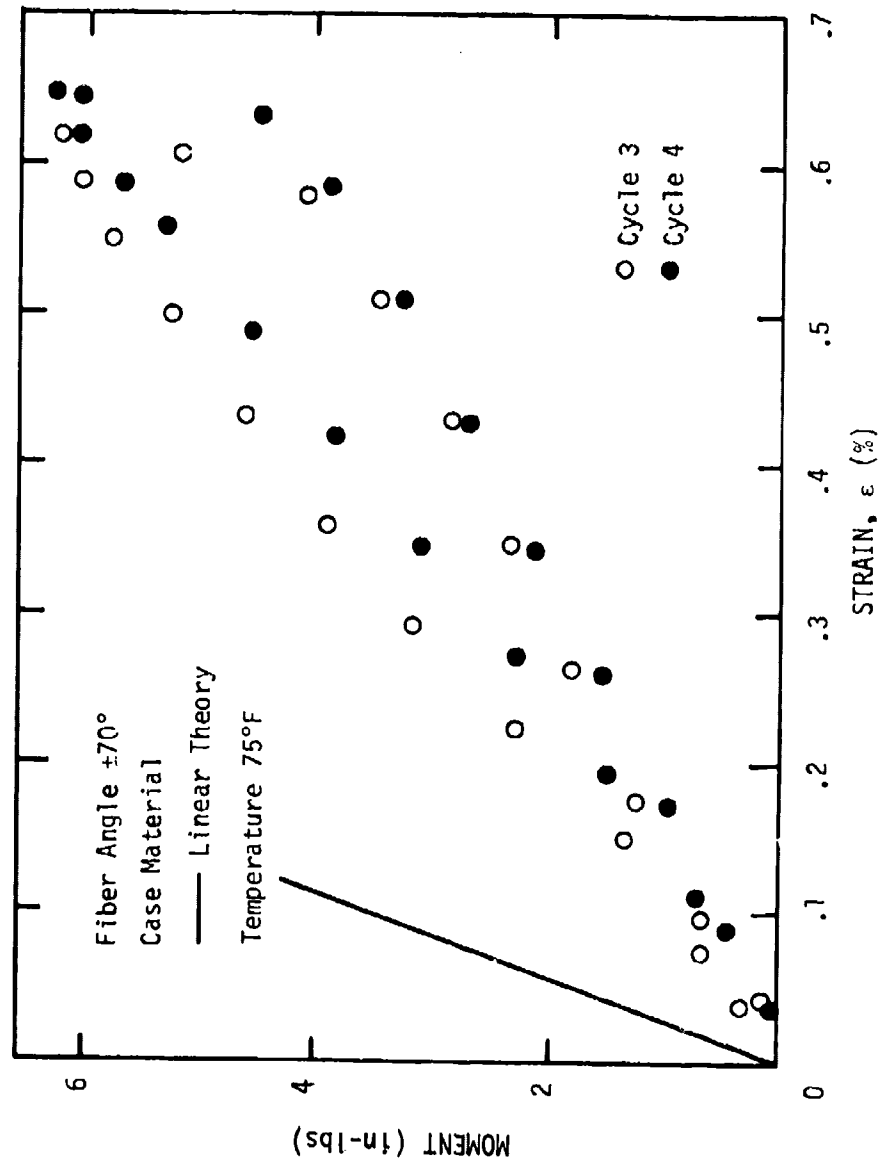


Figure 168. Effect of cyclic loading of  $\pm 70^\circ$  beam cut from motor case material (Cycles 3 and 4).



for the  $45^\circ$  unidirectional glass/epoxy composite (Figure 30).

The  $0^\circ/90^\circ$  beam behavior was predicted by using the corresponding  $0^\circ$  and  $90^\circ$  unidirectional stress-strain curves (Figures 28 and 31, respectively). The moment was determined by employing the following procedure:

1. Select several strain levels, e.g., 1000, 2000, . . . , 10,000  $\mu\epsilon$ , etc., corresponding to the maximum outer fiber strain. The data for the  $\pm 45^\circ$  and  $0^\circ/90^\circ$  specimens indicates the output from both gages (tension and compression surfaces) is relatively close; therefore, only the tension strain gage output is used here.
2. Using the assumption of a linear strain distribution, determine the strain at the mid-point of each layer and the corresponding moment arm measured from the neutral axis of the beam (assumed fixed for all strain levels).
3. Use the strains established for the individual layers to determine the average stress in the layer from the stress-strain curve representing that particular fiber angle. (Some of the stress-strain curves, e.g.,  $45^\circ$ , had to be extrapolated to higher strain levels).
4. The stress acting on a given layer, multiplied

times the area of the layer cross-section and the moment arm yields the incremental moment for that layer.

5. Add all of the incremental moments to give the total moment for a specified strain level.

The linear theory is shown in the  $\pm 45^\circ$  and  $0^\circ/90^\circ$  beam results. The agreement is very good over a large portion of the range. In fact, the presence of the strain gradient greatly reduces the softening effect. In Figure 160 it can be seen that the nonlinear theory predicts a significant decrease in the applied moment. The  $45^\circ$  data used to predict the bending behavior results in conservative predictions of moment. Remember that we have already noted significant crack growth during the first few cycles in the  $45^\circ$  unidirectional composite specimen with crack arrest probably occurring only when the crack reaches another fiber. The  $\pm 45^\circ$  tensile specimen exhibited more crack arrest during the first few cycles and this was attributed to the layering effect.

The beam appears much stiffer than nonlinear theory predicts (Figure 160). In the beam crack growth must occur at the outer fibers where the stress is highest and then work inward toward the center. The cracks are immediately retarded by the interface at the second layer and must be redirected before proceeding. However, the cracks have now moved into a region of lower stresses which reduces the growth rate. It could also be argued from a statistical

viewpoint, that there is a much larger percentage of critical cracks at a given stress level in a tensile specimen than a beam.

The cyclic loading of the motor case materials appears to have reached an equilibrium behavior. The hysteresis loop remains essentially unchanged from cycle to cycle except at the highest moments (Figure 168). However, by using Figure 111, we can predict the linear behavior using the linear viscoelastic creep compliance. The material exhibits considerable softening in the initial compliance (see Table 17) although the creep coefficient which reflects time-dependent crack growth appears to remain unchanged with successive cycles.

#### Plate Twist Tests

The case of plate bending under the action of twisting moments is discussed by Timoshenko and Woinowsky-Krieger [183] and Lekhnitski [25]. The specific test outlined earlier in Section III is commonly called the "plate twist test". Several authors [184, 191-193] have applied the test to anisotropic, and more specifically, orthotropic materials such as plywood [191] and fiber-reinforced composites [192, 193]. Whitney [184] and Tsai [193] have used the test to determine the elastic material properties of glass/epoxy and boron/epoxy composites using linear theory. The purpose of these tests in this particular program was to investigate the effects of multiaxiality on the behavior of the

glass/epoxy composite.

### Creep and Recovery Tests

Since only one plate was available for the plate twist tests, low load level creep and recovery tests were conducted first. Two load levels were used as a check for linearity. The average strain along the two diagonals (using the absolute value) was found to be very small for the load levels used. Again, the strain was found to fit a power law with  $n = 0.19$ . Bryzgalin [148, 194] conducted similar tests on a glass/epoxy plate and found the power law behavior. In order to accurately measure the effects of damage using this test it would be necessary to use higher loads, considerably longer time periods and higher temperatures. At the load levels which we tested there was no measured amount of damage. The surface strains were below  $600 \mu\epsilon$ , which, from Figure 30, can be seen to be well within the linear region. Further creep testing was discontinued and attention was shifted to conducting the constant rate tests to higher load levels.

### Constant Crosshead Rate Tests

The constant crosshead rate tests were conducted to loads which caused large deflections at the plate tips. In addition to the large deflections encountered, the plate was loaded in a manner different from that which is normally treated by the analysis.

The analysis used within the linear region assumes that the plate is loaded at the corner. Experimentally this causes localized deformations at the tip due to the concentrated load at the edge. The test also requires excellent balancing between the four load points to prevent the plate from slipping off the edges. It was also noted that the tests are often conducted with the loads concentrated a short distance in from the edge, but using the original analysis [195]. Although not evident, it is believed that this is common practice because of the experimental difficulties.

In the Appendix the plate twist test is studied analytically by using an energy method and a technique is proposed to take into account the corner effect. The incorporation of large deflection theory in the energy formulation results in a nonlinear load-deflection relationship, Equation (A-13), which predicts that the load depends on the cube of the deflection in the nonlinear range.

Equation (A-13) represents the case of an isotropic material. The load-deflection data for the aluminum plate is plotted on a log-log scale in Figure 169. The cubic behavior in  $w_0$  is not clearly evident until the linear contribution is subtracted out as in Figure 170, after which the data clearly indicate the cubic behavior. In fact, apart from the differences due to the material properties, the glass/epoxy plate would also display the same functional behavior in  $w_0$ . This cubic variation results from the form of assumed displacement function as long as the material properties

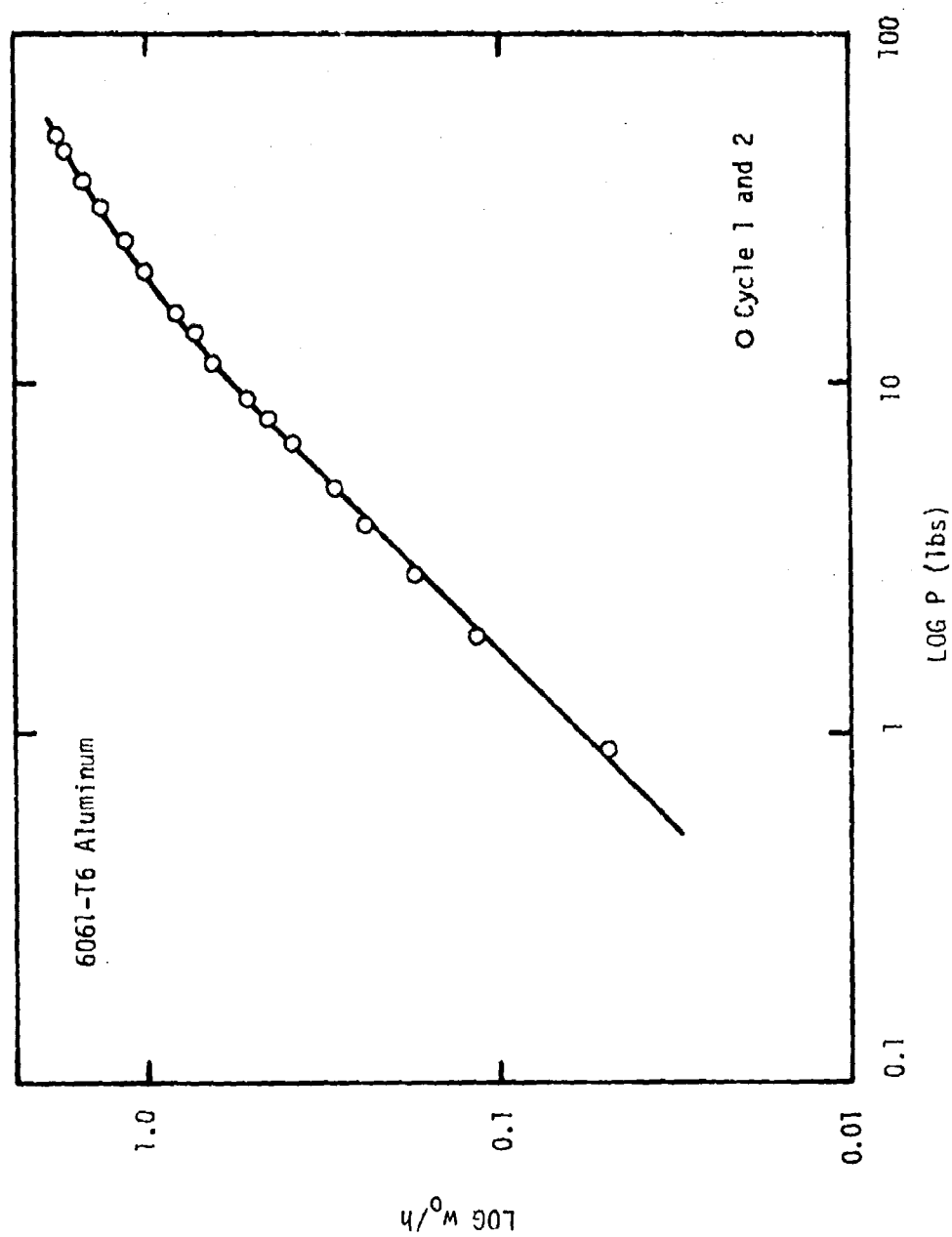


Figure 169. Evaluation of load-deflection behavior of aluminum plate.

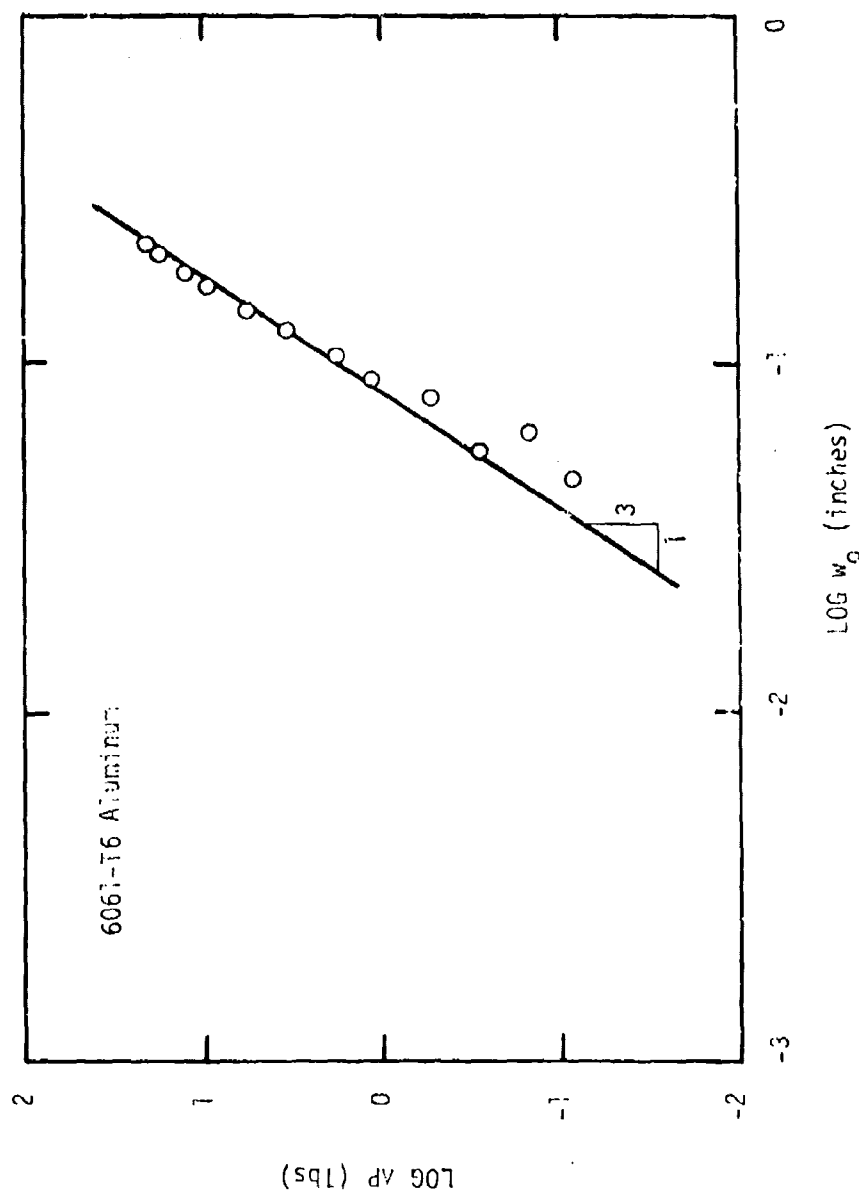


Figure 170. Large deflection contribution,  $\Delta P$ , to total plate load versus deflection for aluminum plate.

do not depend on strain.

The load-deflection curve for the aluminum is shown in Figure 171. The linear theory is given by the first term in Equation (A-13) using the correction for the corner effect. Linear theory predicted by this method shows good agreement up to deflections on the order of one-half the plate thickness. This is the normal limit for linear theory in plates and shells [183] work. The nonlinear theory predicted by Equation (A-13) exhibits considerably more stiffness than noted experimentally. This is probably the result of the choice of the displacement functions, Equation (A-1). It would be possible to obtain better agreement by selecting more suitable displacement functions compatible with loads removed from the corners a finite distance. The plate also exhibits an instability which will be discussed later. This behavior creates larger deflections for a given load and the displacements appear to reflect single curvature. Therefore, the assumed displacement functions are valid only in a very small range.

The load deflection curves for the  $\pm 45^\circ$  glass/epoxy are shown in Figures 172 through 174 for increasing load levels. The linear theory for the  $\pm 45^\circ$  fiber angle is given by Tsai [193] as

$$w_0 = \frac{3Pl^2}{4h^3} S_G \quad (154)$$

where  $P$  is the applied corner load,  $l$  is the length of the side,  $h$  is the plate thickness and  $S_G$  is given as



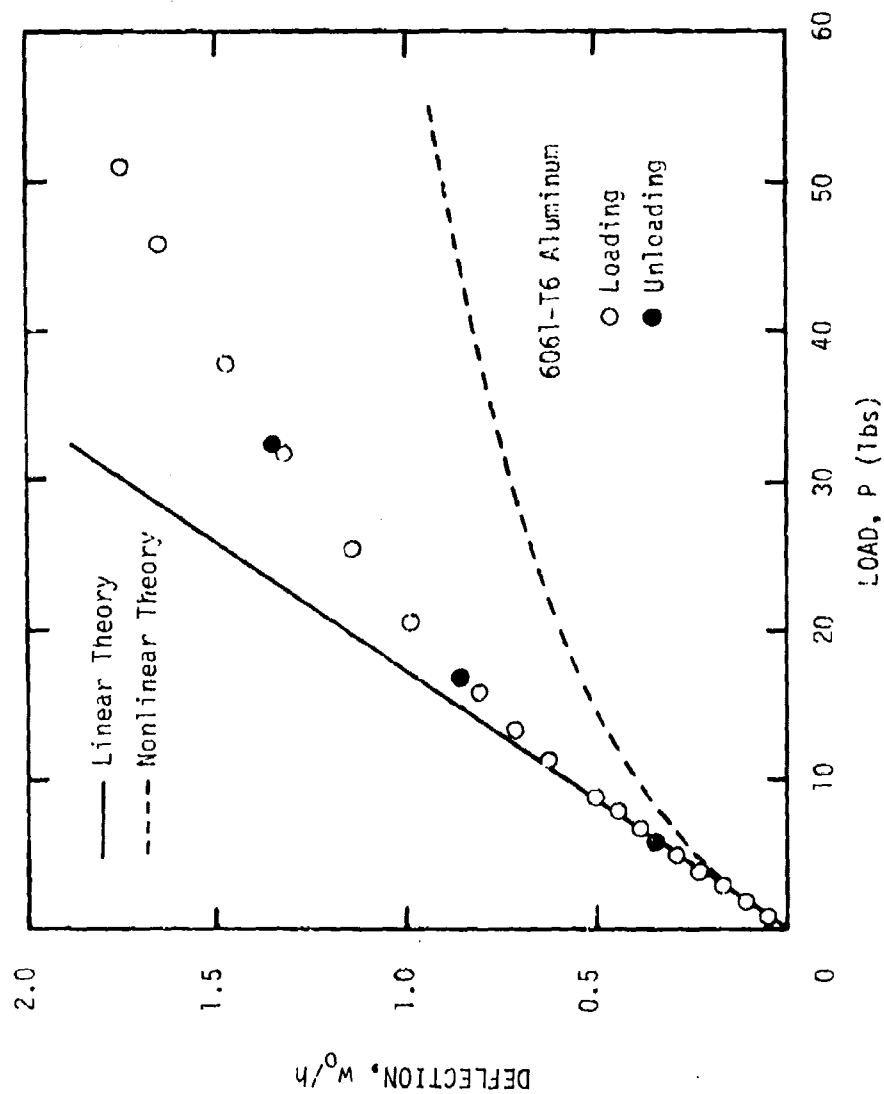


Figure 171. Load-deflection curve for 6061-T6 Aluminum plate.

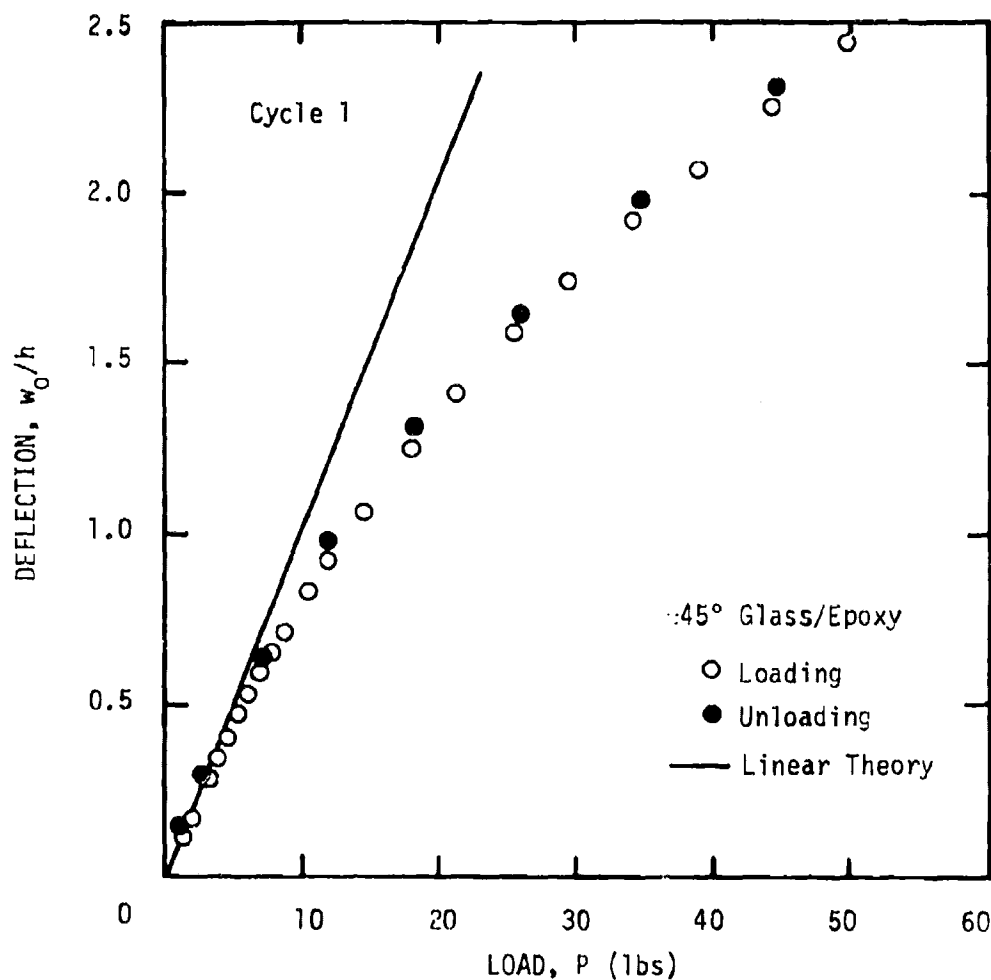


Figure 172. Load-deflection behavior of  $\pm 45^\circ$  glass/epoxy plate (Cycle 1).

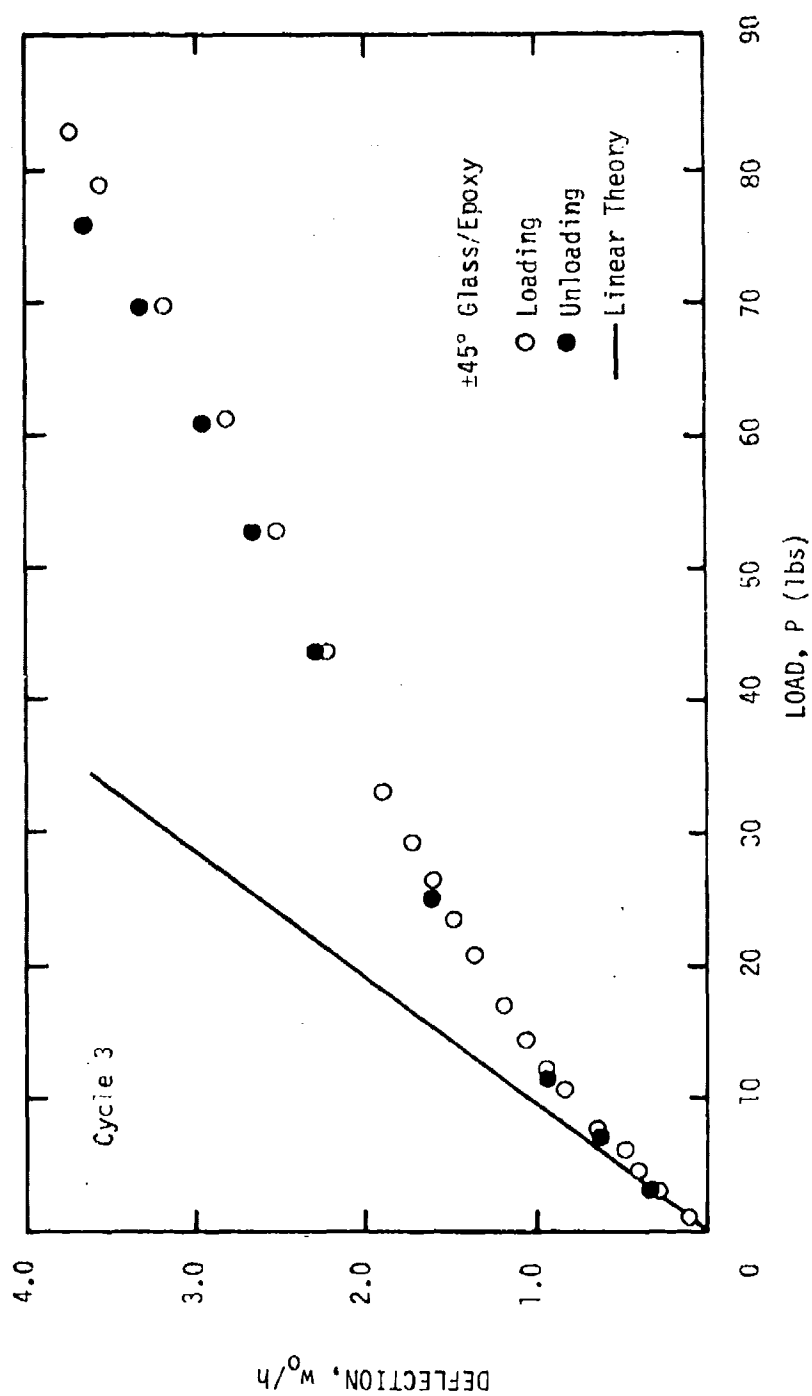


Figure 173. Load-deflection behavior of  $\pm 45^\circ$  glass/epoxy plate (Cycle 3).

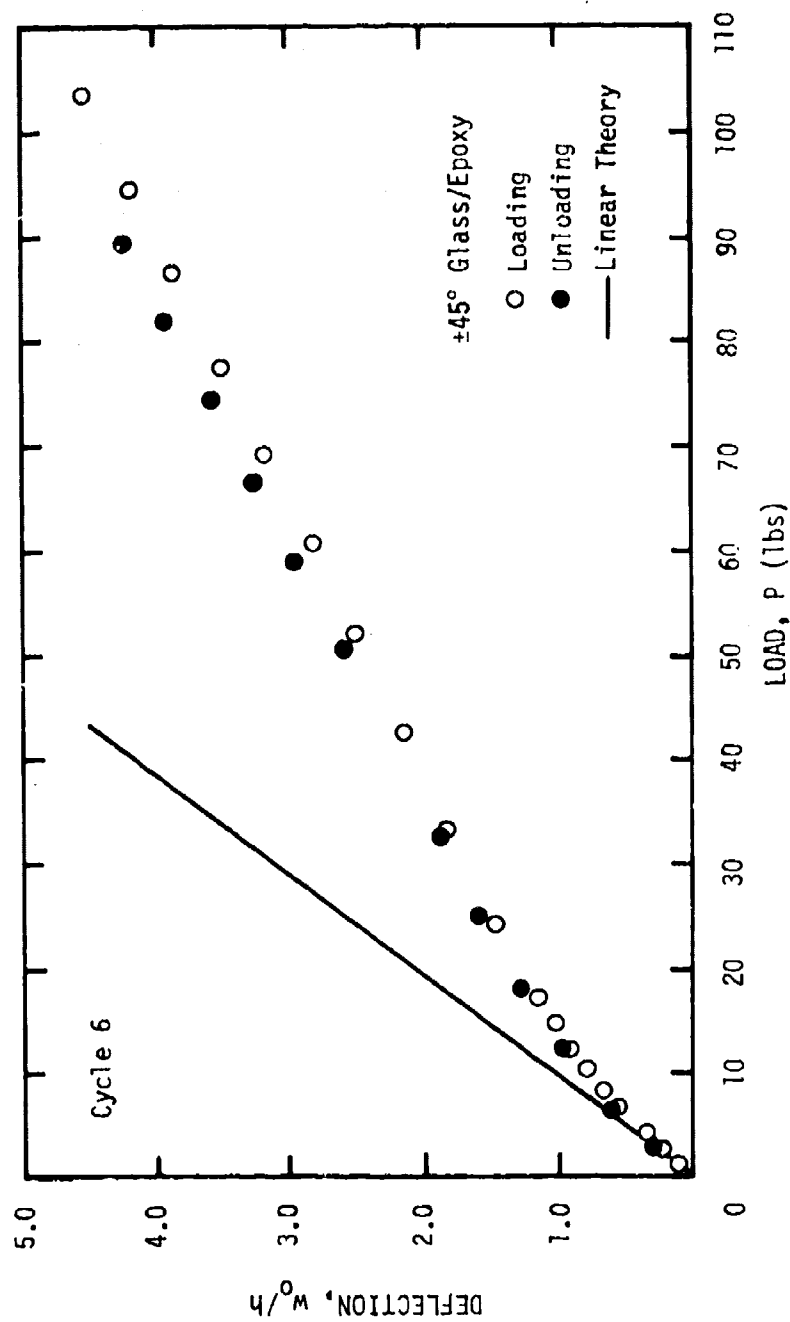


Figure 174. Load-deflection behavior of  $\pm 45^\circ$  glass/epoxy plate (Cycle 6).

$$\theta = +45^\circ \quad S_G = 2(S_{22} - S_{12}) \quad (155a)$$

$$\theta = -45^\circ \quad S_G = 2(S_{11} - S_{12}). \quad (155b)$$

The  $\pm 45^\circ$  glass/epoxy plate consisted of 15 layers; therefore, the average value of  $S_G$  was used in Equation (154). The elastic values of  $S_{11}$ ,  $S_{12}$  and  $S_{22}$  are given in Table 15. The predicted linear theory is shown on the figures after correcting for the corner effect as we did before. Linear theory agrees reasonably well up to plate deflections on the order of one-half the plate thickness.

At the higher loads the load-deflection curves indicate what appears to be a softening effect. When plotted as a load-strain curve, as in Figures 175 through 177, the same effect is seen upon unloading. However, in view of the surface strain levels which are seen to be less than 1400  $\mu\epsilon$ , one would not expect significant non-linear behavior such as this. By plotting the load-deflection curves for cycles 1 and 6 on log-log paper (Figure 178), it can be seen that there are three linear regions. This behavior has been described qualitatively by Foye [196] to consist of a linear range followed by the nonlinear region which possesses an unstable branch. After reaching this unstable point, the load-deflection relationship again becomes linear. Closely examine the edges of the plates shown in Figures 179 and 180. The low level creep and recovery test shows that the plate edge is essentially straight.

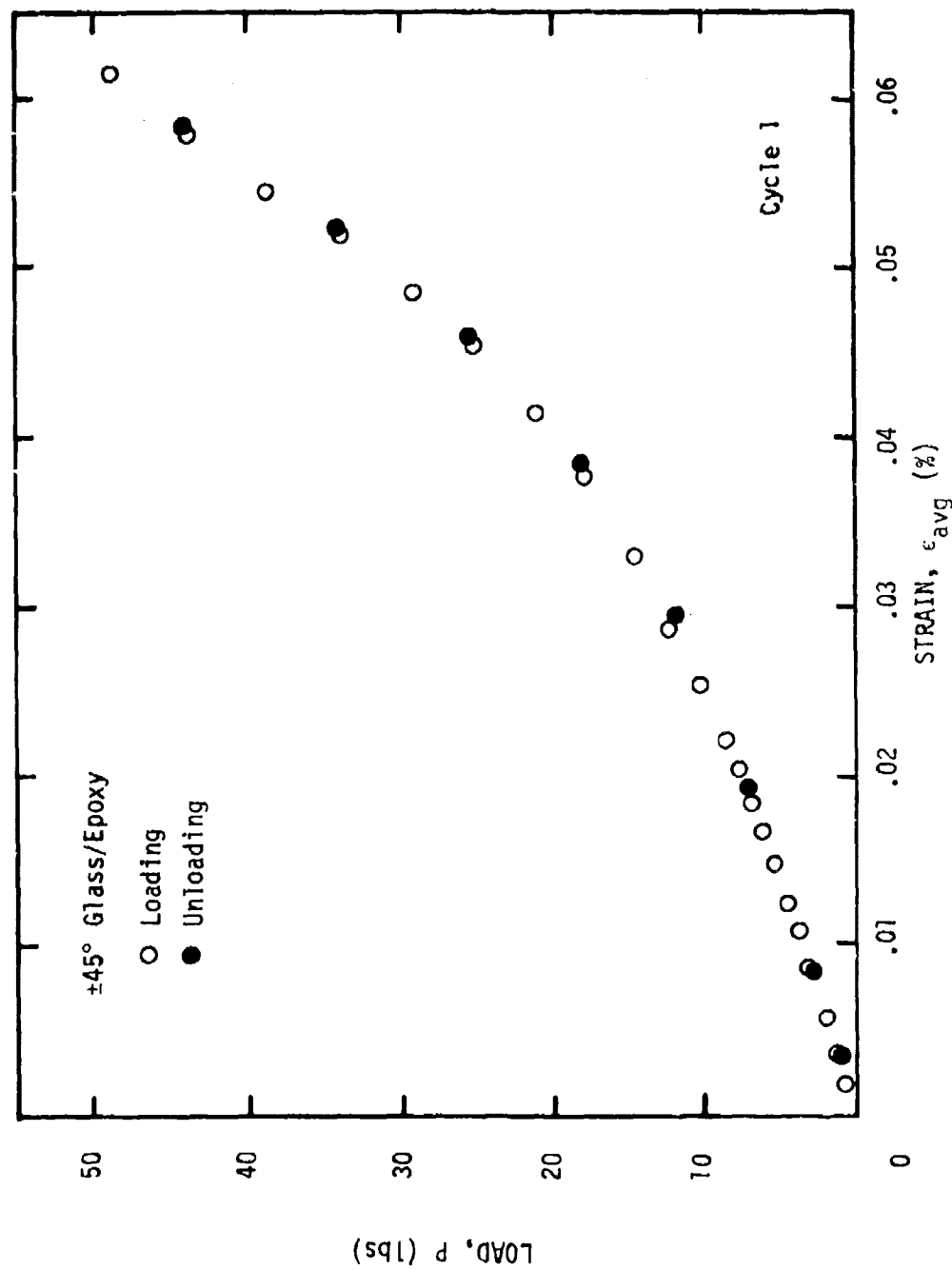


Figure 175. Load versus average surface strain for ±45° glass/epoxy plate (Cycle 1).

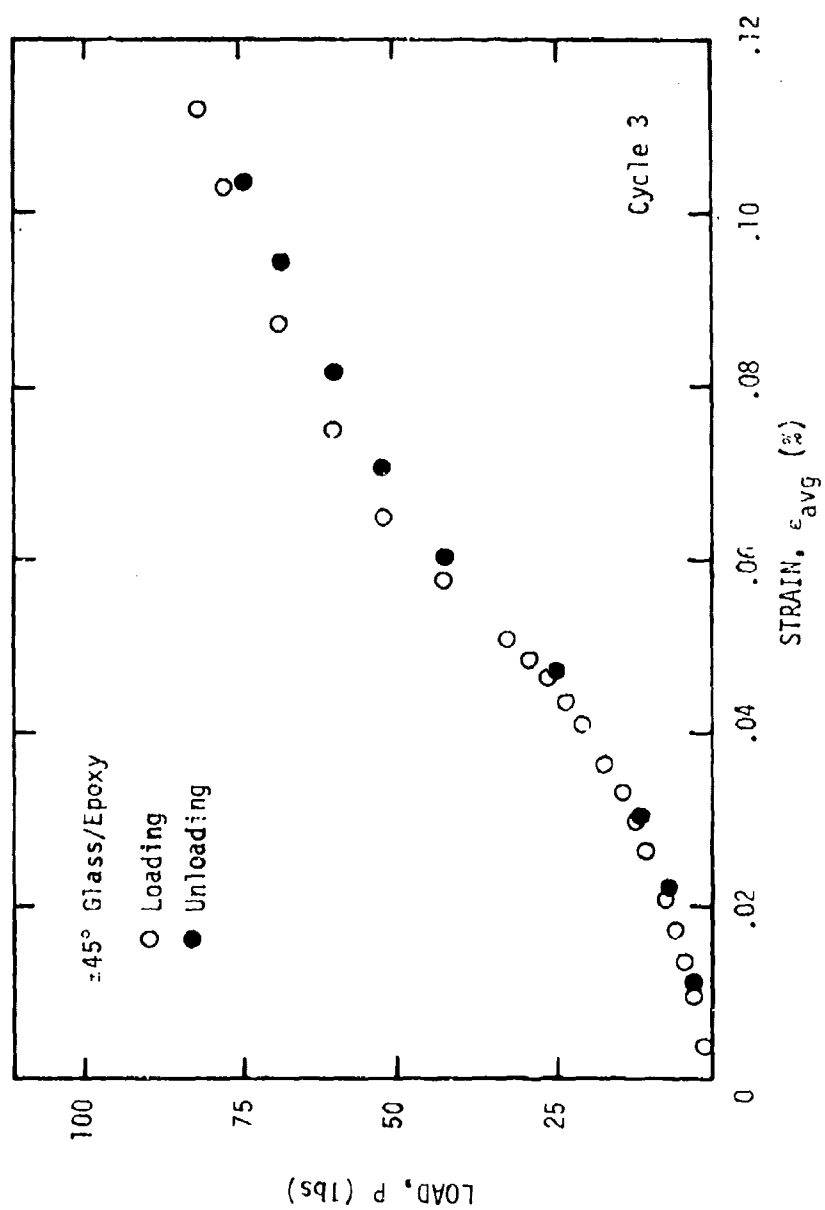


Figure 176. Load versus average surface strain for  $\pm 45^\circ$  glass/epoxy plate (Cycle 3).

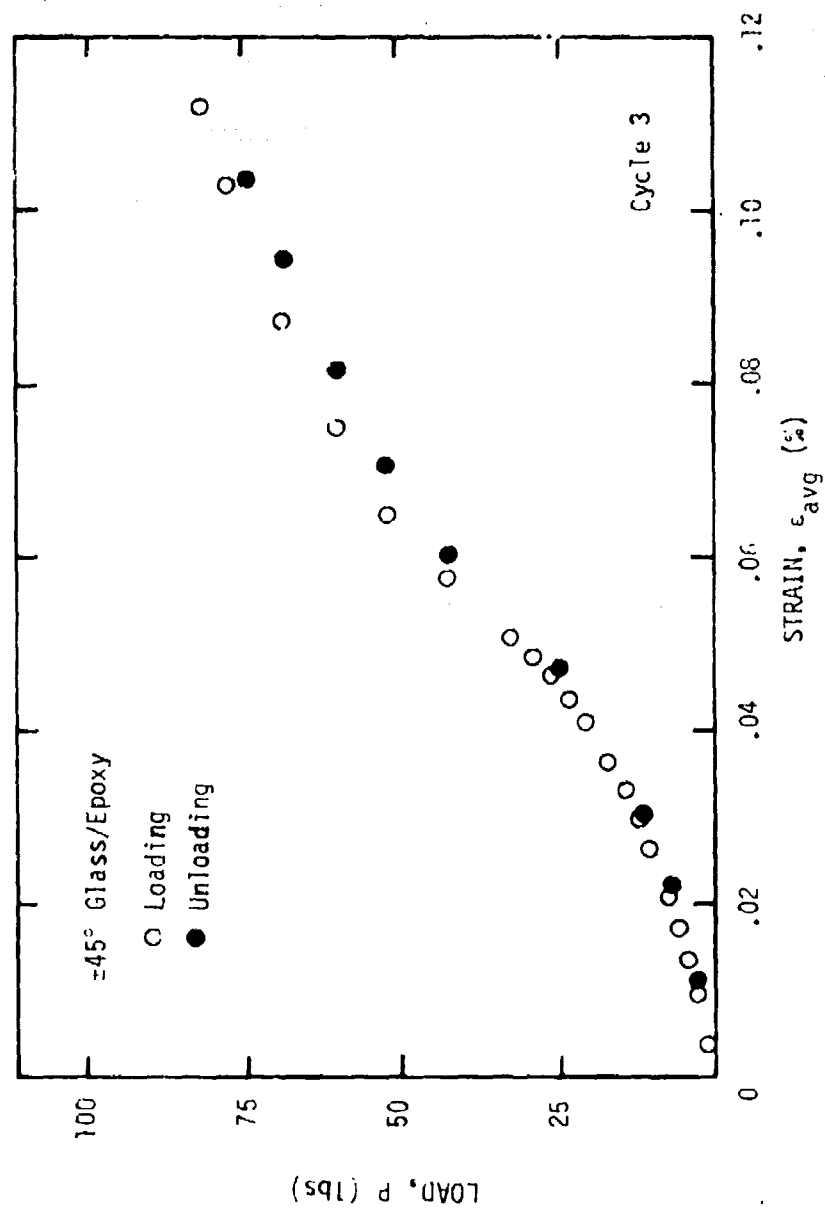


Figure 176. Load versus average surface strain for  $\pm 45^\circ$  glass/epoxy plate (Cycle 3).



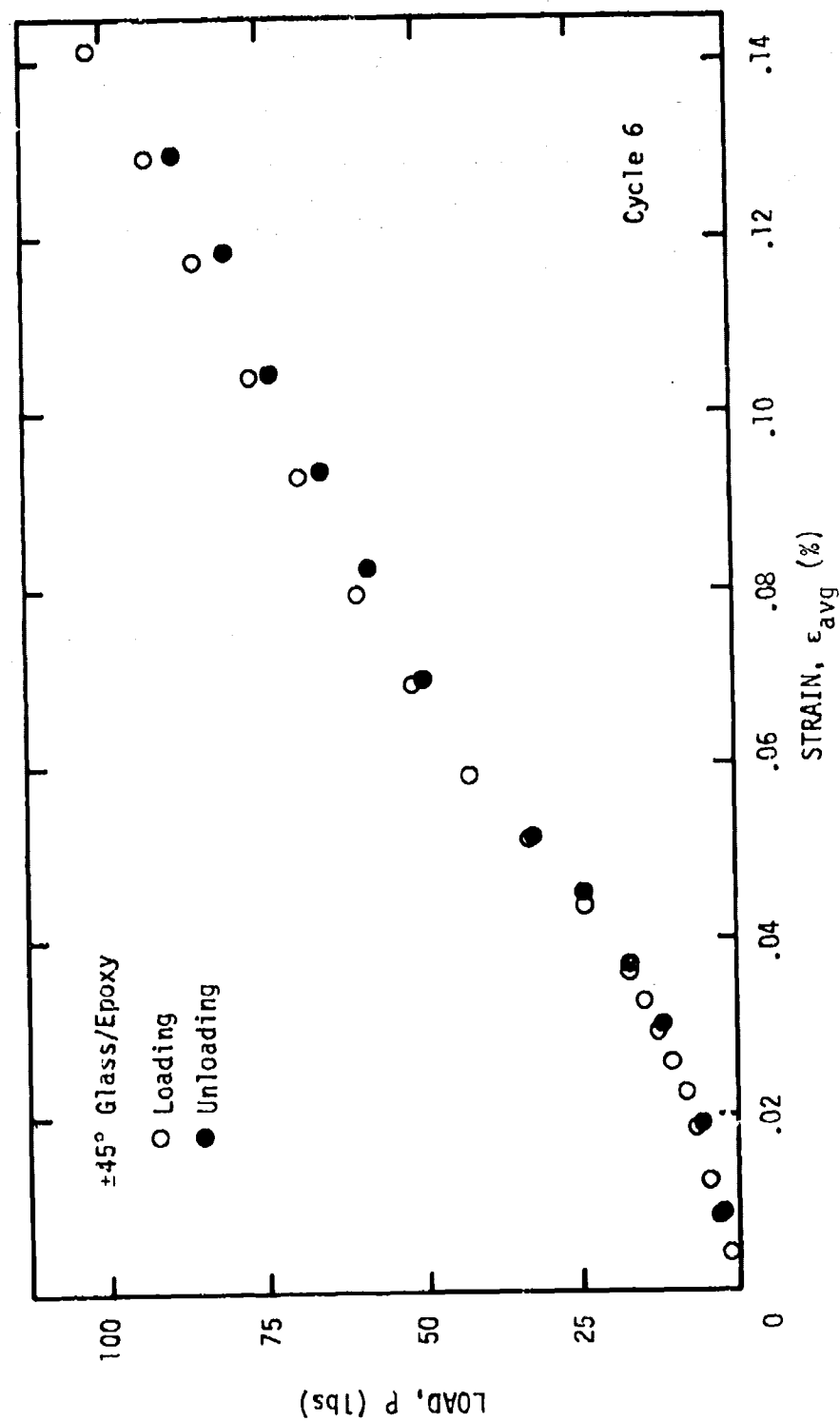


Figure 177. Load versus average surface strain for  $\pm 45^\circ$  glass/epoxy plate (Cycle 6).

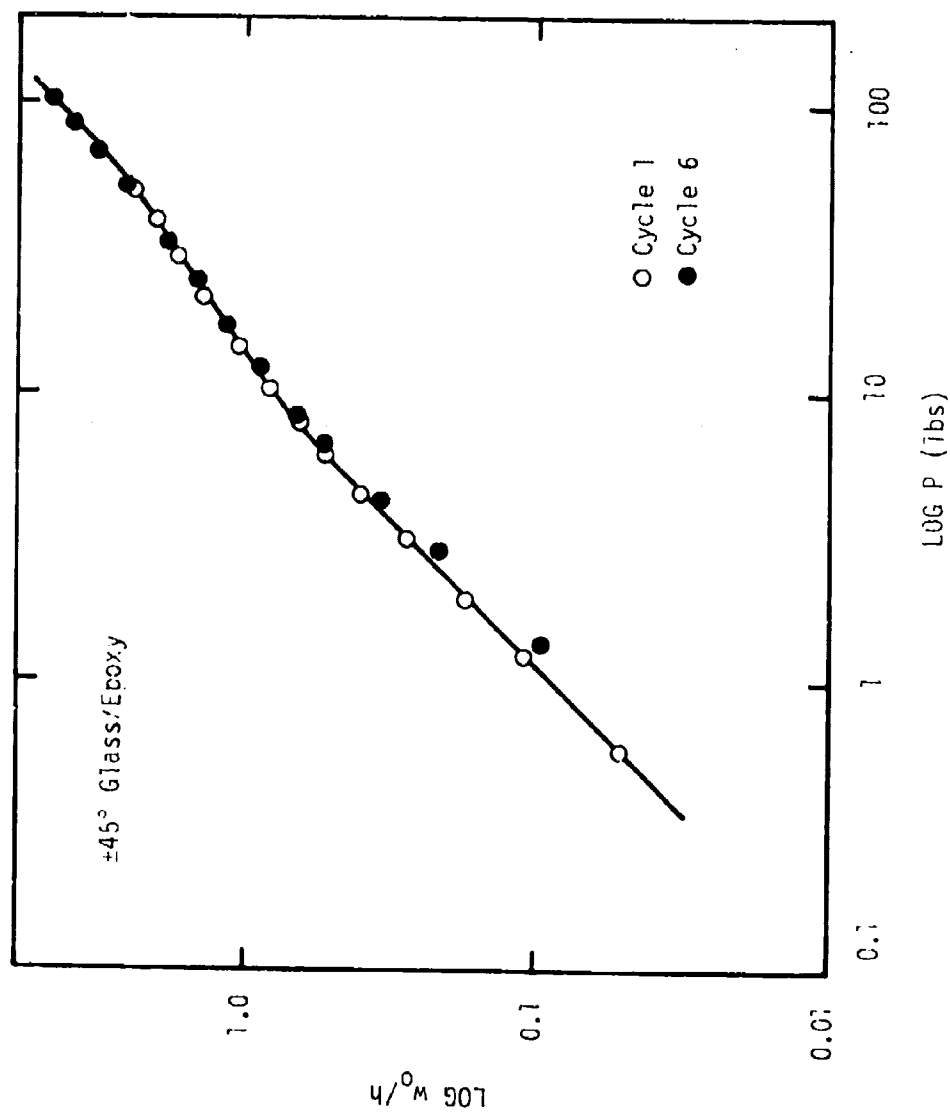


Figure 178. Evaluation of load-deflection behavior of  $\pm 45^\circ$  glass/epoxy plate.

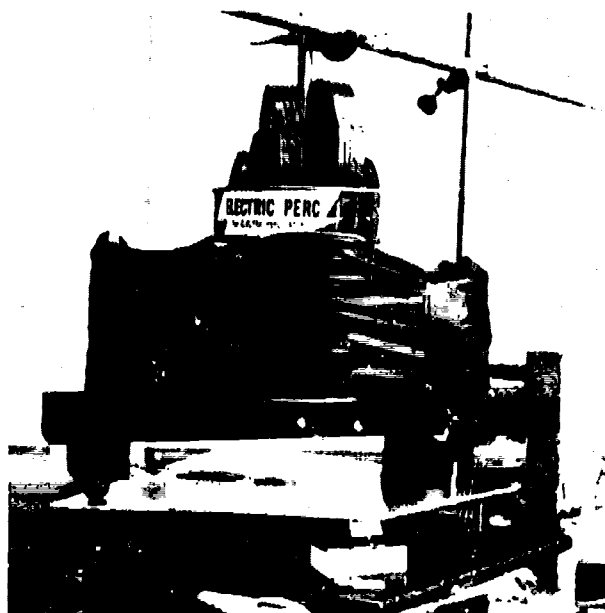


Figure 179. Low load level creep and recovery test within linear range ( $\theta = \pm 45^\circ$ ).

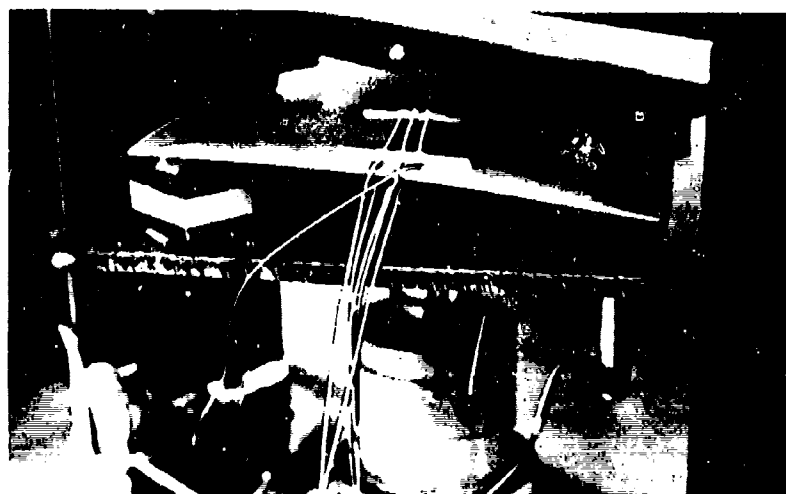


Figure 180. High load level constant crosshead rate test after buckling ( $\theta = \pm 45^\circ$ ).

In Figure 180 the edge shows considerable curvature as a result of the high load which has caused the plate to become unstable with respect to the twisting moments. Also noticeable is the lack of double curvature (saddle effect) after the plate becomes unstable.

Once instability has occurred the plate should be treated differently analytically. The plate could possibly be considered as a triangular plate loaded at the corner as a cantilever beam. A single parabolic displacement function would appear to be a reasonable choice.

## SECTION V

### APPLICATION TO MOTOR CASE DESIGN

The observations and results found in the previous sections on the effects of stress, temperature and multiple cycling on the glass/epoxy composite strongly suggest a means for improved design methodology. In this section, we shall first review the present problem associated with solid rocket motor case design and analysis and existing technology. Lebesgue norms are used to predict the effects of stress and multiple cycling for conditions which are typical of the motor case as a result of hydrotesting and subsequent mission loads.

#### Review of Present Technology

The present design and analysis of fiber-reinforced composite solid rocket motor cases is firmly entrenched in the use of linear, orthotropic elastic analysis coupled with the application of "experience" factors to account for effects such as temperature, case thickness, hydrotesting, etc. [13-17]. It should be noted, however, that in the absence of any sound theoretical baseline, experience carries considerable weight. Under certain conditions, such as low stress levels, short time periods and moderate temperatures, a linear, orthotropic elastic analysis using either measured or predicted (micromechanics) properties may be adequate. In this

same context one may extend the approach to linear viscoelasticity in the absence of significant crack growth.

However, Rawe [197] has pointed out the need to assess the damage created during hydrotesting of filament-wound motor cases such as that shown in Figure 5b. Rawe observed that the cracks become visible at pressures which were only 40% of the required burst pressure. The number of cracks was found to increase with pressurization and became a permanent feature of the chamber's appearance upon release of the pressure. He also noted that a disproportionate amount of cracking occurred during the first (hydrotest) cycle. In addition to the obvious concern for the softening effect created by the crack growth, the presence of cracks leads to eventual reduction in strength as a result of moisture penetration during prolonged storage. We have also noted the effect of moisture on the volumetric expansion (see Figure 26) and the evidence suggests [198] that moisture is present in the composite as the result of small microcracks.

Crownover [14] suggests that a pressure level of 80% of the burst pressure causes significant damage to the case material. His results showed that the strength reduction was a function of both the pressure level and the duration of the holding period. Although his observations were qualitative, they are consistent with the use of Lebesgue norms to describe the time-dependent crack growth effects.

In the Minuteman III motor case the design loads are nominally determined for a safety factor of 1.25 [17]. The hydrotest pressure is 5% higher than the mean operating pressure and 80% of the minimum burst pressure. For design considerations the factor of safety is applied to the mean operating pressure and not the hydrotest pressure. The properties used in the motor analysis are based on a fiber volume content of 0.657 which is slightly higher than that reported in Table 3. In order to account for damage due to the hydrotest cycle, secant moduli determined from strain measurements on the surfaces of several 6-inch diameter and full scale pressure chambers were compared by ASPC [17] with the moduli predicted from the "rule of mixtures" and laminated plate theory.

These correction factors on stiffness were found to be on the order of 0.4-0.7, depending on the load (strain) level and motor location (fiber angle and layer sequence).

Temperature degradation factors were determined by comparing the flexural stiffness of glass/epoxy specimens at various temperatures. As expected, these "temperature degradation factors" actually reflect the viscoelastic temperature dependence of the composite as well as crack growth behavior as the strain level increases. These factors on stiffness were found to be approximately 0.7-1.0 for the specified operating temperatures. Certain locations of the motor case actually reach temperatures approaching 250-300°F for short periods of time. It is entirely possible that the

time-dependent growth of cracks during this period is more significant than the effect of hydrotesting. However, the effects of the higher temperatures are not known.

The present approach, therefore, is based on prior motor case experience and utilizes an empirical method for correcting temperature and multiple cycle effects. No effort has been made, to the author's knowledge, to correct for more than one loading cycle (hydrotest) or the time-dependent effects due to crack growth.

#### Prediction of Multiple Cycling Effects

We have already shown that the linear viscoelastic properties can be predicted reasonably well using the Halpin-Tsai Equations (120) and the "rule of mixtures" Equation (118) in the absence of crack growth. However, we also noted that the crack growth is significant even at low stress levels when the temperature increases. Experimental evidence shows that there is considerable softening of the off-angle glass/epoxy composite which must be considered in the dome areas of the motor case due to the fiber angles employed. Multiple cycling effects were noted in Figures 100 through 105 where it was found that the nonlinear behavior depended primarily on the stress normal to the glass fibers,  $\sigma_n$ . However, the nonlinear property,  $g_0$ , reflects stress dependence and, as shown in the figures, does not explicitly account for the cycle-to-cycle damage.



In Section II the constitutive relationships were given for materials exhibiting damage due to the time-dependent growth of microcracks, viz., Equations (102), (106) and (107). The constitutive theory is based on fracture mechanics and involves the Lebesgue norm functions of stress given by

$$||\sigma||_p = \left[ \int_0^t \sigma^p dt \right]^{1/p} \quad (156)$$

where  $||\sigma||_p$  is normally called the  $p^{\text{th}}$  order Lebesgue norm or  $L_p$  norm. In Equation (105) the value of  $p$  was defined in terms of the matrix exponent,  $n$ . Fracture mechanics implies the use of the  $L_2$  norm when the crack tip velocity is proportional to the square of the stress intensity factor [199]. Both norms were studied in order to determine which one fit the observed data.

Using the form of Equation (106), the constitutive relationship for the glass/epoxy may be written as

$$\epsilon = \int_0^t S(t-\tau) \frac{d\sigma_{ef}}{d\tau} d\tau \quad (157)$$

where  $S(t)$  is the linear viscoelastic creep compliance for the specific fiber angle,  $\theta$ , and  $\sigma_{ef}$  is the "effective stress" given by

$$\sigma_{ef} = \sigma [1 + f(||\sigma||)] \quad (107b)$$

The function  $f$  is dependent upon the stress level through Lebesgue norms. The problem involves measuring the experimental strains,  $\epsilon$ , due to an applied constant stress,  $\sigma$ , and then determining the function  $f$ .

The form of Equation (157) may be inverted in the usual sense to obtain (after using the quasi-elastic approach),

$$\sigma_{ef} = \int_0^t \frac{1}{S(t-\tau)} \frac{d\epsilon}{d\tau} d\tau \quad (158)$$

where we can now consider the measured strains as input strains by fitting the experimental data to a power law

$$\epsilon = \epsilon_0 + \epsilon_1 t^m \quad (159)$$

where  $\epsilon_0$  and  $\epsilon_1$  have the usual definition and reflect the stress dependence due to crack growth. Also,  $m = n$  in the linear visco-elastic region but  $m > 0.19$  in the presence of crack growth.

The reciprocal of  $S(t)$ , which obeys the power law form, is found to be approximated by

$$\frac{1}{1+x} = 1 - x + x^2 - x^3 + \dots \quad (160)$$

The first few terms are given by

$$\frac{1}{S_0} \left[ 1 - \frac{S_1 t^n}{S_0} + \left( \frac{S_1}{S_0} \right)^2 t^{2n} - \left( \frac{S_1}{S_0} \right)^3 t^{3n} + \dots \right] \quad (161)$$

using the form of  $S(t)$  given by Equation (135).

Equation (158) was solved for  $\sigma_{ef}$  using the experimental data, Equation (159), as the strain input and the approximation given by Equation (161) to obtain

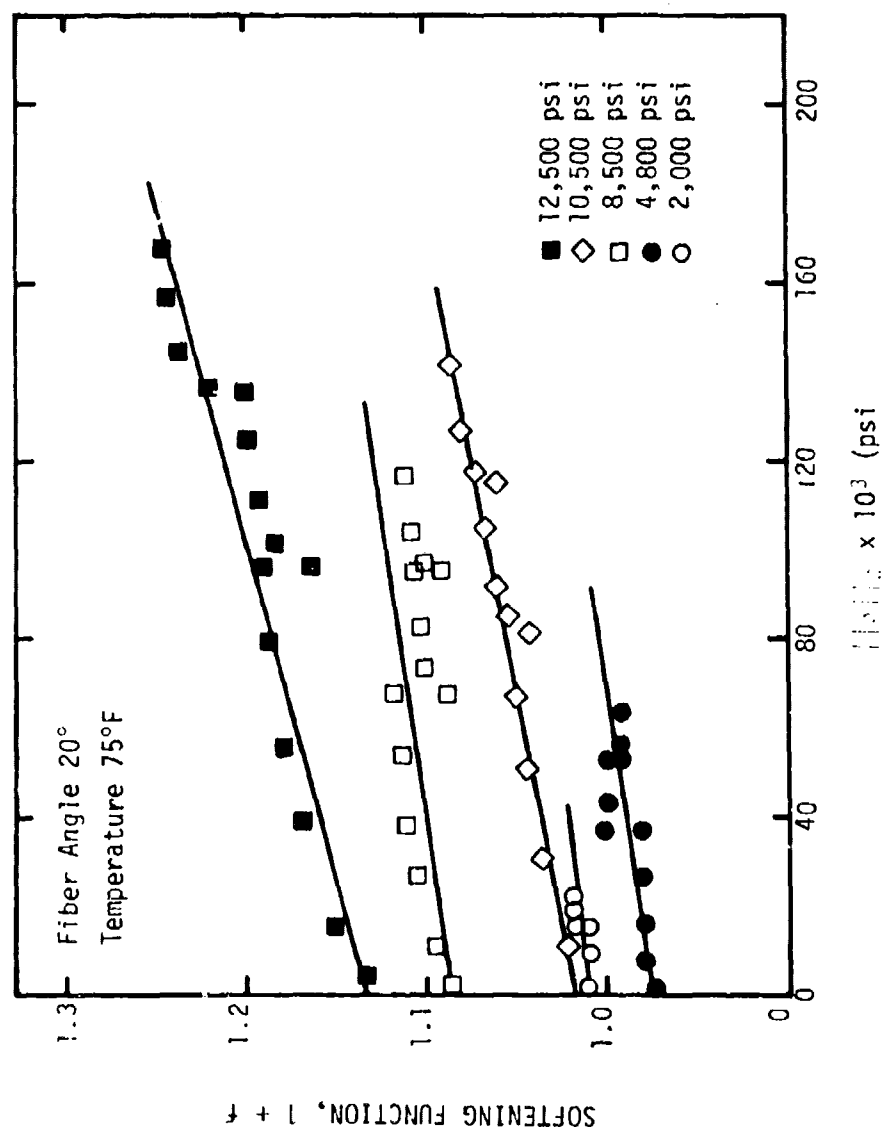
$$\sigma_{ef} = \frac{\epsilon_0}{S_0} \left[ 1 - \frac{S_1 t^n}{S_0} \right] + \frac{\epsilon_1 t^m}{S_0} - \frac{m \epsilon_1 S_1 t^{m+n}}{S_0^2} \left[ \frac{\Gamma(1+n)\Gamma(m)}{\Gamma(1+m+n)} \right] \quad (162)$$

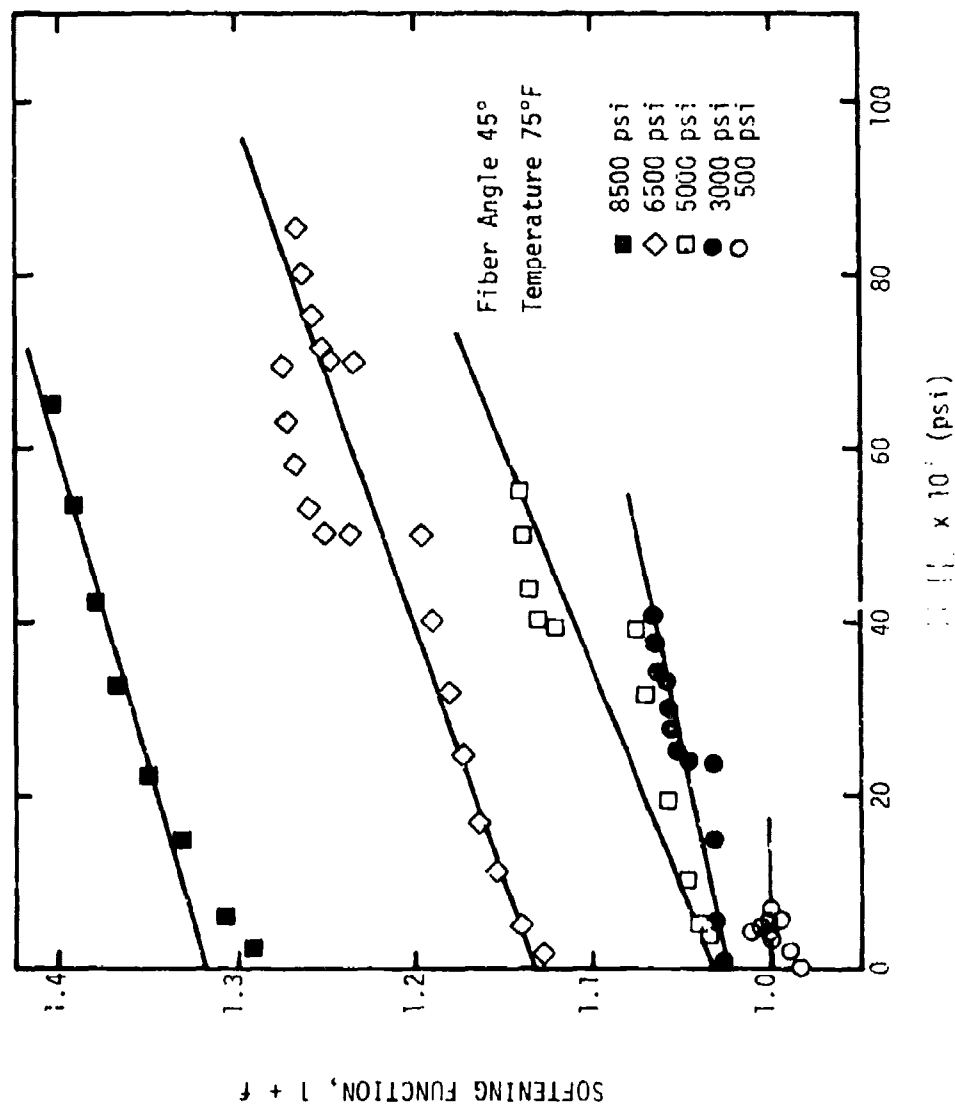
by neglecting the terms of order  $t^{2n}$  and higher in Equation (161).

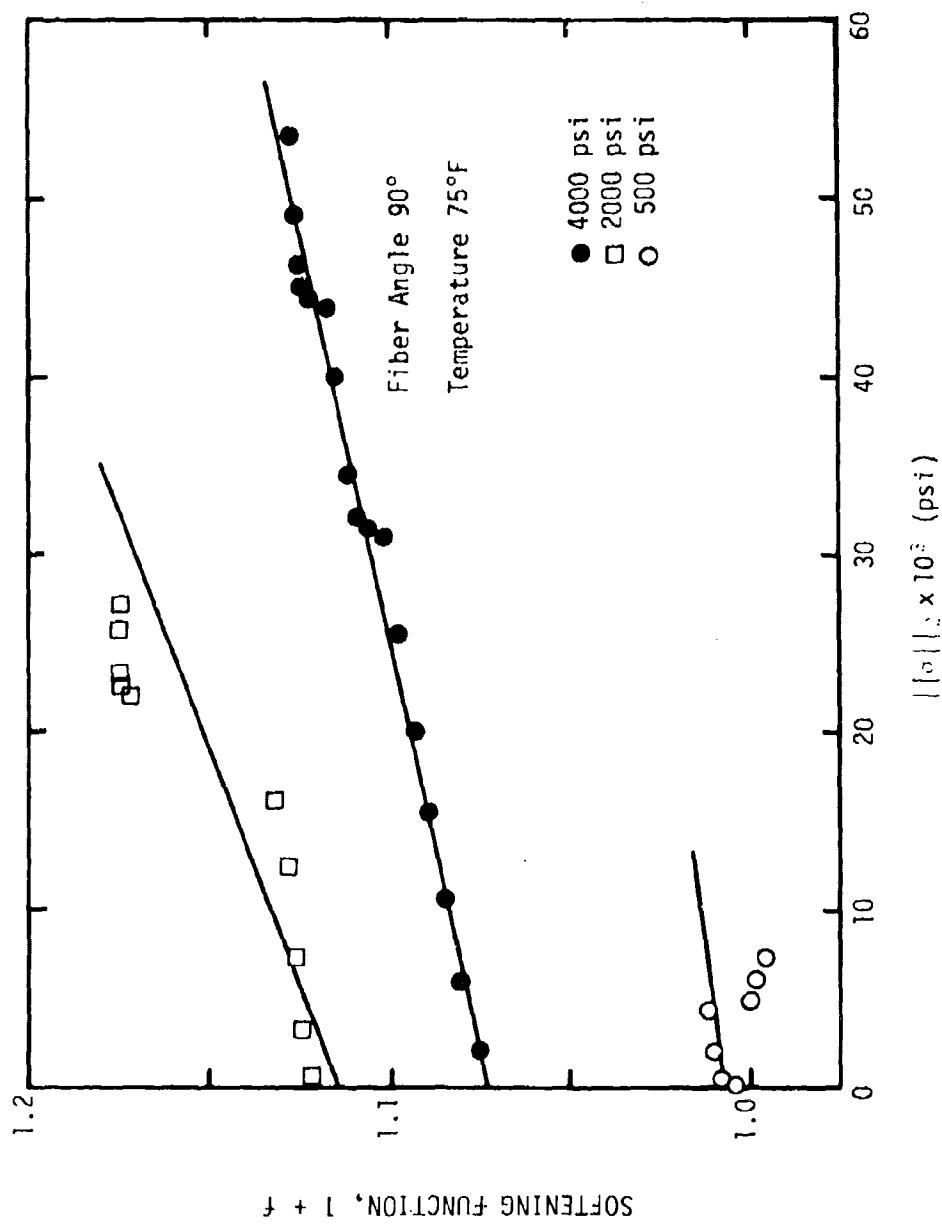
(Note: In the actual reduction of the data, all of the terms shown in Equation (161) were used; however, the difference was found to be insignificant). The function,  $f$ , or more exactly, the function,  $(1+f)$ , was found by using Equation (107b).

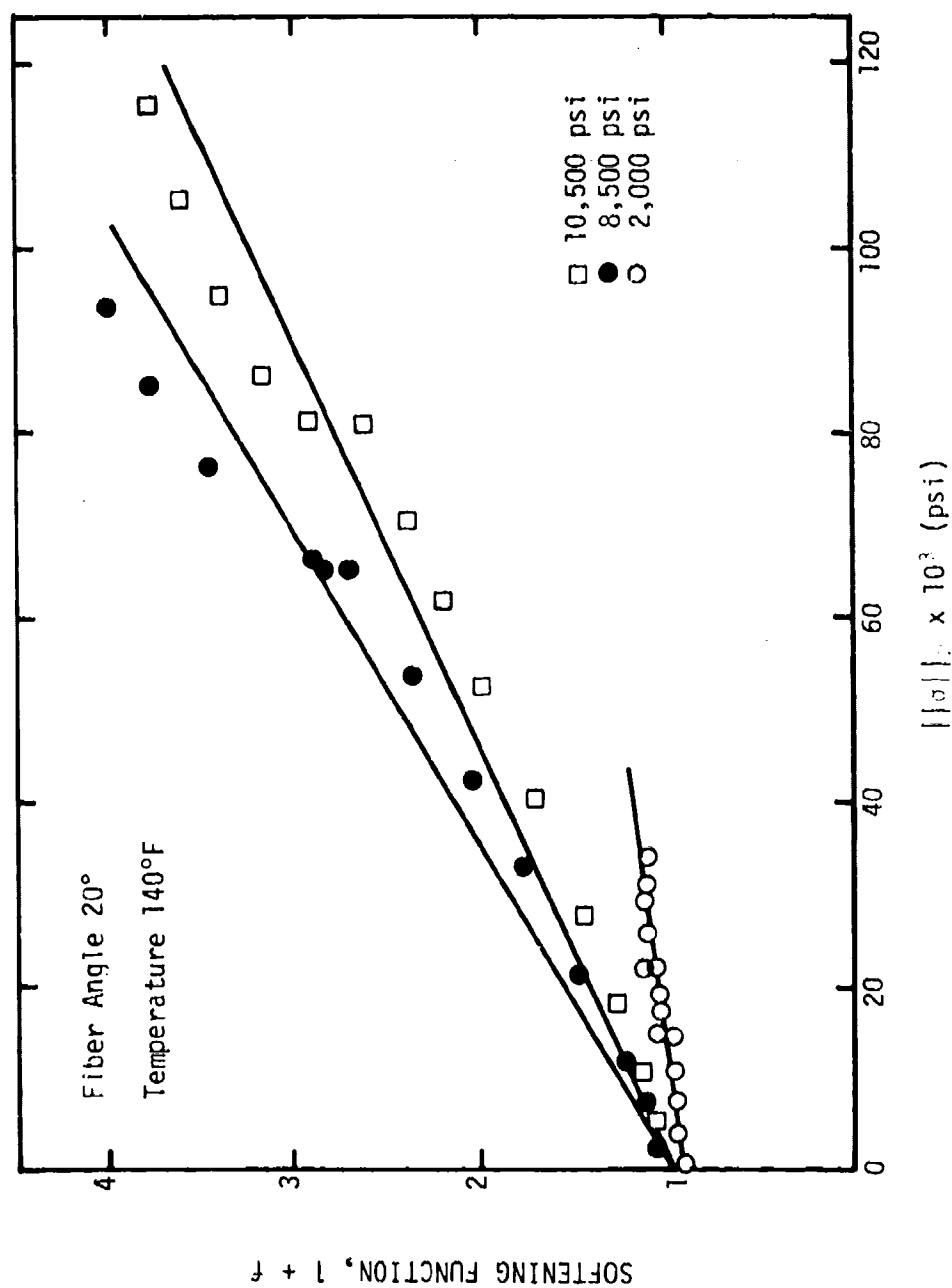
Data from the 20, 45 and 90° fiber angles at the 75°F and 140°F temperatures was used to examine the multiple cycle effects. The data is shown in Figures 181 through 185 as a function of the  $L_2$  norm. The  $L_2$  norm was found to describe the behavior better than the norm using  $n = 0.19$  defined by Equation (105). The data clearly indicated the softening effect in  $f$  through several cycles. However, it appears that the  $L_2$  norm does not completely separate out the effects of stress level which appear to reflect more crack growth effects in the initial loading. Evidence of this is reflected by the small jumps within each cycle.

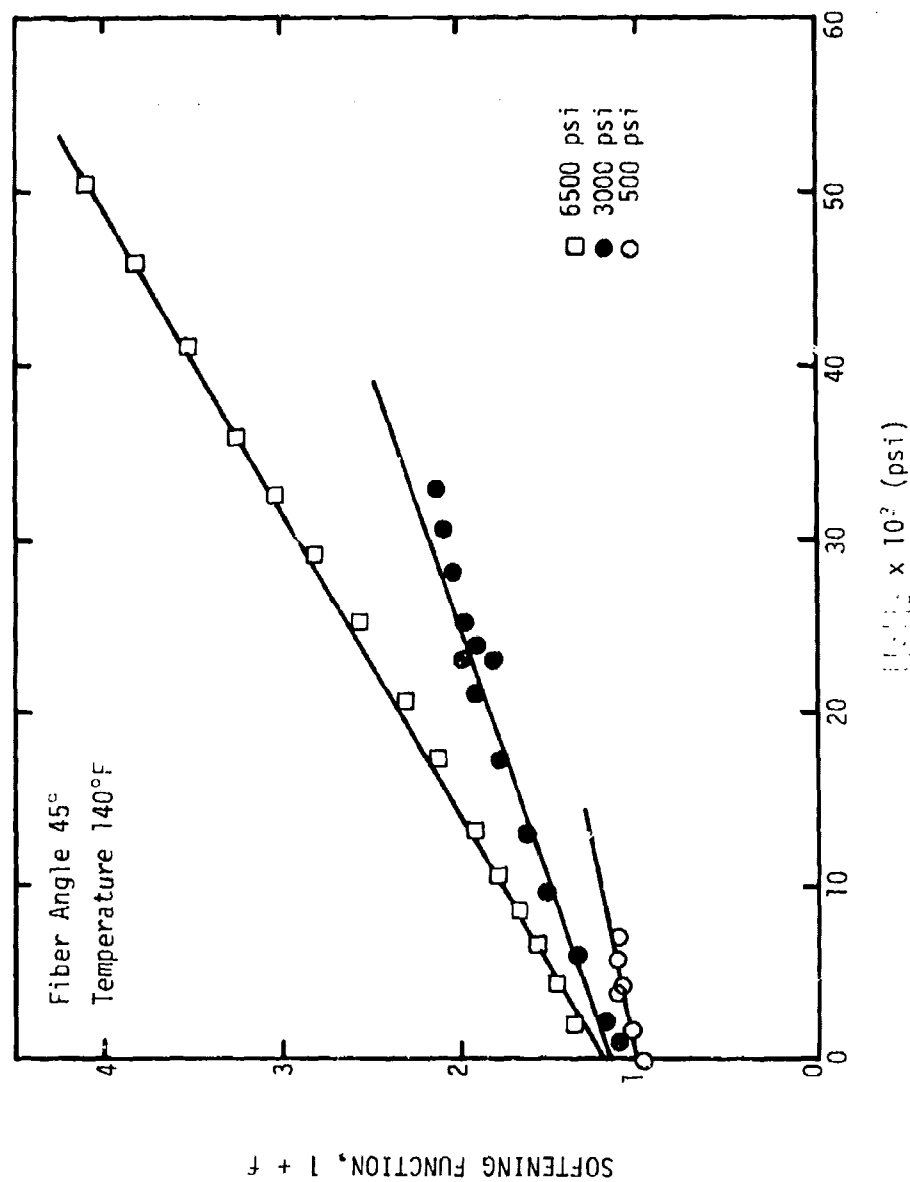
Examination of the curves suggests that they may be approximated by a straight line given by

Figure 181. Softening function,  $1 + f$ , for  $\psi = 20^\circ$  at  $75^\circ\text{F}$ .

Figure 182. Softening function,  $1 + f$ , for  $\theta = 45^\circ$  at  $75^\circ\text{F}$ .

Figure 183. Softening function,  $1 + f$ , for  $\theta = 90^\circ$  at  $75^\circ\text{F}$ .

Figure 184. Softening function,  $1 + f$ , for  $\alpha = 20^\circ$  at  $140^\circ\text{F}$ .

Figure 185. Softening function,  $1 + f$ , for  $\theta = 45^\circ$  at  $140^\circ\text{F}$ .



$$1 + f = A(\sigma) + B(\sigma) \|\sigma\|_2 \quad (163)$$

where  $A(\sigma)$  and  $B(\sigma)$  exhibit stress dependence and  $\|\sigma\|_2$  is the  $L_2$  norm. As a result of the earlier studies we have found that  $A(\sigma)$  and  $B(\sigma)$  depend primarily on the stress normal to the fiber,  $\sigma_n$ . The functions are shown in Figures 186 through 189. The values for  $A(\sigma_n)$  and  $B(\sigma_n)$  are given in Table 18.

Table 18. Softening Parameters for S-901  
Glass/Shell 58-68R Epoxy

Temperature (°F)	$A(\sigma_n)$	$B(\sigma_n)$
75	$1 + 38.5(10^{-6})\sigma_n$	$6.41(10^{-10})\sigma_n$
140	$1 + 288.3(10^{-6})\sigma_n$	$222.0(10^{-10})\sigma_n$

At low stress levels the value of  $f$  approaches unity as predicted by linear viscoelastic theory in the absence of crack growth. The curves also show the strong dependence on temperature.

At 75°F the softening arises mainly from the  $A(\sigma_n)$  contribution. The slope of the curves,  $B(\sigma_n)$ , at 75°F could be considered constant; however, there is not enough data available for various fiber angles and stress levels to assess this assumption. The data at 140°F suggests that the  $B(\sigma_n)$  contribution is considerably more significant.

The softening effect which occurs in the dome region of the

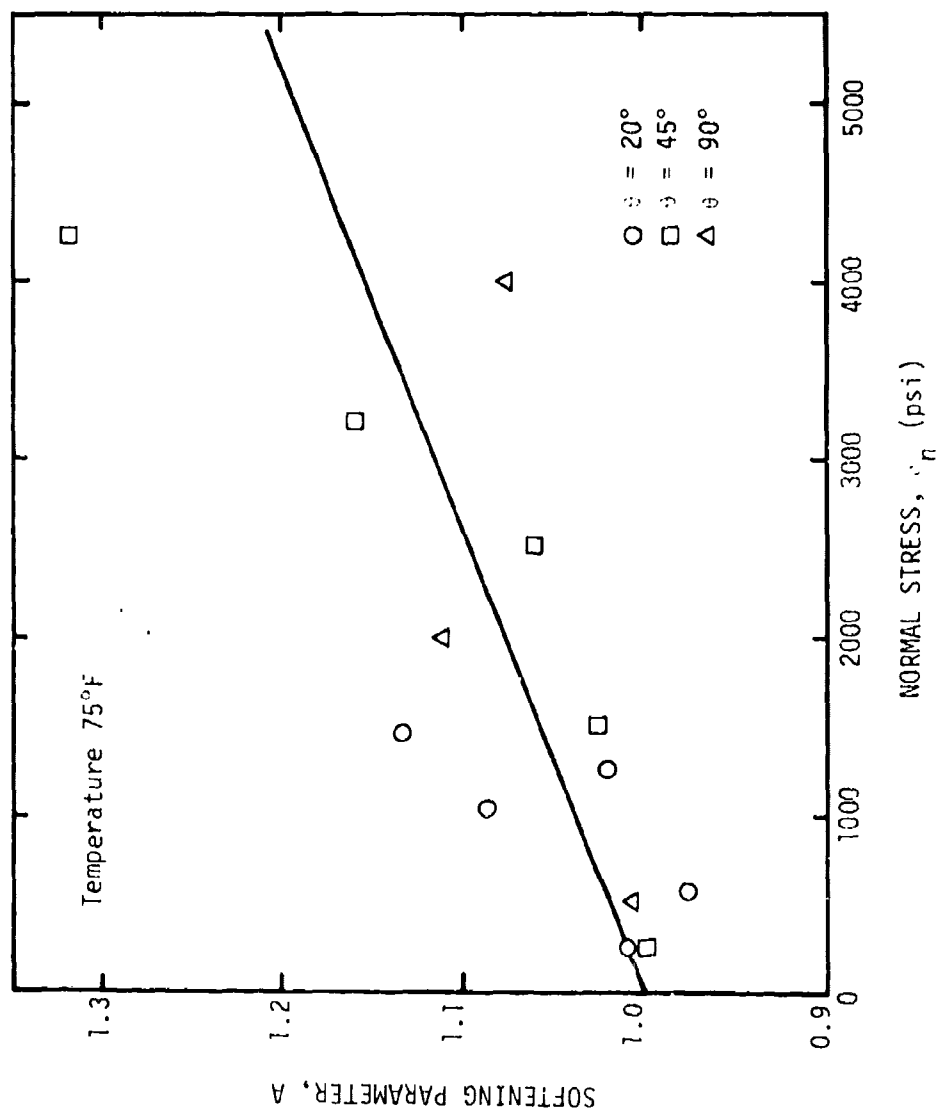


Figure 186. Normal stress dependence of the softening parameter, A, at 75°F.

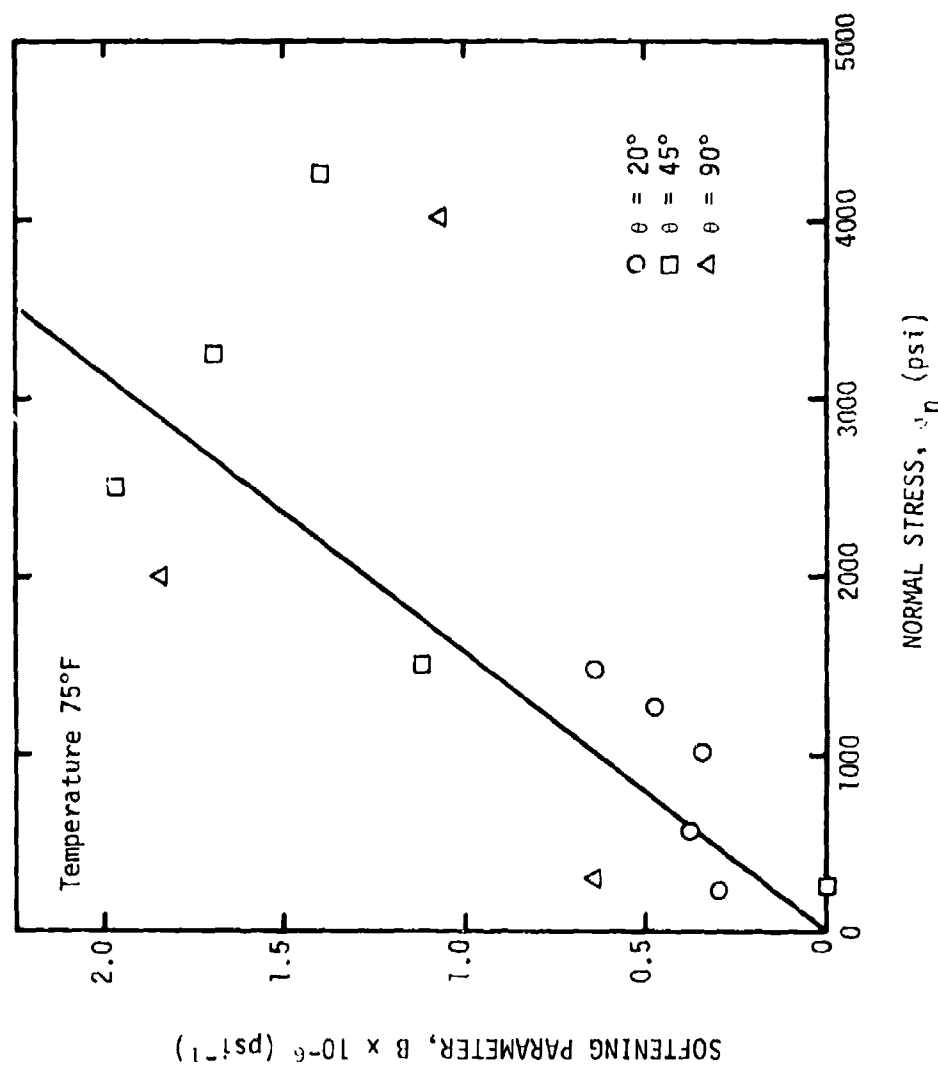


Figure 187. Normal stress dependence of the softening parameter,  $B$ , at 75°F.

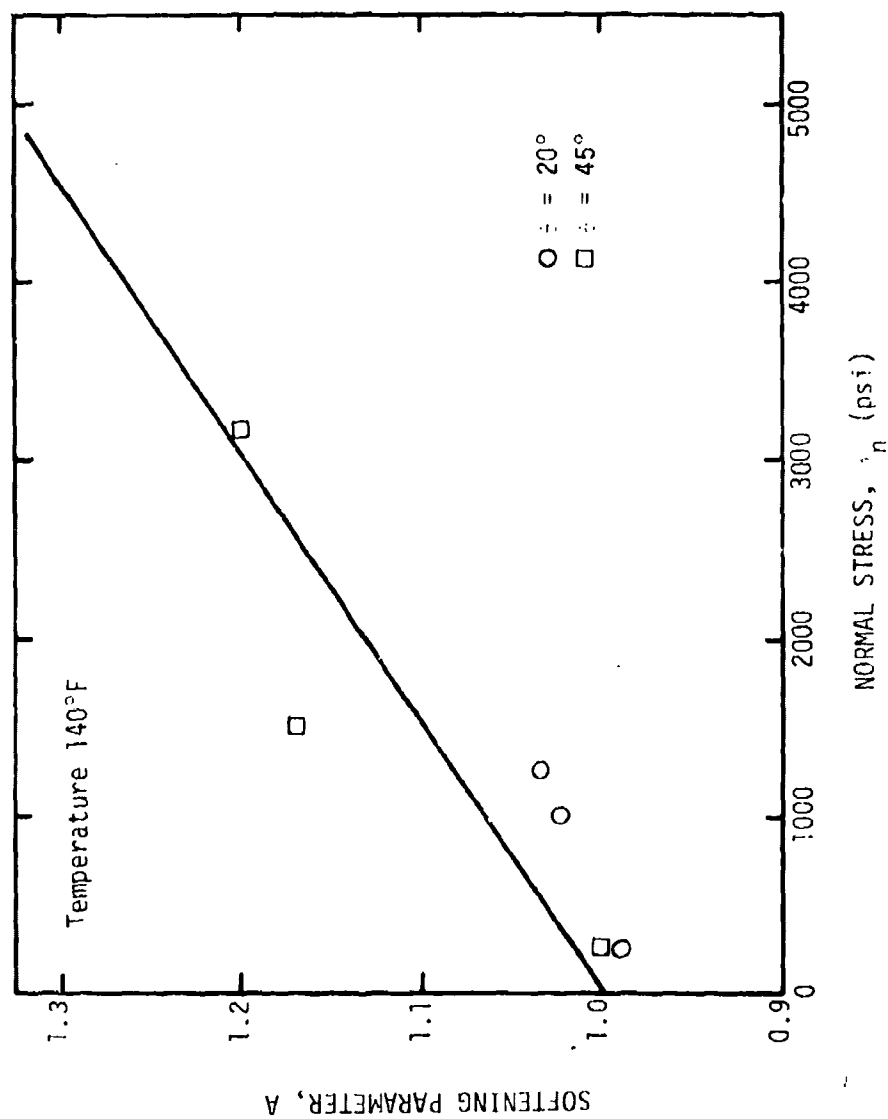


Figure 188. Normal stress dependence of the softening parameter, A, at 140°F.

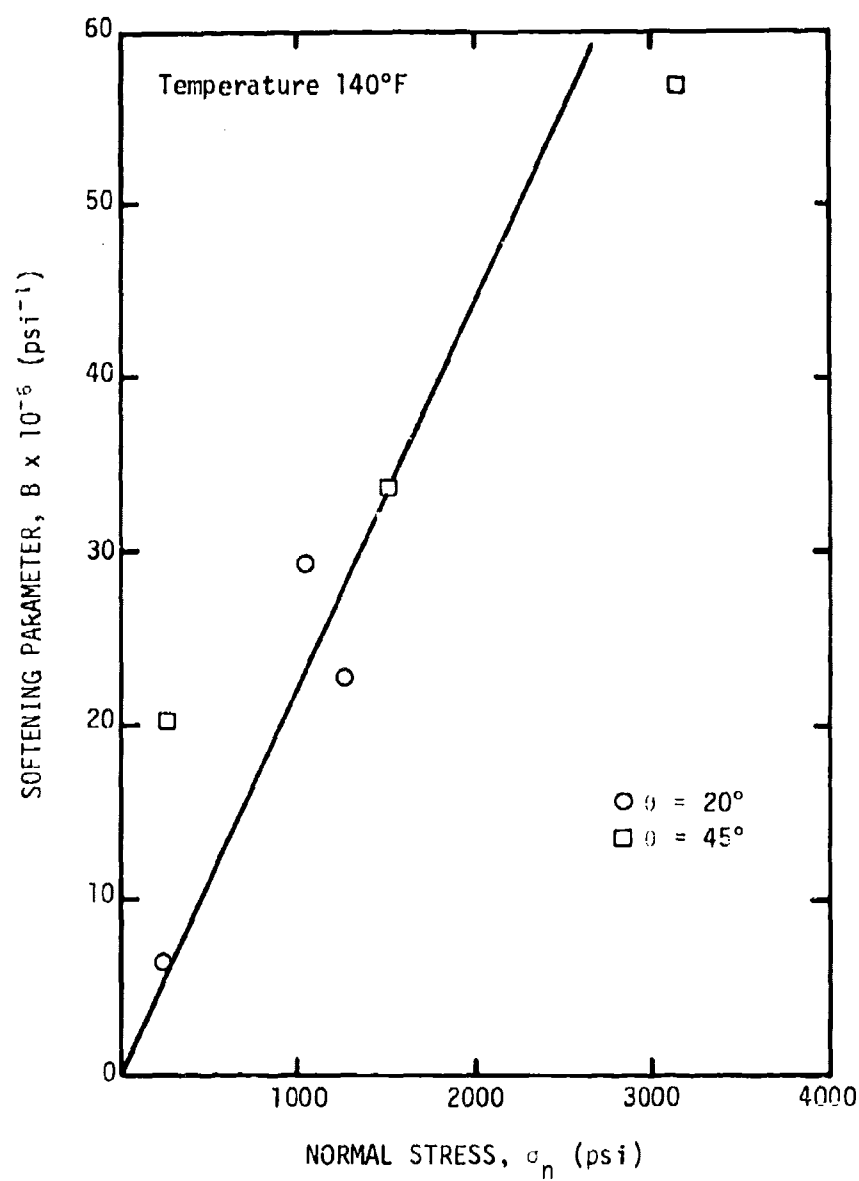


Figure 189. Normal stress dependence of the softening parameter,  $B$ , at 140°F.

motor case, as a result of the stress levels and fiber angles, can be accounted for by using the  $L_2$  norm and the softening parameters given by Table 18 in Equation (163). The effects of multiple cycles such as hydrotesting, motor handling and subsequent firing can be predicted through this procedure. It is interesting to note that the  $L_2$  norm given by

$$||\sigma||_2 = \left[ \int_0^t \sigma^2 dt \right]^{1/2} \quad (164)$$

is actually the root mean square (RMS) value of the stress,  $\sigma$ , times  $t^{1/2}$ . This implies that the motor case analysis can incorporate the use of the local RMS value of the stress, or the normal stress, into existing analyses to determine the amount of softening with each loading cycle. Laboratory data from tensile coupons, such as used here, can be used to determine the functional relationships between the desired  $L_p$  norm and stress.

## SECTION VI

## CONCLUSIONS

The Shell 58-68R epoxy resin was found to exhibit linear viscoelastic behavior for the stress levels studied, which cover the range from 5 to 50% of ultimate. Isothermal data indicated the epoxy to be thermorheologically simple except for temperature dependence of the initial compliance with the creep compliance represented by a power law in time with a constant exponent  $n = 0.19$ .

Evaluation of the S-901 Glass/Shell 58-68R epoxy composite under uniaxial tensile loading showed that the creep compliance could also be represented by a power law in time in the range of linear viscoelastic behavior with the same exponent  $n = 0.19$ . However, the glass/epoxy composite was found to exhibit a strong nonlinearity with both stress and temperature. Temperature dependence analogous to that of the epoxy was found. At the higher temperatures and stress levels, the nonlinearity was attributed primarily to crack growth in addition to the normal reversible nonlinearity. During the first few loading cycles the exponent in the power law representation,  $n$ , was found to be considerably greater than 0.19. The value of the exponent decreased with each subsequent loading cycle. The rate of decrease depended upon the particular stress level as well as the temperature. The nonlinear properties were found to depend primarily on the stress normal to

the fibers rather than the shear stress, which implies agreement with the crack opening mode of growth behavior; for reversible nonlinearity dependence on the octahedral shear stress was found [9].

The time-dependence of the principal creep compliances,  $S_{11}$ ,  $S_{12}$ ,  $S_{22}$  and  $S_{66}$ , was determined from experimental data using fourth-order tensor transformations. Using these tensor relations, the angular dependence of the compliances was also predicted as a function of fiber angle and found to agree with the experimental results for all but the highest temperature of 140°F; at this temperature the disagreement appears to be a result of significant crack growth and possible reversible nonlinearity even at low stress levels.

Crack growth during the first cycle seems to cause a disproportionate amount of damage compared to subsequent cycles. This behavior is reflected in both the unidirectional and laminated composites. However, it appears that there is a difference in the crack growth and arrest in the laminated composites in tension. Both the creep and recovery and constant crosshead rate tests indicate that the angle-ply (10) composites probably further reduce crack growth as a result of the barriers created by the layer interfaces. Consequently, the angle-ply composites were found to be stiffer than their corresponding unidirectional counterparts in tension.



The motor case materials were also found to obey the power law creep compliance with  $n = 0.19$ . They exhibited the same characteristics as the composites fabricated in plate form. Experimental data indicate that the off-angle composites exhibit considerable softening due to crack growth. This behavior will affect the stiffness of the dome regions of the motor case appreciably more than the barrel section.

The "rule of mixtures" and Halpin-Tsai relations, Equations (118) and (120), respectively, were found to describe the principal creep compliances in the linear viscoelastic range reasonably well in the absence of significant crack growth. The adjustment factors were found to be approximately equal with a value of  $\zeta_E = \zeta_G = 3.14$ . Effective epoxy resin compliances predicted by using  $\zeta_E = 2$  and  $\zeta_G = 1$  were found to be considerably lower than the bulk epoxy compliances. Determination of the theoretical upper and lower bounds on compliance suggests that the way in which the fibers are distributed in the cross-section contributes most of the additional stiffness to the Halpin-Tsai model rather than the in-situ matrix as previously suggested by Sims and Halpin [62]. The experimental data fall within the established bounds, except for  $S_{22}$  at  $140^\circ\text{F}$ . Opening mode crack growth at low stresses appears to exist at that temperature.

Bending tests conducted using beams and plates indicate a strong influence of the strain gradient on reducing the softening

of the material. The beam tests show that linear theory agrees very well for laminated composites. The surface cracks are apparently arrested rapidly by the layer interfaces and concurrent movement into a region of lower stress (strain). Nonlinear beam theory, based on the unidirectional data underpredicts the actual stiffness considerably. The bending tests imply that stretching, rather than bending, creates significantly more softening in the composite.

The experimental plate data show good agreement with linear theory for small deflections. A nonlinear theory, developed using the energy method for large deflections, shows that the load-deflection relationship exhibits cubic dependence on the deflection. The experimental results indicate that an instability occurs in the plate twist test at higher loads which agrees qualitatively with Foye's results [196]. Creep and recovery bending tests on the plate in the linear range also follow the power law behavior.

Multiple cycling effects on the glass/epoxy composite showed that the response was independent of earlier lower stresses. Viscoelastic fracture mechanics theory, together with the observed behavior, suggested the use of Lebesgue norms to model multiple cycling effects. The second-order, or  $L_2$  norm, was used to represent the softening effect for various stress levels and numerous loading cycles. Higher order,  $L_{p>2}$  norms, were examined but the best agreement was obtained using the  $L_2$  norm. The softening

effect was found to depend primarily on the stress normal to the fiber. The  $L_2$  norm, which is equal to the root mean square (RMS) of the stress multiplied by the square root of time, may be used to determine the softening at various locations within the motor case. The use of the  $L_2$  norm to model time-dependent crack growth softening during the hydrotesting and subsequent motor case loads is, therefore, proposed.

Finally, it was found that several experimental factors should be considered in terms of refining the determination of the non-linear effects. The errors resulting from gage misalignment, assumed fiber orientation (due to sample fabrication), and general sample-to-sample variability may easily be corrected by normalization. Thus to achieve greater correlation with the data, all specimens should first be tested at a low stress level (without crack growth if possible) in order to determine the linear visco-elastic compliance for the specific specimen. The nonlinearity resulting from stress dependence in the absence of cracks must be determined after crack growth has substantially arrested. Non-linearity due to crack growth can be determined more accurately by subtracting out the effects due to stress dependence on the viscosity. Healing effects were not investigated but previous work [9] showed that they may be significant for long rest periods.

## REFERENCES

1. L. Holliday, Composite Materials, Elsevier Publishing Co. (1966).
2. J. E. Ashton, J. C. Halpin and P. H. Petit, Primer on Composite Materials: Analysis, Technomic Publishing Co., Inc. (1969).
3. G. Lubin, Handbook of Fiberglass and Advanced Plastics Composites, Van Nostrand Reinhold Co. (1969).
4. S. W. Tsai, J. C. Halpin and N. J. Pagano, Composite Materials Workshop, Technomic Publishing Co., Inc. (1968).
5. "Advanced Composites Design Guide," Rockwell International Corp., AFML Contract No. F33615-71-C-1362, January 1973:
  - Vol. I - Design
  - Vol. II - Analysis
  - Vol. III - Manufacturing
  - Vol. IV - Materials
  - Vol. V - Applications
6. S. W. Beckwith, R. A. Schapery and L. D. Webb, "Literature Survey of the Field of Fiber-Reinforced Plastic Composites: Part I (1958 - August 1970)," Texas A & M University, CMR-1, September 1970.
7. S. W. Beckwith, R. A. Schapery and L. D. Webb, "Literature Survey of the Field of Fiber-Reinforced Plastic Composites: Part II (August 1970 - July 1971)," Texas A & M University, CMR-2, August 1971.
8. S. W. Beckwith, "Literature Survey of the Field of Fiber-Reinforced Plastic Composites: Part III (July 1971 - September 1973)," Unpublished Work.
9. Y. C. Lou and R. A. Schapery, "Viscoelastic Characterization of a Nonlinear Fiber-Reinforced Plastic," Journal of Composite Materials, Vol. 5 (1971), p. 208.
10. J. E. Ashton, "Non-Linear Viscoelastic Response of Fibrous Composites," Journal of Composite Materials, Vol. 2 (1968), p. 116.
11. J. C. Halpin, "Introduction to Viscoelasticity," in Composite Materials Workshop, edited by S.W. Tsai, J.C. Halpin and N. J. Pagano, Technomic Publishing Co., Inc. (1968).

12. R. A. Schapery, S. W. Beckwith and N. Conrad, "Studies on the Viscoelastic Behavior of Fiber-Reinforced Plastic," Air Force Materials Laboratory, AFML-TR-73-179, July 1973.
13. A. C. Kneell, "Structural Design and Stress Analysis Program for Advanced Composite Filament-Wound Axisymmetric Pressure Vessels (COMTANK)," Jet Propulsion Laboratory, Technical Report 32-1531, June 1971.
14. W. S. Crownover, "Demonstration of High Strength Fiberglass Reinforced Composite Motor Case Technology," Army Propulsion Laboratory and Center, RK-TR-69-5, April 1969.
15. W. M. Jensen, A. C. Kneell and C. Zweben, "Development of Boron Epoxy Rocket Motor Chambers," Proceedings of 27th Annual Technical Conference, Society of the Plastics Industry, Inc. (1972), p. 17-C-1.
16. J. F. Fulton, "Structural Design and Analysis of Filament-Wound Rocket Motor Cases," Rohm and Haas Company, Technical Report S-267, November 1970.
17. "Stress Report for the Design Submittal of the Improved Stage III Minuteman Motor," Aerojet Solid Propulsion Company, Technical Report MM-101, January 1968.
18. R. A. Schapery, "Viscoelastic Behavior and Analysis of Composite Materials," Texas A & M University, Mech. and Mat. Res. Ctr., Technical Report MM-72-3, August 1972.
19. R. A. Schapery, "A Theory of Crack Growth in Viscoelastic Media," Texas A & M University, Mech. and Mat. Res. Ctr., Technical Report MM-2764-73-1, March 1973.
20. R. J. Farris and R. A. Schapery, "Development of a Solid Rocket Propellant Nonlinear Viscoelastic Constitutive Theory," Air Force Rocket Propulsion Laboratory, AFRPL-TR-73-50, June 1973.
21. A. E. H. Love, A Treatise on the Mathematical Theory of Elasticity, Dover Publications (1963).
22. I. S. Sokolnikoff, Mathematical Theory of Elasticity, 2nd ed., McGraw-Hill (1956).
23. Y. C. Fung, Foundations of Solid Mechanics, Prentice-Hall, Inc. (1965).

24. S. G. Lekhnitskii, Theory of Elasticity of an Anisotropic Body, translated from the Russian by P. Fern, edited by J. Brandstatter, Holden-Day (1963).
25. S. G. Lekhnitskii, Anisotropic Plates, translated from the 2nd Russian Edition by S. W. Tsai and T. Cheron, Gordon and Breach (1968).
26. S. A. Ambartsumyan, Theory of Anisotropic Plates, translated from the 1st Russian Edition by T. Cheron, edited by J. E. Ashton, Technomic Publishing Co., Inc. (1970).
27. J. E. Ashton and J. M. Whitney, Theory of Laminated Plates, Technomic Publishing Co., Inc. (1970).
28. S. B. Dong, R. B. Matthiesen, K. S. Pister and R. L. Taylor, "Analysis of Structural Laminates," University of California, Aeronautical Research Laboratory, ARL-76, September 1961.
29. D. F. Sims, "Viscoelastic Creep and Relaxation Behavior of Laminated Composite Plates," Ph.D. Dissertation, Southern Methodist University (1972).
30. J. E. Fitzgerald and W. L. Hufferd, Handbook for the Engineering Structural Analysis of Solid Propellants, University of Utah, UTEC CE 71-089, May 1971.
31. JANNAF Solid Propellant Structural Integrity Handbook, edited by W. L. Hufferd and J. E. Fitzgerald, University of Utah, UTEC CE 72-160, September 1972.
32. R. A. Schapery, "Stress Analysis of Viscoelastic Composite Materials," Journal of Composite Materials, Vol. 1 (1967), p. 228.
33. J. C. Halpin, "Characterization of Orthotropic (Fiber-Reinforced) Polymeric Solids," Ph.D. Dissertation, The University of Akron (1969).
34. Z. Hashin, "Theory of Fiber Reinforced Materials," University of Pennsylvania, NASA-CR-1974, November 1970.
35. R. A. Schapery, "On the Characterization of Nonlinear Viscoelastic Materials," Polymer Engineering and Science, Vol. 9 (1969).

36. P. M. Ogibalov and I. M. Tiuneeva, "Linearity Range of the Mechanical Properties of Reinforced Plastics," Mekhanika Polimerov, Vol. 5, March 1969, p. 366.
37. P. M. Ogibalov and I. M. Tiuneeva, "On Linearity of the Viscoelastic Properties of the EDF Glass-Plastic (Glass Cloth Impregnated with Epoxide Phenolic Formaldehyde Resins)," translated from Vestn. Mosk. Univ., Ser. 1: Mat. i Mekhan., No. 1 (1968), p. 110.
38. Iu. N. Rabotnov, L. Kh. Papernik and E. I. Stepanychev, "Nonlinear Creep of the Glass Plastic TS8/3-250," Mekhanika Polimerov, Vol. 7, May 1971, p. 391.
39. M. M. Martirosian, "Creep in SVAM Glass Plastics in the Early Post-Production Period," Akademiia Nauk Armianskoi SSR, Izvestiia, Seriia Fiziko-Matematicheskikh Nauk, Vol. 17, No. 5 (1964), p. 51.
40. M. M. Martirosian, "Taking into Account the Effect of the Orientation of a Specimen on the Relation between Creep Stresses and Strains of SVAM Fiber-Glass Reinforced Plastic," Akademiia Nauk Armianskoi SSR, Izvestiia, Seriia Fiziko-Matematicheskikh Nauk, Vol. 18, No. 3 (1965), p. 74.
41. M. M. Martirosian, "Transient Creep of Glass-Reinforced Plastic," Mekhanika Polimerov, Vol. 1, No. 2 (1965), p. 47.
42. M. M. Martirosian, "Effect of Aging on Creep of SVAM Glass-Reinforced Plastic in Tension with Allowance for the Orientation of the Fibers," Mekhanika Polimerov, Vol. 1, No. 6 (1965), p. 20.
43. M. L. Williams, P. J. Blatz and R. A. Schapery, "Fundamental Studies Relating to Systems Analysis of Solid Propellants," California Institute of Technology, GALCIT SM 61-5, February 1961.
44. J. E. Fitzgerald and R. J. Farris "Deficiencies of Viscoelastic Theories as Applied to Solid Propellants," University of Utah, UTEC TH 70-204 (1970).
45. V. Volterra, Theory of Functionals and of Integral and Integro-Differential Equations, Dover Publications, Inc. (1959).
46. A. C. Pipkin, Lectures on Viscoelasticity Theory, Springer-Verlag (1972).

47. M. A. Biot, "Theory of Stress-Strain Relations in Anisotropic Viscoelasticity and Relaxation Phenomena," Journal of Applied Physics, Vol. 25 (1954), p. 1385.
48. R. A. Schapery, "Thermal Expansion Coefficients of Composite Materials Based on Energy Principles," Journal of Composite Materials, Vol. 2, No. 3 (1968), p. 380.
49. L. W. Morland and E. H. Lee, "Stress Analysis for Linear Viscoelastic Materials with Temperature Variation," Trans. Society of Rheology (1960), p. 233.
50. R. A. Schapery, "Application of Thermodynamics to Thermo-mechanical, Fracture and Birefringent Phenomena in Viscoelastic Media," Journal of Applied Physics, Vol. 35 (1964), p. 1451.
51. F. Schwarzl and A. J. Staverman, "Time-Temperature Dependence of Linear Viscoelastic Behavior," Journal Applied Physics, Vol. 23 (1952), p. 838.
52. J. D. Ferry, Viscoelastic Properties of Polymers, 2nd Ed., Wiley (1970).
53. E. Krokosky, "Behavior of Time-Dependent Composite Materials," Modern Composite Materials, edited by L. J. Broutman and R. H. Krock, Addison-Wesley Publishing Co. (1967), p. 120.
54. R. A. Schapery, "Effect of Cyclic Loading on the Temperature in Viscoelastic Media with Variable Properties," AIAA Journal, Vol. 2 (1964), p. 827.
55. F. R. Eirich, Rheology, Vols. 1-3, Academic Press (1956-60).
56. A. E. Moehlenpah, O. Ishai and A. T. DiBenedetto, "The Effect of Time and Temperature on the Mechanical Behavior of a 'Plasticized' Epoxy Resin under Different Loading Modes," Journal of Applied Polymer Science, Vol. 13 (1969), p. 1231.
57. H. Leeming, "Solid Propellant Structural Test Vehicle Program," Lockheed Propulsion Co., AFRPL-TR-72-29, April 1972.
58. R. J. Farris, "Application of Nonlinear Viscoelasticity and Cumulative Damage (A Realistic Evaluation of Real Propellant Behavior)," Aerojet Solid Propulsion Co., NOSC Contract No. N00017-70-C-4441 (1970).



59. T. A. Johnson, C. W. Fowlkes and E. H. Dill, "An Experiment on Creep at Varying Temperature," Proceedings, 5th International Congress on Rheology, Vol. 3 (1970), p. 349.
60. L. A. Watkins, "Creep of an Epoxy Resin under Transient Temperatures," Master's Thesis, Texas A & M University, August 1973.
61. J. Kabelka and J. Vejchar, "Creep in Polyester Resin Laminates at Varying Temperatures," Kunststoff-Ger Plast, Vol. 58 (1968), p. 946.
62. D. F. Sims and J. C. Halpin, "Methods for Determining the Elastic and Viscoelastic Response of Composite Materials," Composite Materials: Testing and Design, 3rd Conference, ASTM STP-546 (1974), p. 43.
63. D. G. Fesko and N. W. Tscheogl, Journal of Polymer Science: Part C, Vol. 35 (1971).
64. A. Tobolsky and H. Eyring, "Mechanical Properties of Polymeric Materials," Journal of Chemical Physics, Vol. 11 (1943), p. 125.
65. A. V. Tobolsky, Properties and Structure of Polymers, John Wiley (1962).
66. T. Kê, "Experimental Evidence of the Viscous Behavior of Grain Boundaries in Metals," Physical Review, Vol. 71 (1947), p. 533.
67. N. G. McCrum and E. L. Morris, "Measurement of the Activation Energies for Creep and Stress Relaxation," Proceedings of Royal Society (London), Vol. A281 (1964), p. 258.
68. J. D. Ferry and E. R. Fitzgerald, "Method of Determining the Dynamic Mechanical Behavior of Gels and Solids at Audio-Frequencies," Journal of Colloid Science, Vol. 8 (1953), p. 224.
69. R. A. Schapery and R. E. Martin, "On the Thermal Diffusivity of Filled Elastomers," Texas A & M University, Mech. and Mat. Res. Ctr., MM-72-2, June 1972.
70. N. G. McCrum and G. A. Pogany, "Time-Temperature Superposition in the  $\alpha$  Region of an Epoxy Resin," Journal of Macromolecular Science and Physics, Vol. B4, March 1970, p. 109.

71. R. A. Schapery, "A Simple Collocation Method for Fitting Viscoelastic Models to Experimental Data," Calif. Inst. Tech., GALCIT SM 61-23A (1961).
72. M. L. Williams, "Structural Analysis of Viscoelastic Materials," AIAA Journal, Vol. 2 (1964), p. 785.
73. D. McCarmond, Transactions of Journal of Plastics Institute, Vol. 35 (1967), p. 409.
74. I. M. Ward, Mechanical Properties of Solid Polymers, Wiley-Interscience (1971).
75. W. N. Findley, American Society of Testing Materials, Symposium on Plastics, (1944), p. 118.
76. R. L. Thorkildsen, "Mechanical Behavior," Engineering Design for Plastics, edited by E. Baer, Reinhold Publishing Corp. (1964), p. 277.
77. A. E. Green and R. S. Rivlin, "The Mechanics of Non-Linear Materials with Memory, Part One," Arch. Rat. Mech. Anal., Vol. 1 (1959), p. 1.
78. R. S. Rivlin, "Non-Linear Viscoelastic Solids," SIAM Review, Vol. 7 (1965), p. 323.
79. B. D. Coleman, "Thermodynamics of Materials with Memory," Arch. Rat. Mech. Anal., Vol. 17 (1965), p. 1.
80. W. Noll, "On the Continuity of Solid and Fluid States," Journal Rat. Mech. Anal., Vol. 4 (1955), p. 3.
81. C. Truesdell, The Elements of Continuum Mechanics, Springer-Verlag, Inc. (1966).
82. C. Truesdell, Continuum Mechanics, Gordon and Breach, Vol. 1 (1966); Vols. 2, 3 and 4 (1965).
83. C. C. Wang, "Stress Relaxation and the Principle of Fading Memory," Arch. Rat. Mech. Anal., Vol. 18 (1965) p. 117.
84. C. C. Wang, "The Principle of Fading Memory," Arch. Rat. Mech. Anal., Vol. 18 (1964), p. 343.
85. A. C. Pipkin, "Small Finite Deformations of Viscoelastic Solids," Rev. Modern Physics, Vol. 36 (1965), p. 1034.

86. A. C. Pipkin and T. G. Rogers, "A Non-Linear Integral Representation for Viscoelastic Behavior," Journal of Mech. Phys. Solids, Vol. 16 (1968), p. 59.
87. L. R. Herrmann, "On a General Theory of Viscoelasticity," Journal of Franklin Inst., Vol. 280 (1965), p. 244.
88. C. W. McGuirt and G. Lianis, "Experimental Investigation of Non-Linear Non-Isothermal Viscoelasticity," Int. J. Eng. Sci., Vol. 7 (1969), p. 579.
89. G. Lianis, "Integral Constitutive Equations on Non-Linear Thermo-Viscoelasticity," Purdue University, Astronautics and Engineering Sciences, Report 65-1 (1965).
90. R. A. Schapery, "Theory of Non-Linear Thermoviscoelasticity Based on Irreversible Thermodynamics," Proceedings 5th Nat. Congress of Applied Mech. (1966), p. 511.
91. R. A. Schapery, "On a Thermodynamic Constitutive Theory and Its Application to Various Nonlinear Materials," Proceedings IUTAM Symposium on Thermoelasticity, Springer-Verlag (1969).
92. N. C. Huang and E. H. Lee, "Nonlinear Viscoelasticity for Short Time Ranges," Journal of Applied Mechanics, Trans. ASME., June 1966, p. 313.
93. R. G. Dong, "Constitutive Equations Involving Chronological Variables," University of Calif. Radiation Lab, Report 12228, December 1964.
94. R. G. Dong, "Studies in Mechanics of Non-Linear Solids," Ph.D Dissertation, University of California (1964).
95. A. V. Tobolsky, "Stress Relaxation Studies on the Viscoelastic Properties of Polymers," Rheology, edited by F. R. Eirich, Academic Press, Inc. (1958), p. 63.
96. T. Alfrey, Mechanical Behavior of High Polymers, Interscience Publishers, Inc. (1948).
97. M. Fréchet, "Sur Les Fonctionnelles Continues," Ann. de L'Ecole Normale Sup., Vol 27 (1910).
98. A. C. Eringen, Mechanics of Continua, John Wiley and Sons, Inc. (1967).

99. A. C. Eringen, Non-Linear Theory of Continuous Media, McGraw-Hill Book Co. (1962).
100. L. E. Malvern, Introduction to the Mechanics of a Continuous Media, Prentice-Hall, Inc. (1969).
101. B. D. Coleman and V. J. Mizel, "On the General Theory of Fading Memory," Arch. Rat. Mech. Anal., Vol. 29 (1968), p. 19.
102. B. D. Coleman and V. J. Mizel, "Norms and Semi-Groups in the Theory of Fading Memory," Arch. Rat. Mech. Anal., Vol. 23 (1966), p. 88.
103. R. J. Rivlin, "Red Herri and Sunday Unidentified Fish in Nonlinear Continuum Mechanics," LeHigh University, Technical Report CAM-100-9, September 1969.
104. N. C. Eringen and R. A. Grot, "Continuum Theory of Nonlinear Viscoelasticity," Mechanics and Chemistry of Solid Propellants, Proceedings 4th Symposium on Naval Structural Mechanics, Pergamon Press (1965).
105. J. G. Oldroyd, "On the Formulation of Rheological Equations of State," Royal Society Proceedings, Vol. 200 (1949).
106. C. C. Hsiao, S. R. Moghe and H. H. R. Von Schmelling, "Time-Dependent Mechanical Strength of Oriented Media," Journal of Applied Physics, Vol. 39 (1968), p. 3857.
107. O. Nakade, "Theory of Nonlinear Responses," J. Physical Soc. of Japan, Vol. 15, No. 12 (1960), p. 2280.
108. J. S. Y. Lai and W. N. Findley, "Prediction of Uniaxial Stress Relaxation from Creep of Nonlinear Viscoelastic Media," Transactions of the Society of Rheology, Vol. 12 (1968), p. 243.
109. J. S. Y. Lai and W. N. Findley, "Stress Relaxations of Nonlinear Viscoelastic Material under Uniaxial Strain," Transactions of the Society of Rheology, Vol. 12 (1968), p. 259.
110. W. N. Findley and K. Onaran, "Product Form of Kernel Functions for Nonlinear Viscoelasticity of PVC under Constant Stresses," Transactions of the Society of Rheology, Vol. 12 (1968), p. 217.

111. K. Onaran and W. N. Findley, "Combined Stress-Creep Experiments on a Non-Linear Viscoelastic Material to Determine the Kernel Functions for a Multiple Integral Representation of Creep," Transactions of the Society of Rheology, Vol. 1 (1965), p. 299.
112. W. N. Findley and J. S. Y. Lai, "A Modified Superposition Principle Applied to Creep of Nonlinear Viscoelastic Material under Abrupt Changes in State of Combined Stress," Transactions of the Society of Rheology, Vol. 11 (1967), p. 361.
113. J. S. Y. Lai and W. N. Findley, "Behavior of Nonlinear Viscoelastic Material under Simultaneous Stress Relaxation and Creep in Torsion," Brown University, Technical Report No. 3, January 1968.
114. W. G. Gottenberg, J. O. Bird and G. L. Agrawal, "An Experimental Study of Nonlinear Viscoelastic Solid in Uniaxial Tension," Journal Applied Mechanics, Transactions of ASME, Vol. 1 (1969).
115. F. J. Lockett and R. O. Stafford, "On Special Constitutive Relations in Non-Linear Viscoelasticity," Inter. J. Eng. Sci., Vol. 7 (1969), p. 917.
116. F. J. Lockett, "Nonlinear Viscoelasticity of Almost-Elastic Materials," Stanford University, Dept. of Applied Mechanics, Technical Report No. 195 (1969).
117. K. C. Valanis and R. F. Landel, "Large Multiaxial Deformation Behavior of a Filled Rubber," Transactions of the Society of Rheology, Vol. 11 (1967), p. 243.
118. T. Nicholas and A. M. Freudenthal, "The Mechanical Behavior of a Filled Elastomer at High Strain Rates," Transactions of the Society of Rheology, Vol. 13 (1969), p. 323.
119. I. M. Ward and E. T. Onat, "The Nonlinear Mechanical Behavior of Oriented Polypropylene," Journal of Mech. Phys. Solids, Vol. 11 (1963), p. 217.
120. I. M. Ward and J. M. Wolfe, "The Nonlinear Behavior of Polypropylene Fibres under Complex Loading Programs," Journal Mech. Phys. Solids, Vol. 14 (1966), p. 131.

121. D. W. Hadley and I. M. Ward, "Nonlinear Creep and Recovery Behavior of Polypropylene Fibres," Journal of Mech. Phys. Solids, Vol. 13 (1965), p. 397.
122. C. A. Berg, "A Unified Derivation of Constitutive Relations for Irrecoverable Deformations," Transactions of the Society of Rheology, Vol. 9 (1965), p. 159.
123. J. M. Kelly, "Generalization of Some Elastic-Viscoplastic Stress-Strain Relations," Transactions of the Society of Rheology, Vol. 11 (1967), p. 55.
124. V. V. Nais and J. L. Sachin, "An Experimental Study of a Nonlinear Material with Memory," Transactions of the Society of Rheology, Vol. 11 (1967), p. 307.
125. R. I. Tanner, "Comparative Studies of Some Simple Viscoelastic Theories," Transactions of the Society of Rheology, Vol. 12 (1968), p. 155.
126. H. B. Bird and B. D. Marsh, "Viscoelastic Hysteresis Part I, Model Prediction; Part II, Numerical and Experimental Examples," Transactions of the Society of Rheology, Vol. 12 (1968), p. 489.
127. J. B. Adeyeri, R. J. Krizek and J. D. Achenbach, "Multiple Integral Description of the Nonlinear Viscoelastic Behavior of a Clay Soil," Transactions of the Society of Rheology, Vol. 14 (1970), p. 375.
128. R. J. Farris, "Homogeneous Constitutive Equations for Materials with Permanent Memory," Ph.D. Dissertation, University of Utah (1970).
129. R. J. Farris, "Applications of Viscoelasticity to Filled Materials," Master's Thesis, University of Utah (1969).
130. A. E. Green, R. S. Rivlin and A. J. M. Spencer, "The Mechanics of Non-Linear Materials with Memory, Part Two," Arch. Rat. Mech. Anal., Vol. 3 (1959), p. 82.
131. H. Leaderman, F. McCrackin and O. Nakada, "Large Longitudinal Retarded Elastic Deformation of Rubberlike Network Polymers. II. Application of a General Formulation of Nonlinear Response," Transactions of the Society of Rheology, Vol 7 (1963), p. 111.

132. K. G. Nolte and W. N. Findley, "A Linear Compressibility Assumption for the Multiple Integral Representation of Nonlinear Creep of Polyurethane," Journal of Applied Mechanics (1970), p. 92.
133. J. Smart and J. G. Williams, "A Power-Law Model for the Multiple-Integral Theory of Non-Linear Viscoelasticity," Journal of Mech. Phys. Solids, Vol. 20 (1972), p. 325.
134. H. Leaderman, Elastic and Creep Properties of Filamentous Materials and Other High Polymers, The Textile Foundation (1943).
135. R. A. Schapery, "Further Development of a Thermodynamic Constitutive Theory: Stress Formulation," Purdue University, School of Aero. Astro. Eng. Sci., AA & ES 69-2 (1969).
136. S. Timoshenko and J. N. Goodier, Theory of Elasticity, McGraw-Hill Book Co., Inc. (1951).
137. Z. Hashin, "Viscoelastic Fiber Reinforced Materials," AIAA Journal, Vol. 4 (1966) p. 1411.
138. M. P. Hanson, "Effect of Temperature on Tensile and Creep Characteristics of PRD49 Fiber/Epoxy Composites," National Aeronautics and Space Administration, NASA D-7120, November 1972.
139. T. R. Bott and A. J. Barker, "Creep in Glass Fiber Reinforced Plastics," Industrial and Engineering Chemistry Journal, Vol. 59, July 1967, p. 46.
140. J. DeMonte, "Creep Characteristics of Laminated Epoxy Plastics," Plastics Technology, October 1958, p. 913.
141. V. Zvonar and J. Tamchyna, "Elastic and Viscoelastic Behavior of Glass-Reinforced Plastics," Journal of Polymer Science: Part C, Vol. 16 (1967), p. 1969.
142. V. P. Antans and A. M. Skudra, "Creep of Reinforced Plastics in Uniaxial Tension along the Fibers," Polymer Mechanics (1965), p. 41.
143. A. M. Skudra and V. P. Antans, "Some Problems in the Thermorheology of Reinforced Polymers," Polymer Mechanics (1966), p. 59.

144. F. Ya. Bulavs and A. M. Skudra, "Rheology of a Viscoelastic Body under Constant Load and Prestressed with Viscoelastic Reinforcing," Polymer Mechanics (1965), p. 40.
145. N. T. Smotrin and V. M. Chebanov, "Creep of SVAM (5:1)-B in Different Directions in the Plane of the Sheet at Low Stresses," Polymer Mechanics (1967), p. 21.
146. A. L. Rabinovich, Introduction to the Mechanics of Reinforced Polymers, Academy of Sciences USSR, Lenin Institute of Chemical Physics, Nauka Press (1970).
147. Yu. M. Tarnopol'skiy and A. M. Skudra, Construction Strength and Deformation Properties of Fiber Glass Reinforced Plastics, Zinatne Publishing House (1966).
148. G. I. Bryzgalin, "Anisotropic Creep of Glass Plastics," PMTF-Zhurnal Prikladnoi Mekhaniki i Tekhnicheskoi Fiziki, November 1963, p. 177.
149. G. I. Bryzgalin, "Calculation of Creep of Glass Plastic Plates," Journal of Appl. Mech. and Tech. Phys., Vol. 4, April 1967, p. 201.
150. A. Kaye and D.W. Saunders, "Creep in an Anisotropic Medium," Brit. J. Appl. Phys., Vol. 15 (1964), p. 1103.
151. L. C. Cessna, Jr., "Stress-Time Superposition of Creep Data for Polypropylene and Coupled Glass-Reinforced Polypropylene," Polymer Engineering and Science, Vol. 11, No. 3 (1971), p. 211.
152. W. N. Findley, C. H. Adams and W. J. Worley, "The Effect of Temperature on the Creep of Two Laminated Plastics as Interpreted by the Hyperbolic-sine Law and Activation Energy Theory," Proceedings, ASTM, Vol. 48 (1948), p. 1217.
153. W. J. Worley and W. N. Findley, "The Effect of Temperature on the Creep and Recovery of a Melamine-Glass Fabric Laminate," Proceedings, ASTM, Vol. 50 (1950), p. 1399.
154. H. Eyring, "Viscosity, Plasticity and Diffusion as Examples of Absolute Reaction Rates," Journal of Chemical Physics, Vol. 4 (1936), p. 283.
155. E. J. McQuillan, "Viscoelastic Creep and Relaxation in Laminated Composites," Naval Air Development Center, NADC-AM-7115, June 1971.



156. E. H. Lee, "Stress Analysis in Viscoelastic Bodies," Quart. Appl. Math., Vol. 13 (1955), p. 183.
157. M. A. Biot, "Dynamics of Viscoelastic Anisotropic Media," Proceedings of the 4th Mid-Western Conference on Solid Mechanics (1955), p. 94.
158. R. A. Schapery, "Approximate Methods of Transform Inversion for Viscoelastic Stress Analysis," Proceedings of the 4th U.S. National Congress of Applied Mechanics, ASME (1962), p. 1075.
159. R. A. Schapery, "A Method of Viscoelastic Stress Analysis Using Elastic Solutions," Journal of the Franklin Institute, Vol. 279 (1965), p. 268.
160. R. M. Hackett, "Viscoelastic Stresses in a Composite System," Polymer Engineering and Science, Vol. 11, No. 3 (1971), p. 220.
161. R. J. Farris, "Dilatation of Granular Filled Elastomers under High Rates of Strain," Journal of Applied Polymer Science, Vol. 8 (1964), p. 25.
162. R. J. Farris, "The Character of the Stress-Strain Function for Solid Propellants," Transactions of the Society of Rheology, Vol. 12 (1968), p. 308.
163. S. W. Beckwith, Unpublished Research.
164. Y. C. Lou and R. A. Schapery, "Viscoelastic Behavior of a Nonlinear, Fiber-Reinforced Plastic," Air Force Materials Laboratory, AFML-TR-70-113, May 1970.
165. R. J. Farris, "The Stress-Strain Behavior of Mechanically Degradable Polymers," Polymer Networks: Structural and Mechanical Properties, edited by A. J. Chompff and S. Newman, Plenum (1971).
166. R. J. Farris, "The Influence of Vacuole Formation on the Response and Failure of Filled Elastomers," Rheology, Vol. 12 (1968), p. 315.
167. A. Y. C. Lou, "Viscoelastic Characterization of a Nonlinear, Fibrous Composite Material," Ph.D. Dissertation, Purdue University (1969).

168. L. B. Greszczuk, "New Test Technique for Shear Modulus and Other Elastic Constants of Filamentary Composites," ASTM, Testing Techniques for Filament Reinforced Plastics, AFML-TR-66-274, September 1966.
169. C. C. Chamis and G. P. Sendekyj, "Critique on Theories Predicting Thermoelastic Properties of Fibrous Composites," Journal of Composite Materials, Vol. 2, No. 3 (1968), p. 332.
170. N. J. Pagano and S. W. Tsai, "A Review of Research in Micromechanics of Composite Media," Air Force Materials Laboratory, AFML-TR-67-348, March 1968.
171. J. C. Halpin, "Effects of Environmental Factors on Composite Materials," Air Force Materials Laboratory, AFML-TR-67-423, June 1969.
172. S. W. Tsai, "Structural Behavior of Composite Materials," Philco Corp., NASA-CR-71, July 1964, p. 27.
173. R. Hill, "Elastic Properties of Reinforced Solids: Some Theoretical Principles," Journal of Mech. Phys. Solids, Vol. 11 (1963), p. 357.
174. R. Hill, "Theory of Mechanical Properties of Fibre-Strengthened Materials: I. Elastic Behaviour," Journal of Mech. Phys. Solids, Vol. 12 (1964), p. 199.
175. R. Hill, "Theory of Mechanical Properties of Fibre-Strengthened Materials: II. Inelastic Behaviour," Journal of Mech. Phys. Solids, Vol. 12 (1964), p. 213.
176. B. Paul, "Prediction of Elastic Constants of Multiphase Materials," Transactions of the Metal. Soc. of AIME, Vol. 218, February 1960, p. 36.
177. J. J. Hermans, "The Elastic Properties of Fiber Reinforced Materials When the Fibers Are Aligned," Proceedings, Konigl. Hederl. Akad. van Wetenschappen Amsterdam, Vol. B70, No. 1 (1967), p. 1.
178. E. H. Kerner, "The Electrical Conductivity of Composite Media," Proceedings, Phys. Soc., Vol. B69 (1956), p. 802.
179. L. M. Soffer and R. Molho, "Cryogenic Resins for Glass Filament-Wound Composites," Aerojet-General Corp., NASA CR-72114, January 1967.

180. A. Feldman and J.J. Damico, "Graphite Filament-Wound Pressure Vessels," Martin Marietta Corp., NASA CR-120951, November 1972.
181. Structural Composites Industries, Private Communication (1972).
182. "Standard Methods of Test for Flexural Properties of Plastics," ASTM Test Method D790-71, American Society for Testing and Materials.
183. S. Timoshenko and S. Woinowsky-Krieger, Theory of Plates and Shells, McGraw-Hill (1959).
184. J. M. Whitney, "Application of the Plate Twist Test to Laminated Composites," Air Force Materials Laboratory, AFML-TR-67-407, March 1968.
185. N. J. Pagano and J. C. Halpin, "Influence of End Constraint in the Testing of Anisotropic Bodies," Journal of Composite Materials, Vol. 2 (1968), p. 18.
186. Y. C. Lou and R. A. Schapery, "Viscoelastic Behavior of Fiber-Reinforced Composite Materials," Air Force Materials Laboratory, AFML-TR-68-90, Part I, April 1968.
187. W. T. Freeman and M. D. Campbell, "Thermal Expansion Characteristics of Graphite Reinforced Composite Materials," Composite Materials: Testing and Design, 2nd Conference, ASTM STP 497 (1972), p. 121.
188. "Plastics for Flight Vehicles - Part I: Reinforced Plastics," MIL-HDBK-17, February 1971.
189. Z. Hashin and B. W. Rosen, "The Elastic Moduli of Fiber Reinforced Materials," Journal of Applied Mechanics, Vol. 31 (1964), p. 223.
190. R. A. Schapery, "Application of Viscoelastic Fracture Mechanics to Nonlinear Behavior and Fracture of Solid Propellants," Texas A&M University, Mech. and Mat. Res. Ctr., Technical Report MM-2995-74-5, July 1974.
191. R. F. S. Hearmon and E. H. Adams, "The Bending and Twisting of Anisotropic Plates," British Journal of Applied Physics, Vol. 3 (1952), p. 150.

192. R. K. Witt, W. H. Hoppmann and R. S. Buxbaum, "Determination of Elastic Constants of Orthotropic Materials with Special Reference to Laminates," ASTM Bulletin, No. 194 (1953), p. 53.
193. S. W. Tsai, "Experimental Determination of the Elastic Behavior of Orthotropic Plates," Journal of Engineering for Industry, Vol. 83B (1965), p. 315.
194. G. I. Bryzgalin, "Creep Tests on Glass-Reinforced Plastic Plates," Journal of Applied Mechanics and Technical Physics, Vol. 1 (1965), p. 136.
195. J. M. Hennessey, J. M. Whitney and M. B. Riley, "Experimental Methods for Determining Shear Modulus of Fiber Reinforced Composite Materials," Air Force Materials Laboratory, AFML-TR-65-42, September 1965.
196. R. L. Foye, "Deflection Limits on the Plate-Twisting Test," Journal of Composite Materials, Vol. 1 (1967), p. 194.
197. R. A. Rawe, "Craze Cracking in Glass Filament-Wound Pressure Chambers," Symposium on Standards for Filament-Wound Reinforced Plastics, ASTM STP-327 (1963), p. 248.
198. M. B. Desai and F. J. McGarry, "Failure Mechanisms in Glass Fiber-Reinforced Plastics," ASTM Bulletin, No. 239 (1959), p. 76.
199. R. A. Schapery, Texas A & M University, Private Communication (1974).

## APPENDIX

## APPENDIX

## Analysis of Plate Twist Test

In this Appendix the energy method is used to obtain a large deflection solution for the plate twist test [191-193] for the case of an isotropic material. The analysis is then corrected for the experimental application of loads at points removed from the corners of the plate. Finally, extension of the approach to include orthotropic materials is indicated.

Consider a square plate with the coordinate system  $(x, y)$  as shown in Figure A-1 where  $a$  is one-half the length of the diagonal. A pure twisting moment is imposed on the plate by loading all four corners with equal forces. The forces are perpendicular to the plate with those forces at the first and third (diagonal) corners being downward and the other two forces upward. The corner loads cause the square plate to assume a hyperbolic paraboloid of saddle-shaped surface [183, 184].

Displacement functions are assumed to take the form

$$w = \frac{w_0}{a^2} (x^2 - y^2) \quad (A-1a)$$

$$u = Ay^2x + Cx \quad (A-1b)$$

$$v = -Ax^2y + Cy \quad (A-1c)$$

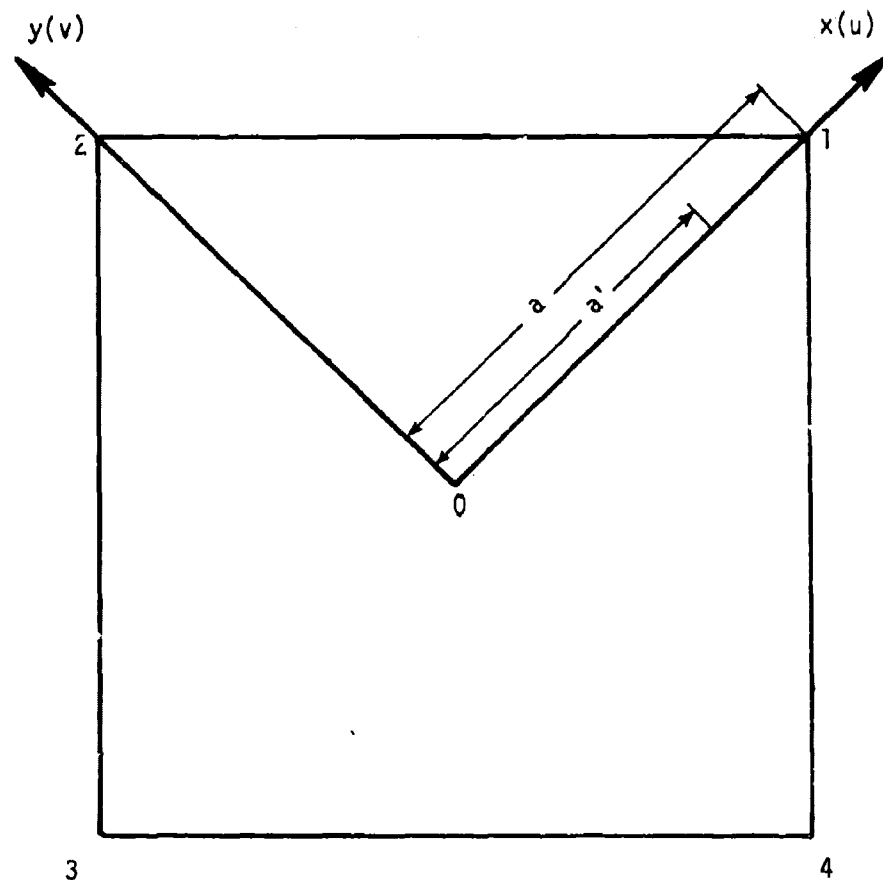


Figure A-1. Plate notation for plate twist test.

The deflection,  $w$ , follows the form for linear theory given by Timoshenko and Woinowsky-Krieger [183] and reduces to the tip deflection,  $w_0$ , when  $x = \pm a$  or  $y = \pm a$ . The displacements  $u$  and  $v$  are even functions of  $y$  and  $x$ , respectively, as a result of symmetry. The coefficients  $A$  and  $C$  will be found by minimizing the potential energy [183].

The equilibrium equation for small deflections is given by [183]

$$\frac{\partial^4 w}{\partial x^4} + 2 \frac{\partial^4 w}{\partial x^2 \partial y^2} + \frac{\partial^4 w}{\partial y^4} = 0. \quad (A-2)$$

The assumed displacement functions automatically satisfy equilibrium for small deflections. For large deflections, in-plane forces  $N_x$ ,  $N_y$  and  $N_{xy}$  are developed which, if exact, will satisfy the following equilibrium equations,

$$\frac{\partial N_x}{\partial x} + \frac{\partial N_{xy}}{\partial y} = 0 \quad (A-3a)$$

$$\frac{\partial N_{xy}}{\partial x} + \frac{\partial N_y}{\partial y} = 0. \quad (A-3b)$$

The strain-displacement relationships for large deflections must include the strain in the middle surface of the plate during bending. The strain components are



$$\epsilon_x = \frac{\partial u}{\partial x} + \frac{1}{2} \left( \frac{\partial w}{\partial x} \right)^2 \quad (\text{A-4a})$$

$$\epsilon_y = \frac{\partial v}{\partial y} + \frac{1}{2} \left( \frac{\partial w}{\partial y} \right)^2 \quad (\text{A-4b})$$

$$\gamma_{xy} = \frac{\partial u}{\partial y} + \frac{\partial v}{\partial x} + \frac{\partial w}{\partial x} \frac{\partial w}{\partial y} \quad (\text{A-4c})$$

For an isotropic material the constitutive equation is given by

$$\epsilon_x = \frac{1}{hE} (N_x - \nu N_y) \quad (\text{A-5a})$$

$$\epsilon_y = \frac{1}{hE} (N_y - \nu N_x) \quad (\text{A-5b})$$

$$\gamma_{xy} = \frac{1}{hG} N_{xy} \quad (\text{A-5c})$$

where  $h$  is the plate thickness,  $E$  is the elastic modulus and  $\nu$  is Poisson's ratio.

The strain energy arises from the pure bending contribution and the additional energy which results from the stretching of the middle surface. The bending strain energy is given by

$$V_B = \frac{D}{2} \int_A \left\{ \left( \frac{\partial^2 w}{\partial x^2} + \frac{\partial^2 w}{\partial y^2} \right)^2 - 2(1-\nu) \left[ \frac{\partial^2 w}{\partial x^2} \frac{\partial^2 w}{\partial y^2} - \left( \frac{\partial^2 w}{\partial x \partial y} \right)^2 \right] \right\} dA \quad (\text{A-6})$$

where  $D$  is the flexural rigidity given by

$$D \equiv \frac{Eh^3}{12(1-\nu^2)} \quad (\text{A-7})$$

The strain energy due to stretching is given by the expression

$$V_S = \frac{Eh}{2(1-\nu^2)} \int_A \left[ \epsilon_x^2 + \epsilon_y^2 + 2\nu\epsilon_x\epsilon_y + \frac{1}{2}(1-\nu)\gamma_{xy}^2 \right] dA. \quad (A-8)$$

The total strain energy is the sum of  $V_B$  and  $V_S$ . The area integration may be performed over one quadrant to obtain the strain energy in terms of the three unknown parameters,  $w_0$ ,  $A$  and  $C$ , by applying Equations (A-1), (A-4), (A-6) and (A-8). The total potential energy of the system is

$$U = V_B + V_S - Pw_0 \quad (A-9)$$

where the last term represents the potential energy due to the applied load acting at the corner with the tip deflection  $w_0$ . The coefficients may now be determined by minimizing the total energy with respect to the coefficients

$$\frac{\partial U}{\partial A} = 0 \quad (A-10a)$$

$$\frac{\partial U}{\partial C} = 0 \quad (A-10b)$$

$$\frac{\partial U}{\partial w_0} = 0. \quad (A-10c)$$

The coefficients  $A$  and  $C$  are found to be

$$A = \frac{2w_0^2}{a^4} \left[ \frac{7 - 11\nu}{15 - 11\nu} \right] \quad (A-11)$$

$$C = - \frac{22w_0^2}{3a^2} \left[ \frac{1 - \nu}{15 - 11\nu} \right]. \quad (A-12)$$

Equation (A-10c) yields the load-deflection relationship after some rearrangement

$$P = \left[ \frac{Eh^3}{3a^2(1+\nu)} \right] w_0 + \left[ \frac{4Eh(43+33\nu)}{45a^2(1+\nu)(15-11\nu)} \right] w_0^3. \quad (A-13)$$

The first term represents the linear contribution while the second term, cubic in  $w_0$ , is the membrane or stretching contribution.

Recall that Equation (A-13) gives the corner load and tip deflection ( $w_0$ ) when the plate is loaded at the corner. Using Equation (A-1a) we can write the deflection  $w'$  at a distance  $a'$  along the diagonal as

$$w' = \left( \frac{a'}{a} \right)^2 w_0. \quad (A-14)$$

Now let us examine the last term in Equation (A-9) more closely. We may rewrite this term using Equation (A-14) to obtain

$$Pw_0 = P \left( \frac{a}{a'} \right)^2 w' \quad (A-15)$$

which gives the same energy contribution if the load acting at  $a'$  were given by

$$P' = P \left( \frac{a}{a'} \right)^2. \quad (A-16)$$

Consequently, Equation (A-14) may be rewritten in terms of the experimental load,  $P'$ , and corresponding deflection,  $w'$ , acting at point  $a'$  on the plate's diagonal,

$$P' = \frac{P}{\lambda} = \left[ \frac{Eh^3}{3a^2(1+\nu)} \right] w' \lambda + \left[ \frac{4Eh(43+33\nu)}{45a^2(1+\nu)(15-11\nu)} \right] (w' \lambda)^3 \quad (A-17)$$

where

$$\lambda \equiv \left( \frac{a}{a'} \right)^2. \quad (A-18)$$

Following this technique we can approximate the load  $P'$  and corresponding deflection  $w_0'$  without having to assume a more complicated set of displacement functions to account for the contribution of the region past the loads.

Note that the procedure for transferring the point of load application is completely independent of the type of material, differing only in the coefficients in the load-deflection terms. Consequently, we can apply the procedure equally as well to anisotropic materials.

## VITA

Scott Williams Beckwith, the son of John Williams and Alba Coffrini Beckwith, was born in New York, New York on February 1, 1942. He is married to Mary Louise Beckwith and has two children, Mary Christina and Michael Williams Beckwith. He graduated from Texas A&M University in May 1964 with a B. S. degree in Aerospace Engineering and from the California Institute of Technology in June 1965 with a M. S. degree in Aeronautics.

After receiving a commission as an officer in the United States Air Force, he served at the Air Force Rocket Propulsion Laboratory, Edwards, California during the period from October 1965 through August 1969. While there he conducted research in the area of solid propellant characterization, analysis and fracture behavior. In September 1969, he began working on a Ph.D degree at Texas A&M University where he was employed as an Engineering Research Associate with the Texas Transportation Institute and the Mechanics and Materials Research Center. He also held an appointment as an instructor within the Civil Engineering Department.

He is currently employed as a Technical Specialist with Hercules Incorporated, Magna, Utah.

Permanent address: Hercules Incorporated  
Bacchus Works  
P. O. Box 98  
Magna, Utah 84044

This dissertation was typed by Mrs. Mary Lou Beckwith.